NASA
TT
F-511
c.1

K. Ya. Kondrat'ev, E. P. Borisenkov and A. A. Moroz

LOAN COPY:
AFWL (
KIRTLAND AF

INTERPRETATION OF OBSERVATION DATA FROM METEOROLOGICAL SATELLITES

TECH LIBRARY KAFB, NM
0068981

Translated from Russian

Published for the National Aeronautics and Space Administration and the National Science Foundation, Washington, D.C. by the Israel Program for Scientific Translations

TECH LIBRARY KAFB, NM
0068981

K.Ya. Kondrat'ev, E.P. Borisenkov
and A.A. Morozkin

INTERPRETATION OF OBSERVATION DATA FROM METEOROLOGICAL SATELLITES

(Prakticheskoe ispol'zovanie dannykh meteorologicheskikh sputnikov)

Gidrometeorologicheskoe Izdatel'stvo
Leningrad 1966

Translated from Russian

Israel Program for Scientific Translations
Jerusalem 1970

NASA TT F-511
TT 68-50310

Published Pursuant to an Agreement with
THE NATIONAL AERONAUTICS AND SPACE ADMINISTRATION
and
THE NATIONAL SCIENCE FOUNDATION, WASHINGTON, D.C.

Copyright © 1970
Israel Program for Scientific Translations Ltd.
IPST Cat. No. 5143

Translated by A. Wald and M. Levi
Edited by P. Greenberg

Printed in Jerusalem by Keter Press
Binding: Wiener Bindery Ltd., Jerusalem

Available from the
U.S. DEPARTMENT OF COMMERCE
Clearinghouse for Federal Scientific and Technical Information
Springfield, Va. 22151

V/16/3

TABLE OF CONTENTS

	Page
LIST OF ABBREVIATIONS	v
FOREWORD	1
INTRODUCTION	3
Chapter 1. THE POTENTIALITIES OF SATELLITE-BORNE EQUIPMENT FOR METEOROLOGICAL RESEARCH	5
1.1. The Main Problems	5
1.2. Selection of Orbits	7
1.3. The U.S. Program for Meteorological Satellites	9
1.4. Meteorological Satellites and their Equipment	11
1.5. Global Meteorological Observation System	43
Chapter 2. THE USE OF RADIATION DATA OBTAINED WITH METEOROLOGICAL SATELLITES	56
2.1. The Radiation Balance of the Earth Surface—Atmosphere System	56
2.2. Spatial Structure of the Outgoing-Radiation Field	79
2.3. Cloud Identification. Radiation Forecasting	86
2.4. Determination of Surface Temperature, Cloud Height, and Moisture in the Troposphere	100
2.5. Analysis of Infrared Cloud Pictures	107
2.6. Outgoing Radiation and Radiant Heat Input. Connection with Other Forms of Heat Input	119
2.7. Relationship Between Outgoing Heat Radiation and the Field of Mean Temperatures in the Troposphere and Lower Stratosphere	125
Chapter 3. THE PROCESSING OF METEOROLOGICAL SATELLITE DATA	137
3.1. Geographical Correlation of Television Pictures and the Elimination of Distortion Factors	138
3.2. Geographical Orientation of APT Data	155
3.3. Interpretation of Nephanalysis Data	164
3.4. Processing of Outgoing-Radiation Data	174
Chapter 4. THE PRACTICAL USE OF TELEVISION AND INFRARED PICTURES OBTAINED FROM METEOROLOGICAL SATELLITES	191

Page

4.1. General Appraisal of Practical Possibilities in the Interpretation of Satellite TV Cloud Patterns 191
4.2. Identification of Clouds on TV Pictures, and their Relationship with Synoptic Elements 198
4.3. Identification of Ice, Snow, and Fog from Satellite Pictures 214
4.4. Determination of Characteristics of Extratropical Cyclones 222
4.5. Identification of Atmospheric Fronts 239
4.6. Analysis of Tropical Zones. Tropical Cyclones 244
4.7. Determination of Wind and Jet-Stream Direction 266
4.8. Reconstruction of the Geopotential and Wind Field from the Cloudiness Field 275
4.9. Practical Nephanalysis 278

APPENDIX 1 296

APPENDIX 2 297

PHOTOGRAPHS TAKEN BY METEOROLOGICAL SATELLITES 299

EXPLANATORY LIST OF ABBREVIATIONS APPEARING IN THE BIBLIOGRAPHIES

Abbreviation	Full name (transliterated)	Translation
AANII	Arkticheskii i Antarkticheskii Nauchno-Issledovatel'skii Institut	Arctic and Antarctic Scientific Research Institute
AN ESSR	Akademiya Nauk Estonskoi SSR	Academy of Sciences of the Estonian SSR
AN KazSSR	Akademiya Nauk Kazakhskoi SSR	Academy of Sciences of the Kazakh SSR
AN SSSR	Akademiya Nauk SSSR	Academy of Sciences of the USSR
GGO	Glavnaya Geofizicheskaya Observatoriya	Main Geophysical Observatory
ISZ	Iskusstvennyi sputnik Zemli	Artificial Earth Satellite
KhGU	Khar'kovskii Gosudarstvennyi Universitet	Kharkov State University
LGU	Leningradskii Gosudarstvennyi Universitet	Leningrad State University
MMTs	Mezhdunarodnyi Meteorologicheskii Tsentr	World Meteorological Center
TsIP	Tsentral'nyi Institut Prognozov	Central Forecasting Institute

FOREWORD

Meteorological satellites have existed only since 1960, but their data has already proved useful in many fields of meteorology. K. Ya. Kondrat'ev's book "Meteorologicheskie sputniki " ("Meteorological Satellites") (Gidrometeoizdat, 1963) was a first attempt to generalize results achieved in the field of satellite meteorology. The purpose of the present book, which partly uses data from the above-mentioned monograph, is to discuss in detail practical applications of meteorological information obtained by means of meteorological satellites. The discussion is restricted to data from American meteorological satellites, since most experience has been gained by interpreting these data. The authors have benefitted much from the WMO Seminar on the interpretation and use of meteorological satellite data held in Tokyo during 1964. Different problems of applied satellite meteorology were discussed in great detail during the Seminar in which one of the present authors participated. Two interesting and fully illustrated volumes of data and methodically well-designed exercises on nephanalysis were prepared by members of the staff of the U.S. Weather Bureau for practical work at the Seminar. Part of this material was used by the authors in preparing this book.

The Soviet artificial Earth satellite COSMOS-122, containing equipment for meteorological research, was launched on 25 June 1966. The apparatus included: 1) TV cameras to obtain information on the distribution of cloud, snow, and ice cover; 2) IR (infrared) radiometer device operating at the atmospheric window to obtain cloud pictures from the night side of the Earth. The above equipment differed from its American counterpart in that it also provided IR cloud pictures from the sunlit Earth surface; 3) equipment for measuring the different components of the radiation budget of the Earth and the atmosphere.

The results of this experiment show that the data obtained may be successfully used in routine weather forecasting. Unfortunately this cannot be discussed in detail in the present book. However, the practical methods for analyzing and interpreting information supplied by a meteorological satellite which are considered in this monograph may be applied to the measurement results obtained by Soviet meteorological satellites.

The Introduction and Chapter 1 were written by K. Ya. Kondrat'ev. After a brief appraisal of the importance of the problem considered, the main possibilities of meteorological research by means of satellites are discussed. The meteorological satellites launched before this monograph was completed, as well as their scientific equipment, are described. Chapter 2 was written by K. Ya. Kondrat'ev (except for section 2.2 written by Borisenkov and section 2.5 by Morozkin and Puchkov). In this chapter problems of the interpretation and practical use of radiation data obtained

by meteorological satellites are discussed. Chapter 3 (by Borisenkov) examines methods of processing information from meteorological satellites. The most important section of the book is Chapter 4 (by Borisenkov and Morozkin), in which different problems on the practical use of cloudiness data are dealt with in detail, followed by examples and exercises. To make the discussion clearer, photographs obtained from meteorological satellites are presented in Appendix 2.

The authors express their gratitude to Smirnov, scientific editor of the book, as well as to Zabrodskii, for their valuable remarks and advice, which were taken into account when preparing the manuscript for publication.

The present monograph should be looked upon as a first attempt to summarize the latest advancements in applied satellite meteorology, and obviously much will have to be revised in the future. Readers comments would therefore be much appreciated, and should be sent to: Gidrometeoizdat, District 53, Section 2, House 23, Leningrad, USSR.

INTRODUCTION

Artificial Earth satellites opened a new era in the study of the upper atmosphere and space. For the first time processes developing in the upper atmospheric layers can be studied directly. The possibility of sending equipment to altitudes at which the parasitic influence of the atmosphere on celestial bodies can be practically eliminated is of major importance for space research. The availability of rockets and spacecraft makes direct space probing possible. It is natural that the first projects for the scientific utilization of these satellites were aimed at exploring phenomena which were beyond the reach of indirect ground-based methods of investigation or very poorly studied. This concerns, first of all, the upper layers of the atmosphere and outer space. However, it is obvious that satellites can provide extremely valuable information on large-scale processes which take place in the lower layers of the atmosphere and which play a major role in weather changes.

There are at present thousands of meteorological stations all over the world which conduct systematic weather observations. Numerous aerological stations are carrying air soundings up to altitudes of 20—30 km. Observational data obtained by these stations are used to plot synoptic charts, which are the principal tool for weather forecasting. It should be remembered, however, that about $^4/_5$ of the globe is covered by oceans and seas, and also that significant parts of the land areas are more or less inaccessible (polar regions, deserts, etc.). Consequently, most of the Earth surface is not really covered by meteorological observations, except for incidental ship observations and a few Arctic and high-mountain meteorological stations. Consequently, despite the dense network of meteorological stations in the most populated regions of the globe, there are still many gaps on the synoptic charts which the weather forecaster must fill by intuition and experience.

It is obvious that these difficulties could be overcome if atmospheric parameters were measured by instruments mounted on a satellite. Even a single satellite placed into a polar orbit (oriented at 90° to the equitorial plane) and completing one circuit every 90 minutes may provide information on the global weather situation within a relatively short period of time. Using a number of such satellites, values of meteorological elements may be obtained almost simultaneously, thus replacing, to some extent, a global meteorological network.

Although this increase in volume of meteorological information provided by satellites is quite important, the main advantage of using satellites in meteorology is that it would be possible to make a detailed study of the laws governing the processes of weather formation. A better understanding of these processes may lead to an improvement in weather forecasting and it will undoubtedly have a major impact on the solution of problems of weather and climate modification.

Chapter 1

THE POTENTIALITIES OF SATELLITE-BORNE EQUIPMENT FOR METEOROLOGICAL RESEARCH

We will consider first the actual prospects for the use of satellites in meteorology /1, 2, 78/.

1.1. THE MAIN PROBLEMS

The main tasks of a scientific program for using meteorological satellites are those of obtaining primary information about meteorological processes on a world-wide scale and developing methods for using this information in weather-forecasting and climatic studies. Ways of solving the second of these tasks are still being investigated, especially in the case of numerical weather forecasting, although some progress has recently been made in the above field /3/. However, more meteorological information can considerably improve the reliability of weather forecasts based on conventional synoptic analysis.

The most important meteorological elements for weather prognosis are cloudiness, precipitation, air temperature and humidity, atmospheric pressure, wind speed, and solar and terrestrial radiation. Methods for determining the above-mentioned elements by means of satellite-borne instruments will probably be developed in the future, but at the moment the number of parameters which can be determined is rather limited.

Many suggestions have recently been made for the use of satellites for meteorological purposes. Problems of major interest are listed below.

Cloud-cover observation by TV. The object of this type of observation is to provide information on the distribution of cloud cover over the Earth. Since conventional TV cameras can only observe cloudiness during the daytime, infrared cameras or ultrasensitive TV cameras could be used at night.

Valuable information on cloudiness distribution at night may be obtained by means of high-resolution radiometers, using data on the space distribution of the outgoing long-wave radiation from the Earth-atmosphere system within given spectral intervals. Cloud data of a quantitative nature would be extremely valuable if the brightness (TV displays) and intensity of outgoing radiation (IR displays) are measured.

Cloud data are of special interest, being sensitive and visual indicators of weather-formation processes. Determination of weather disturbances

from observed changes in cloudiness, so-called nephanalysis, played an important role in weather forecasting in the past. Later, with the advent of more objective and accurate methods, nephanalysis lost its importance. Today we go back, to a certain extent, to the nephanalysis concept, but on a much higher, "satellite" level (from the viewpoint of the technique adopted and with regard to a deeper understanding of the phenomena observed).

Radiation budget of the Earth (Earth surface-atmosphere system). Measurements of the radiation budget and its components using satellite-borne instruments supply data on the laws governing the energy budget of the Earth. The importance of these data can be seen from the following example. Simple calculations /78/ show that a 1% increase in the estimated mean annual radiation inflow to the Earth results in an increase in the mean temperature of the atmosphere by 7°C. This would be so if all excess energy were used to heat the atmosphere. The above corresponds to the temperature change from the last ice age to the present time.

This calculation is, however, obviously exaggerated, since in reality excess energy will only partly be used to heat the atmosphere. However, even if the above-mentioned rate of atmospheric heating were reduced by an order of magnitude, it would still result in a significant temperature variation.

Radiation field of the Earth. A comprehensive program to study the laws governing the radiation distribution of the Earth in different regions of the spectrum, especially using spectometric methods, is intended. Data will first be obtained on the spectral and angular distribution of outgoing radiation. Optical methods for investigating the composition and structure of the atmosphere may then be developed on the basis of data thus obtained. They will be discussed later.

Vertical air-temperature distribution, and composition of the atmosphere. The emission of heat from the Earth-atmosphere system (so-called outgoing radiation) is determined by the vertical distribution of temperature as well as by the absorption and emission of radiation by the atmospheric components (primarily water vapor and carbon dioxide). The measurement data on outgoing radiation may therefore be used to determine the temperature distribution and composition of the atmosphere. In this way, e.g., the temperature of the Earth surface or of the clouds may be determined.

Radar investigation of cloudiness and precipitation. Ground-based radar has proved highly successful in cloud and precipitation studies and one can thus hope that radiometeorology will play an important role in meteorological-satellite observations. Meteorological satellites may also be used for investigating atmospherics with the purpose of studying the distribution of thunderstorm centers over the Earth and their location; these data aid weather forecasting.

The height of the upper boundary of clouds. There are different ways of using data of spectral measurements of outgoing radiation in the visible and near-ultraviolet region of the spectrum to determine the height of cloud tops. Laser techniques may also be used for this purpose. Methods recently adopted will be considered in Chapter 4.

Investigation of the wind field. To obtain data on the terrestrial wind field it is suggested that about two thousand transosondes be launched at

different points around the world and their drift tracked by a system of satellites. Indirect methods may also be applied, particularly those based on the use of observational data on the so-called "solar path" /7, 8/.

Energy distribution in the ultraviolet solar spectrum. The purpose is not only to investigate the spectral composition of the ultraviolet solar and scattered radiation and its variation, but to use these data to determine the ozone content of the atmosphere and to solve some other problems connected with the study of the optical properties of the atmosphere.

In addition to these important problems there are others, for which a solution could not even be outlined until now (investigation of atmospheric turbidity, measurement of the mass of the atmosphere and atmospheric pressure near the ground, etc.).

Any scientific program involving meteorological satellites must include equipment capable of carrying out reliable measurements of the parameters of interest. The use of satellite data is completely dependent on the reliability of such equipment.

The creation of a routine weather-satellite system cannot be achieved without a radical change in meteorological-data processing methods. The huge body of information which will be obtained from satellites will have to be processed automatically by means of computers. Processing must begin at the satellite-signal stage and continue right up to synoptic-chart plotting and numerical weather prediction. This gives rise to automation of data processing and interpretation.

It should be noted that an operational system of meteorological satellites must be able to transmit measurement results to weather-forecasting centers as quickly as possible. Ground-based processing centers will be required to transmit and process information. In certain cases communication satellites may have to be used.

1.2. SELECTION OF ORBITS

The main advantage of meteorological observations from satellites is that they provide information on different processes occurring throughout the total depth of the atmosphere and around the entire (or almost the entire) globe. The development of processes occurring over certain large areas of the Earth can also be tracked continuously. This brings us to the problem of selecting the best satellite orbit.

Circular orbits are the most suitable for meteorological investigations, since then there is no need to introduce corrections due to the varying altitude above the Earth surface. As regards the angle of inclination of an orbit, polar and equatorial orbits are of greatest interest.

The entire globe can be "viewed" by instruments mounted on a satellite moving in a polar orbit. A satellite placed at noon local time in a northern direction into a polar orbit and carrying out an integral number of circuits during 24 hours, will have appeared in all latitudes up to the North Pole by noon. Passing the pole, the satellite will enter the shadow of the Earth and cross all latitudes by local midnight. Due to the Earth revolution around the Sun, the local time at which a satellite crosses a given latitude

will be advanced by four minutes every 24 hours. To eliminate this influence, and to ensure the appearance of the satellite above a point of given latitude at exactly local noon (on the day side) and local midnight (on the night side), respectively, the orbital plane should be inclined by a small angle toward the west with respect to the equatorial plane. The precession of the satellite orbit should also be taken into account /13/.

According to tentative calculations, with an orbital altitude of 500 km a satellite should be placed into an orbit inclined at an angle of 7° toward the west with respect to the pole. Atmospheric processes can be tracked continuously by using a system of quasipolar satellites launched so that they will cross all the latitudes within determined time intervals. According to Haviland (quoted in /29/), two satellites having polar orbits situated in perpendicular planes might be enough, provided the orbital altitudes are 3,600 and 7,200 km, respectively. In this case, however, the charts of geographic distribution of the investigated parameters will be on an extremely large scale.

Wexler /79/ considered a system of seven meteorological satellites orbiting at an altitude of 6,000 km as optimum. He suggested that six quasi-polar satellites (three "day" and three "night" satellites) and one equatorial satellite should be launched. With this system any significant area of cloudiness would not be lost from sight for a period exceeding one hour, and global charts of the geographic distribution of satellite data could be plotted every six hours.

Glaser and Christensen have discussed in detail the requirements for a simple system consisting of two meteorological satellites of the TIROS type to be placed into identical orbits in opposition phase (angle of inclination 58°, altitude 740 km). They considered the following factors that cause perturbations in satellite motion: 1) nonspherical shape (oblateness) of the Earth; 2) interaction of electrical and magnetic fields of both the satellite and the Earth; 3) aerodynamic drag; 4) heterogeneity of the Earth; 5) influence of other celestial bodies; 6) the satellite's own motion.

The first two factors are the most significant for TIROS satellites. Optimum orientation of the satellite spin axis for outgoing-radiation measurements and photography is ensured by matching these two principal factors and by controlling the satellite magnetic moment with a special device. It appears, however, that favorable illumination conditions over an extended period can only be achieved by a significant latitude variation of the investigated regions with time (for example, cloud pictures in the Northern Hemisphere cannot be obtained over extended periods).

The above shortcoming may be eliminated almost completely using two satellites in opposition phase. To ensure opposition phase, the second satellite should be launched 40 days after the first /22/. Glaser and Christensen also considered possible changes in the phase difference of the satellites under the influence of various factors. If the inclination angles of the orbits and the altitudes of the satellites do not differ by more than 0.5° and 40 km, respectively, the shift of the satellites with respect to the opposition-phase position will not exceed 20° during their lifetime (six months). The importance of adding two ground-based receiving stations in Western Europe and Japan to existing stations in the U.S.A. (on Wallops Island, Va., and Point Mugu, Calif.) should be mentioned here. They will

enable information to be received from every satellite circuit. The authors of /22/ did not take into account, however, such an important factor as unavoidable errors arising when the satellite is injected into orbit, which might affect orbit stability and satellite position significantly.

The most rigorous mathematical solution to the problem of choosing an optimum meteorological-satellite system was given by Luders /6/ and Gobetz /35/. It is shown in /23/, for example, that six satellites in two polar orbits at an altitude of about 9,500 km above the Earth surface must be used for total coverage of the Earth surface (i.e., at least one satellite will be in the field of view of any point on the surface). With a special set of orbits it is also possible to solve the above problem by means of five satellites. With a smaller number of satellites a continuous survey of the entire Earth surface is impossible.

In view of the large-scale nature of atmospheric processes, in addition to data averaged over large areas, information concerning local processes must also be obtained. The above requirements are taken into account when determining the type of satellite equipment as well as when choosing the optimum orbits.

As interesting as the "polar" satellite is one launched into an equatorial orbit. When at an altitude of 1,000 km such a satellite may supply information on processes occurring in the near-equatorial zone (approximately from 30°S to 30°N). The use of equatorial orbits with an altitude of 35,700 km is also interesting. A satellite moving in such an orbit will always remain above the same point of the Earth surface.* A system of such satellites positioned above different geographical areas may efficiently be used to collect and transmit information from other meteorological satellites.

1.3. THE U.S. PROGRAM FOR METEOROLOGICAL SATELLITES

An optimum system of meteorological satellites and some indication of their scientific program was mentioned above.

The successful launching of ten meteorological satellites of the TIROS series in the U.S.A. in 1960—1965, as well as the later series of NIMBUS satellites, were instrumental in the use of satellite data for routine weather forecasting. It is assumed that by 1966 a system of meteorological satellites for routine use will be in full operation /76, 20/.

There are, however, considerable delays in realizing the above program. For example, the first NIMBUS satellite was only launched on 28 August 1964, and the TIROS IX, launched on 22 January 1965, was only partly successful (the satellite was injected into a different elliptic orbit than the one calculated; it had a perigee of 740 km and an apogee of 2,580 km).

A diagram of a weather service utilizing NIMBUS satellite data is shown schematically in Figure 1.1, and provides for the use of satellite meteorological data not only by national and regional meteorological centers, but also by local weather services.

* Such an orbit, as well as the satellite moving along it, are referred to as stationary or synchronous.

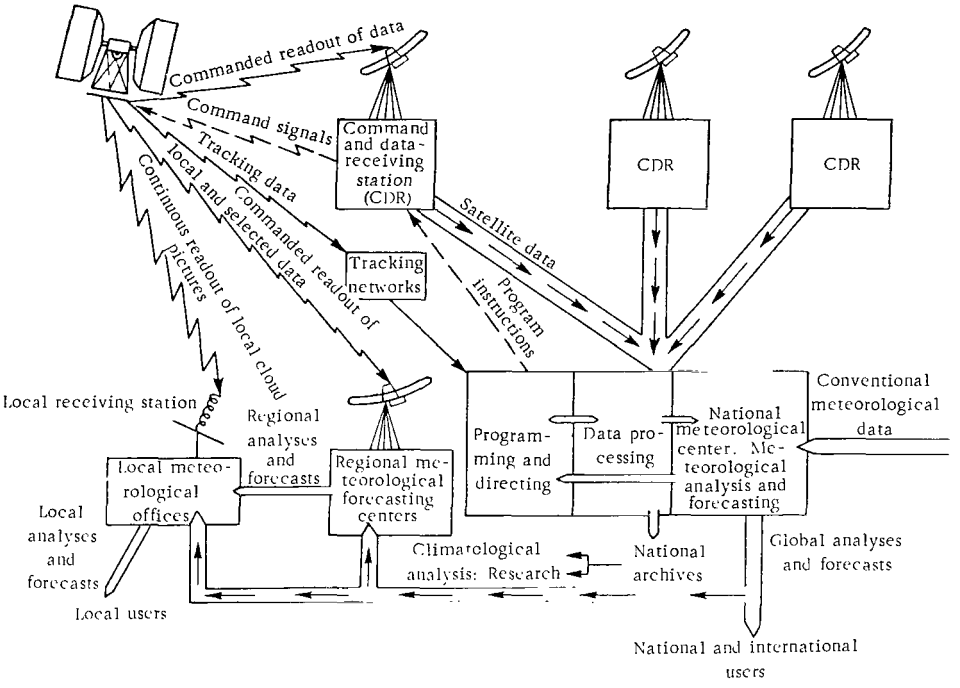

FIGURE 1.1. Diagram showing the operation of a weather service utilizing NIMBUS satellite data.

Due to technical difficulties, which cropped up while arranging the NIMBUS series of satellites, the amount of originally planned scientific equipment of the satellite, the requirements for orientation accuracy, and the service life had to be reduced /80, 41/. Taking into account the above changes and the high cost of NIMBUS satellites, the U.S. Weather Bureau decided not to use NIMBUS satellites in the first stage of operation of the routine meteorological-satellite system. Only two NIMBUS satellites for research purposes were planned to be launched by NASA.

A temporary system of routine meteorological satellites, scheduled for operation in 1966 /20/, will consist of improved TIROS-type satellites.* They will be delivered into a circular polar orbit with an altitude of about 1,000 km. Television cameras should provide for an areal resolution of 4—6 km. In addition to solar cells provision will be made for using other power sources. Radiational effects on the above power sources are one of the main factors limiting the service life of satellite scientific equipment.

It is assumed that when the principal national meteorological satellite system is established the satellites used will have a service life of 3 to 5 years. They will provide data on the global distribution of the cloud cover, day and night, as well as on the degree of cloudiness and on cloud tops. It is also intended to use satellites to determine wind speed and direction, vertical profile of temperature, and state of sea surface.

The problem of finding orbits suitable for the principal satellite system has not yet been solved (the use of synchronous satellites is also

* These satellites are called ESSA.

considered). In a review /41/ it is pointed out that the previously planned synchronous satellites of the AEROS series (as predecessors of the principal system) will not be built, but will be replaced by other types of synchronous satellites which are in the design stage. Preliminary experience using meteorological satellite information has already proved extremely promising.

There are yet more promising prospects of using satellites for various investigations in the field of outgoing radiation, to obtain information on the composition and structure of the atmosphere, as well as the possibility of applying lasers to determine the upper boundary of clouds, recording and tracking the displacement of thunderstorm centers, etc. However, experimentation with satellites can hardly be continued until very serious consideration is given to problems of processing, analyzing, and disseminating meteorological-satellite information.

The amount of this information can be seen by comparing the information in a single TV display of cloud cover obtained from a TIROS satellite, which is 10^7 bits, with the 10^4 bits in a ground synoptic chart of the Northern Hemisphere /42/. It is assumed that by 1975 the daily amount of satellite meteorological information will reach 10^{10} bits, which means an increase of several orders of magnitude. There is no doubt that under these conditions, processing, analysis, and dissemination of information can only be carried out by resorting to full automation.

Cloud-cover and outgoing-radiation data can be applied in numerical weather-forecasting schemes provided that methods of their effective use will be developed and more complex models of atmospheric processes will be elaborated. Increased areal resolution means more complicated models, which increases the difficulties of data processing and analysis.

It should be mentioned here that other computers besides digital computers could be used in meteorology, e.g., so-called teaching machines suitable for pattern recognition. Attempts to use such machines for interpreting synoptic charts have shown that they distinguish satisfactorily between precipitation zones and regions without precipitation. Similar machines may be useful for analyzing cloud-cover photographs, as well as outgoing-radiation fields and analog forecasts.

1.4. METEOROLOGICAL SATELLITES AND THEIR EQUIPMENT

The first experiments in satellite meteorology were carried out with the VANGUARD II and EXPLORER VII satellites, launched only partly successfully in the U.S.A. Between 1960 and 1965 NIMBUS satellites were launched and operated quite satisfactorily. Some data describing the American meteorological satellites are given in Table 1.1 /11, 12, 66, 67/.

A more detailed description of these satellites follows.

1. VANGUARD II. This satellite was launched on 17 February 1959 and used for the first investigations of the global cloud-cover distribution. It was spherical, had a diameter of 50.8 cm, weighed 9.8 kg, and was placed into an elliptic orbit with a perigee of 628 km and an apogee of 3,380 km.

The orbit had an angle of inclination of 32.2° with respect to the equatorial plane /18/.

The satellite carried two photoelectric cells (Figure 1.2, 1 and 5) sensitive to radiation between wavelengths of about 0.6 and 0.8μ and with an acceptance angle of 1°. The photoelectric cells were mounted in such a way that their receiving apertures were located at 45° to the spin axis of the satellite. It was assumed that as the spinning satellite moved in its orbit, one of the two photo cells would always point to the Earth surface, scanning the brightness distribution on the ground in a way similar to a TV scan of an image. Due to the high albedo of the clouds compared with the lower albedo of land and sea (excluding, naturally, regions covered with snow or ice), clouds may be identified by the maximum values of brightness. The actual movement of the satellite turned out to be so complex, that location of the measured values of brightness at particular points was impossible. This was the main reason for the failure of VANGUARD II.

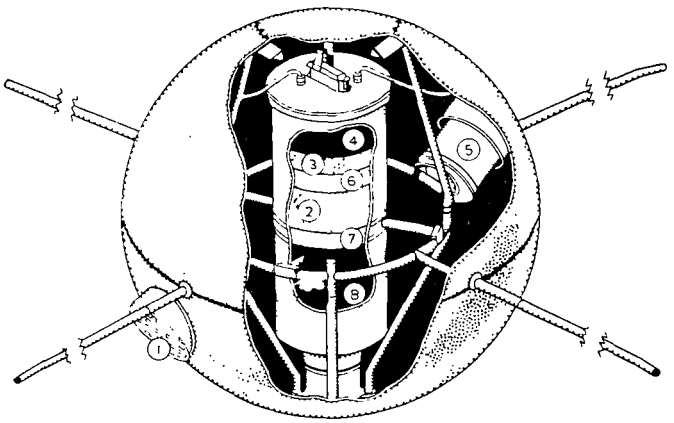

FIGURE 1.2. VANGUARD II satellite:

1,5 – photoelectric cells; 2 – register; 3, 4, 6, 7 – electronic units; 8 – power supply.

2. EXPLORER VII. This satellite was launched on 13 October 1959 and designed to carry out geophysical and other investigations. It weighed 37 kg, and had an orbit with a perigee of 550 km and an apogee of 1,100 km (the initial period of revolution was 101.2 min). The orbital inclination angle was 50.3° /81/. By October of the same year the transmitter of the satellite had failed, the period of observation by this satellite thus being very short.

The middle section of the satellite container represented a cylindrical body, on the side surface of which were mounted five radiation sensors in the shape of thin hemispherical membranes, heat-insulated from the satellite body. Two of the sensors were blackened and one white-coated (for short-wave radiation). The fourth sensor was made of a gold-coated hemisphere, and the surface of the fifth was shielded from the solar rays

TABLE 1.1. American meteorological satellites

Satellite	Launching date	Type of rocket	Angle of inclination of orbit, deg	Stabilization	Meteorological research equipment
VANGUARD II	17 Feb. 1959		32.2	Not oriented	Two photoelectric cells
EXPLORER VII	13 Oct. 1959		50.3	" "	Outgoing-radiation sensors
TIROS I	1 Apr. 1960	Thor-Able II	48.6	Spin axis stabilized	Two TV cameras
TIROS II	23 Nov. 1960	Thor-Delta	48.53	" " "	The same; outgoing-radiation sensors
TIROS III	12 July 1961	" "	48.53	" " "	" " " " "
TIROS IV	8 Feb. 1962	" "	48.30	" " "	" " " " "
TIROS V	19 June 1962	" "	58.10	" " "	" " " " "
TIROS VI	18 Sept. 1962	" "	58.32	" " "	Two TV cameras
TIROS VII	19 June 1963	" "	58.23	" " "	The same; outgoing-radiation sensors
TIROS VIII	21 Dec. 1963	" "	58.50	" " "	Two TV cameras
NIMBUS I	28 Aug. 1964	Thor-Agena	99.0	Oriented toward the Earth surface	Four television cameras: IR scanning radiometer
TIROS IX	22 Jan. 1965	Thor-Delta	96.4	Spin axis stabilized	TV cameras
TIROS X	1 July 1965	" "	98.64	" " "	" "
ESSA I	3 Feb. 1966	—	97	" " "	" "
ESSA II	28 Feb. 1966	—	(circular orbit, apogee 1,390 km, perigee 1,360 km) perigee 1,360 km)	" " "	The same: operating in the direct-transmission schedule

by a special screen and provided with an outer cover of high reflectivity both for short-wave radiation and long-wave heat emission of the satellite itself.

In addition to the hemispherical sensors, there was a black, spherical radiation detector /14/. That part of the satellite surface falling into the viewing field of the radiation detector is a metallic mirror, which eliminates the influence of heat emission of the satellite body. As the satellite is spinning rapidly (360 rpm), the spin axis being parallel to the mirror surface, it is assumed that the hemispherical sensor behaves like a sphere located above the Earth surface at the satellite level.

The temperatures of the hemispheres and the metallic mirror are measured directly. Temperature readings are taken every 42 sec, which corresponds to a latitude difference of about 2.5°.

The field of view of the spherical detector obviously depends on the solid angle β, within which the Earth is seen from the point where the satellite is observed. Table 1.2 presents Bignell's values of the radii r of an area on the Earth surface viewed from different altitudes h, as well as of $r_{0.5}$ and $r_{0.75}$, the radii of areas comprising 0.5 and 0.75 of the total area viewed /14/.

TABLE 1.2. The field of view of a spherical radiation detector

	h km								
	200	300	400	500	600	700	800	900	1000
r km	1591	1912	2190	2450	2670	2680	3040	3200	3360
$r_{0.5}$ km	258	366	465	555	640	723	795	870	930
$r_{0.75}$ km	450	615	770	905	1030	1135	1255	1360	1475

Data in Table 1.2 correspond evidently to the fields of view of a flat receiving surface parallel to the Earth surface. It should be mentioned, however, that under actual conditions it is the concept of the effective solid angle (the corresponding cross section) over which a certain part (e.g., 0.5 or 0.75) of the radiation flux is incident, that is of significant interest. Obviously, the magnitude of the effective solid angle depends on the nature of the angular distribution of radiation. Only for an isotropic radiation field do the effective viewing fields coincide with the values given in Table 1.2.

We now consider the method proposed by Suomi /56/ for deriving a relationship between the measured temperatures of hemispherical radiation detectors and the radiation-balance components. If r is the radius of the hemispheres, and a_S and a_L the absorptivity for short-wave and long-wave radiation, respectively, the following approximate equation for the radiation balance of the sphere is valid, provided the satellite is on the sunlit side of the Earth:

$$\pi r^2 (a_S S_0 + a_S D_\infty + a_L F_\infty) = 4\pi r^2 a_L \sigma T^4, \qquad (1.1)$$

where S_0 is the solar constant; D_∞, F_∞ are fluxes of outgoing short-wave radiation and thermal radiation incident on the detector; T is the temperature of the hemisphere surface. It is assumed in this case that the radiation detector is not shaded by the satellite.

For a black hemisphere it may be assumed that $a_S = a_L = 0.95$. According to (1.1) we have

$$0.95S_0 + 0.95D_\infty + 0.95F_\infty = 4 \cdot 0.95\sigma T_B^4. \tag{1.2}$$

where T_B is the temperature of the black hemisphere. If the hemisphere is painted white so that it reflects the short-wave radiation (e.g., $a_S = 0.05$), but absorbs the heat radiation ($a_L = 0.95$), then (1.2) is replaced by

$$0.05S_0 + 0.05D_\infty + 0.95F_\infty = 4 \cdot 0.95\sigma T_W^4. \tag{1.3}$$

where T_W is the temperature of the white hemisphere.

With known solar constant S_0, the radiation-balance components D_∞ and F_∞ can be determined from the latter two equations. For example, the outgoing short-wave radiation is given by

$$D_\infty = \frac{4 \cdot 0.95}{0.90} \sigma (T_B^4 - T_W^4) - S_0. \tag{1.4}$$

This formula, however, is not very convenient for computing outgoing short-wave radiation for large zenith angles of the Sun and low albedo of the underlying surface, since D_∞ in (1.4) represents a small difference of two considerably larger values. In this case, the computation error according to (1.4) will naturally be significant. Much more reliable is the use of a radiation detector having optical features different from that of the black and white detectors (and being insensitive to heat radiation). In addition, if such a detector is shielded from the Sun, its temperature will be determined mainly by the magnitude of the outgoing short-wave radiation. For the above reason, Suomi suggested using spherical detectors shielded from the Sun and having the optical parameters $a_S = 0.90$ and $a_L = 0.10$. By combining two types of screens (rings and disks) one of the two detectors would be shielded for any position of the satellite with respect to the Sun. The problem of determining the components of the Earth radiation balance is solved in this case by using a predetermined system of three equations for the two unknown values. If the three above-mentioned equations are considered as equations for the three unknown values, it is obvious that an independent determination of the solar constant is then possible.

When the satellite is in the Earth shadow ($S_0 = D_\infty = 0$) the temperature of any of the radiation detectors is determined by the value of the outgoing radiation F_∞.

At present, only radiation data measured from the night side of the Earth have been published /81/. For processing data obtained from the white radiation detectors the following equation was used, being more general than the above-mentioned simple formulas:

$$a_L \beta \frac{F_\infty}{2} = 2\pi\varepsilon\sigma T_W^4 + H \frac{\partial T}{\partial t} + k(T_W - T_M). \tag{1.5}$$

Here β is the solid angle within which the Earth is viewed; $\varepsilon = a_L$ is the absorptivity of the hemisphere surface; H is the specific heat of the radiation detector (the term $H \frac{\partial T}{\partial t}$ represents the influence of the nonsteady

nature of thermal conditions in the detector); k is the thermal conductivity between the detector and the mirror; T_M is the temperature of the mirror. The last term in (1.5) is a correction for the heat exchange by conduction between the radiation detector and the satellite skin (metallic mirror).*

An estimation of the measurement accuracy, using formula (1.5), gave the value of the relative error at about 10% /81/.

The above-described method of processing radiation-balance data is very general. For the described radiation detectors it is mandatory to allow for the possibility of spurious radiation incident on the detectors due to reflections from the satellite body. It is also obvious that the assumption of equality between the amounts of radiation absorbed by a sphere, and a flat surface equal to the cross section of the sphere, is valid only approximately. The formulas considered above were based on this assumption. The reflectivity of actual coatings (lampblack, magnesia, etc.) always depends on the angle of radiation incidence (such coatings are actually nonorthotropic). Therefore the nonorthotropic character of the hemisphere surface, and hence the actual geometry of the radiation detector, should be taken into account when determining the amount of radiation absorbed by the hemisphere. The equivalence of a rotating hemispherical radiation detector to a spherical one as assumed in /81/ cannot be considered as proven. A detailed study of the theory of radiation detectors advanced by Suomi can be found in /9, 14/.

Bignell /14/ analyzed the effect of the anisotropy of the outgoing-radiation field on the relationship between the outgoing-radiation that is incident on spherical and flat surfaces, assuming that the receiving surfaces are absolutely black. Computations, made with allowance for the leveling of the nonuniform angular distribution of the outgoing radiation along the satellite trajectory due to the large time constant of the radiation detectors (5 min), show that for long-wave radiation the difference between the radiation fluxes on the surface of a sphere and a flat surface equivalent in size to the cross section of the sphere, does not exceed 2%. For short-wave radiation the above difference may reach 10%, but should usually be considerably less. If, however, the time constant of the radiation detector is small, the above differences may reach 30—40%.

An interesting result of Bignell's computations /14/ is that aerodynamic heating has a considerable influence on the readings of the radiation detectors at an altitude of 200 km: it creates an additional heat flux of 0.15 cal cm^{-2} min^{-1}. However, at an altitude of h=400 km this heat flux drops to 0.002 cal cm^{-2} min^{-1}. Hence, measurements of outgoing radiation fluxes cannot be carried out from satellites with relatively low orbits.

An important conclusion from the investigation of Malkevich et al. /9/ is that the heat exchange by conduction between the radiation detectors and the satellite skin (metallic mirror) significantly affects the measurement results of outgoing radiation.

3. TIROS. The series of TIROS satellites launched during 1960—1965 was intended to create prerequisites for their gradual utilization as meteorological satellites in routing weather services. The main orbital characteristics of ten TIROS (Television and Infrared Observation Satellite) satellites are given in Table 1.3. A detailed description of these satellites can be found in /10—12, 18, 24, 30—35, 45, 57—64, 66—68, 82/.

* Note that in /81/ the signs of the last two terms of (1.5) are incorrect.

TABLE 1.3. Orbital parameters of TIROS satellites

Main characteristics	TIROS I	TIROS II	TIROS III	TIROS IV	TIROS V
Launching date	1 Apr. 1960	23 Nov. 1960	12 July 1961	8 Feb. 1962	19 June 1962
Period of revolution, min.	99.19	98.27	100.42	100.40	100.47
Inclination angle, deg	48.36	48.53	47.53	48.30	58.10
Apogee, km	749.6	728.9	814.8	844.4	971.7
Perigee, km	689.8	622.7	741.7	709.9	589.5
Eccentricity	0.0042	0.0074	0.0050	0.0094	0.0267

Main characteristics	TIROS VI	TIROS VII	TIROS VIII	TIROS IX	TIROS X
Launching date	18 Sept. 1962	19 June 1963	21 Dec. 1963	22 Jan. 1965	1 July 1965
Period of revolution, min	98.73	97.42	99.35	119.1	100.78
Inclination angle, deg	58.32	58.23	58.50	96.4	98.64
Apogee, km	711.3	649.2	754.8	2,579.	839.2
Perigee, km	684.3	621.2	701.6	701.0	752.1
Eccentricity	0.0019	0.0020	0.0038	0.117	0.0061

Table 1.3 shows that the orbits of TIROS satellites are almost circular. The inclination angle of the orbital plane of the first four satellites provides a latitude coverage of about $\pm 55°$; the coverage provided by subsequent satellites increases to $\pm 63.5°$. TIROS IX and TIROS X were placed into polar orbits.

To track the cloudiness distribution around the globe TV cameras were mounted on the satellites of the TIROS series provided with wide-angle, medium-angle, and narrow-angle lenses; the main characteristics of this equipment are given in Table 1.4.

The optical axes of the TV cameras in all cases (with the exception of TIROS IX) were oriented parallel to the satellite spin axis. The position of the latter with respect to the stars is maintained approximately constant. The satellite can therefore be regarded as spin stabilized [space-oriented]. TIROS II started a series of measurements of the outgoing radiation in different spectral regions (TIROS V was launched with outgoing-radiation sensors disconnected because of a malfunction; no radiation equipment was installed on TIROS VI, TIROS VIII, TIROS IX, and TIROS X).

Table 1.5 presents a general description of the radiation sensors used on TIROS satellites, with brief indications of the purposes of the corresponding measurements /61, 70/. A device for determining the horizon position (and the local vertical of the satellite), using the brightness difference in the infrared portion of the spectrum at the Earth-space interface, was employed in addition to the above-mentioned radiation detectors. Channel 1 on the TIROS VII satellite responded to the long-wave (14.8—15.5μ) band.

Structurally the design of the first 8 TIROS satellites was almost identical. All of them have a "pillbox" structure, the side walls of which are filled with 9,200 solar cells that provide electric power and recharge the nickel-cadmium batteries. The satellite has a diameter of 107 cm and a height of 48 cm. The weight of the satellites is also almost standard. For example, TIROS I weighed 110 kg, and TIROS IV 129 kg. Figure 1.3 shows the TIROS II satellite, which is typical of the whole TIROS series.

The equipment carried aloft by the TIROS satellites consisted of the following seven subsystems, each performing a specific function /57/.

TABLE 1.4. The main characteristics of the TV cameras mounted on TIROS satellites*

Main characteristics	TIROS I		TIROS II		TIROS III	TIROS IV	
	camera I	camera II	camera I	camera II	camera I	camera I	camera II
View angle, deg	104	12.7	104	12.7	104	104	80
Field of view (from average height of satellite and zero nadir), km	1,200 × 1,200	120 × 120	1,200 × 1,200	120 ×120	1,200 × 1,200	1,200 × 1,200	725 × 725
Resolution per raster line (zero nadir), km	2.5–3.0	0.3–0.8	2.5–3.0	0.3–0.8	2.5–3.0	2.5–3.0	2
Shutter speed, sec	1.5		1.5		1.5	1.5	
Lines per frame	500		500		500	500	
Video band width, kHz	62.5		62.5		62.5	62.5	

* Wide-angle cameras were carried aloft by all satellites of the TIROS series, narrow-angle cameras only by TIROS I and TIROS II. Medium-angle cameras were mounted on TIROS IV and TIROS VI.

TABLE 1.5. General characteristics of the radiation detectors carried by TIROS satellites

Channel	Spectral-band response, μ	Purpose of measurements
	Detectors with narrow angles of view (5 × 5°)	
1	6.0—6.5	Investigation of heat radiation from the water-vapor band in order to measure the temperature of the water-vapor layer at an average altitude somewhat below that of the tropopause. The altitude to which the measured temperature corresponds varies with the vertical distribution of water vapor.
2	8.0—12.0	Investigation of the outgoing radiation lost in space through the atmospheric window. These measurements should provide data on: a) cloud-cover distribution, especially at night when TV cameras are not operated; b) cloud-top temperatures and, accordingly, approximate cloud-top heights; c) surface temperatures and horizontal temperature gradients over cloud-free areas.
3	0.2—6.0	Investigation of the combined outgoing short-wave radiation and albedo of the Earth surface—atmosphere system.
4	8.0—30	Integrated long-wave radiation emitted by Earth and atmosphere simultaneously.
5	0.55—0.74	Study of the Earth brightness distribution over that part of the visible spectrum where the vidicon tubes of the TV system are sensitive. Comparison of such brightness distributions with TV pictures, and reception of these data when TV pictures are unavailable.
	Wide-angle detectors (cone with a 35° aperture angle)	
a	Integrated outgoing radiation (black detector)	Investigation of radiation-budget components of the Earth surface-atmosphere system.
b	Integrated short-wave outgoing radiation (white detector)	
	Hemispherical detectors (angle of view 2π)	
a	Black	Investigation of radiation-budget components of the Earth surface-atmosphere system.
b	White	

The dynamic control sybsystem is intended for the control and correction of the satellite orientation in space (more precisely, spin axis orientation) in order to create optimum conditions for the functioning of scientific equipment.

As the satellite separates from the booster rocket it acquires a high angular rotation velocity (spin) of 125 rpm. After separation, the spin rate drops to 9—12 rpm. This is accomplished by ejecting two counterweights of about 400 g each, at the ends of lightweight steel cables. For the maintenance of the required spin rate ten small spin-up rockets are used. When a pair of rockets, mounted at diametrically opposite points around the periphery of the satellite, is fired, the spin rate increases by about 3 rpm. The precession of the satellite spin axis is reduced to a minimum (deflection of the spin axis does not exceed 0.5°) with the aid of two counterweights, which can slide along two rods parallel to the spin axis. The position of

the spin axis is controlled by means of a magnetic device consisting of a coil wound around the side surface of the satellite.

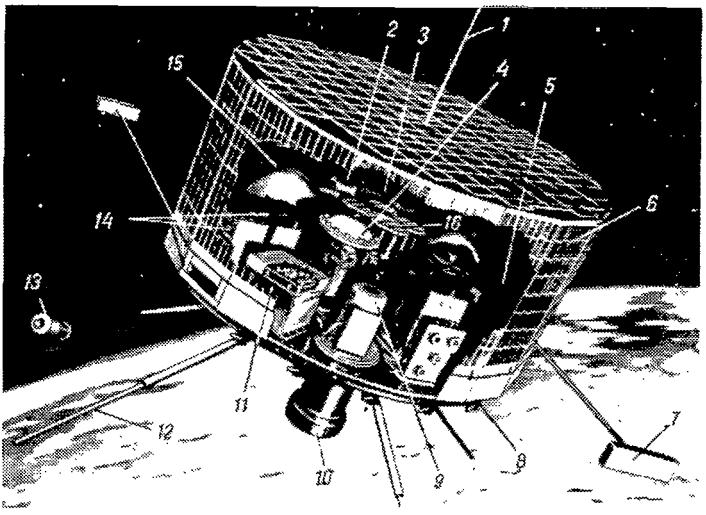

FIGURE 1.3. *TIROS II satellite:*

1 — receiving antenna; 2 — receiving tube of the narrow-angle camera; 3 — battery-charging regulator; 4 — timer; 5 — tape recorder; 6 — solar cells; 7 — spin-decreasing counterweight; 8 — spin-up rocket; 9 — receiving tube; 10 — wide-angle camera lens; 11 — teletransmitter; 12 — transmitting antenna; 13 — the third-stage rocket after separation; 14 — control circuits; 15 — tape recorder; 16 — batteries.

The programming and command subsystem ensures the switching-on and off of the equipment within the range of the ground station. Similar operations are accomplished in any region according to a predetermined program (in the latter case the time interval between the transmission of the command and carrying it out does not exceed 5 hours). In addition, the above-mentioned subsystem switches on the spin-up rockets, controls the operation of the magnetic orientation devices and performs some other functions.

The television subsystem consists of two identical TV cameras with two self-contained tape recorders and transmitters. Operation of the cameras is controlled by commands from ground stations. The TV cameras mounted on the first two TIROS satellites differed in their optical systems: one gave high-resolution pictures of the Earth surface (with a field of view 120 × 120 km at zero nadir angle) and the second giving low-resolution pictures (field of view 1,200 × 1,200 km). The third and subsequent satellites carried only two wide-angle cameras. The television vidicon tubes, especially designed for the satellites, are able to keep the image on the screen for 2 sec, the minimum interval between two images being 10 sec. The shutter placed in front of the vidicon tube screens ensures an exposure

of 1.5 milliseconds. The television equipment was so designed as to ensure that not only the relative, but also the absolute brightness distribution could be determined from the pictures. The TV pictures are transmitted by frequency modulation (the frequency bandwidth ranged from 22.5 to 147.5 kHz). Reception of the tape-recorded information, consisting of 32 pictures (the capacity of the magnetic memory), takes 100 sec. At the receiving stations the TV information is tape-recorded and simultaneously displayed on a picture tube and photographed on a 35-mm film /83/, from which cloud-cover pictures are then printed. In addition, the process of obtaining picture negatives is repeated three times, using tape-recorded data. Then, the negative of best quality is selected. From this negative are printed six positive pictures sent to the main consumers and one main (master) picture used for the preparation of duplicate negatives (the master negative is stored in the archives and is used only when the master positive is no longer suitable for reproduction). At present, work is under way to create two improved systems for the preparation of television data for viewing and analysis. One of the methods consists in the preparation of a composite set of 64 pictures on a film 21.2 × 27.5 cm. Such a picture size is convenient for analysis and display.

The telemetry and trajectory-measurement subsystem is responsible for the reception and transmission of information. It also turns on two beacon transmitters operating continuously, utilized for trajectory measurements.

The satellite position-indicator subsystem serves for determining the position of the satellite with respect to the Sun; it uses nine solar-radiation sensors provided with focal-plane (slit-type) shutters located on the side surface of the satellite parallel to the spin axis. A crude determination of the satellite position with respect to the Earth is carried out with an infrared-radiation sensor pointing in a direction perpendicular to the spin axis and scanning the horizon. The infrared radiation readouts of the five-channel radiometer, mounted on TIROS II, TIROS III, and TIROS IV, were also used for this purpose. In addition, photographs of the Earth surface may serve as a good means for determining the position of the satellite.

The electrical power sources (solar cells and NiCd-batteries) and the instruments measuring the outgoing terrestrial radiation were also self-contained subsystems of the meteorological satellites.

On the whole, the satellite-borne equipment operated satisfactorily. However, the most serious troubles arose in the wide-angle TV camera on TIROS II as a result of decreased sharpness of camera lenses apparently caused by deposition of exhaust gases from the third-stage rocket on the lens surface (later, the quality of the pictures was somewhat restored since the substances on the lens surface probably evaporated in the meantime).

The TIROS satellites were not Earth-stabilized. As the system was placed into orbit, the third-stage rocket, with the satellite attached to it, was given a spin of 125 rpm for stabilization purposes. After separation from the third-stage rocket, the satellite reduced its spin rate to 9—12 rpm by means of a "despinning" mechanism. The spin axis should remain fixed in space. Since the TV cameras are mounted with their optical axes in parallel to the spin axis they look toward the Earth only at determined points of the orbit. The position of the camera optical axes was established

so that the axes face the Earth at optimum illumination conditions. Thus, e.g., the spin axis of TIROS III was pointed vertically to the Earth surface at 20.8°N.

In practice, it was found that the position of the satellite spin axis does not remain constant due to fluctuations in the magnetic and gravitational fields of the Earth /15/. This, in turn, produced considerable difficulties in the processing of observational data, since the precession of the spin axis reached 3—5° during 24 hours. Powers /52/ mentioned three main factors responsible for precession: a) interactions of the satellite magnetic moment and the magnetic field of the Earth; b) nonuniformities in the gravitational field of the Earth caused by its oblateness, and differing moments of inertia of the satellite with respect to its main axes (the moment of inertia with respect to the spin axis is maximum). Another, though minor, disturbing factor is the effect of eddy currents created by satellite rotation in the magnetic field of the Earth.

For the program control of the satellite operation a special theory was developed to predict the satellite orientation. The true position of the spin axis was checked from ground stations, utilizing data on the horizon position in the received pictures, readings from the horizon scanner and from the five-channel radiometer (for the atmospheric window at the 8—13μ waveband). The discrepancy (for 36 hours) between the predicted and observed orientation of the spin axis did not exceed $\pm 1.5°$.

All the satellites, starting with TIROS II, had an electromagnetic coil around their body consisting of several wire turns; if electric current flows through the coil, the magnetic moment of the satellite is markedly compensated [and thus its axis stabilized]. The launching time was calculated so that, for 7—10 days, the precession of the spin axis would not change the given maximum values of the angle between the spin axis and the Sun vector by more than 20—70°. Such an arrangement ensures sufficient illumination necessary for operating the television equipment, as well as for shielding the five-channel infrared radiometer from the Sun.

Ten photoresistors, mounted behind slit-type shutters, were placed in the plane of the spin axis and had an angle of view of about 180° along the slit. This makes it possible not only to determine the position (azimuth) of the Sun, but also to monitor independently the satellite spin rate.

Widger and Wood /84/ analyzed the influence of various factors that limit the region from which information on cloud-cover distribution over the Earth surface can be collected by means of TV equipment, mounted on TIROS meteorological satellites. They found an easy explanation for the influence of the following factors: the angle of inclination of the orbit to the equatorial plane, sufficient illumination for the reception of TV pictures, limitations in the magnetic memory utilized on the satellites, orientation of the TV cameras with respect to the Earth determined by the space stabilization of the spin axis. The effect of orbit precession with respect to the Sun, and the correct location of the station that receives data from the satellite, pose more complex problems. A detailed discussion of the influence of these two factors is presented in /84/.

The time of launching the TIROS satellites was chosen so that the northern part of the orbit was oriented toward the Sun. In this case, the satellite passes over the sunlit (daytime) side of the Earth through the

latitude range 0—50°N. Due to the precession of the orbital plane with respect to the Sun, caused by the oblateness of the Earth, that point of the orbit closer to the Sun slowly shifts southward (the precession period is about ten weeks). As a result, about $3^1/_2$ weeks after the launch, for example, the southern part of the orbit will be at a point closest to the Sun and the satellite will therefore pass over the sunlit side of the Earth within the latitude range 20—50°S (in this case photographic data cannot be obtained for the Northern Hemisphere). An opposite situation takes place roughly eight weeks after launching, when the northern part of the orbit is again at a point closest to the Sun and the satellite passes over the sunlit side of the Earth only within the latitude range 20—50°N. The cycle is completed after ten months. The television equipment can therefore only function over a determined latitude range. Thus, the region from which information on cloudiness can be obtained (coverage zone) has definite latitudinal boundaries. There are also longitudinal boundaries for the coverage zone, however, for quite different reasons. Collection of data from the satellite can be accomplished only within that time interval during which the satellite remains within the direct line of sight for electromagentic radiations of the ground station. This interval depends substantially on the height of the orbit. For TIROS satellites it amounts to several minutes. For the same reason the ground station cannot receive information from orbits which do not enter within its line of sight. For a given receiving station part of the information will be lost entirely due to the limited data-storage capacity of the satellite. In order to get data from each satellite turn of given orbit, a sufficient number of ground stations and sufficient data-storage capacity of the satellite are required. The problem of ground station acquisition effectiveness has been analyzed in detail in /54/.

TIROS IX and TIROS X were placed into quasipolar, sun-synchronous orbits (see Table 1.3), meaning that the precession of the orbital plane is identical with the speed of revolution of the Earth around the Sun. In this case, the satellite will always cross the equatorial plane at the same time.

Auxiliary satellite-borne and ground-based equipment ensure data storing, transmission, reception and primary processing of information, as well as transmission of such command signals from the Earth that control the operation program of the TV cameras during the corresponding favorable time intervals, when the cameras are pointed toward the Earth.

To solve the above-mentioned programming problem charts were plotted showing the distribution of the illuminated areas within the coverage zone of the satellite. The TV cameras were pointed at the sunlit part of the Earth during approximately $^1/_3$ of the orbit period. The magnetic memory of the satellite permits the storage of TV signals and radiation data transmitted to the Earth as the satellite passes over one of the two ground stations (the radius of the receiving range is about 1,800 km). The stations were located on Wallops Island (Virginia) and on San Nicolas Island (California). Later, the station at Fairbanks (Alaska) was also used.

The outgoing radiation was measured continuously. However, recording duration cannot exceed 100 min (since for longer duration, the primary record on 1 hr tape starts to be erased). The ground station therefore received outgoing-radiation data over a time interval of 100 min preceding the commencement of data reception.

The photographs of cloud-cover distribution, 32 pictures in each set, were taken every 30 seconds. The overall length of a strip of successively photographed Earth-surface areas was about 9,600 km. In general, every 24 hours observational data were received from seven orbits (about 450 pictures of cloud distribution and seven tapes of radiation-data records). Data were transmitted by two 2-watt radio transmitters. Cloud-cover pictures and radiation data were immediately transmitted, or else stored for later transmission, upon command from TIROS IV at 235 MHz and 237.8 MHz, respectively. The satellites of the TIROS type will probably be used in the future as well, though with considerable changes in their operation program, design, and orbit parameters.

Much attention is now being paid to the development of a system for automatic transmission of television and infrared radiation data from the satellite to the ground stations, which may be located at any point on the Earth surface (for a polar orbit). With the above in view, TIROS VIII was equipped with an automatic data-transmission system permitting reception of data from the satellite by means of a relatively simple low-cost (about 50,000 dollars) ground station located at any point on the Earth.

A specific feature of the TV cameras utilized in this case is the capability of read-off scanning of the recorded image at a slow rate (approximately during 208 sec). Three pictures, each covering an area of about $2.5 \cdot 10^6 km^2$, can be received as the satellite passes within the coverage range of the station.

It is assumed /25, 71/ that wheel-type TIROS satellites put into polar orbits will be chosen for the U. S. A. routine weather-satellite service. The launching of the first experimental satellite of this type was planned for summer 1964 (which, however, did not take place) as a preliminary stage for routine launching intended for 1965. In fact, the first experimental satellite of the above series (TIROS IX) was launched on 22 January 1965.

TIROS IX differed from previous satellites of the TIROS series (the orbit inclination of which was 47° and 58°, respectively) and was considered as a prototype of the satellites intended for the establishment of an operational meteorological-satellite system called TOSS (TIROS Operational Satellite System). The choice of a wheel-shaped satellite was determined by the tendency to ensure the most favorable condition for obtaining the largest number of TV cloud-cover pictures in the absence of Earth stabilization of the satellite. After delivery into the orbit, the satellite must be oriented with the spin axis perpendicular to the orbital plane. The satellite, as it spins, would roll as a wheel along its orbit. In this case, one of the two TV cameras, mounted on the instrument container of the satellite at 26° to the vertical and pointing in opposite directions (one to the West and the other to the East), will permanently look straight down to the Earth. Systems for the automatic triggering of the cameras when their axes are closest to the vertical are under development (one of these systems consists of a computer connected to infrared horizon sensors). A device comprising a magnetic coil and accelerating rockets will also be provided in order to keep the spin axis of the wheel satellite in a horizontal position and to control the spin rate, which must equal 10 ± 0.5 rpm. Due consideration is given to increasing the reliability of the whole equipment.

It was assumed that the TOSS program would start in the fourth quarter of 1965 with two satellites of the same type as TIROS IX and TIROS X,

which would have a polar orbit with an altitude of about 1,350 km (the period of revolution would be 113 min). However, the TV cameras of the TOSS satellites would differ from their predecessors. According to one version there would be two cameras operating in an automatic picture-transmission system. Improved cameras of the type installed on the NIMBUS satellite would be utilized in another satellite. These cameras transmit an image consisting of 800 lines, thus giving a resolution of about 3 km for a single camera at zero nadir angle. From an altitude of 1,350 km such a camera would produce an image of a square with a side of 3,100 km, i.e., a single camera would provide global coverage every day.

It is believed that on implementation of the TOSS program, it is intended to keep two satellites of the above type in orbit simultaneously. With this in mind, measurements of the outgoing radiation are planned to obtain data on the radiation budget of the Earth. The development of a new camera, capable of operating both in a storage and immediate-data transmission schedule simultaneously, was scheduled for 1966. An infrared device for the collection of data on cloud-cover distribution at night is in the design stage. Two ground stations, at Hillmore Creek (Alaska) and on Wallops Island, will be used for the reception of basic information and for the transmission of data to the National Meteorological Satellite Center.

It is intended that TIROS XI be launched into an elliptical orbit with a perigee of about 500 km and an apogee of 43,000 km. TIROS XII, similar in design to TIROS IX, will be equipped with an automatic data-transmission system.

Let us consider now in detail three groups of devices used to measure outgoing radiation.

As was already mentioned, outgoing radiation in different spectral regions is measured by means of a five-channel radiometer having a small angle of view (5 × 5°) /10, 36/. Its optical axis is inclined to the satellite spin axis at 45° (the instrument has two viewing ports, one located at the end of the satellite cylindrical container and the second on its side surface). The radiometer scans the Earth surface thanks to the satellite orbital motion and its spin rate of about 10 rpm.

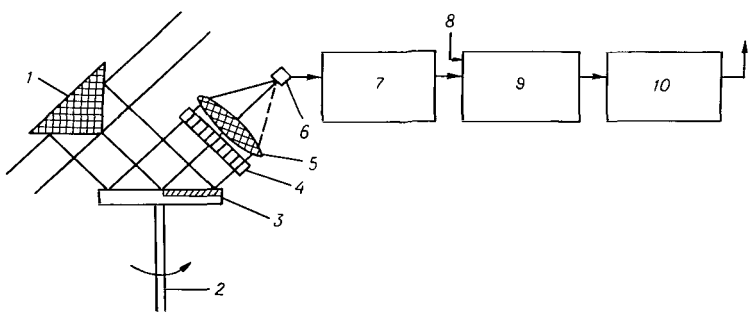

FIGURE 1.4. Block diagram of the five-channel radiometer:

1 — prism; 2 — chopper axis, parallel to satellite spin axis; 3 — chopper disk; 4 — light filter; 5 — lens; 6 — thermistor bolometer; 7 — preamplifier; 8 — other channels; 9 — tape recorder; 10 — transmitter.

The horizon sensor has a small angle of view (1.3 × 1.3°) and is oriented perpendicular to the spin axis. Its purpose is to generate pulses at the moment the Earth-space interface is crossed by the field of view of the instrument. The time interval between the pulses characterizes the satellite spin rate and the angle of inclination of the spin axis with respect to the local vertical.

The five-channel radiometer (Figure 1.4) operates by measuring the difference between the radiation fluxes from the Earth and space, entering its inlet apertures that face in opposite directions (the incoming radiation from space is practically zero).

The radiation is reflected by a silver-coated prism (1) onto the chopper disk (3), one half of which is black and the other half reflecting. Alternating the reflection of radiation from the reflecting half of the disk onto the thermistor bolometer (6) (by focusing lens (5)) with a modulation frequency of 44 Hz permits measurement of the absolute values of radiation flux from the Earth within the radiometer angle of view. For satellite positions when both inlet apertures are pointed toward space, zero-reading is recorded.

The radiometer consists of five separate radiation sensors, each provided with a corresponding light filter (filter (4) is placed in front of the focusing lens (5)). Only the driving motor is common for the five channels of the radiometer as it rotates all chopper disks at 44 rpm.

The five-channel radiometer is 15 × 11 × 11 cm in size and weighs 1.8 kg. Total power consumption of the device is 1 watt. The sensor, measuring radiation in the spectral region of 5.7—6.9μ, is provided with a germanium immersion-type focusing lens. The other sensors have conventional lenses.

TABLE 1.6. Characteristics of lenses, light filters, and regions of spectral sensitivity of the five-channel radiometer

Channel	Spectral region, μ	Focusing lens		Immersion-type lens	Light filter
		L_1	L_2		
1	5.7—6.9	Ge	Ge	Ge	Of the interference type
2	7.5—12	Ge	Ge	—	ZnSb, As_2S_3
3	0.2—5.5	Sapphir	BaF_2	—	
4	7.5—30	KRS-5	—	—	ZnSb
5	0.55—0.75	Sapphir	Quartz	—	Of the interference type

The characteristics of the optical system of the five-channel radiometer are given in Table 1.6. Spectral-sensitivity curves for each of the five channels can be found in /55/. It can be seen from data on channel 5 that it has a noticeable sensitivity also in the near-infrared spectral region. Figure 1.5 shows the radiometer. At the upper part of the instrument there are five pairs of receiving apertures.

Trouble-free operation of the five-channel radiometer in deep vacuum during a six-month period presents a difficult problem, requiring precautionary measures.

Amplifier circuits for both high and low gain bolometers are described in /10/. High gain was only used in the radiation detector operating in

the 5.7—6.9μ bandwidth, the energy here being much lower than in other spectral regions (for the same reason an immersion-type lens was used in this case).

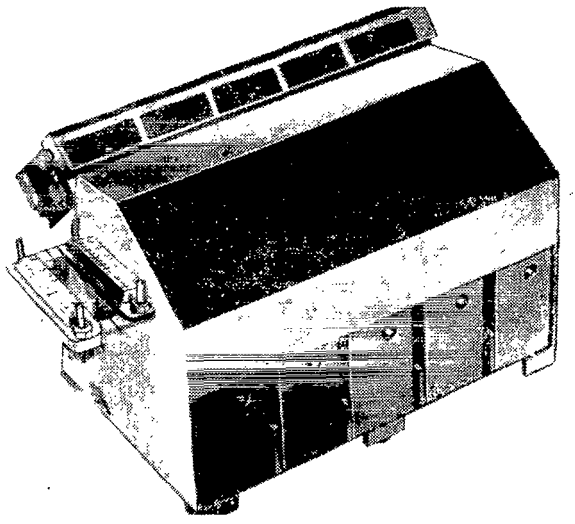

FIGURE 1.5. Exterior view of the five-channel radiometer

The main sources of measurement errors are drifts, caused by temperature variations, and distortions during telemetric data transmission (the temperature dependence of the radiometer readings is quite substantial; the temperature of the radiometer body was measured in order to introduce the necessary corrections).

The wide-angle dual-channel radiometer consists of two mylar cones with a mirror (aluminum-coated) inner surface, having a base of about 7.5 cm in diameter and a height of 5 cm. The top of one cone has a blackened resistance thermometer, while the second has a white-painted resistance thermometer (for short-wave radiations). In the first case, the temperature to be measured is determined by the magnitude of the integrated short- and long-wave radiations, and in the second case only by the short-wave radiation. Hanel /32/ developed the theory and method of processing the instrument readings. A compensation-measuring scheme was used to minimize and allow for the influence of the radiometer-body temperature on the readings. Calibration tests of the instrument revealed a significant nonlinearity and temperature dependence of the dual-channel radiometer readings. A noticeable aging of the white paint under the influence of ultraviolet radiation was found also to take place.

As was already pointed out, the infrared horizon sensor used in TIROS satellites serves two purposes: 1) determination and control of satellite spin rate (the spin rate is maintained at slightly above minimum value and may be increased by means of small solid-fuel accelerating rockets);

2) determination of the satellite spin-axis position, fixed in space with respect to the local vertical (this determination is necessary for a correct analysis of cloud-cover pictures, as well as for the interpretation of the radiation-sensor data).

Due to the nonuniform angular distribution of outgoing-radiation intensity, caused mainly by the influence of cloudiness (the great difference between the temperature of clouds and the Earth surface), the readings of the horizon sensors on TIROS I and TIROS II were not fully single-valued. However, after some experience in the interpretation of horizon-sensor records the discontinuities in the radiation field at the Earth-space interface could easily be identified, the above being imperative for determination of both the spin rate and the position of the fixed spin axis with respect to the local vertical.

A temperature-compensated thermistor bolometer oriented perpendicular to the spin axis is used as a radiation receiver in the horizon sensor. The bolometer uses a differential electronic circuit, only recording the passage from Earth to space and vice versa. The bolometer optical system carries on its inlet side a germanium lens, having good transmittance in the 1.8—20-μ waveband and an effective collecting surface of about 1.3 cm^2. The bolometer is placed very close to the lens. Due to the high refractive index of germanium, the germanium immersion lens focuses the radiant energy, incident on its upper surface, to the radiation sensor; the sensitivity of the system is thus increased.

The principal characteristics of the horizon sensor and a brief description of the bolometer electronic circuits are given in /58/. The authors of /10/ consider the measurements made by the horizon sensor to be insufficiently reliable. This is determined by two factors: 1) the differential-signal level depends on the duration of intersection (scanning) of the Earth-space interface, which varies considerably depending on the angle at which the detector viewing beam intersects the horizon line; 2) the radiation background of the Earth is extremely nonuniform (both by day and by night). Sometimes, the brightness gradients of the Earth background emission may be of the same order of magnitude as the contrast in brightness at the Earth-space interface which is probably due to the nonuniform cloud distribution.

The five-channel radiometer with three light filters translucent to infrared radiation was calibrated with the aid of two blackbodies, the temperature of one of which equaled the temperature of liquid nitrogen, and of the other varied over the range 250 to 320°K /46/. The instrument readings were expressed in terms of the effective blackbody temperature T_{BB}, taking into account the relationship

$$\overline{W} = \pi \overline{N} = \int_0^\infty W_\lambda (T_{BB}) \Phi_\lambda \, d\lambda. \qquad (1.6)$$

where $\overline{W}$ is the effective (equivalent) radiation flux of a blackbody (W m^{-2}); $\overline{N}$ is the effective (equivalent) intensity of this emission (W m^{-2} sr^{-1}); Φ_λ is a function characterizing the spectral sensitivity of the given radiometer channel.

Interpretation of the measurement results showed that the sensitivity of the radiometer varies with time (however, these variations could not be determined with sufficient reliability due to the absence of a sensitivity-

checking device on the satellite). In order to convert the radiometer readings to values of hemispherical outgoing-radiation fluxes, it is necessary to allow for the angular distribution of the intensity of outgoing radiation. The processing of measurement results is thus very complicated.

Analyzing data from TIROS VII, Bandeen et al. /11/ concluded that the total outgoing long-wave radiation can be determined most reliably by utilizing the readings of channel 2 of the radiometer. In this case, the total outgoing radiation F_∞ can be determined from the relationship

$$F_\infty = 0.986 \{ h_2(t) W - 0.141 [h_2(t) - 1] \}, \qquad (1.7)$$

where $h_2(t)$ is a function characterizing the relative change (decrease) of radiometer sensitivity (in this case $h_2(t)$ reached 1.25). The factor 0.986 was introduced to allow for the anisotropic angular distribution of the outgoing radiation; F_∞ is given in cal cm^{-2} min^{-1}.

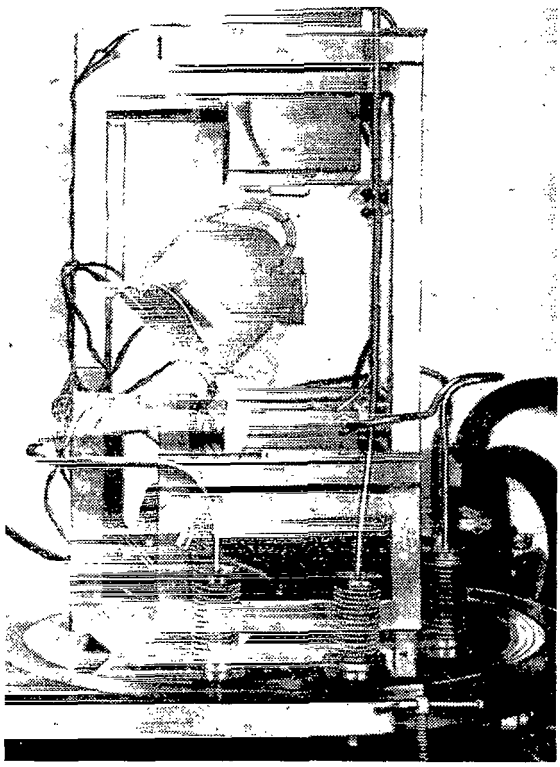

FIGURE 1.6. Setup for calibrating infrared sensors of the five-channel radiometer

Figure 1.6 shows a photograph of the calibration setup. The radiometer inlet apertures face the rectangular parts of the blackbodies, placed on both sides (above and below) of the radiometer. Those radiometer apertures that are placed at the lower base (bottom) of the satellite (the lower receiving apertures) face downward. The receiving apertures placed at the side walls of the satellite (the wall receiving apertures) face the opposite direction. The calibration setup is housed in a vacuum chamber (with the bell of the latter raised upward), which is evacuated to a high vacuum (10^{-6} mm Hg).

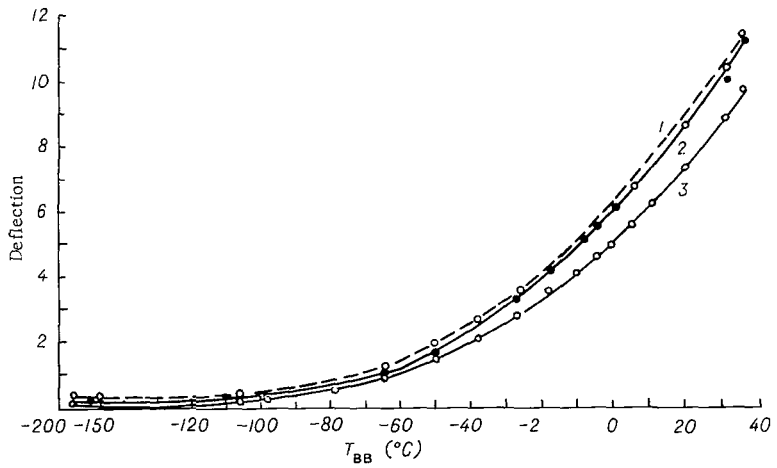

FIGURE 1.7. Calibration diagram for the detector that measures integrated long-wave radiation:

1 — temperature of the radiometer body is 25°C with the lower receiving aperture facing the blackbody of varying temperature; 2 — the same, with reversed position of the receiving apertures; 3 — the same as 1, but with a radiometer body temperature of 45°C.

Figure 1.7 shows the calibration diagram of the detector that measures the integrated long-wave radiation (channel 4). These data show not only the symmetric fluxes of the radiometer inlets but also a considerable dependence of the radiometer readings on the radiometer body temperature (during calibration one of the receiving apertures faces the blackbody which is at the temperature of liquid nitrogen and the other faces a blackbody of temperature that varies along the abscissa as T_{BB}).

Roche et al. /55/ also found a considerable temperature dependence for channel 5 (for an increase of temperature from 30 to 42°C sensitivity dropped by 40%).

The conversion factor of the five-channel radiometer for short-wave radiation (two light filters) is determined by calibration with a standard tungsten quartz lamp of 1.5 kW, introducing a correction for the temperature difference between the Sun and lamp.

In this case

$$\overline{W} = \pi \overline{N} = \frac{1}{R^2} \int_0^\infty J_\lambda \rho_\lambda \Phi_\lambda \, d\lambda, \qquad (1.8)$$

where R is the distance (in m) at which a standard lamp with a known spectral energy distribution J_λ ($W\,sr^{-1}\mu^{-1}$) is positioned so as to illuminate perpendicularly a white diffusely reflecting piece of paper of reflectivity ρ_λ.

Variations in the sensitivity of "short-wave" channels 3 and 5 of the radiometer during operation of the setup were so considerable and difficult to assess that it made the determination of the absolute values of outgoing short-wave radiation insufficiently reliable.

The value of the albedo of the Earth surface-atmosphere system can be evaluated with higher reliability. Let us introduce the effective solar constant

$$\bar{W}^* = \int_0^\infty S_{0,\lambda}\,\Phi_\lambda\,d\lambda. \tag{1.9}$$

where $S_{0,\lambda}$ is the spectral energy distribution of the extraterrestrial Sun spectrum. Assuming the field of reflected radiation to be isotropic and the reflectivity to be independent of the long-wave radiation, we obtain

$$A_S = \frac{\bar{W}}{\bar{W}^* \cos\zeta_\odot} R_a^2. \tag{1.10}$$

where $\zeta_\odot$ is the zenith distance of the Sun and R_a is the distance Earth-Sun expressed in astronomical units.

This formula needs an additional correction for the time-dependence of sensitivity. Analysis of TIROS VII data carried out in /11/ showed the radiometer reading for channel 5 (0.55—0.75μ) to be more reliable than for channel 3 (0.2—6.0μ). For the determination of the albedo we may thus use the relationship

$$A_S' = A_S h_S(t). \tag{1.11}$$

where A_S' is the corrected value of the albedo. The computation of the Earth albedo made in this way gave a value of 20.1%. The equation of the radiation balance (on the basis of measurements of outgoing long-wave radiation) yielded an albedo of 32.2%. Since the latter value is doubtlessly more correct we decided to introduce in (1.11) the correction factor $\frac{32.2}{20.1} = 1.6$.

Thus, expression (1.11) is replaced by

$$A_S' = 1.60 h_S(t) A_S. \tag{1.12}$$

Figure 1.8 shows a calibration setup with the lamp and radiometer placed below it on the left side. On its right side two diffusely reflecting screens are fixed to illuminate the receiving apertures of the radiometer (the direct light from the lamp does not fall onto the radiometer). Roche et al. /55/ carried out a more reliable calibration using an integrating hemisphere.

The two-channel radiometer fixed to a metallic frame was calibrated in a vacuum chamber with respect to a blackbody whose temperature varied

from -130° to +60°C, and also with respect to the Sun and a lamp (in this case the radiation from the diffusion screen was directed to the radiometer through a square window). The temperature of the frame varied from -10° to +60°C. Details of the calibration are given in /16/. The radiometer setup was built as a self-contained unit (independent of the television cameras) with the exception of the power source, antennas and some command units. A study /16/ presents block diagrams of the systems for recording, transmission, reception, and processing of information, as well as examples of oscillograms which show basic and auxiliary measurements (temperature and pressure inside the satellite, time marks, etc.).

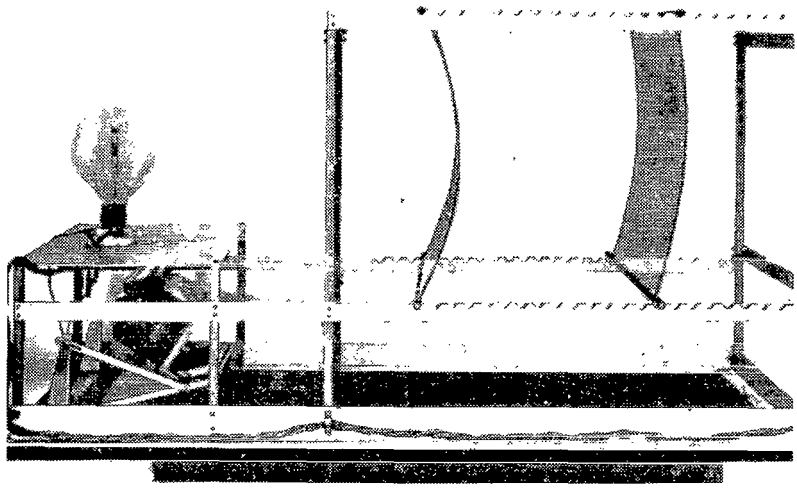

FIGURE 1.8. Calibration setup for short-wave radiation of the five-channel radiometer

Primary data processing is achieved with an IBM-7090 computer. The information is given out as tables, charts, and as special recording forms for further machine processing.

Alongside with calibrations, preflight tests of the main scientific and auxiliary installations on the meteorological satellites are also very important. Goldberg /26/ described the test programs and results of tests of the following satellite subsystems: 1) television cameras of high, medium, and low resolution; 2) command and control; 3) telemetry and radio beacon; 4) radiometers (five-channel scanning; two-channel wide-angle and single-channel radiometer horizon sensor); 5) spin-rate checking; 6) transducers of satellite position relative to the horizon; 7) altitude transducers; 8) magnetic control. In the first stage, independent tests were carried out of the various instrument packages, in order to obtain data on their characteristics and operating reliability. These tests were conducted so as to ensure as complete a simulation of working conditions as possible. Antenna tests were conducted to study the dependence of the emitted signal on the shape and orientation of the antenna. The isotropicity of the antenna

was determined with an accuracy of ±3 dB in the 236-MHz band and from +4 to -8 dB in the 108-MHz band (for the TIROS IV and VI the deviation was +4 to -8 dB in the 136-MHz band). Tests of the television cameras involved the determination of their spectral sensitivity and the dependence of obtained results on the brightness of the picture reproduced by the camera. Brightness calibration showed the cameras to be able to successfully operate from about 5,000 lux (lx); the level of saturation is reached at about $1.3 \cdot 10^5$lx.

Solar cells were calibrated both under laboratory and field conditions. In view of the large number of elements of the solar cells, a special "mass" tester was designed to check one thousand elements during 24 hours under varying operating conditions. This particularly refers to varying illumination conditions of the cells by the Sun for the standard day of 21 June over an altitude range from sea to orbit level. Each of the cell elements was also checked against the Sun by means of a pyrheliometer after their installation on the satellite.

A special setup was designed for the investigation of weight characteristics (mass distribution) of the satellite by giving the balanced satellite a load of about 40 g (corresponding to 80% of the rated load). A special testing method was developed for the speed-reducing device of the satellite that ensures a slowing down of the spin rate from 120 to 9—12 rpm. Although these tests were carried out only at atmospheric pressure, their results can be extrapolated to orbital conditions.

A special instrument package was developed for testing the influence of a magnetic field up to 200 gauss on the behavior of the satellite in orbital conditions (in this case extrapolation was also carried out from ground testing data). The satellite heat conditions were checked with a 120-cm vacuum chamber which simulated space environment for the instruments. For this purpose, a heat source was installed in the upper part of the chamber and [the satellite] was heated to 122°C while the chamber walls were cooled to -78°C. The satellite temperature was measured at 22 points. Of the environmental factors that affected the operating conditions of instruments in the satellite the following elements were taken into consideration: overloads, deep vacuum, thermal and radiational factors. Accidental vibrational stresses were checked over a range of from 20 to 2,000 Hz, exceeding approximately three times the expected overloads. When investigating sinusoidal overloads, vibration frequencies of 550 to 660 Hz were reached with overloads of up to 50 g. These are resonance vibrations that might be caused by firing the third stage of the rocket.

Results of testing TIROS I for accidental overloads up to 21 g showed the existence of some constructional defects and stressed the necessity of building a more rigid structure. Some insufficiencies of instruments were revealed during thermal vacuum tests. After the tests for overloads, all fastening elements, contacts, etc., were thoroughly checked.

A special test and calibration program was carried out on the firing range before launching the satellite. The task of these tests was mainly to check instrument operation and not quantitative calibration.

Till the moment of launching, the satellite underwent on the range daily inspection and operating tests (on the "yes-no" principle) of all instrument packages. Shortly before launching TIROS I these tests were carried out three times: 505, 195, and 95 minutes before launching. The achievement

of such an involved test program ensured successful operation of instruments after launch. The calculated data for the heat conditions of the satellite proved entirely reliable. However, the calculated precession of its spin axis owing to gravitational perturbations gave underestimated values since the values of the magnetic disturbances also proved to be appreciable. On the other hand (as was already shown), correct allowance for these disturbances makes the prediction of spin-axis orientation more reliable. After the data of TIROS I had shown the influence of the Earth magnetic field, this fact was taken into account in all subsequent satellites of this series for the orientation of the satellites by special magnetic coils. The instruments were of such a high dependability that, during the launching of the TIROS satellites, not one gave any trouble or failed. It should also be noted that all the launchings were carried out by the same crew. All TIROS satellites (except for the first) functioned more than three months, but even TIROS I operated on the whole satisfactorily as shown by an operator analysis during the first three months /18/. The first malfunctioning occurred on the 22nd orbit: the clock of the narrow-angle camera went out of action, but was subsequently restored after the 572nd orbit. On the 395th orbit, a temporary malfunctioning occurred in the magnetic recording system. After 1,000 orbits, serious troubles occurred in the telemetry system stopping the transmission of pictures from the wide-angle television camera, but the narrow-angle camera continued to transmit normally. Data reception from the satellite came to a halt at the end of the third month after launch. As we shall see later, the quality of cloud photographs obtained with the TV cameras on TIROS I was rather high.

The accuracy of the telemetry system was within 5%, with a deviation along the whole scale. The 40 parameters transmitted by telemetry were read off (and recorded) in 30 seconds. The unsatisfactory operation of the infrared horizon sensor was already mentioned above. The sensor recording the satellite-altitude with respect to the Sun worked very well. The same can be said of the control instruments of the satellite (excluding the above-mentioned electronic clock), which functioned normally during $2^1/_2$ months. So did the solar cells and NiCa batteries, ensuring stable voltage within the rated limits of 26—31 V. The satellite temperature was preliminarily regulated by selecting suitable time of launch and by allowance for radiation properties for its surface with heat exchange between its different elements. The thermal conditions were checked with temperature sensors (thermistors). Unexpectedly, considerable divergences between calculated and observed temperature values were observed during the first few days after launch which were explained by disturbances (precession) in the orientation of the satellite spin axis with respect to the calculated position.

The dynamic control subsystem functioned rather well. The perturbations in the spin-axis orientation observed soon after launch caused some difficulties at first, particularly in connection with the unsatisfactory operation of the attitude control system. Detailed analysis of the disturbance factors showed the main influence to be the interaction of the magnetic dipole of the satellite with the Earth magnetic field. Gravitational disturbances had a much smaller influence. After these facts were established, it was possible to calculate quite reliably the satellite attitude.

4. NIMBUS. The satellites of the NIMBUS series were planned in the U.S.A. for the coming years (the first satellite of the series was launched on 28 August 1964).

The scientific program of the NIMBUS satellites, details of which are dealt with in /28, 44, 47, 48, 51, 53, 62, 73, 74, 85/, mainly consisted in obtaining more detailed data on the global distribution of cloud cover to be used in routine weather forecasting. For this purpose, three television cameras were installed on the satellite to observe cloud distribution by day. One camera was to be directed at nadir and the other two at 35° to the vertical and perpendicular to the flight direction of the satellite. With such an arrangement of the cameras it is possible to photograph an area of 800 × 2,400 km, with an overlap of 10% between successive pictures. A completely overlapping strip of the Earth surface along a given orbit is obtained with 32 pictures (the capacity of the magnetic memory permits the recording of 64 pictures). The resolving power of the television camera at nadir is about 0.8 km (800 lines per frame), the exposure is 40 millisec; readout of 64 pictures takes 10 minutes. For surveying the cloud cover on the night side of the Earth a scanning infrared radiation sensor with a narrow field of view was used, giving information on outgoing nighttime radiation. This sensor has an angle of view of $8.4 \cdot 10^{-3}$ rad and a scanning rate of 0.67 rev/sec. Within a 122° angle (from one intersection of the horizon to the other) this instrument records 260 readings (width of scanned strip is 2,000 km and space resolution is 8 km).

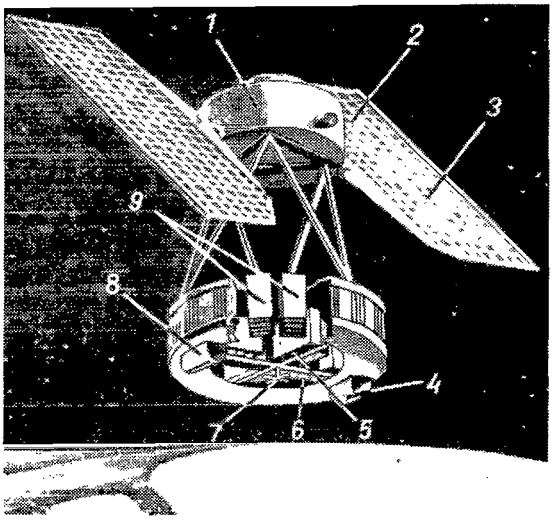

FIGURE 1.9. The NIMBUS satellite:

1 — monitoring compartment; 2 — horizon indicator; 3 — solar cells; 4 — infrared radiation sensors (high resolution); 5 — electrostatic camera; 6 — television camera; 7 — antenna; 8 — infrared radiation sensor (low resolution); 9 — electronic equipment.

The satellites of the NIMBUS series were to be launched in a quasipolar orbit of about 100° inclination (retrograde orbit) so as to satisfy the requirement for their passage over each point at the same local time (see section 2.1). The planned altitude above the Earth surface was about 1,100 km and the orbiting time 108 min (NIMBUS orbit differed from circular).

Figure 1.9 shows schematically the NIMBUS satellite consisting of two separated containers.

The satellite has the following dimensions: height about 2.5 m, diameter 1.4 m. The satellite weight was to be 220—240 kg, but actually reached 360 kg. The bottom of the lower container was pointed by day continuously toward Earth with the aid of a pneumatic mechanism and inertial wings (accuracy of orientation had to be approximately ± 1° with respect to the local vertical, and the speed of reorientation had to be not less than 0.1° per second).

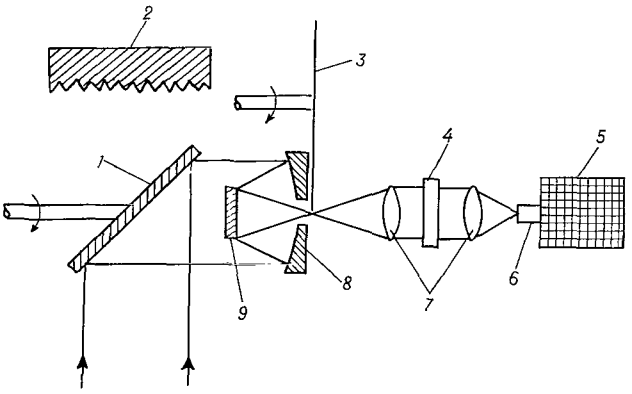

FIGURE 1.10. Block diagram of the scanning narrow-angle radiometer:

1 — scanning mirror; 2 — blackbody; 3 — modulator; 4 — light filter; 5 — condensing cooler; 6 — radiation sensor; 7 — lenses; 8 — primary mirror; 9 — secondary mirror.

The scientific equipment, including television cameras, radiation sensors of small, medium, and wide angle of view and some auxiliary apparatus, were located in the bottom part of the satellite. In particular, it was intended to install on these satellites two types of scanning radiometers /35, 37, 43/, one with high resolution and small angle of view, permitting the measurement of the angular distribution of outgoing radiation in the regions of the atmospheric window for the 3.5- and 4.2-μ bands (Figure 1.10).

The scanning of the Earth is carried out by scanning mirror (1) inclined at 45° with respect to the incident radiation (the direction of the scanning beam is perpendicular to the satellite speed vector, and scanning velocity is 44.7 rev/min). Space resolution of sensor scanning is somewhat lower than with television cameras, but by about one order of magnitude higher compared with the above-mentioned 5-channel radiometer on TIROS. The solid angle of the radiometer is 0.5° which, at an altitude of 920 km, ensures

a space resolution of about 8 km. The radiation sensor consisted of a selenium-lead photoresistance (6), cooled to -75°C. This radiometer permits the measurement of a radiation temperature over the 210—330°K range with a "noise" temperature of 1° for a radiation temperature of 260°K. The data of the high-resolution scanning radiometer were used to obtain information about the cloud cover on the Earth night side and also to track frontal systems and storms.

The NIMBUS satellites will continue to measure angular distribution of outgoing radiation with medium-resolution radiometers similar to the 5-channel radiometers used on the TIROS satellites, but with the use of scanning mirrors (Figure 1.11). However, the ranges of spectral sensitivity of the 5-channel radiometer will have to undergo some changes: instead of measurements at the atmospheric window of the 8—12-μ band, measurements in the 10—11-μ band are planned, and channel 3 is to measure radiations in the 14—16-μ band.

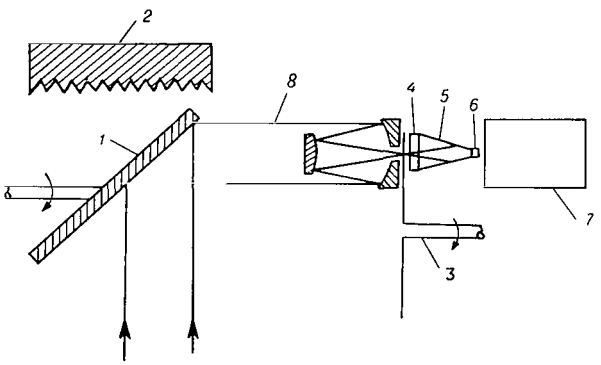

FIGURE 1.11. Block diagram of the medium-angle scanning radiometer:

1, 2, 3, 4, 6 — the same as in Figure 1.10; 5 — light conductor; 7 — pre-amplifier; 8 — focussing system.

A very important improvement in the radiometric instrumentation of the NIMBUS satellites compared with the TIROS series consists in the facilities for checking the radiometer sensitivity on board the satellite. Apart from the zero reading, which, on TIROS satellites, was taken with the receiving aperture pointed toward space, radiometers on NIMBUS will record during each scanning the emission from a standard blackbody of known temperature (see Figures 1.10 and 1.11). In order to check the radiometer sensitivity during the measurement of short-wave radiation it is intended to use direct solar radiation reflected by a special mirror in the direction of the radiometer optical axis.

The NIMBUS satellites are also intended for some new experiments. Thus, e.g., the use of an electrostatic camera will make it possible to house in a common unit both the television cameras and the recorders of the received television pictures. An infrared spectrometer is in the design stage for the spectral measurement of outgoing heat radiation with the

object of solving the problem of determining the vertical distribution of temperature in the atmosphere. Furthermore, it is also planned to use this instrument for the measurement of radiant heat emitted by the Earth surface-atmosphere system.

For the approximate determination of the vertical temperature profile in the layer from 1 to 500 mb it is intended to carry out measurements of outgoing infrared radiation in four narrow regions (width of 5 cm^{-1}) of the 15-μ band where carbon dioxide has a strong absorption band. Further, it is intended to measure outgoing radiation in the region of maximum absorption of the 15-μ band which will permit data to be obtained on the temperature at large altitudes of the atmosphere and on their basis to investigate the sudden warming-up of the stratosphere. In addition, in the first stage it is intended to measure the narrow spectral range (width 7 cm^{-1}) in the long-wave 11.1-μ band, where the atmosphere has maximum transparency for infrared radiation. These data permit conclusion on the global temperature distribution of the underlying surface.

Dreyfus and Hilleary /17/ described an infrared spectrometer intended for the solution of the above problems. The spectrometer has a field of view of 0.04 sr, which, at an altitude of about 1,000 km of the satellite, would cover at nadir a 200 × 200 km area of the Earth surface. The instrument was built according to the Fast-Ebert model and has a diffraction screen of 12.5 × 12.5 cm with 500 lines/cm. A 40-cm diameter focussing mirror (focal length of 62.5 cm) directs the outgoing radiation onto a two-sector disk of the modulator inclined at 45° to the spectrometer optical axis. As the disk is turned toward the entrance slit of the spectrometer the Earth radiation and space radiation (zero signal) fall alternately on it, since the instrument has a second entrance port pointed in a direction away from the Earth. The directly measured signal difference between Earth and space yields the outgoing radiation. In order to check the sensitivity during measurements the focussing mirror swings such that the radiation of an absolute blackbody of known temperature falls on the entrance slit (and in this case the difference between the blackbody and space radiations is measured).

The temperature of the blackbody is not kept constant and may vary from 0 to 60°C. After entering the entrance slit the incoming radiation falls on the collimator mirror and is then reflected by the diffraction grating back to the same mirror which focusses the spectrum onto the five exit slits corresponding to the number of investigated regions of the spectrum (four in the carbon-dioxide band and the fifth in the atmospheric transparent window). The simultaneous measurement of radiation flux in the five spectrum regions is made with immersion-type thermistor bolometers placed close to the exit slits. The spectrometer is designed to measure radiation fluxes in the range of 25—180 erg/cm^2 sec sr cm^{-1}, which corresponds to equivalent temperatures from -70 to +60°C. It is also intended to record changes in the radiation flux of at least 0.25 erg/cm^2 sec sr cm^{-1}, corresponding to a temperature variation of 0.25°C at an equivalent temperature of -70°C. The time constant is about 6 sec. The spectral calibration of the spectrometer may be checked by introducing an interference light filter into the light beam from the blackbody falling on the exit slit (the change in the expected signal level on using the light filter shows the shift of graduation along the wavelength). Laboratory tests of

the spectrometer showed it to be able to record temperature changes of about 0.2°C at room temperature. The next stage of work was the preparation of an instrument prototype which was used for measurements on balloons. Experimental balloon ascents with the spectrometer /39/, and subsequent processing of measurements, gave very promising results: the accuracy of determination of the vertical temperature profile over almost the entire altitude range reached ± 2°C.

Information on atmospheric temperature will be supplemented with data of measurements of outgoing radiation with interference spectrometers. At present, such an instrument is being built, on the basis of the Michelson interferometer /53/. The instrument will enable the measurement of spectral distribution of outgoing radiation in the long-wave region of the 5—20-μ band with a resolution of about 5 cm^{-1}.

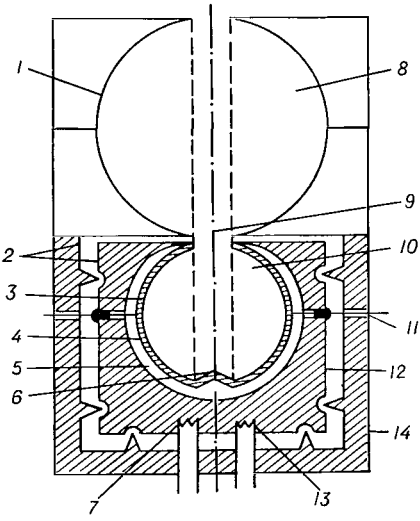

FIGURE 1.12. Satellite-borne pyrheliometer:

1,4 — black surface; 2 — polished metal; 3,6 — polished aluminum; 5 — polished gold; 7 — thermostat container; 8 — aperture (cold) blackbody; 9 — blackbody receiving aperture; 10 — blackbody band; 11 — wire sensors at temperature corresponding to that of blackbody; 12 — thermostat; 13 — thermostat heater; 14 — satellite body.

Hanel /38/ designed a satellite-borne pyrheliometer intended to measure the solar constant with an accuracy of at least ± 0.2%. Functionally, the instrument operates (Figure 1.12) using as a radiation sensor an absolute blackbody in the form of a thin spherical metal shell (10) with a circular opening (9), immersed in a constant-temperature vessel (12). The spherical shell (10) is attached to the inner walls of vessel (12) by thin wires (11) which serve at the same time to measure the temperature of the blackbody cavity. In order to keep the temperature difference between the blackbody and the constant-temperature vessel at a minimum, the latter is kept at a temperature corresponding to that of the blackbody, with the solar constant being 2 cal cm^{-2} min^{-1}. This means that the mentioned temperature difference must not exceed ± 4°C. The blackbody temperature is measured with a resistance thermometer having the form of a foil wound helically on the outer surface of the blackbody casing. The receiving aperture (9) of the blackbody is closed by the aperture (cold) blackbody (8) specially provided to permit installation of the pyrheliometer on the satellite.

A closer analysis of the basic theory of the instrument led Hanel to the conclusion that with a high quality of the blackbody and an accuracy of temperature measurements of blackbody (10), of the aperture blackbody (8), and of constant-temperature vessel (12) of about 0.1°, the measurement error of the solar constant should not exceed ± 0.2%. This estimate,

however, does not take into account the errors connected with transmission, reception and processing of information, so that the actual measurement errors will considerably exceed 0.2%.

The upper container of the satellite houses the maintenance installation and the infrared horizon sensor. The solar cell "paddles" are also fixed to this part. (In addition, the satellite has nickel-cadmium batteries.)

Reception and processing of data and the transmission of commands to the satellite are made from a ground station in Fairbanks, Alaska. The task of this station is also the immediate transmission of the television cloud-cover data to the National Meteorological Center. The station will also be able to receive during 24 hours data for the satellite time intervals between the 9th and 13th orbits.

In order to obtain more complete information on the different regions of the globe it will probably be necessary to use a station on the east coast of the U.S.A. The reception of data for the entire globe will only be possible by using a third station in Great Britain or northwestern Europe.

A study in /47/ presents a detailed account of the planned use of cloud data gathered by NIMBUS for routine weather forecasting.

As mentioned before, NIMBUS I was launched on 28 August 1964 at 0756 GMT into a quasipolar orbit (perigee 423 km, apogee 933 km) from the Vandenberg base in California. Because of the premature firing of the second carrier-rocket stage the satellite could not be placed into the calculated circular orbit of 925 km. This satellite was launched in order to solve the following problems /86/: 1) running-in of instrumentation directed toward the Earth surface in three coordinate axes; 2) the testing of the modified television system supplemented by an improved memory package and by facilities for the reception of information from the satellite from any point (automatic data-transmission system); 3) improvement of television pictures of the Earth surface and cloud cover compared with earlier pictures, supplemented with automatic data transmission; 4) testing of the high-angular resolution radiometer intended for the production of infrared pictures of the Earth surface and its cloud cover. Particular attention given to the running-in of the automatic television data transmission system is explained by the fact that by 1964 there were 62 ground stations and four privately-owned stations on the territory of the U.S.A. and in 12 other countries for the reception of satellite cloud photographs, using the automatic data-transmission system (this system functioned successfully already in TIROS VIII). In conformity with the tasks /75/ the scientific instrumentation of NIMBUS I consisted of a wide-angle television camera providing round-the-clock automatic data transmission; three television cameras with an angle of view of 37° having a data-storage capacity of 64 pictures; a high-angular resolution infrared scanning radiometer sensitive in the 3.4—4.2-μ band (for the reception of infrared cloud pictures and the Earth surface). The coverage angle of the radiometer is 0.45°, corresponding to a diameter of an area on the Earth surface of 3.3 km at perigee and of 7.3 km at apogee /21/. The rotation period of the scanning mirror (scanning was made in a plane perpendicular to the velocity vector) is 1.341818 sec (during this time the satellite travels 9.1 km). One of the three television cameras points to nadir and the other two at an angle of 35° to nadir, relative to the plane perpendicular to the movement of the satellite. Three simultaneous photographs cover a strip of 2,400 km along the parallel and

of 800 km along the meridian. A sequence of pictures is received at intervals of 91 sec, and overlaps 10%; 32 photographs provide a complete coverage of the illuminated part of the Earth surface along a given orbit. Photographs for adjoining orbits, which are shifted approximately by 25°, overlap with the preceding photographs in increasing steps in the direction of the pole. The television cameras give pictures consisting of 800 lines, with a resolution varying from 0.8 km at nadir to 2.4 at the borders of the picture (at perigee). Exposure is 40 millisec., and the time of picture recording by the electronic vidicon tube is 6.5 sec. The time of transmission and reception of these pictures is 10 minutes. A detailed description of the NIMBUS I equipment is given in /49, 53/.

Data from satellites are received at stations in Gilmore Creek near Fairbanks, Alaska and at Rosman, North Carolina, the second of them being auxiliary. The use of only the first station for an orbit height of about 1,000 km permits data reception in minimum time (from 5 to 10 minutes) for 10 orbits out of 14. At the auxiliary station it is possible to receive data for two out of the remaining four orbits. For the reception of information from all orbits it is intended to either set up a third receiving station or to increase the altitude of the satellite.

The heat-control facilities on the satellite keep the satellite temperature constant within 25° ± 10°C with much less temperature fluctuations of its various components.

The study in /75/ describes the testing of the satellite and its different instrument packages; the study also contains computed values of shock-resistance tests and a description of the satellite maintenance equipment. The silicon solar cells of the satellite with a total "reception" area of approximately 13.2 m^2 generate 300 W and serve for recharging the nickel-cadmium batteries.

The power required for the satellite facilities is 206 W in daytime and 170 W at night. On request, it may be increased to 400 and 342 W, respectively. The unit time of the satellite is provided by a quartz-stabilized frequency and by a corresponding succession of commands and time marks. The satellite telemetry provides for two ways of data transmission: 1) preliminary storage and readout on command from the Earth and 2) immediate [nonstored] transmission.

Already several hours after launch of the satellite NIMBUS I on 28 August 1964 the first television pictures of the Mexican Gulf cloud cover could be received /19/. On 31 August, NASA reported that the photographs received from NIMBUS during the preceding days made available data on cloud cover at night for nearly the whole Earth surface. Because of the high eccentricity of the orbit the quality of television pictures varied during changes in the orbit height (the parameters of the television cameras are optimum for a height of 900 km). The satellite is pointed to the Earth with respect to three axes by means of two scanning infrared horizon sensors, sensitive in the 12—16-μ band, a rough sensor facing the Sun, and by a gyrostabilization system. The calculated accuracy of orientation for all three axes is ± 1°. The actual accuracy was, according to /53/, ± 2° for pitch, ± 3° for roll, and ± (8—10°) for yaw. A forced change in orientation (attitude) of the satellite in space was carried out by eight freon-gas fuelled nozzles and three electric motors with flywheels. The motors were used for small attitude corrections. Larger corrections are obtained with

gas nozzles, whose operation is controlled by a satellite-borne computer. On 21 September 1964, a malfunctioning in the system of solar-cell orientation occurred, as a result of which the output capacity of the solar cells in NIMBUS I sharply dropped, and from 23 September the satellite instruments stopped operating. According to Tepper /75/, the volume of meteorological information received during the total satellite life period can be seen from the following figures: the number of separate cloud-cover pictures obtained by the improved television cameras was 12,137. Simultaneously, 1,931 transmission cycles were relayed by the automatic data transmission system. The high space-resolution radiometer (for infrared photographs) worked for 6,881 minutes.

During 3.5 weeks the satellite instruments worked satisfactorily.

Press /53/ presented some interesting data on the operation of the various instrument packages on NIMBUS I.

The subsystems of the ground command stations and the time-control services worked quite satisfactorily. During more than 612 hours, 9,025 commands from the satellite ground time-control subsystems provided an accuracy deviating not more than one second from the standard ground time. Loss (or gain) of the satellite clocks during the last 300 orbits was 70 millisec during 24 hours. (During the first 60 orbits it was 100 millisec per 24 hours.) During the entire time of the successful operation of the scientific instruments there were 25 malfunctionings in the working of the time-control subsystems, two of which were connected with the operation of the ground command stations.

Some insignificant shortcomings were observed in the operation of the telemetry subsystems. Thus, e. g., in the first checking after satellite launch there was a recurring disturbance of the synchronization system. The data-reception center at Gilmore Creek noticed some effect of the aurora borealis on the reception conditions.

On the whole, the improved television subsystem worked excellently. However, some small overexposures over the equator and underexposures near the poles resulted from a not quite satisfactory operation of the automatic [camera] shutter control.

The placement of the satellite into a noncalculated orbit led (because of the low perigee) to incomplete coverage of the Earth surface, which made the use of cloud-cover photographs less effective. On the other hand, the actual elliptic orbit made it possible to obtain useful pictures with different space resolution. The television cameras of the automatic data-transmission and storage system worked troublefree.

The photographs obtained by the improved high-space-resolution television camera were of excellent quality. One of the series of these pictures taken on the 272nd orbit is shown on Photograph 2.9. A particular feature of the processing of these television data from NIMBUS I was the automatic overlay of a coordinate grid (dotted line) on the photographs. The space resolution of photographs near nadir reached 0.8 km.

The pictures obtained with the TV camera operating within the automatic photograph transmission system were less sharp (the space resolution was in this case intentionally much lower). An example of such pictures is shown in Photograph 1.1.

The infrared instrumentation worked excellently, permitting the transmission and reception of cloud-cover distribution on the Earth night side;

the pictures thus obtained were of a quality similar to that of the television photographs (see Photographs 2.6, 2.7, and others).

1.5. GLOBAL METEOROLOGICAL OBSERVATION SYSTEM

After an outline of basic information on meteorological satellites, let us dwell on the problem of future creation of a global observation system in which satellites constitute one of the main links.

Doubtlessly, at present, meteorology and physics of the atmosphere have entered a period of revolutionary transformations. This is connected to a considerable extent with the development of new research methods. On the one hand, in the years to come, the possibility will first arise to establish a data collection system on a global scale suited to synoptic observation times; on the other hand, the considerable achievements in computer techniques permit the design of high-speed electronic computers equipped with large storage capacities. This, in turn, makes it possible to achieve efficient data processing and interpretation for weather and climate forecasting. Although many processes determining the change of weather and climate (in particular the extremely diversified quantitative characteristics) still remain unclear or insufficiently investigated, there is no doubt that improved quality of primary meteorological information and more efficient methods of processing and interpretation should lead to a considerable improvement of forecasts.

In our opinion, a global meteorological system should be based on the following component elements.

1. The totality of conventional observation methods (ground-based meteorological, aerological, radiometric, ship- and aircraft-instrument observations, etc.).
2. Meteorological satellites.
3. A system of meteorological sounding balloons [and radiosondes], ocean buoys, and ground-based automatic weather stations operating jointly with satellites that carry out collection and transmission of the received data.
4. Manned orbiting space laboratories.
5. Lunar meteorological stations for Earth observations.

There is no need to dwell more in detail on the role of conventional observation methods. However, it should be noted that despite the creation of new systems for gathering meteorological observations, the importance of conventional methods still remains considerable. This is particularly shown by the experience in the use of satellite data. Of course, these methods will have to be improved, especially in terms of automation of measurements, data reception, and transmission.

Basically, the importance of data obtained from meteorological satellites was outlined in section 1.3: such data are a very important supplement to conventional meteorological information. If such information is lacking (as over oceans or regions of difficult access) the role of satellite data is unique.

Since, for the time being, satellite information only contains data on cloud-cover distribution and outgoing radiation, it has been suggested to combine conventional automatic measurements carried out by sounding balloons and ocean buoys with the collection and transmission of data on pressure, temperature, and wind parameters for inaccessible areas by means of satellites to ground stations. For such cases, it was also proposed to use the satellites to track the movement of sounding balloons and buoys in order to determine wind direction and force and also ocean currents. In this connection the third, above-mentioned component element of the global observation system becomes of interest. Let us call this component global automatic meteorological station (GAMS) (among these we also include Arctic and Antarctic automatic meteorological ground stations).

At present, there exist several projects for GAMS /40, 65, 77/. Let us dwell at first on the characteristics of the GAMS proposed by a group of French experts /40/. This system comprises: sensors for basic meteorological elements (atmospheric pressure, temperature, etc.) installed on sounding balloons or ocean buoys equipped with pulse-type receiver-transmitters; satellites carrying a receiver, a transmitter and a medium-capacity memory; ground stations for the precise determination of satellite ephemerides and for data reception from the satellites (on request). The ground stations will also carry out processing and transmission of the received information to the consumers.

The satellites shall fulfill the following functions: 1) identification and interrogation of GAMS; 2) determination of GAMS coordinates at different time intervals for the computation of wind parameters or ocean currents; 3) reception and storage of information received from GAMS; 4) if possible, primary processing of these data; 5) transmission of data received from GAMS to ground stations.

Basically two types of meteorological satellites can be used: 1) those intended for the reception of meteorological data by instruments carried aloft by the satellite; 2) those serving as means for the collection of meteorological information from ground, ship, or aircraft observations, automatic meteorological stations and transosondes, as well as for their subsequent transmission to ground stations. As pointed out before, satellites of the first type cannot obtain sufficiently detailed information on various meteorological elements, and this determines the necessity for satellites of the second type and a corresponding observation system. Apparently, one should consider as most successful the planned complex NIMBUS B satellite intended to operate simultaneously both as an ordinary meteorological satellite and a communications orbiter. Such a multi-purpose satellite may also carry out collection and transmission of information from meteorological rockets launched at the moment the satellite passes over them. The most important meteorological elements to be measured should be pressure, temperature, and air humidity, temperature of the ocean surface, as well as wind direction and velocity. When launching radiosonde balloons wind velocity can be determined from data on the drift of the radiosonde in the atmosphere.

An important point is the choice of the orbit and the optimum number of satellites carrying out collection and transmission of information from the GAMS. The necessity for a circular orbit is obvious. The orbital altitude should not be too large: to determine by triangulation the coordinates of

moving GAMS it is important to foresee the possibility for measuring the distance from the satellite to each of the GAMS twice or even more, as the case may be, provided the position of the satellite changes during this time appreciably. The authors of /40/ proposed a system of three satellites with identical circular orbits at an altitude of 1,800 km and inclined at 83° to the equator. These satellites should be phase-shifted between each other by a distance equal to a third of an orbit. In this case the interrogation of the whole GAMS could be made during one circuit (122 minutes). If we proceed from the necessity of establishing contact by each satellite with the ground stations on each orbit, it will be sufficient to have two stations in the Arctic Circle. Such stations are already in existence (Fairbanks in Alaska and Kiruna in Sweden).

There is much interest in using three synchronous satellites whose orbital planes would be spaced 120° apart. In this case the collection and transmission of data from GAMS, placed between 70°S and 70°N, could be made during a few minutes, i. e., almost simultaneously (but the above-mentioned triangulation determinations would be very difficult). In such a case the polar regions could be covered by two satellites circling the Earth in the same polar orbit at a height of about 800 km but placed in opposite phases (this permits collection of information in about 50 minutes only).

Despite limited use of such satellites (data collection and transmission), they would have to fulfill the same technical requirements as does a communication satellite: their weight should be about 50 kg, the power source (solar cells and NiCd batteries) should produce at least 30 W. The telecommunication system should ensure telemetric communication with the ground stations and remote control of their performance as well as the site location and interrogation of the GAMS. The problem of providing a telecommunication link between satellites and ground stations basically presents no serious difficulties because of the possibility of using powerful and highly-efficient ground stations (an important limitation would only be the duration of reception of information from the satellites which does not exceed several hundred seconds).

The situation is quite different regarding the communication link between the satellite and the GAMS, requiring an optimum choice of a whole series of parameters and, above all, possibly a large network of GAMS, permitting a sufficiently great volume of information to be collected at unit time with a high accuracy in determining the satellite-GAMS distance. It is also very important to find the most effective solution to the problem of interrogation of GAMS and subsequent transmission of received information to ground stations (choice of a particular interrogation system, frequency bands, codes, etc.). The simplest solution to these problems consists in the performance of collective calls and the successive reception of data from each GAMS. However, such a solution presents certain technical difficulties (the principal difficulty being the accurate successive connection of a large number of GAMS for the transmission of data after reception of the general interrogation signal from the satellite). Another possibility is the individual interrogation of each GAMS. A third variant to be considered is the collective interrogation of those GAMS situated in the receiving zone.

Taking into account the limited data-storage capacity of the satellite and the necessity of transmitting a very great volume of data, it would

TABLE 1.7. Comparative characteristics of GAMS systems

Characteristics	SWAMI	DATACOL	IRLS	STROBE	BP	EOL (experimental)	EOL
			Satellites				
Number	3	1	1	1	3	1	3
Type of orbit	Circular	Circular	Elliptical	Elliptical	Circular synchronous	Circular	Circular
Inclination of orbit to equatorial plane, deg	90	90	90	90	0	5	Three different inclinations
Period of revolution, min	1,338	106	100	100	1,436	98	105
Mean height, km	2,200	1,100	800	800	36,000	750	1,000
Coverage of Earth surface, %	100	100	100	100	90	40	100
Power requirements, watt	80	25					10–20
Type of interrogation	Programmed	Programmed	Programmed			At regular intervals	
Type of storage		Recording					
Volume of control memory, bits		65,000	640				
General volume of memory, bits		1,000,000	20,000				
Number of GAMS interrogated on each orbit	5,000	600	20				
Number of interrogations of each PAMS during one orbit	1	2	2	3.3	Continous interrogation of each GAMS		
Duration of interrogation of each GAMS, sec	0.25	3	3				

Sounding balloons							
Number	3,200	300	Up to 2048 GAMS each of which sends a report consisting of 1,000 bits	300—600	0	1,000	2,000
Volume of data sent per interrogation, bits		50					
Mean power, watt	0.54	0.25		0.150			
Automatic ground stations							
Number	600	200		0	0	0	1,000
Volume of information sent per interrogation, bits		300					
Buoys							
Number	1,200	700		0	300	20	1,000
Volume of information sent per interrogation, bits		300			100		
Mean power, watt	0.74						

doubtlessly be expedient to carry out part of the processing already on board the satellite. This refers in particular to the coordinates of the GAMS and the subsequent determination of wind velocity.

Sounding balloons and ocean buoys that could be used in a GAMS are still in the design stage; different alternatives and suggestions still need practical tests. Besides difficulties in the optimum choice of such characteristics as power consumption and sources, service life, etc., a critical aspect in the use of such balloons is their potential danger to aviation. The practical realization of GAMS depends to a large extent on problems of state sovereignty, since in the past such sondes have been used for intelligence purposes.

Up till now several variants of GAMS have been proposed. Table 1.7 shows on the basis of data from /40, 65, 77/ comparative characteristics of those systems which were prepared by different organizations in the U.S.A. (SWAMI, DATACOL, IRLS, STROBE, BP) and France (EOL).

According to the DATACOL project developed by the Electronic Systems Sylvania Company, the location of 80% of sounding balloons can be made with an accuracy of ±18.4 km, and that of 99% of buoys with an accuracy of ±9 km. The maximum communication distance GAMS-satellite would be 3,400 km for balloons and 1,900 km for buoys.

With the IRLS project prepared by NASA, the location error for GAMS will reach ±12.5 km, although in principle it may be reduced to ±90 m (the actual limit reached is apparently ±500 m).

The STROBE project, of the Joint Committee for Meteorological Satellites, proceeds from the possibility of using a combination of meteorological satellites and data-collecting systems basically used for the DATACOL project but with some modifications.

The BP project of the U.S. Weather Bureau plans the use of an anchored buoy system (this eliminates the difficulty of determining the coordinates).

The French EOL project, suggested by the Center of Cosmic Research, intends in its experimental stage to use one satellite and a system of 1,000 sounding balloons and 20 buoys. On the whole, the project is designed for the reception of worldwide meteorological data every few hours. The sounding balloons are to measure atmospheric pressure (accuracy about ±1 mb), temperature (±0.5°), vertical gradient of temperature (error ±0.1° for a gradient calculated per 100 m; the measurement of the vertical gradient is made possible by using a second temperature sensor suspended from the balloon at a distance of 100 m). The buoys measure atmospheric pressure (accuracy ±1 mb) and air temperature (±0.5°).

The global meteorological observation system SWAMI was developed at Stanford University /65/ and envisages the use of three satellites in circular orbit at a height of about 2,200 km, shifted at 120° (it is intended to orient the satellites in space by gravitational stabilization). The source of meteorological information is provided by 3,200 sounding balloons drifting at 5.4 and 15 km, by 1,200 free-drifting ocean buoys, and by 600 ground-based automatic weather stations. The method proposed in /65/ for determining the coordinates of the GAMS assure a determination accuracy of about 2—3.5 km. With such a three-satellite system one could obtain a global coverage of meteorological data every 2 hours, data being received by one station at Fairbanks, Alaska. A feature of the SWAMI

project is the possibility of partial processing of data on board the satellite and their transmission to ground stations in a digital form. It is proposed to choose the method of individual interrogation of each GAMS from the satellite.

The table does not mention the GHOST project /77/ which was developed at the National Meteorological Center, U.S.A. The project is based on the use of 1,000—1,500 sounding balloons drifting at six atmospheric-pressure levels (700, 500, 300, 200, 100, and 30 mb). The first operation tests of such balloons which are actually transosondes are planned after the launch of NIMBUS B.

Despite some differences in details of implementation, the characteristics of the GAMS system are as follows: the satellites collect meteorological information from sounding balloons, buoys, ground automatic stations and observatories, aircraft, large and small ships as well as from rocket-borne sondes (collection system of rocket data RODACOL). This body of information is transmitted to ground stations which pass it on to computing centers for final processing, weather forecasting and dissemination to consumers. According to a resolution of the World Meteorological Organization (WMO) on the project of a World Weather Service, most data processing and dissemination will be carried out by three World Meteorological Centers (WMC's): Moscow, Washington, and Melbourne. From these WMC's information is to be sent to Regional Meteorological Centers (RMC's) and then to the consumers. Of course, the successful operation of such a global weather service is only possible with adequate communication channels between its linking elements and with high-capacity computing techniques, permitting routine data processing.

Of the five components of GAMS enumerated at the beginning of this section, the most important are doubtlessly the first three. The role of manned orbital laboratories and lunar meteorological observatories, although very important, can only be an auxiliary one.

In the following we shall briefly dwell on the possibilities of a manned orbital complex laboratory. It must first be stressed that the participation of man in the realization of scientific programs on board a satellite has the following advantages: 1) the possibility of deliberate choice of the object to be investigated: 2) supervision (monitoring) of the complex instrumentation; 3) the testing of new instruments (and the checking of calibration which is difficult to carry out automatically); 4) visual observations.

The latter advantage is particularly attractive from the meteorological point of view. Obviously, if on board the spaceship there is a qualified synoptist, this will permit "visual" synoptic analysis and prognosis on the basis of cloud-cover observations. Storm fore-warnings are one example of these possibilities.

Experience in the interpretation of data on outgoing radiation recorded by meteorological satellites of the TIROS series showed convincingly the importance of man observations from space. Let us remember that the quality of all measurements of outgoing radiation proved to be partly or entirely unsatisfactory because changes in the sensitivity of the radiometers with time were not checked (the causes of these changes are not yet quite clear). In the future, it will, of course, be possible to check automatically

instrument sensitivity, which will considerably improve the reliability of data. However, the presence of an observer on board the satellite will be a decisive contribution to the discovery of the causes of this phenomenon. Moreover, an observer on board the satellite has the possibility of making a timely analysis of the meteorological situation and selecting particular objects for investigation. Thus, data received from TIROS revealed the existence of aerosol layers in the upper troposphere (apparently cirrus clouds) which are optically ineffective in the visible region of the spectrum and do not appear on television cloud pictures, but are an intensive source of infrared heat radiation. Naturally, the choice and investigation of such sporadic phenomena are better made with direct participation of an observer on board the satellite. In the future, space engineers and technicians will also be able to carry out preventive inspection and maintenance of satellite installations.

There is already much experience in the taking of cloud photographs by astronauts and in the subsequent analysis of the data obtained. A photo-album /4/ contains 20 color photographs taken by Soviet astronauts. Similar photographs were obtained by American astronauts.

Thus, astronauts James McDivitt and E. W. White (Gemini 4) took black-and-white photographs (using various light filters) as well as color photographs (the mean height of the spacecraft was about 160 km). The pictures /50/ clearly prove the possibility of a detailed analysis of convective (cellular) cloudiness when the convection cell varies in size between 40 and 80 km. The high resolution of the pictures thus obtained, the availability of color photographs, the possibility of photographing the same cloud system at successive small intervals, all these are important advantages of photographs taken by astronauts compared with the television cloud pictures obtained from meteorological satellites.

Cloud photographs taken earlier by American astronauts from piloted spacecraft confirmed the assumption that the optimum spectral range of sensitivity of the television tube must be limited to the long-wave band of 5,000—7,200 A. According to projects the series of Gemini (including Gemini 4 to 7) flights were intended to continue the program of photographing the cloud cover.

Photographs from spacecraft were taken with a camera having a view angle of 35° and equipped with 5 casettes of 70-mm films each containing 55 frames 60 mm^2 in size (only one casette was intended for cloud photography). About 12 cloud features were chosen as objects to be photographed: vortices, cellular clouds, thunderstorm clouds, shadows of cirrus clouds, tropical storms, and others. During flight, the astronauts received instructions as to which objects to choose, based on an analysis of the synoptic situation, using conventional and satellite meteorological observations. Altogether McDivitt and White shot about 200 frames, of which about 100 were of meteorological interest. The pictures were taken over southern U.S.A., Africa, South Asia, and over the oceans within a belt between 32.5°S and 32.5°N. Objects of 18—24 m in size can well be distinguished on these photographs (roads, airfields, ship wakes, etc.). Because of the relatively low altitude of the spacecraft in a number of cases, the astronauts could not identify characteristic spiral-shaped storm-cloud systems. In /50/, seven photographs are shown and commented on.

In particular, the absence of large cumulus clouds over vast regions of the oceans is pointed out. For subsequent flights, it is intended that preference be given to consecutive pictures (during several orbits) of one and the same cloud system.

A lunar meteorological observatory (LMO) for Earth observations, proposed in /5/, can play an important role in the visual or instrumental tracking of large-scale atmospheric processes. The absence of atmosphere on the Moon makes it possible to carry out on the lunar surface measurements of the solar constant; data of such measurements are instrumental for solving the problem of the Sun's influence on weather. Of considerable interest are also measurements of the Earth outgoing radiation by instruments mounted on the Moon surface. This same installation could also be used to measure components of the radiation budget on the lunar surface and the radiation temperature of the latter. Since the Moon always turns the same face toward the Earth it suffices to set up on its surface a single station for the observation of the entire Earth surface and atmosphere as the Earth rotates about its axis. Of particular meteorological interest will be the transmission of infrared pictures of the Earth which will permanently supply data on the distribution of cloud cover, temperature, and height of cloud tops, as well as information on the temperature of the underlying surface in cloud-free regions for the whole hemisphere.

Undoubtedly, much time will be required before the above-described global system of meteorological observations will be operative. However, it is important that at present various components of this system already exist or are in the stage of development and testing.

Bibliography

1. Kondrat'ev, K. Ya. Meteorologicheskie issledovaniya s pomoshch'yu raket i sputnikov (Meteorological Research by Rockets and Satellites). — Leningrad, Gidrometeoizdat. 1962.
2. Kondrat'ev, K. Ya. Meteorologicheskie sputniki (Meteorological Satellites). — Leningrad, Gidrometeoizdat. 1963.
3. Kibel', I. A. Vvedenie v gidrodinamicheskie metody kratkosrochnogo prognoza pogody (Introduction to Hydrodynamic Methods of Short-Range Weather Forecasting). — Moskva, Gostekhizdat. 1957.
4. Kondrat'ev, K. Ya., M. G. Kroshkin, and V. G. Morachevskii. Nasha planeta iz kosmosa (Our Planet as Seen from Space), Edited by Acad. E. K. Fedorov. — Leningrad, Gidrometeoizdat. 1964.
5. Kondrat'ev, K. Ya., V. L. Gaevskii, V. N. Konashenok, and A. I. Reshetnikov. Lunnaya meteorologicheskaya observatoriya dlya nablyudenii Zemlii (A Lunar Meteorological Observatory for Observation of the Earth). — Kosmich. issled. Vol. IV, No. 2. 1966.
6. Luders, R. D. A Satellite Network for Continuous Zonal Survey. Rocket Technique. — ARS Journal, Vol. 31, No. 2. 1961.

7. Mullamaa, Yu. R. Otrazhenie pryamoi radiatsii ot poverkhnosti morya (Reflection of Direct Radiation from the Ocean Surface).— Izvestiya AN SSSR, Seriya geofizicheskaya, No. 8. 1964.
8. Mullamaa, Yu. R. Atlas opticheskikh kharakteristik vzvolnovannoi poverkhnosti morya (Atlas of Optical Characteristics of the Agitated Ocean Surace).— Institut fiziki i astronomii AN ESSR, Tartu. 1964.
9. Malkevitch, M.S., V.M. Pokras, and L.I. Yurkova. Ob izmereniyakh radiatsionnogo balansa na sputnike "Eksplorer-VII" (Measurement of the Radiation Budget with EXPLORER VII).— ISZ, No. 14. 1962.
10. Astheimer, R.W., R. De Waard, and E.A. Jackson. Infrared Radiometric Measurements on TIROS II.— J. Opt. Soc. Am., Vol. 51, No. 12. 1961.
11. Bandeen, W.R., M. Halev, and J. Strange. A Radiation Climatology in the Visible and Infrared from TIROS Meteorological Satellites.— NASA Goddard Space Flight Center, X-651-64-218. August 1964.
12. Butler, H. Meteorological Satellite Data Systems.— NASA Goddard Space Flight Center, X-650-24-241. September 1964.
13. Bandeen, W.R. Earth Oblateness and Relative Sun Motion Considerations in the Determination of an Ideal Orbit for the NIMBUS Meteorological Satellite.— NASA, Techn. Note, D-1045. July 1961.
14. Bignell, K.J. Heat Balance Measurements from an Earth Satellite — An Analysis of Possibilities.— J. Roy. Met. Soc., Vol. 87, No. 372. 1961.
15. Bandeen, W.R. and W.P. Manger. Angular Motion of the Spin Axis of the TIROS I Meteorological Satellite Due to Magnetic and Gravitational Torques.— J. Geophys. Res., Vol. 65, No. 9. 1960.
16. Bandeen, W.R., R.H. Hanel, J. Licht, R.A. Stampfl, and W.G. Stroud. Infrared and Reflected Solar Radiation Measurements from the TIROS II Meteorological Satellite.— J. Geophys. Res., Vol. 66, No. 10. 1961.
17. Dreyfus, M.G. and D.T. Hilleary. Satellite Infrared Spectrometer. Design and Development.— Aerospace Eng., Vol. 21, No. 2. 1962.
18. Final Report on the TIROS I Meteorological Satellite.— NASA, Techn. Rep., R-131, Wash. 1962.
19. Fritz, S. Pictures from Meteorological Satellites and their Interpretation.— Space Science Rev., Vol. 3, No. 4. 1964.
20. Fritz, S., A.W. Johnson, V.J. Oliver, and R.L. Pyle. Synoptic Use of Meteorological Satellite Data.— U.S. Weather Bureau. April 1965.
21. Fujita, T. and W. Bandeen. Resolution of the NIMBUS High-Resolution Infrared Radiometer.— J. Appl. Met., Vol. 4, No. 4. 1965.
22. Glaser, A.H. and F.E. Christensen. TOSS: TIROS Operational Satellite System.— Astronaut. and Aerospace Engin., Vol. 1, No. 3. 1963.

23. Gobetz, W. F. Satellite Networks for Global Coverage.— J. Astronaut. Sci., Vol. 8, No. 4. 1961.
24. Goetze, D. Accuracy and Range of Infrared Horizon Sensors as Limited by Detector Noise.— ARS Journal, Vol. 32, No. 7. 1962.
25. Glaser, A. H. and F. E. Christensen. TOSS: TIROS Operational Satellite System.— Astronaut. and Aerospace Engin., Vol. 1, No. 3. 1963.
26. Goldberg, E. A. TIROS Preflight Testing and Postlaunch Evaluation.— J. Spacecraft and Rockets, Vol. 1, No. 4. 1964.
27. Good Pictures from NIMBUS I.— Flight Internat., Vol. 86, No. 2896. 1964.
28. Goldberg, I. L., L. Foshee, W. Nordberg, and C. E. Catoe. NIMBUS High-Resolution Infrared Measurements.— The Univ. of Michigan, Inst. of Science and Techn. 1965.
29. Holmes, J. Satellite Weather Forecasts Now Sure to be Reality.— Missil. and Rock., Vol. 7, No. 11. 1960.
30. Hall, F. F., Jr. and C. V. Stanley. Infrared Satellite Radiometry.— Appl. Optics, Vol. 1, No. 2. 1962.
31. Hanel, R. A. and D. Q. Wark. TIROS II Radiation Experiment and its Physical Significance.— J. Opt. Soc. Am., Vol. 51, No. 12. 1961.
32. Hanel, R. A. Low-Resolution Unchopped Radiometer for Satellites.— ARS Journal, Vol. 31, No. 2. 1961.
33. Hanel, R. A. and W. G. Stroud. The TIROS II Radiation Experiment.— NASA, Techn. Note, TND-1152. October 1961.
34. Harper, M. H. Optical Instrumentation for TIROS.— Appl. Optics, Vol. 1, No. 2. 1962.
35. Hanel, R. A. Radiometric Measurements from Satellites.— Aerospace Engin., Vol. 21, No. 7. 1962.
36. Hanel, R. A. and W. G. Stroud. Infrared Imaging from Satellites.— Journal SMPTE, No. 69, p. 25. 1960.
37. Hanel, R. A. Radiometric Measurements from Satellites.— IAS Papers, No. 83. 1962.
38. Hanel, R. A. An Instrument to Measure the Solar Constant from a Satellite.— NASA, Techn. Note, D-674. April 1961.
39. Hilleary, D. T., D. Q. Wark, and G. James. An Experimental Determination of the Atmospheric Temperature Profile by Indirect Means.— Astronaut. and Aeronaut., Vol. 205, p. 489. 1965.
40. Lajeunesse F., G. Millardet, and J. Turrière. Global Meteorological System Using Satellites.— Lab. Central de Telecommunications Paris Pl. 185A, Issue 1. 5 April 1965.
41. Meteorological Satellites.— Space and Astronautics, Vol. 41, No. 1. 1964.
42. Meteorological Satellite Systems of the Future.— Stanford Res. Institute J., Vol. 7, No. 2. 1963.
43. Maykut, E. S. An Experiment in Objective Nephanalysis Using Proposed HRIR Satellite Infrared Radiation Data.— J. Appl. Met., Vol. 3, No. 3. 1964.
44. Meteorological Observations with NIMBUS I.— Trans. Amer. Geophys. Un., Vol. 46, No. 1. 1965.
45. Neiburger, M. and H. Wexler. Weather Satellites.— Sci. Amer., Vol. 205, No. 1. 1961.
46. Nordberg, W. Physical Measurements and Data Processing.— The International Meteorological Satellite Workshop, Abstr. and Fig. of Lectures, Wash. 13—22 November 1961.

47. NIMBUS Data Utilization Plan.— Meteor. Sat. Labor. Rep., No. 6, Wash. 1961.
48. NIMBUS Weather Satellite-More Data from NASA (U.S.A.).— Interavia Air Letter, No. 4889. 1961.
49. NIMBUS I High-Resolution Radiation Data Catalog and User's Manual, Vol. 1.— Goddard Space Flight Center. 15 January 1965.
50. Nagler, K.M. and S.D. Soules. Cloud Photography from Gemini 4 Spaceflight.— Bull. Amer. Met. Soc., Vol. 46, No. 9. 1965.
51. Nordberg, W. The NIMBUS I Meteorological Satellite — Geophysical Observations from a New Perspective.— Science, Vol. 150, No. 3696. 1965.
52. Powers, E.F. TIROS Operations. — Astronaut. and Aerospace Engin., Vol. 1, No. 3. 1963.
53. Press, H. The NIMBUS Meteorological Satellite Program.— Goddard Space Flight Center. July 1965.
54. Pyle, R.L. and S.F. Singer. Dependence of Ground-Station Acquisition Effectiveness on Geographic Location and Satellite Orbit.— J. Spacecraft and Rockets, Vol. 2, No. 3. 1965.
55. Roche, J.J., A.J. Drummond, and D.T. Hilleary. Report on the Test and Calibration of a TIROS III Five Channel Radiometer.— The Eppley Lab., Inc. 6 April 1964.
56. Suomi, V.E. The Radiation Balance of the Earth from Satellites.— IGY Annals, Vol. 6. 1958.
57. Schnapf, A. TIROS I, II and III, Design and Performance.— IAS Papers, No. 79. 1962.
58. Schwartz, F. and W. Chou. Infrared Circuits in TIROS Weather Satellite.— Electronics, Vol. 34, No. 39. 1961.
59. Sternberg, S. and W.G. Stroud. TIROS I Meteorological Satellite.— Astronautics, Vol. 5, No. 6. 1960.
60. Sternberg, S. and A. Schnapf. Performance and Evaluation of Satellites TIROS I and TIROS II.— ARS Journal, Vol. 31, No. 11. 1961.
61. Stroud, W.G. The TIROS Satellite.— The International Meteorological Satellite Workshop, Abstr. and Fig. of Lectures, Wash. 13—22 November 1961.
62. Stampfl, R. and H. Press. NIMBUS Spacecraft System.— Aerospace Engin., Vol. 21, No. 7. 1962.
63. Schnapf, A. TIROS: The Television and Infrared Observation Satellite.— J. Brit. Interplant. Soc., Vol. 19, No. 9. 1964.
64. Schnapf, A. The Performance of the TIROS IX Wheel Satellite.— Intern. Astronautical Congress, Athens. September 1965.
65. Talbert, L.R. editor. Stanford Worldwide Acquisition of Meteorological Information.— Stanford Univ., Dept. of Aeronautics and Astronautics. 1964.
66. TIROS II Radiation Data Users' Manual.— NASA Goddard Space Flight Center. 1961.
67. TIROS III Radiation Data Users' Manual. Supplement.— NASA Goddard Space Flight Center. December 1963.
68. TIROS V Orbit Elliptical, but Photos Good.— Aviation Week and Space Tech., Vol. 76, No. 26. 1962.
69. The TIROS IV Meteorological Satellite.— Trans. Amer. Geophys. Un., Vol. 43, No. 2. 1962.

70. The International Meteorological Satellite Workshop. Facts and Figures on TIROS Satellites, Wash. 13—22 November 1961.
71. TIROS Selected for Weather Net.— Aviation Week and Space Techn., Vol. 80, No. 6. 1964.
72. TIROS Operational Satellite System.— Mariners Weather Log., Vol. 8, No. 4. 1964.
73. Tepper, M. The NASA Meteorological Satellite Plans for the Future.— Intern. Met. Sat. Workshop, Abstr. and Fig. of Lectures, Wash. 13—22 November 1961.
74. Tepper, M. Meteorological Satellites. Space Exploration (Ch. 13).— N.Y., McGraw-Hill. 1964.
75. Tepper, M. Meteorological Satellite Flight Programs.— NASA, Washington, D.C. 1964.
76. Tepper, M. and D.S.Johnson. Toward Operational Weather Satellite Systems.— Astronaut. and Aeronaut., Vol. 3, No. 6. 1965.
77. The Feasibility of a Global Observation and Analysis Experiment.— National Academy of Sciences, Washington. 1965.
78. Wexler, H. and D.S.Johnson. Meteorological Satellites.— ICSU Rev., Vol. 3, No. 2. 1961.
79. Wexler, H. Meteorology.— N.Y., McGraw-Hill. 1961.
80. Weather Satellites: Operational System Planned.— Flight, Vol. 8, No. 2751. 1961.
81. Weinstein, M. and V.E.Suomi. Analysis of Satellite Infrared Radiation Measurements on a Synoptic Scale.— Month. Weath. Rev., Vol. 89, No. 11. 1961.
82. Wormser, E.M. and H.A.Morris. Infrared Navigation Sensors for Space Vehicles. Progress in Astronautics and Rocketry, Vol. 8. Guidance and Control.— Acad. Press. 1962.
83. Weather Satellites Create Problems on the Earth.— Industr. Photogr., Vol. 13, No. 7. 1964.
84. Widger, W.K.Jr. and C.P.Wood. An Explanation of Limitations to the Coverage Provided by TIROS.— Weatherwise, Vol. 14, No. 6. 1961.
85. Weather Satellite System due by 1965—66.— Aviation Week and Space Techn., Vol. 77, No. 1. 1962.
86. Wendel, C. NIMBUS: A Launch Due Friday.— Electron. News, Vol. 9, No. 445. 1964.

Chapter 2

THE USE OF RADIATION DATA OBTAINED WITH METEOROLOGICAL SATELLITES

The collection of data on the principal meteorological elements (atmospheric pressure, temperature and humidity, cloudiness, etc.) in the lower atmospheric layers by means of satellites is a very complicated task. In any case, the only source of information that can be obtained with satellite-borne instruments is the radiation emitted by the Earth surface and the atmosphere, since no other physical characteristics can be directly measured from the satellite.

For this purpose, the use of television and photography seems to be the simplest way. Television and photographic pictures of the cloud cover, combined with satellite data on global observations, are extremely useful in the analysis of laws governing the various weather processes. This is why satellite nephanalysis has now gained widest acceptance as the basic method for the practical application of satellite meteorological data to weather forecasting.

At the same time, it is obvious that the potentialities of satellite meteorology are much wider. Using data on the global radiation field of the Earth it is possible to considerably supplement information provided by television and photography.

In the present brief survey, the author intends to dwell on those results of interpretation of radiation data obtained by meteorological satellites that may be used for immediate practical application.

Chapter 1 presented various problems connected with methods of measuring the outgoing radiation. For such problems, conversion of sensor data on outgoing radiation to physical values (e.g., fluxes of outgoing radiation) is extremely important. For more details, the reader is referred to the monograph /1.2/* and a number of articles published in /38/.

2.1. THE RADIATION BALANCE OF THE EARTH SURFACE—ATMOSPHERE SYSTEM

One of the basic problems of long-range weather forecasting is the necessity to take into account the energy budget of large-scale atmospheric processes. This involves a detailed study of the laws that govern heat

* In the following, when referring to bibliographical sources of other chapters the first figure denotes the number of the chapter.

distribution caused by radiative processes: the Earth receives energy only from the Sun and loses it into space by radiation alone. In this context it is important to study the global distribution of the radiation balance R_S of the surface—atmosphere system which can be expressed as follows:

$$R_S = Q_0(1 - A_S) - F_\infty. \qquad (2.1)$$

Here Q_0 is the inflow of solar radiation from outside the atmosphere; A_S is the albedo of the surface—atmosphere system; F_∞ is the outgoing long-wave radiation. Since the magnitude of the solar constant that determines the value of Q_0 is sufficiently well known, it suffices to have experimental data on the albedo and the outgoing radiation, which can only be obtained with the aid of satellites.

Since, as pointed out in Chapter 1, the accuracy of satellite measurements of outgoing radiation is not yet sufficiently reliable, results of theoretical calculations are still of great value.

Results of theoretical calculations. The components of the radiation balance of the surface—atmosphere system were first calculated at the beginning of the century, and their records can be found in various monographs /19—21/.

Here, we shall consider only results obtained during recent years. Apart from the comprehensive study of Fritz /53/ numerous papers of a very specific character were published /1, 18, 22, 29, 36, 39, 40, 50/, and the components of the radiation balance of the surface—atmosphere system were calculated in detail /57—60, 63, 66, 67/.

1. Albedo of the Earth surface—atmosphere system. Since the value of the solar constant is known with sufficient accuracy, the basic problem of determining the incoming part of the radiation balance — the absorption of solar radiation — consists in determining the values of the short-wave radiation reflected by the planet. Knowing the reflected radiation, the absorbed radiation can easily be found as the difference between the solar constant and the reflected radiation. On the other hand, a knowledge of the planetary albedo permits the independent determination of the absorbed radiation.

The most reliable way to determine the absorbed radiation (and hence the Earth albedo) is the direct measurement of this value from rockets or satellites. However, there is also an indirect method of determining the albedo, based on photometric measurements of the lunar earthlight. Since the brightness of this light, i.e., the brightness of the dark part of the Moon, only illuminated by the sunlight reflected from the Earth, considerably depends on the Earth albedo, the measurement of this brightness can serve to determine the Earth albedo. In the USSR, such a method was used in studies by Fesenkov /40/, Barabashev /3—4/, Orlova /36/, Markov /29/, and Kazachevskii et al. /18.23/.

Unfortunately, the measurement of the Earth albedo from the earthlight brightness of the Moon only yields values for the visible range of the spectrum. In order to find the total albedo over the entire range of the long-wave solar spectrum (which is of particular interest for the investigation of the Earth radiation balance), it is necessary to calculate the albedo figures for the ultraviolet and infrared regions of the spectrum.

This is why the above-mentioned observation results can only play an auxiliary role. As a basis for the determination of the albedo of the surface—atmosphere system we may use the results of calculating the share of solar radiation scattered by clouds, reflected from the cloud-free part of the atmosphere and from the Earth surface in the global albedo. Fritz /53/ carried out a most detailed calculation of the global albedo. He obtained a mean value of 35% and showed that it is the radiation scattered by clouds that mainly contributes to the global albedo.

The share of radiation scattered from the cloud-free atmosphere and reflected from the Earth surface is relatively small (these conclusions of course only refer to determination of the mean global albedo). Calculations made later by Bagrov /1/ yielded figures not far from the above value: between 37 and 40%. Houghton /60/ obtained a value of 35%.

Kano /64/ calculated the albedo in the ultraviolet, visible and infrared regions of the spectrum for a Rayleigh atmosphere and found a mean global albedo of 6.6% in the absence of clouds. The corresponding value, obtained earlier by Fritz /53/, was 8%.

TABLE 2.1. Global albedo for a Rayleigh atmosphere

Spectral region	Albedo, %	
Ultraviolet ($\lambda < 0.4\,\mu$)	23	1.9
Visible (0.4—0.7 μ)	9.6	4.3
Infrared ($\lambda > 0.7\,\mu$)	0.75	0.75
Integrated	6.6	6.6

Table 2.1 shows the distribution of albedo over the regions of the spectrum. The extreme right-side column shows the value of the albedo calculated in relation to the value of the integrated solar constant (data of this column show the share of various regions of the spectrum in the albedo).

Fedoseeva /39/ made the first attempt to calculate the geographical distribution of the albedo of the surface—atmosphere system. For the calculation of the albedo A_S she used the formula

$$A_S = (A_1 + A_2)(1 - n) + (A_3 + A_2')\,n. \qquad (2.2)$$

where A_1 is the albedo of the underlying surface; A_2 is the albedo of the atmospheric layer extending from the surface to the cloud base; A_3 is the albedo of the clouds; A_2' is the albedo of the atmosphere above the clouds; n is the degree of cloudiness.

In this case, the albedo of both the underlying surface and the clouds is determined in relation to the total radiation reaching the Earth surface or the clouds. The albedo of cloud-free atmospheric layers (A_2 and A_2') is found in relation to the flux of extra-atmospheric solar radiation. It is obvious that in this way the determination of the Earth albedo is not very

accurate since in the first case (when determining A_1 and A_2) the modification of the albedo by the atmospheric layer is not allowed for. Since the radiation flux reflected from the Earth surface or from the clouds is considerably weakened by the above-lying atmospheric levels, it is clear that computations with formula (2.2) result in overrated values of A_S. This explains why the mean global albedo of 41% obtained by Fedoseeva exceeds all other values mentioned above.

Notwithstanding the inaccuracy of formula (2.2), the geographical distribution of the albedo of the surface—atmosphere system calculated by Fedoseeva is doubtlessly of great interest. Figure 2.1 shows the geographical distribution of the mean annual planetary albedo. Here, it is interesting to note the relative stability of the albedo values in the equatorial area (latitudes 0—40°) where it has minimum values (35—40%). The albedo increases with latitude, reaching about 60% within 70—80°N and 60—70°S. This is due to the increase in cloudiness and to the persistence of snow and ice cover with latitude. The distribution of albedo isolines in northern latitudes has a sharper zonal character than in the South (in the European USSR, the curvature of the isolines depends on the persistence of the snow cover increasing from the West to the East). On the other hand, the non-zonal distribution of albedo in the equatorial regions is caused by the nonuniform distribution of the cloud cover and nonuniform underlying surface. Lowest albedo is found in particular regions with the minimum cloud cover and over oceans (in low latitudes the albedo of the ocean is less than that of the land). Maximum albedo noticed over the Sahara is caused by the high reflectivity of the desert surface. Similar maxima found over South America and central Africa are caused by the higher cloudiness of these regions compared with the surrounding territories.

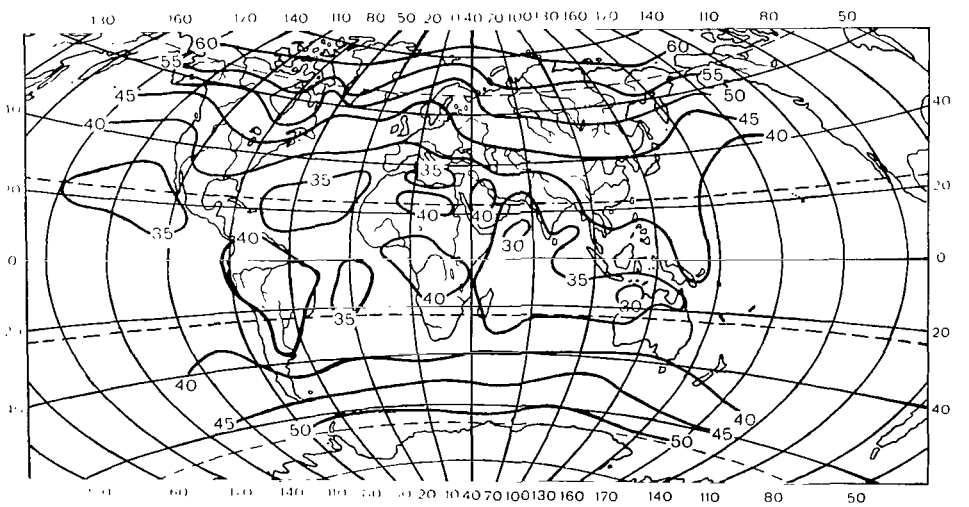

FIGURE 2.1. Global distribution of the mean annual albedo of the Earth surface-atmosphere system (according to Fedoseeva)

In general, the geographical distribution of the Earth albedo varies with the months. Thus, maxima are found in July near the equator (0—10°N) while minima are observed in the latitude belts 10—20°S and 20—30°N, increasing with latitude. Maps for January and February very clearly show in the Northern Hemisphere the heterogeneity of the underlying surface (especially at the boundary between the ice-free oceans and land areas covered with snow). However, in this case too, formula (2.1) yields slightly overrated values for the influence of nonuniformity of the underlying surface and nonuniform distribution of cloud cover on the Earth albedo.

The most accurate calculations of the ableda of the surface-atmosphere system were made by London /66/ and Vinnikov /15/.

TABLE 2.2. Seasonal distribution of the components of the mean global albedo for a cloudless sky (Northern Hemisphere)

Albedo components	Winter	Spring	Summer	Autumn
Reflection from surface	9.0	7.4	5.0	6.0
Atmospheric scattering	8.3	7.6	8.5	7.4
Total global albedo	17.3	15.0	13.5	13.4

Table 2.2 presents data on the seasonal distribution of global albedo for the Northern Hemisphere /66/. As may be seen, the share of solar radiation backscattered by the cloud-free atmosphere is almost stable throughout the year (the same is valid for the latitudinal variation of backscattered radiation). Such a small variation may be explained by the fact that small [optical] air masses occur over a large part of the Earth during summer (for large solar altitude) and throughout the year (for small solar altitude) in combination with large contents of water vapor. The converse relationship is also valid. Therefore, the optical thickness of the atmosphere (and consequently the intensity of backscattering) depends only slightly on the seasons or latitude.

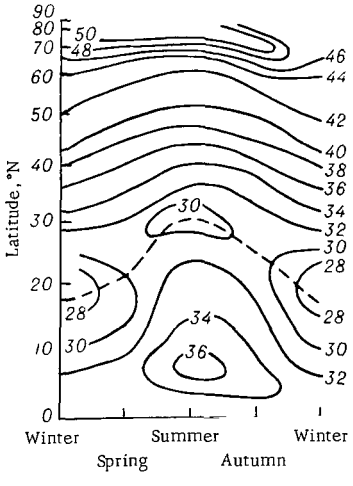

FIGURE 2.2. Mean latitudinal distribution of albedo (%) of the Earth-atmosphere system per season

The reflection of solar radiation from the Earth surface increases with decreasing solar altitude. This circumstance, as well as the prevalence of an ice cover in high latitudes and in winter, increases the amount of radiation reflected by the Earth surface. Therefore, the global albedo increases somewhat in the cold half of the year and in high latitudes. The mean annual global ableda in cloud-free areas is 14.7%.

In the presence of clouds the main component of global albedo is solar radiation reflected from clouds. This reflection varies within very wide

limits, and therefore it is the main cause of variations in the Earth albedo. The share of solar radiation reflected by clouds in the mean global albedo is 24%. According to London /66/, the total global albedo, calculated with allowance for the mean cloudiness of the entire globe, is 35%. It is interesting that the mean global albedo has almost no seasonal variation, being in winter 35.6% and in summer 36.3%. This is apparently so because the increase in cloudiness during the transition from winter to summer compensates for the decreasing albedo of the Earth surface.

Figure 2.2 shows the mean latitudinal albedo of the surface-atmosphere system during the seasons, according to London /66/. Here, as in Figure 2.1, minimum albedo occurs in the subtropics (the region of minimum cloudiness where albedo decreases to 27%). This minimum is displaced to the North during summer and shifts toward the equator during winter. The increase in albedo toward the North, observed during the entire year up to 60—70°N, is caused by the increase in cloudiness and by backscattering of solar radiation from the surface (the latter increases with decreasing solar altitude toward the North; the influence of these two factors is particularly manifest in winter). The summer maximum of albedo in the equatorial region (10—15°N) is caused by the northward shift of the thermal equator accompanied by increase in cloudiness. A small decrease in albedo during summer at 35—50°N is caused by the northward displacement of the main cloud systems of the temperate latitudes during this season.

Vinnikov /15/ used the following formula for computing the albedo of the surface—atmosphere system:

$$A_S = f(\alpha_1)(1 - n) + \alpha' n, \qquad (2.2')$$

where $f(\alpha_1)$ is the variation of A_S with the value of albedo of the Earth surface α_1 for clear sky; α' is the mean value of the albedo of the surface—atmosphere system for an overcast sky.

An analysis of the existing data showed that $f(\alpha_1)$ may be expressed as $f(\alpha_1) = 0.66\,\alpha_1 + 0.10$ with $\alpha' = 0.47$.

Applying formula (2.2'), Vinnikov calculated the albedo and the outgoing short-wave radiation for 260 points evenly distributed over the Earth, and plotted world maps for the geographical distribution of the albedo and the outgoing radiation. These maps confirm the above conclusion on the overrated values of albedo obtained by Fedoseeva /39/. According to /15/, the mean annual values of albedo for the surface—atmosphere system vary over the sunlit part from 30 to 50%. The qualitative characteristics of the geographical distribution of albedo determined in /15/ somewhat differ from the data reported by Fedoseeva; this may be explained by the less reliable data used by Fedoseeva.

2. The outgoing long-wave radiation. Theoretical calculations of the heat radiation emitted by the surface—temperature system have a long history. A survey of research in this field is presented in /21/. The most convenient method for computing emitted heat radiation is the use of a radiation nomograph. This method was used in /22, 37, 57—60, 66, 68/. The absence of data on the vertical stratification of the atmosphere over sufficiently high altitudes (e.g., data on the concentration

of water vapor in the stratosphere) makes it impossible to calculate the true outgoing radiation. In /22/, the outgoing radiation was assumed to be identical with the ascendent radiant-heat flux at the tropopause level, and it was shown that this assumption did not introduce an error exceeding 6% of the calculation accuracy. Similar results were obtained in other studies (e.g., /57/).

Figure 2.3 shows the results of calculations by London /66/ on the mean latitudinal distribution of the ascending radiant-heat flux at the tropopause level for the four seasons of the year over the Northern Hemisphere (under mean cloudiness conditions). The figure clearly shows a summer maximum of outgoing radiation at nearly all latitudes which mainly depend on the maximum temperatures in summer. The latitudinal dependence of outgoing radiation has maximum values in the subtropics because of the existence of minimum cloudiness in this area (the outgoing radiation increases with decreasing cloudiness). The magnitude of the outgoing radiation varies from 0.20 (in polar regions) to 0.36 cal cm^{-2} min^{-1} (in the subtropics).

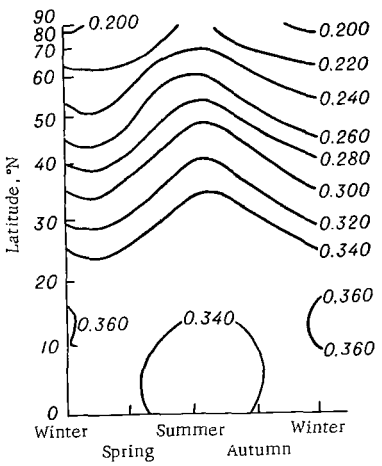

FIGURE 2.3. Mean latitudinal distribution of outgoing heat radiation at the tropopause level for the four seasons of the year over the Northern Hemisphere (cal cm^{-2} min^{-1})

It must, however, be stressed that these figures are only extreme values. Obviously, the variability limits of instantaneous values must be broader. According to /57/, in tropical maritime atmosphere without clouds $F_{\infty} = 0.394$ cal $cm^{-2}min^{-1}$. For other cases, with high and cold clouds, the outgoing radiation decreases to 0.14 cal $cm^{-2}min^{-1}$ This conclusion is supported by results of experimental investigations which we shall consider later.

3. Radiation balance. Very thorough calculations of the radiation balance were made by London /66/ and Vinnikov /13/. However, these computations only refer to the mean latitudinal distribution of the radiation balance and its components.

Table 2.3 shows, according to /66/, the mean values of the seasonal distribution of the radiation balance and its components for the Northern Hemisphere.

Table 2.3 shows the existence of a relationship between the different components of the radiation balance. In the input part of the radiation balance, the main contributor is absorption of short-wave radiation by the Earth surface. Far less radiation is absorbed by the atmosphere, and still less by clouds.

Accordingly, the greatest loss of short-wave radiation is caused by its backscattering into space by clouds and atmosphere. All components of absorbed and reflected radiation exhibit an annual variation cycle. Thus, e.g., the radiation flux, scattered by clouds and atmosphere, is highest in summer because of maximum extraterrestrial insolation at this time of

the year and of increasing cloudiness. Radiation reflected from the Earth surface has a minimum in spring. Although maximum albedo occurs in winter, the minimum insolation at this season causes the maximum of reflected radiation to occur only in spring when the insolation increases considerably and large parts of the hemisphere are still covered by snow.

TABLE 2.3. Seasonal distribution of the mean radiation balance and its components over the Northern Hemisphere under conditions of mean cloudiness (cal cm^{-2} min^{-1})

Radiation-balance components	Winter	Spring	Summer	Autumn	Year
Incoming short-wave radiation					
1. Insolation at the upper limit of the atmosphere	0.348	0.580	0.645	0.424	0.500
2. Absorption of radiation in the atmosphere:					
a) by ozone	0.011	0.016	0.019	0.010	0.014
b) by water vapor and dust	0.044	0.067	0.092	0.057	0.065
c) by clouds	0.005	0.010	0.011	0.007	0.008
Total absorption	0.060	0.093	0.122	0.074	0.087
3. Reflection and backscattering of radiation into space:					
a) by the atmosphere	0.023	0.037	0.048	0.028	0.034
b) by clouds	0.078	0.141	0.162	0.103	0.121
c) by the Earth surface	0.015	0.029	0.024	0.018	0.021
Total reflection	0.116	0.207	0.234	0.149	0.176
4. Absorption of radiation by the Earth surface:					
a) by insolation	0.085	0.142	0.129	0.091	0.112
b) passed through the clouds	0.045	0.091	0.090	0.064	0.072
c) scattered	0.043	0.050	0.070	0.048	0.053
Total absorption by the Earth surface	0.173	0.283	0.289	0.203	0.237
Long-wave radiation					
1. Effective emission by the Earth surface:					
a) heat radiation by the Earth surface	0.530	0.564	0.614	0.581	0.572
b) counterradiation by the atmosphere	0.439	0.473	0.523	0.494	0.482
Effective emission	0.091	0.091	0.091	0.087	0.090
2. Heat radiation by the troposphere:					
a) emission of radiant heat absorbed by the troposphere	0.501	0.535	0.588	0.555	0.545
b) heat radiation by the troposphere proper	0.716	0.749	0.817	0.778	0.765
Balance of long-wave radiation emitted by the troposphere	0.215	0.214	0.229	0.223	0.220
3. Heat radiation into space:					
a) by the Earth surface (in the transparent window)	0.029	0.029	0.026	0.026	0.027
b) by the troposphere	0.277	0.276	0.294	0.283	0.283
c) by the stratosphere	0.011	0.016	0.019	0.010	0.014
Total outgoing radiation	0.317	0.321	0.339	0.319	0.324

The heat loss of the Earth surface—atmosphere system is mainly due to heat radiation of the troposphere, the main contributor to outgoing radiation. Radiation emitted by the Earth surface (in the transparent window of the atmosphere) is less than 10% of the outgoing radiation, while the heat radiated by the stratosphere into space is still smaller, not exceeding 3—6% of the outging radiation. Both the outgoing radiation and its components have very small seasonal variations. The mean value of the outgoing radiation for the Northern Hemisphere is 0.324 cal cm^{-2} min^{-1}, which corresponds to an effective temperature of -22°C. The deviation of the seasonal value from the mean annual figure does not exceed 2—5%. The small variability of the radiation emitted by the Earth surface is explained by the mutual compensating effects of the surface temperature increasing from winter to summer on the one hand, and by the increasing cloudiness and decreasing transparency of the atmosphere as a result of increase in total water—vapor content on the other hand. However, the conclusion on the small variability of the outgoing radiation is only valid for figures averaged over the Northern Hemisphere. As mentioned above, there is a considerable latitudinal variation in the outgoing radiation.

According to Table 2.3, the radiation balance of the surface—atmosphere system averaged over the whole Northern Hemisphere is positive in spring and summer and negative in autumn and winter. Maximum radiation balance in summer is + 0.072 cal cm^{-2} min^{-1}; the minimum value in winter is -0.084 cal cm^{-2} min^{-1}.

TABLE 2.4. Mean annual latitudinal distribution of the radiation balance of the surface-atmosphere system and its components (cal cm^{-2} min^{-1})

Latitudinal belt, °N								
0—10	10—20	20—30	30—40	40—50	50—60	60—70	70—80	80—90	Mean
Absorbed solar radiation									
0.403	0.409	0.387	0.341	0.276	0.224	0.169	0.122	0.106	0.324
Outgoing radiation									
0.347	0.354	0.353	0.327	0.306	0.287	0.270	0.253	0.245	0.324
Radiation balance									
0.056	0.055	0.034	0.014	-0.030	-0.063	-0.101	-0.131	-0.139	-0.000

Since the absorbed solar radiation and the outgoing radiation have a clear latitudinal march, the radiation balance also depends to a considerable extent on latitude. Table 2.4 gives the mean annual values of the radiation balance and its components for different latitudinal belts, as calculated in /66/.

This table shows the radiation balance to vary, depending on latitude, not only quantitatively but also in its sign. The change of sign occurs around 40°N. Naturally, the latitudinal march of the radiation balance and its components during the seasons considerably differ from its mean annual value. Thus, e.g., during winter the passage of the radiation balance through zero occurs near 20°N and in summer near 80°N.

The values of the radiation balance also vary considerably. In summer, in the subtropics (30—40°N), the positive radiation balance is slightly higher than 1 cal cm^{-2} min^{-1}

TABLE 2.5. Mean latitudinal distribution of the radiation balance of the surface-atmosphere system (kcal cm^{-2})

Latitude	January	July	Annual
70--60° N	—10	3.9	—49
60—50	—8.7	4.4	—30
50—40	—6.8	4.9	—12
40—30	—4.7	4.8	4
30—20	—2.6	4	14
20—10	—0.5	3.2	23
10—0	1.5	2.4	29
0—10° S	3.4	1	31
10—20	4.9	—1	28
20—30	6.1	—3	20
30—40	6.8	—5.3	9
40—50	6.7	—7.3	—8
50--60	--	—	29

Tables 2.5 and 2.6 present data on the mean latitudinal variation of the outgoing radiation obtained by Vinnikov (quoted in /2/) and Berlyand /7/. Comparing these data shows their good agreement.

TABLE 2.6. Mean latitudinal march of monthly radiation balance of the surface-atmosphere system and its components (kcal cm^{-2})

Latitude	June			December		
	$Q_0(1-A_S)$	F_∞	R_S	$Q_0(1-A_S)$	F_∞	R_S
70° N	15.4	12.9	2.5	0.0	11.4	--11.4
60	17.2	13.4	3.8	0.7	11.7	--11
50	18.3	13.6	4.7	2.6	12.3	9.7
40	19	14.1	4.9	5.7	13.1	7.4
30	19.1	14.6	4.5	9.6	14.3	4.7
20	18.5	14.2	4.3	12.8	11.8	2
10	17.2	13.3	3.9	15.5	14.1	1.4
0	15.5	12.7	2.8	16.9	13.1	3.8

As may be seen from Table 2.5, the radiation balance of the Southern Hemisphere is larger than that of the Northern Hemisphere.

Vinnikov plotted monthly and annual maps for the geographical distribution of the radiation balance of the surface—atmosphere system. The most characteristic feature of the radiation-balance distribution is its zonality, a fact that confirms the important role of astronomic factors in the radiation regime. However, zonality is upset in the desert regions. The heterogeneity of the underlying surface at the ocean—land interface is clearly seen in the radiation-balance field as a discontinuity in the isolines.

The radiation balance of the surface—atmosphere system is only positive for the whole year in the narrow equatorial region of ± 10° latitude. Over all the remaining regions it changes sign twice during the year. For about three months (in summer) the radiation balance is positive in all regions of each hemisphere. The zone of negative balance appears near the poles in summer, and then gradually extends southward, remaining south of the 30° parallel for 5 months. Spring heralds the northward "retreat" of the zero isoline of the radiation balance. The maximum positive value is 40 kcal cm^{-2} per year and the negative value reaches 60 kcal cm^{-2} per year.

In this connection, it is interesting to calculate the radiation balance of the atmosphere as a component of the radiation balance of the surface—atmosphere system. This component is determined by three elements: the effective emission F_0 of the underlying surface, the outgoing radiation F_∞, and the absorption q' of solar radiation by the atmosphere. Calculations and observations show the average values of solar radiation absorbed by the atmosphere to be much less than the other elements of the balance. Therefore, the radiation balance of the atmosphere is mainly determined by the influx of radiant heat F_0 F_∞. It is easy to see that on the average $F_0 < F_\infty$, and consequently the radiation balance of the atmosphere is negative. This is the result of the fact that the atmosphere, while mainly absorbing the heat radiated from the Earth surface (and to a much lesser degree solar radiation), radiates both to the Earth surface and into space.

TABLE 2.7. Comparison of calculation results for the atmosphere's radiation balance and its components (cal cm^{-2} per day)

	30–50° N	40–60° N	60–90° N		30–50° N	40–60° N	60–90° N
	Baur and Phillips (1934)				London (1957)		
q'	90	82	81	q'	96	83	65
$F_\infty - F_0$	217	233	227	$F_\infty - F_0$	305	280	230
$\lvert R_a \rvert$	127	151	146	$\lvert R_a \rvert$	209	197	165
	Houghton (1954)				Möller (1959)		
q'	212	99	59	q	92	79	55
$F_\infty - F_0$	359	333	287	$F_\infty - F_0$	300	291	262
$\lvert R_a \rvert$	238	234	228	$\lvert R_a \rvert$	208	212	207

Möller /67/ investigated the laws of the annual march of the atmosphere's radiation balance in different climatic zones and concluded that the maximum absolute value of the balance always occurs in November being 250—300 cal cm^{-2} per day. The minimum value is observed in the period from March to July and varies from 140 to 190 cal cm^{-2} per day. In Table 2.7, Möller presents for comparison the mean annual values of the radiation balance R_a of the atmosphere for various latitudinal belts calculated by different authors. This comparison shows good agreement between the data obtained by various authors, whereas earlier values for the radiation balance are either underrated (Baur and Phillips) or overrated (Houghton).

It was Vinnikov who carried out the most complete computations of the components of the atmosphere's heat balance. Table 2.8 presents data on the mean latitudinal distribution of the annual total of the heat-balance components for different latitudinal belts. In this table, P designates the turbulent heat transfer from the underlying surface to the atmosphere, Lr the heat input from condensation, and C the advective heat transfer brought about by horizontal currents in the atmosphere.

TABLE 2.8. The components of the atmosphere's heat balance (kcal cm^{-2} per year)

Latitude	R_a	P	Lr	C
70 - 60° N	70	9	29	-32
60 - 50	60	13	45	-2
50 - 40	60	17	46	3
40 - 30	69	23	45	-1
30 - 20	82	24	44	-14
20 - 10	83	15	72	4
10 - 0	76	9	119	52
0 - 10° S	74	8	94	28
10 - 20	76	11	77	12
20 - 30	74	15	53	-6
30 - 40	71	11	57	-3
40 - 50	64	9	63	8
50 - 60	57	8	61	12
The Earth as a whole	72	13	59	0

Table 2.8 shows that the radiation balance of the atmosphere varies little latitudinally.

Berlyand /7/ plotted monthly (for four seasons) and annual maps of the geographical distribution of the atmosphere's radiation balance for the Northern Hemisphere. These maps also confirm the relatively small spatial variation of the radiation balance. The field of the radiation balance is especially "vague" in summer because of the small latitudinal changes in absorbed solar radiation and outgoing radiation (the values of the balance vary from -4 to +6 kcal cm^{-2} per month). In December a greater variation in the radiation balance is observed: from -10 (in high latitudes) to -4 kcal cm^{-2} per month (in the lower latitudes). The annual radiation balance also has a considerable geographical variation.

Similar results were obtained by Vinnikov for the whole globe. Yearly totals of the radiation balance vary for the entire globe approximately from -40 to -100 kcal cm^{-2} per year. The smallest sum totals (in absolute figures) of the radiation balance occur in summer in the temperate and high latitudes, where the atmosphere absorbs a large amount of solar radiation.

The instantaneous values of the radiation balance of the surface—atmosphere system are extremely variable. The corresponding values obtained by satellites will be discussed later. Möller et al. /67, 63/ calculated the geographical distribution of the radiation balance for the troposphere over western Europe for different synoptic situations. However, this investigation was limited to only one of the components of the radiation balance — the atmosphere. Möller's results bear witness to the extremely nonuniform geographical distribution of the troposphere's radiation balance.

Recent investigations into the radiation balance of the surface—atmosphere system show the considerable potentialities of artificial Earth satellites as a tool for obtaining data on the global distribution of the radiation balance. Let us now analyze some of these data.

Results of measurements. Despite the yet insufficient accuracy of data on outgoing radiation and particularly on albedo obtained from satellites in recent years, experimental data have been obtained for the first time characterizing the spatial and time variation of A_S, F_∞, and R_S. These data clearly confirm the earlier theoretical assumption that the outgoing long-wave radiation has a minimum near the equator, nearly symmetrical maxima in the subtropics, and then decreases monotonically toward the poles. Similar results were obtained in /87, 88/ (data from the TIROS II 5-channel radiometer, Figure 2.4), in /61/ (TIROS IV hemispherical sensors for outgoing radiation, Figure 2.5), and in /44/.

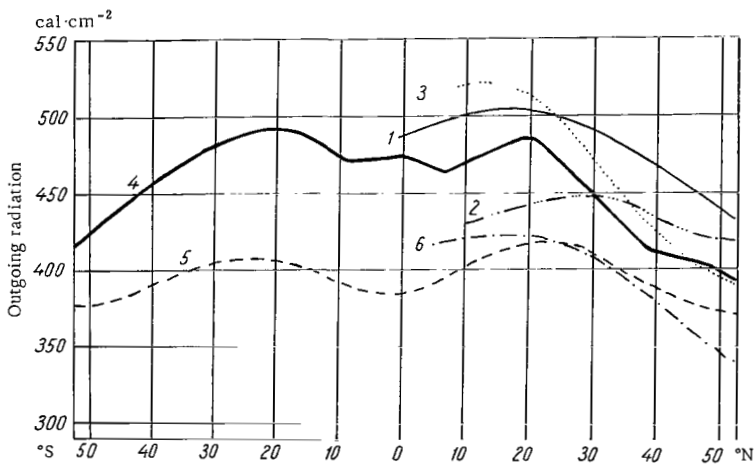

FIGURE 2.4. Daily mean latitudinal distribution of the outgoing long-wave radiation according to data from TIROS II for 26 days, compared with theoretical calculations:

1 — Houghton (mean annual); 2 — Raethjen (winter); 3 — London (winter); 4 — TIROS II (November—January); 5 — Simpson (November—December); 6 — Baur and Phillips (January)

Rao /78/ investigated the annual variation of the outgoing heat radiation using data from TIROS II and III and processed the measurement results on the latitude belts between 55°S and 55°N. The data in Figure 2.6 show that in the temperate latitudes of the Northern Hemisphere the outgoing radiation increases from winter to summer. This may be caused both by the decrease in cloudiness and the increase in temperature of the underlying surface. An opposite variation in the outgoing radiation is found in the temperate latitudes of the Southern Hemisphere. Attention is drawn to the two minima in the outgoing radiation near the equator according to TIROS II data. This may be explained by the presence of two zones of increased cloudiness.

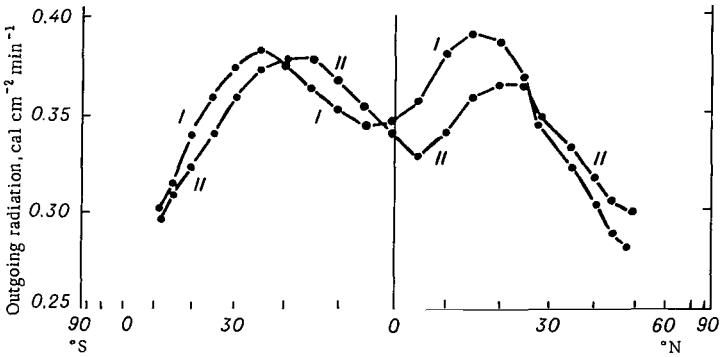

FIGURE 2.5. Latitudinal variation of outgoing long-wave radiation according to TIROS IV data (hemispherical sensor):

I — 8 February through 10 April 1962, daily mean value for the territory 48°N to 48°S equal to 510 cal cm^{-2}; II — 11 April through 10 June 1962, daily areal mean value 501 cal cm^{-2}.

With the aid of the orbital solar observatory OSO-1 launched on 7 March 1962 into a circular orbit at a height of about 560 km, investigations were made of the long-time resistance to cosmic influences of various protecting layers used for controlling the heat regime of satellites. At the same time, these experiments made it possible to obtain data on the flux of outgoing radiation and long-wave radiation /71/.

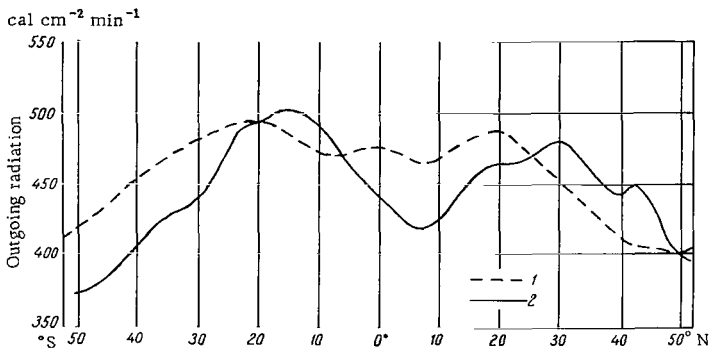

FIGURE 2.6. Latitudinal march of long-wave radiation during winter and summer:

1 — according to data from TIROS II (November—December 1960, January 1961; total for 26 days); 2 — according to TIROS III data (July 1961, 9 days).

Using the heat-balance equation of a flat (plate-type) radiation detector one side of which faced space while the other was heat-insulated, Millard and Neel /71/ derived a formula for determining the albedo of the surface—atmosphere system for short-wave radiation and outgoing long-wave

radiation. The directly measured quantity is the temperature of the sensor plates, differing in their optical properties. One of the plates, particularly resistant to cosmic influence thanks to its special engineering properties, is used both as a reference element and as a sensor for short-wave radiation (this plate is actually a set of several razor blades with blackened ends representing the radiation-receiving surface with properties close to those of an absolute blackbody). Two other plates (out of six), chosen as radiation sensors because of the higher stability of their optical properties, were coated with an epoxy-bonded mixture of aluminum powder, titanium dioxide and silicon. The last plate of the set served as a sensor for the radiation emitted from the night (dark) side of the Earth. Measurements were taken for approximately 5 minutes on every orbit, only within the range of the ground stations in North and South America. The entire period of measurement was about two months (during this time the spatial orientation of the instrument container could still be controlled). During this period the measured values of the long-wave radiation varied from 0.42 to 0.51 cal cm^{-2} min^{-1}, which exceeded considerably the generally accepted mean global value of 0.33 cal cm^{-2} min^{-1} and also the values obtained from measurements with the TIROS satellites. Such a discrepancy was probably caused by nonuniform measuring conditions (time, geographical location, etc.). Albedo data obtained from TIROS IV throughout February and March 1962 showed much closer agreement with the theoretically calculated values. However, the best agreement was observed in the equatorial regions. Values of the albedo vary from 10 to 38%. Estimates of measurement errors both for the albedo and outgoing radiation give values of ± 0.10 (in fractions) and ± 0.04 cal cm^{-2} min^{-1}, respectively.

The most thorough investigation into the laws governing the variation of the radiation balance components of the atmosphere--surface system was made in /44/ on the basis of TIROS VII data, obtained during 14 months of uninterrupted measurements. The methods used in /44/ for processing these measurements are described in Chapter 1.

TABLE 2.9. Seasonal and annual sum totals of the radiation-balance components for the globe

Period	Outgoing long-wave radiation, 10^{15} cal min^{-1}	Solar radiation, 10^{15} cal min^{-1}		Earth albedo, %
		reflected	incident	
June–Aug.	1,725.2	699.0	2,457.8	28.4
Sept.–Nov.	1,725.2	922.2	2,574.8	35.8
Dec.–Feb.	1,712.2	859.7	2,609.8	32.9
Mar.–May	1,746.5	796.0	2,544.2	31.3

Table 2.9 presents the seasonal sum totals of the radiation-balance components for the Earth as a whole. Figures 2.7 and 2.8 show curves of the latitudinal march of mean annual values of the outgoing long-wave radiation and the albedo compared with the results of London /66/.

In Table 2.9 attention is drawn to the small variability of the seasonal sum totals of outgoing long-wave radiation. The seasonal variations in the latitudinal profile of outgoing radiation investigated in /44/ show that

the tropical minimum during the whole year, except for the period December to February, extends to the Northern Hemisphere (the tropical minimum located at 5°N (cf. Figure 2.7) points to the existence of an asymmetry between the hemispheres). In the Northern Hemisphere we also find (except for the months June through August) an absolute maximum of outgoing radiation (the corresponding asymmetry is clearly seen in Figure 2.7). As a rule, in extratropical latitudes of the Northern Hemisphere the outgoing radiation is larger than in the Southern Hemisphere, but in equatorial regions the opposite relationship holds; however, this leads to a certain leveling of radiant-heat losses in both hemispheres.

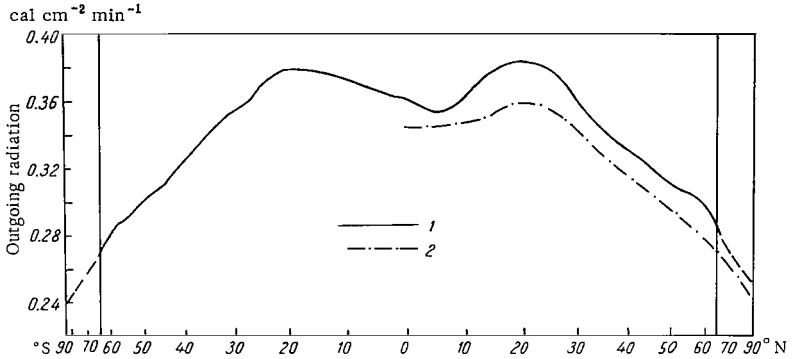

FIGURE 2.7. Latitudinal march of the mean annual values of outgoing radiation (scale of abscissa is proportional to the area of the latitude belts):

1 — TIROS VII data (spectrum regions 8—12 μ, June 1963 to May 1964); 2 — values calculated by London.

The latitudinal march of albedo reflects almost in a mirrorlike fashion (i.e., in the opposite sense) the variation in the outgoing radiation which is determined by the influence of cloudiness (see Figures 2.8 and 2.9 taken from /61/). The dashed curves in Figure 2.9 show the possible influence of measuring errors. The maximum albedo near the equator extends to about 5°N (Figure 2.8), coinciding with the minimum of outgoing long-wave radiation. However, minimum albedo is found at 16°N, i.e., slightly displaced to the South relative to the maximum outgoing radiation. In the region between the equator and 12°N the albedo of the Northern Hemisphere is larger than that of the Southern Hemisphere, but smaller in higher latitudes.

An analysis of the annual march of the albedo shows the smallest values to occur around July and the maximum near October. This is also reflected in the variability of seasonal albedo values (Table 2.9).

The mean latitudinal distribution of the radiation balance of the surface—temperature system is asymmetrical with respect to the equator, and therefore the transition from a positive balance in low latitudes to a negative in high latitudes occurs in different latitude belts of the Northern and Southern hemispheres. This is clearly seen in Figure 2.10 /61/.

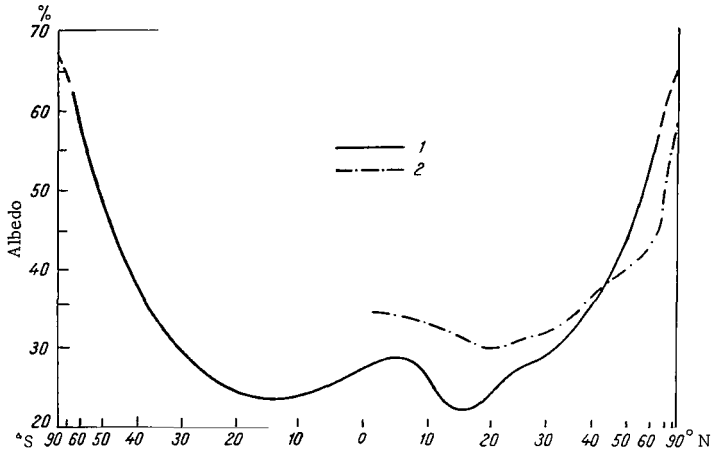

FIGURE 2.8. Latitudinal march of mean annual values of the global albedo (scale of abscissa is proportional to the value of the incoming solar radiation beyond the atmosphere as related to the corresponding latitude belts):

1 — TIROS VII data (spectrum regions 0.55—0.75 μ, June 1963 to May 1964);
2 — values calculated by London.

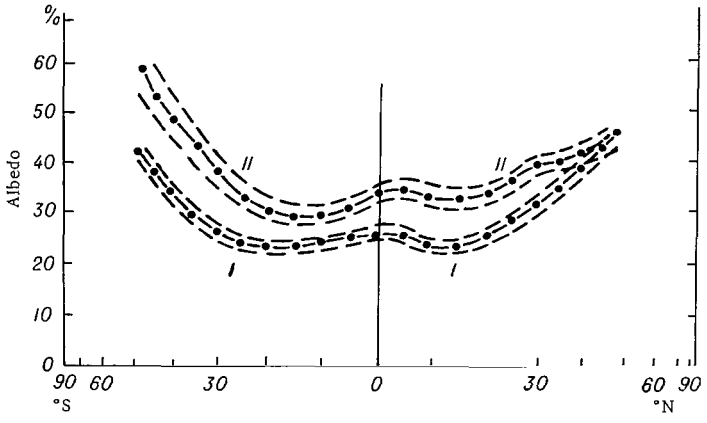

FIGURE 2.9. Latitudinal variation of albedo according to TIROS IV data (hemispherical sensors):

I — 8 February through 10 April 1962, areal means 48°N to 48°S, albedo 28.9%; incoming daily radiation 598 cal cm^{-2}; II — 11 April through 10 June 1962, areal means 48°N to 48°S, albedo 37.2%, incoming daily radiation 500 cal cm^{-2}.

Astling and Horn /41/ calculated the mean latitudinal distribution of outgoing long-wave radiation for the entire Earth surface and separately for the continents and oceans; for these calculations they used data from TIROS II for 27 days between 26 November 1960 and 6 January 1961. These data cover rather completely the latitudes 50°S to 50°N except for parts of

Central Asia and the northern areas of South America, including adjoining parts of the Pacific and Atlantic oceans. The starting data for each day were averaged (over at least 10 values) using squares which had on the equator a side of 2.5° latitude; these data were then used to plot maps showing the geographical distribution of the outgoing radiation for each of the 27 days. All measurements were related to a minimum nadir angle of 56°. The averaged meridional profiles of the outgoing radiation were computed by taking data on outgoing radiation from these maps (with 7, 269 grid points). The mean-latitudinal radiation values were calculated for 5° latitude belts.

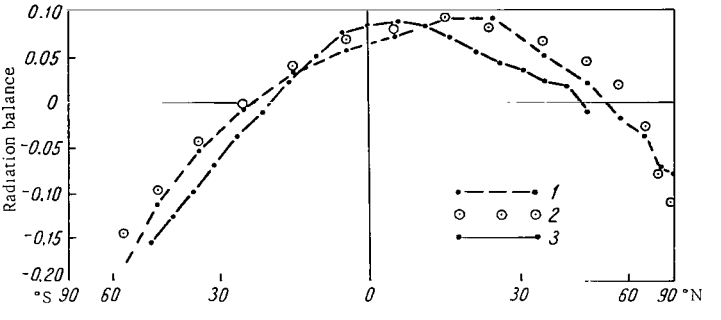

FIGURE 2.10. Latitudinal variations of the radiation balance according to TIROS IV data (hemispherical sensors):

1 — Simpson (1928) for March, April, May; 2 — London (1957) for autumn and spring; 3 — TIROS IV data for March, April, May 1962.

The meridional profile of outgoing radiation obtained in this way exhibits (as in the above-mentioned studies) the presence of a minimum near the equator, a maximum in the warm and relatively cloudless subtropics and a decrease in outgoing radiation with increasing latitude.

The absolute values of outgoing radiation are seen to be smaller (especially in the belt from 5°N to 10°S) than the data obtained earlier by EXPLORER VII and by actinometric radiosondes. This discrepancy may probably be explained by the inaccurate allowance for the effect of darkening toward the borders of the Earth disk in processing TIROS II data (the values of outgoing radiation measured at a large nadir angle were underrated owing to the effect of darkening compared with the corresponding subsatellite values). These conclusions are supported by the fact that comparing the average values of all measurements of the outgoing radiation with the mean values obtained by selected data relating to nadir angles of less than 26°, shows that the former were underrated. However, since even the subsatellite values of outgoing radiation obtained by TIROS II data are smaller than those of EXPLORER VII, one must conclude that one of the reasons of these discrepancies is also the different calibration of the instruments installed on the above-mentioned satellites. According to data for nadir angles less than 26°, the daily values of outgoing radiation in the zones of subtropical maxima (15—25°N and 10—35°S) are about 480 cal cm^{-2}.

Astling and Horn /41/ found a considerable difference between the meridional profiles of the outgoing radiation as related to the continents and oceans. Whereas over the continents a sharp minimum of outgoing radiation is observed between 5°N and 15°S, this minimum is less strongly expressed over oceans and is displaced toward a belt within 5° and 10°N. The southward displacement of the minimum over the continents is probably caused by the influence of cloudiness connected with the intertropical convergence zone. Another important difference was found in the subtropical regions and is connected with the temperature of the underlying surface in these relatively cloud-free regions: over the oceans (small temperature variations), the daily values of the outgoing radiation in the subtropics over both hemispheres are about 500 cal cm^{-2}; the corresponding daily values above the continents are 540 cal cm^{-2} (for the summer hemisphere and high temperatures), and 475 cal cm^{-2} (for the winter hemisphere and low temperatures).

The data obtained in /41/ for the variation of mean values of the outgoing radiation show a sharper variation over the continents. An experimental estimate of the mean values of outgoing radiation and of the albedo for the whole Earth on the basis of TIROS II data, using calculated values for high latitudes, yielded a global mean value of 0.311 cal $cm^{-1} min^{-1}$ for the outgoing radiation and 38% for the albedo. It should be noted that the usually accepted value for the albedo is 34%, while the value obtained by EXPLORER VII was 33%. This discrepancy should be attributed both to the insufficient amount (due to limited time) of available data and to measuring errors. By processing data of TIROS III Wexler /89/ obtained an albedo varying from 4 to 10% for a cloudless sky to about 30% in the presence of a continuous cloud cover (it should, however, be added that in clear weather the albedo over the Sahara reaches 20%). Only during the first five orbits did the satellite record albedo values of 54% in channel 3. The mean value of albedo for all data during the first five orbits was 20%. If one considers that according to aircraft measurements the mean albedo of clouds is 50%, while individual values reach 80%, it becomes clear that the satellite measurements must be considerably underrated.

Nordberg et al. /72/ analyzed the results of the determination of effective temperatures and albedo from data on outgoing rddiation recorded by TIROS III, using at the same time wide-angle pictures of cloud-cover distribution (a similar analysis was later made in /75/).

In /72/ three typical cases were studied, one for the Atlantic Ocean, one for North Africa (two examples for a cloudless atmosphere) and one for the eastern U.S.A. (cloudy sky). All data were obtained at near-noon local time. It should be noted that in all three cases the television cameras and the wide-angle radiometer were pointed at nearly exactly nadir angle. For the 5-channel radiometer the nadir angle of sighting varied from 0 to 45°.

Photograph 2.1 and Figures 2.11—2.15 show data for the Atlantic Ocean in the region of the northeastern coast of Brazil (in the left upper corner of Photograph 2.1 the coastline is clearly discernable). The dot—dash curves in Figures 2.11—2.15 represent the projection of the satellite trajectory on the Earth surface. The dashed oval curves show the area scanned by the wide-angle radiometer. The figures marked GMT represent the time for the corresponding points of the satellite trajectory.

As can be seen in Photograph 2.1, nearly the whole examined ocean area was cloudless.

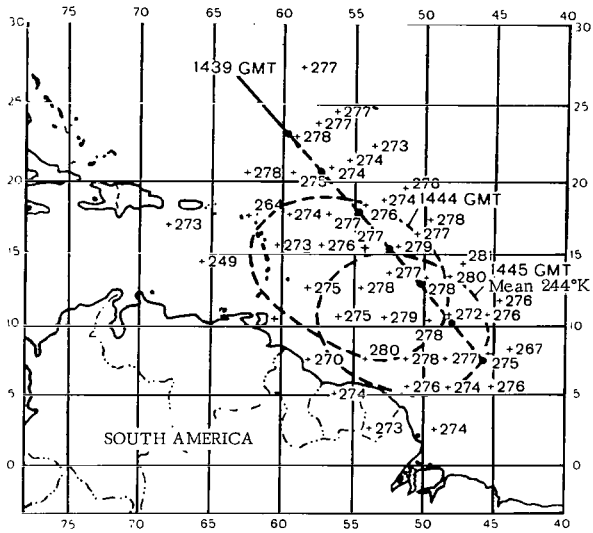

FIGURE 2.11. Distribution of effective temperatures (°K) according to measurements of outgoing radiation in the transparent window of 7.5—13.5 μ for 20 July 1961, 1439 GMT.

Analysis of data relating to the transparent window (Figure 2.11) shows that despite the cloudless sky the values of effective temperatures are approximately 20° lower than the water-surface temperatures. This points to a considerable attenuation of the atmospheric infrared emission even in the transparent window, and probably to measurement errors. Low values of effective temperature (small magnitude of outgoing radiation) were obtained from measurements in the 5.9—6.7-μ band (Figure 2.12) and for the integrated long-wave radiation (Figure 2.13). In the given case the reflected short-wave radiation has also small values. This is confirmed by the low albedo values of the surface—atmosphere system (Figures 2.14 and 2.16); the albedo values being determined from data on the integrated short-wave radiation (Figure 2.14) are improbably low. The albedo values obtained from measurements of the outgoing radiation in the visible range of the spectrum (Figure 2.15) are much more reliable. Probably the reasons for the above-mentioned discrepancies also noticed in other cases are explained by calibrational errors in the measurement of the integrated short-wave radiation. However, distortions introduced by a defective radiometer should also be discounted.

In the above instance the wide-angle radiometer recorded an albedo of 9% (constant value for two measurements). This agrees satisfactorily with the mean albedo of 7% for the spectrum regions 0.50—0.75μ (the mean albedo for the integrated short-wave radiation was 4%). As can be seen

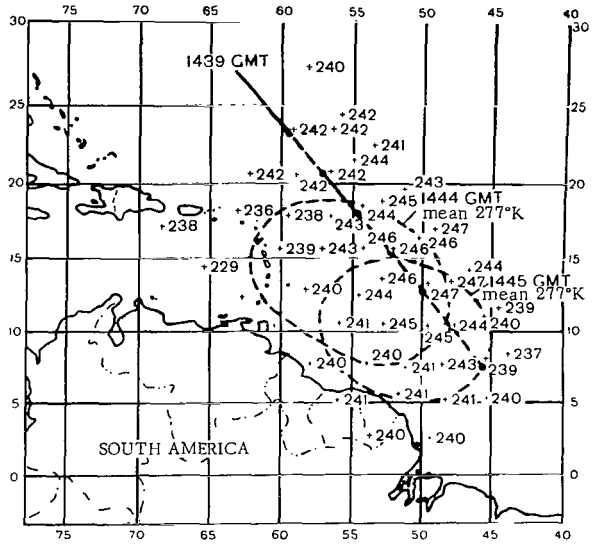

FIGURE 2.12. Distribution of effective temperatures (°K) according to measurements of outgoing radiation in the wavelength band of 5.9—6.7 μ for the same period as in Figure 2.11.

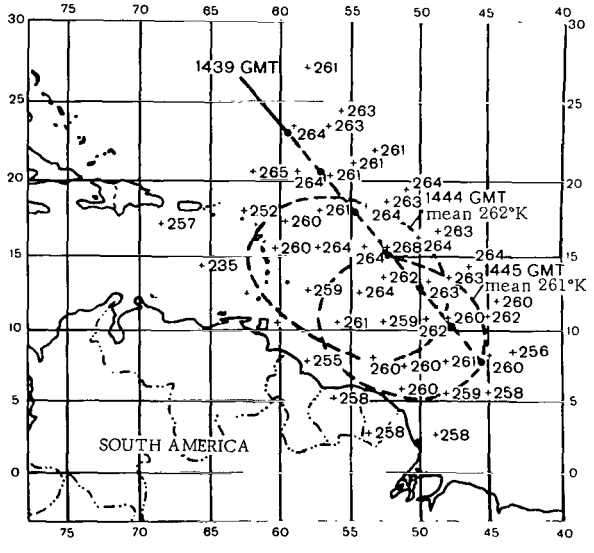

FIGURE 2.13. Distribution of effective temperatures (°K) according to measurements of outgoing integrated long-wave radiation (7.0—32.0 μ) for the same period as in Figure 2.11.

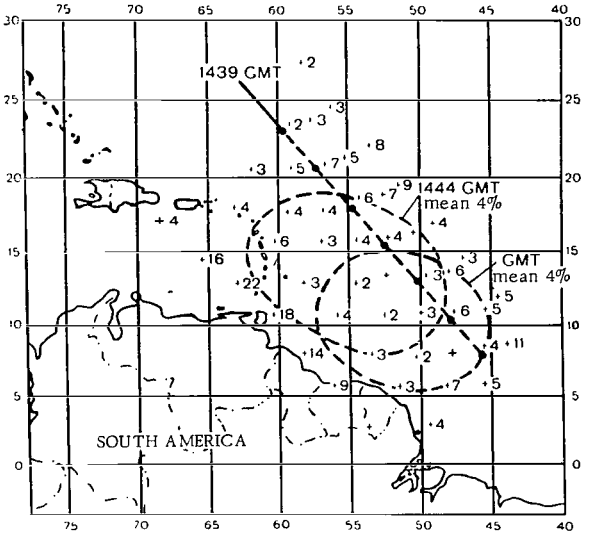

FIGURE 2.14. Albedo, determined from measurements of outgoing integrated short-wave radiation (0.2—7.0 μ) with the 5-channel radiometer for the same period as in Figure 2.11.

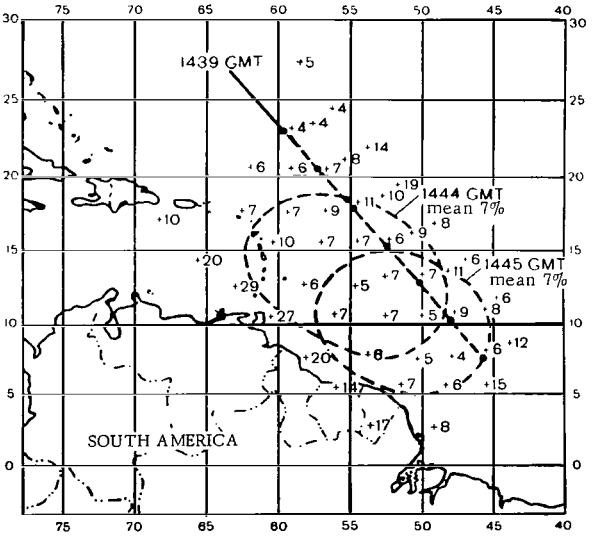

FIGURE 2.15. Albedo, determined from measurements of outgoing short-wave radiation in the visible range of the spectrum (0.5—0.75 μ) for the same period as in Figure 2.11.

from Figures 2.14 and 2.15, in both cases, the coastline can be clearly discerned in the field of the albedo values (the albedo of the land is much larger than that of the ocean).

The measurement of outgoing integrated long-wave radiation with the wide-angle radiometer yields data that show a good agreement with similar data for the spectrum regions 7.0—32.0μ obtained with the 5-channel radiometer. According to the wide-angle-radiometer data, the effective temperatures were 258°K at 1444 GMT and 260°K at 1445 GMT. The corresponding mean values according to data from the 5-channel radiometer were 262°K and 261°K. The overrated temperature values as recorded by the wide-angle radiometer are probably caused by the great time lag (about 1.5 minutes) of this instrument (till the moment of measurement the radiometer was facing into space or down to the very cold underlying surface in the North).

For a continuous cloud cover (the data relate to the eastern U.S.A., 12 July 1961) the albedo increases to 40—50% (as before, the integrated albedo is smaller than the visual albedo). The mean values of the visual albedo for two extensive areas of territory, which also included a small part of cloud-free atmosphere, are 28% and 37%. Wide-angle-radiometer measurements for the same areas yielded 26% and 32%, respectively. The effective temperatures for all spectrum regions are very low, a fact which shows the presence of high clouds. Thus, e.g., for the transparent window the effective temperature of an area with a dense cloud cover is 239°K. For the 5.9—6.7-μ band the effective temperature is by 10° lower. Measurements of long-wave radiation both by the 5-channel and the wide-angle radiometers showed satisfactory agreement.

Of particular interest is the third example, which characterizes the field of emission for the Mediterranean Sea and North Africa (measurements on 15 July 1961) for a very small degree of cloudiness. Three consecutively taken photographs (Photographs 2.2—2.4) show the variable nature of the underlying surface during the movement of the satellite from the cloudless water body of the Mediterranean (Photograph 2.2) over the Libyan desert (Photograph 2.3) to the mountainous area at the border between Sudan and Ethiopia (Photograph 2.4).

An analysis of the measurement data on outgoing radiation shows the considerable variation in albedo with changes in the underlying surface: as the satellite moves from the Mediterranean Sea to desert regions, albedo tends to increase, but the region of the El Haruj oasis (the dark spot in the middle of Photograph 2.4) exhibits a clearly defined area of low albedo. On the other hand, the presence of cloudiness is characterized by zones of high albedo. All these features are clearly seen in Figure 2.16, which presents albedo and the effective temperature data obtained with the wide-angle radiometer. The increase in albedo from 14 to 29% between 1053 and 1058 hr is connected with the motion of the satellite from the Mediterranean to the desert region with a high albedo of the underlying surface. The lowest albedo measured at 1100 hr occurs in the region of vegetation near the Nile, while the subsequent increase is connected with the displacement of the satellite over Ethiopa. A decrease in the albedo at the end of the considered time interval is connected with the displacement of the satellite to the Indian Ocean (1105 hr).

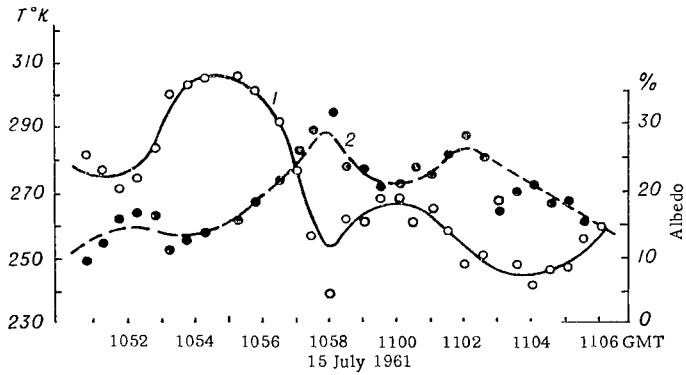

FIGURE 2.16. Time dependence (along the satellite trajectory) of the effective temperature and albedo according to measurements with the TIROS III wide-angle radiometer on 15 July 1961:

1 — effective temperature; 2 — albedo.

The march of the effective temperature is also very interesting. Over desert regions (from 1054 to 1055 hr) the wide-angle radiometer recorded a temperature peak of 305°K. At about 1057 hr the effective temperature decreased sharply to about 260°K and remained nearly stable. This is due to the very rapid and considerable increase in the atmospheric humidity south of 15°N as the satellite moves over the tropical region of the Sudan. This conclusion is supported by similar results on the outgoing long-wave radiation measured with the 5-channel radiometer. According to measurements in the transparent window, the effective temperature over the desert reaches 310°K, which is probably very close to the temperature of the surface (this proves the extremely low humidity of the atmosphere). However, in the southern Sudan the effective temperature in the window falls to its lowest values of about 280°K. The determination of mean-noon values of outgoing integrated long-wave radiation gave the following results: 192 W/m^2 (eastern U.S.A. with dense and continuous cloud cover); 250 W/m^2 (Atlantic Ocean, tropics, clear sky); 265 W/m^2 (eastern U.S.A. with clear sky); 340 W/m^2 (African desert, clear sky).

Satellite measurements of the Earth radiation-balance components carried out so far point to the necessity for further measurement data and, in particular, for much greater measurement accuracy.

2.2. SPATIAL STRUCTURE OF THE OUTGOING-RADIATION FIELD

The results of investigations into the spatial distribution of the radiation-balance components of the surface—atmosphere system are based on an analysis of individual (although in many cases averaged) fields of outgoing radiation. Naturally, the large body of available information and its global coverage suggest the application of statistical methods to the processing and integration of the available data.

Let us therefore consider some statistical estimates of the radiation field, obtained from TIROS II and TIROS III data and based on results of published studies /11, 12/.

The importance of statistical processing of radiation-field data is determined by several factors. In view of the considerable errors of radiation measurements it is important to statistically estimate the reliability of determining nonuniformities in the radiation fields, so as to compare them with fields of other meteorological elements which may be characterized by these nonuniformities.

Moreover, for objective analysis of the radiation field one should use optimum schemes that would allow for the statistical structure of the analyzed element. This requires a knowledge of the correlation, structural, and spectral functions. Such characteristics could also form a reasonable basis for establishing optimum frequency of measurements of high measurement accuracy.

With data from /85, 86/ the Ural-2 electronic digital computer calculated the correlation, structural, and spectral functions for this purpose; the TIROS III radiometer readings were reduced to data from TIROS II for comparing the characteristics thus obtained /12/.

TABLE 2.10. Mean values of radiation fluxes (W/m^2) for different regions of the spectrum

Channel No.	TIROS II		TIROS III		
	number of fields used	mean radiation values	number of fields used	mean radiation values without accounting for differences in light filters used	after reduction of TIROS II data to TIROS III readings
1	51	0.426	22	0.305	0.479
2	56	32.18	42	36.20	34.50
3	Defective readings		11	7.86	—
4	62	40.76	25	90.28	46.70
5	Defective readings		22	1.19	—

Table 2.10 presents the mean values of emitted radiation fluxes obtained with different channels. As can be seen, the mean radiation fluxes according to TIROS III data are somewhat larger than those obtained with TIROS II. This may be explained by the seasonal march of the outgoing radiation, since data from TIROS III refer to the summer while those of TIROS II refer to winter measurements.

Table 2.11 presents the dispersions, averaged from data on various radiation fields.

Calculations showed that although, on the average, conditions of local isotropicity apply to the field of outgoing radiation, its nonuniformity is large, and for different regions the structural and correlation functions may differ considerably from each other.

Figure 2.17 presents averaged values for the structural functions $b(l)$ of the radiation fields. As may be seen, the structural functions for the two

satellites differ from each other, and this can hardly be explained by the difference between the seasons of the year. A dependence of the structural functions on the applied point grid has been observed, although no such dependence has been noticed for other meteorological fields /12/.

TABLE 2.11. Mean dispersion of the outgoing radiation fields

Channel No.	Dispersion averaged from data for individual radiation fields	Channel No.	Dispersion averaged from data for individual radiation fields
TIROS II, grid pitch 40 miles			
1	0.0126	TIROS III, grid pitch 2.5°	
2	21.90		
4	18.85	1	0.0133
TIROS III, grid pitch 1.25°		2	45.56
1	0.00894		
2	45.24	3	—
3	—		
4	139.65	4	136.16
5	0.414		
		5	0.931

Such a nonuniformity may be explained both by the quality of starting data and by the applied method of objective analysis which does not allow for the structure of the radiation fields. This again stresses the necessity of using the laws of statistical structure for establishing an optimum scheme for the objective analysis of radiation data. Since the transmissivity of the light filters for the 5-channel radiometer varies for different satellites, it is more convenient to use correlation functions for a joint analysis of measurements, because this limiting factor does not affect these functions.

The above-considered structural characteristics may be used for the solution of numerous practical problems connected with the objective analysis of radiation fields, as well as for establishing optimum frequency of satellite measurements.

According to Kotel'nikov's theorem, any function $f(t)$ that has a frequency spectrum with an upper frequency ω_c is determined completely by the sequence of its values read for the interval $\Delta t = \frac{1}{2\omega_c}$. Here t is a time or space coordinate (for a uniform or isotropic field). To represent the function $f(t)$ in the interval T_c it is necessary to have $n = 2T_c\omega_c$ ordinates with a time interval Δt. In this case function $f(t)$ in the interval T_c is analytically expressed in terms of its instantaneous values $f(t - p\Delta t)$ by the following formula:

$$f(t) = \sum_{p=1}^{n} f(p\,\Delta t)\,\frac{\sin 2\pi\omega_c (t - p\,\Delta t)}{2\pi\omega_c (t - p\,\Delta t)} \qquad (2.3)$$

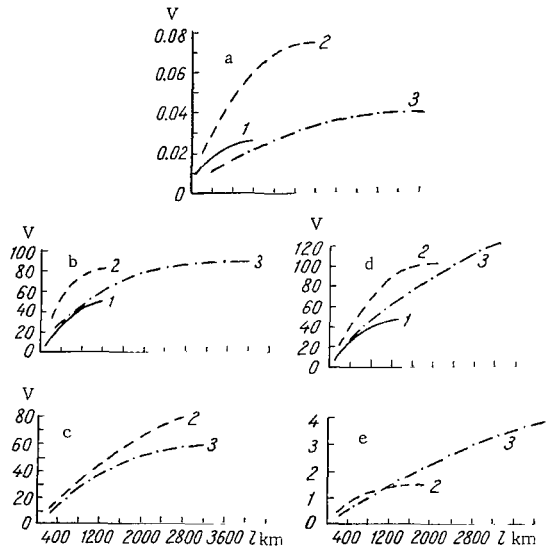

FIGURE 2.17. Structural functions of the radiation field using radiation data chosen from nodes of a grid with a pitch of 40 miles (1), 1.25° (2), and 2.5° (3):

a — channel 1; b — channel 2; c — channel 3; d — channel 4; e — channel 5.

For the determination of the frequency spectrum the spectral density $S(\omega)$ is calculated by the formula

$$S(\omega) = \frac{2}{\pi} \int_0^\infty k(\tau) \cos \omega\tau \, d\tau, \qquad (2.4)$$

where $k(\tau)$ is the correlation function of the given element.

The area of the essential frequencies is usually taken from the region of frequencies between 0 and ω_c, where ω_c is the frequency for which

$$S(\omega_c) \leqslant 0.05 S(0).$$

Such an approach permits the structural characteristics thus obtained to be used for determining the spectra of characteristic frequencies of the radiation fields (both in time and space), and also to establish optimum measurement frequencies from a satellite.

For the determination of the time-frequency spectrum it is necessary to know the time correlation function of the radiation field. Knowing the time correlation function of a certain meteorological element, measured from a satellite, the frequency spectrum of this element can be determined; using the above considerations, the time interval Δt can be found. Since, however, the velocity of the satellite exceeds many times the displacement velocity of the observed meteorological elements, the problem may be solved in another way, using data on the spatial structure of the radiation field.

In a study /11/ it was shown that within a range of about 1,000—2,000 km the radiation field, like fields of other meteorological elements, is isotropic, i.e., the direction of reading does not influence the form of the correlation function. Results of processing TIROS III data support this conclusion.

This makes it possible to calculate the spectral density and to evaluate the area of essential frequencies. We then may assume $\omega = \frac{2\pi}{l}$, where l is the linear scale. Let d_c designate the critical scale corresponding to the frequency ω_c where $\omega_c = \frac{2\pi}{d_c}$. Then for the general case the interval of distances through which measurements have to be carried out is

$$\Delta d = \frac{d_c}{4\pi}. \tag{2.5}$$

The critical scale d_c can be estimated with sufficient accuracy if the spatial and correlation functions are known. This scale should correspond to the scale for the limits of which conditions of local isotropicity are fulfilled. This scale may be taken as the distance for which the correlation function becomes zero. Thus, e.g., for channel 1 this distance is approximately 1,000—2,000 km, which corresponds to an optimum measurement density over intervals of 80—150 km. For channel 2 the value of d_c varies within 600—1,600 km, which corresponds to a measurement interval of from 50 to 130 km. For the short-wave radiation, $d_c \approx 1{,}000$—2,000 km and consequently the measurement interval must be 80—150 km.

Thus, for a sufficiently full representation of the field of outgoing radiation the measurement interval should be within 50—150 km. The description of a finer structure of the radiation fields involves larger measurement frequencies. However, as it results from estimates of the influence of observation errors for the existing measurement accuracy of satellites, observation data obtained with larger measurement frequencies do not furnish additional information either for objective analysis of the radiation field or for assessing its structure.

In these determinations it is important to estimate the spectral density of the radiation field, and consequently also the scale of perturbations most significant in terms of the energy budget.

For this purpose, the spectral density was computed on the Ural-2 electronic computer, using the correlation functions of the radiation fields for the different regions of the spectrum. The values of the spectral functions were obtained for frequencies ω corresponding to $l = h, 2h$, etc., h being the grid pitch, varying for different satellites.

It should, however, be noted that since the correlation function, with $l > 10h$, is not determined with sufficient reliability, the value $S(l)$ for $l > 10h$ should be considered with much caution.

Figure 2.18d shows three curves characterizing the spectral densities of the field of integrated outgoing radiation for three kinds of correlation functions, calculated for grid pitches of 40 miles, 1.25° and 2.5° of the meridian arc. As is seen, the most probable scales of perturbation in the field of integrated outgoing radiation with $h = 40$ miles are 350 and 800 km. Considering the fluctuation limits for the correlation function, the minimum

scale of perturbation is between 200 and 500 km and the maximum between 600 and 800 km. Perturbations of such scales are also observed in the fields of other meteorological elements, particularly in the pressure and geopotential fields.

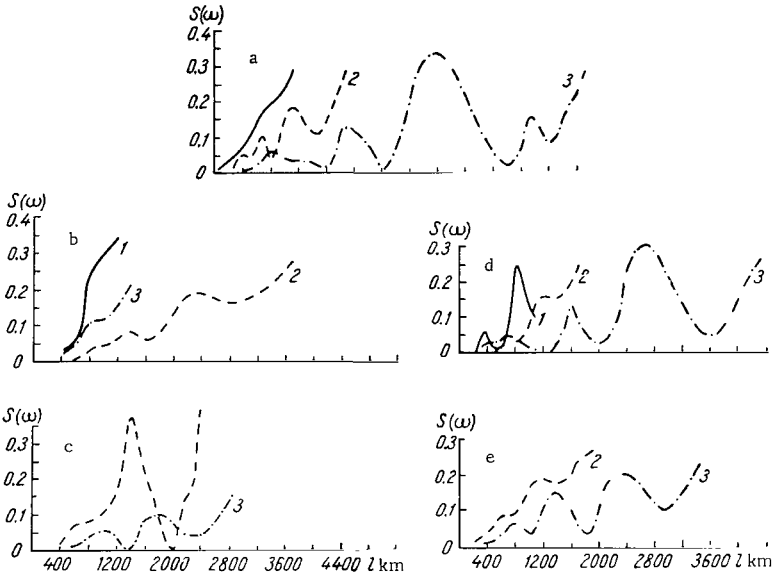

FIGURE 2.18. Spectral density of the radiation field with radiation data chosen from the nodes of a grid with a pitch of 40 miles (1), 1.25° (2), and 2.5° (3).

a — channel 1; b — channel 2; c — channel 3; d — channel 4; e — channel 5.

If the radiation data are chosen from a grid with a pitch $h = 1.25°$ the spectral functions calculated with these data reveal two perturbation scales of 400 and 700 km. The spectrum of these perturbations is very weak and shows up in the spectral functions of different fields.

With allowance for the possible deviations of the correlation functions from mean values, the scale of small perturbations varies within 250—500 km, and for large perturbations within 700—900 km. In addition, some, even larger perturbations are revealed whose scale is of the order of 1,100—1,700 km.

It is easy to see that in spite of the discrepancy between channel-4 data from TIROS II and TIROS III the spectral characteristics of perturbations were rather close. The same figure shows a curve that characterizes the spectral density for the field of outgoing radiation according to data from channel 4 of TIROS III with a grid pitch of 2.5°.

It is only natural that in the given case we cannot obtain a perturbation spectrum with dimensions of 200—500 km; on the other hand, we obtain perturbations with a scale 800—1,000 km or even larger (on a global scale), the dimensions of which vary from 1,600—2,000 to 2,500—3,500 km.

The radiation flux in the 6.0—6.5-μ band is determined in practice by the radiation of atmospheric water vapor, with a maximum value at an altitude of 7—8 km. Therefore, from the spectral density of these fields (Figure 2.18a) we can conclude that scales of the energetically significant perturbations have an order of magnitude of 400, 700, and also 1,100—1,700 km (curve 2). However, curve 3, characterizing the spectral density of emission according to data from TIROS III, with $h = 2.5°$, has only one maximum at $l \approx 800$ km that coincides with the analogous curves of Figure 2.18d. Further on the two curves are nearly a mirror image of each other. The absence of any perturbation on the curves of spectral density obtained from data of TIROS III seems to be very strange. On the other hand, the maxima at distances of 350 and 800 km stand out very clearly. In the region of the atmospheric window (Figure 2.18b) perturbations with a scale of about 800 km can be seen (curve 3).

According to curve 2, in this portion of the spectrum perturbations with the scale 1,200—1,600 km can be noticed. In general, in Figure 2.18 the perturbations are less noticeable than for the fields of integrated radiation or for water-vapor radiation. This may be explained by the considerable influence of cloud fields which determine the perturbation scales in the region of the atmospheric window. However, large perturbations of global scale are most noticeable in radiation fields that, to a large extent, are formed by the whole mass of troposphere, i. e., in the spectrum regions singled out by channels 1 and 4 of the radiometers.

In the region of the integrated short-wave radiation (Figure 2.18c) perturbations on the scales 500—800 and 1,200—1,500 km are seen on curve 2.

The same magnitude of perturbations of the radiation field appears in the range of channel 5, using data chosen from grid nodes with a 2.5° pitch (curve 3 in Figure 2.18e). The same curve shows another maximum at $l \approx 2{,}400$ km. On the other two curves (curve 3 in Figure 2.18c and curve 2 in Figure 2.18e) it is difficult to determine the scales of perturbations: the former only exhibits perturbations with $l \approx 500$—1,300 km and $l \approx 1{,}500$—2,100 km, while on the latter curve the perturbations with $l \approx 500$—1,100 km are weakly marked. Since the errors in the starting measurement data for these two channels were particularly large it is also natural to expect large errors in the calculated spectral density. Thus, e. g., the curves of spectral density for channel 3 with $h = 2.5°$ and for channel 5 with $h = 1.25°$, calculated according to the maximum and minimum envelopes of the field of auto-correlation coefficients, are almost a mirror image of each other. Therefore the curve of spectral density, calculated from a mean $k(\tau)$, has a very smooth course.

Such a spectral analysis may be very useful when comparing the emission fields plotted from satellite data with fields of the principal meteorological elements, in particular pressure, temperature, and cloudiness.

Such a relationship is supported by experiments and has a physical basis. Thus, the study in /11/ obtained a sufficiently high correlation between the radiation values of channels 2 and 4, and between the structural functions for the same channels. According to recent studies, integrated radiation, potential and kinetic energy of a certain atmospheric layer, outgoing radiation, the cooling of the atmosphere and other meteorological elements

are intimately interrelated. There exists in particular a connection between emission and the temperatures of the mean energy level /25, 11/.

Further achievements in the methods of statistical processing of radiation data will considerably promote their effective use and practical interpretation.

2.3. CLOUD IDENTIFICATION. RADIATION FORECASTING

The amount of heat (infrared) radiation depends on the temperature of the radiating body. Since, as a rule, cloud tops are colder than the Earth surface, this permits identifying the cloud cover from measurements of the outgoing infrared radiation. In the following this is illustrated by results obtained by Rasool /76/. *

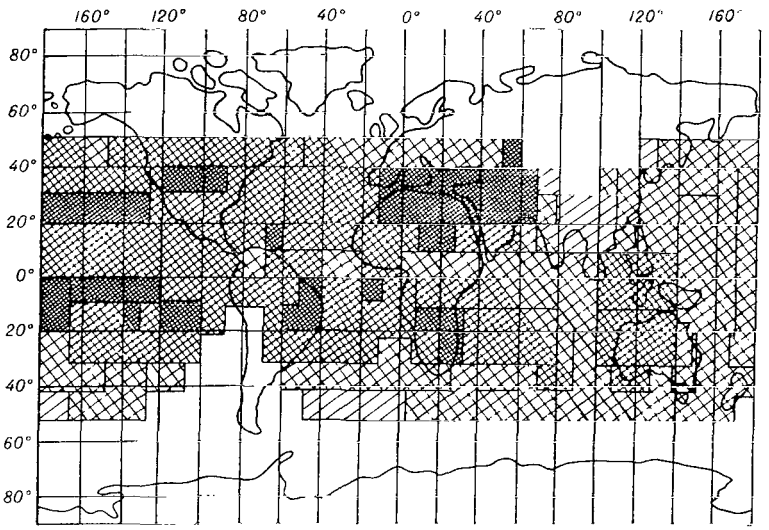

FIGURE 2.19. Global distribution of effective temperatures, measured by satellite TIROS III (channel 2) for the period from 12 July to 10 September 1961. The darkest shadings correspond to $T > 295$°K and the brightest to $T < 255$°K

Rasool processed the data from measurements of outgoing radiation in the transparent window of 8—12μ from data obtained by TIROS III during the period July through September 1961, with the purpose of studying the distribution of cloud cover on the Earth's night side (Figure 2.19). As is seen from these studies, the geographical distribution of the effective radiation temperature in the transparent window, averaged from squares of 10° latitude X 10° longitude over a time interval from 0600 to 1800 hours local time, clearly reflects the characteristic features of the planetary

* Some statements in this study have been criticized by Winston /92/.

cloud distribution: 1) a belt of relatively low temperatures near the equator, corresponding to the zone of considerable cloudiness observed in this region; 2) subtropical belts of high effective temperature located on both sides of the equator, characterizing the zones of relatively low cloudiness in the subtropics; 3) exceptionally low effective temperatures in east Pakistan and India, corresponding to considerable cloudiness with a high upper boundary.

The possibility of using measurement data on outgoing radiation for the detection of cloud systems and for the determination of cloud tops was discussed in /77/, where characteristic features of the radiation field in the region of a quasistationary front passing through the area of the Great Lakes and the central U.S.A. (27 November 1960, TIROS II data) were analyzed. Both ground-based and aerological data were used for comparison. These studies showed the field of effective temperatures to clearly reflect the characteristic distribution of cloudiness. Thus, e.g., a sharp increase in cloud heights is clearly evidenced from the reduction in effective temperature. However, the lowest effective temperatures were found in the region of broken cloud cover in the higher layers. It is possible that this discrepancy is due to errors in localizing the data of radiation measurements. An attempt to estimate the height of cloud tops on the basis of measurements, corrected for the influence of atmospheric layers, turned out to be a failure since the discrepancy between the calculated and measured cloud heights was too great. Apparently, this failure can be explained by the influence of partially obscured or semi-transparent sky cover of the upper layer and by the inaccuracy of corrections for the atmospheric layer. In another case, the calculated cloud heights coincided quite well with the measured heights in the region of a zone of continuous cloud cover with a rather high upper boundary (above 8 km).

The second example of data analysis refers to the region of a cold front and an occlusion in the eastern U.S.A. (29 November 1960). In this case a sharp gradient of the effective temperature (more than 20 deg/160 km) was observed across the frontal zone. Again, the field of effective temperatures reflects very well the cloud-cover distribution, but the calculated values for cloud tops differed in a number of cases considerably from the observed ones for the same reasons as those mentioned before. In all cases, the computed values of cloud heights of the upper layer were underrated because of the presence of lower clouds, while those for the lower layers were overrated (because of the presence of clouds located at higher layers).

The study in /77/ discusses in detail the possible application of measurements of the effective temperature in the transparent window for determining the temperature of the underlying surface (land, water surfaces, and snow cover) in cloudless regions. Comparing maps of both the geographical distribution of effective temperature and the air temperature as measured in the meteorological shelter screen shows that on the whole there is a qualitative coincidence between both types of temperatures in cloudless regions, although there are also some considerable discrepancies.

The study of observational data obtained during a cloudless night on 18 December 1960 in a coastal region of the Atlantic Ocean showed the

field of effective temperatures to reveal quite well the position of the coastline (as evidenced by the form of the isolines) and a considerable temperature gradient between the land and the oceans. There are, however, considerable differences between the effective temperature and the temperature of the underlying surface (up to 16—18°C) which may be explained either by the influence of possibly unobserved clouds or by the existence of aerosol layers near the tropopause. For snow-covered areas (in the border region between the U.S.A. and Canada) the values of the effective temperature were found to be lower than for the cloudy region located near it. In the absence of any other meteorological information than that supplied by the satellite, these data may mistakenly be interpreted as being caused by the presence of clouds in higher and lower layers. The quoted example shows the impossibility of a single-valued (unique) solution to the problem of investigating the cloud-cover distribution using data on the radiation field in the transparent window under any meteorological conditions. The condition of uniqueness can, however, be excluded if use is made of successive photographs from satellites and radiation measurements received every day for the same region. In this connection, climatological data may also be very useful.

Cloud distribution, as is well known, serves as a good index of the peculiarities of weather processes. Considering the relationship between cloud-cover distribution and radiation fields, the most typical weather systems can be easily identified from the features of the radiation-field distribution. At present plenty of information is available to support this conclusion and to speak of a new branch of meteorology — radiation forecasting. Of course, in the first stage of investigation with the still insufficient accuracy and reliability of satellite measurements of outgoing radiation, the easiest way in this study is to compare the synoptic charts and the fields of outgoing radiation and then to establish an empirical correlation between cloud-cover distribution, pressure patterns, and outgoing radiation. This method of interpreting data received from EXPLORER VII and TIROS II was used in various studies /6, 47, 55, 87, 90, 91/.

In /91/ measurement results were analyzed by comparing composite maps of geographical distribution of outgoing long-wave radiation from data on nocturnal measurements for 1—3 December 1959 during time intervals of several hours with maps of cloud distribution and 500-mb charts plotted for the same region and time intervals.

Comparison of the above maps immediately shows an intimate correlation between the fields of outgoing radiation and cloud-cover distribution. Let us examine, e. g., the maps of distribution of cloud cover and outgoing long-wave radiation in Figures 2.20 and 2.21 covering regions of North America and vast areas of the Pacific and Atlantic oceans. Here, the fluxes of outgoing radiation reach 10^{-3} cal cm^{-2} min^{-1}.

This comparison shows a perfect coincidence in the western parts of the investigated region between areas of lowest outgoing radiation (L-R-1, L-R-3, L-R-5) and zones of continuous cloud cover. It is obvious that the reason for this correlation is due to the presence of cloud systems of great vertical extent and with cold upper boundaries in these regions. On the other hand, the region of low cloudiness in the center of the considered

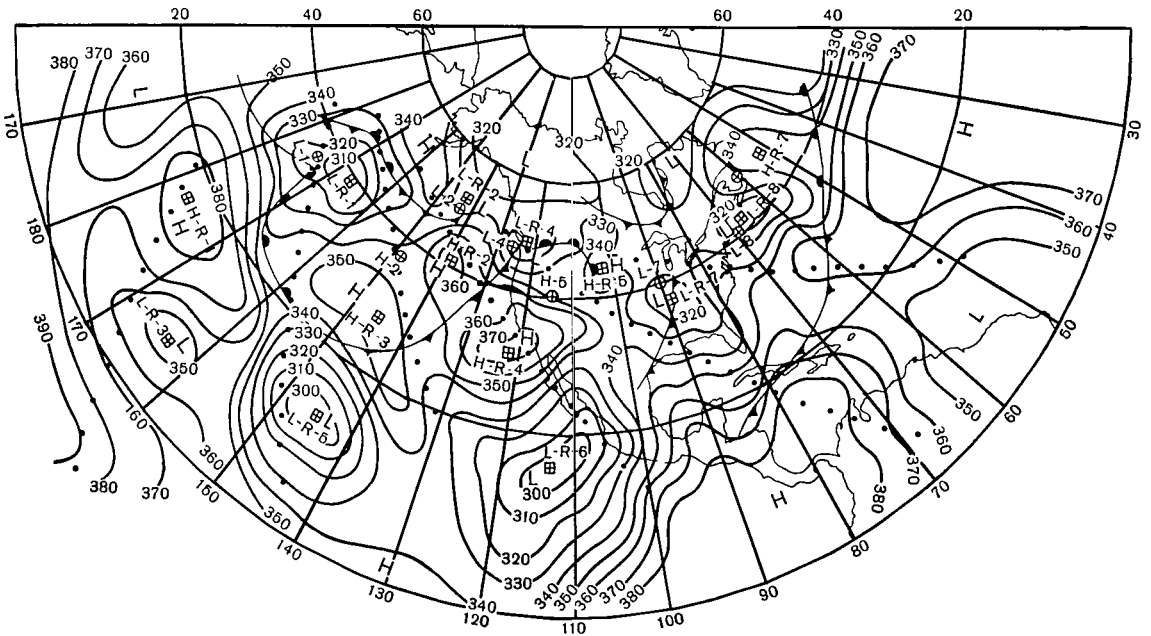

FIGURE 2.20. Geographical distribution of outgoing long-wave radiation according to measurements on 2 December 1959 (10^{-3} cal cm^{-2} min^{-1}). The circles and letter–figure combinations (e.g., L-1) designate centers of low and high pressure, respectively, at the ground level. The positions of surface fronts are also marked on the map. The extreme values of the radiation field are marked by squares and also by the combinations with an added R (e.g., L-R-1: region of low values of outgoing radiation connected with the center of low pressure L-1). The dots mark the points to which refer radiation-detector readings of the satellite.

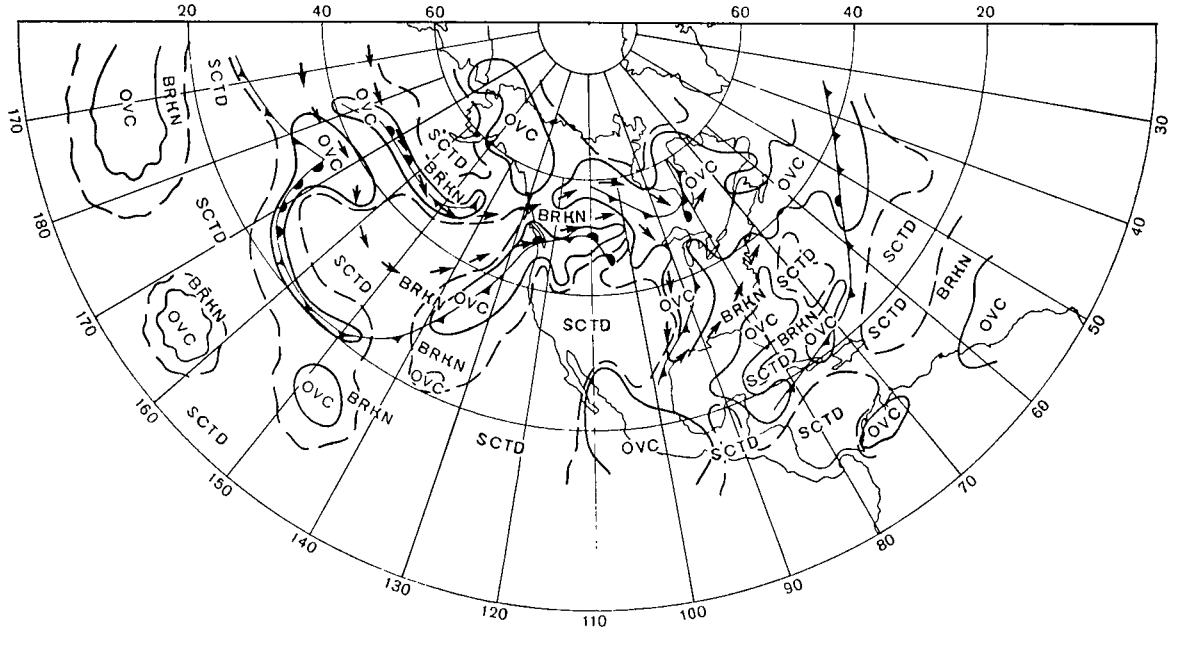

FIGURE 2.21. Geographical cloud-cover distribution on 2 December 1959 according to observational data at 0000, 0600, and 1200 GMT: Regions of continuous cloud cover (OVC) are enclosed by thick solid curves; areas of broken sky cover (BRKN) are enclosed by dashed curves; the remaining areas are either cloudless or with scattered clouds (SCTD). Arrows indicate the position of maximum wind speeds at 0000 hr at the 300-mb level.

area coincides with the position of the center of high outgoing radiation H-R-1 Since cloud-cover distribution reflects specific features of weather processes in a certain region, there is also a clear connection between extreme values of the pressure field, the position of fronts, and the field of outgoing radiation. Thus, e. g., in areas of cyclones (lows) or with a very active front, the upper limit of clouds is higher and cooler, and, therefore, such areas exhibit minimum outgoing radiation. The highest values of outgoing radiation are noticed in the central and eastern regions of anticyclones. In 24 out of 25 instances recorded between 1 and 3 December 1959 observational data for the temperate latitudes of the Northern Hemisphere showed a clear correlation between the position of surface lows and anticyclones on the one hand, and regions of minimum and maximum outgoing radiation on the other. For this area, the minimum of outgoing radiation is displaced to the east of the center of the low, while the maximum of radiation is displaced to the east of the anticyclonic center.

The field of outgoing radiation not only reflects the position of fronts but also their intensity, since "sharpness" and depth of "radiational" troughs are closely connected with the intensity of fronts. The daily change of the form of radiational troughs therefore characterizes the changes in intensity of fronts during 24 hours. Thus, e. g., the weakening of the radiational trough in the coastal region of the Pacific Ocean between 1 and 2 December reflects the decreasing intensity of the surface cold front. The same is valid for the evolution of lows. As a low is intensified, cloudiness increases both in the horizontal and vertical directions, and the horizontal temperature gradient increases as well. These changes, in turn, cause changes in the field of outgoing radiation. Moreover, there is a close connection between the movement of the low and the regions of minimum outgoing radiation. This is clearly seen from Figure 2.22, which presents the trajectory of the surface centers of low and high pressure (dashed lines) and the regions of minimum and maximum outgoing radiation (solid lines) for the period 1—3 December 1959 (see, e. g., the trajectories L-1 and L-R-1; H-5 and H-R-5, etc.). Six (out of seven) of the investigated displacements of regions with maximum outgoing radiation coincided with the displacement of high-pressure centers with an accuracy of not less than 20° in terms of direction and 18 km/hr in terms of speed (the seventh instance, the movement of H-4 and H-R-4, was complicated by the fact that during its motion H-4 merged with H-2). In all seven cases the displacements of the minima of both outgoing radiation and pressure centers were interrelated.

The displacement of regions of minimum outgoing radiation was found to be positively correlated with the movement of the mean geostrophic wind at 500 mb over corresponding areas. A somewhat poorer correlation is noticed in the analysis of motion of regions with maximum outgoing radiation.

The external appearance of the outgoing-radiation isolines very closely resembles the pattern of cyclone families reflected by the pressure field; the above-mentioned facts provide evidence that this similarity is not only an exterior feature (cf. the system of areas with minima of outgoing radiation from L-R-4 to L-R-1). Thus, the already mentioned correlation between the position of a cyclone family and jet streams corresponds to a similar correlation with regard to the field of outgoing radiation (see in

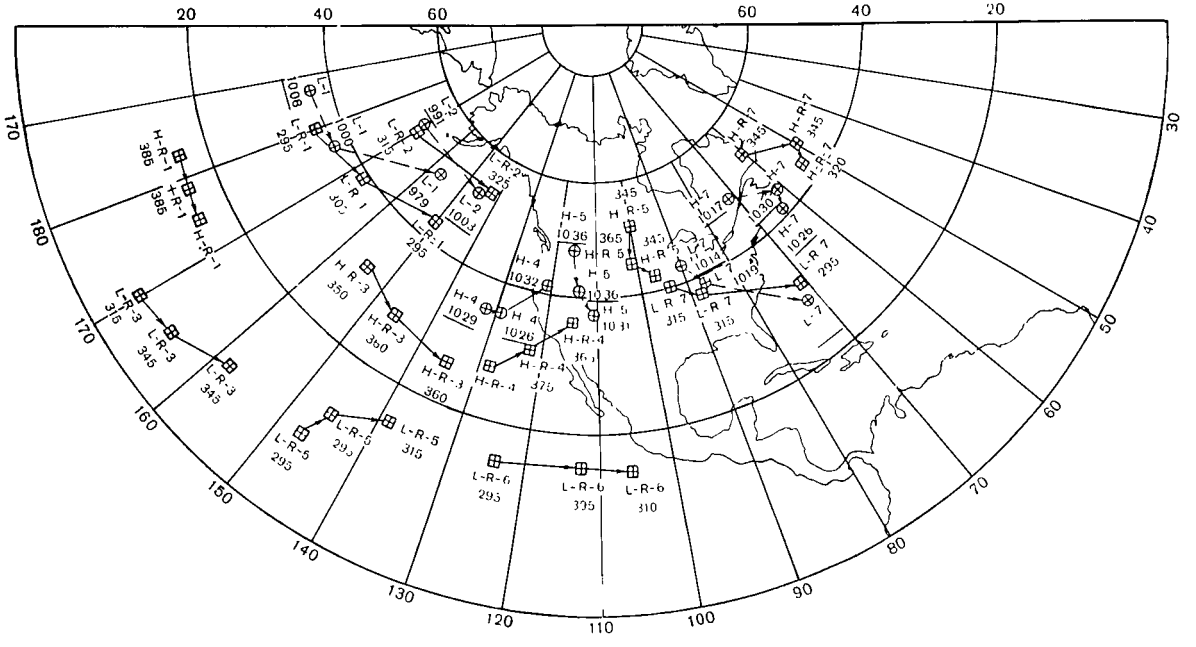

FIGURE 2.22. Trajectory displacement of extreme values of surface pressures and outgoing radiation (1—3 December 1959). For notation see legend of Figure 2.21.

Figures 2.20 and 2.22 the coincidence of wind-speed direction with the position of the chain of low-radiation centers). Minimum outgoing radiation may be associated not only with lows or fronts, but also with the presence of a cold underlying surface or a snow cover, as well as with an extensive cloud cover in the upper layer. However, an analysis of the outgoing-radiation field often permits the specific reasons for the decrease in outgoing radiation to be established.

Corcoran and Horn /48/, when studying problems of generation of usable potential energy by means of differential radiant cooling, performed an interesting analysis of characteristic features of outgoing long-wave radiation as applied to various synoptic instances.

According to Fritz and Winston /55/, the greatest difficulty arises when it becomes necessary to distinguish between low cloudiness and the Earth surface. For such cases, a unique solution is not always available (it should be noted that in /55/ only measurements of outgoing radiation in the atmospheric window 8—12μ were analyzed).

Thus, the field of outgoing radiation reflects fairly completely the properties of meteorological processes, and in the absence of conventional meteorological data it often provides an idea on the position of lows and anticyclones, changes in intensity and speed of movement, the position of fronts, and other features of meteorological processes. There is also a possibility to determine wind velocity at the 500-mb level and tropospheric jet streams.

Although the results obtained by Weinstein and Suomi /91/ are very tempting, they require a serious statistical substantiation by expanding the amount of available data. Measurements of outgoing radiation should also become much more accurate. This was illustrated with particular clarity in /43/ by the example of the characteristic shape of hurrican Anna in the field of radiation of various wavelengths. In this paper, the authors investigated the properties of the field of outgoing radiation of various wavelengths over the area of hurricane Anna from measurements of the TIROS III 5-channel radiometer on 21 July 1961. They were able to reveal the distinctive appearance of the hurricane against the background of the infrared-radiation field as a zone of very low radiation values, caused by the presence of clouds with high and cold upper boundaries in the center of the hurricane. This is clear from Figure 2.21, which shows the field of outgoing radiation in the transparent window of the 7.5—13.5-μ band. Figure 2.23 shows values of the effective (radiation) temperature corresponding to different isolines. As is seen, the temperature in the center of the hurricane decreases to 220°K.

Boldyrev /6/ analyzed the radiational synoptic situation over the territory of the U.S.A. on 27 November 1960. He established three outgoing radiation minima that covered the center of the cyclone, and a region of maximum radiation in the Gulf of Mexico corresponding to a cloudless zone.

Winston and Rao /88/, when analyzing TIROS II data, showed that the field of outging long-wave radiation reflects well the characteristic features of weather processes in various regions of the Earth. They also plotted maps of diurnal geographical distribution of the outgoing radiation supplemented with most detailed information on radiation.

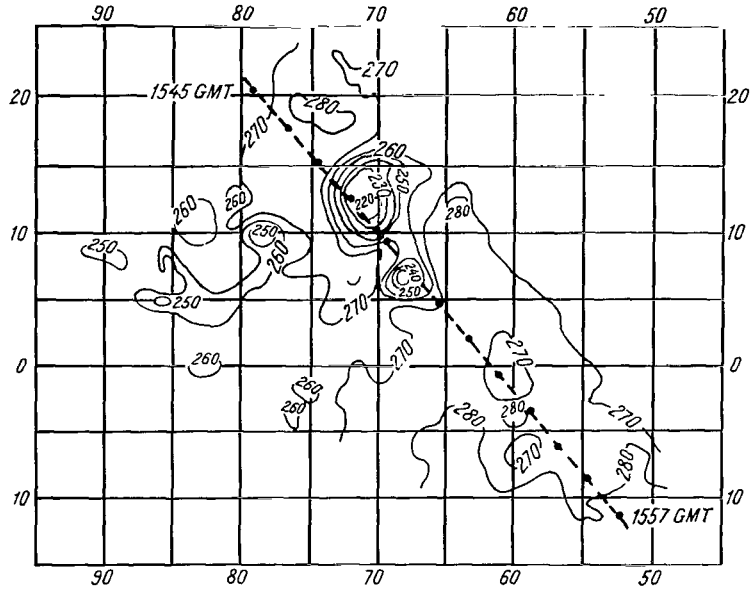

FIGURE 2.23. Radiational-synoptic chart. Geographical distribution of outgoing radiation in the transparent window of the 7.5—13.5-μ band. Orbit 132 on 21 July 1961, 1545 to 1602 GMT.

Despite the considerable leveling of data, the maps reveal an extremely nonuniform distribution of the cloud cover. It is for this very reason that the field of long-wave radiation reflects the characteristic features of weather processes in different regions of the Earth. (One can, e.g., clearly discern the intertropical convergence zone. In temperate latitudes the regions of lowest radiation values correspond to places of lows and fronts, whereas regions of radiation maxima coincide with the location of anticyclones in the regions of the westerlies and with the subtropical anticyclones to the south of this zone.)

Comparing maps of the distribution of outgoing radiation with data from nephanalyses shows that the minimum radiation mostly coincides with large areas of continuous or considerable cloudiness, while maxima coincide with regions of low cloudiness. Occasional discrepancies may be explained both by the schematical character and insufficient reliability of nephanalyses because of the low quality of pictures obtained with TIROS II and by the fact that even with continuous cloud cover and low boundaries the outgoing radiation may reach large values.

Winston and Rao analyzed four composite maps of the geographical distribution of outgoing radiation plotted by averaging observational data for four to five days. These maps were compared with maps of absolute topography of isobaric 700-mb surface averaged for five days. These results revealed an interesting fact: a sharp decrease in outgoing radiation at the end of November and till mid-December, associated with the intrusion of westerlies into the Subtropics where till then ancicyclones prevailed. In the Northern Hemisphere from the middle of December till the beginning

of January the field of outgoing radiation was relatively stable. In the Southern Hemisphere the outgoing radiation usually has less variability in time that that in the Northern Hemisphere. The most significant time-dependent variations in the radiation on the analyzed maps reflect the transition from zonal to meridional circulation.

It should be noted that the characteristic features of geographical distribution of the long-wave radiation, being determined by the specific distribution of the cloud cover, are closely connected with the position and intensity of lows, anticyclones, fronts, and other meteorological phenomena, but only generally do they reflect the characteristic features of the airflow in the atmosphere.

A very interesting and useful experiment of obtaining infrared pictures of the cloud cover on the Earth's night side was carried out by means of a high-resolution scanning radiometer with maximum sensitivity in the transparent window of about 4μ installed on NIMBUS I (see Chapter 1).

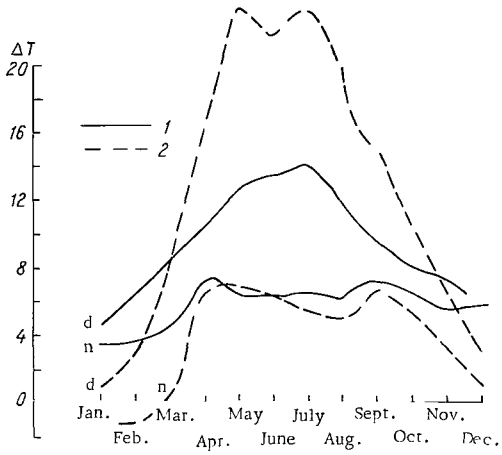

FIGURE 2.24. Annual variation of temperature differences between the Earth surface and cloud tops. Moscow:

1 — low clouds; 2 — high clouds; d — day; n — night.

In connection with the possibility of obtaining infrared cloud pictures it is interesting to study both the conditions that favor the solution of this problem and those in which the interpretation of data may prove erroneous. The latter may arise, e.g., for temperature inversions, when the Earth surface may be colder than the cloud tops, or else the temperature difference between the surface and cloud tops may be very small. Such conditions are quite typical of high latitudes, especially in winter. Thus, Nordberg /75/, when analyzing infrared pictures of the Greenland region, obtained cloud-top temperatures by 20°C higher than those of the underlying surface. For the study of a similar situation Kondrat'ev and Ter-Markaryants /24/ investigated the annual variation of temperature difference between the ground surface and cloud tops in different climatic zones and for clouds at different levels. Figure 2.24 clearly shows how much the problem of cloud identification by measurements of the outgoing long-wave radiation tends to become complicated in winter. Data from NIMBUS I showed that from this point of view the use of the transparent windows of 3.4—4.2μ is preferable to those of 8—12μ. This conclusion was theoretically substantiated in /35, 28/.

As shown by Malkevich /30, 31/, in such cases very reliable data can be obtained by using the results of measurements of outgoing radiation not

only in the transparent window, but also in the absorption bands. Obviously, the brightness contrasts between the atmosphere radiation window and the absorption bands will be largest for the Earth surface and should decrease with increasing cloud height, as seen from Figure 2.25. Even if the Earth surface and the cloud tops have the same temperature, the use of the above-mentioned contrasts makes it possible to distinguish between clouds and the Earth surface.

Finally, let us consider an example of analysis of infrared cloud pictures from NIMBUS I data, reported in /14/.

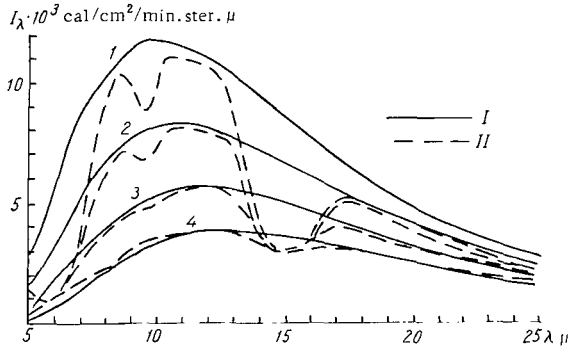

FIGURE 2.25. Spectral distribution of the absolute blackbody radiation at the upper cloud boundaries (curve I) and of the outgoing long-wave radiation (7—35 μ) for different heights z of cloud tops (curve II):

1 — z = 0 (Earth surface), T = 288°K; 2 — low clouds, T = 273°K; 3 — middle clouds, T = 250°K; 4 — high clouds, T = 223°K.

Photograph 2.5 shows a cloud picture in the region of Siberia obtained on 6 September 1964 at 0030 hr local time for the meridian of 75°E in the 3.7—4.2-μ wavelength bands.

The infrared picture covers a belt about 1,300 km wide (eastward from the Ural Mountains), stretching from southern Kazakhstan and the southern Ural Mountains (lower part of the picture) to the Laptev Sea (upper right corner).

The brightest parts of the picture correspond to clouds with the largest altitude (i.e., with the lowest temperatures at their upper boundaries); the less bright parts correspond to clouds with lower tops, while the dark-gray parts show cloudless areas of the Earth surface. At the lower right (A) of the photograph banks of high and cold clouds can cearly be seen. Analysis of routine meteorological observations shows these clouds to be connected with a cold front in the region of which rain showers are observed. This front extends somewhat eastward of the Ob' River, nearly parallel to its upper course.

The cyclone to which the front belongs, i.e., the lower isobaric system, can only be traced up to the 850-mb surface.

In the lower left of the picture (BB') an area of rather high clouds is seen which is connected with a second cold front extending along the 70th meridian from Salekhard to Tselinograd. Local rain showers are observed in the region of this front.

Between these cloud complexes an area of light-gray shade (C) is found corresponding to regions with clear weather in the rear of the cold front.

The darker middle part of the photograph (D) coincides with a cloudless area determined by the anticyclone located over the central Siberia plateau. This anticyclone is a high-pressure system with an almost vertical space axis; this system can be tracked up to the tropopause. On the right of the picture one can discern a somewhat brighter portion indicating the northwestern, highest ridges of the plateau.

On the left of the photograph (about 75—80°N) a rather large complex of high clouds (E) appears, extending to the right. This is connected with the frontal part of a low and with warm fronts where local overcast, rains, and drizzle are observed. In the upper part of the picture, belts with less bright white and gray shades are clearly seen; in the uppermost part of the photograph these belts are twisted. The direction of these cloud belts and their twisting coincide more or less exactly with the direction of the wind and the center of the low at the 300-mb level.

The dark spots in the upper left corner of the photograph (D) are apparently areas of partly open water between the ice floes in the Arctic Ocean. (According to airborne surveys, zones of ice-free water were observed in this region.)

Figure 2.26 shows for comparison ground-observation data on cloud cover distribution for 0000 hr local time on 6 September 1964, and corresponding satellite cloud pictures (hatched areas). The figure shows a good coincidence between cloudy areas observed from the surface and from the satellite. There are, however, some discrepancies which may be explained either by difficulties in cloud observations from the ground at night or by inaccurate geographical location of satellite data.

However, as can be seen from Photograph 2.5, infrared cloud pictures obtained by satellites afford, in general, a good idea of cloud distribution.

In Photograph 2.5, the region D with cloudless sky (the Yenisei river basin) is relatively darker than region C, which is also cloud-free according to observations from meteorological stations. This difference may be explained using aerial synoptic data. The brighter shade of the infrared picture of the southern cloudless zone is caused by the lower temperature of that zone in the atmospheric boundary layer up to an altitude of about 3 km, which is seen from Table 2.12.

TABLE 2.12

Region	Temperature, °C		
	at the ground surface	at 850 mb	at 700 mb
South (C)	5—6	0—2	-5, -10
North (D)	10—15 (along the river) 5—6 (in the mountains)	8—10	0, -2

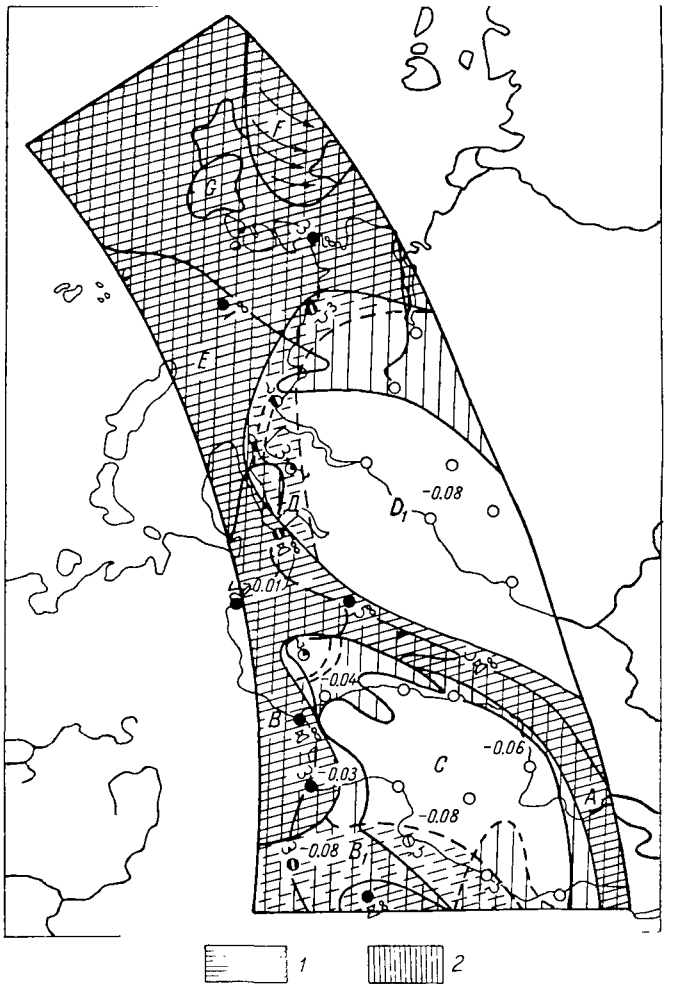

FIGURE 2.26. Schematic map of cloud distribution according to ground-based data (1) and observation results from satellite NIMBUS I (2) for 6 September 1964, 0030 hr local time

It should be pointed out that the barometric ridge which causes cloudless weather in region C is a low formation hardly trackable to the altitude of the 850-mb surface. Higher up, a well marked cyclonic circulation exists over that region which may lead to the formation of ascending currents in the upper layers of the troposphere and of thin cirrus clouds, which cannot be observed at night from the ground.

On the other hand, in the north, the ridge connected with cloudless weather may be tracked to larger heights. On the 300-mb (H_{300}) map a vast upper-level anticyclone extends over this region, and therefore this region must have descending currents that inhibit cloud development.

From an emagram analysis it is seen that the height of cloud tops in the region marked B and B' varies from 3.5 to 4 km, while cloud temperature at this height varies from -10 to -15°C. Over the Perm and Sverdlovsk regions and the region east of Novosibirsk (zone A) the cloud tops are at 10 to 11 km and their temperature is about -50°C.

The analysis of Figure 2.26 shows that data on cloud distribution obtained from a satellite [except for infrared pictures] do not always agree with data from ground observations. In such cases the above data may be checked against the values of the radiation balance obtained by actinometric ground stations.

Figure 2.26 presents values of the radiation balance (in cal cm^{-2} min^{-1}) for 0030 hr local time obtained on 6 September 1964. As may be seen, the most characteristic values for cloudless areas are -0.06 to -0.011 cal cm^{-2} min^{-1} (with an average of -0.08 cal cm^{-2} min^{-1}); for cloudy regions they are much smaller: between -0.01 and -0.04 cal cm^{-2} min^{-1}.

Nordberg /75/ made a very interesting analysis of infrared photographs of clouds and different parts of the Earth surface. These data proved particularly useful in determining the temperature of open water surfaces. The temperature of relatively small lakes can be determined rather reliably. In principle, even ocean currents may be detected from the temperature contrasts [on the pictures].

Fujita and Bandeen /1.21/ discussed the possibility of analyzing the fine spatial structure of the underlying ground surface from data supplied by infrared photographs on the Earth taken by NIMBUS I with a high-resolution infrared scanning radiometer. They analyzed three infrared pictures of cloudless parts of the U.S.A. (Grand Canyon, Death Valley, and Sierra Nevada) taken about midnight. This analysis was supplemented by data on the outgoing radiation recorded for separate picture lines. The analysis showed a double form of noise of a periodic and oscillatory character to be superimposed on the useful signals. The oscillatory noises can be eliminated by averaging the intervals of scanning angle of approximately one degree. The periodic noise does not affect the resolving power and accuracy of the geographic location of the infrared pictures.

Fujita and Bandeen showed that the fine structure of the distribution of outgoing radiation (as evidenced by the infrared pictures) is a very sensitive index of the heterogeneity of the underlying surface. Thus, a lake 20 × 30 km in size or less, or even the dried-up beds of lakes, appear as spots of elevated temperatures. The determination of the temperature of the underlying surface for points at different heights above sea level made it possible to obtain a value of 6°/km for the vertical temperature gradient. Topographical features are also clearly seen on the infrared pictures. It was found, e. g., that the bottom of Grand Canyon is warmer than its slopes. The estimated vertical temperature gradient in this instance was 10°/km.

The ice fields and their structure were also clearly revealed in these pictures. Different information may be obtained about the properties of the underlying surface: topographic features, tentative data on the heat capacity and moisture of the soil, etc. Nordberg /75/ pointed out that data from daily measurements of the infrared radiation in the transparent window of 3.4 to 4.2 μ may be used for determining the emissivity of the underlying surface. Preliminary interpretation of the observational data

showed that for large parts of the underlying surface (oceans, clouds, snow, vegetative cover) the emissivity factor exceeds 0.9.

From infrared pictures of the Earth surface it is possible to study soil moisture /1.51/, thanks to the horizontal temperature gradient which exists by day owing to the differences in soil moisture.

2.4. DETERMINATION OF SURFACE TEMPERATURE, CLOUD HEIGHT, AND MOISTURE IN THE TROPOSPHERE

The main contributor to the outgoing radiation through the transparent window of the atmosphere is the radiation of the Earth surface (or of the cloud tops). This permits the determination of the surface temperature by measuring the outgoing radiation. Of course in crude measurements the introduction of appropriate corrections for the influence of the intervening atmospheric layers above the ground is essential.

Airborne measurements conducted by Gaevskii and Rabinovich /16/ showed that in the 8—12-μ window the magnitude of the above-mentioned corrections may reach 15° when the water-vapor content of the atmosphere is 3.6 cm (these experiments yielded much lower values than those obtained by theoretical computations). However, it is possible to plot correlation graphs for the dependence of corrections on the values of the effective (radiation) temperature of the ground surface using only one parameter, namely, the moisture content over the whole mass of the atmosphere. Thus, knowing this moisture content, we can find the correction for the effective temperature, and thus the actual surface temperature (the ozone effect, which has to be allowed for in interpreting satellite data, can be determined theoretically).

Another way of taking into account the influence of the intervening atmosphere layer is the introduction of a so-called transfer function suggested in /9/. The transfer function is defined as the ratio of the true surface radiation to the radiation of an absolute blackbody at the Earth surface temperature; this function mainly depends on the equivalent water-vapor content of the whole atmosphere. A practical example for this method is presented in /5, 8/.

The above theoretical studies /5, 8, 9, 32/ only take into account the absorption of radiation by the whole atmosphere. Zdunkowskii et al. /96/ calculated the effect of the invisible thin cirrus clouds on the outgoing long-wave radiation in the following spectral ranges: 6—6.5μ; 8—12μ; 8.75—12.25μ; 13.5—16.5μ, as well as the integrated long-wave (outgoing) radiation. According to some authorities, haze represents a layer of monodisperse spherical ice particles (of radius 120μ and in concentrations varying from $5 \cdot 10^{-4}$ to $1 \cdot 10^{-1}$ cm^{-3}); the layer has a thickness of 1 km and its top is 1 km below the troposphere. The authors of /96/ also present data on the dependence of the length of attenuation, scattering and absorption on wavelength (for 120-μ particles) and show this dependence to be less markedly pronounced than the wavelength dependence of the attenuation (absorption) coefficient. In calculating outgoing radiation, the above authors assumed the upper boundary of the atmosphere to be at 45 km for a haze layer. They

also present the results of calculations of the latitudinal march of outgoing radiation along the 80°W meridian. Both in the absorption belt (wavelengths 6—6.5μ) and the transparent window (8—12μ) the effect of the haze layer on outgoing radiation is very considerable, especially for a particle concentration of 10^{-2} cm^{-3}. At a particle concentration of 10^{-1} cm^{-3} even an inversion of the latitudinal variation is noticed; there is a decrease in the outgoing radiation at smaller concentrations of ice particles. This considerable influence of haze on the integrated outgoing radiation is supported by data of actinometric soundings. Estimates show that invisible cirrus clouds may lower the integrated outgoing radiation by about 10%. Using data from measurements of outgoing radiation in the atmospheric window for the determination of ground temperature without allowing for the influence of haze may yield overrated temperatures (by 3—4°C larger for tropical air masses and by 2—3° larger during winter in mid-latitudes). It has been noted that with observations at zenith viewing angles between 0 and 45° the transition from invisible to discernible brightness of clouds occurs at an increase in the particle concentration from $1.5 \cdot 10^{-3}$ to $1.5 \cdot 10^{-2}$ cm^{-3}. The transition from partially translucent to nearly "black" clouds in the infrared region of the spectrum occurs over a particle-concentration range of 10^{-2}—10^{-1} cm^{-3}. The influence of a stratospheric aerosol layer (assumed to consist of carbon particles) at a height of 10—30 km on the transfer of long-wave radiation is negligible.

Kuhn and Suomi /65/ analyzed the results of two actinometric night soundings in a desert region (California) carried out on 20 February 1964 under a cloudless sky and in a very dry atmosphere; these soundings were supplemented by visual observations of haze layers from a jet plane at a height of about 12.9 km. Separate temperature measurements of the ground surface were made with thermistors and a radiometer. A comparison of the radiometer and thermistor readings yielded an emissivity of the surface of 0.95. Analysis of the first actinometric sounding revealed the presence of a continuous cloud or haze layer at altitudes of 10.5—12.9 km. This was confirmed by visual airborne observations. The outgoing-radiation flux computed at the probe ceiling, without allowing for the influence of the haze layers, was by 0.041 cal cm^{-2} min^{-1} larger than the measured value. However, for haze layers with a relative emissivity of 0.11, the calculated values coincide with the measured ones. Such an agreement was also observed when the temperature of the underlying surface was taken as 3.0°C instead of the observed 8.7°C. Such discrepancies (5.7°) are likely to arise when determining the ground temperature from satellite data on outgoing radiation without taking into account the influence of aerosol layers. The air temperature in the meteorological shelter was 12.2°C. At the time of the second (later) ascent of the probes only remainders of the earlier observed thin clouds were found. The above-mentioned paper also estimated possible errors in the above-examined measurements and calculations.

Once the temperature of the cloud tops is found, it becomes possible to determine the height of the cloud tops if data on the vertical temperature distribution are available. Fritz and Winston /55/ developed a method for solving such problems, using isotherm maps for 700-, 500-, and 300-mb surfaces, plotted at the U.S. National Meteorological Center. The ground

charts may be plotted using routine meteorological observations. Results thus obtained proved in many cases to be quite satisfactory.

Möller /69/ proposed a simple method for determining the temperature of the Earth surface (or of the cloud tops) and the relative humidity, using observational data received from TIROS satellites.

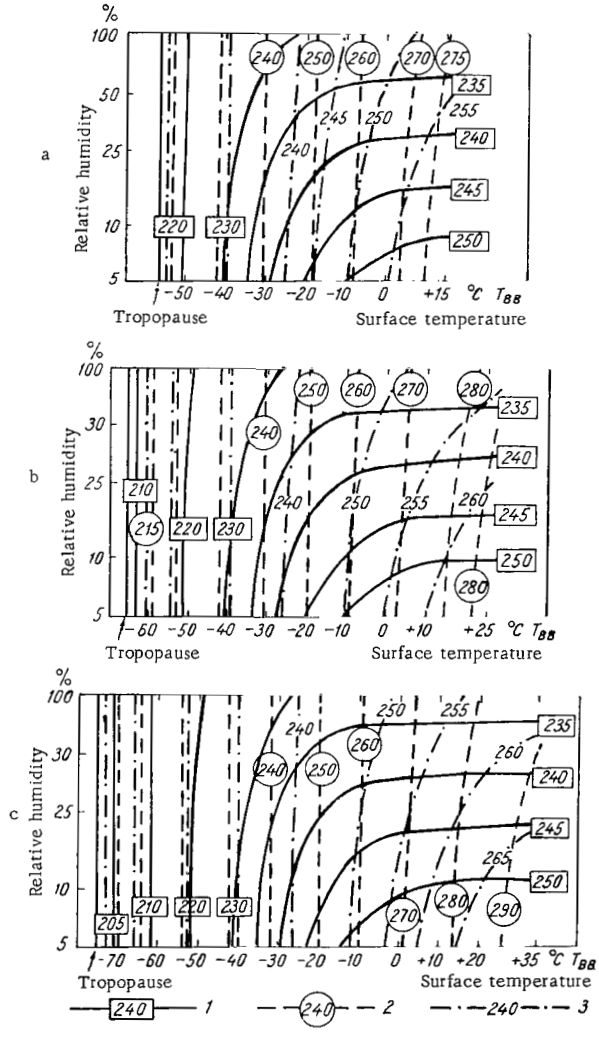

FIGURE 2.27. Nomographs for calculating surface temperature and relative humidity:

a — atmosphere I (ARDC); b — atmosphere II (subtropical); c — atmosphere III (tropical); 1 — channel 1 (5.6—6.8 μ); 2 — channel 2 (7.5—13.5 μ); 3 — difference of readings (12.0—32.5 μ).

From available data on outgoing radiation over the spectrum ranges 5.6—6.8μ (channel 1 of the 5-channel radiometer of the TIROS satellites), 8—13μ (channel 2), 7.5—32.5μ (channel 4) and 12.0—32.5μ (difference between readings of channels 2 and 4), it is possible to draw isolines of computed values of outgoing radiation (or effective temperature) in a coordinate system of surface temperature vs. relative humidity (Figure 2.27a,b,c). If the relative humidity is plotted on the ordinate and the surface temperature on the abscissa, the isolines relating to channel 2 are almost parallel to the ordinate. With the measured values of outgoing radiation (effective radiation temperatures) on hand the surface temperature may be determined with the aid of the diagram. Then, from the isolines for channel 1 with the available values of surface temperatures, we determine the relative humidity of the upper half of the troposphere. The difference between readings of channel 1 and channel 2 on the one hand and channel 4 on the other hand, yields values of relative humidity for the lower half of the troposphere.

Möller and Raschke /70/ have shown that the above-mentioned isolines should be drawn for different model atmospheres that relate to certain latitude belts, and only then applied to the specific conditions of observations.

Figure 2.27 shows the corresponding diagrams for standard, subtropical, and tropical atmospheres. Using the above method, Raschke and Tannhäuser /79/ plotted maps of the quasiplanetary distribution of the Earth surface temperatures and of relative humidity of the upper troposphere from data received by TIROS III during the first six days of its functioning.

This method is also applicable for the determination of the water content of the whole atmosphere by using the formula

$$w = \int_{z}^{\infty} \frac{e_s(T(z))\, r(z)}{T(z)\, R^* m_w}\, dz,$$

where $T(z)$ is the vertical temperature profile (the profile corresponding to the standard atmosphere for a temperature value at the level z according to observational data may be taken as the vertical profile); e_s is the saturation water-vapor pressure; $r(z)$ is the relative humidity; R^* is the universal gas constant; m_w is the molecular weight of water vapor.

As level z one may take the 500-mb level, remembering that the outgoing radiation in the 6.0—6.5-μ band mainly forms in the atmospheric layers above this level.

Let us consider Möller's method with an example.

Assume that observations furnished the following values of the effective temperature:

Channel	Temperature, °K
1	237.5±2.5
2	272.5±2.5
(4—2)	257.5±2.5

Using a set of three diagrams plotted by Raschke for three model atmospheres, we obtain Table 2.13.

TABLE 2.13

Model atmosphere	Temperature of the Earth surface, °C	Relative humidity, %
Channels 1 and 2		
I	9	40
II	8	45
III	7	55
Channels 2 and (4 minus 2)		
I	7	
II	6.5	
III	6	22

As may be seen, surface temperature decreases somewhat and the relative humidity increases from atmosphere model I to model III.

Assuming that in our case there is a continuous cloud cover, and taking 10°C as the temperature of the cloud top, then, depending on the selected model atmosphere, the height of the cloud top must be as follows:

Model atmosphere	I	II	III
Level of cloud top (in mb)	930	770	650

This table shows that the choice of model atmosphere is very important in determining cloud height.

A similar method for determining cloud height was suggested in /76/. For a quantitative interpretation of measurement results, Rasool computed the effective temperatures in the transparent window for ten model atmospheres without clouds for ten-degree latitude belts over the range of 50°N to 50°S. Similar computations were also made for different cloudiness conditions (different degree of cloudiness and cloud height). These computations were used to correlate the difference between effective temperature and surface temperature with the degree of cloudiness for different humidity of the atmosphere (cloud height being used as a correlation parameter). If the Earth surface temperature, degree of cloudiness, and atmospheric humidity are known they can be used for an approximate evaluation of the temperature and height of cloud tops by correlating them with data from satellite measurements of the effective temperature. The use of climatic data for determining the temperature of the underlying surface permitted the study of the latitudinal dependence of the difference between effective temperature and surface temperature for day and night.

With satellite television data on the latitudinal distribution of cloudiness in daytime and with the above relationship, it is possible to compute the mean latitudinal distribution of cloud-top heights at night. Comparing the mean latitudinal cloud distribution by day and night shows that in the Southern Hemisphere cloudiness during nighttime is much larger than by day. On the contrary, in the Northern Hemisphere, night cloudiness is about 20% smaller in the latitude range of 20—40°. It should, however, be stressed that these results are based on the (disputable) assumption that cloud height is the same at night and during daytime for a given latitude belt

The processing of data obtained from measurements by a high-resolution radiometer installed on the NIMBUS satellite /75/ made it possible to receive very detailed information (in terms of spatial resolution) on the height of the cloud cover.

Gaevskii and Guseva /17/ discussed the possibility of determining the height of cloud tops from data of satellite measurements of the radiation temperature of clouds when the vertical temperature gradient (lapse rate) is not known, and thus a mean value of the temperature gradient has to be used. For this purpose, the vertical temperature gradient from the Earth surface to the cloud top has been computed from airborne soundings in the Leningrad Region (for 923 instances). From the results it is seen that in 80% of the cases the vertical temperature gradient varies between 0.4 and 0.75 deg/100 m, and only with stratus clouds it increases from -0.1 to + 0.9 deg/100 m. If we assume a mean temperature gradient of 0.55 deg/100 m, the error in determining the height of two clouds whose tops are, e. g., at 7 and 3 km, respectively, will be 1 km and 500 m, respectively, the error being larger for stratified clouds. It has been noted that values obtained for the radiation temperature of the Earth surface may differ by 3—10°C from the actual air temperature at this level. Such large differences limit the applicability of this method for determining cloud-top height, and the above-mentioned errors may be considered as real only for clouds whose thickness does not exceed 400 m. Such clouds can often (but not always) be distinguished on satellite cloud pictures. The Earth surface temperature can be determined by satellite radiation measurements in the breaks between the clouds.

Winston and Rao /88/ have shown that several cloud layers observed simultaneously make it very difficult to determine temperature and height of cloud tops. A significant source of errors may be caused by failing to take into account the presence of thin cirrus clouds otherwise invisible to the naked eye /96/. Other difficulties may arise as a result of insufficient knowledge of the radiational characteristics (the emissivity) of the clouds in different layers. According to data from /1.51/ the emissivity of most cloud types in the spectrum range of $3.4 - 4.2\,\mu$ is about 0.75.

The height of cloud tops can also be determined by measuring absorption of solar radiation in the 0.76-μ oxygen absorption band in the atmospheric layer about the cloud.

The study in /82/ describes a spectrograph for measuring the height of cloud tops by this method. In the spectrograph (which combines a photographic camera with a spectroscope) the dispersing element serves to analyze the spectral components of the solar radiation reflected by the clouds in the oxygen absorption band of $0.76\,\mu$, and is a replica grating of 3.0×3.2 cm with 1,200 lines/mm with a brightness of the first order for the 0.76-μ band. Its spectral resolving power is about 5 Å and it weighs about 1.65 kg. For radiation intensity the device is calibrated by exposing a film through a number of slots of different width. The method of processing the results consists in comparing the measured values of the solar radiation transmitted through the atmospheric layer above the clouds (i. e., the ratio between the intensity of radiation in the absorption band for wavelengths of 7,630 Å and beyond them) with the corresponding values, computed for different atmospheric pressures at the upper cloud limit.

After comparison, we determine the atmospheric pressure and then the height of the cloud top. Airborne tests of the device during a flight at a height of 30 m above a uniform altocumulus cloud deck with the device aimed at the nadir angle, showed the device to yield overrated values of the atmospheric pressure compared with the actual 137-mb level; this in turn leads to underrated values of the cloud height. However, the error in measuring radiation transmitted through the atmosphere did not exceed ± 0.01, corresponding to an error of ± 30 mb in determining the pressure. The above-mentioned discrepancy may be explained by the distorting influence of absorption of solar radiation on the radiation reflected by the cloud mass. This definitely proves the necessity to take into account the differences in the cloud albedo within and beyond the oxygen-absorption band. An approximate theoretical calculation confirms this assumption. The authors of /82/ proposed a method for introducing the necessary corrections that allow for the cloud albedo difference within and beyond the absorption band as a function of the cloud-cover thickness. Without such a correction the error in determining the height of cloud tops may vary from 300 to 2,200 m. It is therefore very important to check this method experimentally for middle and high clouds, as well as for semi-transparent clouds. Theoretical estimates of the influence of solar-radiation absorption within the cloud mass are only valid for such cases in which the solar zenith distance is about 67°. It is quite possible to exclude the radiation—absorption effect within the cloud body by using measurement data for two spectral intervals in the oxygen-absorption band corresponding to different absorption coefficients. The above instrument was used during the flight of astronauts Cooper and Conrad. A preliminary processing of data yielded very promising results /95/.

Wark and Mercer /94/ discussed the theoretical interpretation of data from measurements of the outgoing radiation in the oxygen band of 0.76μ to be used for the determination of cloud heights. These authors recalculated the absorption of solar radiation by the atmosphere caused by the oxygen band and detailed the fine structure of this band. They presented the molecular constants for O_2^{16}, $O^{16}O^{17}$ and $O^{16}O^{18}$, as well as data for calculating the intensity of spectrum lines that make up the band (probability of transitions, statistical weights, and half-width). The absorption of solar radiation was calculated for a standard atmosphere, using spectrum intervals containing about 10 lines. A comparison of the calculation results with measured values showed fairly good agreement. The authors emphasize the importance of choosing sufficient spectrum intervals for carrying out satellite experiments and show that the use of a single interval is insufficient for determining the cloud tops both of the lower and higher level. For the wavelengths 7,607 and 7,632 Å they show that the first cannot be used for the determination of cloud tops of the lower level (the absorption is too strong), while the second length is useless for measuring cloud tops of higher level (absorption is too weak). However, the joint use of both wavelengths makes it possible to obtain a reliable solution of the problem. Calculations of the derivative function of absorption in terms of cloud height led to the conclusion that the variation of absorption with height of cloud cover is relatively small, and therefore the influence of measurement errors on the final results is considerable. Thus, with a measurement error of 4% the error in determining cloud height is around

one kilometer if the values of the absorption function vary from 0.31 to 0.91. This may include a cloud-height range from zero to 12 km. If it is required to raise the ceiling it becomes necessary to reduce the measurement error to 2%. Calculations of the radiation absorption for the above wavelengths under conditions of tropical and arctic atmospheres show that deviations from values for standard atmosphere do not exceed 1%.

Usually (but not always) the field of cloudiness coincides with regions of ascending air currents, while descending motion is associated with cloudless regions. Therefore, information on cloudiness also permits, at least, general conclusions on the field of vertical motions. This was convincingly shown by Musaelyan /33, 34/, who established the existence of linear correlation between the coefficients of Fourier series that determine the field of vertical motions in clouds.

Shenk /80/, obtaining a correlation between Earth—surface temperatures at cloudless sky and outgoing radiation in the 8—12-μ transparent window, first computed from measurements the differences between the fluxes of outgoing radiation for cloudless and overcast sky that characterize the temperature difference between the Earth surface and cloud tops and hence the vertical temperature gradient. Since the latter characterizes the nature of vertical currents, data on them may be obtained from measurements of outgoing radiation. Moreover, since vertical currents are connected with the meridional components of the atmospheric circulation, these components may also be determined. It should be noted that the correlation between the difference of outgoing radiation fluxes and vertical currents is linear. For the 700-, 500-, and 300-mb levels the correlation coefficients are 0.768, 0.569, and 0.564, respectively. The weaker correlation for higher levels is explained by the lower accuracy of computations for these levels. Studies also established a linear correlation between the outgoing radiation flux and the meridional wind-velocity component.

2.5. ANALYSIS OF INFRARED CLOUD PICTURES

The TV system, which operates in the visible part of the spectrum and is intended for the detection of clouds by artificial Earth satellites, can discern clouds against the background of the underlying surface when illumination conditions exceed the lower limit of the sensitivity threshold of the TV camera. Therefore, the method of television cloud tracking can only be applied over a limited region of the Earth. Moreover, the TV system can hardly discern clouds over an underlying surface that has an albedo similar to that of the clouds. This restricts still more the application range of satellite observations.

Nowadays, the presence of cloud cover on the Earth night side is detected by infrared cameras sensitive to the radiation of natural objects and being able, in principle, to detect cloud covers over the whole globe at any hour of the day.

As pointed out in Chapter 1, NIMBUS I carried out the first experiment for investigating planetary cloud-cover distribution on the Earth night side with the aid of an infrared high-resolution radiometer.

Photographs 2.6 and 2.7 present typical pictures of the Earth surface and of clouds in the infrared part of the spectrum at night. Photograph 2.6 shows a strip along the satellite trajectory, including an area from the South Pole to 45° latitude; the width of this strip is about 2,700 km. With the radiometer resolving power of 7 × 7 km, this strip consists of approximately 2,300 scanning lines.

Since the outgoing radiation in the spectrum range of the infrared radiometer is hardly weakened by the absorption components of the atmosphere the picture brightness (shading) of any object on the infrared photograph mainly depends on the temperature of the radiating surface and its spectral coefficient of relative emissivity. The lower the temperature of the radiating surface (the Earth surface or clouds) and the smaller its spectral coefficient, the brighter it will appear on the negative of the infrared picture. As a result, the brightness contrasts observed on the infrared pictures correspond to temperature contrasts between the underlying surface and the clouds.

The existence of heat contrasts, exceeding the lower sensitivity threshold of the infrared camera, makes it possible to study the structure of investigated objects, and hence the analysis of satellite pictures to reveal clouds against the background of the Earth surface, to determine their properties and to distinguish between details of the surface such as coastlines, lakes, bodies of water, snow- and ice-cover lines, rivers, etc. In such determinations the brightness (shading) and structure of the picture serve as distinguishing features.

Clouds, having mostly a lower temperature than the underlying surface, will show up on the infrared pictures as bright (white) areas on the dark background of the ground. However, under inversion conditions, it is almost impossible to obtain a clear identification of clouds.

Photograph 2.6 also reveals several zones of cloudiness. High cirrus clouds, corresponding to very bright zones, extend over China (upper part of the picture), over the tropical part of the Pacific Ocean (upper third of the picture) and over the Indian Ocean (lower third). The bright zone in the Antarctic reveals an ice cover of very low temperatures. Areas of lesser brightness over the oceans show the presence of low and middle clouds. To the right of the center of the picture the western coast of Australia can clearly be seen.

If the viewing field of the infrared radiometer covers cloud-free areas of the Earth surface, these areas, because of the difference in temperature and spectral coefficients of emissivity, will reveal orographic and hydrographic features of the Earth, if their horizontal dimensions are at least 3—4 times larger than the resolving power of the radiometer. Such features are large mountain massifs, areas with uniform surface (e.g., deserts), large lakes, rivers, etc.

Photograph 2.7, showing the southwest part of Africa, was taken at midnight from an altitude of 560 km. The east coast of Mozambique and South Africa can be well discerned. Because of the night cooling of the Earth surface under conditions of a cloudless sky, the water temperature is higher than that of the land, and on the picture the parts with water surface are therefore much darker than the land. The coastline is clearly discernible. On the upper left the Nyasa Lake can be seen as a dark spot. In the center of the right part of the picture, the west coast of Madagascar can be seen. The identified topographical and hydrographical heterogeneities,

and also the contour of the coastline make easier the geographical location of objects revealed by infrared pictures.

Several brightness gradations appear on infrared cloud pictures. Since brightness is connected with the temperature of the radiating surface, there appears the possibility to determine temperature and from it the height of cloud tops. For this purpose, the right side of the picture is provided with an optical wedge in which each brightness gradation corresponds to a given temperature (Photgraph 2.8). However, the accuracy of determining temperatures by this method with allowance for brightness contrasts is not higher than 4—8°C. Differences in quality of photographic processing of the pictures and the subjective choice of brightness gradations by the operator increase the error to 12—16°C.

However, Earth and cloud temperature can be more easily determined from measurements of the absolute magnitudes of the emitted radiation with the same high-resolution radiometer. Temperatures and height of cloud tops can thus simply be determined with electronic computers.

In determining the temperatures of cloud tops and of the underlying surface one must take into account their spectral coefficient of relative emissivity. To a first approximation the natural radiating surfaces may be assumed to be a perfect blackbody. According to data in /95/ this assumption appears justified for water surfaces, land covered by vegetation and for the upper surface of dense clouds.

It can also be assumed that the cloud-top temperature is equal to the air temperature at this level. In this case, by using radiosonde measurements closest in terms of space and timing to the satellite observations, one can determine the height of cloud tops.

The experiment carried out on NIMBUS I showed that from the brightness of infrared pictures alone the form of clouds cannot always be identified. This, however, is relatively simpler (of course with certain limitations) using TV cloud pictures. Consequently, the most complete analysis of cloud systems can be made by a joint study of infrared and TV pictures of the same cloud fields. This analysis is the more interesting as the much larger horizontal resolving power of the TV camera (0.8—1 km) can be used to reproduce those small-scale features of the cloud field that are not discernible on the coarser infrared pictures obtained with radiometers. In addition, from TV cloud pictures, it is possible to determine whether a given cloud system is uniform or not within the limits of the field of vision of the infrared radiometer: this is very important, since for a closed cover consisting of different elements whose horizontal sizes are smaller than the resolving power of the infrared radiometer, the outgoing radiation registered by the radiometer is the sum total of the radiation emitted by both the surface and cloud tops. Such cloud elements may not be discernible at all on the infrared pictures, and consequently, the temperature of the underlying surface or of the cloud tops will be determined with a certain error. Television pictures taken during the day and night and infrared photographs may be used to study the transformation of cloud systems from day to night.

The diagnosis of synoptic situations from infrared cloud pictures should be made in the following order:

1) assessment of the general synoptic situation in the region of interest by visual analysis of the position, orientation and heights of cloud systems on the infrared cloud pictures;

2) determination of the temperature of cloud tops and of the underlying surface in cloudless areas;

3) determination of upper boundary of each large cloud body additionally resorting to radiosoundings and climatological data;

4) comparison of analysis results of the infrared-pictures interpretation both with data of ground synoptic charts of the considered region for the time nearest to the time of satellite observation and with charts of baric topography (height and pressure patterns).

This analysis should be supplemented by an analysis of TV cloud pictures received during the following 12 hours.

Below we shall discuss two examples of cloud pictures relating to the North Pacific Ocean from the equator to 50°N, approximately along the 160°W meridian. The first case was observed from midnight 14 September local time till midnight on 16 September 1964, and the second example is for noon and midnight on 20 September 1964. Of greatest interest for analysis of these pictures are the cloud belts in the upper right corner of each picture, where a multi-layer structure is clearly visible.

On all infrared cloud pictures, dark areas represent regions with relatively high temperatures of the radiating surface, while the white areas are those with relatively low temperatures. This means that the darkest spots are the ocean surfaces and the brightest ones represent high clouds of considerable vertical development. Intermediate brightness characterizes cloud fields lying between these height limits.

An analysis of the above example is given in the form of an exercise. The data are taken from /92/.

EXERCISE I

Determination of the radiating-surface temperature and of cloud-top height

Initial data

1. Infrared cloud photographs of the Earth night side taken on 15 September (Photograph 2.8), 16 September (Photograph 2.10), and on 21 September 1964 (Photographs 2.14 and 2.15).

2. Radiosounding data (Figure 2.32).

Order of work

1. Select the brightness shades of the cloud systems on each of the four pictures in order to obtain an optimum match with the corresponding brightness gradations on the optical wedge. It is expedient to consider the following brightness gradations:

a) the brightest cloud belt on the upper parts of each picture;

b) the different darker strips between relatively bright cloud masses in the upper parts of the pictures near 38°N and 154°W on 15 September 1964 and in the region 38°N and 140°W on 16 September 1964 (Photographs 2.8 and 2.10);

c) the bright cloud belts in the lower part of Photographs 2.8 and 2.14;

d) a separate bright cloud in the region 30°N and 146°W on Photograph 2.10;

e) the broken gray cloud mass in the lower right corner of Photograph 2.10;

f) the relatively gray cloud field in the center of Photograph 2.14:

g) the bright cloud vortex in the center of Photograph 2.15;

h) the cloudless water surface at 30°N on Photographs 2.8, 2.10, and 2.15 and near 38°N and 140°W on Photograph 2.14.

2. Determine the temperature corresponding to each brightness shade of the clouds and the underlying surface according to the optical wedge, taking into account the fact that the brightness shades of the optical wedge are identical for each infrared picture.

3. Note on the left of the picture the temperature values for the ocean surface, and on the right the temperature of the cloud tops, and indicate by arrows the place of their determination.

4. Using data of vertical atmosphere radiosounding from Figure 2.32 and the temperatures of the cloud tops, determine the heights of the cloud tops for all brightness gradations of the cloud field. Write the heights of the cloud tops as denominator under the corresponding temperature values.

EXERCISE II

Comparison of infrared cloud pictures with synoptic charts, height- and pressure-pattern charts and TV cloud pictures

In this exercise infrared pictures for a corresponding synoptic situation are compared with TV cloud pictures. The time at which ground-based synoptic charts and height- and pressure-pattern charts were obtained nearly coincides with the reception time of the infrared pictures. The TV photographs were taken approximately 12 hours after this region was scanned by the infrared radiometer.

As an example, we present both a comparative analysis of infrared and TV cloud pictures for a given synoptic situation and in special cases for independent analysis.

Initial data

1. Infrared and TV cloud photographs, ground-based synoptic charts and 300-mb charts all of them characterizing the same cloud system during 36 hours (Figures 2.28 to 2.33 and Photographs 2.8 to 2.13).

2. The same initial data for 0000 to 1200 hr [local time] on 21 September 1964 (Figures 2.33, 2.34; Photographs 2.12 to 2.15). In the series of infrared and TV cloud pictures received by NIMBUS I (Photographs 2.8 to 2.11) successively taken from day to night, the advance of a cold front over the eastern Pacific Ocean during 36 hours can be tracked. The position of

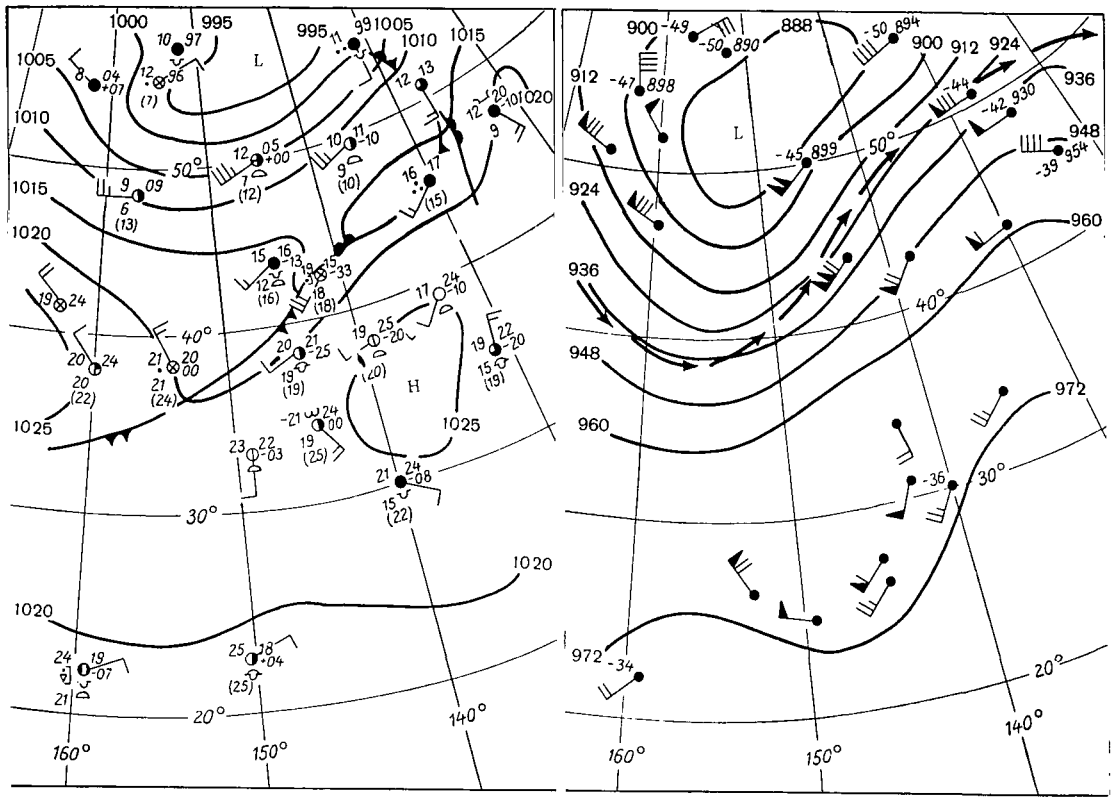

FIGURE 2.28. Surface weather chart and 300-mb chart for 1200 hr on 15 September 1964

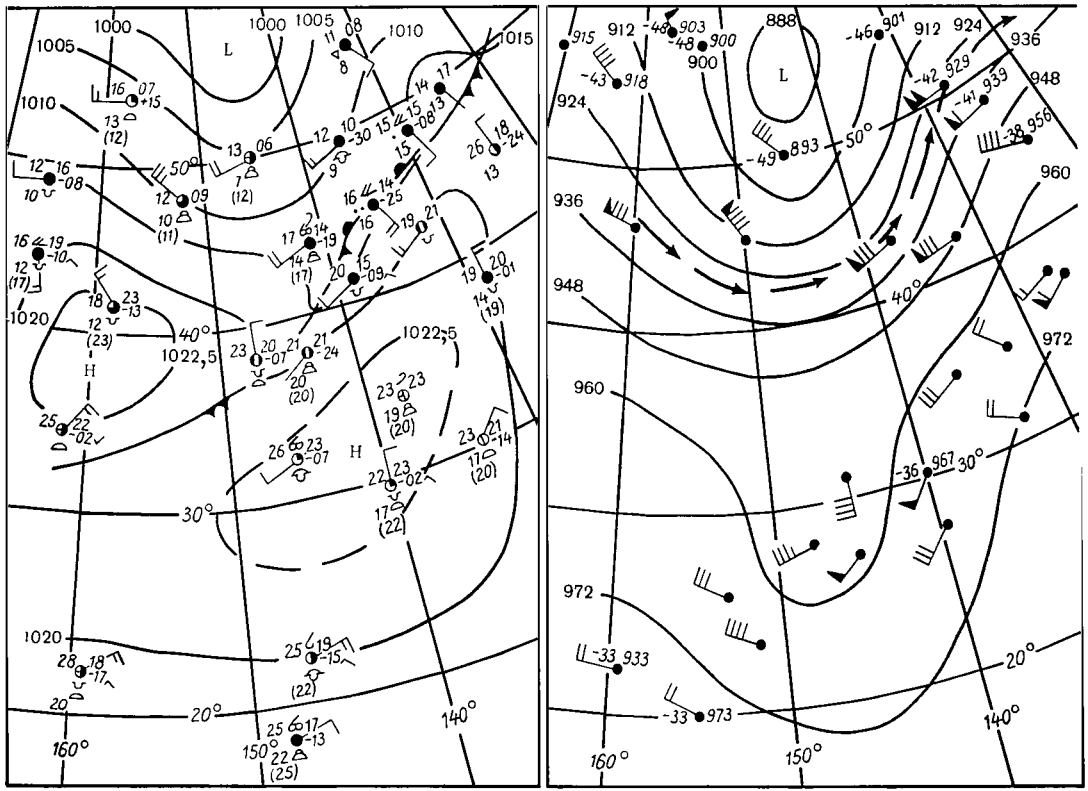

FIGURE 2.29. Surface weather chart and 300-mb chart for 0000 hr on 16 September 1964

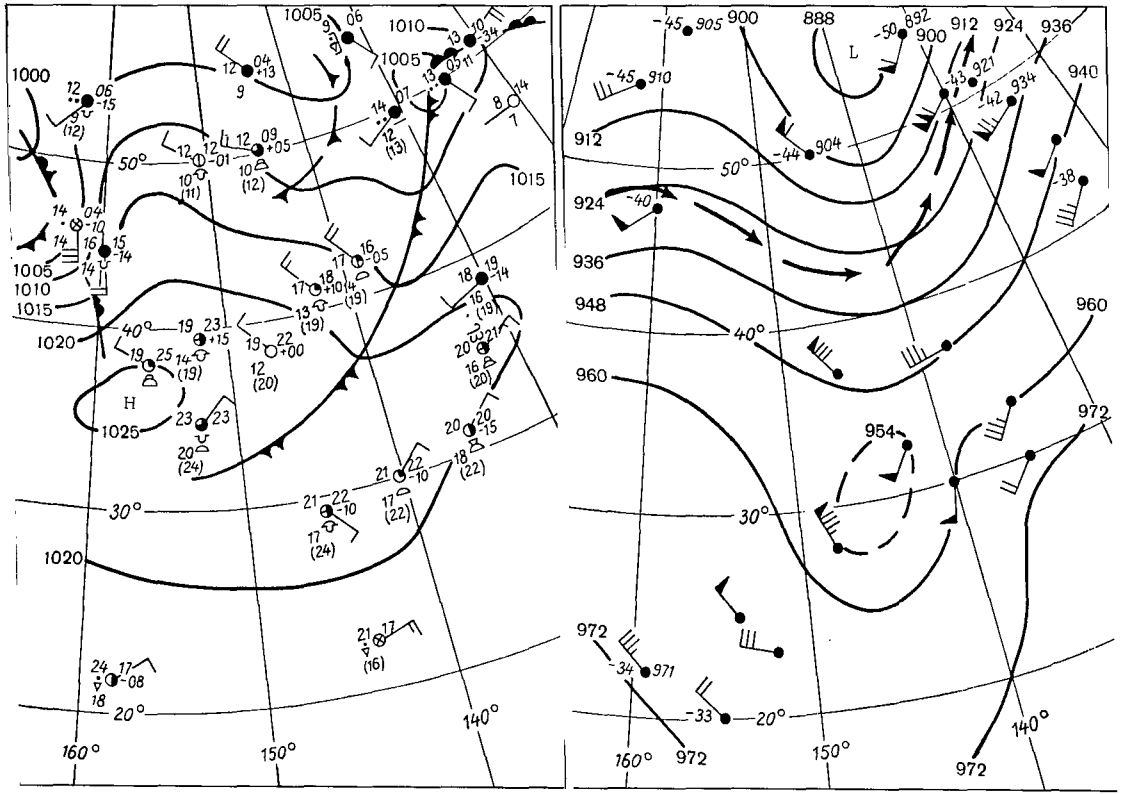

FIGURE 2.30. Surface weather chart and 300-mb chart for 1200 hr on 16 September 1964

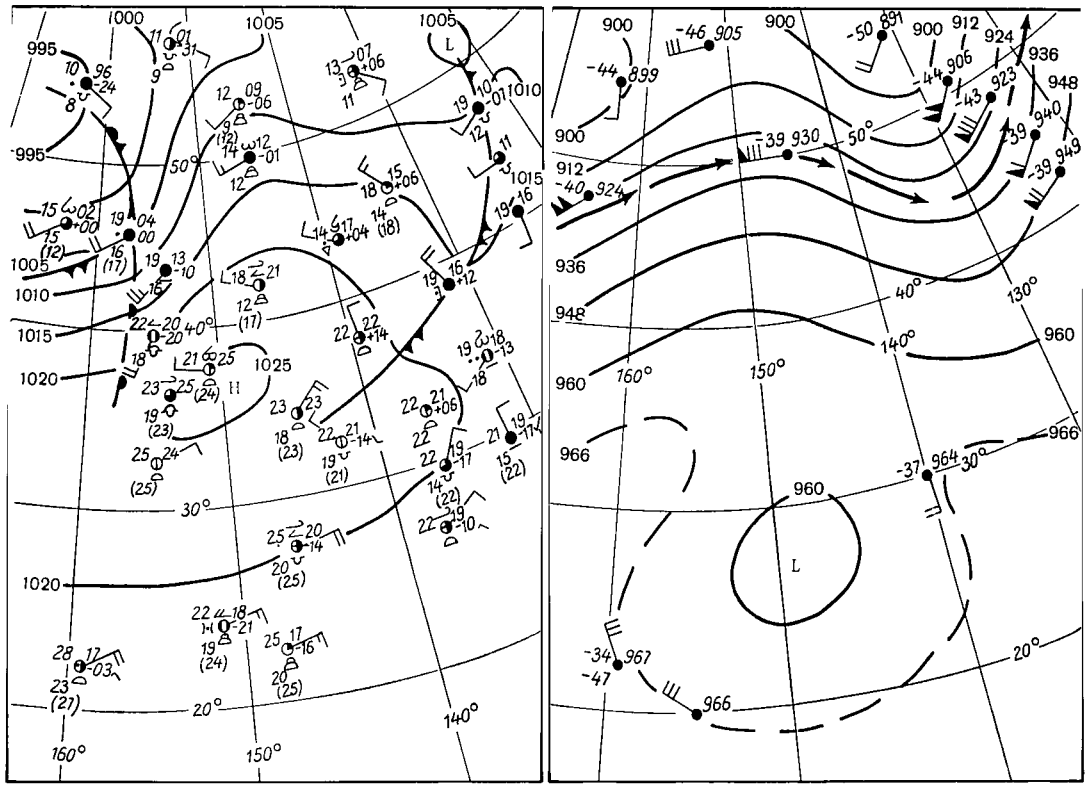

FIGURE 2.31. Surface weather chart and 300-mb chart for 0000 hr on 17 September 1964

this front with a wave disturbance is quite accurately recorded on the surface weather charts (Figure 2.28). On the 300-mb chart the axis of the trough, oriented from north to south, along 155°W intersects the frontal zone at approximately 35°N.

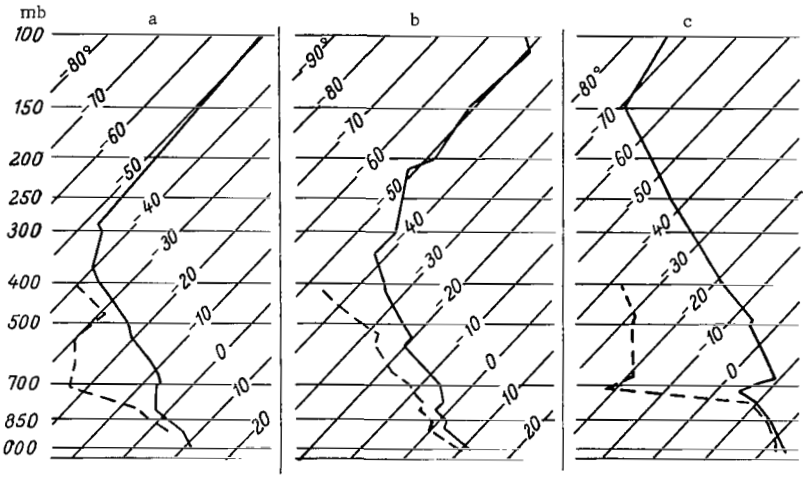

FIGURE 2.32. Radiosounding data for 1200 hr:

a — 15 September 1964, Ship P (150°N, 145°W); b — September 1964, Ship P; c — 16 September 1964, Honolulu.

The thermodynamic processes in that part of the frontal zone lying to the right of the trough axis are the most active. In this part, multilayer cloud systems leading to precipitation are observed. To the west of the trough axis, where the vertical motion usually has a negative sign, the front in the cloud field near the Earth surface is weakly expressed.

The infrared cloud pictures received from NIMBUS I confirm this convincingly. Photograph 2.8 clearly displays a frontal cloud system (upper right corner). The vertical structure of the cloud field, characterized by changes in the temperature of the cloud tops with their height, is seen from the changes in brightness of the cloud appearing along the frontal zone at 34°N and 154°W. As the height of cloud tops diminishes, the brightness of the cloud picture changes from white to gray and dark gray.

To the north of the main frontal zone another belt of cold clouds is seen in the region of 44°N and 150°W. These are cirrus clouds which usually extend south of the jet-stream axis. As the picture shows, they too break off at the axis of the trough on the 300-mb chart.

Near 44°N and 155°W cold, broken clouds are seen without the characteristic banded structure of frontal cloud systems. These white spots, as seen on the infrared pictures, represent the tops of thick cumulus and cumulonimbus clouds, lying to the south of the low-pressure center on the 300-mb chart.

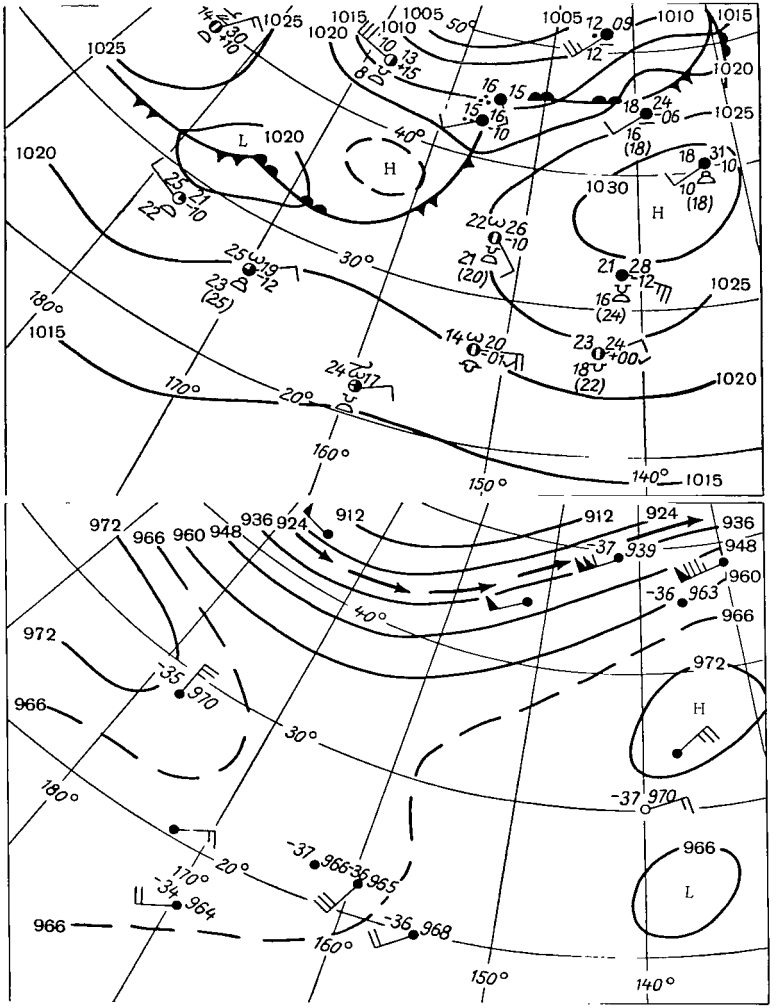

FIGURE 2.33. Surface weather chart and 300-mb chart for 0000 hr on 21 September 1964

It should be noted that the infrared pictures present a clear tracking of the distribution of air masses. Comparatively cold air masses and low humidity appear on Photograph 2.8 in shades brighter than warm and moist air masses which show up relatively darker. This permits the conclusion that the position of frontal zones, centers of major pressure systems and axes of jet streams, may be determined from satellite infrared pictures.

The same front is shown on Photograph 2.9 12 hours later. The frontal zone stretching from 37°N and 150°W to 35°N and 165°W appears in the form of numerous thin cloud bands, cloud spots of varying size, and several continuous cloud masses of fairly uniform character. Such conglomerations of varying sizes and forms are typical of that part of the front lying at the

rear of the upper trough. Twelve hours earlier, this part of the frontal zone appeared on the infrared photograph (Photograph 2.8) as a gray area with some white spots.

To the west of the frontal zone the distribution of cumuliform clouds can be tracked on Photograph 2.9. Cirrus and nimbostratus clouds near the vortex center are located too far to the east and west to be covered by the field of vision of the TV camera on the satellite. Much farther to the south of the frontal zone, near 10°N, clouds can be seen that were not intercepted by the infrared radiometer.

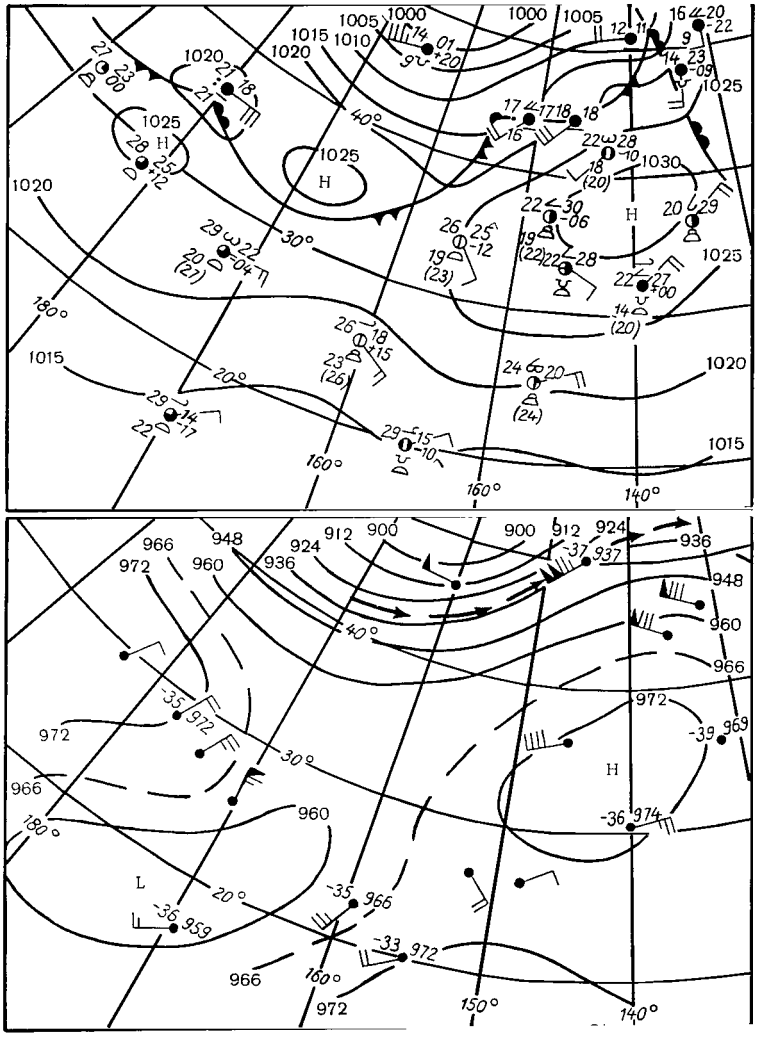

FIGURE 2.34. Surface weather chart and 300-mb chart for 1200 hr on 21 September 1964

In the region 21°N and 161°W the picture shows part of Hawaii, to the east of which is located an area of thin spiral clouds with their center at 20°N and 155°W.

On Photograph 2.10 the same front is seen 12 hours after Photograph 2.9, and 24 hours after Photograph 2.8.

As can be seen from Figure 2.30, the main frontal zone at the Earth surface and the trough axis on the 300-mb chart intersect near 35°N and 143°W. On the picture (Photograph 2.10) high cold clouds are seen to break off sharply near 40°N and 138°W. This leads to the conclusion that the trough on the 300-mb chart (Figure 2.31) probably passes near the front at a point near 40°N and 138°W. The frontal clouds extending southwest from this point toward 35°N and 150°W on the infrared picture (Photograph 2.10) are more grayish, which points to their location at lower levels. Here, only some cold spots are seen. In the northwestern part (Photograph 2.10) the picture shows frontal cirrus clouds which are connected with the cyclonic vortex at 47°N and 165°W.

Another area of high cold clouds is seen near 28°N and 146°W. These are cumulonimbus clouds. Ground observations (see Figure 2.30) confirm that there were showers in this region.

The TV picture (Photograph 2.11) shows the above-mentioned frontal zone as tracked 12, 24, and 36 hours after Photograph 2.8.

This picture shows cirrus clouds connected with another front located to the northwest of the front just discussed, a front dispersing at 33°N and 145°W, and a filling tropical cyclone in the region between 15°N and 137°W.

EXERCISE 3
(for independent analysis)

Compare each TV (Photographs 2.12 and 2.13) and infrared (Photographs 2.14 and 2.15) cloud picture with the corresponding synoptic situation (Figures 2.33 and 2.34) and identify on them the following features:

1) frontal zones;
2) low-pressure areas;
3) subtropical jet stream;
4) low stratified clouds and fog;
5) isolated thunderstorms;
6) fair-weather cumulus clouds.

2.6. OUTGOING RADIATION AND RADIANT HEAT INPUT. CONNECTION WITH OTHER FORMS OF HEAT INPUT

Satellite measurements of the integrated fluxes of outgoing radiation are of considerable interest for the study of the radiation balance of the surface—atmosphere system. However, another important problem, namely, the determination of the radiant-heat input to the entire atmosphere, is connected with the interpretation of these data.

Particular attention has been given of late to methods of nonadiabatic weather forecasting, with particular stress on the effect of radiant-heat input. With this approach, and in the simplest case of a single-level model atmosphere, it is necessary to obtain data on the radiant-heat input for the entire atmosphere. This flux can only be calculated from data on the radiation balance at the Earth surface and at the upper limit of the atmosphere. However, this problem is not easy to solve, since satellite measurements have a global coverage while the network of ground-based actinometric stations only covers a small part of the Earth surface. Moreover, with the use of actinometric data from ground and satellite observations, the problem is complicated by the large differences in scale when averaging the ground-based and satellite measurements. Thus, the search for a solution that would permit the determination of radiant-heat input for the whole atmosphere only from data on outgoing radiation becomes a pressing problem.

Sabatini and Suomi /81/ analyzed measurements of the radiation balance of the Earth surface—atmosphere system at night using data from actinometric soundings, and revealed a rather good correlation between the outgoing long-wave radiation and the radiant-heat inflow throughout the atmosphere. Table 2.14 gives measurement results for varying cloudiness, the data being presented as a regression function for the outgoing radiation F_∞ and the radiant heat input (the radiational-temperature changes C). The table also presents values of the correlation coefficient R.

TABLE 2.14. Correlation coefficient and regression function characterizing the connection between outgoing radiation and radiant-heat input

Cloudiness	R	Regression function
Clear	0.87	$C = 6.43\ F_\infty - 0.98$
Scattered clouds	0.90	$C = 5.52\ F_\infty - 0.74$
Broken clouds	0.95	$C = 5.53\ F_\infty - 0.66$
Overcast	0.85	$C = 5.46\ F_\infty - 0.53$
Mean	0.88	$C = 5.14\ F_\infty - 0.53$

According to /81/, the correlation between F_∞ and C is very high, which means that at night the values of the radiant-heat input for the entire atmosphere can be obtained with sufficient reliability from data on outgoing radiation.

Davis /51, 52/ also studied the relationship between outgoing radiation and radiant-heat input using values averaged for 4 × 4° latitude squares (in the temperature latitudes), and measurement results for channel 2 (8—12μ) for four orbits of TIROS III (mid-July 1961).

Davis /51/ deals with the causes of the correlation between outgoing radiation and radiant-heat input at night. Obviously, in this case both processes mainly depend on cloudiness conditions.

Outgoing long-wave radiation is mainly determined by the height of the cloud tops, while the effective emission of the Earth surface depends on the height of the cloud base. The radiant-heat input, as the difference between these two values, depends on the heights of the cloud base and tops.

TABLE 2.15. Mean values and standard deviations of components of the heat input for the entire atmosphere

Components of heat input	3rd orbit		4th orbit		29th orbit		44th orbit	
	mean	standard deviation	mean	standard deviation	mean	standard deviation	mean	standard deviation
Total radiant-heat input, cal cm^{-2} min^{-1}	0.1347	0.0277	0.1408	0.0228	0.1394	0.0262	0.1451	0.0233
Long-wave heat input, cal cm^{-2} min^{-1}	0.2436	0.0258	0.2551	0.0219	0.2578	0.0231	0.2535	0.0327
Absorbed solar radiation, cal cm^{-2} min^{-1}	0.1090	0.0155	0.1143	0.0187	0.1183	0.0128	0.1084	0.0192
Outgoing long-wave radiation, cal cm^{-2} min^{-1}	0.3580	0.0513	0.3633	0.0481	0.3359	0.0360	0.3846	0.0494
Sum total of potential and internal energy in the layer from the surface to the 100-mb level, J/m^2	205.0	9.66	211.2	12.76	220.4	6.01	203.6	13.96
Total degree of cloudiness (in fractions of unity)	0.4896	0.3153	0.4375	0.3171	0.5840	0.2098	0.3479	0.3261
Effective temperature (channel 2, °K)	268.7	11.28	271.9	11.74	263.3	9.85	268.0	8.80
Reflected solar radiation (channel 3), W/m^2	94.4	46.7	129.6	62.2	—	—	—	—
Height of cloud tops, expressed as fraction of atmospheric humidity below the cloud top	0.4609	0.2997	0.4168	0.3048	0.5616	0.2093	0.3207	0.3020

Maximum radiant-heat input must occur in the presence of ground fog when the effective emission is zero and the outgoing radiation is considerable. Minimum heat flux must occur when both the outgoing and effective radiation are small (e.g., for clouds of vertical development, with low bases but with their tops reaching the tropopause). From the above examples it is clear that the correlation between outgoing radiation and radiant-heat input cannot be perfect: e.g., in the presence of fog the outgoing radiation remains almost stable, while the effective radiation undergoes sharp changes.

Davis used the results of calculating the mean meridional profiles of the outgoing long-wave radiation, the reflected solar radiation, the radiant-heat input (both its total and long-wave component) as well as the total heat input, taking into account radiation, phase changes of water, and the turbulent heat transfer, to analyze the correlation between the above parameters and actual outgoing radiation. His analysis proved the unsatisfactory correlation between outgoing radiation and total heat input.

In the same study /51/, Davis made an analysis, using the above synoptic data on outgoing radiation (averaged over 24 hours) and the results of calculating the principal components of the atmosphere's heat balance. Some papers /27, 42, 49/ also deal with the analysis of the relation between components of the atmosphere's heat balance. The purpose of all these studies was to compare only those values which can be, at least in principle, obtained by measurements from meteorological satellites. This, by the way, concerns especially the sum total of potential and internal energy which is determined by the vertical temperature distribution and surface pressure.

Table 2.15 presents mean values and standard deviations (from data of separate orbits) of components of the heat input and other values. This table clearly shows the considerable variability of the reflected solar radiation and of the cloud cover. On the other hand, radiant heat input and outgoing long-wave radiation are rather stable. An analysis of the correlation between the values referred to in Table 2.15 yielded the following results (see in Table 2.16 an example of computation of correlation coefficients according to data for the 44th orbit; in brackets are given the values of correlation coefficients for those magnitudes one of which is the component of the other).

TABLE 2.16. Correlation coefficients between different components of the heat input flux and other values (according to data for the 44th orbit of TIROS III)

	Long-wave radiant-heat input	Absorbed solar radiation	Outgoing long-wave radiation	Total energy	Degree of cloudiness	Effective temperature for the transparent window
Total radiant-heat input	(0.818)	(0.182)	(0.422)	-0.022	-0.025	0.495
Long-wave heat input		0.715	(-0.141)	0.398	0.529	-0.024
Absorbed solar radiation				0.706	0.933	-0.643
Outgoing long-wave radiation		-0.754		-0.567	-0.892	0.956
Total (potential + internal) energy					0.667	-0.571
Degree of cloudiness						-0.815
Height of cloud tops						-0.825

Parameters such as outgoing long-wave radiation and effective temperature, outgoing radiation or absorbed solar radiation and degree of cloudiness, height of cloud tops and effective temperature, are closely correlated. It is interesting to note that the outgoing radiation has a much higher correlation with the total radiant-heat input than with the long-wave radiant-heat input (the same also applies to the correlation with the Earth surface temperature).

The existence of a small negative correlation between the total radiant-heat input and the total energy can be explained by the generation of some potential energy from radiant-heat input.

Computations in /51/ revealed a very significant correlation between the reflected solar radiation (outgoing short-wave radiation) and the following quantities: solar radiation absorbed by the atmosphere, effective temperature, and the parameter that characterizes the thickness of a cloud and the height of its tops. This confirms the large "information" value of measuring the outgoing short-wave radiation.

Difficulties in estimating quantitatively the heat input caused by phase changes of water in the atmosphere and by turbulent heat exchange did not permit the determination of correlation coefficients for these parameters. Semi-quantitative estimates based on climatological data led to the following conclusions: 1) a negative correlation is observed between the heat of condensation and the total radiant-heat input (the same is valid for effective temperature); 2) a rather high correlation exists between the heat of condensation and the height of cloud tops; 3) a quite well-defined connection exists between effective temperature and total heat inflow, taking into account radiation and condensation; 4) the effective temperature also correlates well with the value of the turbulent heat exchange between the Earth surface and the atmosphere.

The results presented in /51/ show that satellite measurements of outgoing short-wave radiation and of effective temperature in the transparent window of 8—12μ are very important for the determination of the heat input and its components.

Using data from TIROS II for the period between 26 November 1960 and 7 January 1961, Corcoran and Horn /49/ studied the influence of atmosphere cooling, caused by long-wave emission, on the generation of vorticity components of the available potential energy (those parts of the potential energy which can be converted into kinetic energy and are determined by the longitudinal variation of the temperature field). The above authors pointed to the contradictory results of potential-energy calculations carried out by various authors; these results show that the nonadiabatic processes may cause both generation and dissipation of potential energy. Corcoran and Horn computed the correlation between the deviation from mean zonal radiational cooling and the height of the relative baric topography of the 1,000—500-mb level for different wave disturbances at the 500-mb level. In processing the experimental data they obtained averages for ten or more discrete values using data only for nadir angles larger than 56°. The investigated region includes the latitude belt 30—50°N from Europe to Western Japan. Values of the radiant-heat input (i.e., of the radiational cooling of the entire atmosphere) were obtained by measuring the outgoing radiation, using a correlation derived from data on long-wave radiation input obtained by actinometric radiosondes.

The above authors showed that the generation of potential energy is negative for long-wave and positive for short-wave perturbations. Such a wavelength dependence is apparently caused by the specific features of cloud-cover distribution. It has been suggested that cloudiness also leads to the generation of potential energy as a result of air heating by absorbed solar radiation and of the release of the latent heat of condensation. Turbulent heat transfer probably leads to dissipation of potential energy. A direct generation of vorticity components of available potential energy, caused by nonadiabatic processes, must be more important in earlier stages of development of the pressure perturbations (with short wavelengths).

Fritz et al. /56/ attempted to determine the amount of solar radiation absorbed by the whole atmosphere using data from satellite measurements of the solar radiation reflected by the Earth and the results of pyranometric measurements of the total and the reflected radiation carried out by the U.S. network of actinometric stations. They stressed that their results may only have theoretical importance, since the satellite data on reflected solar radiation are not sufficiently accurate. The data referred to were obtained by TIROS III on 12 July 1961 and mainly relate to the eastern half of the U.S.A.

Fritz et al. /56/, using satellite data on reflected solar radiation, plotted charts showing the distribution of this radiation over the territory of the U.S.A.; for these charts they also resorted to calculated values of solar-radiation input on a horizontal surface beyond the atmosphere (assuming a solar constant of 2 cal cm^{-2} min^{-1}). The data thus obtained were used to plot a chart of albedo distribution.

Albedo values vary from 0.65 over bright clouds at the border of Indiana and Kentucky, to 0.15 in the region of scattered clouds (Illinois, Arkansas) and to 0.05 over the cloudless areas of Lake Michigan and the Pacific Ocean.

The above comparisons showed the distribution of albedo to fully correspond to the brightness distribution in the satellite pictures. Analysis of observational data from ground-based actinometric stations shows that, although this station network is quite dense over the U.S.A., these data are insufficient to permit such a detailed geographical distribution of the short-wave radiation as can be provided by satellite measurements. Therefore, a comparison of ground-based and satellite measurements can only be done for separate (individual) points by using ground-based data averaged over an hour. This is done to take into account the scale differences between spatial distribution of ground-based and satellite measurements. Errors in the geographical location of satellite data should also be allowed for, since even under the most favorable conditions (e.g., distinct landmarks on the cloud photographs) they may amount to 50—100 km.

The albedo A_S of the surface—atmosphere system is linearly connected with the relative value of solar radiation q_t transmitted through the atmosphere: $A_S = 0.63—0.64\ q_t$. The correlation coefficient is -0.9. With thick bright clouds q_t is 0.25 and the albedo is 0.47. For a relatively clear sky these values are 0.8 and 0.12, respectively. According to aircraft and balloon measurements, the albedo A of the Earth surface varied from 0.10 to 0.15 during the considered period. For these albedo values and for different relative values of the solar radiation q' absorbed by the atmosphere the authors plotted the relationship between A_S and q_t, permitting the calculation of q' when A_S, q_t and A are known. A calculation of absorbed

radiation gave values from 0.07 to 0.37 for $A = 0.10$. Comparing the results of aircraft and balloon measurements shows that satellite albedo measurements are underrated while data on absorbed radiation are overrated.

The study in /56/ analyzes in detail the influence of various factors (and their corresponding measurement errors) on the calculation results for absorbed radiation (these factors are the albedo of the Earth surface, influence of anisotropy of the angular radiation distribution when calculating the radiation flux according to measured intensity, the height limitation in the case of aircraft measurements, and errors of radiometer calibration). The influence of calibration errors and uncontrollable variations in radiometer sensitivity is very considerable. For further measurements it is therefore important to ensure adequate sensitivity control of instruments carried by satellites, aircraft. and balloons, and to compare these instrument data with independent ground-based measurements.

The authors of /84/ plotted meridional profiles on the strength of averaged values of solar radiation absorbed by the atmosphere, using data on the albedo of the surface—atmosphere system obtained from TIROS III measurements of the outgoing short-wave radiation. The shape of these meridional profiles satisfactorily agrees with the values calculated by London /66/ (absolute values obtained from geographical location and from the author's own data).

Despite the first, successful attempts to measure outgoing radiation with the aid of satellites and thus to determine the input of radiant heat, further research is necessary, based on more reliable measurement data.

2.7. RELATIONSHIP BETWEEN OUTGOING HEAT RADIATION AND THE FIELD OF MEAN TEMPERATURES IN THE TROPOSPHERE AND LOWER STRATOSPHERE

Radiant heat back-reflected into space through the transparent window mainly depends on the radiation from the Earth surface and the cloud tops. In the absorption bands, depending on their intensity, the outgoing radiation is affected by the various atmospheric layers. Obviously, the sources of the integrated outgoing heat radiation are both the Earth surface and the entire mass of the atmosphere. However, it is only natural to try and find a correspondence between the integrated outgoing radiation and the temperature of some mean [atmospheric] layer. Such an attempt was made by Kolosov /25/, who found a satisfactory relationship between the ascending current of the integrated heat radiation at the tropopause level (this value may be regarded as approximately identical with the value of the outgoing radiation) and the temperature at the 400-mb level. This relationship is even closer if we use the temperature corresponding to the mean energy level, given by

$$gz_{av} = RT_{av} ,$$

where z_{av}, T_{av} are the height and temperature of the mean energy level; g is the acceleration of gravity and R is the gas constant. Kostyanoi /26/

markedly refined these conclusions; using data from 20 actinometric soundings over the USSR during 1961—1963 he showed that the correlation between outgoing radiation and the temperature corresponding to a single (mean average) energy level is weak. In view of the complex character of the relationship between the outgoing radiation and atmosphere layering (stratification) it is not possible to establish a universal relationship between the outgoing radiation and the temperature of a certain, definite level. The position of such a level depending on the observed actual conditions is extremely variable.

An interesting experiment was carried out to determine the mean temperature of the lower stratosphere by measuring the outgoing radiation in the 15μ CO_2 absorption band (the investigated interval included the 14.8—15.5-μ band) with a radiometer carried on board TIROS VII /44, 45, 73, 74/. The main purpose of this experiment was to compare the satellite measurements with calculated values of the outgoing radiation.

An analysis of these measurements for 19 June 1963, undertaken in /45/, showed good agreement with theoretical computations. This particularly refers to the dependence of the outgoing radiation on cloudiness, latitude, and on the small increase in intensity of the outgoing radiation toward the rim of the Earth disk.

Such information about the variability of the outgoing radiation is essential for determining the horizon line from data on infrared emission. For this determination it is important to note that the outgoing radiation in the center of the 15-μ band is practically unaffected by cloudiness.

One of the examples considered in /45/ clearly reveals the increase in intensity of the outgoing radiation toward the rim of the Earth disk in the 15-μ band and the effect of "darkening" in the spectral intervals 8—12 and 8—30μ. The values of outgoing radiation in the 15-μ band averaged over each scanning had minimum figures in the high latitudes of the Southern Hemisphere during the antarctic winter, and maximum figures in the high latitudes of the Northern Hemisphere (during summer). The values of the effective radiation temperature in the middle and tropical latitudes vary but little (225—240°K).

Calculations show that the main contribution to outgoing radiation in the spectral region of the 15-μ heat-sensitive radiometer is made by the atmospheric layer at a height of 15—25km. The height of this effective layer slightly increases when the viewing angle of the radiometer covers regions close to the horizon (this fact produces the "brightening" effect at the horizon, since the temperature of the effective layer increases with its height). However, in general the values of the outgoing radiation for the 15-μ channel reflect the variability of temperatures in the lower stratosphere. This conclusion permits the use of these data for the study and tracking of the well-known phenomenon of sudden stratospheric warming up. Thus, with data of measurements at small and large nadir angles, it is possible to evaluate the vertical temperature gradient between the lower and upper stratosphere.

Using data of measurements for June 1963 till March 1964, Nordberg et al. /73, 74/ plotted the first maps of the planetary distribution of temperatures in the lower stratosphere. One of these maps is shown in Figure 2.35 (for their preparation, measurements for nadir angles between 0 and 40° were used). In the case shown in this figure the range of

temperature variations covers values from 240°K near 60°N to 215°K near 60°S. As can be seen,the temperature distribution has an almost zonal character and reflects the well-known existence of an intensive cyclonic circulation near the winter pole. Over the summer pole, on the other hand, circulation has an anticyclonic character. It is interesting that over the winter hemisphere the meridional temperature gradient is larger than over the summer hemisphere. This reflects the fact that the cyclonic circulation is more intense than the anticyclonic.

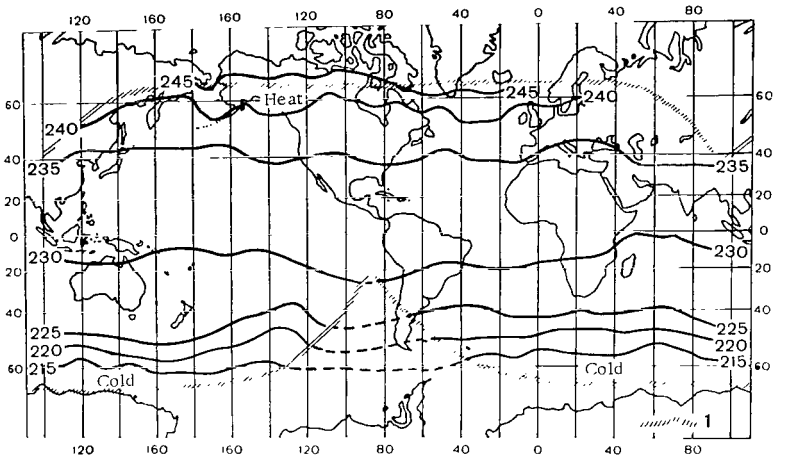

FIGURE 2.35. Planetary distribution of effective temperature in the 15 μ, CO_2 band, averaged for one week from 19 to 25 June 1963:

1 — limit of the region to which the data refer.

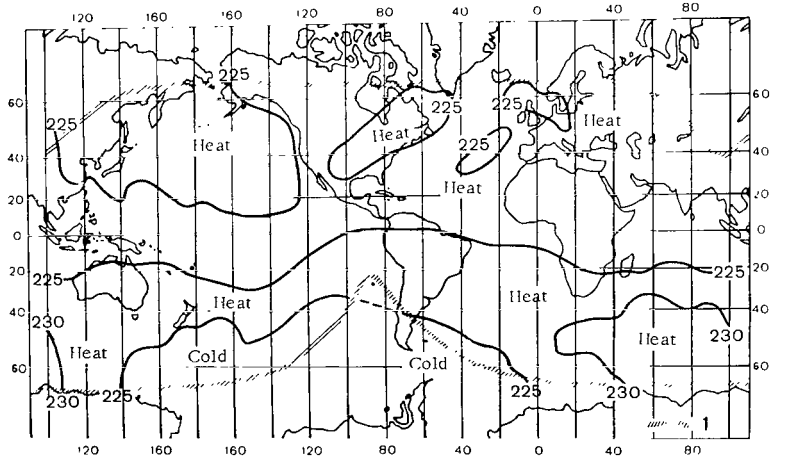

FIGURE 2.36. Planetary distribution of effective temperature in the 15 μ, CO_2 band, averaged for one week from 25 September to 1 October 1963:

1 — limit of the region to which the data refer.

A map, similar to that shown in Figure 2.35 but for measurements at nadir angles of 52—58°, affords an idea on the temperature field for a mean level lying at 3—4 km. A comparison of both maps permits the evaluation of the vertical temperature gradient.

Considerable azonality of the temperature field occurs in the transition seasons of the year. This can be seen on the map in Figure 2.51 which refers to September 1963. The stratosphere temperature in the Northern Hemisphere hardly changes with latitude, but individual temperature-anomaly centers are seen to develop. It should be noted that the temperature values on the maps in Figures 2.35 and 2.36 and the subsequent values are underrated by about 7°, because the reduction in the radiometer sensitivity was not allowed for.

A comparison of the maps for 15—22 January 1964 with data in Figure 2.35 shows the nature of the temperature field in summer to be similar both in the Northern and Southern hemispheres. This, however, is not valid for winter. In the Northern Hemisphere, during winter, a sharp anomaly is caused by the Aleutian low (center of action).

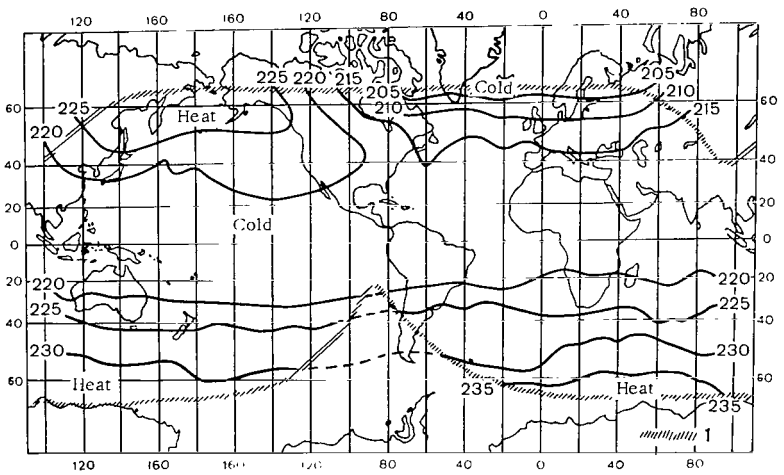

FIGURE 2.37. Planetary distribution of effective temperature in the 15 μ, CO_2 band, averaged for 15—22 January 1964:

1 — limit of the region to which the data refer.

Analyzing the maps of the planetary temperature field in the lower stratosphere permits the study of the dynamics of different large-scale temperature anomalies, in particular, sudden stratospheric warmings. Figures 2.37 and 2.38 show measurement results for January 1964. These data clearly prove the appearance of a moderate stratospheric warming up during the last week of January over the Caspian Sea, extending to the Himalaya Mountains and the Black Sea. Compared with the preceding week (Figure 2.37) the temperature increased by 8°. An analysis of Figure 2.37 shows that in the period between 15 and 22 January there were no temperature anomalies over this region. If, however, we analyze the data

for this period for nadir angles of 52—58° we can notice signs of a temperature rise over Central Asia which probably proves that the warming spread from the upper stratosphere. The daily maps of the temperature field (distribution) reproduced in /73/ reveal rather fine details of the extension and development of this sudden stratospheric warming.

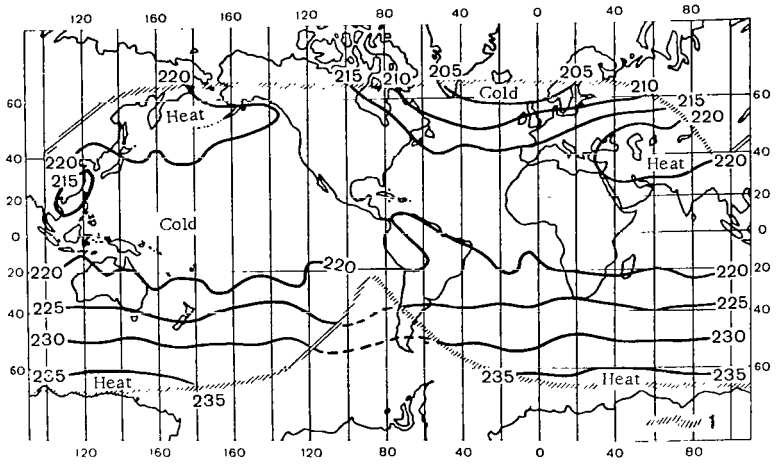

FIGURE 2.38. Planetary distribution of effective temperature in the 15 μ, CO_2 band, averaged for 22—29 January 1964:

1 — limit of the region to which the data refer.

Houghton /62/ proposed a more subtle method for determining the temperature of the stratosphere, but this has not yet been applied in practice.

When studying the relationship between outgoing radiation and meteorological parameters, Belov and Kivganov /10/ established a significant correlation between the radiant-heat input and the geopotential. Based on several examples they show that the contribution of radiational factors to changes in the geopotential on the 850-, 500- and 200-mb surfaces is 24%, 2%, and 12%, respectively. This doubtlessly proves the significant role of the radiant-heat input in the heat budget and dynamics of the atmosphere.

Bibliography

1. Bagrov, N.A. Planetarnoe al'bedo Zemli (The Planetary Albedo of the Earth).— Trudy TsIP, Issue No. 35(62). 1954.
2. Budyko, M.I. and K.Ya.Kondrat'ev. Teplovoi balans Zemli (The Heat Balance of the Earth).— Kosmicheskie issledovaniya, No.1. 1964.

3. Barabashev, N.P. Opredelenie al'bedo zemnogo shara (Determination of the Earth Albedo).— Russkii astronomicheskii Zhurnal, Vol. 1, Issue No. III—IV. 1924.
4. Barabashev, N.P. Issledovanie fizicheskikh uslovii na Lune i planetakh (Investigation of the Physical Conditions on the Moon and the Planets).— Izd. KhGU. 1952.
5. Boldyrev, V.G. K voprosu ob ispol'zovanii izmerenii ukhodyashchei radiatsii dlya rascheta temperatury zemnoi poverkhnosti i verkhnei granitsy oblakov (The Use of Measurements of Outgoing Radiation for Calculating the Temperature of the Earth Surface and of the Cloud Tops).— Trudy MMTs, Issue No. 8. 1965.
6. Boldyrev, V.G. Ob ispol'zovanii radiatsionnykh izmerenii, osushchestvlennykh s pomoshch'yu sputnikov v sinopticheskom analize (The Use of Satellite Radiation Measurements in Synoptic Analysis).— Meteorologiya i Gidrologiya, No. 10. 1962.
7. Berlyand, T.G. Teplovoi balans atmosfery severnogo polushariya. A.I. Voeikov i sovremennye problemy klimatologii (The Atmospheric Heat Balance of the Northern Hemisphere. A.I. Voeikov and Contemporary Climatological Problems).— Collection of Papers. Gidrometeoizdat. 1956.
8. Boldyrev, V.G. Raschet peredatochnykh funktsii atmosfery v intervale 8—12μ dlya territorii severnogo polushariya (Calculation of Transfer Functions of the Atmosphere in the 8—12-μ Band for the Northern Hemisphere).— Izv. AN SSSR, seriya fizika atmosfery i okeana, Vol. 1, No. 7. 1965.
9. Boldyrev, V.G., L.I. Koprova, and M.S. Malkevich. Ob uchete variatsii vertikal'nykh profilei temperatury i vlazhnosti pri opredelenii temperatury podstilayushchei poverkhnosti po ukhodyashchemu izlucheniyu (Allowance for the Variation of Vertical Temperature and Humidity Profiles in Determining the Temperature of the Underlying Surface, from Data on Outgoing Radiation).— Izv. AN SSSR, seriya fizika atmosfery, Vol. 1, No. 7. 1965.
10. Belov, P.N. and A.F. Kivganov. Ob izmeneniyakh temperatury i geopotentsiala, obuslovlennykh radiatsionnym pritokom tepla (Variations in Temperature and Geopotential, Caused by the Radiant-Heat Input).— Trudy MMTs, Issue No. 8. 1965.
11. Borisenkov, E.P., Yu.P. Doronin, and K.Ya. Kondrat'ev. Strukturnye kharakteristiki polya izlucheniya Zemli kak planety (Structural Characteristics of the Earth Radiation Field).— Kosmicheskie issledovaniya, Vol. 1, Issue No. 1. 1963.
12. Borisenkov, E.P., Yu.P. Doronin, and K.Ya. Kondrat'ev. Strukturnye kharakteristiki polei ukhodyashchei radiatsii po dannym ISZ "Tairos-II" i "Tairos-III" (Structural Characteristics of Outgoing Radiation Field from Data Obtained by TIROS II and TIROS III).— Kosmicheskie issledovaniya, Vol. 3, Issue No. 3. 1965.
13. Vinnikov, K.Ya. Novyi raschet teplovogo balansa sistemy Zemlya-atmosfera (New Calculations of the Heat Balance for the Earth—Atmosphere System).— Meteorologiya i Gidrologiya, No. 8. 1965.

14. Vetlov, I.P., V.I. Gaevskii, L.N. Guseva, E.P. Dombkovskaya, K.Ya. Kondrat'ev, W. Nordberg, and N.E. Ter-Markaryants. Opyt analiza infrakrasnogo izobrazheniya oblachnosti, poluchennogo pri pomoshchi meteorologicheskogo sputnika "Nimbus-I" (Analysis of Infrared Cloud Photographs, Obtained by NIMBUS I).— Meteorologiya i Gidrologiya, No. 9. 1965.
15. Vinnikov, K.Ya. Al'bedo sistemy Zemlya-atmosfera i pole ukhodyashchei korotkovolnovoi radiatsii (Albedo of the Earth—Atmosphere System and the Field of Outgoing Short-Wave Radiation).— Trudy GGO, Issue No. 170. 1965.
16. Gaevskii, V.L. and Yu.I. Rabinovich. Ob uchete vliyaniya atmosfery na rezultaty izmereniya radiatsionnoi temperatury zemnoi poverkhnosti s iskusstvennykh sputnikov Zemli (Allowance for the Effect of Atmosphere on the Measurements of Radiation Temperature of the Earth Surface by Artificial Earth Satellites).— Trudy GGO, Issue No. 170. 1965.
17. Gaevskii, V.L. and L.N. Guseva. Opredelenie vysoty verkhnei granitsy oblakov po dannym meteorologicheskikh sputnikov (Determination of Cloud-Top Heights with Data from Meteorological Satellites).— Trudy GGO, Issue No. 170. 1965.
18. Dzazhybekova, E.K., V.M. Kazachevskii, and A.V. Kharitonov. Opredelenie al'bedo Zemli (Determination of the Earth Albedo).— Astronomicheskii Zhurnal, Vol. 37, No. 1. 1960.
19. Kondrat'ev, K.Ya. Perenos dlinnovolnovogo izlucheniya v atmosfere (Propagation of Short-Wave Radiation in the Atmosphere).— Leningrad, Gostekhizdat. 1950.
20. Kondrat'ev, K.Ya. Luchistaya energiya Solntsa (Radiant Energy of the Sun).— Leningrad, Gidrometeoizdat. 1954.
21. Kondrat'ev, K.Ya. Luchistyi teploobmen v atmosfere (Radiant-Heat Exchange in the Atmosphere).— Leningrad, Gidrometeoizdat. 1956.
22. Kondrat'ev, K.Ya. and O.P. Filipovich. Ob ukhodyashchem izluchenii (Radiation).— Vestnik LGU, No. 6. 1962.
23. Kazachevskii, V.M. Opredelenie otrazhatel'noi sposobnosti zemnogo shara (Determination of Reflectivity of the Earth).— Izvestiya Astrofizicheskogo instituta AN KazSSR, Vol. 1, Issue Nos. 1—2. 1955.
24. Kondrat'ev, K.Ya. and N.E. Ter-Markaryants. O vozmozhnosti nablyudenii oblachnogo pokrova na nochnoi storone Zemli s pomoshch'yu ukhodyashchego izlucheniya v okne prozrachnosti (The Possibility of Observing the Cloud Cover on the Earth Night Side Using the Outgoing Radiation in the Transparent Window).— Trudy GGO, Issue No. 170. 1965.
25. Kolosov, S.G. Svyaz' polya voskhodyashchego izlucheniya Zemli i troposfery s polem temperatury (Outgoing Radiation of the Earth and Troposphere and its Relationship with the Temperature Field).— Iskusstvennye sputniki Zemli, No. 14. 1962.
26. Kostyanoi, G.N. O svyazi voskhodyashchikh potokov dlinnovolnovogo izlucheniya Zemli i troposfery s temperaturoi sredneenergeticheskogo urovnya (The Ascending Fluxes of Long-Wave Radiation of the Earth and Troposphere and their Relationship

with the Temperature Corresponding to the Mean Energy Level).— Izvestiya AN SSSR, seriya fizika atmosfery i okeana, Vol. 1, No. 7. 1965.

27. Kurilova, Yu. V. O vozmozhnosti meteorologicheskoi interpretatsii dlinnovolnovoi radiatsii (Meteorological Interpretation of Long-Wave Radiation).— Trudy MMTs, No. 8. 1965.
28. Kondrat'ev, K. Ya., E. P. Novosel'tsev, and N. E. Ter-Markaryants. Opredelenie temperatury postilayushchei poverkhnosti i oblakov s meteorologicheskikh sputnikov Zemli (Determination of the Temperature of the Underlying Surface and Clouds from Data of Meteorological Satellites).— Trudy GGO, Issue No. 183. 1966.
29. Markov, A. V. Otrazhatel'naya sposobnost' i pokazateli tsveta Zemli i detalei Luny po elektrofotometricheskim promeram (Reflectivity and Color Indexes of the Earth, and Moon Details as Measured from Electrophotometric Surveys).— Byulleten' Abastumskoi astrofizicheskoi observatorii, No. 11. 1950.
30. Malkevich, M. S. and V. I. Tatarskii. Opredelenie vertikal'nogo profilya temperatury atmosfery po ukhodyashchemu izlucheniya v polose CO_2 (Determination of Vertical Temperature Profiles of the Atmosphere Using Data on Outgoing Radiation in the CO_2 Band).— Kosmicheskie issledovaniya, Vol. III, No. 3. 1965.
31. Malkevich, M. S. Nekotorye voprosy interpretatsii polya ukhodyashchei radiatsii Zemli. 2. Razlichenie oblakov na fone estestvennykh poverkhnostei (Problems in the Interpretation of Data on the Outgoing Radiation of the Earth. 2. How to Distinguish Clouds against the Background of the Earth Surface).— Trudy GGO. Issue No. 166. 1964.
32. Malkevich, M. S. Nekotorye voprosy interpretatsii polya ukhodyashchei radiatsii Zemli. 1. Opredelenie temperatury podstilayushchei poverkhosti i vysoty verkhnei granitsy oblakov (Some Problems in the Interpretation of Data on the Outgoing Radiation of the Earth. 1. Determination of the Temperature of the Underlying Surface and Cloud Tops).— Trudy GGO, Issue No. 166. 1964.
33. Musaelyan, Sh. A. and A. Z. Chekirda. O chislennoi interpretatsii informatsii, postupayushchei s iskusstvennykh sputnikov Zemli (Numerical Interpretation of Data from Artificial Earth Satellites).— Trudy GGO, Issue No. 166. 1965.
34. Musaelyan, Sh. A. Nekotorye voprosy chislennoi interpretatsii oblachnoi informatsii postupayushchei s iskusstvennykh sputnikov Zemli (Some Problems in the Numerical Interpretation of Cloud Data Obtained from Artificial Earth Satellites).— Trudy GGO, Issue No. 166. 1964.
35. Novosel'tsev, E. P. O vybore spektral'nogo diapazona dlya tselei opredeleniya temperatury podstilayushchei poverkhnosti i oblakov pri pomoshchi radiometra (The Selection of the Spectrum Range for Radiometric Determinations of Temperature of the Underlying Surface and Clouds).— Trudy GGO, Issue No. 170. 1965.
36. Orlova, N. S. Opredelenie otrazhatel'noi sposobnosti planety Zemlya (Determination of the Earth Reflectivity).— Uchennye zapiski LGU, No. 82. 1941.

37. Rakipova, L.P. O raschete ukhodyashchego izlucheniya Zemli po izmereniyam s iskusstvennykh sputnikov Zemli (Calculation of the Earth Back Radiation from Satellite Data).— Kosmicheskie issledovaniya, Vol. III, Issue No. 4. 1965.
38. Trudy GGO, Issue No. 166. 1964.
39. Fedoseeva, A.I. Al'bedo sistemi Zemlya-atmosfera i ego raspredelenie po zemnomu sharu (Albedo of the Earth—Atmosphere System, and its Global Distribution).— Trudy GGO, Issue No. 41 (103). 1958.
40. Fesenkov, V.G. Gornaya astrofizicheskaya observatoriya AN KazSSR i nekotorye rezul'taty ee raboty (The Mountain Astrophysical Observatory of the AN KazSSR and Some Results of its Work).— Izvestiya AN KazSSR, No. 9. 1950.
41. Astling, E.G. and L.H. Horn. Some Geophysical Variations of Terrestrial Radiation Measured by TIROS II.— J. Atm. Sci., Vol. 21, No. 1. 1964.
42. Adem, J. Preliminary Model for Computing Mid-Troposphere and Surface Temperatures from Satellite Data.— J. Geophys. Res., Vol. 70, No. 12. 1965.
43. Bandeen, W.R., B.J. Conrath, W. Nordberg and H.P. Thompson. A Radiation View of Hurricane Anna from the TIROS III Meteorological Satellite.— Proc. JRSME, Amsterdam. 1962.
44. Bandeen, W.R., M. Halev, and J. Strange. A Radiation Climatology in the Visible and Infrared Band from the TIROS Meteorological Satellites.— NASA Goddard Space Flight Center, X-651-64-218. August 1964.
45. Bandeen, W.R., B.J. Conrath, and R.A. Hanel. Experimental Confirmation from the TIROS VII Meteorological Satellite of the Theoretically Calculated Radiance of the Earth Within the 15-μ Band of Carbon Dioxide.— J. Atm. Sci., Vol. 20, No. 6. 1963.
46. Bandeen, W.R., V. Kunde, W. Nordberg, and H.P. Thompson. TIROS III Meteorological Satellite Radiation Observations of a Tropical Hurricane.— Tellus, Vol. 16, No. 4. 1964.
47. Clapp, P.F. Comments on "Analysis of Satellite Infrared Radiation Measurements on a Synoptic Scale" and "Synoptic Use of Radiation Measurements from Satellite TIROS II".— Mon. Weath. Rev., Vol. 90, No. 7. 1962.
48. Corcoran, J.L. and L.H. Horn. The Role of Synoptic-Scale Variations of Infrared Radiation in the Generation of Available Potential Energy.— Dept. of Meteor., Univ. of Wisconsin, Annual Rep. Oct. 1964.
49. Corcoran, J.L. and L.H. Horn. The Role of Synoptic-Scale Variations of Infrared Radiations in the Generation of Available Potential Energy.— J. Geophys. Res., Vol. 70, No. 18. 1965.
50. Danjon, A. Nouvelles recherches sur la photometrie de la lumière cendrée et albedo de la terre.— Ann. de l'Obs. Strasbourg, Vol. 3. 1936.

51. Davis, P.A. Satellite Radiation Measurements and the Atmospheric Heat Balance.— Fin. Rep., Contr. NASA 5—2919. July 1964.
52. Davis, P.A. TIROS III Radiation Measurements and some Adiabatic Properties of the Atmosphere.— Mon. Weath. Rev., Vol. 93, No. 9. 1965.
53. Fritz, S. The Albedo of the Planet Earth and of Clouds.— J. Met., Vol. 6, No. 4. 1949.
54. Vassy, A. and E. Vassy. Possibilité de mesure de la température moyenne de la stratosphère par satellite.— 14th Int. Astr. Congr., Paris, 1962, Vol. 2. Paris-Warsaw. 1965.
55. Fritz, S. and J.S. Winston. Synoptic Use of Radiation Measurements from Satellite TIROS II.— Mon. Weath. Rev., Vol. 190, No. 1. 1962.
56. Fritz, S., P.K. Rao, and M. Weinstein. Satellite Measurement of Reflected Solar Energy and the Energy Received at the Ground.— J. Atm. Sci., Vol. 21, No. 2. 1964.
57. Hales, J.V. and W.G. Zdunkowski. The Long-Wave Flux Density Leaving the Earth under Various Meteorological Conditions.— AFCRC-TN-59-212. 1959.
58. Hales, J.V., T.L. Williams, and D. Henderson. Calculation of Infrared Radiative Flux Emission of the Earth Plus Atmosphere at Various Levels High above the Earth.— Final Rep., AFCRL-TR-60-405. August 1960.
59. Hales, J.V., T.A. Studer, and D. Henderson. Atmospheric Radiation Flux in the 6.3μ to 8.2μ Interval.— Sci. Rep., No. 2, AFCRL-TN-60-638. 1960.
60. Houghton, H.C. On the Annual Balance of the Northern Hemisphere.— J. Met., Vol. 11, No. 1. 1954.
61. House, F.B. The Earth's Radiation Heat Budget as Seen by TIROS IV Satellite.— Radiation Symposium in Leningrad, 5—12 August 1964.
62. Houghton, J.T. Stratosphere Temperature Measurements from a Satellite.— J. Brit. Interplanet. Soc., Vol. 19, No. 9. 1964.
63. Kasten, F., G. Korb, G. Manier, and F. Möller. On the Heat Balance of the Troposphere.— Johannes Gutenberg Univ., Final Rep., Contr. AF 61 (052)-18. 1959.
64. Kano, M. The Albedo of Earth's Atmosphere. A Case of a Rayleigh Atmosphere.— Pap. in Met. and Geophys., Vol. VIII, No. 4. 1958.
65. Kuhn, P.M. and V.E. Suomi. Airborne Radiometer Measurements of Effects of Particulates on Terrestrial Fluxes.— J. Appl. Met., Vol. 4, No. 2. 1965.
66. London, J. A Study of the Atmospheric Heat Balance.— New York Univ., Final Rep., Contr. NAF 19 (122)-165. 1957.
67. Möller, F. Der Strahlungshaushalt der Troposphäre.— Meteorol. Rund., Vol. 13, No. 3. 1960.
68. Möller, F. and W. Zdunkowski. Computational Methods of Long-Wave Atmospheric Radiation.— Meteorol. Inst., Univ. Munich. Contr. AF 61 (052)-493. 1961.
69. Möller, F. Einige vorläufige Auswertungen der Strahlungsmessungen von TIROS II.— Archiv für Met., Geophys. und Biokl., Ser. B, Vol. 12, No. 1. 1962.

70. Möller, F. and E. Raschke. Evaluation of TIROS III Radiation Data.— J. Atm. Sci., Vol. 21, No. 2. 1964.
71. Millard, J.P. and C.B. Neel. Measurements of Albedo and Earth Radiation from OSO-1.— AIAA J., Vol. 3, No. 7. 1965.
72. Nordberg, W., W.R. Bandeen, B.J. Conrath, V. Kunde, and J. Persano. Preliminary Results of Radiation Measurements from the TIROS III Meteorological Satellite.— J. Atm. Sci., Vol. 19, No. 1. 1962; NASA TN D-1338. 1961.
73. Nordberg, W., W.R. Bandeen, G. Warnecke, and V. Kunde. Stratospheric Temperature Patterns Based on Radiometric Measurements from the TIROS VII Satellite.— Goddard Space Flight Center, X-651-64-115. May 1964.
74. Nordberg, W., W.R. Bandeen, G. Warnecke, and V. Kunde. Stratospheric Temperature Patterns Based on Radiometric Measurements from the TIROS VII Satellite.— Space Research. Proc. of the Fifth Intern. Space Sci. Symp., North-Holland Publ. Comp., Amsterdam. 1965.
75. Nordberg, W. The NIMBUS I Meteorological Satellite—Geophysical Observations from a New Perspective.— Goddard Space Flight Center. 1965.
76. Rasool, S.I. Cloud Heights and Nighttime Cloud Cover from TIROS Radiation Data.— J. Atm. Sci., Vol. 21, No. 2. 1964.
77. Rao P.K. and J.S. Winston. An Investigation of Some Synoptic Capabilities of Atmospheric "Window" Measurement from Satellite TIROS II.— J. Appl. Met., Vol. 2, No. 1. 1963.
78. Rao, P.K. Seasonal Variations of Outgoing Long-Wave Radiation Observed by TIROS II and TIROS III Satellites.— Weather, Vol. XIX, No. 3. 1964.
79. Raschke, E. and J. Tannhäuser. Investigation of Atmospheric Properties Based upon Evaluation of Infrared-Radiation Data Obtained from TIROS Satellites.— Fin. Rep., Univ. of Munich. May 1965.
80. Schenk, W.E. TIROS II Window Radiation and Large-Scale Vertical Motion.— J. Appl. Met., Vol. 2, No. 6. 1963.
81. Sabatini, R.R. and V.E. Suomi. On the Possibility of Infrared Cooling Estimates from Satellite Observations.— J. Atm. Sci., Vol. 19, No. 4. 1962.
82. Saiedy, F., D.T. Hilleary, and W.A. Morgan. Cloud-Top Altitude Measurements from Satellites.— Appl. Opt., Vol. 4, No. 4. 1965.
83. Saiedy, F., W.A. Morgan, and D.Q. Wark. Determination of Cloud Altitudes from Gemini-Titan-5.— Nature, Vol. 208, No. 5012. 1965.
84. TIROS III Radiation Data Users' Manual Supplement.— Goddard Space Flight Center. 1963.
85. TIROS II Radiation Data Catalogue, Vol. 1.— Goddard Space Flight Center. 15 August 1961.
86. TIROS III Radiation Data Catalogue.— Goddard Space Flight Center. 1962.
87. Winston, J.S. and P.K. Rao. Preliminary Study of Planetary-Scale Outgoing Long-Wave Radiation as Measured from TIROS II Measurements.— Month. Weath. Rev., Vol. 90, No. 8. 1962.

88. Winston, J.S. and P.K. Rao. Temporal Variations in the Planetary-Scale Outgoing Long-Wave Radiation as Derived from TIROS II Measurements. — Mon. Weath. Rev., Vol. 91, No. 10—12. 1963.
89. Wexler, R. Infrared and Visual Radiation Measurements from TIROS II. — Appl. Opt., Vol. 3, No. 2. 1964.
90. Widger, W.K. Jr., P.E. Sherr, and C.W.C. Rogers. Practical Interpretation of Meteorological Satellite Data. — Aracon Geophys. Co., Fin. Rep., Contr. AF 19 (628)-247. 1 September 1964.
91. Weinstein, M. and V.E. Suomi. Analysis of Satellite Infrared Radiation Measurements on a Synoptic Scale. — Mon. Weath. Rev., Vol. 89, No. 11. 1961.
92. Winston, J.S. Comments on "Cloud Heights and Nighttime Cloud Cover from TIROS Radiation Data." Reply by S.J. Rasool. — J. Atm. Sci., Vol. 22, No. 3. 1965.
93. Wiegman, E.J., R.G. Hadfield, S.M. Serebreny, and W. Viezee. Atlas of Cloud Vortex Patterns Observed in Satellite Photographs. Final Addendum. — Stanford Res. Inst. July 1965.
94. Wark, D.Q. and D.M. Mercer. Absorption in the Atmosphere by the Oxygen "A" Band. — Appl. Opt., Vol. 4, No. 7. 1965.
95. World Meteorological Organization Interregional Seminar on the Interpretation and Use of Meteorological Satellite Data. Part I, Part II. — Tokyo. 27 November—8 December 1964.
96. Zdunkowski, W., D. Henderson, and J.V. Hales. The Influence of Haze on Infrared Radiation Measurements Detected by Space Vehicles. — Tellus, Vol. 17, No. 2. 1965.
97. Zirkind, R. The Near Medium IR Earth Albedo; its Use for Cloud Height Determination. — Planet. and Space Sci., Vol. 13, No. 5. 1965.

Chapter 3

THE PROCESSING OF METEOROLOGICAL SATELLITE DATA

Data processing is one of the most serious problems in satellite meteorology. The reason is the specific character of information from satellites and its large volume. Without automatic data processing and the application of electronic computers the interpretation and practical application of satellite data may prove ineffective or even impossible.

For comparison, let us mention some figures. At present there are some 1,000 aerological stations functioning in the Northern Hemisphere, carrying out radiosonde measurements. With three radiosoundings, every aerological telegram containing 20—30 five-digit groups, we obtain an information volume of $3 \cdot 10^5$ to $4.5 \cdot 10^5$ groups/hour.

A complete and timely processing of this information represents a formidable task and requires the use of highly reliable electronic digital computers with a processing capacity of some hundreds of thousands of operations per second.

The volume of information obtained from satellites considerably exceeds these figures. Thus, according to data from /18/, the volume of information on outgoing radiation for one orbit of TIROS III is $2 \cdot 10^5$ bits of information. To this one must add that every satellite of the TIROS family carried two TV cameras, while the NIMBUS I carried four cameras with which one hundred thousand photographs were obtained (32 pictures per orbit).

In the present chapter we shall consider four groups of problems, relating to the practical processing of satellite data:

1) geographical gridding (correlation) of pictures and the elimination of distorting factors;

2) geographical correlation and rectification of photographs obtained by the APT (automatic picture transmission) system;

3) processing of nephanalysis data;

4) processing of data on outgoing radiation.

Incidentally, we shall also touch in this chapter on a number of other problems connected with satellite data processing.

It should also be remembered that processing methods are continuously being improved and modified. Methods applied nowadays differ considerably from those used a few years ago, that were partly described in /4/. This is only a natural and legitimate development, and it should not be assumed that the methods described here are universally applied and do not change. They will doubtlessly be improved and become more accurate. Different aspects of processing problems are dealt with in /12, 15, 17, 19, 21, 23, 25, 26/.

3.1. GEOGRAPHICAL CORRELATION OF TELEVISION PICTURES AND THE ELIMINATION OF DISTORTION FACTORS

The first step in the analysis of TV pictures of localities and meteorological fields obtained by satellites is the geographical correlation [i.e., determination of the particular geographical location that they reproduce] and the elimination (as far as possible) of all distortion factors. The latter are connected with the specific features of operation of the TV camera and with many other orbital factors.

For solving the problem of geographical correlation the following parameters must be known:

1) the latitude and longitude of the satellite, i.e., of its sub-satellite point (SSP). By the latter is meant the point of intersection of the main vertical (the line satellite—Earth center) with the Earth surface;

2) the satellite height above the Earth surface;

3) the nadir angle, defined as the angle between the main vertical and the satellite spin axis, which usually coincides with the optical axis of the satellite TV cameras. The point of intersection of the optical axis with the Earth surface is called the principal point (PP);

4) the azimuth of the spin axis (optical axis) projected on the Earth surface counted from the meridian passing through the SSP;

5) the angle between the fixed direction on the photographs and the projection line of the spin axis on the Earth surface. The projection line is called the principal or base line.

In addition, for many problems connected with the calculation of all possible distortions, we must know such characteristics as the angle between the projection of the direction of incidence of the solar rays on the TV picture plane and the line of intersection of this plane with the vertical plane on which the optical axis of the TV camera lies; the angle of inclination of the picture; the optical characteristics of the lens system, and others.

The basic orbital parameters must be given as time functions. The above parameters are sufficient to perform geographical correlation.

Initially, correlation was carried out using Canadian grids /24/, well known from photogrammetry. Details of the grids as applied to satellite data are presented in /3—5, 10, 14, 23/. Their use consists in the following. Since the optical axis of the TV camera is usually aimed at some angle at the Earth surface, this leads to the perspective distortion of the picture. This in turn involves the calculation and plotting of a coordinate grid representing the projection of a right-angle grid on the Earth surface in the direction of the optical axis of the TV camera. This grid is superimposed on the photographs of clouds and localities. A set of such grids (Figure 3.1) is prepared for different nadir angles for a given satellite height.

On many photographs the horizon line can be seen, and this permits the quick orientation of the picture by superimposing this line on the corresponding coordinate grid. As will be seen later, the existence of the horizon line on the picture permits numerous distortion effects to be eliminated.

In the earlier stage of application of the satellite photographs at the data-receiving stations, the operator having a set of coordinate grids

performed manual correlation by superimposing the grids on the pictures. Later, the S-15 calculator /16, 24/ was used for this work.

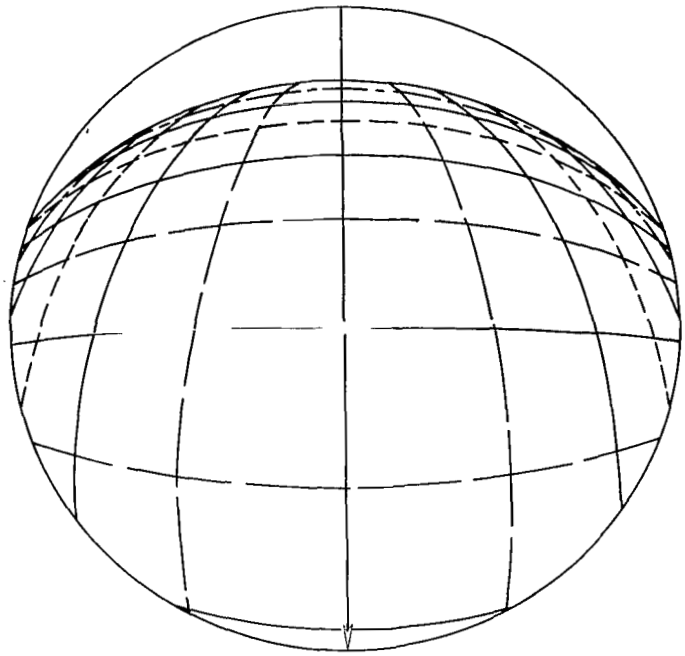

FIGURE 3.1. Perspective coordinate grid for a nadir angle of 25° and a satellite height of 810 km

At present, the coordinate grids are computed by an electronic digital computer, and this arrangement permits the automatic plotting of these grids directly on the pictures. Based on data given in /10/, we shall present more details of this process.

The first experiments for performing automatic correlation and processing the photographs were made with the pictures received from geophysical rockets /10/. With the aid of a special device these photographs were graduated according to the brightness scale with 16 divisions. The data were recorded on a magnetic tape and then fed into an electronic digital computer. For shortening the information in the experimental calculations the magnetic tape contained a record of 99 lines, each of which had 105 information bits. The coordinates of each second point and its brightness grade were calculated and stored in the electronic computer. After brief data processing and calculation of the coordinates with the help of a printing unit these data were printed out. Figure 3.2 shows a model of such a printed table which presents the coordinates of points (latitude and longitude) and the corresponding brightness grades for each point. However, in many cases, in particular for routine application of satellite

ROW 44									
36.12	68.43	6	5	36.10	68.44	5	5	36.09	68.44
36.04	68.46	6	6	36.03	68.46	6	6	36.02	68.47
35.97	68.48	5	5	35.96	68.48	5	5	35.94	68.49
35.90	68.50	3	4	35.89	68.51	4	3	35.87	68.51
35.83	68.52	3	4	35.81	68.53	3	3	35.80	68.53
35.75	68.54	2	2	35.74	68.55	3	3	35.73	68.55
35.68	68.56	5	5	35.67	68.56	4	4	35.65	68.57
35.61	68.58	4	5	35.59	68.58	5	5	35.58	68.59
35.54	68.60	6	6	35.52	68.60	5	5	35.51	68.60
35.46	68.61	4	3	35.45	68.62	2	1	35.43	68.62
35.39	68.63	2	2	35.37	68.63	2	4	35.36	68.64
ROW 45									
36.18	68.69	6	5	36.16	68.69	6	6	36.15	68.70
36.11	68.71	5	6	36.09	68.72	6	6	36.08	68.72
36.04	68.73	5	4	36.02	68.74	4	4	36.01	68.74
35.96	68.75	4	5	35.95	68.76	4	4	35.94	68.76
35.89	68.77	3	2	35.88	68.78	2	2	35.86	68.78
35.82	68.79	2	3	35.81	68.80	4	3	35.79	68.80
35.75	68.81	3	3	35.74	68.82	2	2	35.72	68.82
35.68	68.83	2	4	35.66	68.83	4	4	35.65	68.84
35.61	68.85	5	4	35.59	68.85	3	3	35.58	68.86
35.53	68.87	3	2	35.52	68.87	2	2	35.50	68.87
35.46	68.88	3	3	35.45	68.88	3	5	35.43	68.89
ROW 46									
36.23	68.92	6	5	36.22	68.92	6	6	36.20	68.93
36.16	68.94	6	6	36.15	68.94	6	5	36.13	68.95
36.09	68.96	4	3	36.08	68.97	3	3	36.06	68.97
36.02	68.98	4	4	36.01	68.99	4	5	35.99	68.99
35.95	69.00	2	1	35.94	69.01	1	1	35.92	69.01
35.88	69.02	2	3	35.87	69.02	3	3	35.85	69.03
35.81	69.04	3	2	35.80	69.04	2	1	35.78	69.05
35.74	69.06	1	1	35.73	69.06	1	2	35.71	69.06
35.67	69.07	2	1	35.66	69.08	1	1	35.64	69.08
35.60	69.09	2	1	35.58	69.09	2	3	35.57	69.10
35.53	69.11	3	5	35.51	69.11	5	5	35.50	69.11
ROW 47									
36.28	69.13	6	5	36.27	69.13	6	6	36.25	69.13
36.21	69.15	6	6	36.20	69.15	5	5	36.19	69.16
36.14	69.17	2	2	36.13	69.17	2	2	36.12	69.18
36.07	69.19	4	5	36.06	69.19	4	3	36.05	69.20
36.01	69.21	2	2	35.99	69.21	2	2	35.98	69.22
35.94	69.23	2	3	35.92	69.23	3	2	35.91	69.23
35.87	69.24	1	0	35.85	69.25	0	1	35.84	69.25
35.80	69.26	2	2	35.78	69.27	3	3	35.77	69.27
35.73	69.28	1	1	35.71	69.28	2	1	35.70	69.29
35.66	69.30	3	2	35.64	69.30	1	2	35.63	69.30
35.59	69.31	4	5	35.57	69.32	5	5	35.56	69.32
ROW 48									
36.33	69.32	6	5	36.31	69.32	5	5	36.30	69.32
36.26	69.34	6	5	36.25	69.34	5	4	36.23	69.35
36.19	69.36	3	3	36.18	69.36	3	4	36.16	69.37
36.12	69.38	3	3	36.11	69.38	3	4	36.10	69.38
36.05	69.40	3	3	36.04	69.40	3	3	36.03	69.40
35.99	69.41	1	1	35.97	69.42	2	3	35.96	69.42
35.92	69.43	0	0	35.90	69.44	0	0	35.89	69.44
35.85	69.45	3	1	35.84	69.45	2	2	35.82	69.46
35.78	69.47	3	4	35.77	69.47	5	4	35.75	69.47
35.71	69.48	4	4	35.70	69.49	3	3	35.68	69.49
35.64	69.50	3	4	35.63	69.50	5	6	35.61	69.51
ROW 49									
36.37	69.49	7	5	36.36	69.50	5	5	36.34	69.50
36.30	69.51	5	4	36.29	69.52	3	3	36.27	69.52
36.23	69.53	4	4	36.22	69.54	4	3	36.21	69.54
36.17	69.55	3	4	36.15	69.55	5	5	36.14	69.56
36.10	69.57	3	4	36.09	69.57	4	4	36.07	69.58
36.03	69.59	0	0	36.02	69.59	0	1	36.01	69.60
35.96	69.61	0	0	35.95	69.61	0	0	35.94	69.61
35.90	69.62	4	3	35.88	69.63	1	1	35.87	69.63
35.83	69.64	5	6	35.82	69.64	6	6	35.80	69.65
35.76	69.66	5	6	35.75	69.66	6	6	35.73	69.66
35.69	69.67	5	5	35.68	69.68	6	6	35.66	69.68
ROW 50									
36.41	69.65	7	5	36.39	69.66	5	5	36.38	69.66
36.34	69.67	3	3	36.33	69.68	3	4	36.32	69.68
36.28	69.69	5	4	36.26	69.70	4	3	36.25	69.70
36.21	69.71	4	4	36.20	69.72	3	4	36.18	69.72
36.14	69.73	3	2	36.13	69.73	3	3	36.12	69.74
36.07	69.75	0	0	36.06	69.75	0	0	36.05	69.76
36.01	69.77	0	0	35.99	69.77	0	1	35.98	69.77
35.94	69.78	1	1	35.93	69.79	0	1	35.91	69.79
35.87	69.80	6	6	35.86	69.80	6	6	35.85	69.81
35.81	69.82	5	6	35.79	69.82	6	6	35.78	69.82
35.74	69.83	6	6	35.73	69.84	5	5	35.71	69.84
ROW 51									

FIGURE 3.2. Example of a printed data table for cloud photographs obtained by a rocket in

6	6	36.07	68.45	6	6	36.06	68.45	6	6
6	6	36.00	68.47	6	6	35.99	68.48	6	6
5	4	35.93	68.49	4	4	35.91	68.50	4	3
3	3	35.86	68.51	3	3	35.84	68.52	3	3
2	2	35.78	68.53	2	2	35.77	68.54	1	1
3	4	35.71	68.55	4	4	35.70	68.56	4	4
4	4	35.64	68.57	5	5	35.62	68.58	5	4
5	6	35.56	68.59	6	6	35.55	68.59	5	5
5	4	35.49	68.61	4	3	35.48	68.61	4	5
1	2	35.42	68.62	2	1	35.40	68.63	2	2
4	0								
6	6	36.13	68.70	6	6	36.12	68.71	6	5
6	6	36.06	68.72	6	5	36.05	68.73	5	5
4	4	35.99	68.75	3	3	35.98	68.75	3	3
4	4	35.92	68.77	4	4	35.91	68.77	4	4
2	2	35.85	68.79	3	2	35.84	68.79	2	2
4	4	35.78	68.81	4	4	35.76	68.81	4	3
2	4	35.71	68.82	5	5	35.69	68.83	4	3
5	5	35.63	68.84	5	5	35.62	68.85	5	5
4	5	35.56	68.86	5	5	35.55	68.86	5	5
3	3	35.49	68.87	3	2	35.48	68.88	2	2
5	0								
6	6	36.19	68.93	6	5	36.18	68.94	5	6
5	5	36.12	68.95	5	4	36.11	68.96	4	4
3	3	36.05	68.97	3	4	36.04	68.98	4	4
5	5	35.98	68.99	4	3	35.97	69.00	3	2
2	3	35.91	69.01	3	3	35.90	69.02	2	2
2	2	35.84	69.03	1	1	35.83	69.04	2	2
3	4	35.77	69.05	3	3	35.75	69.05	3	2
3	4	35.70	69.07	3	2	35.68	69.07	3	4
2	3	35.63	69.08	3	3	35.61	69.09	3	2
3	3	35.56	69.10	2	2	35.54	69.10	3	3
4	0								
5	5	36.24	69.14	5	5	36.23	69.14	5	6
5	4	36.17	69.16	3	3	36.16	69.16	3	3
3	4	36.10	69.18	3	3	36.09	69.18	3	3
3	3	36.03	69.20	2	2	36.02	69.20	2	2
3	4	35.96	69.22	3	3	35.95	69.22	3	3
1	1	35.89	69.24	1	2	35.88	69.24	3	2
1	1	35.83	69.26	0	0	35.81	69.26	1	1
2	2	35.76	69.27	2	2	35.74	69.28	2	2
2	3	35.69	69.29	3	3	35.67	69.29	4	4
2	2	35.62	69.31	2	2	35.60	69.31	4	4
5	0								
5	5	36.29	69.33	6	6	36.27	69.33	6	6
3	3	36.22	69.35	2	2	36.20	69.35	2	2
4	4	36.15	69.37	3	3	36.14	69.37	3	2
4	5	36.08	69.39	4	4	36.07	69.39	4	3
4	4	36.01	69.41	2	2	36.00	69.41	2	2
2	1	35.95	69.43	2	2	35.93	69.43	2	0
0	1	35.88	69.44	1	1	35.86	69.45	2	3
2	4	35.81	69.46	4	3	35.79	69.46	3	3
5	4	35.74	69.48	4	4	35.72	69.48	5	5
3	3	35.67	69.49	3	3	35.66	69.50	4	4
5	0								
5	5	36.33	69.50	6	6	36.32	69.51	5	5
3	3	36.26	69.52	3	3	36.25	69.53	3	4
3	3	36.19	69.54	3	4	36.18	69.55	4	3
4	4	36.13	69.56	5	4	36.11	69.57	4	3
3	2	36.06	69.58	1	1	36.05	69.58	0	0
1	0	35.99	69.60	0	0	35.98	69.60	0	0
0	0	35.92	69.62	1	3	35.91	69.62	4	5
0	1	35.86	69.63	2	3	35.84	69.64	5	4
5	5	35.79	69.65	4	3	35.77	69.65	4	5
5	5	35.72	69.67	6	5	35.71	69.67	5	5
5	0								
5	5	36.37	69.67	5	5	36.36	69.67	4	3
4	3	36.30	69.69	4	4	36.29	69.69	5	5
4	5	36.24	69.70	5	4	36.22	69.71	4	4
3	3	36.17	69.72	4	3	36.16	69.73	2	2
2	1	36.10	69.74	0	0	36.09	69.75	0	0
0	0	36.03	69.76	0	0	36.02	69.76	0	0
2	3	35.97	69.78	4	5	35.95	69.78	4	2
1	1	35.90	69.79	1	3	35.89	69.80	5	5
5	3	35.83	69.81	3	2	35.82	69.81	3	5
6	6	35.77	69.83	6	6	35.75	69.83	6	6
5	0								

1959; the table was printed after processing the photographs by an IBM-704 computer

photographs, this method of representing cloud data is inconvenient. The earlier described method of overlaying coordinate grids on the photographs is much more practical.

Below, two programs used for computing the grids are discussed. The first program is used to find the latitude and longitude for each point covered by the viewing field of the satellite TV camera and represented in the local system of right-angle x, y coordinates. The purpose of the second program is to solve the inverse problem, i.e., to find the x, y coordinates in the local right-angle coordinate system of the picture according to the given coordinates of the points of intersection between latitude and meridian circles. Both programs take into account this distortion inherent in the optical system used by the camera.

Before describing these programs let us briefly consider the influence of lens distortion which is not taken into account with the general outlines of coordinate-grid computation.

One of these lens distortions is the radially symmetric circular distortion. The input information that allows for this type of distortion are the optical characteristics of the lenses that connect the true angles under which the light rays from the object enter the TV camera, with the theoretical angles.

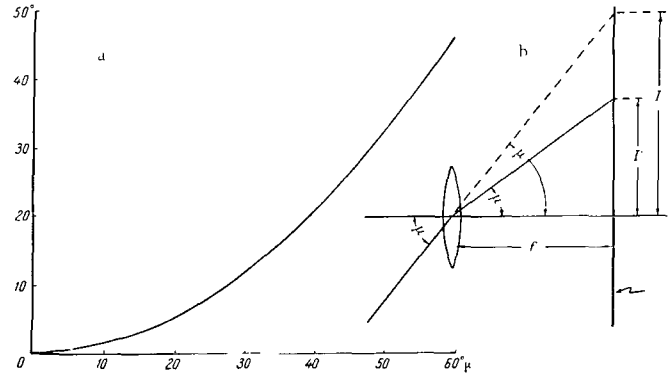

FIGURE 3.3. Lens distortion of the TIROS optical system:

a — diagram for calculating distortion; b — schematic diagram of a light ray passing through the lens.

Figure 3.3a shows a conversion diagram for the TIROS lens system. The necessary explanations are given in Figure 3.3b. Because of lens distortion the light ray entering the system at angle μ will leave it at angle μ'. The ratio $\frac{l-l'}{l}$ 100% is called the resolution ratio. In Figure 3.3a this ratio is represented as a function of μ. where μ is the angle between the optical axis and the light ray from the object, entering the center of the lens. The characteristics of the lens in the form of trigonometric functions are transferred to punchcards and are used simultaneously with the punchcards of the program for the direct geographical correlation. In general, the

allowance for distortion does not depend on the correlation program, but only on the characteristics of the lens and film. For TIROS I $f = 5.33$ mm.

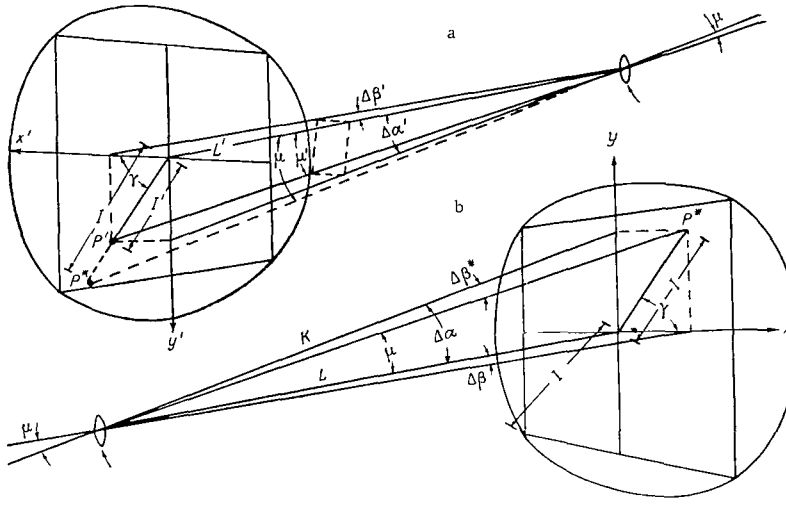

FIGURE 3.4. Picture obtained on the satellite TV camera (a) and on the "true" plane (b)

Figure 3.4 shows a schematic plan view of the section of a locality (b) and its image on the tape after the passage of the rays through the lens (a). In both cases the picture is perpendicular to the optical axis. Owing to the distorting influence of the lens, point P^* falls on point P' on the picture. The diameter of the distorted image is divided into 47 equal parts through which pass concentric circles. In addition, the image is subdivided by radial lines issuing from its center. The intersection points form a network consisting of nodal points, symmetrically located around the axis. In this case, the geographical location of points and the distorting effect of the optical lens are calculated for each nodal point.

In Figure 3.4 the orbital point P' can be defined on the camera plane by coordinates x', y'. Since the focal length of the given lens L' is known, the coordinates of each point on the image can be calculated by the equations

$$\begin{aligned} y' &= L' \operatorname{tg} \Delta\alpha'; \\ x' &= L' \operatorname{tg} \Delta\beta'. \end{aligned} \tag{3.1}$$

However,

$$\operatorname{tg} \mu' = \frac{l'}{L'} = \sqrt{\operatorname{tg}^2 \Delta\alpha' + \operatorname{tg}^2 \Delta\beta'}, \tag{3.2}$$

where l' is the radially distorted distance from the center to point P'.

Using (3.2)

$$\mu' = \operatorname{arc\,tg} \sqrt{\operatorname{tg}^2 \Delta\alpha' + \operatorname{tg}^2 \Delta\beta'}. \tag{3.3}$$

Angle γ, formed between the direction from the center to point P' and axis Ox', is calculated with the following relation:

$$\gamma = \operatorname{arc\,tg}\left(\frac{\operatorname{tg}\Delta\alpha'}{\operatorname{tg}\Delta\beta'}\right). \tag{3.4}$$

The radial distorted distance l' in the image plane corresponds to the radial distance l of point P^* on the locality. We are interested in angle μ which should be the same both in the picture and for the locality. The angle μ is calculated using the angle μ' with allowance for lens distortion. The angles $\Delta\alpha$ and $\Delta\beta$ are computed with the help of angles μ, $\Delta\alpha'$ and $\Delta\beta'$. Actually, on the strength of Figure 3.4b, which shows the passage of the rays from the object to the satellite camera lens, we have

$$\operatorname{tg}\Delta\beta = \frac{x}{L} = \frac{l\cos\gamma}{L} = \operatorname{tg}\mu\cos\gamma. \tag{3.5}$$

Here, L is the distance from the picture center to the lens; x is the coordinate of point P^* on the locality and $\frac{x}{l} = \cos\gamma$, whence

$$\Delta\beta = \operatorname{arc\,tg}\left(\operatorname{tg}^2\mu/(1+\operatorname{tg}^2\gamma)\right). \tag{3.6}$$

Similarly

$$\Delta\alpha = \operatorname{arc\,tg}(\operatorname{tg}\mu\sin\gamma). \tag{3.7}$$

For the allowance of the picture-angle distortions we determine the angle $\Delta\beta^*$, which is a function of $\Delta\alpha$ and $\Delta\beta$. Since

$$\operatorname{tg}\Delta\beta^* = \frac{x}{K} = \frac{x}{L}\frac{L}{K} = \operatorname{tg}\Delta\beta\cos\Delta\alpha,$$

where K is the distance from the lens center to the projection point P^* on the Oy axis (Figure 3.4b), we obtain

$$\Delta\beta^* = \operatorname{arc\,tg}(\operatorname{tg}\Delta\beta\cos\Delta\alpha). \tag{3.8}$$

Finally, the computer output yields the angles $\Delta\alpha$ and $\Delta\beta^*$ in the form of tables. On the true pictures thus obtained the geographical grid is then superimposed.

Usually, test photographs are taken already before the launching of the satellite. Symmetric distortions are eliminated mathematically. The difference between total and symmetric distortions gives the values of the asymmetric distortions, which are then tabulated for points lying on the concentric circles of the video camera, symmetric with the optical axis. Figure 3.5 gives an idea of the symmetric and asymmetric distortions. It should be noted that according to some data /4/ the allowance for asymmetric distortion did not in practice yield the desired results.

Once the distortion characteristics of the lens are obtained, the direct geographical correlation is performed by one of the above-mentioned

programs, the previously made calculations being used as supplementary input information.

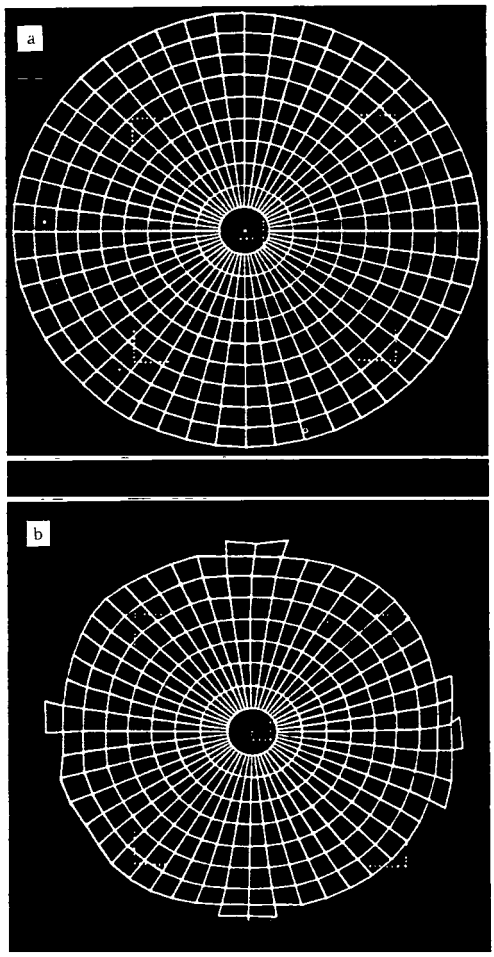

FIGURE 3.5. Relation between angles on the locality and on the picture for symmetrical distortion (a) and for all types of distortion (b)

1. **Program for the determination of geographical coordinates of points with given x, y coordinates.** In this program, the computations are made for a plane normal to the main vertical (Figure 3.6). The y axis points along the line joining the projection of the SSP on this plane as well as the principal point (PP).

In Figure 3.6, the line S—SSP is the line of the main vertical; H is the satellite altitude.

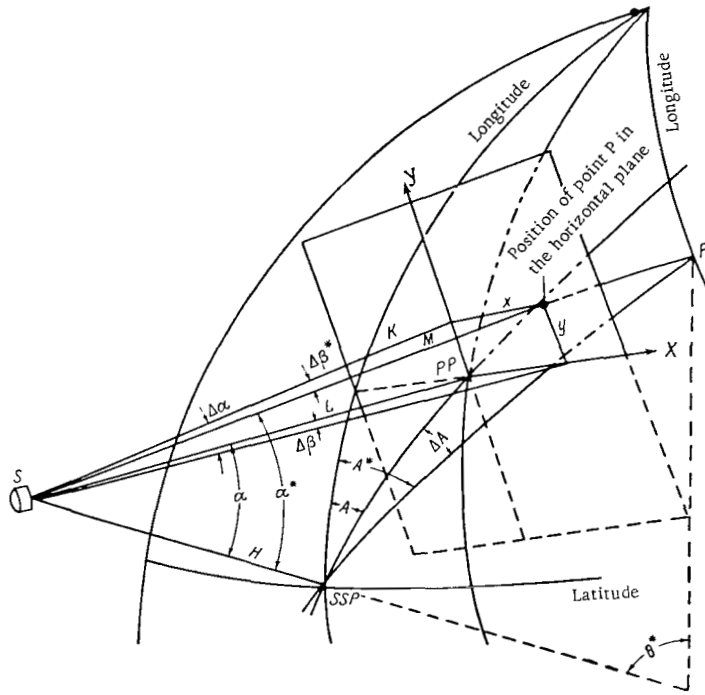

FIGURE 3.6. Location of characteristic points, angles and lines for the preparation of calculation programs for the electronic computer

The arc of the large circle, which passes through the pole and the SSP, is the longitude of the PP. The arc of the large circle that joins the pole and the principal point is the longitude of the principal point. The angle A is called the azimuth. The angle ΔA is the increment of the azimuth on transition from the PP to any other point P on the picture; A^* is the azimuth of this point; L is the distance from the satellite to the picture center; K is the distance from the satellite to the projection of some point of the picture on the y axis; M is the distance from the satellite to this point; α is the nadir angle.

With given length of the base line, azimuth, and geographical coordinates for the PP which were obtained by measuring the position of the optical axis with respect to the main vertical, it is possible to determine from a spherical triangle the pole (SSP—PP) given in Figure 3.7:

$$\begin{aligned} \operatorname{hav}\theta &= \operatorname{hav}[(90-\varphi_{PP})-(90-\varphi_{SSP})]+ \\ &+\sin(90-\varphi_{PP})\sin(90-\varphi_{SSP})\operatorname{hav}\Delta\lambda, \\ \theta &= \arccos(1-2\operatorname{hav}\theta), \\ \operatorname{hav}A &= \frac{\operatorname{hav}(90-\varphi_{PP})-\sin[(90-\varphi_{SSP})-\theta]}{\sin(90-\varphi_{SSP})\sin\theta}, \end{aligned} \tag{3.9}$$

$$A = \arccos(1-2\operatorname{hav}A). \tag{3.10}$$

Here, φ_{PP} is the latitude of the principal point; φ_{SSP} the latitude of the SSP, A is the azimuth and θ is the angular distance of the principal (base) line.

Knowing angle θ and satellite altitude (Figure 3.8), we can compute the nadir angle, and with relationship (3.10) the azimuth A. The angles $\Delta\alpha$ and $\Delta\beta^*$ are computed by using the above formulas for the lens distortion. These data are sufficient for the determination of the geographical coordinates of each point.

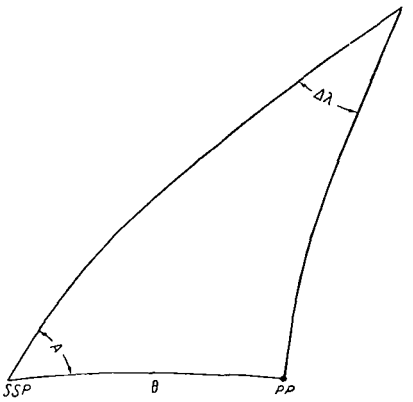

FIGURE 3.7. Spherical triangle for calculating the angles θ and A, and point coordinates

The line parallel to the optical axis, passing through the Earth center (Figure 3.9), intersects the Earth surface at point SAP [Satellite Azimuth Point] and lies on the base line that connects the SSP and the PP; then $\alpha = 0$, $A = A' - 180$ (Figure 3.9). The angles that determine the position of the satellite and its orientation in space are assumed to be known.

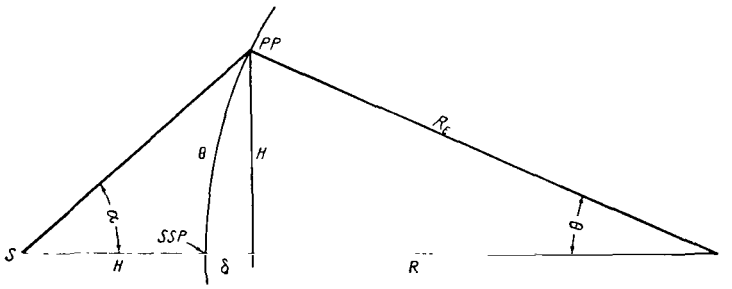

FIGURE 3.8. Relationship between nadir angle α and angle θ.

The nadir angle α is then determined using angle 0 and the satellite height (Figure 3.10). Since the segment N in Figure 3.10 is the perpendicular dropped from the PP onto the main vertical, we have

$$\begin{aligned} N &= R_E \sin 0, \\ \delta &= R_E - R = R_E(1 - \cos 0), \\ \alpha &= \operatorname{arc\,tg} \frac{R_E \sin 0}{H + R_E(1 - \cos 0)}. \end{aligned} \tag{3.11}$$

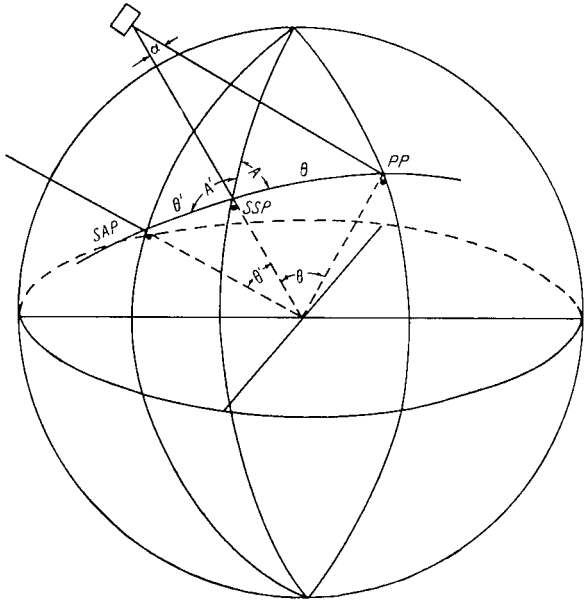

FIGURE 3.9. Determination of the *SAP*

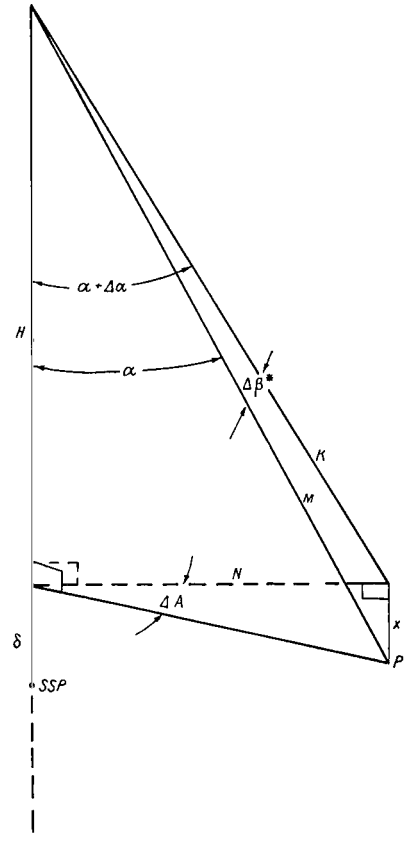

FIGURE 3.10. Diagram for determining the angle increments ΔA and $\Delta\beta$

Here, R_E is the Earth radius and R is the distance from the Earth center to the point of intersection of the perpendicular dropped from the PP onto the main vertical; δ is the distance between this point and the SSP (see Figures 3.6 and 3.8).

For the determination of the geographical coordinates of points we draw a plane normal to the main vertical and tangent to the Earth surface at the SSP. This plane moves parallel to itself until the point for which the calculations are made does not fall on it any more. The angles α, $\Delta\alpha$ and $\Delta\beta^*$ serve for calculating the angles ΔA and α^* (Figure 3.10), which determine the increment of the coordinates when passing from the principal point to point P* (see Figures 3.6 and 3.10).

As is seen from Figure 3.10, the increment of the azimuth of any point with respect to the PP is given by the following expression:

$$\operatorname{tg}\Delta A = \frac{x}{N} = \frac{x}{K}\frac{K}{N}.$$

But

$$\frac{N}{K} = \sin(\alpha + \Delta\alpha), \text{ and } \frac{x}{K} = \operatorname{tg}\Delta\beta^*,$$

hence

$$\Delta A = \operatorname{arc\,tg}\frac{\operatorname{tg}\Delta\beta^*}{\sin(\alpha + \Delta\alpha)}. \tag{3.12}$$

The total azimuth of point P*, for which calculation is made, is obviously equal to the azimuth of the base line (line SSP—PP) plus ΔA (see Figure 3.6), i.e.,

$$A^* = A + \Delta A.$$

The angles α, $\Delta\alpha$ and $\Delta\beta^*$ are then used for calculating the nadir angle α^* of the given point P* according to the formula

$$\cos\alpha^* = \frac{H}{M} = \frac{H}{K}\frac{K}{M},$$

whence

$$\alpha^* = \operatorname{arc\,cos}[\cos(\alpha + \Delta\alpha)\cos\Delta\beta^*]. \tag{3.13}$$

Equation (3.11) can be used for calculations at any point. When α^* is known the equation can be solved for θ^*, i.e.,

$$\operatorname{tg}\alpha^* = \frac{R_E \sin\theta^*}{H + R_E(1 - \cos\theta^*)},$$

$$\operatorname{tg}\alpha^*\cos\theta^* + \sin\theta^* = \frac{H + R_E}{R_E}\operatorname{tg}\alpha^*.$$

Multiplying both parts of the latter equation by $\cos\alpha^* = \frac{\sin\alpha^*}{\operatorname{tg}\alpha^*}$, we have

$$\sin\alpha^*\cos\theta^* + \cos\alpha^*\sin\theta^* = \frac{H + R_E}{R_E}\sin\alpha^*$$

or

$$\sin(\alpha^* + \theta^*) = \frac{H + R_E}{R_E} \sin\alpha^*,$$

whence

$$\theta^* = \arcsin\left(\frac{H + R_E}{R_E} \sin\alpha^*\right) - \alpha^*. \tag{3.14}$$

If θ^* and A^* are given, the equations for the spherical triangle which are equivalent to equations (3.9) and (3.10) are used for calculating the longitude and latitude lines that pass through the required point P*. Finally, we find the working formula for computation as follows:

$$\begin{aligned} \operatorname{hav}(90 - \varphi_{P^*}) &= \operatorname{hav}[\theta^* - (90 - \varphi_{SSP})] + \\ &+ \sin\theta^* - \sin(90 - \varphi_{SSP}) \operatorname{hav} A^*, \\ \varphi_{P^*} &= 90 - \arccos[1 - 2\operatorname{hav}(90 - \varphi_{P^*})], \end{aligned} \tag{3.15}$$

$$\begin{aligned} \operatorname{hav}\Delta\lambda_{P^*} &= \frac{\operatorname{hav}\theta^* - \operatorname{hav}[(90 - \varphi_{SSP}) - (90 - \varphi_{P^*})]}{\sin(90 - \varphi_{SSP})\sin(90 - \varphi_{P^*})}, \\ \lambda_{P^*} &= \lambda_{SSP} - \arccos(1 - 2\operatorname{hav}\Delta\lambda_{P^*}). \end{aligned} \tag{3.16}$$

All these calculations are made for those points which lie on the Earth surface, i. e., for nadir angles not exceeding some critical value α_{cr} above which the optical axis points to space, i. e., for

$$\alpha_{cr} = \arcsin\left(\frac{R_E}{H + R_E}\right) \geqslant \alpha^*.$$

For $\alpha^* \geqslant \alpha_{cr}$ the coordinates are not calculated.

When $\alpha^* = \alpha_{cr}$ and $\Delta\beta^*$ are known one can determine $\Delta\alpha_{cr}$. Using (3.13) we have

$$\Delta\alpha_{cr} = \arccos\left(\frac{\cos\alpha_{cr}}{\cos\Delta\beta^*}\right) - \alpha.$$

Equation (3.8) is used for computing $\Delta\beta_{cr}$:

$$\Delta\beta_{cr} = \operatorname{arc\,tg}\left(\frac{\operatorname{tg}\Delta\beta^*}{\cos\Delta\alpha_{cr}}\right).$$

These angles on the true picture are transformed into the corresponding angles on the video camera of the satellite, using formulas (3.1) to (3.4).

The above-described algorithm was programmed for the IBM-709 and IBM-704 computers. The processing time for one photograph was 10 seconds. For the IBM-709 computer a supplementary input-output program was used.

The use of mechanical printing devices permits the printing of longitude and latitude lines on special paper. An example of such a printout is given

in Figures 3.11 and 3.12. The principle of fixing the points lying on these lines is accomplished by a program described as follows. The points lying on the first interval between two meridians or latitudes are given some figure or letter index, e.g., 1. The points belonging to the second interval have no index. The points belonging to the next interval are given the index 2. This is followed by an interval without index. Next follow the points with index 3, etc. Then, as a result of printing the data, the chart consists of full number strips and empty spaces. The limits between these strips are isolines of meridians (or latitudes). In addition, the corresponding latitude (or longitude) values are printed out at the nodal points of the right-angle grid. This system of graphical representation of information is often used in the automatic processing of meteorological, aerological /3, 16/, and radiation data from satellites /3, 23, 26/.

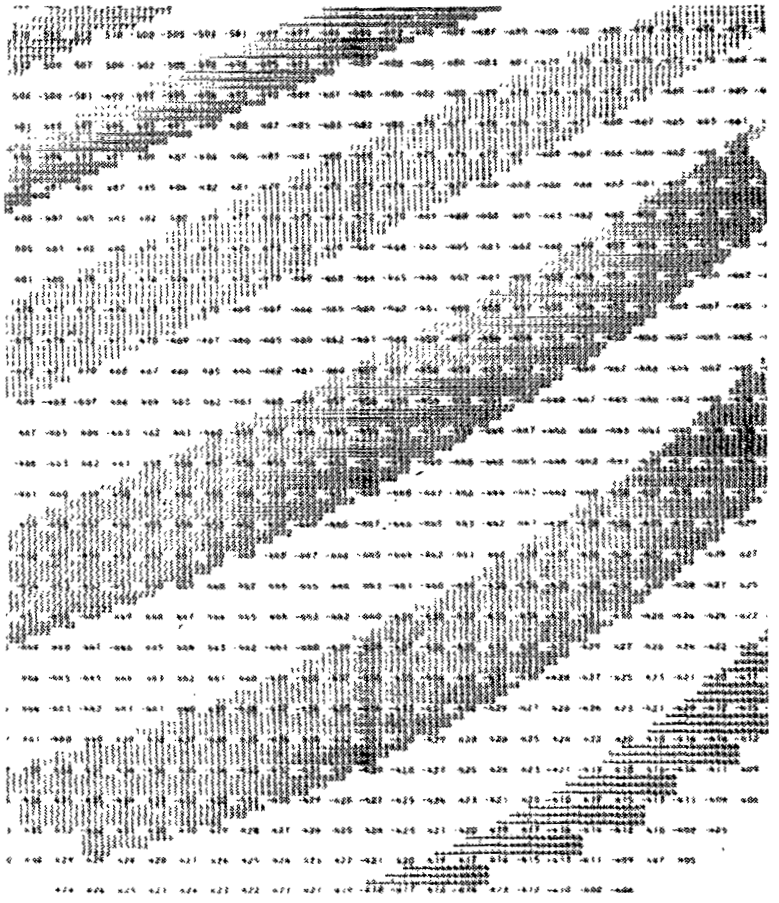

FIGURE 3.11. Example of a latitude-grid printout:

The latitudes are printed out at the nodal points. The limits of the full printed number strips and of the empty spaces represent latitude lines, taking into account perspective distortion.

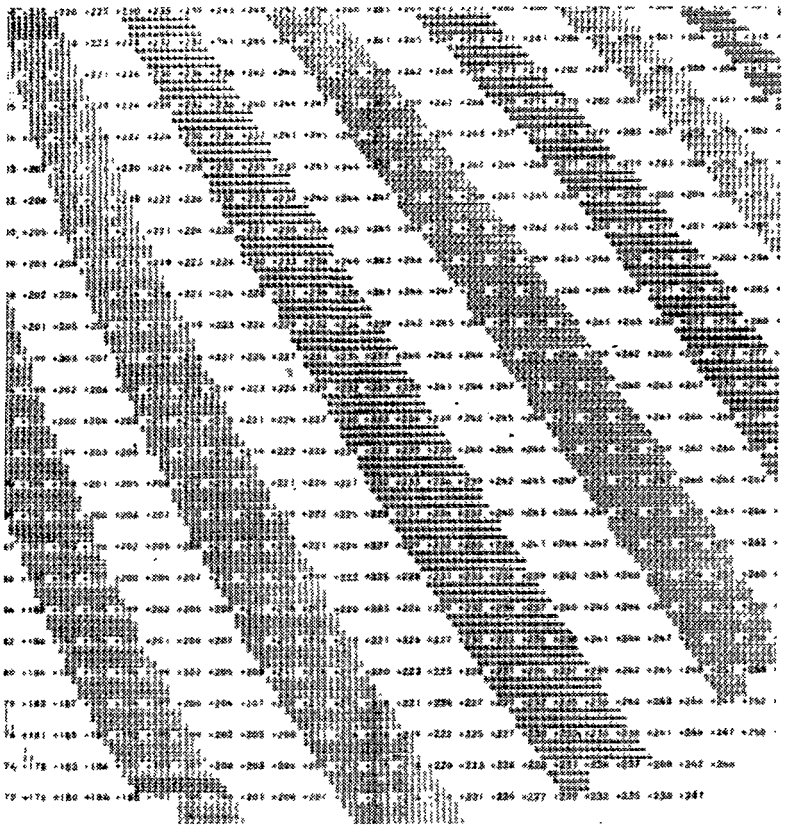

FIGURE 3.12. Example of a longitude-grid printout. The principle is the same as in Figure 3.11

2. Program for determining the x, y coordinates for the video camera at given latitude and longitude lines. In the above-described program the isolines for latitude and longitude are obtained by interpolation between points with given x, y coordinates used for the computation of the geographical coordinates. In general, these do not coincide with the lines $\varphi = \text{const}$ and $\lambda = \text{const}$. Therefore, a second program is prepared, so as to compute the x, y coordinates for the intersection points of latitude and longitude circles that are multiples of a whole number, i.e., according to given criteria $\varphi = \text{const}$ and $\lambda = \text{const}$, the x, y coordinates are computed for the video camera.

The program is prepared so that along the fixed latitude the increments of longitude are calculated; then a new latitude is taken, and again longitude increments are calculated. The operation is repeated until we obtain a grid that covers the entire viewing field.

In order to avoid an excessive crowding of points when approaching the horizon, a special "horizon program" is introduced which should not exceed 95% α_{cr}. In this strip with $0.95\ \alpha_{cr} < \alpha < \alpha_{cr}$ the grid points are not calculated so as to avoid an unwieldy picture, but the position of the horizon

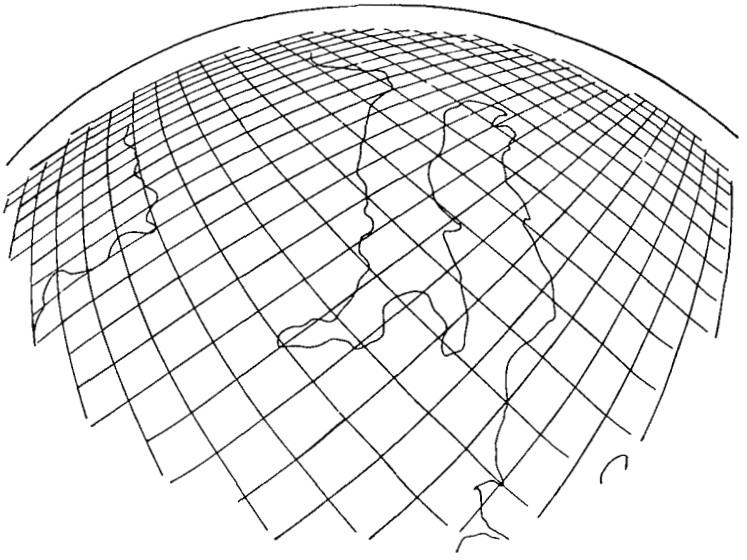

FIGURE 3.13

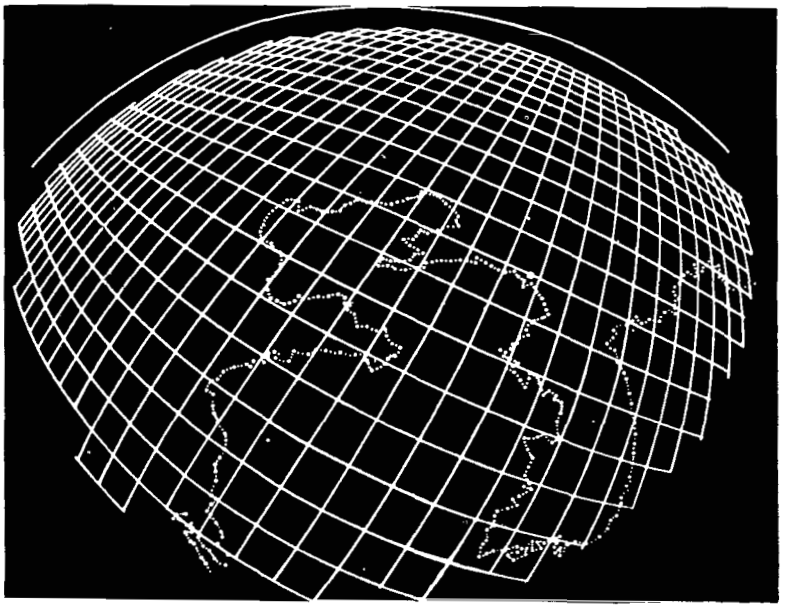

FIGURE 3.14

line is computed. After the geographical grid is determined, it is projected onto the picture plane, applying at the same time a correction for symmetric distortion, and, if necessary, also for asymmetric distortion.

For the solution of the inverse problem, i.e., for the calculation of x and y in a right-angle coordinate system of the photograph with the aid of geographical coordinates, the already mentioned formulas are used, but in a reverse order, i.e., according to given λ^* and φ^* the angles A^*, θ^* and α^* are calculated, with allowance for lens distortion. While processing program tables are included, giving the geographical coordinates of characteristic points of the coastline which fall into the surveyed region, or the whole coastline. In this case, the points of the coastlines are recalculated by the same method as the x, y coordinates of the picture. Further, the geographical grid as well as the coastline can be plotted by a special two-coordinate electronic plotter (for details see Figure 3.13); these parameters can be computed not only with the above plotter (described in /1, 6/), but they may also be reproduced on the screen of a cathode-ray tube and then photographed. An example of such a picture is given in Figure 3.14.

The mechanical tracing of grids and coastlines with a plotter takes about 12—15 seconds per picture. If the picture is projected onto a cathode-ray-tube screen it requires 8—10 seconds.

There are some alternations to the above-mentioned two programs. One of these alternatives provides for the output of geographical grids and coastlines on punchcards. The latter are introduced into the automatic plotter or into the device for data output on the picture tube screen, that operates independently of the electronic computer.

TABLE 3.1. Sequence of data printout on punchcards

Number of column	Content of punched information
1—4	Height of satellite in km and tenths of km (e.g., 712.4 km ~ 7,124)
5—8	Latitude of the SSP in whole and tenths of a degree, and ± sign. Latitude north is positive and south negative (e.g., 2.5°N is + 025; 60.3°S is -603)
9—13	Longitude of the SSP in whole and tenths of a degree measured eastward from zero to 359.9°, or the longitude of the SSP + 180° (e.g., 5.3°E is coded +0053; 73.6°W is coded 0736 or +2864 (360° — 73.6° = 286.4°))
14—17 18—22	Latitude or nadir angle Longitude or azimuth } depending on the code perforated in column 23
23	Code number that defines the data perforated in columns 14—22 0 — latitude and longitude of the PP 1 — nadir angle and azimuth of the PP 2 — latitude and longitude of the SAP (Figure 3.9), i.e., the intersection points of a line that is parallel to the optical axis and passes through the center of the Earth, with the Earth surface. Latitude and longitude are punched in the same way as in columns 5—13. The nadir angle is positive, when reading from the SSP to the PP
24	Sequential number of data transmission
25—29	Frame number
30	Number of receiving station 1 — Fort Mugu; 2 — Wallops Island
31	Method of readout 1 — direct; 2 — magnetic tape
32	Camera number

The geographical grid and the coastline may also be reproduced on special paper or on plastic translucent sheets. The transfer of one drawing onto the special paper takes 20—30 min. This method was used to obtain about 2,000 grids from the TIROS I photographs for the file and for research work. It was also used for filing 8,000 grids of TIROS III.

With small changes in program it is possible, if necessary, to obtain on the output of the high-speed C-4020 machine microfilms of the grid which can then be reproduced in less than one second. Special program alternatives were also used for the correlation of photographs from other satellites of the TIROS family and from NIMBUS.

All the programs are recorded on punchcards, and after being fed into an electronic computer, they are printed out on magnetic tape. Further on, the corresponding punchcards are fed into the computer. A model of these cards is presented in Table 3.1. Finally, the appropriate processing program is applied.

This method of geographical correlation is used at large meteorological centers where a large body of data is received. Below we shall discuss methods of correlation for data obtained with the APT system, which are simpler and more convenient for work at any center.

3.2. GEOGRAPHICAL ORIENTATION OF APT DATA

The use of satellite observational data in routine meteorological work is particularly convenient and important for satellites with automatic picture transmission (APT) directly over the regions viewed by the satellite. Thus, in agreement with the U.S.A., the meteorological weather service of Canada, from November 1961, used the APT system in ice surveys and for routine meteorological work. The ground-based equipment for such a system comprises: tracking facilities (for target homing) with electric drive, antenna control, telemetering receiver, tape recorder, and a high-resolution kinescope connected to a Polaroid camera for photographic recording of TV pictures. Antenna directivity is 10 dB (right-hand circular polarization of the antenna corresponding to an artificial-satellite signal of 136.95 MHz). The antenna ensures step-by-step satellite tracking with one-minute intervals, during which the antenna is displaced through the given observation angle.

The picture signals recorded on the magnetic tape (made of Mylar fiber) at a rate of 38 cm/sec are fed to a two-channel tape recorder; they ensure acoustic checking during the reproduction of recorded signals. Reproduction of the image is based on the television principle and is performed with the aid of a 1,000-line cathode-ray tube. From the tube screen the picture is then recorded on either a reversal or a negative (conventional) film.

In Canada, automatic reception of pictures from TIROS VIII was achieved for the first time on 21 December 1963. The picture quality was excellent.

During April 1964 the equipment was redesigned and provided with special facilities for receiving pictures from the Arctic Zone. From 28 August until the day signal transmission was discontinued (23 September 1964) the meteorological stations in Ottawa and then on Baffin Island

regularly received pictures from the NIMBUS satellite. The experiment showed the high quality of the equipment permitting reception of reliable data from photographs of landscapes, cloud, ice, and other geometeorological fields.

Similar systems were created in numerous countries.* The use of APT systems will no doubt have a favorable effect on the routine processing of satellite data.

In mass interpretation of satellite data, geographical orientation of pictures and grid plotting (gridding) can only be performed using electronic computers. At the APT data-acquisition centers the position is quite different since in this case, the satellite views constantly one and the same area or at least a region of limited area. Therefore, picture orientation and rectification may be performed from a set of maps that allow for these distortions.

However, perspective distortion is not the single factor leading to errors. Other factors should also be taken into consideration so as to ensure correct location of given meteorological and geometeorological phenomena observed from the satellite.

For future satellite launchings it is intended to transmit via the APT system not only the results of TV tracking of the cloud cover but also data on outgoing radiation /25, 26/. For the superimposition of the coordinate grid on the picture received at the APT station, it is necessary to know the space location of the satellite, its coordinates, and the exact time at which the photographs have been taken.

Latitude and longitude of the sub-satellite point (SSP), as well as satellite height given as a function of time for their recording on the coordinate grid, may generally be determined with sufficient reliability. However, data on space location of the satellite [camera], e.g., the angle of picture inclination [with respect to the optical axis of the camera], azimuth of the principal vertical α^{PL}, and time of photography may often contain errors that, in view of the high translational speed of the satellite, might affect the accuracy of the coordinate-plotting grid and hence the reliability of picture orientation. To allow for such distortions, it is advisable to use data on the position of ground-based landmarks clearly visible on the pictures. In this case, coordination and orientation errors may be found by comparing the position of these landmarks with respect to the coordination grid and by allowing for their exact geographical coordinates. If the coordinates of the landmarks are distorted on two or more pictures such regular distortions may easily be detected at the APT reception station and suitably eliminated. The operator at the APT station should study for each particular instance and region the nature of these errors, and after establishing their cause he should present suggestions for their elimination.

The most accurate method for determining and correcting errors of the coordinate grid, applied on the picture, consists in using the above-mentioned ground landmarks; the coordinates of such landmarks can be taken from geographical maps. Photograph 3.1 presents a photograph taken from TIROS VII showing the raised coastline, while the letters *A*, *B*, *C*, *D*, *E*, *F*, *G*, *H*, *I* and *J* designate the particular landmarks on the picture. Figure 3.15 represents the corresponding section of the map in the conventional Mercator projection, with the meridians and parallels drawn at 1° spacings

* In 1966 more than 150 centers in various countries, mostly located in the U.S.A., are using the APT system.

corresponding to these points; the coordinates of the points should be known or else they may be taken from the map. The corresponding coordinate grid (cf. Figure 3.16) is then plotted with due allowance for the nadir angle and the inevitable perspective distortion. The grid is superimposed on the photograph which then takes its final shape as shown in Photograph 3.2. Points *A* through *J* are transferred on Photograph 3.2 either from Figure 3.15 or from a relevant handbook.

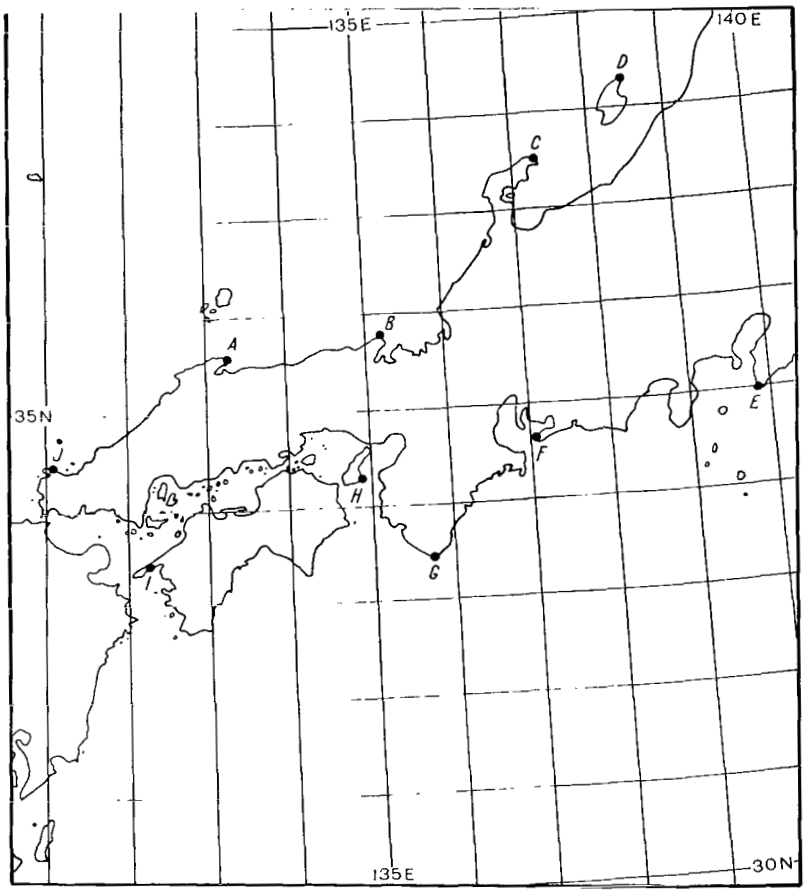

FIGURE 3.15. Same locality as shown in Photograph 3.1; region drawn in Mercator projection

Vectorial errors for each point are determined by comparing the transferred points with the points on the photograph, i. e., by comparing Photographs 3.1 and 3.2. In the case considered, these errors are insignificant. However, in practice, vectorial errors may reach large values, and then the points applied on Photograph 3.2 might not coincide

with their actual geographical position. It is then necessary to analyze the cause of the errors and to eliminate them.

We shall now analyze these additional errors, which in the final run tend to totalize. They may be classified into three types:

a) errors due to inaccurate determination of the time of photography;

b) errors due to inexact determination of the picture-inclination angle;

c) errors due to inexact determination of the azimuth.

Errors of type (a) are apt to cause vectorial errors oriented along the satellite trajectory. Photograph 3.3 is basically the same as Photograph 3.1, but with the time of photography shifted by 15 seconds (i. e., instead of 05 hr 25.50 min local time, the time is 05 hr 25.75 min local time); this in turn caused changes in latitude φ_{SSP} and longitude λ_{SSP}.

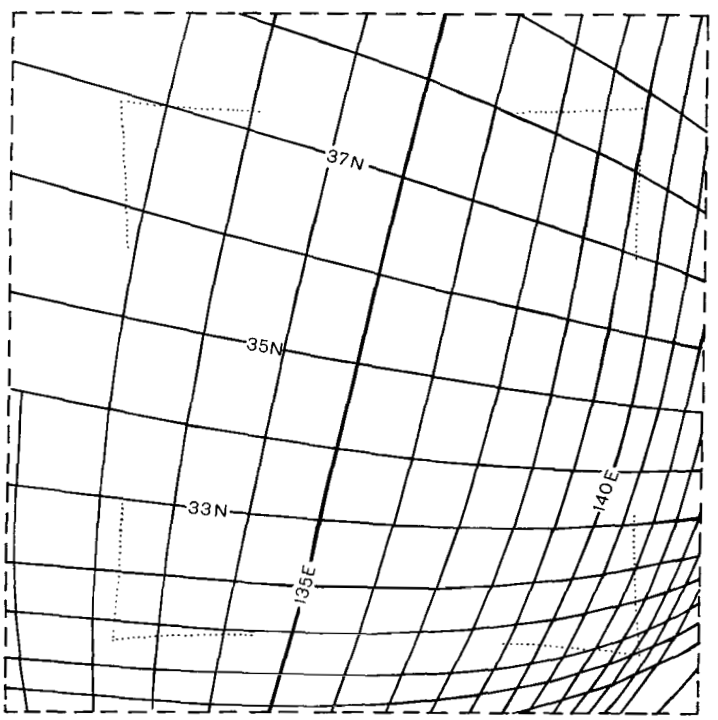

FIGURE 3.16. Prespective grid for given satellite parameters and given position of the TV camera. For input parameters see Photograph 3.1.

Figure 3.17 shows the trajectory of both the SSP and PP. Arrows indicate the calculated vectorial errors (the vector length corresponds to the scale distortion of the map). As is easily seen, these vectorial errors, oriented toward NE, coincide in direction with the trajectory of the SSP. Errors shown in Figure 3.17 were determined by superimposing a correct grid (Figure 3.16) on a grid plotted by using an incorrect photography time (Photograph 3.3). The vectorial errors are plotted for the nodal points of latitude and longitude intersection.

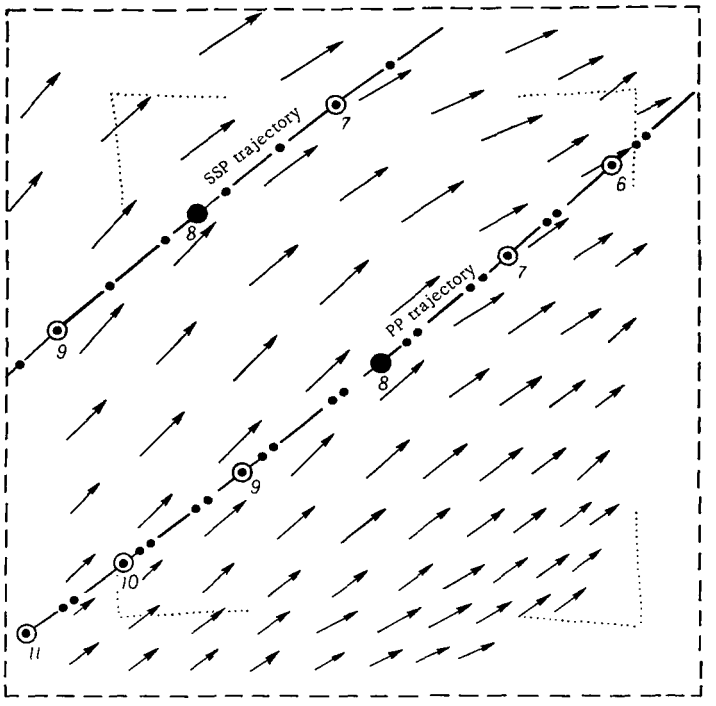

FIGURE 3.17. Field of vectorial errors caused by inexact determination of the time of photography. The actual time was 05 hr 25.5 min, while the time used in calculations was 05 hr 25.75 min.

Under actual conditions, these displacements may be determined not from the displacement of the points of intersection between the meridians and parallels, but from the displacement of the position of the ground landmarks. To correct the whole grid, we must perform either interpolation or extrapolation between the selected landmarks.

Let us now deal with errors of type (b). Photograph 3.4 shows the same perspective grid as above (Figure 3.16), but except that the angle of picture inclination has been changed by 5° (i. e., instead of $\tau = 23.8°$, $\tau = 18.8°$). Superimposing a correct perspective grid on the distorted grid (Photograph 3.4) we obtain, because of picture inclination, a field of vectorial errors resulting from inaccurate determination of the inclination angle. This field is shown in Figure 3.18. Vectorial errors of this kind are oriented almost normally to the trajectory of the SSP. As in the first case, these vectors under actual conditions are plotted from the distortion of landmark position and are then interpolated or extrapolated.

Errors of type (c) are caused by two factors. The first of them is the result of errors in determining the coordinates of the SSP, i. e., the point of intersection of the main vertical with the Earth surface (point SSP in Figure 3.8). This type of error may be quickly found if the nadir angle is such as to permit the horizon line to be seen on the picture. If the line

cannot be seen, this error is determined by comparing the correct geographical grid with the grid distorted as a result of this error (see above).

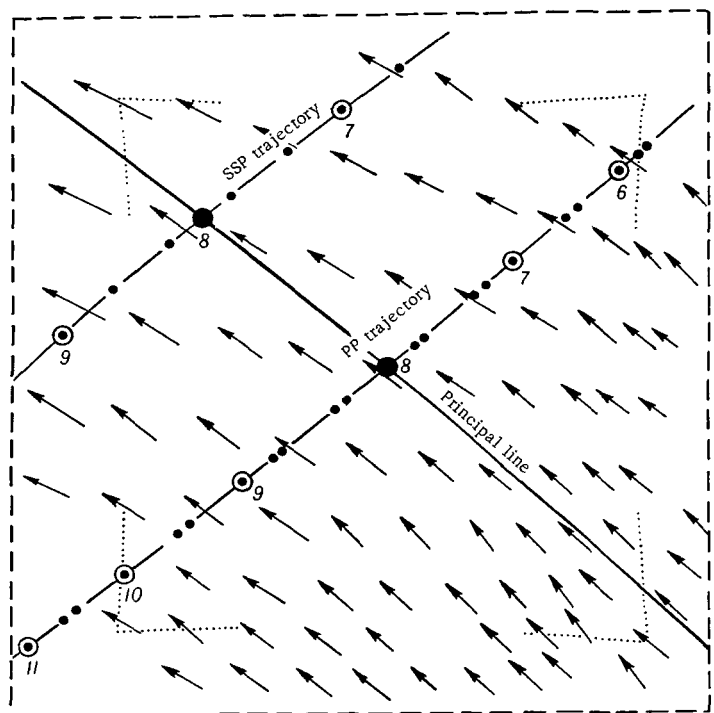

FIGURE 3.18. Field of vectorial errors caused by inexact determination of the picture-inclination angle:

$\tau_{true} = 23.8°$; $\tau_{used} = 18.8°$.

Photograph 3.5 presents the geographical grid calculated with such an error in determining the coordinates of the SSP that would cause an error of 10° in the determination of the azimuth. The field of vectorial errors for this case is shown in Figure 3.19. As may be seen, the vectorial errors rotate about point PP.

The other factor that causes errors of type (c) is connected with the case when the coordinates of the points of intersection of the main vertical with the Earth surface (SSP) are determined correctly, but the azimuth is determined inaccurately. Photograph 3.6 shows such a grid, while the corresponding field of vectorial errors is presented in Figure 3.20. As before, the magnitude of these errors tends to increase toward the edges of the picture, but symmetry is noticed around the SSP.

Figure 3.21a shows the perspective grid. Figure 3.21b presents the field of vectorial errors due to inexact determination of time of photography

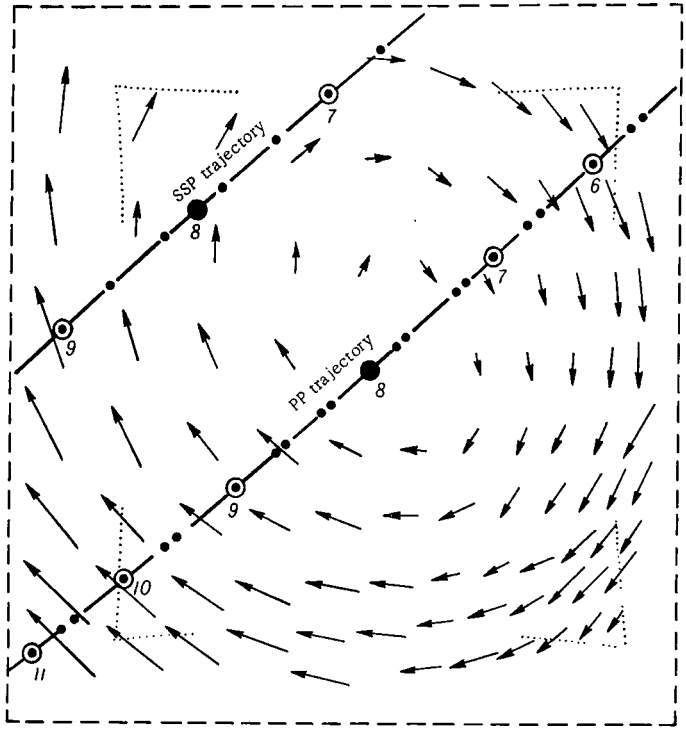

FIGURE 3.19. Field of vectorial errors caused by inexact determination of the azimuth:

A_{true} = 117°; A_{used} = 127°.

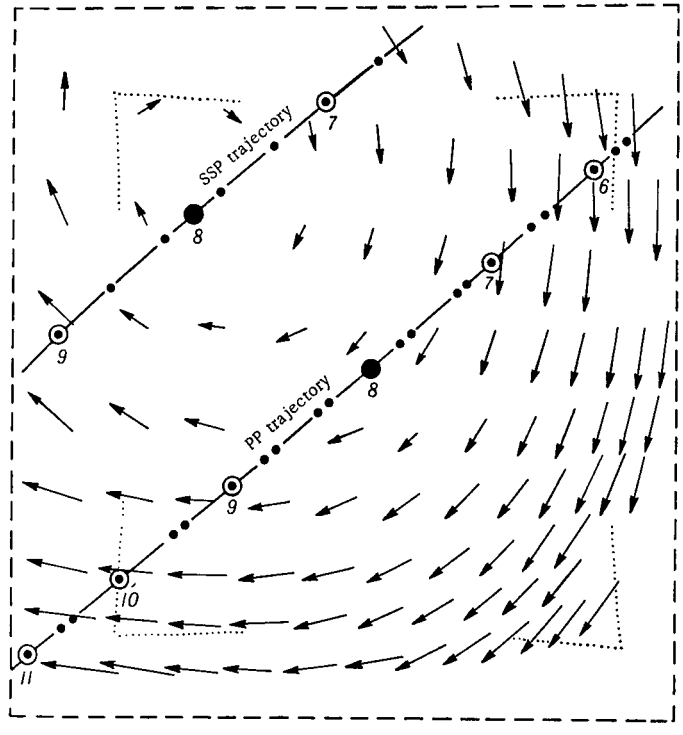

FIGURE 3.20. Field of vectorial errors caused by inaccurate determination of of the azimuth while calculating the SSP coordinates:

A_{true} = 117°; A_{used} = 127°.

(difference of 15 seconds). Figure 3.21c shows the field of vectorial errors due to an error of 5° in determining the picture-inclination angle; in the same figure, the dotted line shows the horizon line calculated for this case. Figure 3.21d shows the field of vectorial errors caused by errors in determining the azimuth. It is easily seen that if the error depends either on the error in determining the photography time or on the error in determining the SSP coordinates and hence the azimuth, both the calculated and actually observed horizon lines will coincide. However, these lines do not coincide if the vectorial errors are caused by errors in determining the picture-inclination angle or by errors in determining the SSP coordinates. For such errors the position of the horizon line may be used in determining the corrections for the geographical grid.

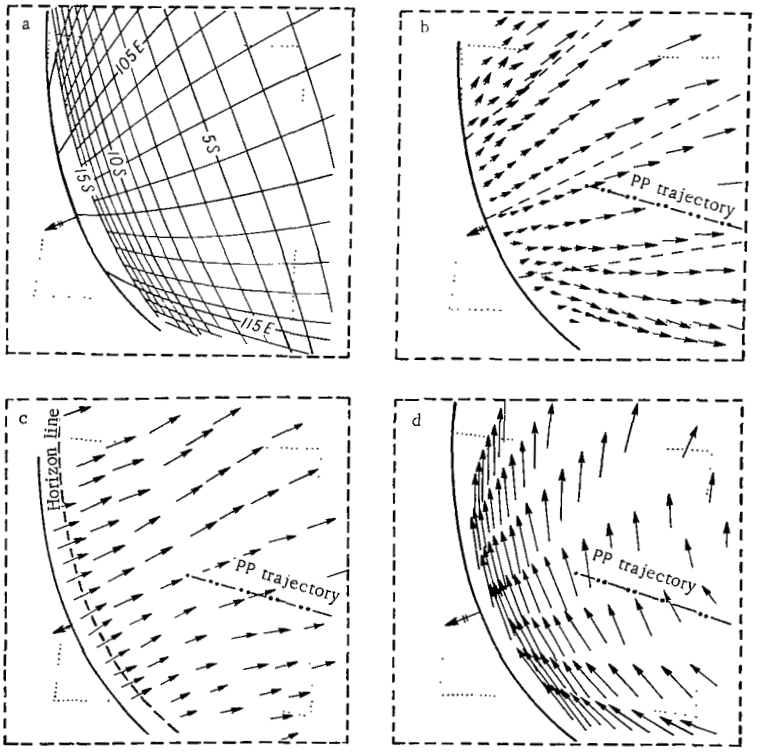

FIGURE 3.21. Field of vectorial errors near the horizon line:

a — graticule with horizon line: time of photography 0.5 hr 13.5 min; $\tau = 44.0°$, $A^{PL} = 117.0°$, $H = 631$ km, $\varphi_{SSP}=0.7°S, \lambda_{SSP} = 108.6°E$; b — field of vectorial errors due to inexact determination of photography time: true time 05 hr 13.5 min, time used 05 hr 13.75 min; c — field of vertical errors due to an error of 5° in determining the picture-inclination angle: $\tau_{true} = 44.0°$, $\tau_{used} = 39.0°$; d — field of vectorial errors caused by errors in determining the azimuth: $A^{PL}_{true} = 177°$, $A^{PL}_{used} = 187°$.

The above method for determining the error vector may be used for any satellite picture with a superimposed grid and with easily discernible landmarks, provided a sufficiently large number of such landmarks is available.

The next step involves the determination of factors causing the above errors. For this purpose, the calculated error field is compared with the actually obtained field, by successively including the errors in the time of photography, picture-angle inclination, and azimuth. Once the causes of these errors are determined, it is usually possible to introduce the corresponding corrections in the geographical grid.*

EXERCISE

Evaluation of distortions in the geographical orientation of APT pictures, and determination of fields of vectorial errors

1. Errors in determining the point coordinates caused by inaccurate determination of the time of photography.

Copy Figure 3.16 on tracing paper. Superimpose this copy on Photograph 3.3. Place a piece of tracing paper over the copy. At each point of intersection of latitudes and longitudes on Photograph 3.3, determine the error vector equal to the difference in the position of intersection points between Photograph 3.3 and Figure 3.16; transfer this vector to the tracing paper. Compare the field of vectorial errors thus obtained with the field of vectorial errors in Figure 3.17. Estimate the magnitude of the errors for points A through J.

2. Errors in determining the point coordinates caused by errors in determining the picture-inclination angle.

Apply the tracing-paper copy of Figure 3.16 on Photograph 3.4. Plot the error vector at each point of intersection of latitudes and longitudes and transfer the vector on a sheet of tracing paper. Compare the field of vectorial errors with Figure 3.18. Estimate their magnitude for points A through J.

3. Errors in determining the point coordinates caused by errors in determining the azimuth.

a) The error in determining the azimuth depends on the error in determining the SSP coordinates.

Superimpose a copy of Figure 3.16 on Photograph 3.5. Place on the copy another sheet of tracing paper, and transfer the error vectors for each intersection point from Photograph 3.5 to this sheet. Compare the field of vectorial errors thus obtained with Figure 3.19. Estimate the magnitude and nature of the errors for points A through J.

b) The error in determining the azimuth caused by other factors. Put the copy of Figure 3.16 on a sheet of tracing paper and place it on Photograph 3.6. As above, estimate the field of vectorial errors for points A through J and compare it with Figure 3.20.

* With the ESSA 2 and NIMBUS 2 satellites photography was performed for zero nadir angles. As a result the effect of perspective distortion is less marked.

3.3. INTERPRETATION OF NEPHANALYSIS DATA

In the U.S.A., the data obtained from meteorological satellites are transmitted through adequate communication lines in the form of two reports /25/:

1. auxiliary reports with data on regions which in the next few days are intended for satellite observation coverage;

2. reports containing the results of nephanalysis of pictures taken from satellites, i.e., a schematic presentation of the results of picture decoding and interpretation.

These reports are subdivided into two kinds: principal and auxiliary. In the following we shall deal with the coding system used for transmitting these reports.

Code used for the transmission of auxiliary reports

TB US KWBC N — distinctive group, group of date and time, TIROS alert—auxiliary report.

Part I. Preliminary data for the next 24—48 hours:

$$n_0n_0n_0n_0 \quad YYGGgg$$
$$QL_aL_aL_0L_0 \quad QL_aL_aL_0L_0 \ldots$$

etc. (the daily transmission program may not include more than nine satellite orbits).

Part II. Preliminary data on the regions covered by satellite observations on the next seven days:

$$YY \quad QL_aL_aL_0L_0 \quad QL_aL_aL_0L_0 \ldots$$
$$YY \quad QL_aL_aL_0L_0 \quad QL_aL_aL_0L_0 \ldots$$
$$YY \quad QL_aL_aL_0L_0 \quad QL_aL_aL_0L_0 \ldots$$

(The bulletins transmitted every Monday, Wednesday, and Friday indicate three regions.)

Designations (Symbols)

TB — reads "Bulletin for TIROS satellite".
US — geographical index (U.S.A.) (this group may not be transmitted).
KWBC — international code for the Central Station of Communications of the U.S. Weather Bureau in Washington.
N — code of the international communication line
TIROS — name of satellite.
alert — the word shows the type of report (in this case, the auxiliary report).

Part I.

$n_on_on_on_o$ — current number of orbit for the given satellite.
YY — day of month
GGgg — time (hours and minutes GMT) at which the PP of the satellite is over the region to be photographed.
Q — octant of the globe (code BMO 3300) which is presented in the following table:

Northern Hemisphere		Southern Hemisphere	
code number	longitude	code number	longitude
0	0–90°W	5	0–90°W
1	90–180°W	6	90–180° W
2	180–90°E	7	180–90° E
3	90–0°E	8	90–0°E

L_aL_a — latitude in degrees of the PP of the picture.
L_oL_o — longitude in degrees of the same point (if the longitude is larger than 100°, the telegram should indicate additionally: longitude minus 100°).

Part II.

YY — day of month GMT.
Q — octant of the globe (code BMO 3300).
L_aL_a — latitude in degrees of the region to be shown on the picture.
L_oL_o — longitude in degrees.

To avoid errors that might arise if the region is located in two or more octants of the globe, the coordinates are given at first for the NE corner of the region and then for the other corners in a clockwise direction. In this way each region is assigned several series like $QL_aL_aL_oL_o$.

Example of notation:

TB KWBC N 12190
TIROS alert

Part I

0032	141 010	33 703	33 625	33 547
0033	141 130	03 305	33 709	33 323
0034	141 310	02 811	02 901	33 009
0035	141 450	02 316	02 309	02 302
0036	141 630	01 821	01 815	01 809
0037	141 810	01 325	01 221	01 117
0038	141 950	00 729	00 625	00 521
0039	142 110	00 234	00 031	50 228

Part II

21	14 040	12 136	22 660	10 280
22	13 165	11 361	11 075	70 975
23	22 270	20 274	20 170	71 950

The first part contains data on the geographical coordinates of three points for each of the 8 orbits on the 14th day of the month.

Part II presents the coordinates of the regions covered by the satellite every 21st, 22nd, and 23rd day of the given month.

Coding of nephanalysis data

These data are transmitted via communication lines every three hours. After the pictures transmitted by the satellite have been analyzed separately, these data only contain three basic characteristics of cloudiness observed from the satellite: observed number of clouds, their shape, and some additional features. These three possible combinations are assigned a given letter. The code for the data transmitted by TIROS III and TIROS IV has been described in detail elsewhere /1.2/. At present, for the recent series of TIROS satellites, some changes have been introduced. In this connection we shall examine the new coding system that takes these changes into account.

Code used for transmitting nephanalysis data

Title — Auxx KWBC N YYGGgg.
Subtitle — nepan TIROS $n_t n_o n_o n_o n_o$ YYGGgg CN
Key for analysis — $AAC_aC_tC_d$ BBC_a $C_tC_dCCC_aC_tC_d$.
Analysis — $QL_aL_aL_oL_o$ ZZZZZ etc.

1. Title

Auxx — distinctive group
KWBC N and YYGGgg — the same as for the auxiliary part.

2. Subtitle

nepan — conventional word for nephanalysis.
n_t — number of satellite of given series (e.g., TIROS IV, TIROS V, etc.).
$n_o n_o n_o n_o$ — current number of orbit.
YY — day of month in which pictures were taken.
GGgg — time (in hours and minutes GMT) at which the satellite PP passed over the given area.
CN — group, showing the quality of geographical orientation; here C is the distinctive letter and N is the estimate of picture-orientation quality.

Orientation quality is estimated using the following scale:
N = 1 — excellent.
N = 2 — good.
N = 3 — average.
N = 4 — poor (as a rule, no report is transmitted with this rating).

When for any reason no nephanalysis is available, the word "none" is entered.

3. Key for analysis

The group of type $AAC_aC_tC_d$, $BBC_aC_tC_d$, $CCC_aC_tC_d$ etc. has the following significance. The letters A, B, C, etc. show the combination of characteristics to be analyzed, as described by the corresponding letters $C_aC_tC_d$. For greater reliability, the letters A, B, C, etc. are repeated (doubled).

The number, shape, and characteristics of clouds are usually coded with the following letters: A, B, C, D, F, G, J, K, L, M, N, V, Z, Q, W, E, R, T, Y, U, P, S, H in this sequence. Decoding is described below.

The whole region covered by the satellite is divided into squares, the sizes of which correspond to one degree latitude and one degree longitude. Each square is assigned a special symbol (letter) that defines the above-mentioned three characteristics of clouds ($C_aC_tC_d$). Thus, each square is represented by a separate letter.

The northernmost latitude belt is coded first. Within the belt the numeration follows from West to East. The subsequent latitude belts are arranged from North to South independently of the Earth octant in which they might be located.

In the given code, the group $QL_aL_aL_oL_o$ is used to designate the coordinates of the most NW square, i.e., of the first square in the first belt. Then, the group is used for the tenth belt, for the twelfth, etc. For intermediate latitude belts, only the longitude group L_oL_o is given since the latitude of the belts is easily determined from the extreme values, each belt being spaced 1 degree latitude from its neighboring belt.

Each line of a given communication text usually contains data on a single latitude belt. These communications, apart from the L_oL_o group, may contain numbers or letters, or else combinations of numbers and letters with the letter *x*. The latter is used to show completion of the last group of data transmission for a given belt.

If a latitude belt contains six or more successively located equal letters, their total number is indicated in the nonmandatory group ZZ_rNNN_t, defined as follows:

ZZ_r is the distinctive sign,

NN is the number of groups (squares) of given combination,

N_t is a check figure equal to the sum of numbers in group NN.

The groups ZZZZZ may be replaced by, or alternated with, the groups ZZ_rNNN_t in any line if this helps to shorten the groups by repeating one and the same letters in the line.

The second to tenth belts have the form L_oL_oZZZZZ (and/or ZZ_rNNN_t if shortening is possible).

The tenth latitude belt in the transmitted communication has a form similar to that of the first belt, i.e., it will be determined by the group

$$QL_aL_aL_oL_o\ ZZZZZ\ (\text{and/or}\ ZZ_rNNN_t).$$

The eleventh to nineteenth belts are similar in form to the second to ninth. The twelfth belt is similar to the first, tenth, etc.

The combination of letters AA, BB, CC, etc. represents the specific features to be analyzed; these features are designated by $C_aC_tC_d$. The symbol C_a shows the number of clouds in a one-degree square. Decoding is performed using Table 3.2.

TABLE 3.2. Decoding the code designations of the amount of clouds C_a

Code number	Amount of cloudiness
0	No cloudiness
1	Large part of the sky is cloud-free (cloud cover extends over 20–50% of the sky)
2	A large part of the sky (50–80%) is covered with clouds
3	Total cloudiness
4	Cloudiness covers less than 20% of the sky
5	Cloudiness is not given
6	The sky more than 80% covered with clouds, but cloudiness is not total
7, 8, 9	Free numbers

Cloud shape C_t in the one-degree square is coded and decoded according to Table 3.3.

TABLE 3.3. Decoding the code designations of cloud shapes C_t

Code number	Cloud forms
0	No clouds
1	Cumulus
2	Stratiform clouds
3	Cirrus
4	Cumulus and cirrus
5	Cumulus and stratiform clouds
6	Cumulonimbus (more or less isolated)
7	Cumulonimbus (together with other cloud forms)
8	Frontal clouds (chaotically mixed types)
9	Unidentified cloud type

Additional cloud characteristics C_d are coded and decoded according to Table 3.4.

```
AUXX KWBC N 120410
NEPAN TIROS 30880 111829 C2
AA000 BB110 CC130 DD231 FF210 GG262
JJ310 KK312 LL350 MM319 NN320 VV510
05175 LL066
75 LL099
75 LL134
75 LL167
75 LL178
75 LL099 AALLL LLLLX
75 LL066 AA066 FFFFL LLXXX
75 AA077 NAAAA FFFFF FFFLX
75 AA077 NNNAA FFFFF FFFLL
75 AAAAA NN066 AFFFF FFFFL FLLXX
04175 AAANN NAAAA AAFFF AAFFF FFFFL LFFFL
75 AA077 FF101 LLLFF FFFFF
75 AA077 FF213
73 AAAA FF224
70 AAFFF FF202
68 FFFCC CCFFF FF123 KFXXX
67 FFCCC CCCCC FCCCC FFBKF KFFFX
65 FCCCC CCCCC CCCBB KFKKK KKKXX
64 GG112 BBKFK KK077
63 GG088 BBBKF KKKKK KKKFF
03162 BBGGG GGBBB KFKKK MKKKK KFFXX
61 BBBBC GBBBB KFKKK KKKKK FFFFX
60 BB101 KFKKK KKKKF FFXXX
58 BB099 KKKKK BKAAF FFXXX
56 BB123 KAAAF FFBXX
54 BB101 AAAAF FFFBX
53 BB088 AFFAA FFFFB BBXXX
52 BBBBF BBAFA AAFFA AFJBB
50 FFFFA FJAAA AAJJJ JJJBX
49 FBBAA JAAAA JJJJJ JJBBX
02148 BAAJA AVVVF AAAJJ JBBBB
47 AAJDK VVFKK KAAJJ BBBBX
46 AJDKV FKKKK KAAJB BBBBX
45 JDKVK FKKKK KAABB BBBXX
44 DKVFF KKKKF AABBB BBBXX
43 KVFKK KMKFB AABBB BBXXX
43 KK077 FFBAB BBBBB
42 KK066 FFBAB BBBBB
41 KKKKV FFBAB BBBBB
41 VVVVV FFBBB BBBBB
01140 VVVVF FBBBB BBBBX
40 VVVFF FBBBB BBBXX
35 FFFFB BBBXX
```

FIGURE 3.22. Telegram with nephanalysis data

Conventional symbols used for plotting maps of schematic nephanalysis are given in Section 4.8.

TABLE 3.4. Decoding of code designations for additional cloud characteristics C_d

Code number	Cloudiness features
0	Cloud structure undetermined or unclear
1	Thin clouds
2	Thick dense clouds
3	Possible haze, snow, etc.
4	Convection cells or bands
5	Bands
6	Transverse bands
7	Frontal clouds
8	Dense frontal clouds
9	Cloud vortex

The sequence for application and use of nephanalysis data consists of the following.

As soon as the given meteorological station or center that uses satellite data has received the telegram with nephanalysis data (Figure 3.22), the data are transferred onto one-degree squares. Such a processed telegram is shown in Figure 3.23. Next, regions with similar cloud characteristics are linked by isolines and an intermediate map is plotted. This map (cf. Figure 3.24) schematically contains additional characteristics. Using this map and the telegram data, the operator draws up the nephanalysis map shown in Figure 3.25.*

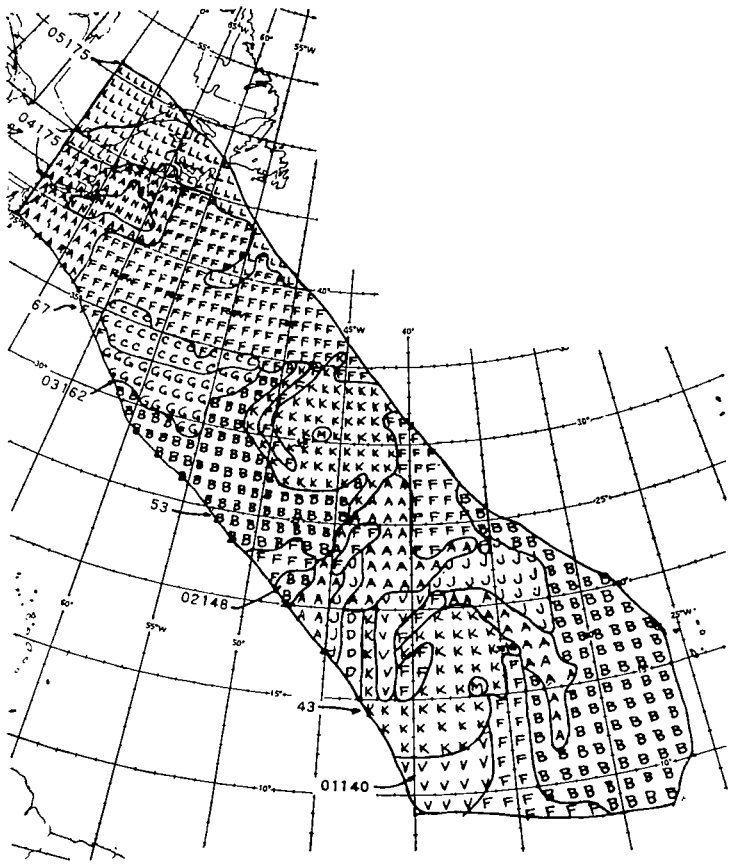

FIGURE 3.23. Example of decoding telegrams and entering data onto one-degree squares

* If the operator is sufficiently experienced, intermediate maps are unnecessary.

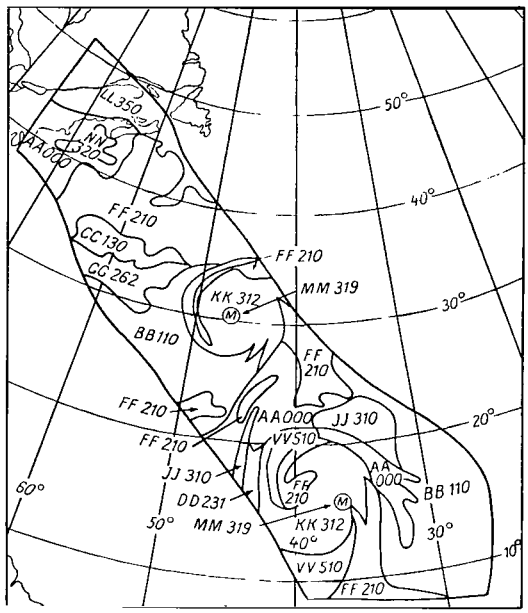

FIGURE 3.24. Schematic intermediate nephanalysis

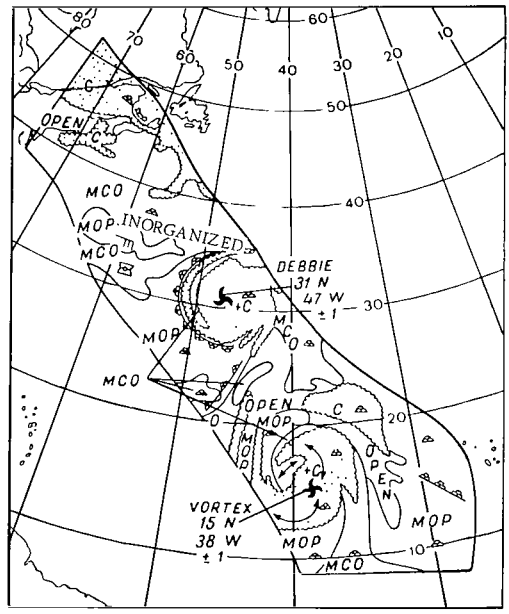

FIGURE 3.25. Final nephananalysis map

Clarity of nephanalysis charts is increased using color shading, particularly for cloudiness (blue or green). Numerous additional symbols and letters are also used (cf. Section 4.8).

The results of nephanalysis [plotted on charts] contain no more information that those provided by pictures. Therefore, much depends on the skill of the meteorologist. Chapter 4 of this book deals in detail with methods used to directly decode photographs. However, most meteorological stations or centers will not always be in a position to receive satellite pictures (except for centers that receive data from satellite APT systems). Therefore, joint use of nephanalysis data with information from other observation devices is extremely important for the routine work of hydrometeorological weather services.

At present, numerous countries, including the USSR, are receiving nephanalysis data furnished by meteorological satellites. In order to ensure the speedy use of information, the World Meteorological Centers in Moscow and Washington are linked by direct communication lines.

Some stages in nephanalysis processing lend themselves to automation. Thus, telegrams with nephanalysis data received directly via the communication line may be fed to an electronic computer, where they are decoded; the results may be printed on special charts using the automatic printing devices available at the stations. It is also possible to transcribe the decoded data and feed them into one of the external storages of the computer, e.g., to carry out statistical routine processing of cloudiness data. This is particularly important for ocean and polar regions, for which data on cloud fields are in general very scarce.

In conclusion, let us dwell on the forms of charts for recording satellite data.

As is well known from cartography, maps plotted in the polar stereographic projection are extremely useful for areas of high latitudes of the Northern and Southern hemispheres, but for lower latitudes such maps lead to considerable distortions.

For moderate latitudes, maps plotted in conical projection yield minimum distortion. Mercator projection, which yields maximum distortion for higher latitudes, is nevertheless more suitable for lower latitudes. It is, of course, difficult to select a standard projection if the maps are to be used on a global scale. Map forms used for synoptic analysis may also be employed for individual regions.

In the U.S.A., the most widely used map scales are 1:30,000,000; 1:20,000,000; and 1:15,000,000.

Maps of a larger scale, e.g., 1:10,000,000, may also be used. Various papers suggest the use of a set of plane tables for the whole globe, the tables being plotted in a projection convenient for the given latitude. One such suggestion is presented in /2/.

In the following an example is presented of plotting a system of map cutouts for a meteorological satellite that moves at a height of 600 km in a circular orbit with an inclination angle of 65°.

Changes in the geographical latitude of the SSP during the movement of the satellite along its orbit are described by the following formula:

$$\sin\varphi = \sin\delta \sin\Omega t,$$
$$\operatorname{tg}(\lambda + \omega t) = \cos\delta \operatorname{tg}\Omega t, \qquad (3.17)$$

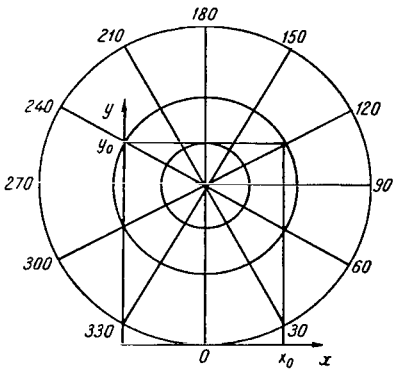

FIGURE 3.26. Schematic position of strips for preparing cutouts in high and moderate latitudes

where φ is the latitude; δ is the orbit inclination angle; Ω is the angular rotational speed of the satellite around the Earth; t is the time counted from the instant the satellite passes through the equator; λ is the longitude; ω is the angular rotational speed of the Earth.

If the critical nadir angle is restricted to 60° for given initial data on the satellite orbit, the processing and mapping of observational data may be done for a strip of width 2,500 km. For this purpose, it suffices to prepare from the hemisphere map two cutouts that cover the high latitudes and the adjacent moderate latitudes. In such a case, the center of the rectangular strip will be at the Pole, while the large diagonal of the rectangle will be along the 0 or 90° meridian (cf. Figure 3.26).

Assuming the direction of the axis of the plane-table coordinates to be the same as in Figure 3.26, we obtain

$$x = \frac{x_0}{2} + 1.866 R_E \bar{M} \operatorname{tg}\left(\frac{\pi}{4} - \frac{\varphi}{2}\right) \sin(\lambda - \lambda_0),$$
$$y = y' - 1.866 R_E \bar{M} \operatorname{tg}\left(\frac{\pi}{4} - \frac{\varphi}{2}\right) \cos(\lambda - \lambda_0), \qquad (3.18)$$

where R_E is the radius of the Earth; $\bar{M}$ is the scale-multiplying (conversion) coefficient; λ_0 and y' are constants determining the origin of coordinates.

For the first two plane tables λ_0 is 0 and 90°, while $y' = \frac{y_0}{2}$. For the remaining plane tables $\lambda_0 = \frac{\pi}{6}(n-1)$, where $n = 1, 2, \ldots 12$ is the current number of the cutout, and $y' = 1.866\, R_E \bar{M}$. In the same way we prepare 14 cutouts for the Southern Hemisphere.

For lower latitudes it suffices to prepare 8 cutouts from the map drawn in Mercator projection. The central line of the rectangle will then coincide with the equator, and the short line with the meridian that is a multiple of 45° (cf. Figure 3.27).

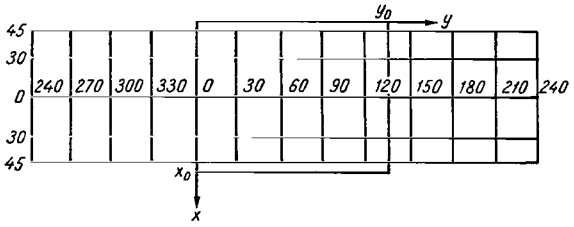

FIGURE 3.27. Schematic position of strips for preparing cutouts in lower latitudes

In this case the formula for the conversion from geographical to plane-table coordinates becomes

$$x = \frac{1}{2}x_0 - \frac{\overline{R}_E \overline{M} \cos\varphi_0}{0.43429} \lg \operatorname{tg}\left(90 - \frac{\varphi_0}{2}\right),$$
$$y = \frac{2\pi R_E \cos\varphi_0 \overline{M}}{360} (\lambda - \lambda_0), \qquad (3.19)$$

where $\varphi_0 = 22°30'$; $\lambda = \frac{\pi}{4}(m-1)$, $m = 1, 2, 3, \ldots, 8$.

A system of 36 plane tables is thus capable of ensuring reliable transmission of satellite data for any region.

Accurate and objective analysis can then be performed using a rectangular coordinate system, as is done for other meteorological elements. Such a system of cutouts is especially convenient for processing radiation data, but may also be used to interpret cloud data.

3.4. PROCESSING OF OUTGOING-RADIATION DATA

The TIROS series of satellites (TIROS II, TIROS III, and later satellites) made it possible to obtain a large body of information on radiation using five-channel scanning radiometers. Such an amount of data makes it almost impossible to ensure manual data processing, and therefore data interpretation is performed using all the available means of modern automation and computing. Electronic computers, if used for this purpose, should meet the following requirements: 1) quick action (10^5—10^6 operations per second); 2) maximum internal-storage capacity; 3) high reliability; 4) possibility of connecting additional external devices to the computer input and output for special processing needs.

The papers in /1.2/ present a review of the first studies on processing radiation data. Various aspects of this problem are also dealt with elsewhere /2.88, 2.89, 8, 19, 21, 22/.

The entire cycle of radiation-data processing is done automatically, from the input of information received from the communication line until the automatic plotting of radiation charts and tables. The processing technique involves the following operations. From the data-acquisition center, information is transmitted through adequate communication lines to the processing center, where it is recorded on magnetic tape and fed to the computer. Data are stored in the form of analyzed Final Meteorological Radiation Tables (FMRT) that are either summarized in catalogs or tabulated. For scientific-research purposes, other forms of data recording are also used. Each tape has its own code and is filed at the data center. The center also keeps a special catalog of stored data with their characteristics /19, 21/.

From the FMRT, data may be transferred and fed to one of the computer storages and then processed according to one of the available programs. There is ample information on the programs for processing TIROS II /19, 20/ and TIROS III data /11, 21, 22/. However, the various programs in general do not vary with the satellites used.

Before describing the date-processing programs for outgoing radiation, let us briefly dwell on the characteristics and quality of information obtaine from satellites, since otherwise it is very difficult to perform efficient data interpretation.

In existing catalogs for TIROS II /19, 20/ the magnitudes of outgoing radiation for all spectral regions are given in W/m^2. For the TIROS III satellite /11, 21, 22/ and subsequent series of the TIROS family, the data of channels 1, 2, and 4 presented the outgoing radiation in actual temperatures that characterize the radiation temperature of an absolute blackbody for the given spectral region. For channel 3, which recorded the reflected short-wave radiation, as well as for channel 5, which recorded radiation in the visible part of the spectrum, the radiation was given, as before, in W/m^2. Table 3.5 presents the characteristics of the channels and the measurement errors for TIROS II and TIROS III /2.12/. The table was compiled from data in /19—22/ and contained the mean absolute errors e_1 of radiation measurements as well as the maximum errors e_2 that allow for distortions arising in the transmission system of the satellite after launching.

TABLE 3.5. Errors in outgoing-radiation measurements conducted for TIROS II and TIROS III

Channel No.	Channel characteristics	TIROS II		TIROS III	
		e_1	e_2	e_1	e_2
1	Spectral band 6—6.5 μ. Satellite recorded the radiation of atmospheric water vapor	±0.06 W/m^2 (±2° at T = 240°K)	±0.18 W/m^2 (±6° at T = 240°K)	± 2°K	± 5°K
2	Spectral band 8—12 μ. The satellite recorded the back radiation reflected through the atmospheric window. About 75% of this radiation is reflected from the underlying surface or the upper cloud boundary	± 1.6 W/m^2 (±2° at T = 270°K)	± 4.0 W/m^2 (±5° at T = 270°K)	± 2°K	± 4°K
3	Spectral band 0.2—6 μ. Satellite recorded the integrated short-wave radiation	±60.0 W/m^2	— Unreliable data	±20 W/m^2	—
4	Spectral band 8—30 μ. The satellite recorded the integrated long-wave radiation of both the underlying surface and the atmosphere	±1.7 W/m^2	±5.0 W/m^2	± 2°K	± 4°K
5	Spectral band 0.55—0.75 μ. Satellite recorded radiation in the visible region of the spectrum	Unreliable data		± 3 W/m^2	±10 W/m^2

Since the data from TIROS III differ from those transmitted by TIROS II due to different measurement units used in both satellites, special calibration graphs /22/ or an empirical formula derived from them /2.12/ is used to compare these data:

$$f_1 = a_1 T^{10}; \quad f_2 = a_2 T^5; \quad f_4 = a_4 T^4,$$

where f_i is the radiation (in W/m^2) for the corresponding channel; $a_1 = 6.17 \cdot 10^{-25}$; $a_2 = 2.83 \cdot 10^{-11}$; and $a_4 = 2.15 \cdot 10^{-8}$.

Table 3.5 shows that errors in measuring the radiation fluxes are still considerable and therefore they must be allowed for when interpreting satellite radiation data.

The following is a description of some principles used in processing outgoing-radiation data and of methods for their presentation in the form of tables and graphs.

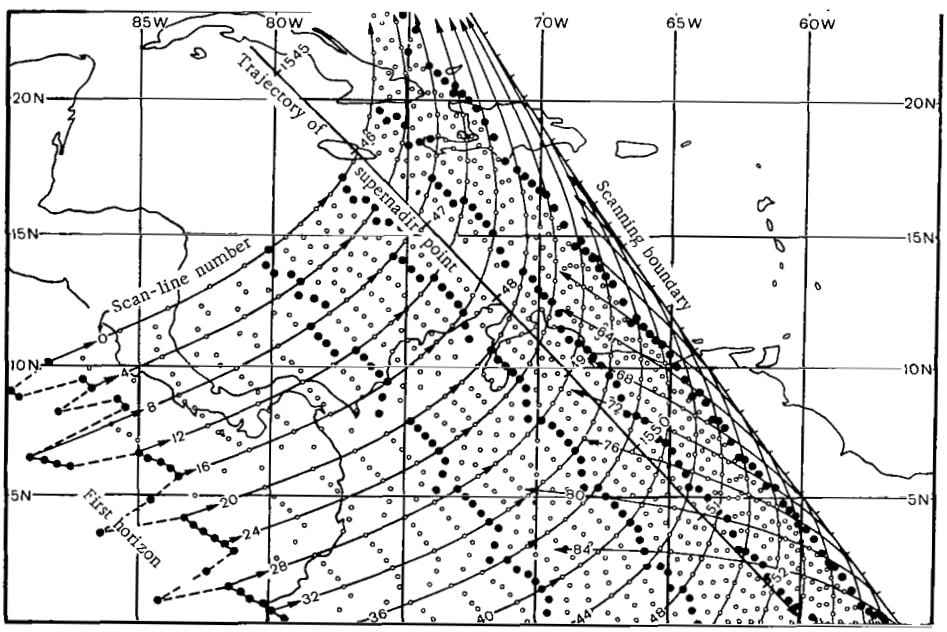

FIGURE 3.28. Position of scan points and scan lines for TIROS III on 21 July 1961

The radiometer installed on the satellite faces the Earth surface at a given nadir angle. The point of intersection of the radiometer's optical axis with the Earth surface is similar to the PP of the TV camera, and is the "supernadir" point /8/, the trajectory of which, like that of the satellite PP, has to be calculated. The radiometer side scanning, as well as scanning during the movement and spinning of the satellite, ensure efficient coverage

of the observed area. Figure 3.28 shows one of the regions scanned by TIROS III and the trajectory of the supernadir points; the figure also shows the regions corresponding to time intervals of one minute as well as the scan lines (the figure separately shows each fifth point). As is seen from the figure, the one-minute interval contains 10 lines. Each fourth line is numerated. Such information, after being recorded on tape, is then processed using an available program.

The first program for data printing (MS-500) involves the performance of two tasks. The first consists in compiling a list of satellite observational data at five-minute intervals; these data are printed on special tape in a definite sequence (there are several versions of this program). Printing is performed either for each scan point or in batches, for each line or for each fourth line. In this case, data for each fourth point are printed on each line (Figure 3.28).

Figure 3.29 presents an example of such a table for two lines. This table, for each fifth point, contains printed data on azimuth, nadir angle, latitude and longitude of the point, and the data from five sensors in the adopted measurement units.

The second task of the MS-500 program consists in compiling the local information report at the reference point grid which is then used for objective analysis. To compile local information at every fifth point (at picture edges it is likely to be every fourth, third, or even second point), a single reference point is selected by interpolating data for every point in the group. If instead of five points the averaging strip turns out to have two points, the interpolation should be linear; if the strip has three points, interpolation should be squared, and finally if the strip has more than three points, interpolation should be cubed. Such a method yields a somewhat averaged image which, with a large density of points and low measurement accuracy, might be very useful.

With the aid of special printing devices, the data for each point may be printed in the corresponding measurement units. Since each point is scanned at a different angle, for channels 1, 2, and 4 one must know the zenith angles at which the observation is being conducted; for channels 3 and 5 we must know the position of the Sun (determined by the zenith angle of the Sun (Figure 3.30)). Figure 3.31 shows an example of such a printout. It is useful to plot the zenith angles as isolines.

It is interesting to note that the position of the supernadir point at 1547 hr was near the NW edge of typhoon Anna /8/. Figures 3.31b and d (upper right corner of picture) for this region clearly show the eye with low actual temperatures; this stresses the importance of using radiation data in routine meteorological work.

According to /19/ the MS-500 program has the following shortcomings:

1. The body of input information does not contain more than 20,000 bits, which corresponds to measurement data obtained during 15—20 minutes of satellite operation. Using electronic computers with a higher storage capacity such limitations may be eliminated.

2. Local information distorts the overall pattern at the boundaries of the scanned region for large nadir angles. This makes it necessary to introduce certain limitations in the analysis /8/.

Two program complexes were developed for further data interpretation, one of which /19, 20/ is intended for data processing from TIROS II. The

SCAN LINE NUMBER 4

AZIMUTH	NADIR ANGLE	LONGITUDE	LATITUDE	6.0-6.5 MU	8.0-12 MU	0.2-5.0 MU	7.5-30 MU	.55-.75 MU
235.98	56.94	86.67	9.34	228.37	247.50	119.12	247.75	18.62
223.30	54.18	84.54	10.32	237.75	263.25	106.37	249.12	11.12
217.06	50.14	82.73	11.19	233.25	268.87	59.25	255.25	3.75
215.69	45.11	81.20	11.97	233.25	268.12	31.50	254.00	0.
217.64	39.41	79.93	12.68	239.50	272.25	24.50	258.62	0.
221.34	33.33	78.89	13.33	237.25	276.75	10.62	263.00	0.
225.25	27.17	78.05	13.92	238.87	281.12	17.62	267.37	0.
227.80	21.24	77.39	14.48	237.75	271.37	31.50	265.25	0.
227.42	15.83	76.88	15.01	242.37	274.00	17.62	261.87	0.
222.57	11.26	76.49	15.53	238.87	278.87	10.62	267.37	0.
211.67	7.81	76.19	16.05	238.37	274.87	0.	265.25	0.
163.36	7.69	75.84	16.59	235.50	275.75	3.75	264.12	0.
113.34	8.83	75.57	17.15	233.25	274.87	10.62	264.12	0.
67.52	11.06	75.35	17.75	236.12	274.87	10.62	260.75	0.
31.78	14.21	75.21	18.39	237.75	278.87	17.62	269.62	0.
12.03	18.12	75.12	19.08	238.87	281.12	3.75	265.25	0.
14.16	22.62	75.11	19.83	238.37	276.75	31.50	265.25	0.
44.05	27.53	75.16	20.67	227.75	274.87	31.50	264.12	0.
107.62	32.69	75.27	21.58	237.25	279.87	10.62	264.12	1.87
210.75	37.92	75.46	22.59	226.50	276.75	10.62	264.12	1.87
359.34	43.06	75.70	23.70	240.12	274.87	17.62	265.25	0.
559.29	47.94	76.02	24.93	234.87	272.25	10.62	263.00	0.
816.49	52.38	76.39	26.29	233.25	268.12	10.62	257.50	0.
1136.83	56.22	76.84	27.78	233.25	262.50	31.50	249.12	0.

SCAN LINE NUMBER 8

AZIMUTH	NADIR ANGLE	LONGITUDE	LATITUDE	6.0-6.5 MU	8.0-12 MU	0.2-5.0 MU	7.5-30 MU	.55-.75 MU
238.39	60.42	89.08	6.59	220.12	230.00	100.00	238.25	14.87
226.93	57.38	86.10	7.88	228.37	261.62	87.12	254.00	13.00
220.92	53.38	83.60	9.01	234.87	270.50	66.25	255.25	0.
219.01	48.63	81.54	9.99	233.75	266.50	73.25	252.75	11.12
219.84	43.35	79.86	10.84	229.62	235.75	138.25	227.00	7.37
222.03	37.77	78.52	11.58	232.62	245.00	73.25	245.00	1.87
224.24	32.09	77.47	12.23	237.75	273.12	10.62	263.00	0.
225.09	26.54	76.68	12.81	241.75	274.87	10.62	259.62	0.
223.23	21.33	76.10	13.34	243.00	276.75	17.62	261.87	0.
217.29	16.69	75.68	13.84	235.50	273.12	59.25	258.62	9.25
205.91	12.83	75.37	14.33	234.37	271.37	80.12	256.37	0.
171.40	10.83	74.98	14.86	232.00	271.37	17.62	260.75	3.75
132.81	9.84	74.65	15.41	240.12	264.12	10.62	251.62	1.87
92.85	9.84	74.39	15.98	230.25	264.12	59.25	255.25	0.
54.26	10.83	74.20	16.58	236.62	277.87	59.25	260.75	0.
19.75	12.83	74.06	17.22	238.37	273.12	17.62	263.00	0.
-3.15	16.69	73.88	17.77	234.37	274.87	38.50	256.37	1.87
-17.74	21.33	73.78	18.41	230.25	274.00	31.50	266.37	0.
-22.49	26.53	73.79	19.18	225.37	279.87	3.75	265.25	0.
-15.88	32.07	73.92	20.13	232.00	282.25	17.62	264.12	0.
3.59	37.73	74.22	21.30	237.75	274.87	10.62	260.75	0.
37.46	43.31	74.69	22.72	232.62	270.50	10.62	256.37	0.
87.23	48.57	75.37	24.45	234.87	272.25	17.62	259.62	0.
154.43	53.30	76.28	26.52	241.25	276.75	17.62	264.12	0.
240.57	57.29	77.44	28.98	230.87	265.62	17.62	257.50	3.75
347.17	60.31	78.87	31.87	227.75	247.50	52.37	237.00	9.25

FIGURE 3.29. Example of printed data on outgoing radiation from TIROS III. Printing was done for two scan lines. Coordinates, azimuth and nadir angle are printed for each fifth point on the given line.

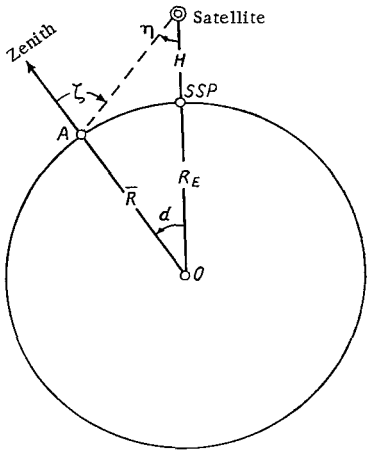

FIGURE 3.30. Scheme for determining the zenith angle

first program of this complex, called AW-950, is intended for plotting low-resolution radiation charts. For plotting charts with this program in the U.S.A., a squared grid is used in the system of routine objective interpretation of aerological data /12, 19/. The grid represents an octagon inscribed in the large latitude of the (Northern and Southern) hemisphere map plotted in the stereoscopic polar projection to the scale $1:5 \cdot 10^7$. This grid is shown in Figure 3.32; for moderate latitudes, the grid pitch is 200 miles. With such a pitch the number of nodal points reaches 1,977, but simultaneously not more than 377 nodal points per channel are processed.

The task involves recording radiation data at the nodes of a regular grid according to data from the local reference grid. The coordinates of the local reference grid are first converted from geographical coordinates to x, y coordinates taking the grid pitch as length unit. The next step is data interpolation and the plotting of isoline charts.

The second program (MS-501) of the above complex is similar to the first one and involves plotting high-resolution radiation charts. The program also uses 1,977 nodal points, but the chart has a different scale ($1:10^7$), which corresponds to a distance of about 40 miles between the nodes of the square grid. In the first processing stage the computer is fed with only 8,200 bits, that correspond to a body of information obtained during 5—10 minutes of satellite operation. The sequence in using the first subprogram of the MS-501 program is similar to that in using the MS-500 program. FMRT data for a single time interval are read off the magnetic tape and stored in the computer. The coordinates of the reference points are converted to x, y coordinates using here as a measurement unit a pitch of 40 miles. This stage is followed by data interpolation intended to record radiation values in the nodes of the regular grid from data of the local reference grid.

The interpolation method is based on the successive correction of the reasonably predetermined initial field. For each nodal point some average values may serve as a zero approximation. This correction is then performed in several stages. At first, for each stage those points of the reference grid are selected that are spaced from the node at a distance not exceeding a value D, expressed by the number of intervals between the points. Interpolation of data for the nodal point yields from each adjacent point of the reference grid a series of corrections for the initial value of the element to be analyzed. The final correction is then found as an average value from the formula

$$E_k = \frac{\sum_{i=1}^{N} w_i g_i}{\sum_{i=1}^{N} w_i}, \qquad (3.20)$$

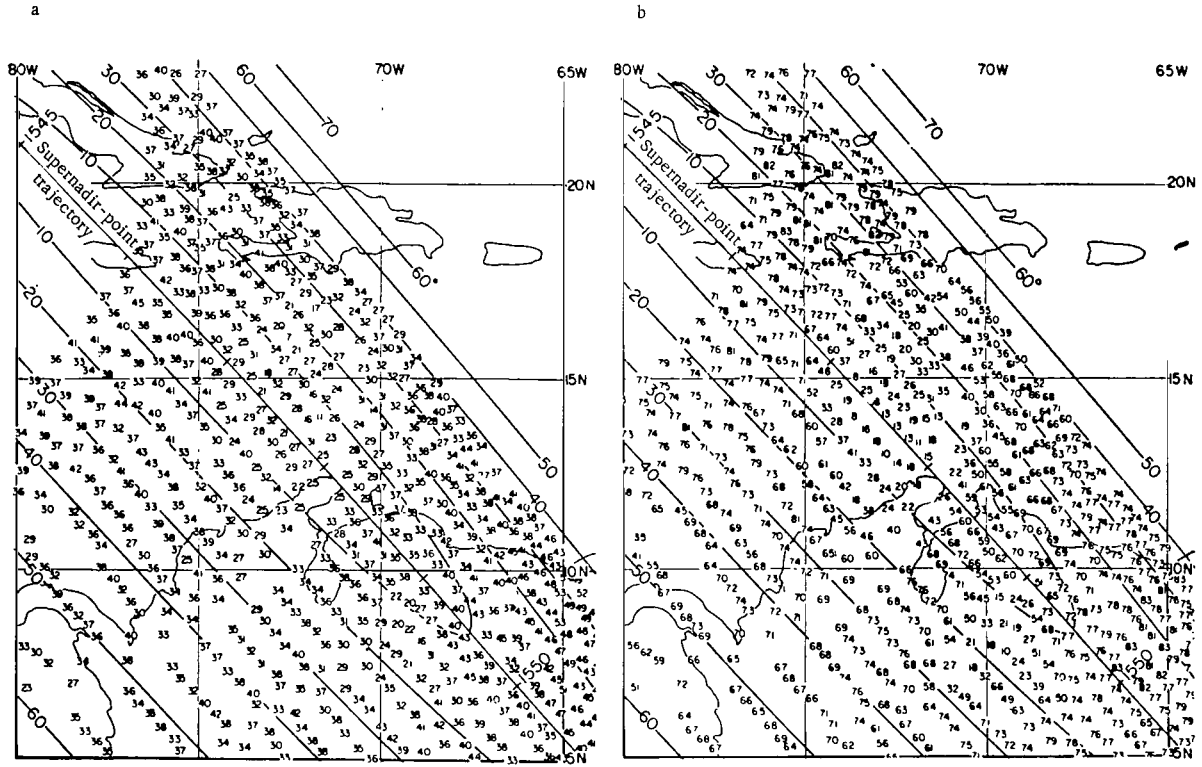

FIGURE 3.31. Outgoing radiation data from TIROS III on 21 July 1961 from orbit No. 132; data are printed on a Mercator-projection map: a – data from channel 1 in degrees of actual temperature (200 + °C); b – data from channel 2. Solid lines designate isolines of zenith angles.

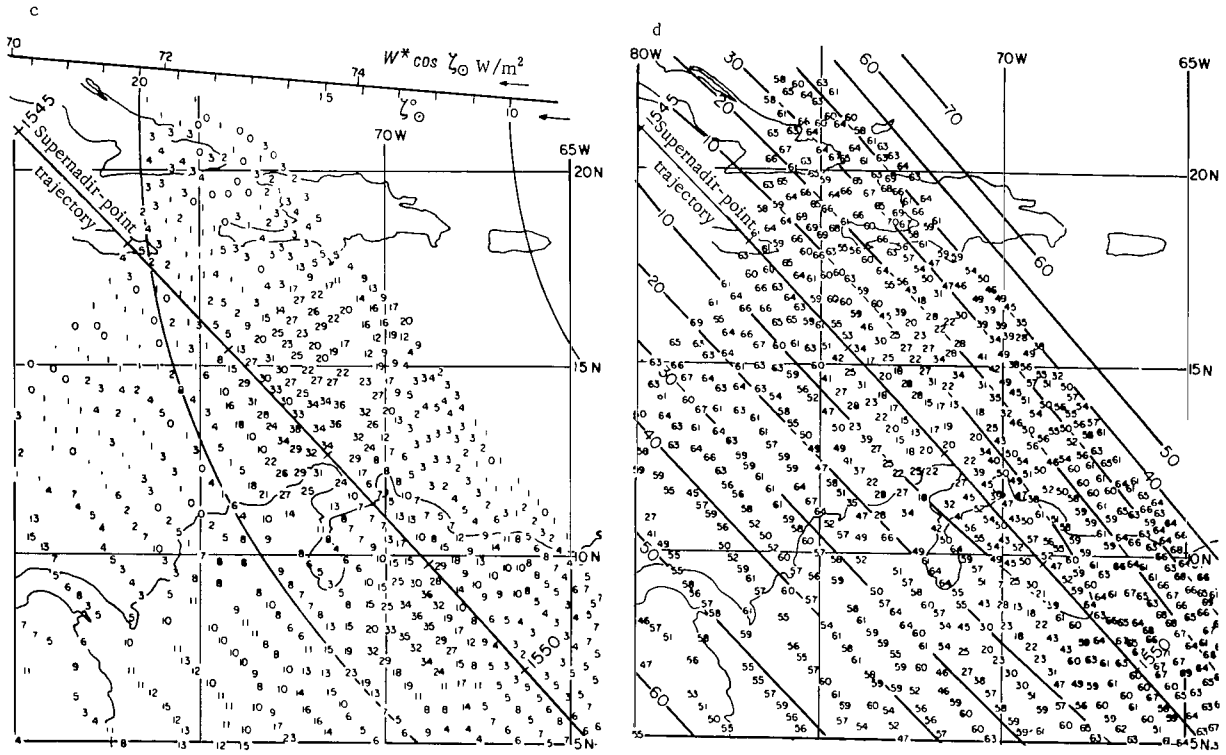

FIGURE 3.31. Outgoing-radiation data from TIROS III on 21 July 1932, from orbit No.132; data printed on a Mercator projection map: c – measurements with channel 3 in tens of W/m²; solid lines designate isolines of the Sun zenith angles; d – measurements with channel 4; designations as in Figure 3.31, a and b.

where g_i is the correction for the value of the initial field in the k-th field obtained by interpolation from the i-th point, N is the number of points used in the analysis of the given node, and E_k is the mean weighted correction; w_i is the weight factor determined by

$$w_i = \frac{D^2 - d^2_i}{D^2 + d^2_i}, \tag{3.21}$$

where d_i is the distance between the i-th point and the k-th node measured in grid pitches of given resolution; D is the distance at which w_i becomes zero. The latter value is found empirically.

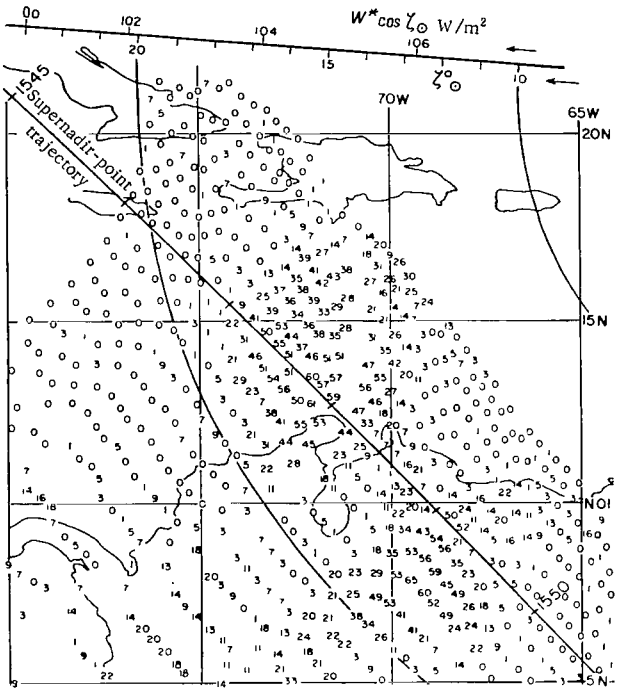

FIGURE 3.31. Outgoing-radiation data from TIROS III on 21 July 1932, from orbit No. 132; data printed on a Mercator-projection map:

e – measurements with channel 5; designations as in Figure 3.31c.

The corrections yield at each point the field of the first approximation. However, this field must also be corrected using the same calculation formulas (3.20) and (3.21), but with smaller values of D. This means that data from the reference stations located nearer the given nodal point are used in the correction. This yields the field of the second approximation. Such a correction is repeated 3 or 4 times. For the correction of the zero-approximation field, D is taken as 3 or 4. In the last stage, $D = 0.9$ and $w_i = 1$.

The corrected data at the nodes of the regular square grid are printed on suitable forms as three-digit numbers with a special printing device.

The isolines on the charts are spaced at 0.1 W/m^2 for channel 1, at 2.0 W/m^2 for channels 2 and 4, and at 20 W/m^2 for channels 3 and 5. The isolines are printed either with mechanical printers or with a two-coordinate electronic plotter /3/. Figure 3.33 shows an example of such a chart.

On the strength of studies published in /8, 21, 22/ the program of data processing for TIROS III and its subsequent series of satellites was improved by developing two alternative programs. One version comprises the low-resolution processing program for stereographic projection used in high and moderate latitudes, and for Mercator projection used in low latitudes. The second version includes the high-resolution programs also for both projections.

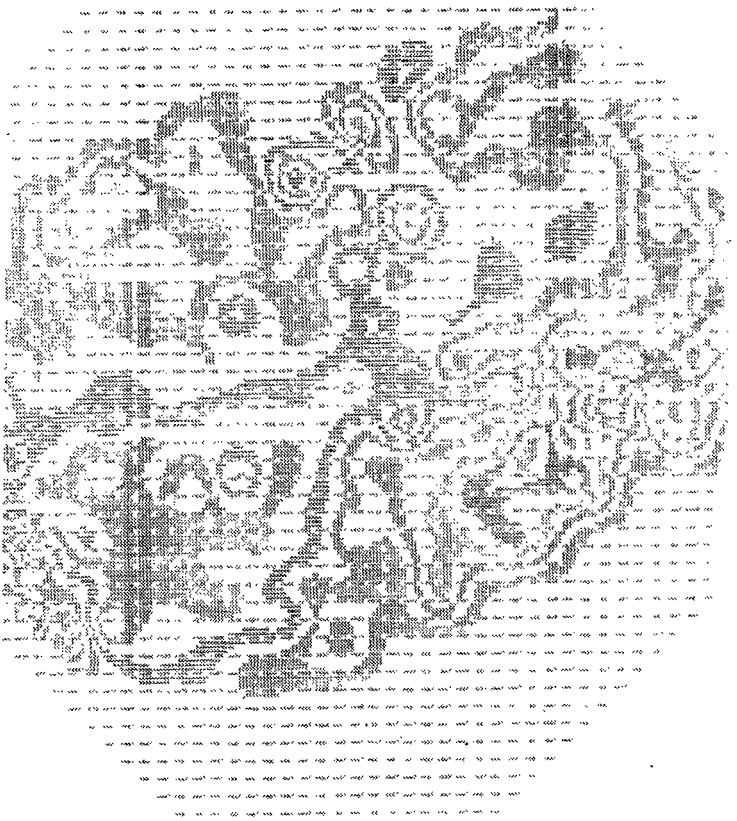

FIGURE 3.32. Distribution of outgoing radiation in the spectral band of 7–30 μ. The printed data are entered at the nodes of a regular square grid. The chart has high resolution

Radiation data from TIROS III for channels 3 and 5 are given in W/m^2, and for channels 1, 2, and 4 in degrees of actual temperatures; these data are interpolated at the nodes of a grid with a pitch of 1, 25, and 2.5° of the

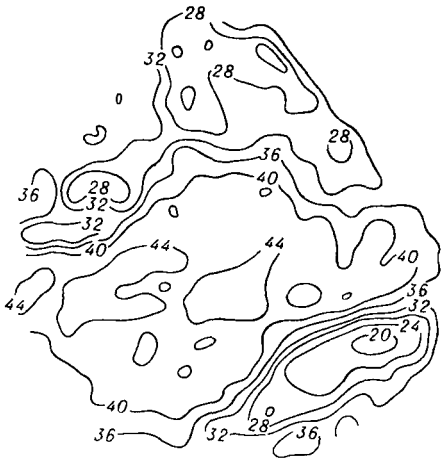

FIGURE 3.33. Chart of outgoing radiation in the 8—12μ-band printed by a two-coordinate electronic plotter

arc of the Equator. The radiation charts of high and low resolution for some orbits of TIROS II and TIROS III are published as catalogs /19, 21/. For geographical orientation and location, these catalogs contain transparent plane tables provided with a geographical grid. For processing, plane tables are selected that carry an index corresponding to the index printed on a special form; superposing these indexes permits suitable geographical orientation of printed data and isolines.

Consider now model punchcards common for all programs. The model shown in Figure 3.34 exhibits the following sequence in data punching. Columns 1, 2, and 3 are provided with the days of the Julian calendar, i.e., the number of the day of the month elapsed since satellite launching. Thus, for TIROS II, readout starts from 23 November 1960, for TIROS III from 12 July 1961, for TIROS IV from 8 February 1962, etc. Columns 4 and 5 are provided with hours, while columns 6 and 7 are with minutes. Columns 8 through 11 contain the length of the working time interval for which readout has to be done. For some processing programs this working interval is 5 minutes. Column 12 receives the current number of the satellite channel from which readout starts.

Station No.
1 = New Jersey
2 = California

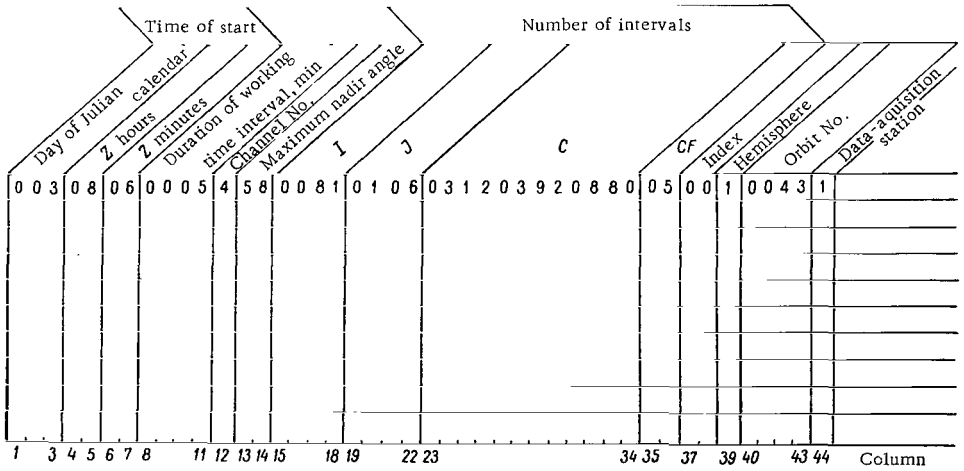

FIGURE 3.34. Model of punchcard for interpreting outgoing-radiation data

Columns 13 and 14 contain the maximum nadir angle. Readout starts for observation at nadir angles below their critical values. Columns 15 to 18 contain the number of intervals of the small-pitch grid; this number is read from some starting ordinate. Columns 19—22 contain the number of intervals read from the initial abscissa; this number represents the displacement of the coordinate origin in the region where the data must be processed.

Columns 23 and 24 contain the number of large intervals between the pole and the Equator on the low-resolution polar-stereographic projection map.

Columns 35 and 36 indicate the number of small intervals in one large interval. For TIROS II the number is five.

Columns 37 and 38 contain a certain distinctive symbol or code number. For TIROS II this code number is 01. Column 39 receives either 1 for the Northern Hemisphere or 0 for the Southern Hemisphere.

Columns 40 to 43 contain the current numbers of the orbits, while column 44 contains the code number of the APT data-acquisition stations. At the eastern coast of the U.S.A. such a station has the number 1, and at the west coast the number 2. The numbers in the model card are not punched but printed, and designate the following: request is made for satellite data from the third day after its launching until 0806 hr; channel 4 data are requested from orbit No. 43, having a nadir angle of $\leq 58°$ for a working time interval of 5 minutes.

FIGURE 3.35. Chart with outgoing radiation data from channel 2; chart was printed after objective analysis (data are limited by a nadir angle of 58°)

In the grid used the origin of coordinates of the small-pitch grid (pitch of 40 miles) is displaced by 81 intervals from the origin of the ordinate and by 106 intervals from the origin of the abscissa.

After the required data are read off, the program most suitable for the particular task is selected.

Fujita /8/ shows that for the efficient utilization of radiation data we should avoid using data obtained from observations at large angle, allow for the position of the Sun, etc.

Presentation of processed data with an indication of all these details is important for the correct use of radiation data both for routine work and scientific purposes.

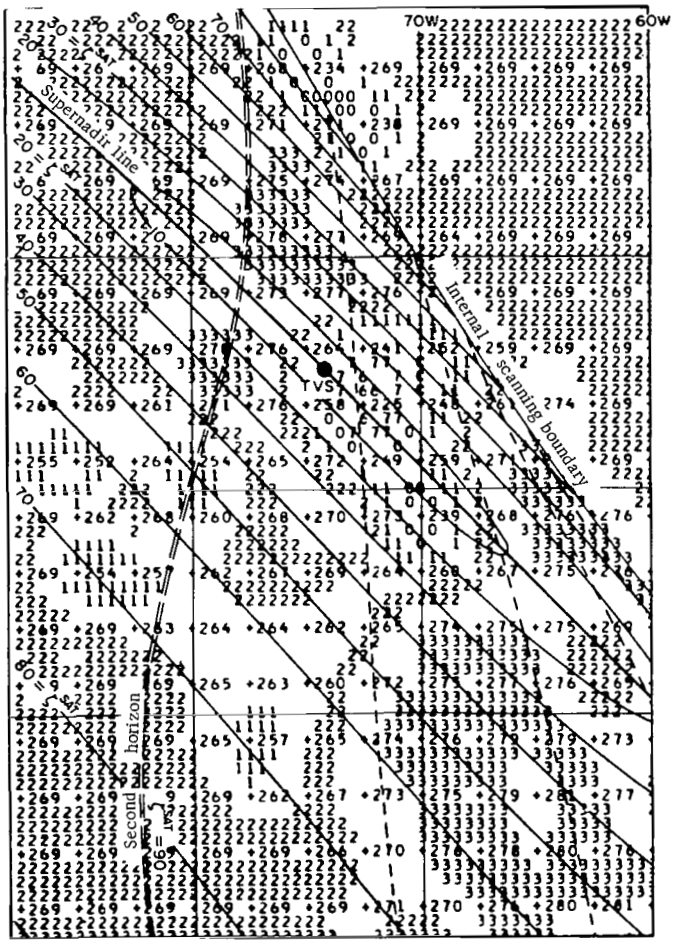

FIGURE 3.36. Chart with outgoing-radiation data from channel 2 and with zenith-angle isolines

Figure 3.35 shows a radiation chart after objective analysis /19, 21/. In this figure, the data on the actual radiation temperature for orbit No. 132 obtained from channel 2 are printed (after objective analysis) at the nodes of the regular grid. The boundaries between the thick numbers, that show the interval between two isotherms, and the empty spaces are isotherm lines. In the given example they are drawn at 5° intervals. This figure also shows the printed data delineated by a zone with nadir angles $\leq 58°$ corresponding to a maximum zenith angle of 72°. The data from the boundary points are transferred to the region of the chart where the measured area terminates.

Figure 3.36 presents the same chart for channel 2 but with zenith-angle isolines. Point TVS on the supernadir line denotes the scan point for zero

scanning angle. The zenith angles are given for two scans; satellite rotation produces two scan lines — one in front of the satellite and the other behind it. The results of the first scanning are presented by solid lines, those of the second scanning by dotted lines. The scanning boundary is delineated by two lines — one being the horizon (thick dots for the first scanning and double dots for the second scanning); the second line represents the scanning delineation.

The radiation chart in Figure 3.37 shows the scan lines (first scan as solid lines, the second scan as dotted lines). The same figure shows the lines of delineation by the nadir angle of 58°.

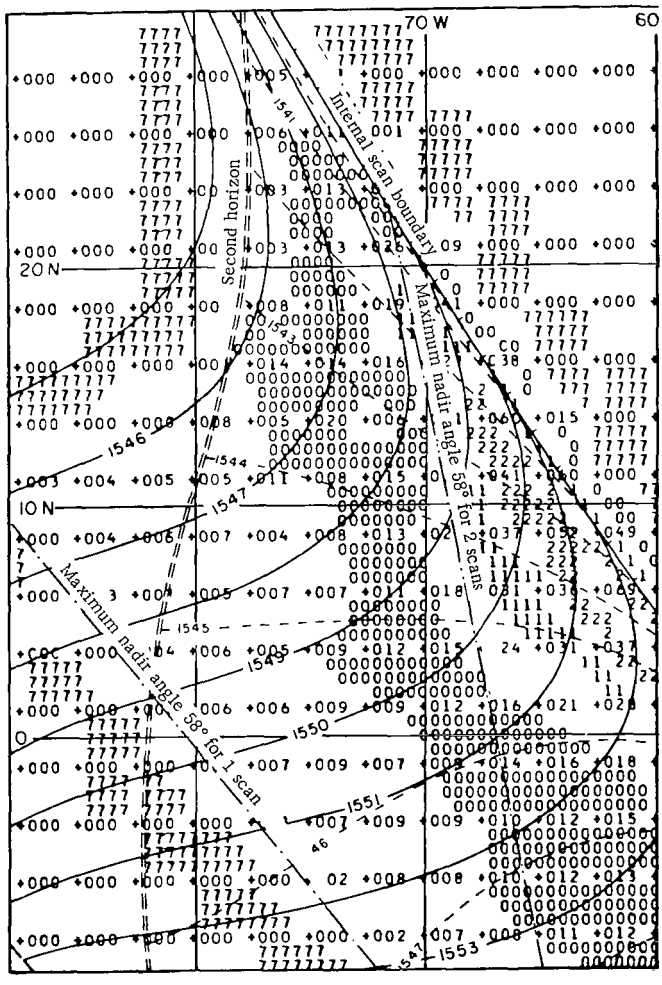

FIGURE 3.37. Outgoing-radiation chart containing scan lines, lines of delineation with nadir angle of 58°, and lines of scanning delineation

Such a processing technique enables the data on outgoing radiation for different spectral bands to be used for various scientific purposes, particularly if they are employed jointly with cloud photographs, nephdata, and other meteorological information.

Routine meteorological work may greatly be enhanced by the use of IR pictures of a particular region, or of cloudiness if the pictures are obtained for the infrared spectral band. Their analysis is extremely important for the study of the dark side of the Earth; for the day side too they may furnish additional information. The practical use of TV and IR cloud photographs has been dealt with in Chapter 2. As far as geographical orientation and location of infrared pictures is concerned these operations are similar to those used for television pictures.

Bibliography

1. Borisenkov, E.P. Fiziko-statisticheskie metody analiza i predvychisleniya meteorologicheskikh polei (Physical and Statistical Methods of Analysis and Calculation of Meteorological Fields).— Trudy AANII, Vol. 263. 1963.
2. Kagan, R.L. and K.Ya. Vinnikov. Voprosy kartirovaniya radiatsionnykh izmerenii meteorologicheskikh sputnikov (Problems of Mapping Radiation Measurement Data Obtained from Meteorological Satellites).— Trudy GGO, Issue 166. 1964.
3. Bristor, C.L. Picture Gridding. Proceedings of the International Meteorological Satellite.— Workshop, NASA/Weather Bureau, Washington. 1961.
4. Dean, C. Grid Program for TIROS Pictures. Final Report.— U.S. Weather Bureau, Contract, No. CWB 10023. 31 March 1961.
5. Doolittle, R.C., L.J. Miller, and J.S. Ruff. Geophysical Location of Cloud Features.— Fin. Rep. on the TIROS I Meteorological Satellite System, TR R-131, NASA. 1961.
6. Electronic Plotter Draws Weather Maps.— Electronics. 16 December 1960.
7. Fujita, T. A Technique for Precise Analysis of Satellite Photographs.— Research Paper 17. Dept. of Geophys. Sci., University of Chicago. 1963.
8. Fujita, T. Outline of a Theory and Examples for Precise Analysis of Satellite Radiation Data. Mesometeorol. Project.— Research Paper 15. Dept. of Geophys. Sci. University of Chicago. 1963.
9. Fujita, T. Use of TIROS Pictures for Studies of the Internal Structure of Tropical Storms. Mesometeorol. Project.— Research Paper 25. Dept. of Geophys. Sci., University of Chicago. 1965.

10. Frankel, M. and C.L. Bristor. Perspective Locator Grids for TIROS Pictures.— Met. Sat. Lab., Rep., No. 11, Washington. 1962.
11. Glaser, A.H. TIROS Meteorology.— Allied Research Associates. Inc. Dac., No. ARA-954. 31 March 1961.
12. Grossman, G. An Operational Objective Analysis System.— Mon. Weath. Rev., Vol. 87, No. 10. 1959.
13. Hubert, L. F. TIROS I. Camera Altitude Data, Analysis of Location Errors and Derivation of Correction for Calibration.— Met. Sat. Lab. Rep., No. 5, U.S. Weather Bureau. 1961.
14. Hubert, L. F. Canadian Grids for TIROS I, Additional Orientation Data, Errata.— Met. Sat. Lab., Rep., No. 5, Washington. 1961.
15. Hubert, L. F. Camera Altitude Data, Analysis of Location Errors and Derivation of Correction for Calibration.— Met. Sat. Lab., Rep. No. 5, Washington. 1961.
16. NIMBUS Data Utilization Plan.— Met. Sat. Lab., Rep. No. 6. Washington. 1961.
17. Negley, R.M. On the Use of High-Altitude Cloud Photographs.— Florida State University Dept. of Meteorology, Scientific Rep., No. 2, Contract AF 19 (604)—1754.
18. Nordberg, W., W.R. Bandeen, B.J. Conrath, V. Kunde, and J. Persano. Preliminary Results of Radiation Measurements from the TIROS Meteorological Satellite.— J. Atm. Sci., Vol. 19, No. 1. 1962; NASA TN D-1338. 1961.
19. TIROS II Radiation Data Catalogue, Vol. 1.— Goddard Space Flight Center, Greenbelt, Maryland. 15 August 1961.
20. TIROS II Radiation Data. User's Manual.— Goddard Space Flight Center, Greenbelt, Maryland. 15 August 1961.
21. TIROS III Radiation Data Catalogue.— Goddard Space Flight Center. 1962.
22. TIROS III Radiation Data. User's Manual Supplement.— Goddard Space Flight Center. May 1962.
23. Technique for Precise Analysis of Satellite Data, Vol. 1: Photogrammetry.— U.S. Met. Sat. Lab. Rep., No. 14. Washington, 1963.
24. Contributions to Satellite Meteorology.— GRD Research Notes, No. 36, AFCRC-TN-60 427, June 1960; AFCRL-438, Vol. 1. 1961.
25. Widger, W.K., P.E. Sheer, and C.W.C. Rogers. Practical Interpretation of Meteorological Satellite Data.— Contract, No. A. F. 19 (628)—2471, Project. No. 6698, Task, No. 699802. September 1964.
26. Inter-Regional Seminar on the Interpretation and Use of Meteorological Satellite Data. Tokyo, 27 November—8 December 1964.— World Meteorological Organization, Japan Meteorol. Agency, Tokyo, Japan.

Chapter 4

THE PRACTICAL USE OF TELEVISION AND INFRARED PICTURES OBTAINED FROM METEOROLOGICAL SATELLITES

In this chapter, main stress is laid on cloud identification, analysis of extratropical cyclones, atmospheric fronts, ice and snow fields, and of mist and fog zones. Much attention is also paid to the tropical zone, particularly to tropical cyclones and to the use of meteorological satellite data in routine work. Cloudiness data obtained from satellite TV pictures have been most immediately useful in passing from the analysis of cloud fields and patterns to the analysis of other meteorological fields, e.g., wind circulation near the ground and at certain altitudes, study of jet streams, baric fields, etc. As is easily seen, satellite TV pictures are useful not only for cloud observations, but also for the study of many other meteorological phenomena. The possibilities afforded by satellite TV pictures are even wider when using IR data. However, the use of satellite-picture data becomes still more effective if we combine satellite data with other meteorological information; later in this text we shall illustrate this statement by practical examples on the use of satellite information.

4.1. GENERAL APPRAISAL OF PRACTICAL POSSIBILITIES IN THE INTERPRETATION OF SATELLITE TV CLOUD PATTERNS

At present, satellite TV pictures are currently used in routine weather forecasting.

Television equipment may operate in two modes: either in satellite storage or in immediate transmission of pictures.

In the first mode, data obtained from the first satellite orbit are recorded by the satellite storage memory from which they are transmitted to ground stations when the satellite passes within the radio-visibility range of the particular station. From the ground station these data are relayed to the National Weather Satellite Center, whence they can be transmitted via facsimile communication lines in the form of photographs to all interested agencies. Television tracking of cloudiness for all orbits provides an efficient global picture of rather high quality.

Satellite TV photographs are used in nephanalysis according to a special procedure. Nephanalysis is performed by a skilled staff which, using TV

pictures, should be capable of correctly estimating cloud distribution and some cloud features in accordance with a given system of gradation provided by the code (cf. Section 3.4). Nephanalysis data may be employed in the form of schematic cloud charts transmitted via facsimile communication lines or in the form of coded telegrams to be decoded at the given station and then to be transferred onto maps. At present, nephanalysis is an essential tool for the weather forecaster, particularly in regions with a sparse meteorological network.

In the second mode, satellite data (i. e., TV pictures) are directly transmitted from the satellite by-passing onboard data storage. However, these data have a local character since on the ground they may be received only for a time interval that is equal to the duration of direct radio visibility of the satellite at the given station or center. The area and sizes of such a range vary with the satellite TV equipment and the orbit height. At present, areas scanned by satellites have a width of 1,000–3,000 km and a length of 4,000–6,000 km. Data from such an area can be transmitted only from satellites provided with automatic picture transmission (APT). Such a system was installed onboard TIROS VIII and the NIMBUS series.

Information is transmitted in the shape of photographs of the mentioned local regions adjacent to the point viewed by the satellite. A ground-based data-acquisition station is rather simple and may be installed almost anywhere, even on ships.

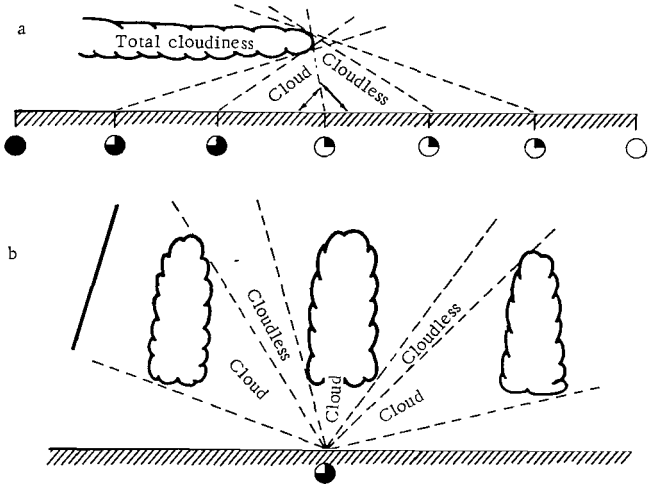

FIGURE 4.1. Schematic diagram illustrating the difference between cloud observations from (a) satellites and (b) the ground

If we compare satellite data with synoptic information, photographs obtained from satellites may be considered as an analog to ring-shaped (annular) charts. The great advantage of such data is that they may be obtained in the shortest time, in just a few minutes.

In principle, TV observations supply the following categories of information:

1) photographs transmitted by the National Weather Satellite Center via facsimile communication lines;

2) photographs of more or less limited regions scanned by the satellite APT; such photographs may be transmitted to a large circle of consumers;

3) results of nephanalysis transmitted in the form of coded telegrams, or via facsimile lines in the form of schematic cloud charts.

With these three types on hand, the meteorologist is in a position to correctly present a general and at the same time differentiated cloud pattern. Of course, photographs cannot be analyzed as the weather forecaster analyzes data from meteorological and aerological stations. From the example of the determination of cloudiness (Figure 4.1) it is seen that without accounting for specific features of satellite data, serious errors are likely to enter the analysis. The specific features of satellite data are self-evident. The vision field of a satellite is (at least) 100 times as large as the field viewed by a ground-based observer. Moreover, ground-based cloud observations to describe cloud patterns have a discrete character. On the other hand, satellite photographs yield an immediate overall cloud pattern which, after careful interpretation and decoding, may be broken down into separate features.

Another specific aspect is the difference in resolution between ground-based and satellite observations. As a rule, ground-based information has a higher resolution than data obtained from satellites. Even for an extremely skilled decoder, photograph decoding presents appreciable difficulties. It should be noted that satellite meteorology is still in its infancy, and methods as well as analysis principles are still in the making.

As far as the area covered by the satellite viewing field is concerned, we must take into account the following.

The satellite appears over one and the same region every 12 hours, i. e., twice a day, during which it may be either in the sunlit or in the dark side of the Earth. Hence, once per day it is possible to take satellite pictures from this region. At high altitudes, as a result of the overlapping of adjacent orbits, several successive photographs may be obtained from one and the same region spaced at a time interval equal to the rotational period of the space vehicle.

Most TIROS satellites had their orbit inclined at 58–65°. The trajectory* of such an orbit is shown in Figure 4.2. The quasipolar orbits of the NIMBUS series are shown in Figure 4.3. The viewing strip of the TV camera follows the trajectory. The width of the strip depends on the specific features of the TV equipment. For the TIROS series the strip was about 1,500 km wide.

As was shown in Chapter 1, the region of possible satellite scanning (viewing) varies over a period of 2.5 months (cf. Figure 4.4). Satellite passage over a particular region is therefore predicted for 7 days in advance and transmitted three times a week.

The scanned area and the resolving power of the satellite equipment depend (apart from the characteristics of the equipment) on the angle at which the given area is scanned (nadir angle).

Thus, for conventional camera lenses and a satellite height of 720 km the area covered by a single picture has a side of 1,500 km if the optical

* Here, trajectory denotes the projection of the satellite motion on the Earth surface.

axis of the camera is vertical (zero nadir angle). If the optical axis is inclined so that some part of the sky is scanned, the side of the scanned area varies from 2,200 to 2,300 km. At very large nadir angles the visible distance along the horizon may exceed 3,800 km. In such a case, however, the resolving power is greatly reduced and only large details can be distinguished on the picture; the errors in determining the geographical location of these details may reach considerable values. In practice, if 85–90% of the picture (scanning) area lies beyond the horizon, such an area (with a few exceptions) cannot be used, except with the greatest caution and due allowance for the above-mentioned distortions.

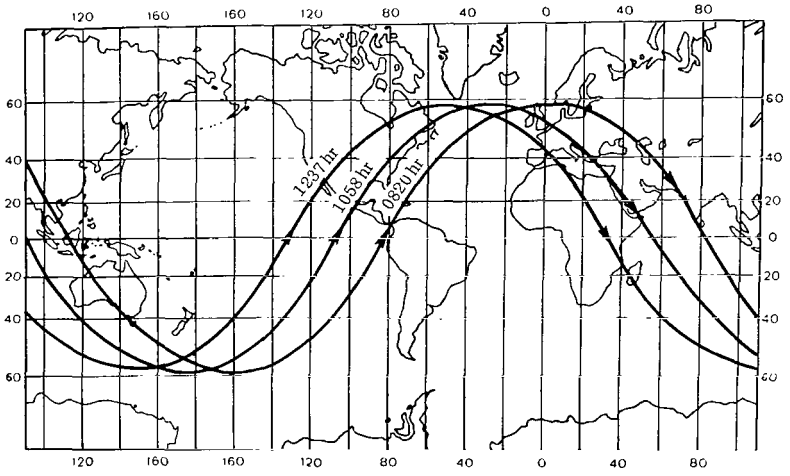

FIGURE 4.2. Trajectory of a satellite with inclined orbit

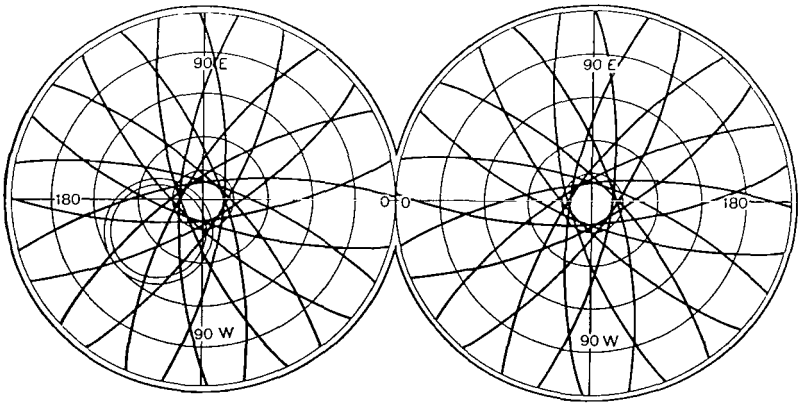

FIGURE 4.3. Quasipolar orbits of the NIMBUS satellite

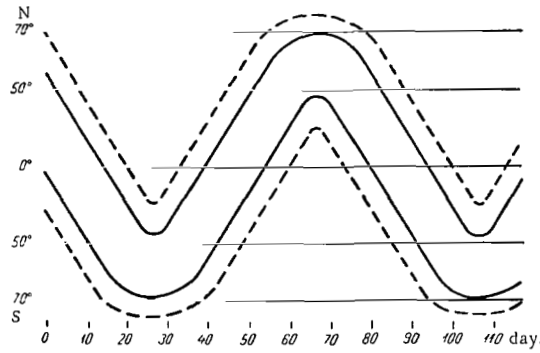

FIGURE 4.4. Diurnal variation in the satellite viewing (scanning) strip for an inclined orbit

In general, the errors in determining the geographical coordinates of a given terrestrial element, except for the above instances of large distortions, rarely exceed 2° latitude; the most probable errors are 50–60 km.

The NIMBUS satellite carried aloft three TV cameras. The optical axis of the central camera coincided with the vertical; the optical axes of the two cameras mounted on the side of the vehicle were slightly inclined with respect to the vertical. Figure 4.5 shows the area scanned by the three cameras.

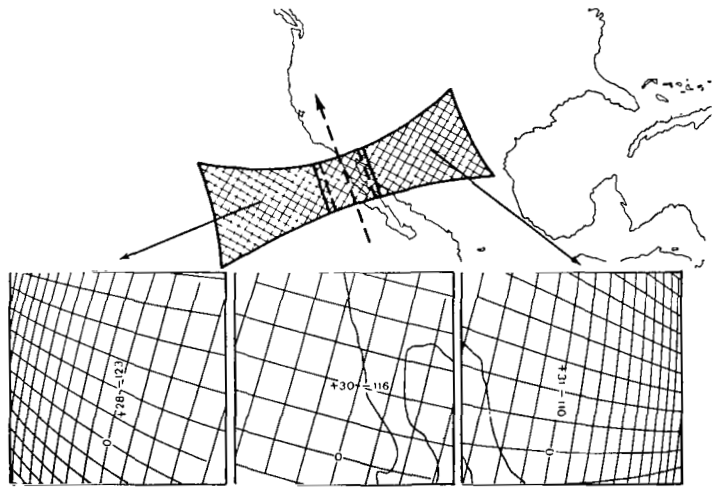

FIGURE 4.5. Area scanned by the NIMBUS satellite with lateral and central cameras

The geographical grid on the figures with intervals of 1° latitude and 1° longitude shows that for laterally mounted cameras distortions at the horizon may be rather large.

Additional distortions are due to the lens system of the camera, electron equipment and communication channels of the satellite, but in general they are negligible.

Limitations introduced by insufficient resolving power depend on the characteristics of the cameras, their position, and on the frequency of scanning lines (cf. Table 4.1).

TABLE 4.1. Resolving power of TV cameras as a function of nadir angle

Type of camera	Relative position	Resolving power, km
	TIROS	
Wide angle	Directly beneath the satellite center . . .	3.6
	Beneath the satellite, close to the picture edge	7.2
	Beneath the satellite, close to the picture corner	12.6
	$^9/_{10}$ of the image lies beyond the horizon	18.0
Narrow angle	Directly beneath the satellite	1.8–0.9
	Directly beneath the satellite near the picture edge	3.6
	Directly beneath the satellite near the picture corner	5.4
	$^9/_{10}$ of the image lies beyond the horizon	14.4
	NIMBUS	
Centrally mounted	Directly beneath the satellite	1.2
	Near the picture edge	1.4
Laterally mounted	Near edge of the picture	1.4
	Far edge of the picture	5.4
APT	Directly beneath the satellite	3.6
	Near the picture edge	7.2
	Near the picture corner	12.6

If the cloud bands are very narrow they are likely to overlap on the lines, thus misleading the decoder as to the direction of the cloud bands. Narrow cloud bands are usually well visible if they intersect the scan at an angle $\geqslant 45°$.

Identification of individual clouds or cloud elements is impossible if their sizes are smaller than the camera resolution. Decoding largely depends on the contrast and brightness of the scanned elements.

Contrast is the difference in brightness between two neighboring details, or between a given detail and its background. Contrast introduces certain limitations in picture decoding. The main difficulties arise if clouds are viewed against the background of a uniform snow cover, or if clouds of the upper level are viewed against the background of total cloudiness of the medium or the lower level.

Against the background of the land surface it is often more difficult to distinguish (decode) thin cirrus clouds than against the background of the sea surface because the land surface is slightly brighter than the sea.

Since the fields of small scattered cloud cells, the sizes of which are smaller than the resolution of the camera, form on the picture a bright veil similar to thin cirrus clouds, it is sometimes very difficult or even impossible to see them against the background of the land surface.

The brightness of a detail to be reproduced on a picture is an important characteristic in picture decoding. To a first approximation, regions differing in brightness may be classified as follows:

1) darkest areas – the space above the horizon;

2) dark regions – oceans, nonfreezing lakes, rivers;

3) dark-gray regions – areas of the continent, particularly if covered with forests or other vegetation;

4) bright-gray areas – thin clouds, small scattered cloud cells, bright sand and deserts, old snow (firn), and ice;

5) white regions – clouds of medium vertical-layer thickness;

6) very white regions – dense clouds of large vertical-layer thickness, particularly large cumulus clouds.

TABLE 4.2. Statistical evaluation of brightness characteristics in TIROS pictures

M_x	D_{xx}	γ_1	γ_2	R_{xx}	M_x	D_{xx}	γ_1	γ_2	R_{xx}
Space					Considerable cloudiness				
1.81	0.01	3.15	11.69	0.18	Above land				
1.65	0.62	8.17	71.76	0.25	4.75	6.52	2.18	5.97	—
1.57	0.23	—0.17	—0.27	0.75	11.29	44.72	0.65	—	—
Low cloudiness					12.95	114.19	0.91	—	—
Above sea					Above sea				
2.35	0.37	4.56	35.82	—					
2.27	1.89	4.21	21.06	—	6.88	16.92	1.56	—	—
2.38	0.64	2.94	19.39	—	25.15	210.15	0.28	—	—
2.52	0.78	1.44	4.02	—	16.11	101.96	0.71	—	—
4.42	11.45	2.34	9.39	—	16.24	158.33	0.97	—	—
Above land					Total cloudiness				
5.57	9.67	3.17	20.68	—	31.00	189.96	0.05	—	—
6.30	21.17	1.91	4.90	—	30.58	316.51	0.08	—	—
3.48	1.02	0.70	—0.05	—	29.81	156.18	0.40	—	—
5.68	14.17	1.72	4.03	—					

As was said above, contrast is an important characteristic in cloud investigations. Sonechkin classified the clouds by their brightness and contrast characteristics by subjecting 13 cloud pictures to photometric analysis and calculating the following parameters: mean brightness or the mathematical expectation M_x, brightness scatter (dispersion) D_{xx}, skewness γ_1 representing the deviation of brightness of given sign from its mean value, kurtosis γ_2 measuring the magnitude of deviation of a given sign, and the normed spatial correlation function R_{xx}.

Table 4.2 presents these parameters as a function of cloud type.

Each cloud type in Table 4.2 corresponded to 3–5 instances of

observation. As is seen from the table, the mean brightness M_x is the most characteristic quantitative parameter. Thus for outer space $M_x < 2$; for low cloudiness above sea $2 < M_x < 5$; above land $5 < M_x < 6$, etc. However, it is difficult to draw conclusions from the dispersion field alone, since noise dispersion increases considerably with signal dispersion. On the other hand, in practice cloud types cannot be determined from the correlation function. Skewness γ_1 and kurtosis γ_2 permit some conclusions on the general nature of pictures, but not on the cloud type. Parameters γ_1 and γ_2 are linked by an almost linear relationship. On the whole, the prevalence of positive values of the above parameters points to the prevalence of bright regions on the photographs.

Quantitative analysis of a few observations from TIROS shows that the number of cloud gradations as seen from the satellite pictures is clearly exaggerated, and does not correspond to the inherent possibilities of the satellite equipment if we only proceed from brightness characteristics. However, if such a quantitative analysis is performed using synoptic and radiation data it yields good results for various cloud types.

The quality of picture interpretation much depends on the time of day (whether day or night), scanning angle, and direction of scanned area with respect to the Sun. Thus, brightness varies four times during the day. Due to the effect of Sun-ray reflection the clouds appear extremely bright if viewed from the satellite oriented toward the Sun. This brightness is particularly pronounced if the normal to the reflecting surface of the cloud lies on the same line as the optical axis of the camera and in the direction of the Sun rays.

Some additional difficulties in picture decoding and interpretation are due to the specific features of the underlying surface.

Bright regions, such as snow fields, ice-covered lakes, sands, areas with solonchaks, deserts, etc., may be mistaken for cloud images. Darker lakes or rivers, if viewed through a uniform cloud cover of considerable thickness, may be taken for clouds of small thickness. Mist and stratiform clouds in river valleys may erroneously be mistaken for cumulus cloud cells.

This is why specialists who deal with the decoding of satellite TV pictures should know the specific features of the underlying surface as they appear during a particular season of the year.

The practical value of synoptic data obtained from satellites is likely to vary with the regions of the orbit, synoptic conditions, and the particular task of the meteorologist.

Thus, in general, a forecaster proceeding from conventional data is unable to infer on the nature and distribution of top clouds, whereas satellite observations permit such conclusions (which are very important for, say, aviation). For oceans and polar regions with their sparse meteorological network, satellite data permit the refining of the position of baric centers and fronts, their linear sizes, etc., in the absence of no other conventional data. This will be discussed later.

4.2. IDENTIFICATION OF CLOUDS ON TV PICTURES, AND THEIR RELATIONSHIP WITH SYNOPTIC ELEMENTS

The possibility of identifying a particular cloud type on TV pictures depends on the following factors:

1) the difference between the sizes of cloud elements and the sizes of the elements on the TV camera (the difference should be as small as possible);

2) difference in contrast between the cloud elements and the background of the underlying surface.

The brightness of cloud pictures (other conditions of photography remaining unchanged) depends on the reflectivity (albedo) /9/. Cloud albedo depends on the number, thickness, microstructure, and phase conditions of the clouds. Since microstructure and phase conditions are distinctive features of cloud forms, definite conclusions on them may be drawn from cloud-picture brightness. However, brightness of clouds of a given form may vary because of particular features of the cloud surface, varying thickness, and conditions of photography.

Thus, a reliable interpretation of cloud pictures needs, apart from brightness analysis, another identification index —structure of the image which is determined from the picture brightness contrast that exceeds the contrast threshold sensitivity of the television camera. It is clear that in determining the cloud structure, the nature of the cloud formations must be allowed for.

Analysis of TV pictures /9, 11, 23/ shows that cloud formations are characterized by a quite regular structure that corresponds to definite processes in the troposphere, mainly of synoptic and medium scale. Therefore, information on the regular character of medium- and particularly of synoptic-scale cloud systems is of primary importance in the diagnosis and prognosis of atmospheric processes. Since cloud systems are frequently conglomerates of differently shaped clouds corresponding to clearly expressed synoptic conditions, identification of individual cloud elements on the basis of an international classification often loses its own importance. Because of difficulties in identifying cloud elements on TV pictures according to standard techniques, meteorologist decoders, in their picture analysis, tended to identify a typical structure of cloud formations corresponding to typical synoptic conditions (e.g., baric formations, atmospheric fronts, air masses, etc.). Picture interpretation, if done in this way, simplifies cloud-form identification, thanks to the relationship between cloud forms and synoptic factors. Thus, e.g., once the typical structure of cold fronts is known, one can determine the individual cloud forms and their particular combination, or at least avoid rough errors when determining cloud forms.

Already the pictures of the first satellites disclosed numerous specific features and details of cloud formations /11, 23/. Later satellite launchings yielded many better quality pictures that permitted numerous details of earlier found structures to be refined and new details to be disclosed. However, we are still far from having a sufficiently close relationship between typical cloud structures as determined from satellite pictures and characteristic synoptic conditions for given geographical regions with which to fully use the information from satellite pictures.

Analysis of a large body of information from satellite TV pictures jointly with data from ground stations, aerial surveys, and synoptic charts made it possible to advance suggestions for the interpretation of cloud formations using satellite cloud pictures /23, 24/. Such an interpretation is based on

the determination of brightness, texture, structure, sizes and types of distribution of clouds on the pictures.

However, in using these recommendations one must bear in mind that typical cloud features, as obtained from satellites and ground stations, are by no means identical. This difference is determined by the inherent possibilities of the particular observation system. Data from satellite observations often cannot be recorded by the existing code system, which is sometimes inadequate even for coding ground observational data. It would, therefore, be impractical to limit the routine work to determine on satellite pictures those features that are necessary for the identification of cloud formations according to the international classification. Nonetheless, even with limitations introduced by the resolving power of the TV camera, photography conditions, and grouping of differently shaped clouds into a single cloud system, the intrinsic utility and superiority of satellite observations yield much valuable information.

1. Characteristic features for the identification of cloud forms according to the international classification

Upper-level clouds

Cirrus clouds (Ci — Photograph 4.1). Thin individual and scattered clouds remain unidentified. Identification is possible for large dense clouds or separate formations appearing as gray or sometimes white bands or streaks usually oriented toward the wind at the cloud level (Photograph 4.1a). The pictures also permit the identification of the wave structure of cirrus clouds; in general, cloud waves are oriented normal to the wind direction (Photograph 4.1b). The upper portions of the cumulonimbus capillatus clouds (Cb) have distinct cirriform elements (incus, anvil) and are oriented along the wind direction at their level; they are identified from the reduction in brightness of the Cb core in the wind direction (Photograh 4.1c).

Cirrocumulus clouds (Cc). Individual, small elements of this cloud type cannot be tracked. Large accumulations of Cc appear on the pictures as cirrus or cirrostratus clouds.

Cirrostratus clouds (Cs)—Photograph 4.2. They are tracked as a gray veil against the visible dark background of the underlying surface, while the dense Cs together with other denser and lower clouds (of the altostratus and stratocumulus types) are sometimes seen as a white veil.

Medium-level clouds

Altocumulus clouds (Ac) — Photograph 4.3. Only large elements can be seen. The pictures of separate elements often have different brightness varying from gray to white depending on cloud density, mutual

location and illumination. Combined with other cloud forms, Ac appears as a bright homogeneous zone.

Altostratus clouds (As) — Photograph 4.4. They are seen as a white compact cloud sheet and often appear as white formations together with nimbostratus clouds (Ns). It is difficult to see them against the background of an ice or snow cover.

Low-level clouds

Stratocumulus clouds (Sc) — Photograph 4.5. On the pictures they are easily identified, since they seldom appear as individual small elements. Their picture brightness varies from dark-gray to white depending on cloud thickness. Some individual cloud elements may form cloud "streets."

Stratus clouds (St) — Photograph 4.6. On the picture they appear as a gray or dark-gray dense layer. Clouds thicker than 300 m are white. Against the background of the underlying gray surface they are but little visible and are hardly distinguishable from fog.

Nimbostratus clouds (Ns) — Photograph 4.7. Large cloud formations of this type have a white or bright-white color.

Clouds of vertical development

Cumulus clouds (Cu) — Photograph 4.8. In fair weather, individual cumulus (of diameter $\leq$ 1 km) cannot be identified on the pictures.* On the picture their accumulations appear as mist formations of relatively low brightness. If the photographs are taken at small nadir angles, cumulus groups appear on the picture in the form of granules. The Cu structure varies only for regions close to the center of the picture. Then, parallel Cu bands are easily visible in the form of streets. Such a linear structure of Cu, however, disappears if Cu are located close to the horizon. Thick Cu are clearly visible as white formations on pictures taken with a narrow-angle camera. Individual tower-like Cu of diameter 1 to 4 km have the characteristic form of true Cu. With a distance between the visible elements of 10 to 30 km, the picture reveals cloud bundles, whereas separate elements cannot be distinguished. A combination of scattered tower-like Cu within the field of nondeveloped Cu or of a larger number of Cu appears on the picture as a spotted or mottled cover, but on too small a scale to be clearly visible.

Cumulonimbus clouds (Cb) — Photograph 4.9. If the cloud elements of this group are relatively large and if they are not covered by other cloud shapes, they appear on the pictures as bright nuclei of diameter 10 to 40 km, or as bright spots of diameter 100 km or more. The spots of large sizes are accumulations of individual Cb; their size on the picture is markedly larger, due to distortions during photography and the presence of dense Ci anvils. If the process of development and decay of Cb is associated with the formation of other cloud shapes (e.g., various Cu, Sc,

* If the television camera has a higher resolution, these forms can nevertheless be identified.

Ac, etc.), the cumuliform structure becomes somewhat diffuse, and then the existence of Cb can only be inferred from the spot-like shape of the cloud masses and from the sharp changes in brightness on the picture.

Frontal Cb, and those Cb that form in troughs, exhibit clearly visible (distinctive) features on the pictures. Combinations of continuous Cb, uniform in shape and almost of equal horizontal sizes, appear on the picture as massive bright nuclei that form a single, very long cloud system (sometimes up to several hundreds of km). Although each such single system has a rather uniform structure, and therefore its individual elements are hardly visible, the convective nature of this cloud group is easily revealed from the teethlike contour of the cloud boundaries and from the uniform brightness of the various sections.

2. Specific features of the medium-scale cloud structures

Conover /11/ classified clouds by their external appearance into two main groups: cumuliform and noncumuliform clouds. The clouds of each group were then subdivided by their shape into banded or nonbanded; from satellite pictures taken with the wide-angle and narrow-angle cameras he determined the typical features of the more detailed medium-scale structure.

On the strength of comparative interpretation of satellite pictures, ground-station data, and aerial photographs, the following seven types of medium-scale cloud structure were established:

1) cumuliform clouds of the nonbanded type, seen as straight or slightly bent strips;

2) cumuliform clouds of the nonbanded type in the form of dense cells;

3) cumuliform clouds of the nonbanded type in the form of hollow cells or half-moon (semicircular) shape;

4) vermicular (zigzag-shaped) clouds of the banded cumuliform type;

5) noncumuliform banded clouds;

6) nonbanded fibrous clouds of the noncumulus type;

7) nonbanded nonfibrous clouds of the noncumulus type.

Figures 4.6 and 4.7 present schematic diagrams of the interpretation of cloud pictures taken with two TV cameras, No. 2 a wide-angle camera and No. 1 a narrow-angle camera. With the aid of these diagrams cloud pictures are identified according to four brightness gradiations: dark gray, gray, white, and very white. The diagrams reproduce the cloud-element sizes and the intervals between the elements. The diagrams are illustrated with typical photographs, shown in Photographs 4.10 (camera No. 1) and 4.11 (camera No. 2). The numbers of the circles in Photographs 4.10 and 4.11 refer to the images selected and are entered in the respective columns (in parentheses) in Figures 4.6 and 4.7. Photographs 4.10 and 4.11 are shown uncorrected. Hence, for the determination of the image scale, each photograph is provided with mutually perpendicular sections, the relative length of which shows the picture—inclination angle with respect to the optical axis of the camera. The short section between the point of

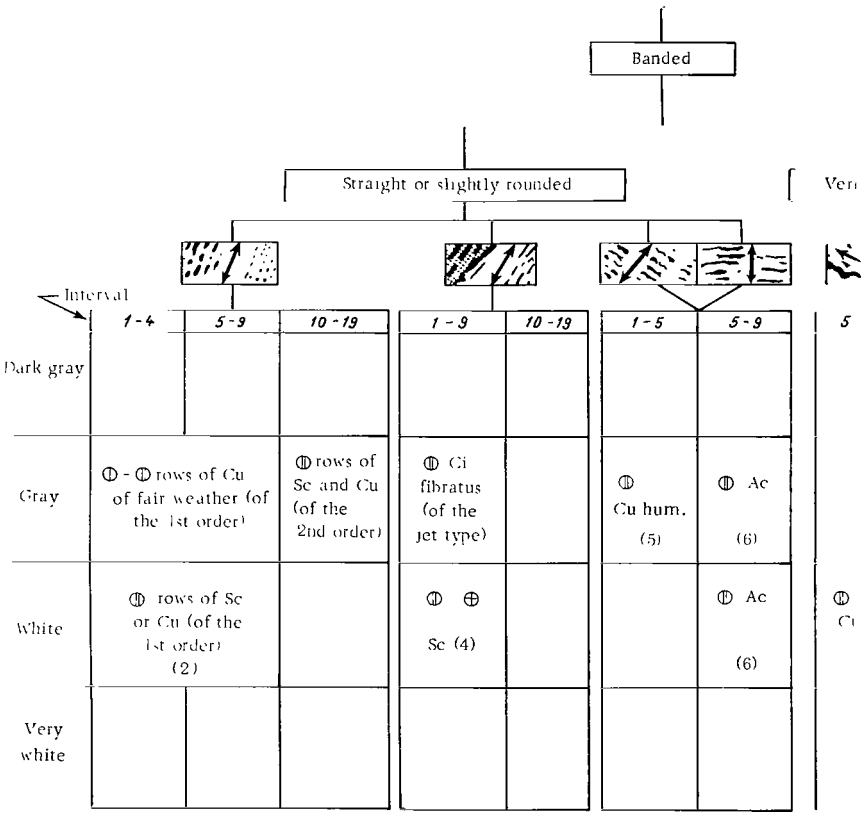

FIGURE 4.6. Schematic diagram of cloud interpretation of satellite pictures taken with narrow-ang

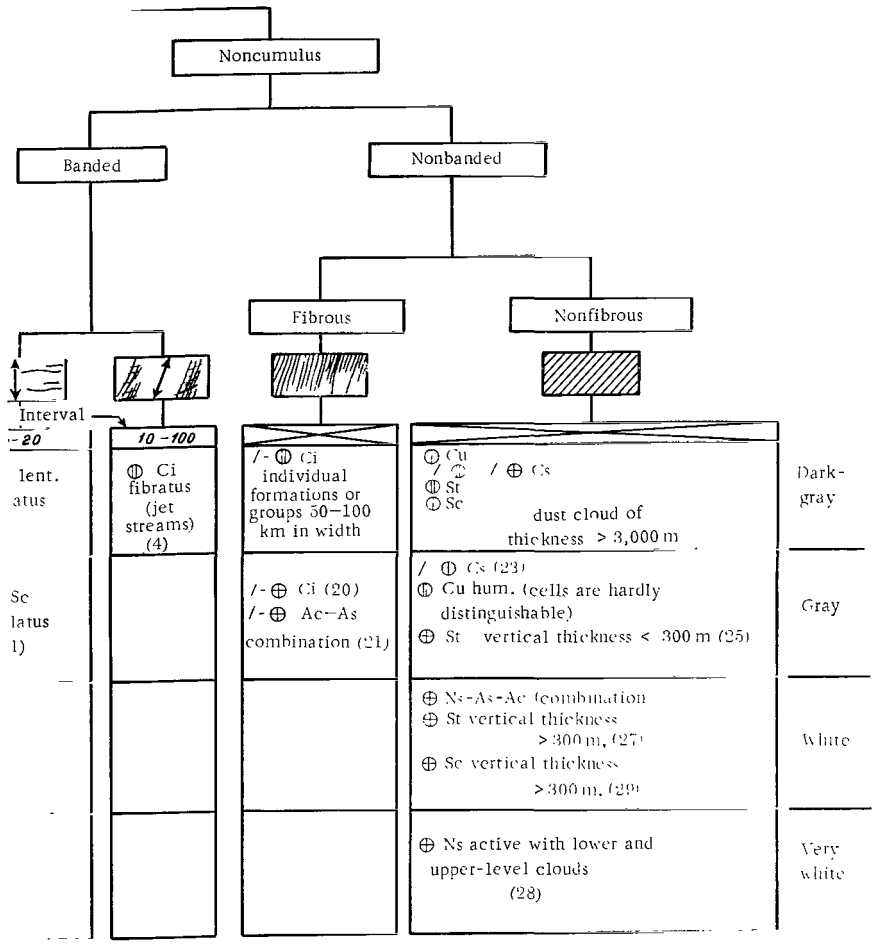

5143/202-203b

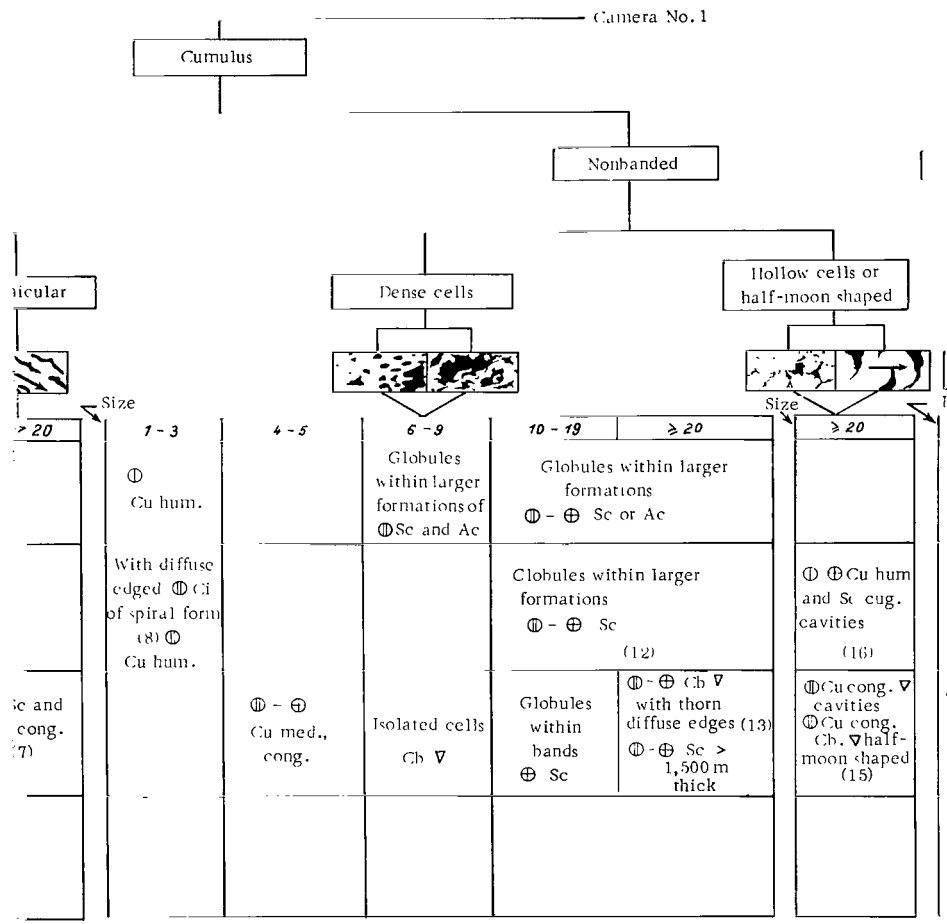

e camera No. 1 onboard TIROS III

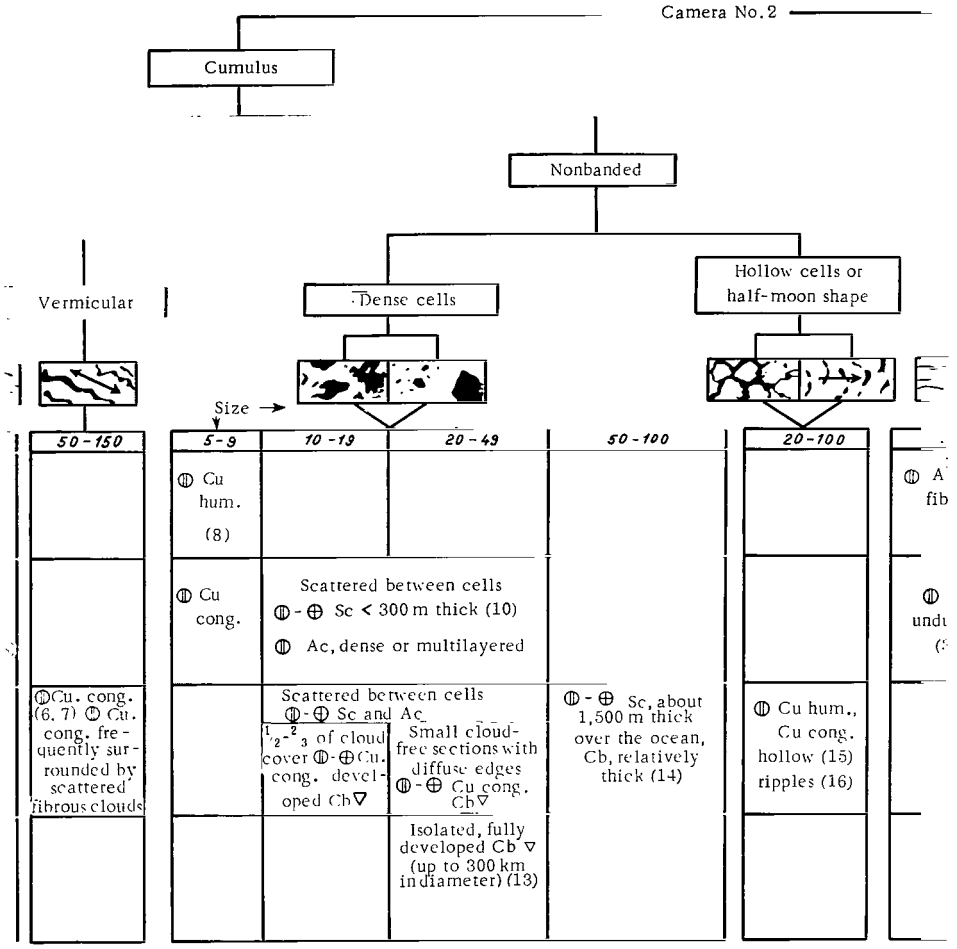

-angle camera No. 2 onboard TIROS III

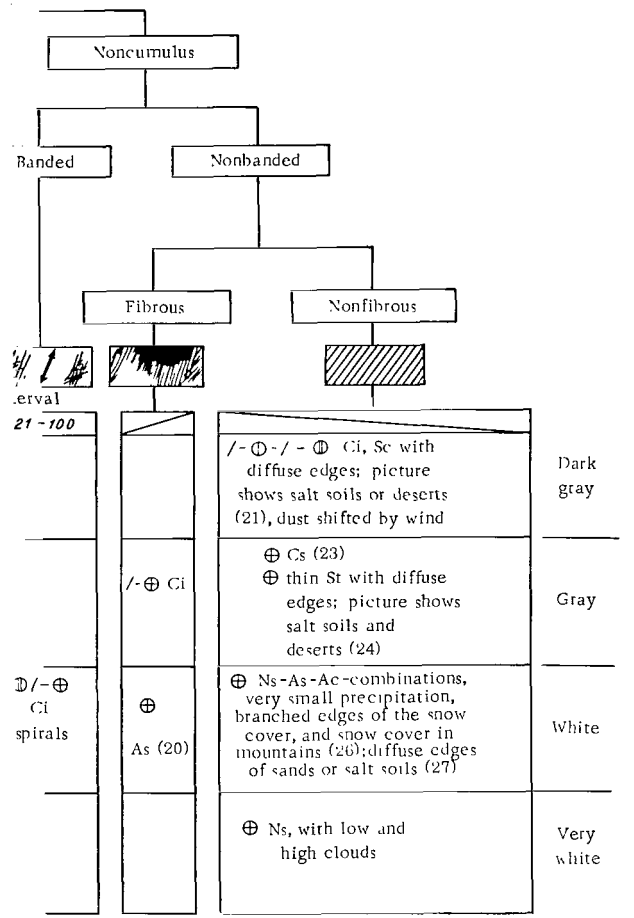

5143/202-203a

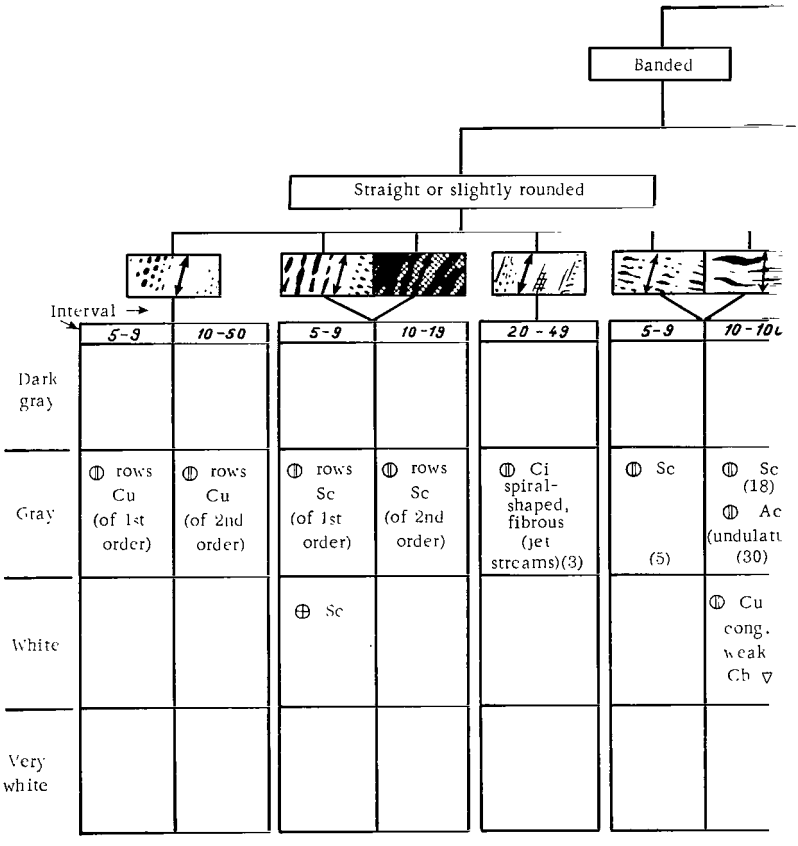

FIGURE 4.7. Schematic diagram of cloud interpretation of satellite pictures taken with wi

intersection with the long section is oriented toward the horizon. The approximate length of sections on Photograph 4.10 is 20 km, and 200 km on Photograph 4.11.

Let us now dwell on the specific features of medium-scale cloud structures using data in /11, 23/.

1. Cumulus in the form of straight or slightly bent bands. This type comprises some variants of Cu, Cb, Sc, and Ci clouds. The elements of these clouds form bands with a variety of structural details that depend on the atmospheric processes. The bands are characterized by the sizes and form of cloud elements, the distance between the rows and chains and by their sizes. Slight differences between the cloud-band structures are linked with specific conditions of cloud formation.

Depending on the band orientation with respect to the wind direction at the level of the upper cloud boundary, the above cloud system is subdivided into parallel and normal (transverse) types. Clouds, the bands of which are parallel with the wind direction or with the direction of the vertical displacement of the wind in the convective layer, belong to the parallel type, while clouds, the bands of which are normal to the wind direction, are called normal clouds (usually, the direction of wind displacement in the convective layer coincides with the wind direction at the level of the top cloud boundary).

The parallel type of clouds is generally formed by small, closely spaced cloud elements of Cu humilis. The normal type is more frequently found with undulated Sc and well-developed elements of Cu and Cb spaced by gaps of several tens of km. The Ci bands on the warm side of jet streams appear as cumulus clouds and belong to the parallel type. Bands of these Ci should not be taken as Cb anvils of cirrus clouds, which may be more than 100 km from the principal bright core of Cb in the direction of the stream.

The first four sketches in Figure 4.7 (camera No. 2) illustrate the structure of parallel clouds: three sketches characterize the transition from lines of individual rounded cloud elements of Cu and Sc to the continuous cloud sheet consisting of bands which have not yet become rounded; the fourth sketch shows the structure of fibrous jet-stream Ci. The fifth and sixth sketches represent clouds of the normal type. The congested clouds of the normal type on the fifth sketch are much wider than the clouds of the parallel type. The sixth sketch shows cumuliform clouds with large intervals between them. Since the edges of the clouds are diffuse, they can easily be mistaken on the pictures taken with camera No. 2 for clouds of noncumulus shape.

In Figure 4.6 (camera No. 1) the first and second sketches represent the parallel type of Cu and Sc clouds: the first sketch shows rows of the first order having intervals of 2.5 to 3 km; the second sketch shows rows of the second order with a length of about 150 km spaced 15—20 km apart. The first-order rows could not be identified in the pictures taken with camera No. 2. Frequently, rows of the second order consist of converging, strongly developed rows of the first order. Photograph 4.10 (No. 2) shows rows of flat inversion-type Sc.

2. Cumulus clouds of the nonbanded type in the form of continuous cells. This cloud type is formed by sparsely scattered or uniformly distributed Cu, Sc, Ac, and Cb (Photograph 4.12). Well developed Cb are identified on the pictures from the attenuation of picture

brightness in the direction of wind (transition from very white to gray). Very often, bright, large formations of developed Cb are surrounded by a ring of small, less developed clouds.

3. Cumulus clouds of the nonbanded type in the form of hollow cells or of a half-moon (semicircles). The cells consist of ring-shaped pure cumulus and towering cumulus clouds with an inner diameter of 20 to 50 km (Photograph 4.13). At their inner side, the rings are cloud-free or else Cu elements of the weak convective type may be seen.

The pictures show that clouds may accumulate in the form of a half-moon of radius about 50 km. The half-moons are spaced 30—50 km apart (Photograph 4.14). At places of most intensive convection, the contour of the cloud rings and half-moons may be upset as a result of the formation of large clouds (of area more than 200 km^2).

Clouds of annular shape were noticed with no marked vertical shift of the wind in the convective layer; clouds in the form of a half-moon were observed with small shift of the wind.

4. Vermicular (zigzag) banded cumulus clouds. This type is characteristic of low latitudes. Photograph 4.15 shows Cu and Sc clouds. The wind in the convective layer may change from weak to strong with a direction close to that of the vermicular elements of clouds. Figures 4.6 and 4.7 show the sizes of this structure.

5. Banded clouds of the noncumulus type. This type consists of waves of Sc, Ac, and Ci clouds spaced 5—20 km apart (Photograph 4.16), as well as of jet-stream clouds in the form of smoothed bands at intervals of 10—100 km.

6. Nonbanded fibrous clouds of the noncumulus type. This type is mainly formed by Ci on the warm side of jet streams. On the pictures, clouds of this type appear almost like Ci clouds observed from the ground (Photograph 4.10, No. 20). Fibers of gray shade extend in the direction of the wind. Such a structure is produced by large horizontal wind displacements. Sometimes, Ci on the warm side of jet streams occur as a single band 50—150 km wide. Thin As may also appear on the picture as fibers of a white shade (Photograph 4.10, No. 21).

7. Nonbanded, nonfibrous clouds of the noncumulus type. This type comprises large-area clouds and dust:

1) Ns—As cloud systems of large vertical development (thickness) appearing on the picture as white and very white shades (Photograph 4.10);

2) gray and dark-gray Cs and thin St (Photograph 4.10, No. 23);

3) white dense St and Sc;

4) dust clouds of thickness greater than 3 km.

Multi-layer clouds of large vertical development appear on the picture as a continuous white veil. Due to the amorphous structure, the images of such clouds can hardly be seen against the background of the underlying surface (snow, ice, deserts, etc.) which has a reflectivity similar to that of these clouds.

3. The structure of large-scale (synoptic) systems

Interpretation of TV pictures yielded a series of typical forms of cloud systems characteristic of synoptic atmospheric processes /23, 24/. These forms appear on the pictures as:

1) spiral clouds or cloud vortices;
2) cloud masses in the form of "commas";
3) principal cloud bands;
4) fields of convective synoptic-scale clouds;
5) fields of stratiform clouds of synoptic scale;
6) large fields of homogeneous microscale cloud cells or of medium-scale clouds (mesoscale bands and rows).

The above types do not reflect the great variety in cloud organization of the large-scale system, and therefore cloud pictures cannot always be related to a more or less general and standard classification.

Let us dwell more in detail on these types.

1. Spiral clouds or cloud vortices. This type is more frequently connected with cyclones in moderate latitudes, and with cyclones, storms, and hurricanes in tropical regions. Cloud spirals, as elements of a cloud system, are more typical of moderate-latitude cyclones in the stage of occlusion and filling, and may be found in horizontally and vertically well developed tropical cyclones. Evolution of cyclones goes hand in hand with evolution of the spiral structure of clouds associated with these cyclones (Photograph 4.17).

Spiral clouds or cloud vortices of relatively small sizes are a frequent phenomenon. In moderate latitudes they are linked with the following processes:

1) secondary cyclonic disturbances at the periphery of deep and extensive troughs at the cold fronts, and less frequently at the warm fronts, as well as at occlusion points;
2) cyclonic disturbances caused by orographic effects;
3) existence, in old filled cyclones, of stratocumulus and convective clouds.

Small-size cloud vortices in tropical regions correspond to tropical cyclonic disturbances and are of smaller scale and intensity than tropical cyclones; they also correspond to disturbances of the atmospheric current at heights that favor conditions of cloud formation. More details on cloud vortices are found in Section 4.5.

2. "Comma" type cloud masses. This type reflects the principal cloud system of cyclones during their initial stage of occlusion. The comma shape of these clouds corresponds to a definite character of the baric cyclone field: the cyclone has a well developed low, with a clearly expressed baroclinic zone, and cyclonic circulation at the 500-mb contour (Photograph 4.18a). In this case, an annular cloud vortex can easily be tracked over the higher cyclonic region while the cloud bands, extending from the ring, are located in front of the low-depth axis. If there is no annular cloud vortex above the cyclone eye which might be due to insufficient vertical development of the cyclone, the main cloud system of the cyclone assumes the shape of a half-moon (Photograph 4.18b). This cloud type is characterized by the absence of extensive cloud systems in the rear region of the cyclone.

3. Principal cloud bands. This cloud type is connected with the following synoptic elements:

1) tropospheric fronts;
2) secondary cold fronts;

3) prefrontal squall (instability) lines;

4) convergence and instability of cold air in the rear part of the cyclone;

5) zones of basic convergence in tropical latitudes;

6) jet streams.

Depending on the synoptic conditions, the principal cloud bands differ in size and structure (Photograph 4.19).

4. Fields of convective synoptic-scale clouds. This group comprises first and foremost the fields of convective clouds in the form of different sized cells in the cold air at the rear part of the cyclone. Because of the different vertical development (thickness) and sizes of individual or grouped clouds, this cloud type tends to form regions of mottled structure (Photograph 4.20).

As we depart from the cold front, cumulus clouds gradually assume a cell-like structure. While grouping, these clouds form arcs (domes) and sometimes circles with a diameter of several tens of km.

5. Fields of stratiform synoptic-scale clouds. In the pictures, this group appears as a wide zone of stratiform clouds. These fields are usually observed during the cold season of the year in the northern and western periphery of anticyclone areas in the warm and humid atmosphere, in warm sections of cyclones and in the northern area of oceans.

6. Large fields of homogeneous types of microscale (cloud cells) or medium scale cloud systems. This type includes internal clouds, the uniform structure of which can be tracked over large geographical regions; this type permits conclusions on the nature of developing synoptic processes:

1) convective cloud cells, pointing to instability in the lower atmosphere and to stability in higher layers (Photograph 4.21a);

2) medium-scale structure of cumulus clouds and of more unstable air masses (Photograph 4.21b);

3) internal clouds, the structure of which to a large extent depends on the underlying topography (Photograph 4.26).

4. Specific features of medium-scale cloud structure connected with orographic effects

Medium-scale cloud disturbances caused by orographic effects on cloud formation, clearly visible on cloud pictures, are of particular interest in weather forecasting. Some of these disturbances were first seen on satellite pictures.

These cloud types are classified as:

1) cloud bands not linked with atmospheric fronts on the windward side of mountain ridges;

2) individual, broken clouds, or gaps in the cloud sheet on the leeside of the mountain ridge, provided there is a considerable or continuous cloud cover on the windward side of the mountains;

3) cumulus clouds, formed by ascending vertical air currents above the mountain ridge (crest clouds);

4) "latent" waves — cloud formations due to wave motions of air currents above mountain regions;

5) isolated lenticular clouds (mountain-wave clouds);

6) cumulus fibrous clouds resembling in their shape converging streams;

7) large, extensive, individual cloud lines over ocean islands;

8) boundaries of cloud zone, coinciding with the coastline;

9) fog, and low stratiform clouds, formation and evolution of which is connected with the underlying relief.

The processes of cloud formation on the windward side of mountain ridges and the phenomenon of foehn on the lee side are clearly seen on weather charts. However, in this case satellite photographs afford a clearer and fuller picture of cloud distribution (Figure 4.8).

Crest clouds (Photograph 4.22) mainly result from cumulus clouds, and their accumulations from stratocumulus clouds and individual cumulonimbus clouds. In their formation, apart from ascending currents of dynamic character over mountain ridges, thermal convection developing under the action of relatively warm mountain slopes plays a prominent role.

Crest clouds may be distinguished from cumulus streets by their configuration, similar to the topography of the particular mountains; crest clouds cannot form at strong winds oriented normally to the mountain ridge. Usually, crest clouds form in a layer 300—1,000 m above the mountain ridge, except for some individual, more developed clouds. On the photographs, crest clouds are hardly distinguishable from the snow cover in mountains.

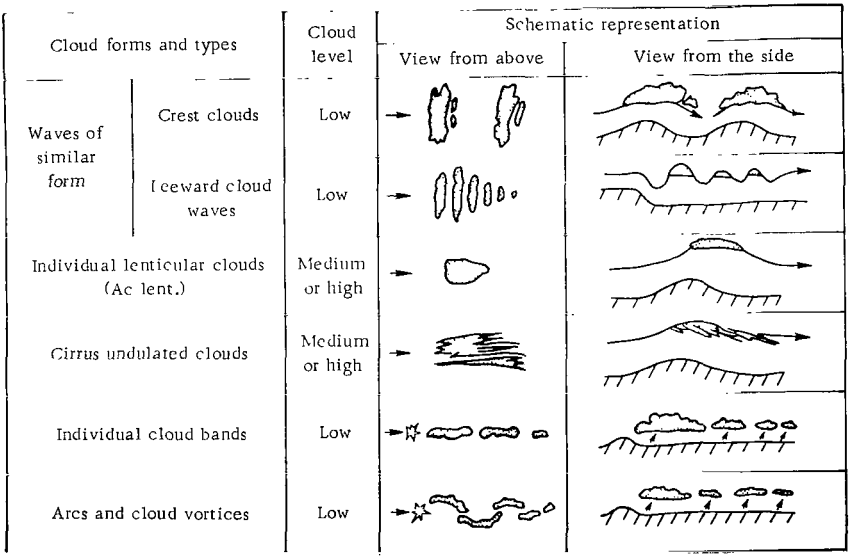

FIGURE 4.8. Schematic diagram of some conditions for the formation of medium-scale cloud over mountain regions

Latent clouds are seen on satellite photographs as parallel, closely and uniformly located cloud bands or billows. Such bands are oriented almost normal to the air current and parallel with the mountain ridges, even if the height of the latter is not considerable. The top of such clouds does not exceed 3,000 m above the elevation of the particular area.

Latent Sc and Ac form as a result of wave movements of the air mass caused by the underlying relief and by the vertical shift of the wind. An indispensable condition for the formation of waves is the considerable effect of wind, oriented normal to the folds and irregularities of the relief. The length of such waves varies from 5 to 20 km.

There is a definite relationship between wave length and mean wind speed in the 10-km layer above the friction level; this relationship, also confirmed by satellite observations, is expressed by the formula /23/

$$\overline{u}=6\lambda+12,$$

where $\overline{u}$ is the mean wind speed (expressed in knots) at the 850—200-mb layer; λ is the wave length (nautical miles) determined from the clouds.

At the leeward side, the base of such clouds lies about 1,000—3,000 m above the area elevation, while the vertical development (thickness) varies from 300 to 600 m.

Isolated lenticular clouds of the mountain-wave type initially form as rather strong cumulus clouds, around which less thick clouds form at the same time. These clouds, being displaced together with the air current under the effect of wave motions, assume a lenticular shape (Photograph 4.23). The clouds can be observed at rather large heights (up to 6 km) and their vertical development may reach or exceed 500 m.

In photographs of mountain relief with a strong wind oriented to the mountain ridge, individual formations of fibrous clouds could be observed in the upper troposphere at heights of 6—7 km; these formations resemble convergent clouds (Photograph 4.24). They are the result of a forced uplift of air to heights of 6—7 km when there is no visible drift of wind in direction and speed.

Individual extensive cloud lines form above islands under the action of the warmer underlying surface of islands compared with the surrounding ocean (Photograph 4.25).

Medium-scale phenomena in low stratiform clouds and fogs in mountain, coastal, and ocean areas (in the absence of other cloud types) are often clearly seen on satellite pictures. Frequently, satellite data are the sole source of information in determining the boundaries of fogs or low stratiform clouds in these areas. The utility of information gathered from pictures or nephanalysis charts naturally depends on the accuracy of geographical orientation and location of the pictures, and on a knowledge of relief details (configuration of valleys, coastlines, etc.).

In view of the rather sparse observation network in sea and ocean areas, weather charts cause considerable difficulties in determining cloud transformations at the boundary between land and sea (ocean). Here, satellite data are of great help. Since such transformation processes are dealt with extensively in the literature, satellite data, while yielding additional information on such transformations, are extremely useful for

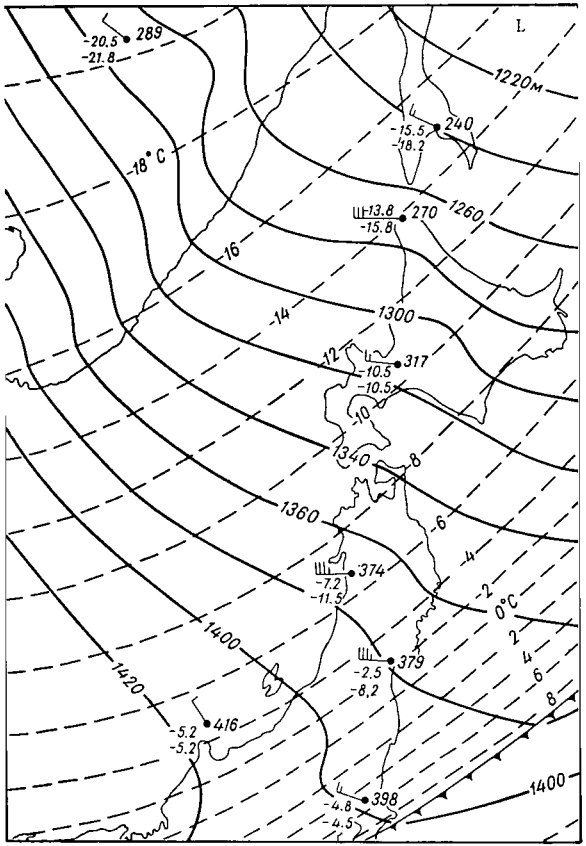

FIGURE 4.9. 850-mb chart at 0000 hr on 14 January 1964

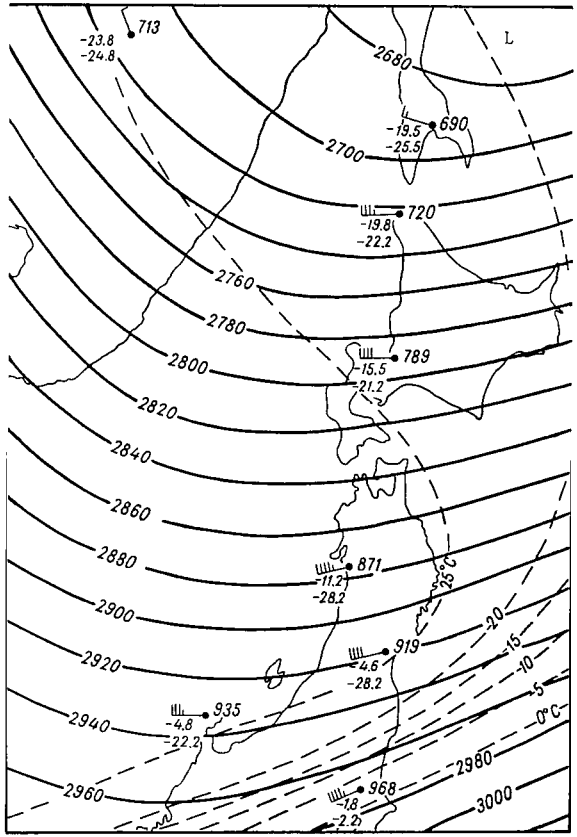

FIGURE 4.10. 700-mb chart at 0000 hr on 14 January 1964

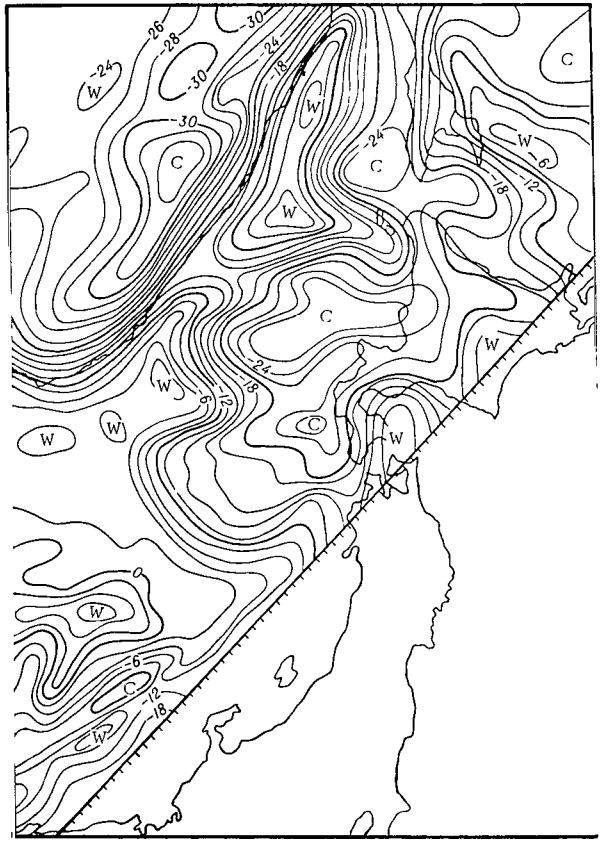

FIGURE 4.11. Chart of outgoing radiation in the 8—12-μ band (channel 2) according to measurement data between 0022 and 0028 hr on 14 January 1964 (measurements from TIROS VII, orbit No. 3085)

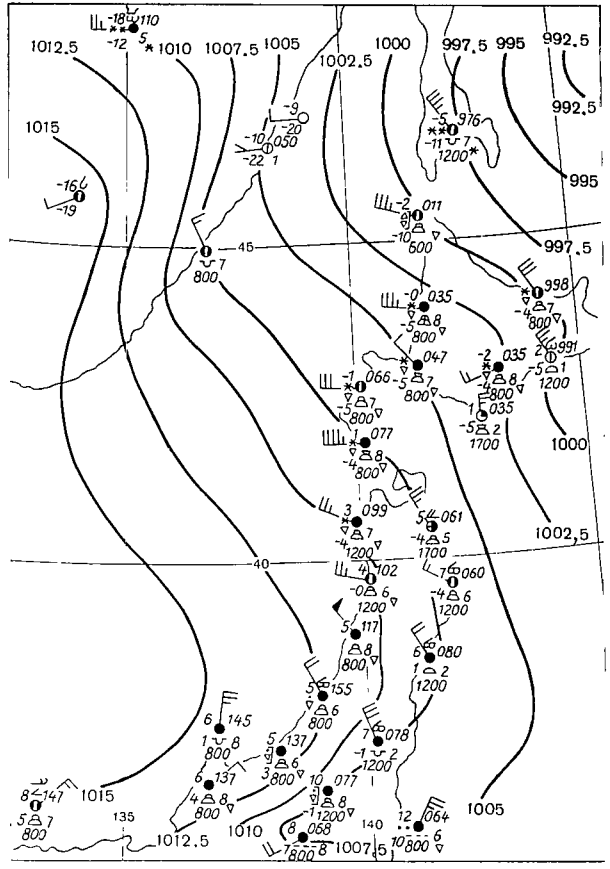

FIGURE 4.12. Bottom-layer weather chart at 0000 hr on 14 January 1964

understanding atmospheric processes at these boundaries (cf. Examples 1 and 2 below).

Two instances of a Far-East monsoon (14 and 20 January 1964) may illustrate the potentialities of satellite picture information.

First example. 14 January 1964 (Figures 4.9—4.12; Photographs 4.26 and 4.27).

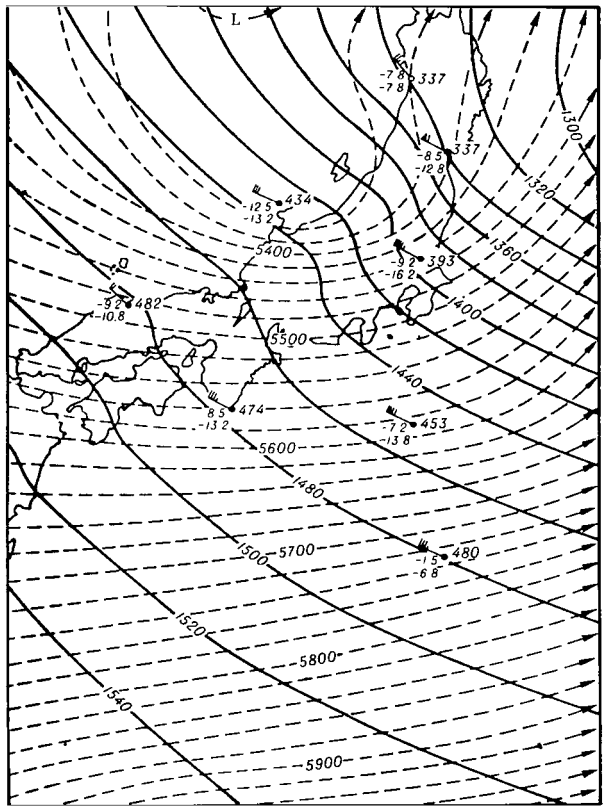

FIGURE 4.13. 850-mb chart at 0000 hr on 20 January 1964

Three frames of the cloud pictures (Photograph 4.26) and the generalizing chart plotted from these pictures (Photograph 4.27) show the distribution and structure of clouds above large geographical areas. Along the sea coast at Sikhote Alin above the sea, a cloud-free band of width 100 km can be noticed. The band is produced by the dynamic heating of the air under the action of descending currents on the leeside of the mountain ridge. At this distance from the coastline and farther in the direction of the air current at the 850-mb level (Figure 4.9), we can see narrow, closely-spaced cloud bands. The bands are obstructed by the southern part of Sakhalin Island,

where the mountains reach a height of about 1,000 m. At the eastern coast of the island there is another cloud-free region. Convective clouds tend to form in front of the southern part of Hokkaido Island with its relatively weak monsoon.

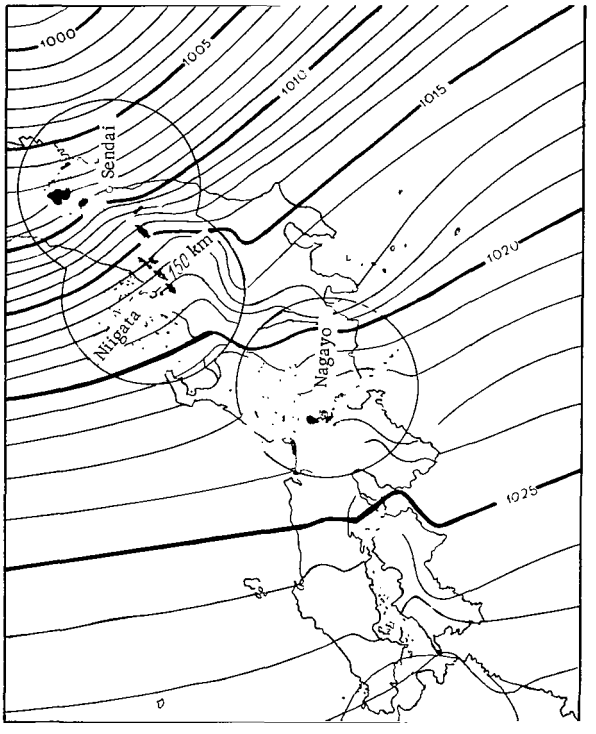

FIGURE 4.14. Nuclei of vertically strongly developed clouds, according to radar data at 0000 hr on 20 January 1964

The thermobaric field at the 700-mb level (Figure 4.10) is characteristic of descending vertical currents above the central region of the Sea of Japan; the top boundary of the clouds was found to be at a height of about 3 km. If one takes into account that the cloudiness is total and compact, the lowest cloud-surface temperatures (-24 to -26°C) correspond to a height of about 3 km (Figure 4.11). Along the coast of the Sikhote Alin area with its cloud-free band the temperature above the ocean surface is near zero; here, a small cloud band can be noticed. The cold low between Sakhalin and Hokkaido islands corresponds to the established cloud pattern. The chart of infrared radiation reflects, on the whole, the temperature conditions of both the underlying surface and the clouds.

This example is rather typical and permits us to conclude that the winter monsoon in the above region causes the formation of cloud bands in the top zone below 3 km. These bands extend in the direction of the air current at the 850-mb level. The weather chart in Figure 4.12 permits these data to be compared and checked.

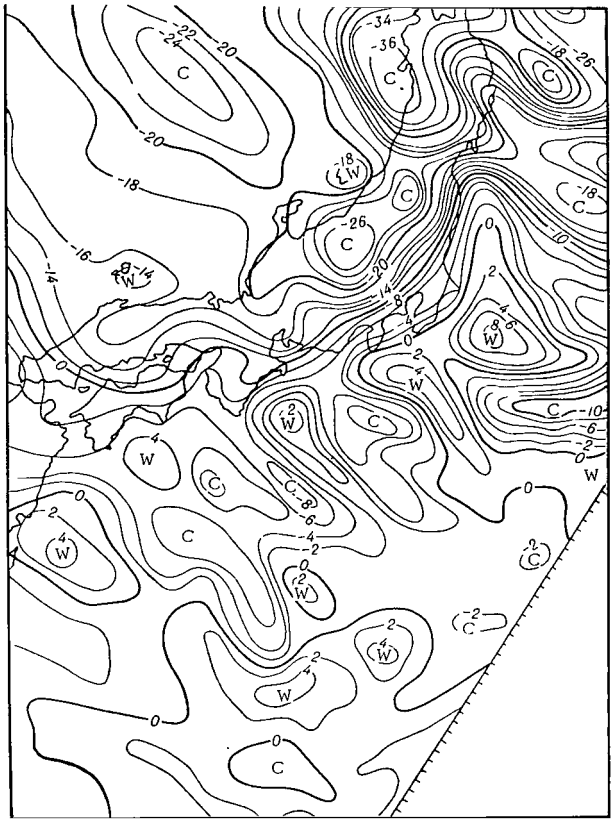

FIGURE 4.15. Chart of outgoing radiation in the 8—12-μ band (channel 2) according to measurement data between 2335 and 2336 hr on 19 January 1964 (measurements from TIROS VII, orbit No. 3172)

Second example. 20 January 1964 (Figures 4.13—4.17; Photographs 4.28 and 4.29). This example refers to a monsoon period in which the wind speed, measured at some stations of Honshu Island, exceeded 12 m/sec.

The factual material in this example may be used for independent study. For this purpose one must determine the utility and potentialities of the pictures for the determination of cloud structures above the Sea of Japan, Honshu Island and its coasts, and in the western and southern islands of the Pacific Ocean, in order to estimate the effect of topography and underlying surface on the formation of clouds of different structure (this particularly refers to clouds of vertical development over islands and their coasts).

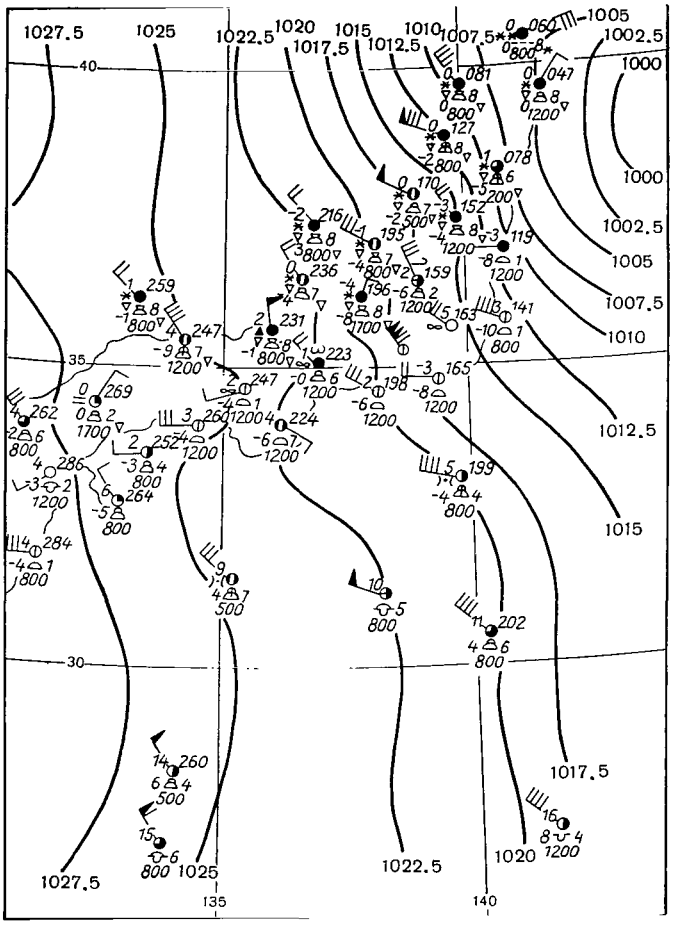

FIGURE 4.16. Bottom-layer weather chart at 0000 hr on 20 January 1964

4.3. IDENTIFICATION OF ICE, SNOW, AND FOG FROM SATELLITE PICTURES

Nearly 10% of the Earth surface is covered with glaciers and sea ice. If all this ice were to melt (the volume of which is about $26.7 \cdot 10^6 km^3$ /21/) the level of the World Ocean would rise by 70 m. This again points to the considerable interest in satellite pictures with information on the icecap of the Earth mantle. When considering the water and heat budget of the Earth we must allow for the advance and recession of glaciers, the boundary of continuous sea ice sheets, icebergs, etc. The latter is particularly important in sea navigation. At present, information on the icecap is obtained from airborne ice surveys, which are not carried out regularly and also scan only a few percent of the area covered with ice. Since the

main mass of ice is concentrated in remote areas, information obtained from satellites moving in quasipolar orbits might be extremely valuable.

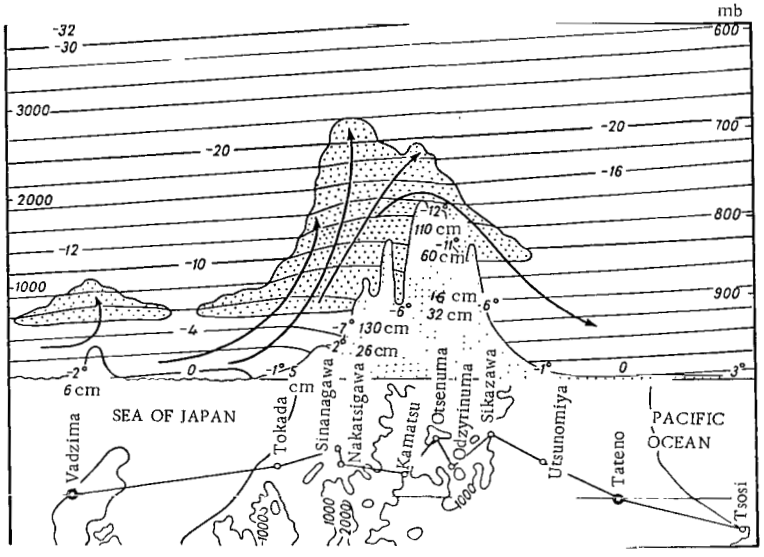

FIGURE 4.17. Vertical section of the atmosphere at 0000 hr on 20 January 1964

The authors of /26/ calculated the economics of satellite data in ice survey and reconnaissance. They found that in 1961, the U.S.A. Navy spent 400,000 dollars on ice survey from aircraft in obtaining the required data. Another 6,650,000 dollars were spent on providing data for the navigation of icebreakers. Canada spent about 3,500,000 dollars for airborne ice survey and icebreaker operation.

A tentative estimate carried out by the Ice Service showed that some ice data obtained from aircraft could easily be received from satellites. In this case satellite information reduces the overall expenses, as it diminishes by 40% the frequency of aircraft flights for data collection. Another 10% saving may be made by reducing the number of icebreaker cruises for ice surveys. Thus, satellite ice information has not only scientific, but also great economic importance.

According to an ice classification outlined in /8/, the ice cover is classified into sea ice and continental ice (Table 4.3).

A continuous ice sheet linked with the coast, or in shallow sea water with the sea bed, is termed inactive ice.

For practical purposes it is sometimes necessary to determine numerous ice characteristics. However, since there is but little experience as yet in satellite ice observations, it is too early to state which of the ice characteristics can and cannot be identified on satellite pictures. It is clear that many of the above ice characteristics cannot be determined from a satellite. Nevertheless, satellite ice observations can and will be useful,

as satellite equipment is steadily being improved and more experience in satellite ice observations is gained.

TABLE 4.3. Characteristics of ice fields

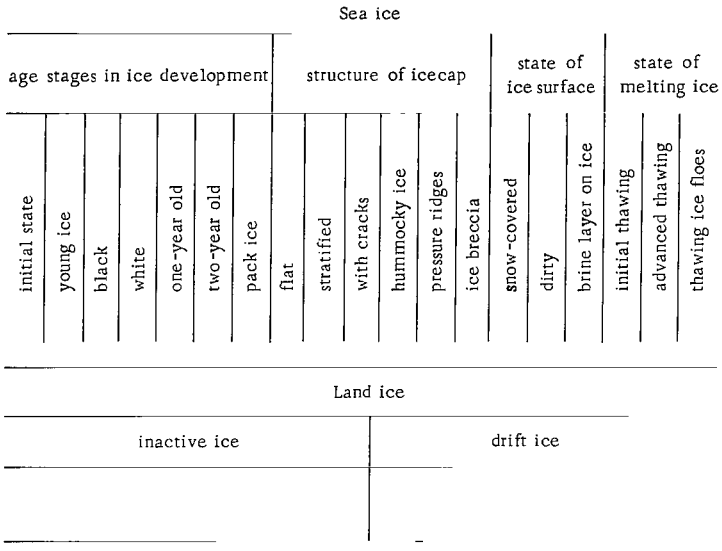

The greatest difficulty in interpreting satellite ice pictures arises when we try to distinguish between a cloud and snow-ice cover, or if we want to identify a particular ice field covered by a cloud sheet. This is why we are unable to determine such ice elements as: age of icecap, existence of snow layers, hummocky ice cracks, etc. Only some general features of the ice (or snow) cover, or its boundaries, can reliably be determined from satellite ice pictures.

During winter and summer, sea ice can be observed from the satellite in the polar regions of the Northern and Southern hemispheres; during winter, it can also be observed in the nonfreezing regions of other seas /22, 23/.

Airborne ice observations have been compared with satellite observations for the regions of the St. Lawrence Bay, Hudson Bay, Sea of Okhotsk, Hokkaido Islands, and the coast of the Antarctic.

Sea ice can be distinguished from clouds by its clear white surface which, unlike the cloud surface, is rather stable in time; another distinctive feature is the sharp contour of the edges, pointing to the existence of open (ice-free) spaces within the icecap.

On satellite pictures, ice-covered lakes usually appear as clear, white spots, even if the transparency of the icecap might be affected by a possible snow layer or by its roughness.

Frozen lakes may be distinguished from clouds by comparing the shape of the white area seen on the picture with the corresponding geographical shape of the lake.

Photograph 4.30 is a satellite picture showing how frozen lakes can be identified.

Snow cover in mountains is easily identified on satellite pictures if it is absent on the adjacent lowland area. In this case, the snow cover appears as an extensive white spot coinciding with the contour of the underlying terrain. If mountain ridges alternate with valleys, the photograph shows a corresponding alternation of bright and dark bands; this permits the snow cover to be easily distinguished from clouds, particularly during the warm season.

Like ice fields, the snow cover is more stable in time than cloud fields. Therefore, analyzing cloud-field pictures taken successively for several days permits the evaluation of position and configuration of both the snow and ice covers, except for periods of thawing or intensive snowfall. Nonetheless, and despite the rapidly changing cloudiness, one can identify areas covered with snow or ice, a fact of particular importance for practical purposes, since no other observations afford so many details as do satellite pictures. However, the decoder should know the geographical, topographical, and other features (e.g., vegetative cover) of the area. Thus, e.g., in his analysis of snow-cover distribution he might be misled by zones of evergreen forest, which have a darker shading than the surrounding open areas. Such details must be suitably allowed for in any picture analysis.

Let us now examine a joint analysis of satellite and airborne ice observations conducted by the Canadian and U.S. Weather Bureaus /22/. According to /22/, charts of schematic analysis of ice fields have the following symbols:

Amount and features of ice

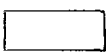 — absence of ice

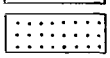 — below 1

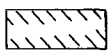 — from 1 to 4

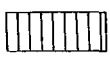 — from 5 to 7

— from 8 to 9

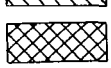 — continuous icecap

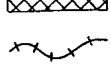 — cracks

— open, ice-free spaces

The extent of cloud cover as seen on ice-survey charts is designated by the following symbols:

○ — below 1

◐ — from 1 to 4

⦶ — from 5 to 9

⊕ — total cloudiness

V — varying cloudiness

⌒⌒⌒ — limited visibility of cloudiness

····· — limited visibility of cloud boundaries

The charts also have some additional (letter) symbols:

A — age of ice, if determined
IC — ice crystals
SL — sludge ice, ice slush
GRS — wet ice
PNK — fast ice
LYPD — white ice interlayers
J — young ice
W — winter ice

The symbols sometimes appear as a fraction; then, if the numerator has the letter *A*, the denominator contains the ice features. For example, $\frac{A}{W}$ and $\frac{A}{8W2J}$ reads as follows, respectively: 1 winter ice; 8 winter ice and 2 young ice. Sometimes, the letters are provided with subscripts, e.g., $\frac{C}{N_1 N_2 N_3}$, where C is the total extent of ice, N_1 is the cracked ice, N_2 is a small or medium amount of ice floes, and N_3 is a large amount of ice floes or ice fields.*

Figure 4.18 shows an ice chart. In the following, an example is discussed of the above-mentioned joint analysis for observations on 22 March 1961.

Figure 4.19 shows a rectangular strip in the region of Newfoundland and Anticosti islands covered by satellite observations. Figure 4.18 also shows a schematic presentation of ice-survey results. To the west of Newfoundland near Anticosti Island, the extent of the icecap is rather large (up to 7—9), the ice being mostly of the winter type. An area of clear water is seen SW of the island coasts. To the west of 62° longitude, no ice-survey data were available. Photograph 4.31 shows a satellite picture covering the observation strip shown in Figure 4.19. The third photograph (from the right) refers to the SW end of Newfoundland Island; the picture clearly shows the coastline, and a small area of ice-free water also seen on the ice-survey chart. Nearer Anticosti Island there are zones of an almost continuous icecap. The seventh and eighth frames show the extreme end of Anticosti Island; to the south of this extends a region of clear water, a fact that could hardly be inferred from airborne data alone. The eighth frame shows the northern extremity of the peninsula and a small ice area. In the bay there is also a zone of clear water.

* The Ice Service of the USSR uses a different system of symbols on ice charts. At present, the possibility is being discussed of creating an international system of ice symbols.

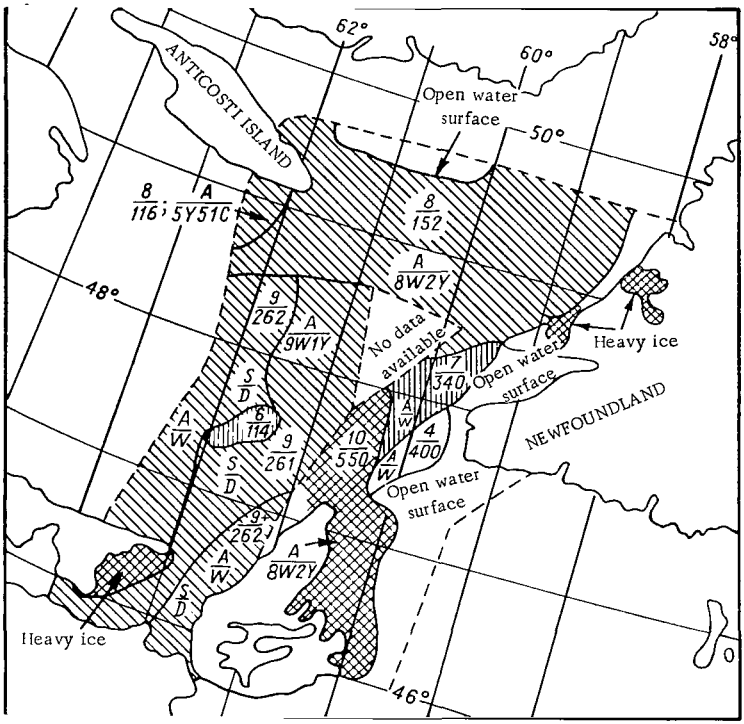

FIGURE 4.18. Chart with data from airborne ice survey on 22 March 1961

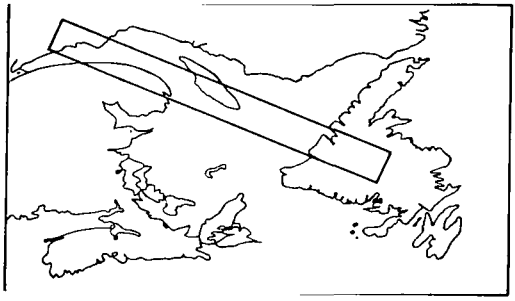

FIGURE 4.19. Satellite-observed strip on 22 March 1961

EXERCISE I

Determination of ice fields from satellite observations

Photograph 4.32 shows a picture from TIROS VI (orbit No. 3227, April 1963) above the St. Lawrence Bay.

Sequence of work

1. Determine the coast outline in the lower part of the picture against the darker background which delineates the boundary between the coast and the shore ice.

2. Determine the area of shore ice in the lower part of the picture.

3. Determine the layered cloud cover in the left top part of the picture.

4. Refine the coast outlines in Photograph 4.33, which shows the same region two days later (orbit No. 3241). Determine the area of shore ice and the zone of clear water on both this and subsequent pictures.

5. Compare the white fields in the top parts of Photographs 4.32 and 4.33, and estimate the nature of the ice fields observed in this part of the picture (clouds, snow, or ice fields are also seen).

6. Examine again Photograph 4.34. It shows the same region photographed on 17 April, in the interval between the two already examined pictures but at a larger nadir angle.

7. Refine the shore line and determine the shore-ice zone. Note how differently the nadir angle alters the viewed zone of the icecap. Estimate the distortion in the linear scale of the viewed field introduced by this change.

In the lower part of Photograph 4.34, Anticosti Island is clearly seen against the dark background of the open-water zone. Compare the outline as seen in the picture with the actual geographical outline of the island.

We now consider the identification of fog.

On weather-satellite photographs, fog is not easily distinguishable from stratiform or stratocirrus clouds, often even from the underlying land surface, and also instances in which on the picture fog converges with clouds or forms immediately beneath the cloud cover.

Fortunately, there are a series of factors (darker background of the underlying surface, relief features, conditions of photography and radiation data) that sometimes permit the clear identification of fog.

This is illustrated by the fog picture taken by TIROS VII (orbit No. 735) over a region in the North Pacific. The pictures were taken at an optical camera angle of about 30° (Photograph 4.35) /24/.

Analysis of the photographs was made easier using an auxiliary chart (Photograph 4.36), that contains reproductions from the photographs and a picture of the Aleutian Islands with the elevations of highest relief points of the island (in m). The strips on both the photograph and the auxiliary chart are similar in structure to stratocirrus clouds; the strips are blocked (delineated) by the islands. The largest strip, shown in Photograph 4.35 by four arrows, is blocked by the western half (highest part) of the island with an elevation of 120 m; the lower half of the island, almost 10 km wide, is obscured by the above strip. The obstruction of the strips by the islands may be explained only by the presence of a southwestern advection of fog or low stratiform clouds. The heating up of the eastern part of the island is insufficient to disperse the fog, while the low elevation of the island does not permit its obstruction (blocking). The fog strip is usually oriented parallel with the vertical drift of wind, in other words, it is oriented almost in the direction of the geostrophic wind (as shown on the surface chart).

The eighth frame in Photograph 4.35 along 172 and 173°E shows a dark narrow strip, the appearance of which may be explained in a twofold manner: as a clearance (gap) between clouds or as a shadow cast by high clouds on lower clouds. The correct answer can be obtained from data on the relative position of the Sun and satellite at the instance of photography, i.e., from the position of the antisolar point. When the antisolar point is projected onto

high clouds or close to their edge, the dark line (if it is actually the shadow) should disappear on the picture (Photograph 4.37).

The series of photographs (Photograph 4.37) confirm the fact that the dark strip disappears if the antisolar point is near it as a result of the satellite moving along its orbit. The dotted circle about the point AS designates the angle of the particular element scanned by the satellite (10° from the point AS). Two clouds indicated by single and double arrows can be tracked on each frame; it is then seen that the dark strip — the boundary between these two clouds — disappears near the antisolar point.

FIGURE 4.20. Chart of outgoing radiation in the 8–12-μ band (channel 2) according to measurement data from 0320 to 0322 hrs on 8 August 1963 (TIROS VII, orbit No. 735)

The chart of outgoing radiation (Figure 4.20) showing the thermal pattern of the underlying ocean surface and the existence of haze and cloudiness, confirms the results of picture interpretation: the zone of large temperature gradients coincides with the shadow cast by the clouds on the surface of the fog; the temperature at the top boundary of the main fog strip is several degrees below the temperature of that part of the fog-free ocean. The surface weather chart in Figure 4.21 serves to check the data of picture interpretation.

EXERCISE 2

Determination of sea fog near the Aleutian Islands

Sequence of work

1. Carefully analyze Photograph 4.35 to determine the structure of the various images, with particular stress on the cloud bands and their

blocking; in other words, try to determine the clear boundaries of the gaps between cloud bands.

2. Using the auxiliary chart (Photograph 4.36), study the blocking of the cloud bands by islands with stress on the large cloud band indicated by four arrows (Photograph 4.35), this strip being blocked by the western part of the islands at elevation 120 m (Photograph 4.36); this is done to identify the fog and the direction of advection.

3. Identify the existence of the shadow strip on frame 8 (Photograph 4.35) between 172 and 173°E using frames 8 through 11 (on Photograph 4.37).

4. Compare the chart of outgoing radiation (Figure 4.20) with the auxiliary chart for the interpretation of pictures of fog strips, high clouds, and shadow strip; this is done to check and confirm the results of the preceding interpretation.

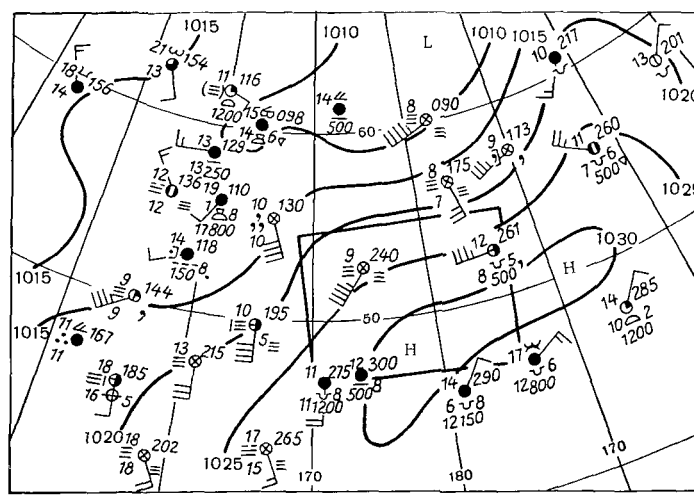

FIGURE 4.21. Surface weather chart at 0000 hrs on 8 August 1963

5. Compare the results of this analysis with the data on the surface weather chart (Figure 4.21).

4.4. DETERMINATION OF CHARACTERISTICS OF EXTRATROPICAL CYCLONES

The following is an analysis of extratropical cyclones. The study in /10/ presents a division of such cyclones into six classes.

Table 4.4 shows the number of instances used in this analysis and the characteristics of the six cyclone classes.

The classification in this table as well as that presented later in this text is almost identical with the classification proposed by N. L. Taborovskii and Kh. P. Pogosyan.

Thus, according to /7/, there are four stages in cyclone formation: the first or wave stage corresponds to class E1 (in Table 4.4); the second or

young stage corresponds to class E2 and to some extent also to class E3; in the third [mature] stage the cyclone reaches its maximum development (corresponding to class E4 and partly to classes E3 and E5); the fourth stage is characterized by cyclone filling, and corresponds to class E5.

TABLE 4.4. Classes of extratropical cyclones

Code letter	Development stage	Number of instances
E1	Frontal wave	3
E2	Preocclusion state	1
E3	Beginning occlusion	9
E4	Occluded cyclone	17
E5	Fully occluded cyclone	30
E6	Filling cyclone	16
	Undetermined	30
		Total 106

The above analysis was conducted in the following order:

1) comparison between the position of cloud vortices and low-pressure centers near the ground;

2) comparison between the position of cloud vortices and the high-level center of the low-pressure region near the 500-mb level;

3) determination of deviation of pressure and height of the 500-mb level from the standard values for the region of cloud vortices, allowing for the effect of season (the correlation was established for the various stages of cyclone evolution).

However, certain difficulties arose in these investigations. For extratropical cyclones it is very difficult to determine the first three stages (classes E1, E2, and E3); for tropical cyclones it is difficult to determine stages T1, T2, and sometimes T5 (cf. Section 4.6).

In the above analysis, particular attention was paid to the photographs of those regions where, according to other indexes, we could have expected the formation of cyclones; but even so, the determination of early stages was difficult for the following reasons:

1) the time during which the developing vortex is in its initial stage is much shorter than for later stages, however, these early stages may sometimes be an excellent index of cyclone development during the next few hours;

2) in the early stage, poorly developed cloud systems may partly or completely be obscured by another, also less well-developed system;

3) cloud systems in their early stages are so poorly visible that they may easily be misrepresented and misunderstood in their analysis at the data-reception center.

Another difficulty in the above analysis was connected with the lack of (synoptic and aerological) data on regions for which satellite pictures were available. For extratropical cyclones the position of low-pressure centers at the 500-mb level, and sometimes the position of these centers near the sea surface, was often uncertain, either due to noncoincident observation times or due to lack of data, particularly for oceans.

TABLE 4.5. Evaluation of correctness in the determination of class of extratropical cyclones

Class according to nephanalysis	Finally determined class after repeated analysis							Total number of instances
	E1	E2	E3	E4	E5	E6	undetermined	
E1	2	1	1	—	—	1	5	10
E2	1	—	1	—	1	—	1	4
E3	—	—	3	3	3	3	6	18
E4	—	—	—	13	5	1	13	32
E5	—	—	4	1	19	5	4	33
E6	—	—	—	—	2	6	1	9

Class according to photographs	Finally determined class after repeated analysis							Total number of instances
	E1	E2	E3	E4	E5	E6	undetermined	
E1	2	1	—	—	—	—	5	8
E2	1	—	2	—	—	—	2	5
E3	—	—	4	4	2	—	7	17
E4	—	—	—	12	1	1	9	23
E5	—	—	2	1	20	3	6	32
E6	—	—	1	—	7	12	1	21
Total number of instances	3	1	9	17	30	16	30	106

The next step in the analysis was dividing the cyclones according to classes (as shown above) using TIROS data both for nephanalysis and the facsimile transmission of satellite pictures. Analysis was done to see how well the nephanalysis data reflect the visual pattern and development stages of the cyclone and how correct was the estimate carried out by an experienced analyst. The results of this analysis are presented in Tables 4.5—4.7.

TABLE 4.6. Total evaluation of correctness in determining the particular phase of extratropical cyclones

	Number of instances	Percent of instances of the determined class	Percent of instances of the total number		Number of instances	Percent of instances of the determined class	Percent of instances of the total number
According to nephanalysis data				According to picture data			
Determined correctly . .	43	57	41	Determined correctly . .	50	66	47
With an error of ± class .	62	82	58	With an error of ± class .	70	92	66
Total determined instances	76	100	72	Total determined instances	76	100	72
Total number	106	—	100	Total number	106	—	100

TABLE 4.7. Instances of extratropical cyclones for which a statistical analysis has been performed

Class	Number of instances
1	3
2	1
3	7
4	14
5	22
6	12
Total number of instances	59

The analysis showed how easily two neighboring classes may be mistaken and, therefore, division of cyclones at such stages is unreliable.

The present state of nephanalysis performance and interpretation may still require much development, but nevertheless much useful information may be obtained. Of the 106 instances for analysis, 47 (for various technical reasons) were excluded from statistical processing. The remaining 59 instances distributed by phases are shown in Table 4.7.

In line with the main task of satellite-data utilization for analyzing regions for which no other information was available, attention was paid to the oceans, particularly to their southern regions for which tropical cyclones were analyzed; but even for moderate latitudes above the ocean, for which the position of baric centers had to be determined with a view to finding the synoptic conditions, the U.S. National Weather Satellite Center used stations spaced 500—800 km apart, and in some cases even 1,500 km. On the other hand, the diameter of the first closed isoline in the baric formations observed from these stations does not exceed 450—500 km.

In using satellite data, the analyst should determine the position of baric formations relative to the center of the cloud vortex. For this purpose, recourse was made to all available and reliable data, including ship observations.

Statistical determination of the centers of baric formations

For the statistical determination of the position of the center of baric formations (pressure patterns) the available data were not sufficiently reliable but nevertheless some conclusions using data in /23/ could be drawn. When processing the starting data we noted the position of the centers of (surface and high-level) pressure patterns with respect to the center of the cloud vortex. The results of this analysis are presented below.

1. Class 3 (onset of occlusion). In this phase of cyclone evolution cloudiness is better developed at the lower and central levels of the troposphere than in its upper levels.

2. Class 4 (occluded cyclone). As is seen from Table 4.7, statistical analysis was performed for 14 instances of this class. Of these, eight

instances permitted the position of the ground center to be determined using additional data. In five instances the position of the center at the 500-mb level was determined with sufficient reliability, and only in one instance could the position of both the surface and high-level center be determined with sufficient reliability.

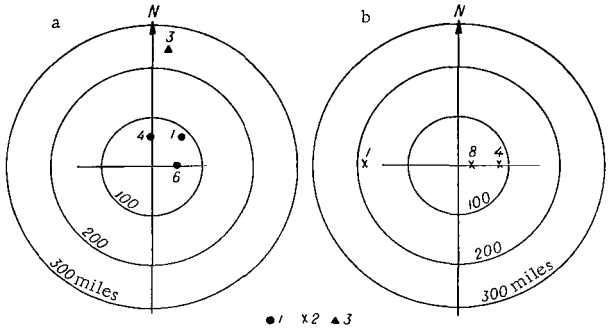

FIGURE 4.22. Position of centers of baric formations relative to the center of cloud vortices (class 3):

a — position of cyclone center at sea level relative to the center of the cloud vortex; b — position of high-level baric centers relative to the centers of cloud vortices; 1 — position of cyclone center; 2 — position of high-level baric centers; 3 — refined position of centers.

Figure 4.23 presents the mutual position of the centers. According to Figure 4.23a, b, only in three instances was the distance between the centers larger than 200 miles (350 km); in two of them the position of the centers, as determined from the initial synoptic analysis, is rather doubtful. At the 500-mb level a distance between the centers larger than 350 km was noticed for two instances; in one instance the synoptic analysis is doubtful. For the first instance use was made only of synoptic data, while for the second instance the position of the center was determined by interpolating data from remote stations.

The above analysis reveals a regularity according to which the center of the cloud vortex lies slightly S or SW of the high-level center.

Figure 4.23c, d shows the slope of the cyclone axis for the investigated instances. As expected, with predominant westerlies in the Northern Hemisphere, the high-level centers are shifted to the North (with respect to the surface centers), and there are almost no instances in which they were shifted to the South.

3. Class 5 (fully occluded cyclone). On the photographs this type is more easily identified than other types. As may be seen from Figure 4.24, in 19 out of 22 investigated instances the distance between the baric centers and the center of the cloud vortex did not exceed 350 km.

One of the three remaining instances could be connected on the picture with the second cloud vortex (but it was not noticed on the nephanalysis); the other two instances were connected with insignificant circulation

currents near the Earth surface and at certain heights, and had no link with high-level or surface centers.

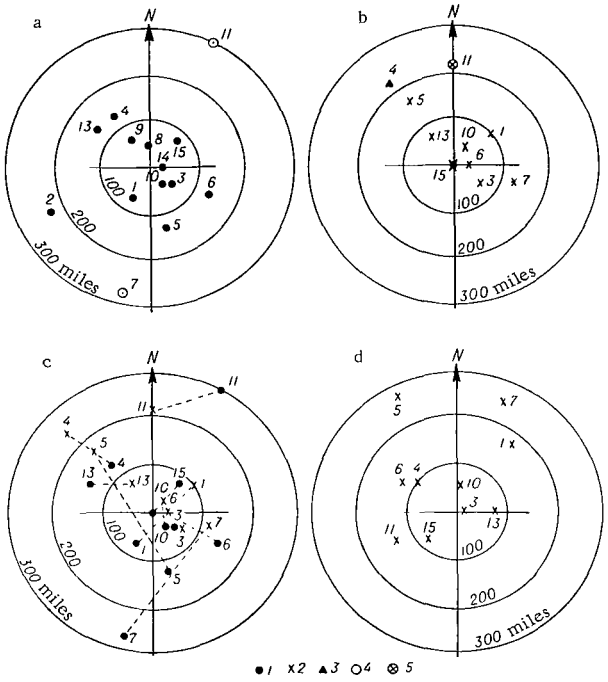

FIGURE 4.23. Position of baric centers relative to centers of cloud vortices (class 4):

a — position of cyclone centers near the ground relative to the centers of cloud vortices; b — position of high-level centers at the 500-mb level relative to the centers of cloud vortices; c — superimposed position of surface and high-level centers of low pressure relative to centers of cloud vortices; d — position of high-level centers of low pressure relative to the cyclone center near sea level; 1 — position of cyclone center; 2 — position of high-level baric centers; 3 — refined position of centers; 4 — dubious position of center at sea level; 5 — dubious position of center at 500-mb level.

Figure 4.24 also depicts the slope of the baric-center axes. The slope is negligible, pointing to the occluding stage of the cyclones.

For the analyst it might be interesting to study the distribution of surface and high-level baric centers, as well as the position of cloud-vortex centers, in various geographical regions (the Atlantic, Pacific, and over land).

As is seen from Figure 4.25a, the position of surface baric centers relative to the center of cloud vortices shows better correlation for the ocean than for land. The same applies to the position of high-level baric centers (Figure 4.25b). This regularity is probably due to the quality of analysis.

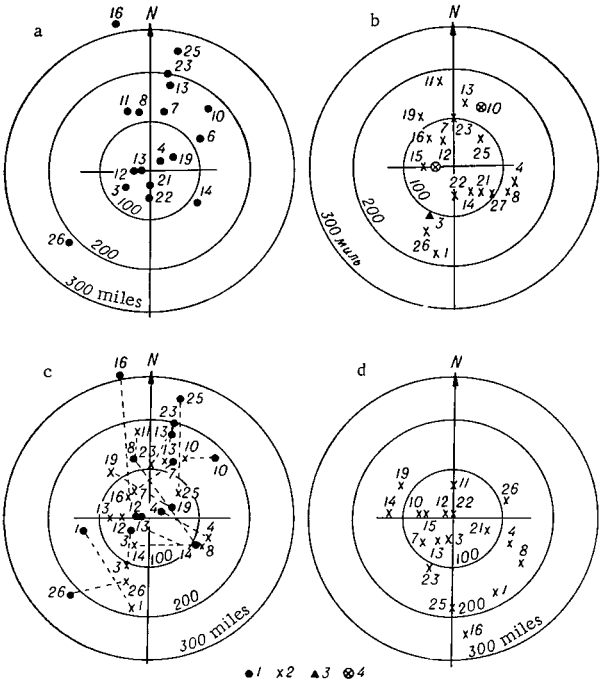

FIGURE 4.24. Position of baric centers relative to the centers of cloud vortices (class 5):

a–d as in Figure 4.23; 1 — position of cyclone center; 2 — position of high-level baric centers; 3 — refined position of centers; 4 — dubious position of the center at the 500-mb level.

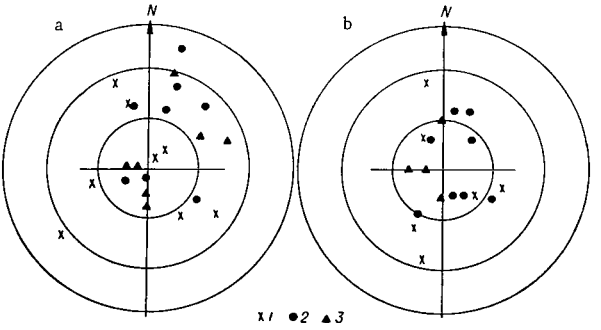

FIGURE 4.25. Position of surface and high-level low-pressure centers relative to the centers of cloud vortices as a function of the character of the underlying terrain:

a — position of cyclone centers near sea level relative to the centers of cloud vortices; b — position of cyclone centers at the 500-mb level relative to the center of cloud vortices; 1 — above the Pacific; 2 — above the Atlantic; 3 — above land.

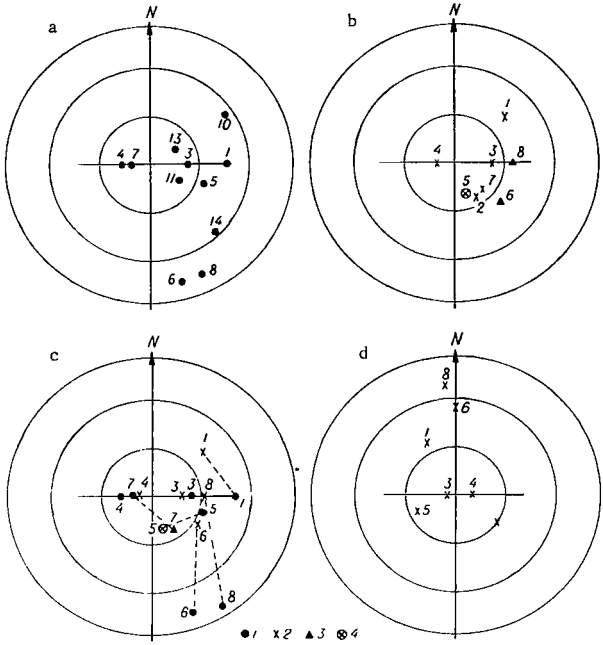

FIGURE 4.26. Position of the surface and high-level low-pressure centers relative to the center of cloud vortices (class 6). For legend see Figure 4.24

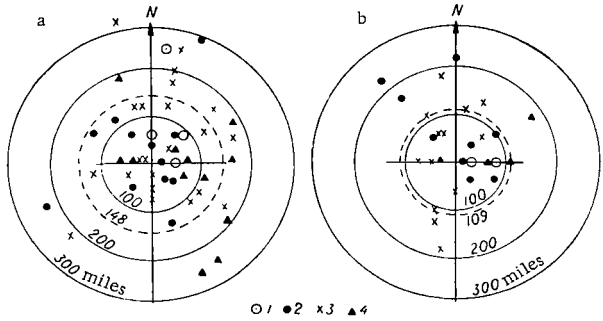

FIGURE 4.27. Position of surface and high-level low-pressure centers relative to cloud-vortex centers (for classes 3, 4, 5, and 6):

a — position of surface cyclones relative to cloud-vortex center; b — position of high-level low-pressure centers relative to the cloud-vortex center.

4. Class 6 (filling cyclone). This class represents an old filling cyclone clearly expressed at the 500-mb level (Figure 4.26). The center of the cloud vortices in this formation stage is located slightly W or NW to the surface center. The same pattern is noticed for the high-level baric centers. However, the high-level baric center is closer to the center of the cloud vortices.

Figure 4.27a shows the position of surface baric centers relative to the centers of cloud vortices for cyclone classes 3, 4, 5, and 6. Figure 4.27b shows a similar pattern, but with allowance for the high-level baric center.

The root-mean-square deviation of the position of the surface center from the vortex center was 266 km, while the deviation in the position of the high-level baric center was 196 km.

TABLE 4.8. Statistical characteristic of reliability in determining the cyclone center

Reliability of initial data	Cyclone classes			
	3 (7)	4 (14)	5 (22)	6 (12)
Percent of total instances in which the cyclone center at sea level was reliably determined	57	61	43	42
Percent of instances in which the cyclone center at the 500-mb level was reliably determined	14	39	47	58
Percent of instances in which neither the position of the cyclone at sea level nor the position at the high level was reliably determined	29	0	9	0
Percent of instances in which the cyclone center at sea level was not farther than 350 km from the cloud vortex center	43	78	73	75
Percent of instances in which the cyclone center at the 500-mb level was not farther than 350 km from the cloud-vortex center	43	57	86	66

Note. The number of instances is given in parantheses.

Table 4.8 presents some statistical data on the position of centers obtained from the analysis of instances in which the position of baric centers was reliably determined. Table 4.9 presents similar data for each cyclone class, except for instances of unreliable determination of baric-center positions.

Minina /4/ investigated 64 instances of cloud vortices reproduced on satellite pictures taken during August 1963. The author was interested in determining the center of the cloud vortex in the pressure field at both the sea and 500-mb levels. The results of the studies are presented in Table 4.10. In 22 instances of observation, the baric centers of tropical cyclones coincide with the centers of their cloud vortices; this may be explained by the near-vertical position of the spatial axis of the tropical

cyclone. The observations for cyclones in temperate latitudes may, for each individual instance, be interpreted by analyzing the thermobaric structure of the cloud cover where a cloud vortex is noticed. The author found a good correlation of the cloud-vortex structure and cloud-vortex center in the baric field with the evolution stages of the cyclone.

TABLE 4.9. Errors in determining cyclone centers

Reliability of initial data	Cyclone class			
	3	4	5	6
Percent of instances in which the distance between the position of low-pressure center and the cloud-vortex center was 350 km	60	78	84	82
Percent of instances in which the distance between the center of high pressure and the cloud vortex center was ≤ 350 km	67	80	100	100

In the following, we shall deal with the structure of cloud systems of extratropical cyclones in their various evolution stages using data from earlier studies /6, 7, 23/.

TABLE 4.10. Characteristics of pressure fields at sea level and of the geopotential field at the 500-mb level for 64 cloud vortices

Characteristics	At sea level	At the 500-mb level			
		center or trough	cyclone center	trough axis	frontal zone
Cyclone region tropical cyclones	22/34	22/34			
Cyclones in temperate latitudes	13/20		8/13	1/1.5	4/6
periphery	19/30		10/16	1/1.5	8/13
Gradient-free baric field	2/3			2/3	
Anticyclonic region, periphery	8/13		1/1.5	1/1.5	6/10

Note. *The numerator shows the number of instances and the denominator percent of the total number of investigated instances.*

1. Stage of frontal wave (wave cyclone). In this stage, the vortex structure of the clouds is generally not tracked. From the cloud pictures alone, without resorting to ground-based data, it is very difficult to ascertain the existence of a wave cyclone and its further evolution.

However, very often the formation of a wave cyclone may be inferred from the widening of the frontal cloud band on the warm section of the front and from the more advanced convection in the cold air both behind and ahead of the cold section of the front. In cold air cumulus clouds may form bent rows or chains of clouds (Photograph 4.38). Cirrus clouds ahead of a young section of the warm front do not spread far from the front line. The center of the cloud system (if identifiable) lies close to the wave crest. When the center of a cloud system coincides with the wave crest at the cold front, in the 500-mb level it will be located in the top part of the high-level trough in the region of considerable wind drift /23/.

A wave cyclone that develops at the relatively slowly moving warm front shows only seldom a cloud-vortex pattern, because it is obscured by the wide zone of warm-front clouds which converge with the postfrontal clouds.

Cyclones that appeared at the occlusion point are preceded by a vertically well-developed cloud layer. Since the nucleus for the appearance of a cyclone at the occlusion point is formed by a well-expressed V-shaped high-level trough, the vortex pattern of clouds forms rapidly and at a relatively high level (Photograph 4.39).

In the cold front, the cloud system of a wave cyclone usually has smaller horizontal sizes than the system of cyclones that form at the warm front and at the occlusion point.

In identifying wave cyclones on satellite pictures from the cloud structure, the analyst would do well to take into account the fact that new cyclones are generated at the cold sections of the front of an earlier cyclone.

2. Stage of pre-occlusion (young cyclone). The wave disturbances of the front caused by the developing initial phase are more pronounced in this stage (Photograph 4.40). The cloud system exhibits an orientation corresponding to the front orientation: the main bands of frontal clouds coincide in direction with the frontal zone on the 1,000-mb map. The vortex structure of clouds is still too unclear to permit the determination of the vortex center. The position of the center of the main cloud system relative to the surface-pressure and 500-mb geopotential fields is nearly the same as in the initial stage.

In the rear part of the cyclone and in its thermal sector, the cloud structure depends on geographical and seasonal features, air humidity, and on the nature of the thermobaric field. All these features are almost fully seen on satellite pictures. Thus, the absence of cloudiness or the existence of low cloudiness in the rear part of the cyclone may be linked with a strong pressure rise, or may point to an inflow of cold and dry continental air into the rear part of the cyclone; on the other hand, a large cumulus cover may point to the inflow of wet unstable air.

In the rear part and in the warm sector of the cyclone, rows and chains of cumulus clouds are usually oriented along the isotherms on the surface weather map or on the 850-mb chart.

3. Stage of onset of occlusion. The evolution of any cyclone, except for rare cases, is not limited to this stage. The initial stage of cyclone occlusion is followed by further cyclone development; the conditions of cyclone deepening continue until the cyclone becomes asymmetric in the temperature field. In this phase, humidity distribution in the cyclone and the nature of the thermobaric field create conditions for the formation of asymmetric cloud systems.

Satellite pictures (their number was small due to the short duration of this stage) permitted the identification of the spiral structure of the main cloud system with the vortex center located rather close to the center of the high-level cyclone or to the axis of the high-level trough (Photograph 4.41). Asymmetrical distribution of the cloud cover may enhance protrusion of the cloud-free wedge of cold air into the rear part of the cyclone, particularly behind the second-order cold front.

4. Stage of cyclone occlusion. Compared with the initial stages, this stage is far longer. During this period, the thermobaric field and the frontal structure of the cyclone undergo a marked evolution. The cyclone reaches its maximum development (maximum depth) followed by filling. The temperature distribution in the surface layer of the central part of the cyclone acquires a less asymmetrical character. Closed cyclonic circulation can be tracked at high levels. In the cyclone area, the heat crest becomes very narrow and shifts to the frontal part of the cyclone periphery. The frontal zone shifts to the cyclone periphery near the warm air front, and thus the zones of maximum advective changes in temperature also shift to the periphery.

The satellite pictures clearly reveal the vortex structure of the cyclone clouds (Photographs 4.42—4.44). The central region of the cloud vortex represents a circle from which spiral cloud bands irradiate toward the periphery. The large principal cloud band oriented along the occlusion front is located ahead of the cyclone, near the occlusion front. The cold air of the rear part of the cyclone usually exhibits spiral bands and small cloud chains. At the cyclone periphery, cloud bands of the cold and warm fronts are less clearly seen; however, cloud bands of the cold front are better expressed, particularly the cloud boundary which is oriented toward the cold air. Cloud bands with a high top boundary in the frontal part of the cyclone are oriented along the air current at the level of the top cloud boundary; at the rear part of the cyclone, cloud bands and series of lower cumulus clouds are located according to a pattern that resembles the flow lines near the Earth surface. The center of the cloud vortex is located close to the high-level center of the cyclone, and instead of departing from the surface center it often approaches it. The various instances of the occlusion stage are seen from the specific features of the cloud vortex structure (Photographs 4.42—4.44).

5. Stage of full cyclone occlusion. This stage is characterized by a temperature leveling in all sectors of the cyclone and by diffuse frontal interfaces (boundaries). The most intensive cyclone circulation is noticed at the top half of the troposphere. Cold air occupies the central part of the cyclone. Heat advection is noticed at the northern and even northwestern periphery of the cyclone, leading to isolation of the cold region in the central part of the cyclone.

Photograph 4.45 shows a typical cloud-vortex structure in this stage. On the picture, the high stratiform clouds are seen as spiral-like bands, the position of which is in good agreement with the closed cyclone configuration on the isohypse charts of high-level baric topography. Cumulus clouds are noticed at the southern part of the cyclone, forming separate cloud groups and short irregularly shaped bands as a result of weakening of air currents in the lower tropospheric layers. On the other hand, the central

part of the cyclone reveals cloud-free sections. The center of the cloud vortex coincides with the high-level center of the cyclone, approaching the surface center. The whole pattern illustrates the process of decay of the basic cloud mass of the cyclone.

In a few instances, during this development stage, secondary cloud vortices were found to the west of the main cyclone center. Such an eddy distribution of cumulus and cirrus clouds is due to the formation of both a clearly expressed cold trough near the bottom layer at the rear of the cyclone, and a trough at the 500-mb level. These troughs may be detected with the aid of satellite pictures, much earlier than from conventional synoptic data.

6. Stage of decay (full filling). In this last stage cloud shapes of the greatest variety tend to assume a vortex pattern (see Photograph 4.46). The stage is characterized by the cloud structure at different levels: at the low level we find mainly cumulus clouds; at the top level the clouds have a stratified and fibrous structure. As the cyclone vortex gradually dissipates, the amount of cloud bands decreases, the gap between them increases and the cloud sheet in the center of the vortex becomes more and more broken. However, these changes, to a large extent, depend on the nature of the underlying surface, season of the year, hour of day and other factors. Not infrequently, the process of cloud decay comes to a halt and cloudiness as well as the old cyclone tend to regenerate.

Most frequently, the center of the cloud vortex of a cold decaying cyclone coincides with the high-level center of the cyclone and, if cyclone circulation near the Earth is preserved, it coincides with the center of circulation. Often, a gradient-free field, and even the periphery of an anticyclone, may be noticed near the Earth surface below the center of the cloud vortex.

The rule that governs the displacement of cloud vortices (systems) of extratropical cyclones is almost the same as for the cyclones themselves. The displacement of cyclones may be estimated from the displacement of cloud vortices.

The following table shows the deviation of pressure level at the Earth surface ($\overline{\Delta p}$) and at the geopotential half of the 500-mb level ($\overline{\Delta H}$) from the climatological standards at baric centers /23/:

Class	$\overline{\Delta p}$, mb	$\overline{\Delta H}$, m
4	18.0	177
5	15.6	194
6	12.4	137

Examples of analysis of extratropical cyclones

The examples below stress the utility of using satellite cloud data to analyze weather charts plotted for regions of cyclonic activity. The satellite pictures supply additional information on forms, structure, and distribution of cloudiness; interpretation of picture data yields the exact position of cyclone centers and thermobaric structure of cyclones on the weather charts.

Example 1. For the analysis of a cyclone at the northern part of the Pacific, the following elements were used:

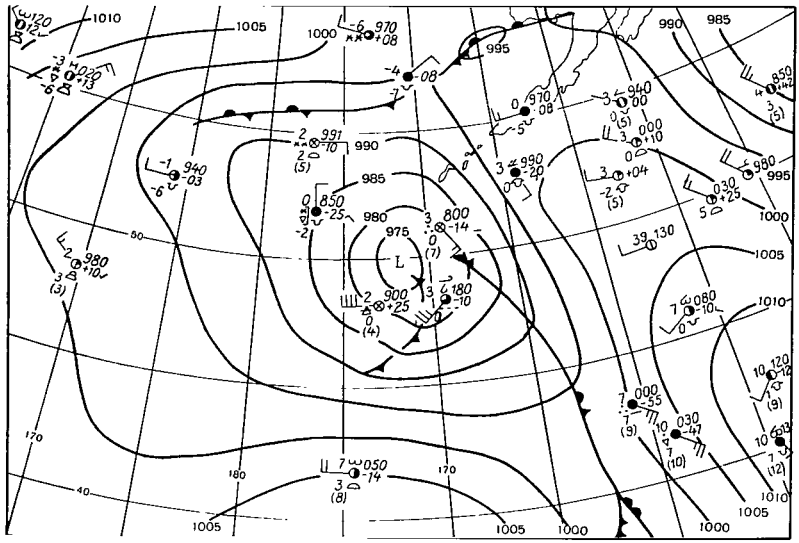

FIGURE 4.28. Surface weather chart at 0000hr on 29 January 1964

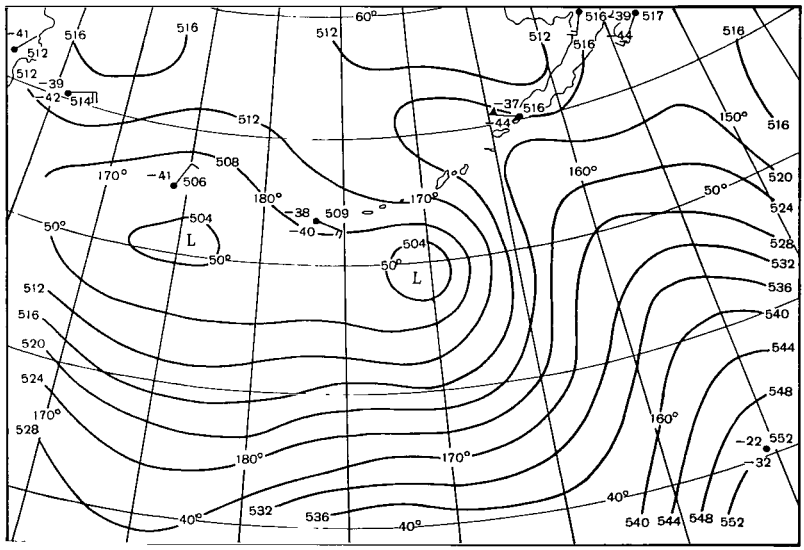

FIGURE 4.29. 500-mb chart at 0000hr on 29 January 1964

1) photograph of cloud cover taken at 0136hrs on 29 January 1964 (Photograph 4.47);

2) surface weather chart at 0000hr (Figure 4.28);

3) 500-mb chart at 0000hr (Figure 4.29).

Difficulties likely to arise in analyzing the surface-weather chart (Figure 4.28) are due to difficulties in finding the various fronts; this is a result of lacking reliable observational data for large areas, particularly close to the cyclone trough where it is quite impossible to obtain any reliable data on weather conditions. Difficulties are still greater in analyzing the 500-mb charts (Figure 4.29), for which the little available data do not permit the determination of the geopotential field at the southern and southwestern part of the territory involved. This is convincingly seen when we attempt to perform analysis only from ground observational data.

Let us now consider satellite cloud pictures (Photograph 4.47). Here the spiral-like structure of the cloud vortex points to the mature stage of cyclone development. According to all signs the cyclone is of the high occluded type. This is borne out by the spiral band of high clouds transferred to the northern and western part of the cyclone, and by the breaking up of the low clouds in the cold air into separate rows at the southwestern part of the cyclone. The orientation of cloud bands and rows is in good agreement with the cyclonic circulation. The main frontal cloud band is directed from the vortex center toward SSE. The photograph supplements the scarce information on the cloud cover over many regions for which ground-based observational data are unavailable. To the NNE of the vortex center (near 51°N, 177°E) we can easily see large Cb clouds together with smaller scattered cloud elements. These data permit us to infer on the existence in this area of a deep trough or even of a partial cyclone at the periphery of the main cyclone (Photograph 4.47). In the northern area we can track the cloud bands of the low frontal section.

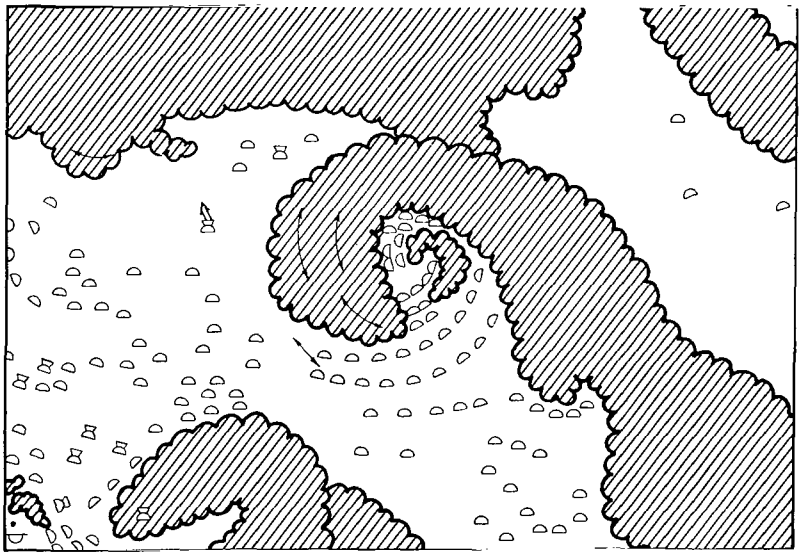

FIGURE 4.30. Schematic nephchart at 0136 hr on 29 January 1964

For the given case, satellite pictures made it possible to determine the thermobaric structure (evolution stage) of a cyclone (without the otherwise inevitable rough errors in determining the position of the surface and high-level centers of the cyclone), and the frontal sections and pressure fields at the sea and 500-mb geopotential level.

As a check it is advisable to compare the results of surface-weather charts and 500-mb charts with the schematic nephanalysis chart (Figure 4.30), allowing for the time difference between satellite- and ground-station observations.

Example 2. For the analysis of cyclonic activity in the same regions as above but 24 hours later, data were taken similar to those in Example 1:

1) cloud photographs taken both at 0157 and 0020 hr on 30 January 1964 (Photograph 4.48);

2) surface weather chart at 0000 hr on 30 January 1964 (Figure 4.31);

3) 500-mb chart at 0000 hr on 30 January 1964 (Figure 4.32).

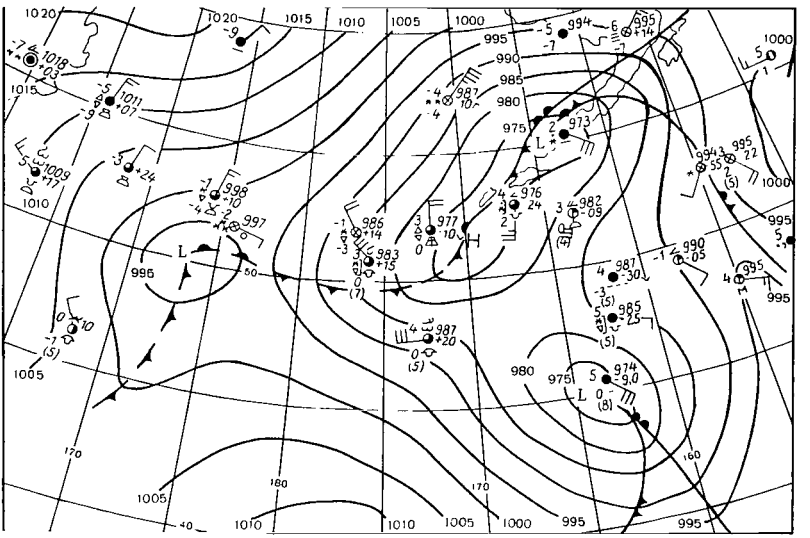

FIGURE 4.31. Surface weather chart at 0000 hr on 30 January 1964

In the analysis of this instance using cloud photographs and its component frames, it is advisable to plot a schematic nephchart to the scale of the surface weather chart as shown in Figure 4.33. This makes easier comparison between the results of the satellite pictures and the weather-chart data. The pictures show the structure of cloud vortices and the development stage of four cyclones: two cold cyclones (the coordinates of their centers are 50°N, 175°E; 52.5°N, 171°E), one occluded cyclone (studied in Example 1) with coordinates about 54°N, 164°E, and a cyclone at the stage of the onset of occlusion at about 45°N, 164°E (24 hours earlier no cyclone was revealed in the region for which the chart was plotted). In the region

of a vast ridge of high pressure at the South, convective clouds in the form of empty cells are clearly visible.

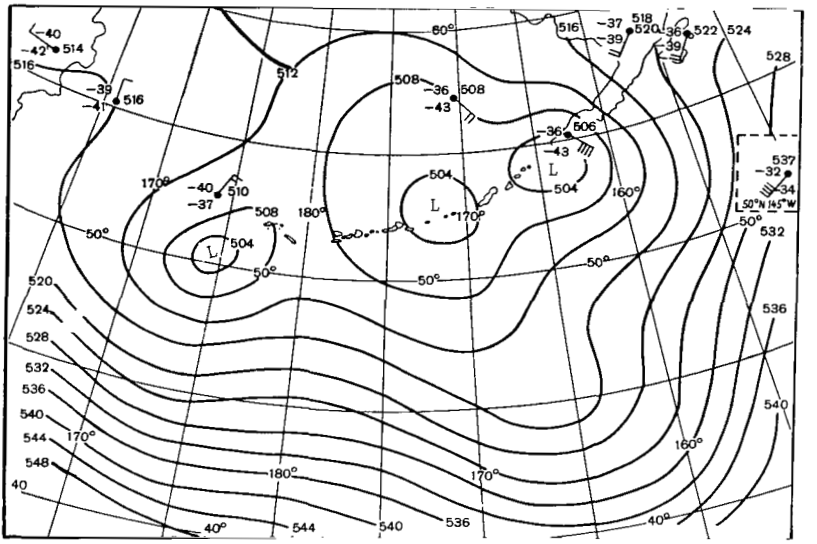

FIGURE 4.32. 500-mb chart at 0000 hr on 30 January 1964

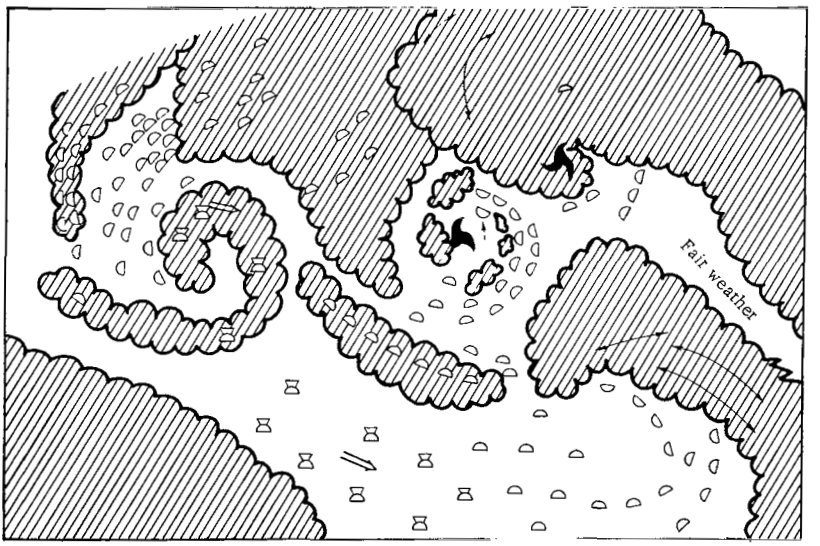

FIGURE 4.33. Schematic nephchart at 0020 and 0157 hr on 30 January 1964

For this instance, the good agreement between the structures of the cloud and wind fields is particularly noteworthy. Without resorting to photographs gross errors in analyzing the 500-mb chart would be unavoidable. The data not analyzed in Examples 1 and 2 may be used as exercises.

4.5. IDENTIFICATION OF ATMOSPHERIC FRONTS

A comparative analysis of satellite- and weather-chart data showed that the structure of frontal clouds, as seen from satellite pictures, to a certain extent reflects the principal specific features of atmospheric fronts confirming our present-day ideas on models of frontal cloud systems /7/.

These features are determined by the character of the wind field and of the vertical distribution of motions in the frontal zone, mainly in the warm air above the frontal surface.

The use of these characteristic features permits the frontal clouds reproduced on satellite pictures to be divided into two basic types:

1) wide bands linked with the upward motion above the frontal surface — the anafront (warm front and cold front of the first order);

2) relatively narrow bands linked with ascending motions in the head part of the cold front during downward movement in the free atmosphere above most of the surface front and above ceilings directed normal to the front — the katafront (cold fronts of the 2nd order).

Although for the time being satellite pictures did not much improve our understanding of the frontal-cloud structure, the large area (of almost global scale) covered by satellite observations increases the practical value of such pictures in the analysis and prediction of atmospheric processes, particularly for regions with a sparse meteorological network.

Cold-front cloudiness. Wide frontal cloud bands were noticed on the pictures along extensive frontal zones and represented the frontal (eastern) part of a high-level trough of large amplitude exhibiting positive vortex advection, ordered ascending motions and a wind parallel to the front in the central and top layers of the troposphere, a fact typical of cold fronts of the 1st order.

On satellite pictures, clouds linked with such fronts appear as combinations of various cloud types both of nonconvective and convective character. Frontal cloud bands of average width about 300 km have a clear-cut edge with one or two sides in which the type and amount of clouds sharply change. When the main cloud band reaches the region of cold air up to the area of jet streams. it contains separate long cloud bands parallel with the wind or else transverse short bands normal to the wind, close to the edge of frontal clouds at the cold air to the right of the jet-stream axis.

The width of the frontal cloud band decreases from the center of the cyclonic area to its periphery. Comparing the position of these cloud bands on satellite photographs and on baric-topography charts for the same observation time shows that the frontal cloud band ends or disintegrates in separate cloud elements in the area of the frontal zone close to the axis of the baric high-level trough.

In warm seasons it is very difficult to identify frontal cloud bands over the ocean as they are obscured by stratus cloud and fog on either side of the front. However, much information can in this case be obtained from data on outgoing radiation and from infrared pictures, since the vertically most developed frontal cloudiness can be tracked from the belt of lowest temperatures on the chart of outgoing radiation and from the brightest strip on the infrared picture.

Cloud bands of cold fronts of the second order have a width of only a few tens of kilometers and are not usually continuous along the whole front.

Their image on the picture can be distinguished by their pronounced cumuliform structure, particularly in the warm season, by their breaking up into irregularly shaped elements oriented parallel with the air-mass current in the central and top layers of the troposphere, but normal to the current in the surface behind the cold front. Sometimes the cloud system of the cold front of the second order cannot clearly be seen on surface weather charts because of the relatively small size of its component elements, and their diurnal variation; but on satellite pictures it is easily identifiable and this helps much in the geographical location of the front usually linked with critical weather processes (storm rainfalls, thunderstorms, etc.).

Satellite pictures often permit the tracking of relatively wide cloud bands parallel to the cold front, but not linked with the principal frontal zone both ahead of the warm-air front and behind the cold-air front. In the former case, they form as a result of converging separate convective clouds along the instability lines in warm humid air at a distance of tens and hundreds of kilometers ahead of the cold front. Here, formation of cloud bands is enhanced by the development of large-scale turbulence. In the latter case, cloud bands are generated by zones of ordered convection and convergence on the lower layer of a greatly unstable air mass in the rear part of a cyclone. When analyzing the surface weather chart, the forecaster does not distinguish between such zones and secondary cold fronts.

Warm-front cloudiness. The analyst is often unable to identify cloud bands, particularly frontal clouds, because of convergence of frontal cloudiness with prefrontal cold-air clouds and postfrontal warm-air clouds. The two latter cloud zones may be of both convective and nonconvective origin, depending on the temperature regime of the underlying surface and stratification. As is well known, formation of postfrontal clouds is markedly enhanced by advection of warm air into the lower troposphere. Therefore, warm-front cloud bands, unlike cold-front bands have, with few exceptions, no sharply defined boundaries.

Occlusion-front cloudiness. On satellite pictures, occlusion-front cloud bands are rather easily identifiable, since by their size and structure they differ from internal discontinuous clouds or from clouds grouped as a result of cyclonic circulation into much smaller bands. The width of such bands is generally much larger in the central part of the cyclone. The western (rear) boundary of the band almost coincides with the trough axis on the 500-mb chart. Often, a parallel band of convective clouds may be observed ahead of the principal frontal band. Distinctive gaps in the internal clouds may be observed behind the principal frontal band, but this does not exclude the existence of cloud bands that are linked with convection and convergence lines including secondary fronts. Of course, instances are also possible when a frontal cloud band may converge with a total low-cloud cover in a relatively warm and stable air mass as, e.g., is often the case with the passage of cyclones from the Atlantic into other regions during the cold season of the year.

If a partial cyclone forms at the occlusion point, the cloud band usually undergoes deformation under the effect of cyclonic circulation: above the occlusion point, it becomes narrower and its boundary recedes, while below the point the band widens.

Examples of analysis of atmospheric fronts

Example 1. In the following, we analyzed a cold front above the ocean near the western coast of North America. For the analysis the following elements were used:

1) surface weather chart at 1800hr on 19 April 1963 (Figure 4.34);

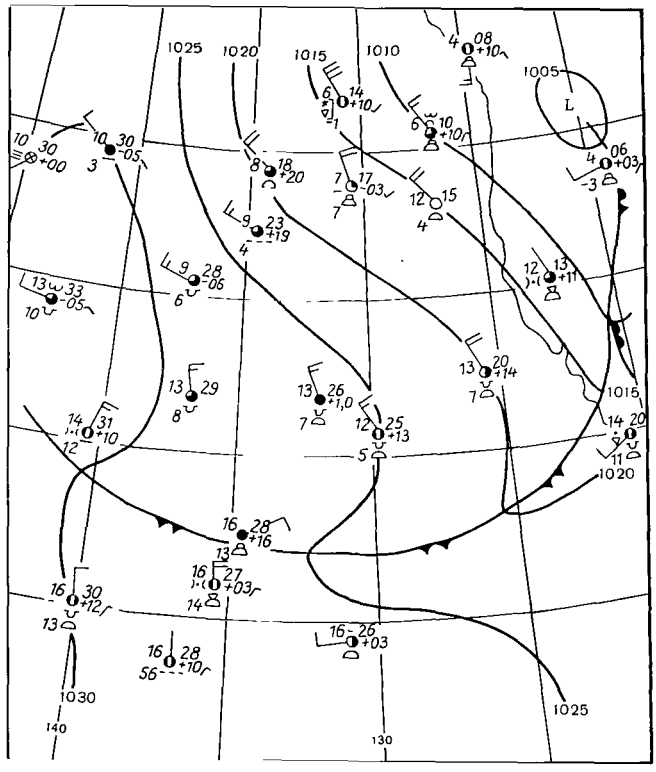

FIGURE 4.34. Surface weather chart at 1800 hr on 19 April 1963

2) the 500-mb chart at 1800hr on 19 April 1963 (Figure 4.35);

3) the 500—1,000-mb chart at 1800hr on 19 April 1963 (Figure 4.36);

4) cloud photographs at 2103hr on 19 April 1963 (Photograph 4.49).

The pictures show cloud systems of different structure: the windward mountain coast covered with a total cloud sheet (almost without gaps); a large region near the coast of width about 400 km covered with cumulus clouds in the form of empty cells; along 32°N a bright cloud band 100—150 km wide with sharp edges at the North and transverse bands extending to the South; further South, the pictures show mainly cumulus cloud cells, chains, and rows; to the North of the sharply outlined edge of the bright band there is a large wedge of white cumulostratus and cumulus clouds adjoining the edge of the band.

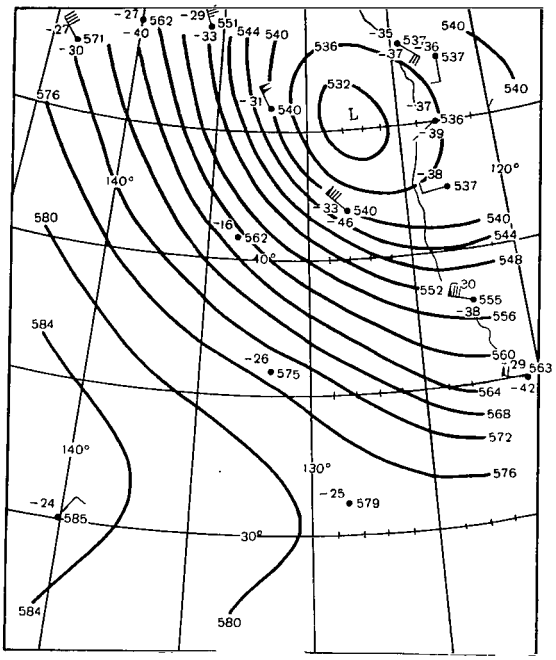

FIGURE 4.35. 500-mb chart at 1800 hr on 19 April 1963

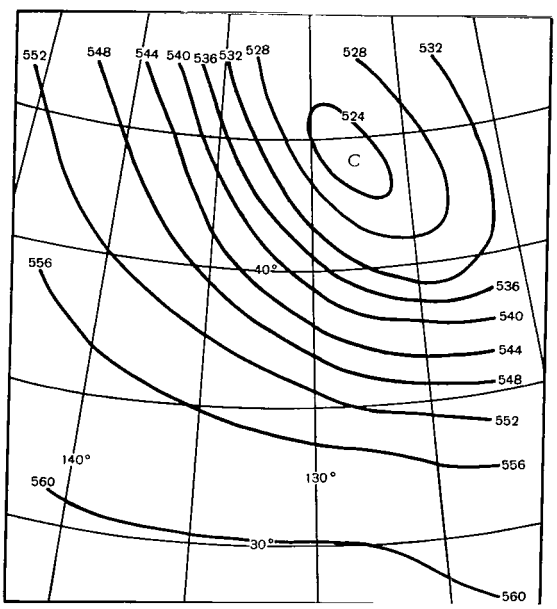

FIGURE 4.36. 500—1,000-mb chart at 1800 hr on 19 April 1963

Comparison is made easy by inspecting the schematic nephchart in Figure 4.37.

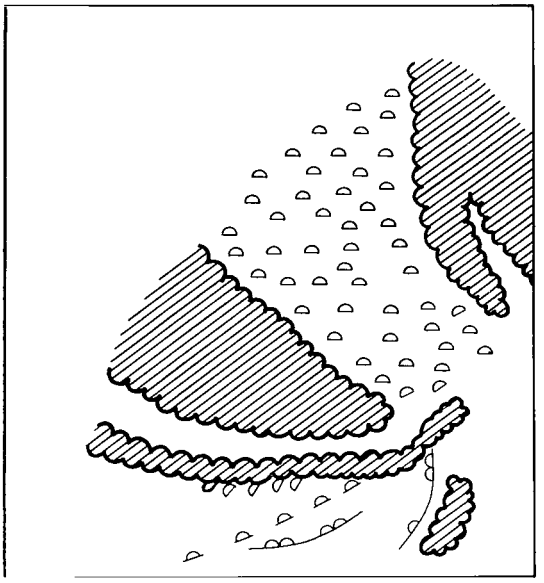

FIGURE 4.37. Nephchart at 2103 hr on 19 April 1963

Near the Earth surface, the cold front is clearly expressed in the wind and temperature fields although the horizontal gradients of the temperature field are small (the sharp temperature discontinuity is not recorded). The position of the front corresponds to the high-level frontal zone.

The weather chart carries almost no information on frontal cloudiness. On the other hand, interpretation of cloud pictures permits not only the position of the front to be refined, but also its structure along its whole length. At a region of the front close to the intersection point of the high-level trough axis and the frontal axis, and slightly further West of it, thin high-cloud bands (presumably of the cirrus type) and a few cumulus clouds can be noticed. On the section between 128 and 142°W and 32°N the cloud front appears as a bright band (see above). By its structure and wind direction in the middle troposphere this front is of the katafront type.

Example 2. The following elements were used for the analysis of the occlusion front and of small areas of cold and warm fronts above the Pacific:

1) surface weather chart at 0000 hr on 29 January 1964 (Figure 4.38);
2) 500-mb chart at 0000 hr on 29 January 1964 (Figure 4.39);
3) 500—1,000-mb chart at 0000 hr on 29 January 1964 (Figure 4.40);
4) cloud pictures at 0136 hr on 29 January 1964 (Photograph 4.50).

In this analysis, particular attention should be paid to wave disturbances at the occlusion front. The crests of these disturbances are defined on

the pictures by the coordinates: 46°N, 164°W and 39°N, 160°W. The cloud band with diffuse edges located between 36 and 33°N corresponds to the position of the cold-front region located at the southwestern point of occlusion. The warm-front region cannot be identified from a single picture, while the wide cloud band limited by the eastern edge of the picture frame only confirms the correctness of the cold-front position as determined on the surface weather chart. Behind the occlusion front we notice the typical pattern of internal clouds appearing as a chain of cumulus clouds together with nuclei of stratocumulus.

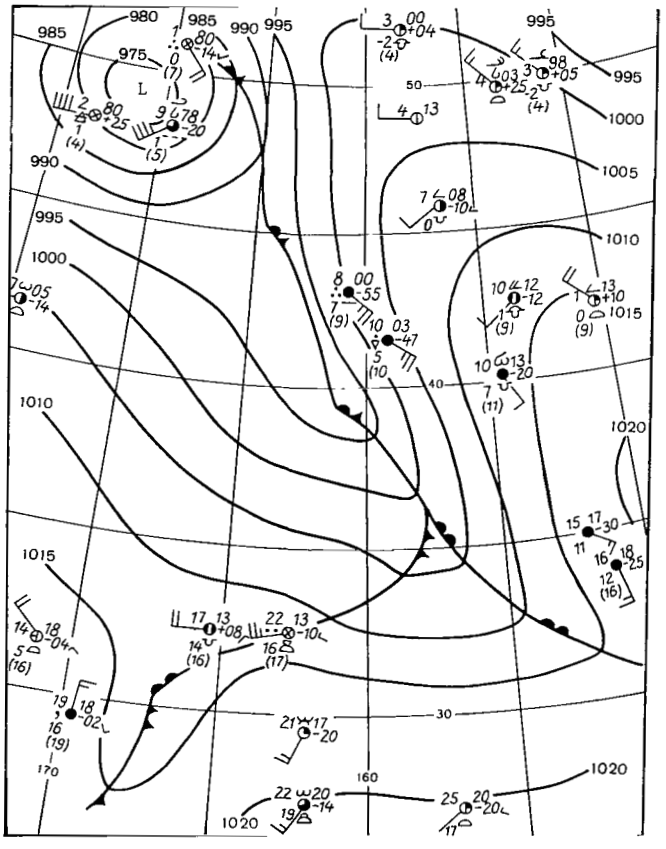

FIGURE 4.38. Surface weather chart at 0000 hr on 29 January 1964

In this example total frontal cloud bands are noticed in areas where the wind exhibits a vertical drift to the right (right turn of wind with height).

4.6. ANALYSIS OF TROPICAL ZONES. TROPICAL CYCLONES

Satellite cloud pictures are of particular value in the analysis of synoptic processes for regions with a sparse meteorological network. One such

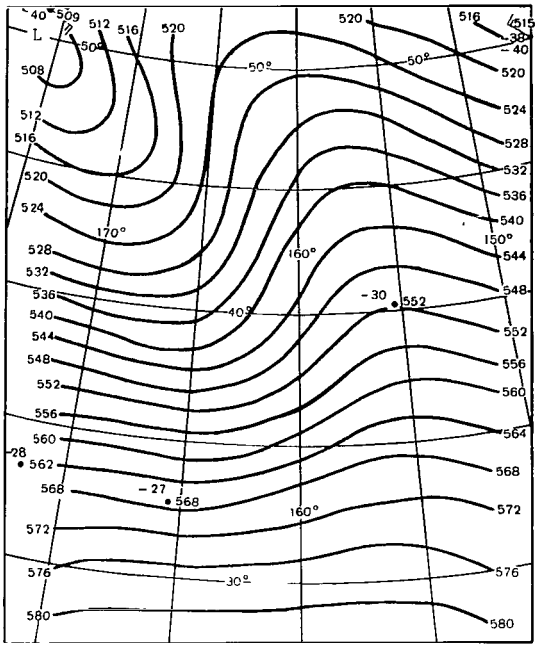

FIGURE 4.39. 500-mb chart at 0000 hr on 29 January 1964

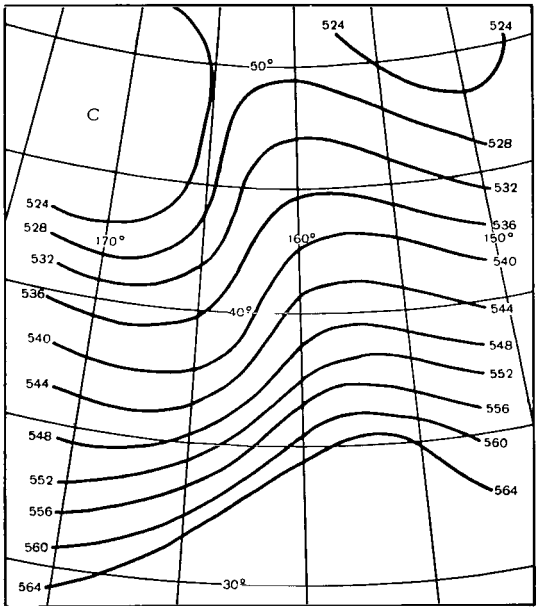

FIGURE 4.40. 500- and 1,000-mb chart at 0000 hr on 29 January 1964

region is the tropical zone which plays an important role in the general circulation pattern of the atmosphere, although weather formation is not only linked with the tropical zone but also to a large extent with temperate latitudes.

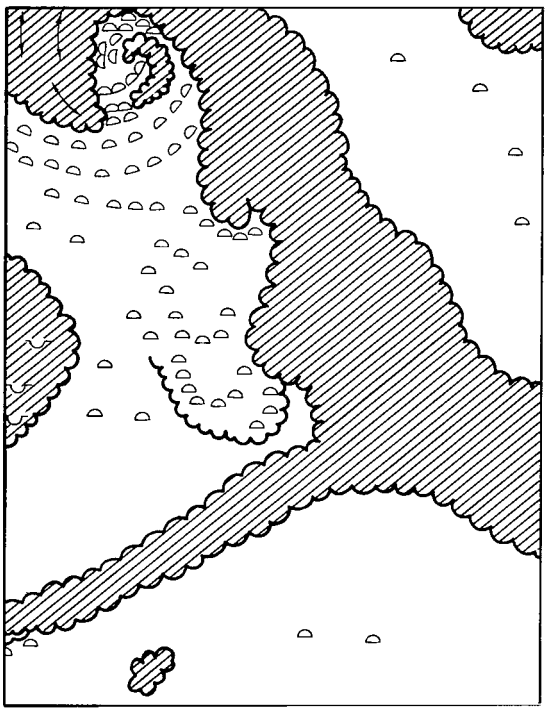

FIGURE 4.41. Schematic nephchart at 0136 hr on 29 January 1964

In the tropics, weather-formation factors are usually trade winds, convergent air currents, and vortices of differing origin and scale.

In recent years atmospheric circulation and weather formation in the tropics has been the object of extensive studies and numerous papers were published in this field. However, weather satellites made an important contribution to a better understanding of these processes, supplying much new information, the amount of which will no doubt increase in the near future.

The practical utility of weather satellites for the study of tropical climate conditions has been vividly illustrated by the launchings of the very first series of the TIROS generation in 1961, when satellite observational data predicted hurricane Esther and permitted the determination of the position and structure of other hurricanes such as Anna, Betsy, Debbie, etc. /23/.

When using satellite data on tropical conditions, they must be compared with observational data obtained by other methods, otherwise the analyst may be misled.

Tropical zones are characterized by a more or less well expressed layering of the troposphere. Thus, according to data in /23/, the tropical atmosphere is (by convention) divided into two and sometimes even three [or more] layers. The lowest layer near the Earth surface is the layer of eastern trade winds (easterlies) with their frequent formation of waves or vortices. The second layer is close to the 200-mb level and has the appearance of high-level vortices. A third layer, at the 600-mb level, with pronounced vorticity and cloudiness is also often noticed. Therefore satellite data alone are insufficient to differentiate between low thermal vortices and vortices that develop in upper layers. On the other hand, even scarce aerological and ground-based meteorological observations permit such errors to be avoided.

When jointly using satellite and ground-based data, the analyst has to take into account the following.

1) In the analysis of tropical cyclones, the continuity of satellite observations has to be preserved.

2) It is very useful to superimpose satellite data on time sections of the atmosphere. In this case, the analyst is able to simultaneously obtain both a spatial and temporal pattern of the tropical atmosphere and to determine the extent to which the shifting of any synoptic elements has caused changes in the atmospheric conditions.

3) In tropical meteorology, the joint analysis of flow lines and cloud pictures is of the utmost importance. Recent data have revealed a relationship between the development of tropical disturbances and flow lines in the central troposphere, approximately at the 500-mb level. In the upper troposphere, flow-line analysis should be made for the 200-mb level.

4) Although basically the relationship between the development of tropical cyclones in one area holds good for other areas as well, for the time being there are but little data to support this conclusion and the meteorologist must study the regional features of the tropical zone.

Principal kinds of cloud pictures for the tropical zone

According to data in /23/, satellite pictures most frequently show three types of cloud distribution in the tropics:

1. Amorphous clouds.* The group comprises randomly located cloud masses without any distinctive forms and boundaries. These masses are linked either with a monsoon equatorial trough or with a convergence zone.

Only a successive analysis of satellite cloud pictures and other observational data permit us to determine whether these cloud masses are linked with a developing tropical cyclone or with other air disturbances at larger altitudes.

2. Cloud bands. The principal cloud bands in the tropics are associated with zones of wind convergence or of horizontal wind drift. Very often, cloud bands form as a result of a cold front moving into the

* Some authorities call such randomly distributed cloud masses "cloud drops."

tropics from mid-latitude regions; they also often form in monsoon troughs or close to them along convergence lines. Sometimes, the relationship between cloudiness and the convergence zone is only manifested in the upper troposphere. Cloud bands may persist in a quasisteady state for a long time causing bad weather without, however, developing into cloudiness of tropical cyclones or into weak displacements. Due to the sparse network [in tropical regions] quasisteady-state cloud bands may escape detection by conventional means even for several days. Here, satellite observations play a special role, the more so as it is the zone of cloud bands that favors formation of tropical cyclones. Therefore, any section of disturbance in the cloud-band zone (bending, curvature, etc.) may indicate the onset of a vortex process.

Cloud bands that form in the zone of cold fronts penetrating from the North are often the only means for detecting such fronts.

The sparse network of tropical meteorological stations does not permit the accurate and reliable determination of the convergence zone from wind data alone. Hence for a reliable analysis, recourse should be made to other information sources.

Cloud bands linked with monsoon activity are usually located some 2 or 3 degrees South of the trough axis in the zone of wind convergence. This is illustrated by Photograph 4.51. In this band, cloud distribution is such that its northern edge has a sharper boundary than the southern edge. In order to identify cloud bands that are only linked with high-level zones of convergence additional information is required.

Sometimes, but infrequently, a secondary convergence line and its relevant cloud bands may also be noticed. It is also shifted to the North of both the trough axis and the convergence line. This band is less intensive than the southern band (Photograph 4.51a).

3. Systems of cloud vortices. Tropical cloud vortices are often linked with disturbances, the intensity of which varies from usual tropical perturbations to severe hurricanes and typhoons.*

The first indication of the possible formation of a tropical cyclone is the existence of cloud bands with discontinuities and other inhomogeneities of the cloud cover (bending, bulging, etc.).

Cloud bands linked with monsoon troughs and the corresponding convergence lines are the main nucleus for the development of tropical cyclones in the western area of the northern and southern regions of the Pacific, in some regions of the Indian Ocean and in the western part of the Caribbean Sea.

However, many disturbances in a cloud band do not develop into severe tropical cyclones. Such disturbances are due to the formation of trade-wind waves. Here, it should again be stressed that from satellite pictures alone, without resorting to additional data, it is difficult to infer on the initial development of a tropical cyclone.

Although the concept of easterly wave (first introduced by Riehl long before the introduction of weather satellites /20/) has been successfully used in the prediction of tropical meteors, satellite observations have shown this concept to be insufficient to describe and explain the extremely varied pattern of cloudiness, precipitation, and wind connected with disturbances in the eastern tropical winds. As shown in /23/, prior to the advent of

* According to the terminology adopted in /23/, a hurricane is an intensive tropical cyclone while a typhoon is a very intensive tropical cyclone of limited size.

satellites, any disturbances in easterlies that did not develop into cyclones were assimilated into easterly waves. Satellite observations showed that it is more correct to call the group of disturbances in the eastern circulation, easterly disturbances. The classical description of easterlies given by Riehl /20/ and confirmed by satellite observations should be referred to easterly waves.

Most frequently, cloud distribution caused by eastern circulation has the form of a closed cyclonic-circulation pattern in the middle troposphere at a height of about 5 km. If this circulation is intensive the disturbances are of the classical, easterly-wave type. Such intensive waves extend over a layer 6—7 km thick, while weak disturbances extend over much thinner layers of thickness 3—3.5 km. If the disturbances develop in the middle atmosphere without any evolution in the surface layers, satellite data imply that such disturbances are an intensive tropical cyclone. Unlike severe cyclones, tropical disturbances and weak tropical lows are characterized by the absence of a regular cirriform cloudiness. Satellite cloud pictures show only the disturbed region of cloud bands and a small amount of cirrus clouds.

A clear indication of disturbances in the eastern circulation passing into a weak tropical cyclone is the successive displacement of the circulation center from the eastern to the western side of the cloud band, and the shift of the boundary between the bright cloud mass and the cloud-free area to the West or toward the direction of cyclone movement as seen on satellite pictures. If, however, the circulation center persists in the eastern or southeastern region of the cloud mass, no increase in the intensity of disturbances may generally be expected for the next few days.

Intensive tropical cyclones are characterized by a dense cover of cirrus clouds. This points to the onset of cyclone deepening; in this case, it is very important to differentiate between the band of cumulus clouds and that of cirrus.

Another indication of increasing cyclonic intensity, alongside with the existence of cirrus clouds, is the formation of convective towers within cirrus clouds. Often, on large-scale pictures, such towers are clearly seen near the circulation centers where they appear as bright spots in the early stage of cyclone development. Photograph 4.52 shows an example of such towers observed on 4 October 1962 in the area of hurricane Daisy. The pictures also show the formation of a dense cirrus-cloud cover in the form of cloud bands, which indicate the development of upper-air currents issuing from the region of the cyclone. These bands are, in general, parallel with the bands of convective clouds in the lower layers that characterize the inflow of air into the cyclone region.

On the satellite pictures, tropical cyclones are clearly seen during their maximum development. This period is characterized by the following features:

1) considerable increase in the brightness of the cirrus-cloud layer, and development of the typical structure of a cyclonic vortex;

2) most of the lower clouds are covered by a relatively symmetric layer of cirrus clouds;

3) formation of a symmetric structure of cumulus bands at the periphery of the cyclone.

Photograph 4.53 shows a tropical cyclone at the onset of its maximum evolution, while Photograph 4.55 presents the picture of a typhoon. The

importance of satellite observations becomes more obvious in the case of typhoons, in view of their enormous destructive force despite their relatively small sizes. Some typhoons may reach a wind speed of up to 60—80 km/hr at a distance of 500—600 km from their center, and of up to 250—300 km/hr at a distance of 60—100 km from the center.

If one assumes that the inflow of air into the lower layers is compensated by the outflow of air into the upper layers (a fact determined from the presence of cirrus clouds), the structure and sizes of such clouds should afford a good idea on the intensity of a tropical cyclone. The conclusions in /10, 23/ confirm this assumption.

In /23/, the evolution of a tropical cyclone as a function of the cloud-cover characteristics is assumed to consist of two stages. The first stage, the cold-eye stage, covers the period of cyclone development until the formation of cirrus clouds. The second stage covers the period of intensive cyclone evolution followed by cyclone decay after the appearance of cirrus clouds (the warm-eye stage).

This stage may be subdivided into three substages:

1) convergent cloud band with clear V-shaped disturbances;

2) weak cloud vortex;

3) well-developed cloud vortex with clearly visible cloud bands.

In general, the warm-eye stage is divided into two (sometimes three) substages /10/:

1) well-developed cloud vortex with cirrus clouds covering most of the cyclone area;

2) well-developed cloud vortex but with smaller cirrus cloudiness. This is the cyclone-decay stage.

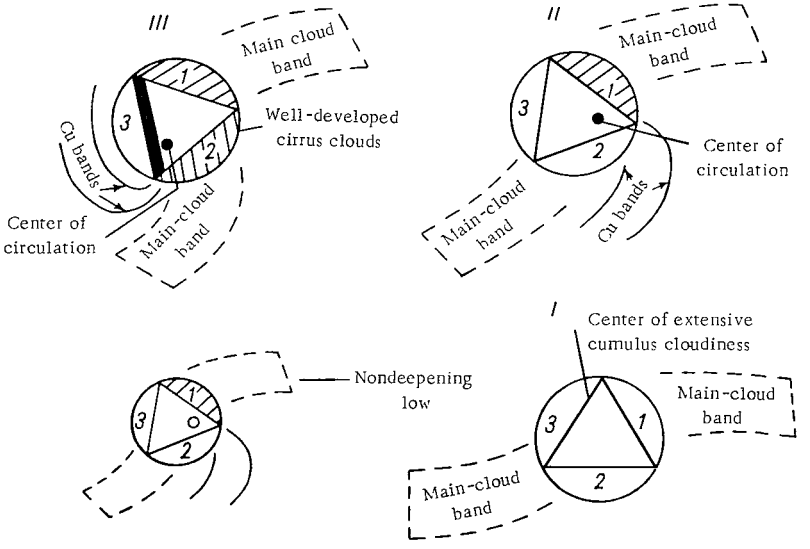

FIGURE 4.42. Schematic diagram of stages in the evolution of the cold eye of a tropical cyclone:

I — weak tropical disturbances, principal cloud bands may be absent; II — tropical disturbance or low, increased amount of well-developed cirrus clouds; III — weakly developed tropical cyclone, western edge with clearly expressed outlines.

Figures 4.42 and 4.43 show schematically the stages of cold and warm cyclone eyes. In these figures, the triangles delineate the extensive system of bright clouds; under real conditions, this system also has a triangular shape. The triangular system of cloud-form designation is convenient, as it permits the differentiation of three important regions that surround the central part of the cloud mass. The position of regions 1, 2, and 3 in the triangles may roughly be characterized in the following way:

1) to the NE or at the rear of the main cloud mass relative to the direction of cyclone movement;

2) to the South or to the left of the cloud-mass center;

3) to the West or in front of the cloud-mass center.

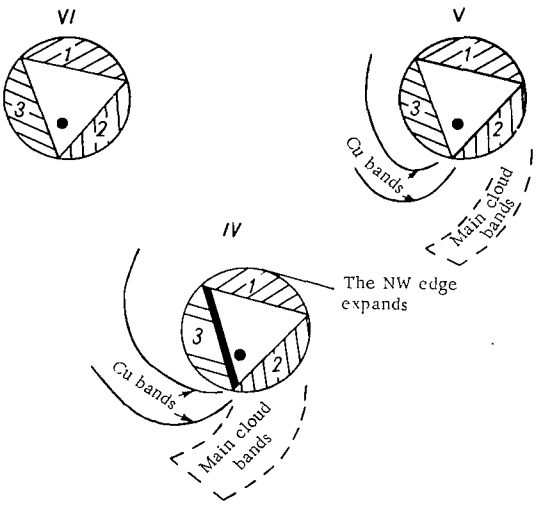

FIGURE 4.43. Schematic diagram of the stages in the evolution of the warm eye of a tropical cyclone:

IV — tropical cyclone, the eye is not shown, cirrus clouds start to fill the western edge; V — hurrican (typhoon), the eye can be tracked, well-developed cirrus clouds over all regions; VI — decay of tropical cyclone, the cover of cirrus clouds decreases in size, the cyclone eye is still visible.

These regions are provided with numbers in the sequence in which they are most frequently filled with cirrus clouds. The main cloud bands where the cyclone develops is designated in Figures 4.42 and 4.43 by dotted quasi-rectilinear lines. The smaller spiral-cloud bands of cumulus extending toward the circulation center are designated by solid lines. Other characteristic features are also seen in the figures.

This model permits a satisfactory representation of the various evolution stages of tropical cyclones. However, alongside with tropical-cyclone cloud masses, vortices, and vortex formations in the middle troposphere, a situation may arise when the same cloud-distribution pattern is linked with intensive circulation nuclei in the upper troposphere. Such

high-level disturbances may sometimes produce a pattern usually typical of eastern disturbances and hence misleading. This stresses once more the necessity for the joint use of satellite and other observational data.

Frequently satellite photographs disclose secondary cloud vortices, the diameter of which is usually equal to half the diameter of the main cloud vortex. The development, movement, and decay of a secondary vortex mainly depends on the main vortex. Most frequently, both vortex types tend to separate to a distance of about 1,500 km; the process of separation usually slows down with increasing intensity of the main vortex. Very often, secondary vortices are located to the South or West of the main vortex, but this rule has many exceptions (Photograph 4.54).

Analysis of tropical cyclones

A special study /10/ was carried out to estimate the potentialities and quality of interpretation of data from tropical zones, for which tropical cyclones hold the main interest. These studies covered the following regions:

1) the northern part of the southern coast of the U.S.A. from 60°W to the central part of the continent;

2) to the North of the equator from 170°E toward Asia.

TABLE 4.11. Characteristics of cloudiness for tropical cyclones in their various evolution stages

Code number	Characteristic features of the cloud field	Number of instances
T1	Small convexity of the main cloud cover . .	2
T2	Considerable convexity of the V-shaped cloud cover	7
T3	Formation of vortex structure in the cloud cover, but absence of cirrus clouds	16
T4	Formation of cirrus clouds over part or the whole vortex	40
T5	Decay of cloud vortex	6
Not recorded	—	7
	Total	78

In this study, the tropical cyclones were divided (as in the case of extratropical cyclones) into five types (see Table 4.11). The characteristics presented in this table are generally in good agreement with the characteristics presented in /23/. According to existing data, the time development of tropical cyclones is symmetrical relative to the instant of maximum intensity. Hence, knowing the given development stage of the cyclone and its history, the meteorologist can predict its further evolution.

After preliminary determination of the cyclone-development stages, the existing data were again analyzed by skilled meteorologists using the same technique as for extratropical cyclones (cf. Section 4.4).

TABLE 4.12. Group classification of tropical cyclones by various methods

Initially established class	Finally established class using additional data						
	T1	T2	T3	T4	T5	Undetermined	Total
According to nephanalysis data							
T1	1					2	3
T2		3		1		3	4
T3		4	12	6			22
T4	1		3	30	2	2	38
T5			1	3	4		8
According to satellite-picture data processed by analysts							
T1	1	1					
T2	1	4	1			4	10
T3		2	13	7			22
T4			1	27		2	30
T5			1	6	6		13
Total	2	7	16	40	6	7	78

From Table 4.12 it is seen that both nephanalysis and satellite pictures yielded a rather reliable group classification of the cyclone.

Table 4.13 presents the reliability (in percent) in determining the particular cyclone class.

TABLE 4.13. Reliability in determining the particular cyclone class

	Number of instances	Percent of instances in which the cyclone class was determined	Percent of total number of instances
Nephanalysis			
Determined correctly	50	70	64
Determined with an error of ± class	68	96	87
Total determinations	71	100	91
Total number of instances	78	—	100
Picture analysis			
Determined correctly	51	72	65
Determined with an error of ± class	70	99	90
Total determinations	71	100	91
Total number of instances	78	—	100

In the following we shall discuss the analysis of satellite cyclone pictures, but before going into details we shall briefly deal with the principles of data analysis.

For analysis, TIROS III, TIROS V, and TIROS VI satellite pictures over tropical regions of the North Atlantic, North Pacific, and adjoining areas were used. Use was also made of microfilm copies (from surface weather

charts and 500-mb charts prepared by the National Meteorological Center). To supplement the analysis with missing data, each picture series was distributed by groups so as to facilitate a rapid comparison of similar instances. For ten analyzed instances observational data for three successive days were available, and for ten other instances observational data were available for two or three successive days. These 20 instances were supplemented by another 12 instances, for which only a single cloud-vortex picture was available (for each of them).

Analysis made by several meteorologists showed that the error in determining the position of the point on the satellite picture was about 2° of an arc on the large circle. This error was the maximum possible for the position of the point near the visible horizon. For a series of 21 instances analyzed by Hubert during the typhoon season of 1961, in 85% of the cases the discrepancy in determining the position of the vortex centers between satellite and airborne data was ≤ 180 km. According to another, similar analysis of 23 instances during 1961—1962, the reliability (in percent) in determining the position of the cyclone center was as follows:

Errors, degree latitude	1	1.5	2
Reliability, percent	74	94	99

The position of the cyclone-vortex center was easily determined using one of the following methods.

1. For a well-developed cyclone eye, the center may be located instantly (cf. Photograph 4.55); in such a case, the determination error may increase only due to distortions resulting from photography at large angles.

2. Where the cyclone eye is not clearly discernible, the center may be determined from the spiral cloud bands at the place of their convergence (Photograph 4.56).

3. Finally, the vortex center may be determined by its identification with the center of the cloud mass. However, as will be seen later in this text, the cloud cover of a tropical cyclone has a certain asymmetry which slightly reduces the determination accuracy.

An analysis was conducted /24/ of pictures of tropical cyclones taken by TIROS satellites. Four successive stages of cyclone development were tracked as a function of the baric field at sea level. The principal characteristic of the first development stage is that near the ground surface at the place of disturbance there are no closed isobars; the subsequent three stages are characterized by closed isobars on the surface weather charts. Near the Earth surface, the wind speed increases with the development of the cyclone and reaches peak values during maximum development.

Figure 4.44 shows schematically these three stages. Arrows show the flow lines of the gradient wind drawn from the schematic cloud pattern of the cyclone shown on satellite pictures. For substages A, B, and C, the figure shows the flow lines of the gradient wind near the surface, while for stage D, the flow lines at the 200-mb level are indicated.

The four stages have various characteristics.

1. Tropical disturbance (stage A). In this development stage the surface weather chart has no closed isobars at the place of tropical disturbance. Cyclonic circulation near the surface is but little developed,

or is absent altogether; at higher levels it may exhibit a better development. A particular feature of this stage, as evidenced by satellite TV pictures, is the intensified convection in or near the region of cloud location.

During such a disturbance, the clouds often extend along the axis of the wave to which they are connected.

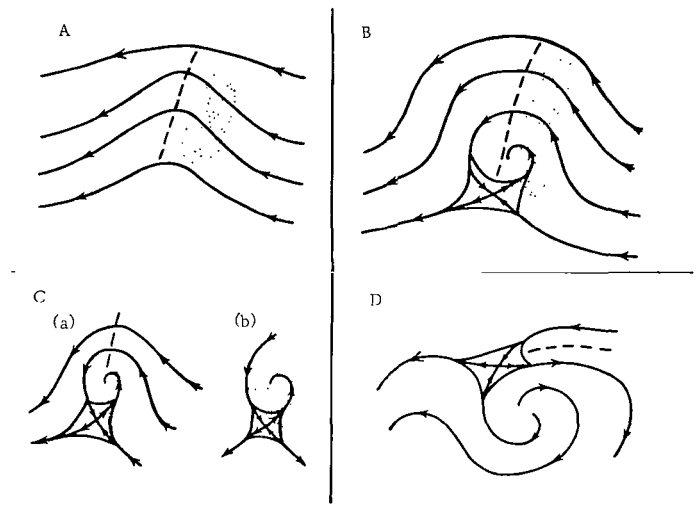

FIGURE 4.44. Schematic representation of development stages of a tropical cyclone:

A — tropical disturbance, closed isobars are absent on the surface weather chart, cloud mass extends along the wave axis; B — tropical low I, maximum wind speed below 10 m/sec, center of the "comma" shape is poorly developed; C — tropical low II, maximum wind speed 10—15 m/sec: (a) — center of "comma" well developed; (b) — onset of darkening, air outflow from the upper layers; D — tropical low III, tropical cyclone I, maximum wind speed 16—20 m/sec, center is darkened, air outflow is seen at the 200-mb level.

In the region of minimum pressure, wind speed is usually low but may attain 12—15 m/sec in the area of flow-line convergence.

Baric topography (high-level pattern) charts above the position of the tropical cyclone in this development stage may exhibit closed isohypses.

2. Tropical low I. Central isotach not above 10 m/sec (stage B). In this stage, the surface weather chart shows at least one closed isobar, which permits the determination of the center of the developing cyclone still not covered by a dense cloud cover.

In the region of such a low, the clouds often have the shape of a "comma" that spreads toward the lower end. The center of the low is located in the region of the upper point of the comma. In the wide region of the comma we can usually notice a dense cloud cover with the tops of cumulonimbus

clouds penetrating the cover. Usually, the zone of this cloud cover does not extend beyond the southeastern quarter of the cyclone.

The most characteristic feature of this development stage is the rounded and sharply outlined western boundary of the commalike cloud cover.

Close to the cyclone center the wind speed does not exceed 10 m/sec; however, in the region of convective clouds it may reach 15—18 m/sec.

3. Tropical low II. Central isotach 10—15 m/sec (stage C). In this development stage, the cloud cover in the cyclone maintains its comma shape; however, the center of the low in which we can notice cloud-free weather becomes more and more pronounced.

Close to the cyclone center the wind speed increases to 10—15 m/sec; in the eastern half of the low, in the region of convective clouds the wind speed may reach 20—25 m/sec.

Instances were observed in which middle and high clouds appeared in the central part of the cyclone as the wind speed at its center approached a value of 15 m/sec. In this case, maximum convergence of currents shifts from the upper end of the comma to the cyclone center, with the region of maximum wind speed also approaching the center.

4. Tropical low III. Tropical storm I. Central isotach 15—20 m/sec (stage D). In this stage, the nature of the circulation is clearly expressed by the cloud distribution. The cyclone center still remains covered with middle and high clouds. The diameter of the cloud cover above the storm center may vary between 100 and 300 km, increasing with the intensity of the tropical storm.

Satellite TV pictures of the tropical storm in this stage frequently show spiral cloud bands up to 200 km wide and even wider; these bands tend to converge toward the center of the tropical cyclone. Most frequently, one of these bands is found in the southwestern part of the cyclone while another part may be found in its northeastern part.

Table 4.14, based on data in /24/, presents cyclone classes according to cloud distribution. The classes in this table correspond, to a large extent, to the classes Ti (i = 1, 2, . . . 5) shown in Table 4.11.

Determination of the zone of strong winds in the region of tropical cyclones

Tropical cyclones are known to have great intensity. Thus, according to Takahashi /25/, the intensity of a tropical cyclone may be determined from the following formula:

$$K = 0.36 \cdot 10^{22} \Delta p r^2 \text{ (ergs)},$$

where K is the kinetic energy of the cyclone; Δp is the pressure gradient between the center and periphery of the cyclone (where the pressure field is undisturbed); r is the radius of that part of the cyclone (in degrees latitude) where the wind speed exceeds 10 m/sec. This radius usually varies from 1 to 9, with an average value of 3.9.

The tropical cyclone has, however, a central area where the wind speed may reach destructive values (25 m/sec and more).

Satellite cloud pictures permit the location of this region of high wind speed. From observations it is known that such regions are associated with the zone of maximum convective activity in the area of a cloud "wall" and with areas of some more active spiral-like cloud bands near the cyclone center. If these areas can be identified on the pictures this permits the determination of position and extent of the storm zone.

In such an analysis it is very important to perform a correct evaluation of cloud characteristics, particularly for the instance in which the cumulus clouds in the lower layers of the troposphere during the first development stages of the tropical cyclone are covered with cirrus clouds that later spread partially or completely over the region of convective clouds forming, as it were, a curtain above this region. Photographs 4.57 and 4.58 illustrate these development stages. In the former case, the spirallike cirrus clouds start to develop above the cumulus clouds of the cyclone except for its center. In the latter case, the cirrus clouds have almost completely formed a curtain. However, the cyclone eye can still be tracked.

The dependence of strong-wind area (in percent of the total cyclone area) on cyclone diameter is as follows:

Cyclone diameter, km . . .	450	450—700	700—1,250
Area, %	40	20	10

Photograph 4.59 shows a typical instance in which the region of strong winds near the typhoon center appears as a bright circle. For such a case, according to shipborne data, the wind speed within this circle reached 20 m/sec, but higher speeds were recorded in an area of radius 350—550 km; such speeds were also recorded both during and after satellite photography. Typhoon Amy, shown on the photograph, was extremely strong with the speed at its center reaching 50 m/sec. The most intensive winds with speeds $\geqslant$ 25 m/sec were recorded within the above-mentioned bright circle of radius 55 km, relative to the typhoon eye.

Another example illustrating the possibility of identifying the region of strong winds near the center is shown in Photograph 4.60. Here, the region is delineated by the diffuse rim of the darker background around the center with brighter convective clouds.

For some typhoons, this region is wider but wind speed is smaller, reaching about 15 m/sec.

Observations have shown that the region of strong winds near the surface is asymmetric relative to the center; wind speeds in the region to the right of the cyclone center (relative to its movement direction) are larger than to the left of the center.

It was also noticed that on satellite photographs cloudiness shows a similar asymmetry. Investigation of ten instances showed that asymmetry of regions of large wind speeds near the surface is found beneath regions of asymmetric clouds. Photograph 4.61 shows an example of asymmetric distribution of a typhoon cloud cover (typhoon Opal photographed on 4 August 1962). The picture permits the exact determination of the eye position, both directly and from the position of the convergence point of spiral clouds. The cloud region to the right of the center is almost three times larger than the region to the left.

TABLE 4.14. Table for determining the class of clouds in a tropical cyclone according to cloud-distribution

Cloud-distribution features	0	1
Cyclone eye or characteristic center of cloud cover	Center of cloud cover is not seen. Dense cloud mass	No cyclone eye visible. Center of cloud-distribution pattern is not clearly seen. It can be determined approximately from the rounded bands in the cloud structure
Furrow bands	No bands are present. No irradiating (divergent) cirrus clouds are noticed	No cloud bands are noticed within the cyclone center. Irradiating cirrus-cloud bands are usually located at the edge of the dense cloud cover (sometimes such bands are noticed only in a quarter of the circle)
Bands	There are no bands that might indicate the center of the cloud mass	Bands poorly developed.* The central cloud mass and its boundaries show the presence of small inwardly extending cloud elements that might be masked by dense cirrus clouds. The periphery of the total cloudiness region shows lower, slightly bent cloud bands that intersect this region at a large angle. The existence of cloud bands is doubtful beyond the total-cloudiness region
Gaps in the region of total cloudiness (including dark-gray spots)	Shape and distribution of the gaps are very irregular	No major gaps are noticed in the cloud cover, and if they exist they are not concentric and have irregular shape
Additional features of cloud distribution	Cloud-shape irregular. Cloud location may be tracked but center of cloud pattern is not discernible	Beyond the region of total cloudiness we notice the cloud cover of a weakly developed cyclone. The central part of the cloud mass better resembles the elements of bright clouds than extended broken cloud bands

* Bands are not present or their presence is doubtful; cloud elements are irregularly distributed; there are no successive linear cloud elements, etc.

** Bands are poorly expressed; cloud elements show the overall location of the cloud pattern, although it is rather difficult to define any isolated cloud group as a cloud band. Weak bands appear either as wide broken and poorly expressed strips, or else they consist of broken, individual elements. The curvature along any cloud band is not constant and the large-scale bands are not parallel. The weak bands of low clouds usually converge in the region of total cloudiness and are not clearly visible.

pattern

Class 2	3	4
No eye is visible, but the cloud-distribution pattern is discernible near the end of the wide band which is bent at a large angle toward the center	The eye is usually visible, but is insufficiently clear and has an irregular shape. No ring-shaped bright cloud cover is present near the eye	The eye may be seen as a dark round spot surrounded by a ring-shaped dense and bright cloud cover. The diameter of the eye does not exceed 30—40 km, while the ring-shaped cloud cover around the eye is of varying size. The edges of the eye are smooth, unlike the broken and diffuse edges of class 3 eye
A few cloud bands are noticed above the cyclone center (sometimes they are not noticed altogether). Several cirrus cloud bands, not necessarily of the divergent type but more expanding than in class 1, may be tracked at the edge of the dense cloud cover	Several expanding cloud bands in the central cloud mass. Cirrus cloud bands are often visible far from the edge of the dense cloud cover	Clearly expressed concentric cloud bands in the central part of the tropical cyclone. Cirrus cloud bands are tracked beyond the region of total cloudiness.
Usually, we can notice a single, wide and long cloud band with broken edges spirally spinning about its wide end and in the central part. The width of this band is about 2 degrees latitude. The band and the region of total cloudiness are often asymmetric, since the single bent cloud band sometimes converges within the "tail" and forms a region of total cloudiness only at one side of the cyclone center. The bands are poorly visible outside the region of total cloudiness.†	Within the region of total cloudiness near the cyclone eye we notice spiral and concentric cloud bands that may be seen rather frequently along an arc of more than 90°. Usually the width of such bands does not exceed 200 km (2 degrees latitude). If the bands have a width of not more than 40—50 km they may form a broken line along a 360° arc. Poorly developed cloud bands may be seen beyond the area of total cloudiness.†	Narrow and extended, spiral, and concentric cloud bands†† are seen in the region of total cloudiness. The concentric bands are located immediately after the mass of bright clouds ("wall" clouds). Unlike class 3, the bands of this class in the region of total cloudiness are better developed, more concentric and located closer to the eye. The bands beyond the region of total cloudiness are also better developed.
A gap in the shape of a long line is the distinctive feature of this class. The gap (covered by thin high clouds) enters the zone of total cloudiness at large angles to its periphery, and penetrates the area of the inner circle without interfering with the rules of its determination. The gap closely resembles a spiral with the wide end at the storm center.	Nearly concentric or strongly extended, somewhat broken gaps covered by thin cirrus clouds	As distinct from class 3, the gaps in this class are more concentric and have smoothened edges. Above, they are covered by thin cirrus clouds
Wide, far extending band in the shape of a bent tail	The clouds have a compact shape which tends to be round, although a tail is still visible	The edges of the main cloud region of circular shape are rather sharp, but within one or two quarters of the circle they are slightly smoothened. A clearly expressed "trench" is delineated by the region of total cloudiness and by strong bands beyond the region

† Moderate bands are of medium size between weak (*) and strong (††) bands.

†† Strong, clearly expressed bands; the elements are characterized by a clear direction, they are long and narrow (1 degree latitude); often they are rounded to 180° forming dense and bright bands with rounded edges. Strong bands usually have no sudden changes of curvature, and create a pattern of concentric circles or ellipses around the center of the cloud mass.

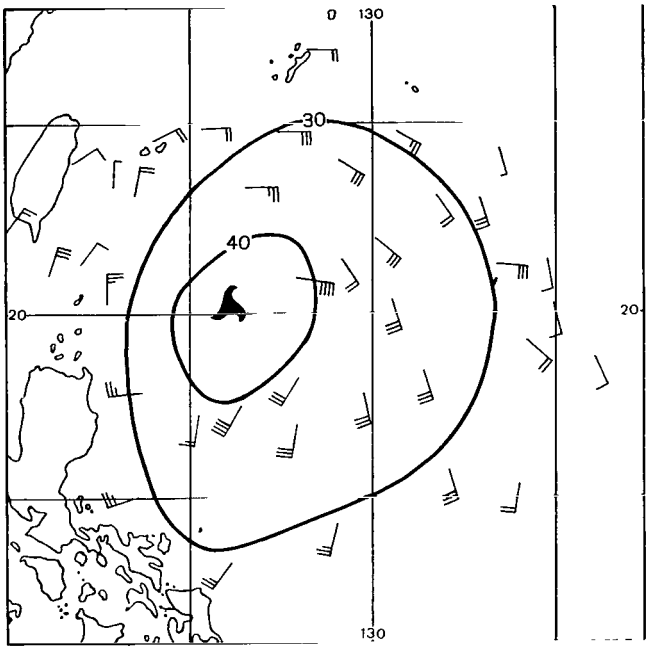

FIGURE 4.45. Field of mean isotachs near the Earth surface (in knots) between 3 and 5 August 1962 (the position of the cyclone on 4 August may be seen at the center)

Figure 4.45 shows the wind field, averaged over a 48-hour period, from 1200 hr on 3 August 1962 to 1200 hr on 5 August. Photograph 4.61 was taken on 4 August 1962 at 0800 hr. The radius of the region where the wind speed was $\geqslant 15$ km/sec was in the eastern part and was about twice that in the western part. This shows a certain asymmetry relative to the movement direction, the reason for which is still not understood; such an asymmetry is useful when determining the direction of cyclone displacement.

Analysis of successive stages in the development of tropical cyclones shows the relationship between maximum wind speed near the surface and evolution of cloud distribution in these cyclones. Using this relationship, Hubert /24/ suggested a method for evaluating the maximum wind speed of tropical cyclones near the surface by interpreting satellite cloud pictures.

The method consists in drawing inner and outer circles, the former of which comprises the cloud field at the storm center, while the latter covers the cloud field associated with tropical cyclones. After the cloud field at the cyclone center is identified, the class of this cloudiness is determined according to the data from Table 4.14. Figure 4.46 shows schematically the distribution of cloud classes at the center of the tropical cyclone, as well as a graph for determining the maximum wind speed (v_{max}) at the Earth surface.

With known class of clouds located in the inner circle and after measuring the outer circle diameter in degrees latitude, one can determine

the maximum probable cyclone speed near the surface (using the graph in Figure 4.46b).

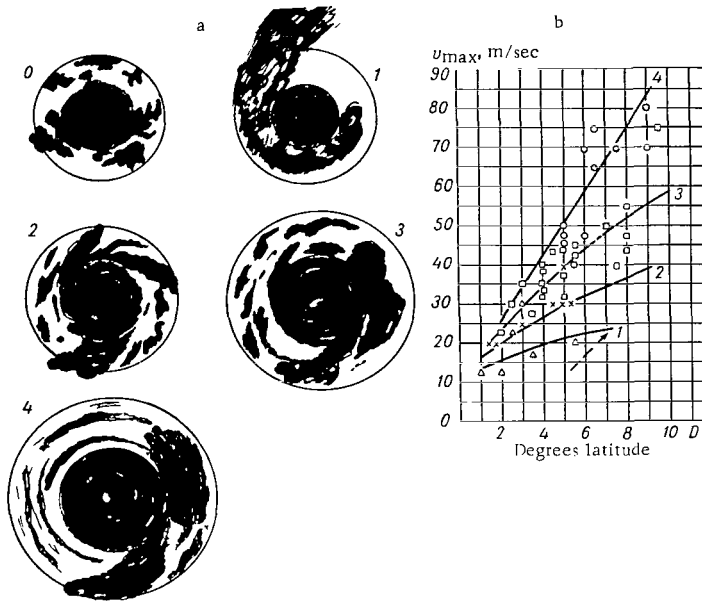

FIGURE 4.6. Variation of wind speed for different classes of cyclone with cloud characteristics:

a — cyclone class; 0 — internal structure-dense cover (no bands), external structure poorly developed; 1 — internal structure comprises cloud bands without spirals, external structure shows an absence of bands or the presence of weak bands; 2 — internal structure comprises diffuse spirals, external structure comprises moderate bands; 3 — internal structure comprises dense spirals, external structure comprises moderate or strong bands; 4 — internal structure comprises very dense spirals, external structure comprises well-developed bands (internal structure is determined from the inner circle); b — graph for determining wind speed.

The graph in Figure 4.46b shows four experimental curves of maximum wind speed near the surface as a function of both cloud class at the center of the cyclone and outer-circle diameter. The abscissa shows the diameter in degrees latitude and the ordinate shows the wind speed in m/sec.

Maximum wind speed with the aid of this graph should be determined in the following order.

1. Plot on the geographical map the contours of the cloud region connected with the tropical cyclone; the region should contain all the gaps and cloud bands from the peripheral area.

2. Plot the inner-circle area, which should include the region of total cloudiness characterized by a relatively high reflectivity. The field of this bright cloud cover may exhibit small dark spots that should correspond to the following requirements:

a) the width of the dark band should not exceed one degree latitude, and its brightness should correspond to that of a thin cloud layer and not to the open areas of the underlying surface;

b) the dark bands should be concentrated at the center of the cyclonic vortex, except for class 2 clouds in the cyclone center. The narrow rounded dark spots oriented toward the center are a distinctive feature of class 2 clouds and belong to the area of the inner circle if they correspond to a thin-cloud sheet, the width of which does not exceed 1 degree latitude;

c) weakly developed dark cloud bands may be detected beyond concentrated gaps.

3. Determine from satellite pictures of tropical cyclones the tropical disturbances (stage A) for which the distribution of cloudiness corresponds to class 0 according to Hubert. In doing so the following points have to be taken into account:

a) the diameter of the inner circle of tropical cyclones of this class does not exceed one degree latitude;

b) the area of the inner circle of these cyclones is up to $^{7}/_{8}$ covered with clouds of relatively high reflectivity. The relatively dark bands should be narrow and correspond to the layer of thin clouds.

Sometimes, the diameter of the inner circle depends on which part of the total-cloudiness region (where brightness gradually decreases as the distance from the tropical cyclone center increases) is located within the inner circle. The gradual reduction in cloud brightness probably occurs in places where no low cloud layers are present. (Such places are beneath thick vertical cloud layers, the vertical thickness or optical density of which decreases with increasing distance from the cyclone center.) In this case, we must include in the circle the thin layer of gray cirrus clouds, leaving along the diameter of the circle the main dense mass of cirrus clouds without the lower-lying cloud cover. With this in mind, the inner-circle periphery should be drawn at the center of the section on which cloud brightness gradually decreases to gray.

4. Draw the periphery of the outer circle that covers the whole cloud mass of the tropical cyclone and measure the diameter of the circle in degrees latitude.

5. Using the graph in Figure 4.46b, determine the maximum probable cyclone speed near the surface.

6. Knowing the maximum wind speed of the cyclone determine its development stage.

Atmospheric currents of the upper troposphere in the region of tropical cyclones

Although a knowledge of the wind-speed field near the Earth surface has much practical importance, the wind field in the upper troposphere above the tropical cyclone is of no less interest both in predicting the path of the cyclone and in ensuring optimum flight conditions.

In the early stage of cyclone development, the cloud field characterizes the field of air-mass disturbances in the lower troposphere. In the later development stage, the cyclone region is covered with a curtain of cirrus

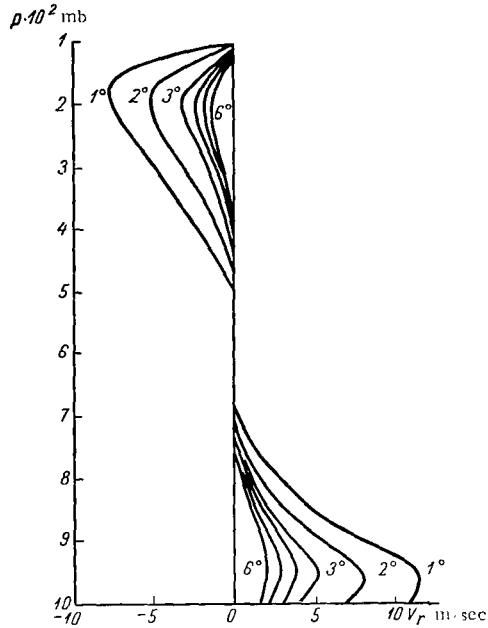

FIGURE 4.47. Vertical profile of radial wind-speed component in a tropical cyclone as a function of distance from cyclone center (according to Palmén and Gill)

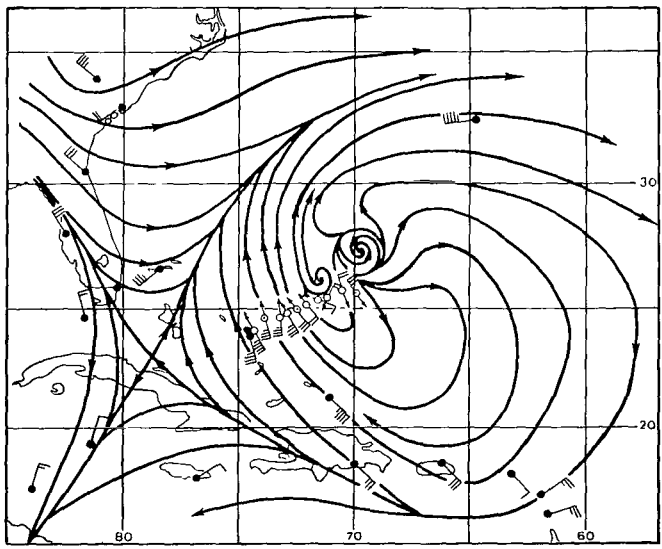

FIGURE 4.48. Flow lines and wind speeds at the 200-mb level at 1200 hr on 5 October 1962 in the region of cyclone Daisy

clouds, the position of which permits the flow direction of upper-air currents to be determined.

Figure 4.47 shows in degrees latitude the vertical profiles of the radial wind-speed component at different distances from the cyclone center. From the figure it is seen that in the lower, 3-km layer the radial component is oriented toward the center. In the upper troposphere it is oriented from the center outwards with its maximum at the 200-mb level. These data are in good agreement with results obtained earlier by Palmén, Jordan, Riehl, and others prior to the first satellite launchings. Thus, the observed cirrus bands permit the evaluation of wind direction in the upper troposphere. An example of such an evaluation is presented in Figure 4.48 and Photograph 4.62, showing the flow lines and the wind at the 200-mb level at 1200hr on 5 October 1962. With the aid of cloud pictures (cirrus bands) it is easy to show that the bands coincide in direction with the flow lines.

How to determine squall lines

Usually, a well-developed tropical cyclone shows in its frontal part a linear region of well-developed convective clouds connected with intensive precipitation and a short-time increase in wind speed. This line is called a squall line [also known as instability line] and its passage frequently precedes a tropical cyclone. On satellite pictures the squall line detached from the cirrus clouds is often well developed. Photograph 4.63 shows an example of a cumulus-cloud line not linked with the mass of cirrus clouds. However, squall lines are not always visible and therefore they may be used only as an auxiliary indication of cyclones.

Direction of movement of a tropical cyclone

Using the preceding features, the direction of movement of a tropical cyclone may be evaluated from the following indexes:

1) the tropical cyclone moves normal to the asymmetry line of the cloud cover so that the smaller axis of the cloud mass will be oriented from the center to the left;

2) the tropical cyclone moves in a direction normal to the squall line (if such is noticed);

3) the tropical cyclone moves in the direction of the upper air current as evidenced by the cirrus clouds;

4) the cyclone moves normal to the asymmetry line of the region of maximum wind speed near the surface, as evidenced by the bright circle on the cloud picture near the cyclone center.

If all these indexes are available at the same time, the flow direction of the tropical cyclone can, of course, be determined with far greater reliability.

How to evaluate the intensity of a tropical cyclone

The intensity of a tropical cyclone can be evaluated with empirical formulas that link the diameter of the cirrus-cloud cover with the depth

of the cyclone. Such a relationship has been used /10, 23/. Statistical processing of satellite data permitted the plotting of an experimental curve (Figure 4.49) showing the surface pressure as a function of the horizontal sizes of the cloud cover over a tropical cyclone. In this figure, the abscissa shows the cloud-cover diameter and the ordinate the atmospheric pressure at the cyclone center. Hence, with satellite-picture data on the horizontal sizes of the cloud cover and using the above relationship, one can determine the most probable magnitude of surface atmospheric pressure at the cyclone center.

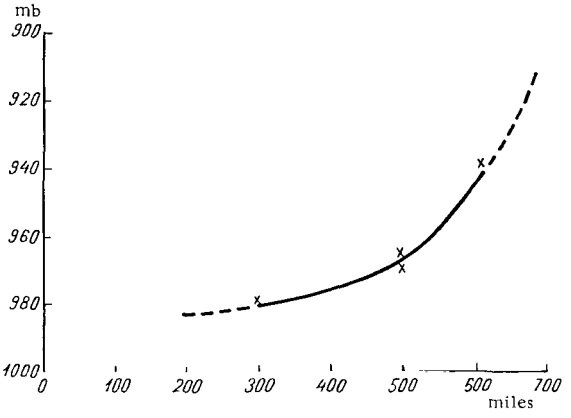

FIGURE 4.49. Relationship between pressure in the typhoon center and diameter of cloud mass

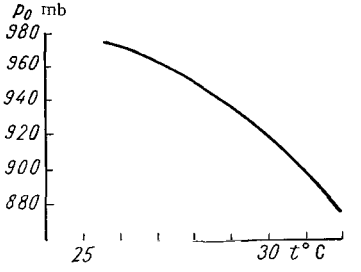

FIGURE 4.50. Depth of tropical cyclone as a function of water-surface temperature

According to existing data, the depth of a tropical cyclone shows a rather good correlation with the temperature of the underlying surface /25/. This relationship is shown in Figure 4.50 and may, to some extent, be used to evaluate the state of the water surface after determining the pressure at the cyclone center.

EXERCISE

Determine the characteristics of tropical cyclones

Starting material

Satellite TV pictures of tropical cyclones (cf. Photographs 4.64 and 4.65).

Sequence of performance

1. Using the TV cloud pictures shown in Photograph 4.64, determine the development stage of each of the eight tropical cyclones.

2. From the cloud pictures shown in Photograph 4.65 determine the class of each of these cyclones according to Hubert, diameter D of the outer circle, maximum wind speed v_{max} at Earth surface, and atmospheric pressure p_0 at the center of the cyclone.

Appendix 1 presents correct solutions to these problems and the actual values of maximum wind speed at the Earth surface obtained with shipborne instruments and other devices. An Appendix also presents surface weather charts and absolute baric topography charts for the cases considered. Correspondence between figures and photographs may be checked using Appendix 2.

4.7. DETERMINATION OF WIND AND JET-STREAM DIRECTION

The troposphere and lower stratosphere have two jet-stream branches. One of them is connected with the polar front and occurs, on the average, in a belt between 30 and 40 degrees latitude. The second branch is connected with the arctic front and occurs between 60 and 70 degrees latitude. Both branches, particularly the first, northern one, is subjected to considerable migration, the rate of which depends on cyclonic activity. To determine the characteristics of jet streams one has to find the details of the wind-speed field; satellite cloud pictures are of considerable aid for this purpose.

The zone of jet streams is connected with the zone of maximum horizontal temperature gradients and hence with the zones of maximum vertical wind-speed gradients.

A considerable horizontal temperature gradient is found in two frontal zones: in the frontal zone of the lower troposphere, and in the height frontal zone of the upper troposphere where it is more intensive. As a result, maximum jet-stream intensity is found in the upper troposphere (at the 200—300-mb level) slightly below the tropopause.

Satellite pictures clearly show the band structure of the clouds, the bands extending in a definite direction. Sometimes, these cloud bands are oriented along the air current at the given baric level, but in some cases the bands are found at some angle (sometimes very large) to the air current at this level. Such a definite orientation and structure of the cloud bands makes it possible to determine numerous characteristics of the jet stream.

With data in /18/ on hand, let us analyze a cloud mass that formed in a layer with lower and upper boundaries z_0 and z_1. For the moment let us assume that at this stage there is no longer any vertical movement in the layer. An x-axis is directed along the wind direction at the lower boundary of the layer. Let u_0 and $v_0=0$ be the wind-speed components along the x- and y-axes of the lower boundary (z_0), and u_1 and v_1 the respective speed components at the upper boundary (z_1) of the layer.

If the wind in a layer with the boundaries $z_0 \sim z_1$ varies linearly over height then, at some intermediate level z, we have

$$u = u_0 + \frac{u_1 - u_0}{z_1 - z_0}(z - z_0),$$

$$v = \frac{v_1 - v_0}{z_1 - z_0}(z - z_0). \qquad (4.1)$$

The coordinates of the position of a cloud point at level z at time t may be found from

$$x = \int_{t_0}^{t} u\,dt,$$
$$y = \int_{t_0}^{t} v\,dt, \tag{4.2}$$

where t_0 is the initial time.

Assuming u_0, u_1, v_0 and v_1 to be constant, equation (4.1) yields

$$x = \left[u_0 + \frac{u_1 - u_0}{z_1 - z_0}(z - z_0)\right] t,$$
$$y = \frac{v_1}{z_1 - z_0}(z - z_0)\, t. \tag{4.3}$$

Eliminating z, z_1 and z_0 with the aid of (4.3) we obtain the following expression for the x coordinate of a cloud mass on a horizontal plane during the time t:

$$x = u_0 t + \frac{u_1 - u_0}{v_1}\,. \tag{4.4}$$

In other words, the cloud mass on the photographs should extend along the vertical wind shift in the given layer, i. e., they should extend along the thermal wind in this layer.

Let us now consider another case for which the above-mentioned conclusions are also valid. In addition, let us assume that the existent vertical movements in this case are only functions of height.

The ratio between z_0 and t for a cloud particle that starts to rise from level z at time $t = \tau$ to level z at time t may be written as

$$\int_{z_0}^{z} \frac{dz}{w(z)} = t - \tau. \tag{4.5}$$

Therefore, the height of this cloud particle is a function $f(t - \tau)$, while

$$z = \begin{cases} f(t-\tau) + z_0 & \text{for } t > \tau \\ z_0 & \text{for } t = \tau. \end{cases} \tag{4.6}$$

The horizontal speed of the cloud particle at time t is found from

$$u(t, \tau) = \begin{cases} u_0 + \frac{u_1 - u_0}{z_1 - z_0} f(t-\tau) & \text{for } t > \tau \\ u_0 & \text{for } t = \tau \end{cases}$$
$$v(t, \tau) = \begin{cases} \frac{v_1}{z_1 - z_0} f(t-\tau) & \text{for } t > \tau \\ 0 & \text{for } t = \tau. \end{cases} \tag{4.7}$$

The coordinates at time t of the particle are found by integrating (4.7) to give

$$x = u_0 t + \frac{u_1 - u_0}{z_1 - z_0} \int_{\tau}^{t} f(t-\tau)\, dt,$$

$$y = \frac{v_1}{z_1 - z_0} \int_{\tau}^{t} f(t-\tau)\, dt. \tag{4.8}$$

The projection of the cloud mass on the horizontal plane is found from (4.8) by eliminating $\int_{\tau}^{t} f(t-\tau)\, dt$; this yields

$$x = u_0 t + \frac{u_1 - u_0}{v_1}\, y. \tag{4.9}$$

Comparing (4.9) with (4.4), we see that the projection of the cloud bands on the horizontal plane should also be directed along the thermal wind.

The above assumptions somewhat simplify the true picture since the cloud may change its contour as a result of other influences, even if it does not move together with the air current. Moreover, vertical movements and the wind speed may be a complex function of height and time. Nonetheless, the general assumptions about the wind-speed field and its connection with the cloud bands remain valid.

Qualitatively, the jet streams may be analyzed from cloud data since the specific features of the spatial cloud distribution in the zone of strong jet streams depend not only on the vertical movement of air, which differs in sign with the orientation toward the jet-stream axis, but also on the air humidity in the region of the high-level frontal zone in which the jet streams develop. Any considerable changes in this complex system of vertical air movements along the jet-stream axis and rapid changes in structure affect cloud distribution. The association of the jet stream to specific high-level frontal zones, changes in the baroclinicity of these zones, and seasonal variations in the jet streams affect both the structure and distribution of cloudiness.

Cloud structure in the jet-stream zone depends on the longitudinal and transverse movements relative to the jet axis as well as on the existence of large-scale vertical eddies in the high-level frontal zone at the cyclonic side of the jet stream.

Numerous studies /18, 19/ have been made on the relationship between cloudiness and jet streams using data from airborne and balloon soundings, as well as satellite pictures and other information. Most of them reached the same conclusions as to the shape of clouds and cloud systems associated with jet streams.

The following, most characteristic features of cloud distribution in the region of jet streams were determined from statistically processed data.

1. To the right of the jet-stream axis in the frontal part of the high-level trough there is a region of stratiform clouds (Cs) resulting from the ordered ascending air movements in this area. To the left of the axis there are Cu, Cb, and Ac clouds, and anvil cirrus clouds; such a distribution of clouds is characteristic of strong jet streams.

2. Cirrostratus and high cirrus clouds are often located above frontal clouds of much lower level.

3. Close to the high-level trough, there is often no cloudiness at all, or else it is present in the form of a narrow cloud band to the right or left of the jet-stream axis.

4. Cloudiness is also often absent to the left of the stream axis in the frontal part of the high-level trough, in which case the axis is determined from the position of the broken boundary of the cirrus cloud bands that are found to the right of the stream.

5. The rear part of the trough is often characterized both by the presence of cirrus cloud bands oriented along the stream axis, and by the absence of clouds to the left of the axis.

6. The top boundaries of the cloud systems to the right or left of the jet-stream axis are usually below the tropopause, and the difference in their position depends to a certain extent on the discontinuity of the tropopause along the stream axis; this difference in position often reaches several kilometers.

7. The clouds of the highest layers to the right of the axis have a more ordered structure than those located to the left; this structure has the shape of a dense wide (400—600 km) band, or of isolated extended strips along the air current. On the other hand, clouds of much lower levels to the left of the axis have a less ordered (cellular or chaotic) structure.

8. The jet-stream axis forms a definite boundary between cloud systems located on either side; a gap in the upper clouds along the jet axis may be noticed even when these clouds are located to the left of the axis.

9. Cirrostratus clouds of jet streams are very often much denser than the same clouds formed under other conditions, and hence they are brighter on satellite pictures.

The above features of jet-stream cloud distribution are certainly not exhaustive, but we have discussed them here since they are easiest to be tracked on satellite cloud pictures, the more so as such satellites with their larger field of view yield a global picture of the distribution and structure of cloudiness and of the position of the jet-stream axis. This is clearly seen from Photographs 4.66 and 4.67.

On Photograph 4.66a the position of the jet-stream axis is easily located in the area between 80 and 85°W from the shadow strip cast by the higher-level clouds located to the right of the axis on the lower clouds located to the left. Such a jet-stream structure is also clearly seen on Photograph 4.66b. Amorphous clouds to the right of the shadow have a well-developed broken edge along the jet-stream axis; airborne soundings, made at almost the same time as the satellite pictures were taken, confirm that the dark strip is the shadow and not a gap between two cloud systems /19/.

Photograph 4.66c shows a more complex case: here, the jet-axis position is determined from the shadow cast by the cirrus-cloud wedge (to the left of the frame between 40 and 45°N) on the cellular convective clouds. On the upper edge of the frame, the position of the frontal cloud system and the center of the cyclonic vortex confirm the position of the jet stream.

On Photograph 4.66d, the position of the jet stream coincides with the broken boundary of the cirrus and cirrostratus clouds in the region between 30 and 32°N; here, the clouds are projected against the dark surface of the ocean. Cloud jets are absent to the North.

Photograph 4.67 contains four frames showing different cloud distributions in the jet-stream area. The first frame (a) shows clouds of

mountain wave over the western part of the U.S.A. The cloud mass, dissected into long cloud bands, extends from the southwestern to the north-eastern region. This cloud mass is bounded by a dark wide cloud-free strip oriented at the NE from 35°N to 100°W. Thin cloud bands are oriented almost normal to the air current. The second frame (b) shows the jet stream as a boundary of cirrus clouds in the form of bright transverse bands normal to the air current.

Sometimes, as may be seen from the third frame (c), jet streams are identified from the narrow cloud bands. On the picture such bands appear against the background of the underlying water surface.

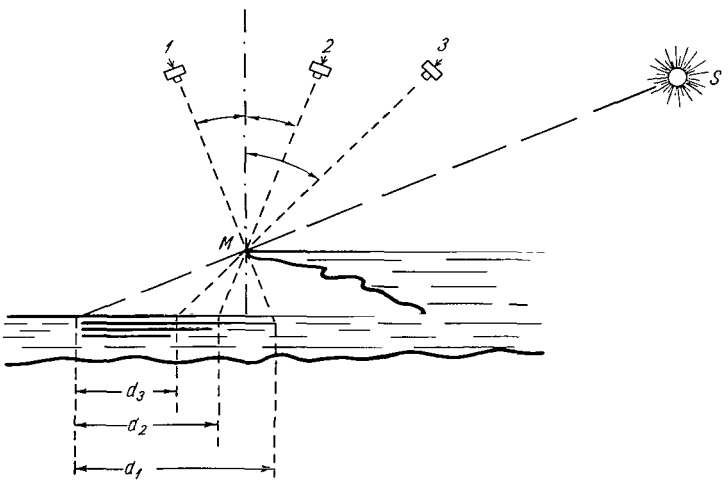

FIGURE 4.51. Schematic representation of the shadow cast by jet-stream clouds

On the fourth frame (d) of Photograph 4.67, the northwestern jet stream is identified from the cirrus-cloud bands located in the SW of the frame against the background of the water surface of the Sea of Okhotsk, west of Kamchatka.

Jet streams often form the border line between cloud systems located to the left or right of the jet axis at different levels and of different structure. Under certain photography conditions upper clouds may cast a shadow on lower clouds. According to data from /19, 24/, the shadow width varies from 10 to 30 km, depending on Sun altitude, the difference in height between the upper boundaries of high- and low-level clouds, and on the angle at which the upper clouds are viewed from the satellite. This is shown schematically in Figure 4.51.

In the following, we present an exercise for the evaluation of satellite cloud pictures to identify jet streams.

In solving the problems of this exercise it is necessary to check the relationship between clouds and jet streams in regions for which ample data are available, and then to use satellite data for identifying jet streams in regions with sparse observations.

EXERCISE

Determination of jet-stream axis

1. Initial data

1. Cutout from surface weather chart plotted at 1500 hr on 20 November 1962 (Figure 4.52).

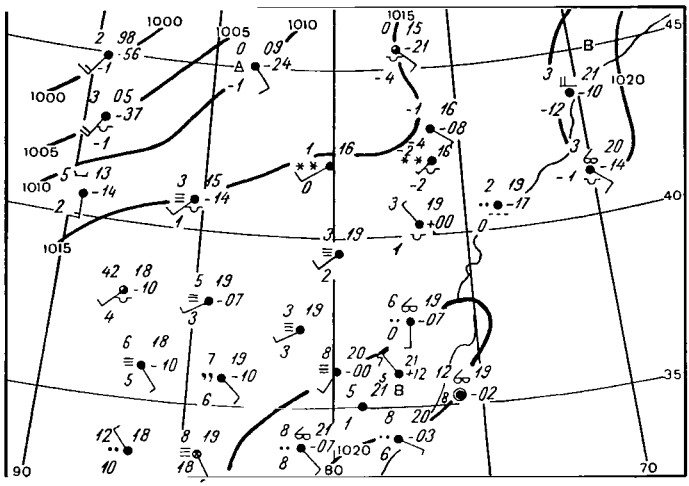

FIGURE 4.52. Cutout from surface weather chart plotted at 1500 hr on 20 November 1962

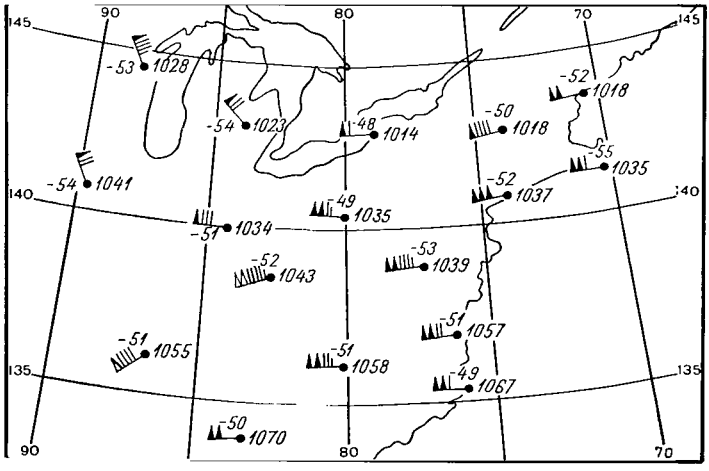

FIGURE 4.53. 250-mb chart plotted at 1200 hr on 20 November 1962

2. Cutout from the 250-mb chart plotted at 1200 hr on 20 November 1962 (Figure 4.53).

3. Cloud pictures taken at 1358 hr on 20 November 1962 by TIROS VI on orbit No. 0922, and at 1447 hr on the same day taken by TIROS V on orbit No. 2209 (Photograph 4.68).

4. Data of radio soundings at 1200 hr on 20 November 1962 (Figure 4.54).

5. Data from airborne soundings of the upper-cloud boundary with an interval of one hour between the time of soundings and satellite photography (Photograph 4.68).

6. Nephchart (Figure 4.55).

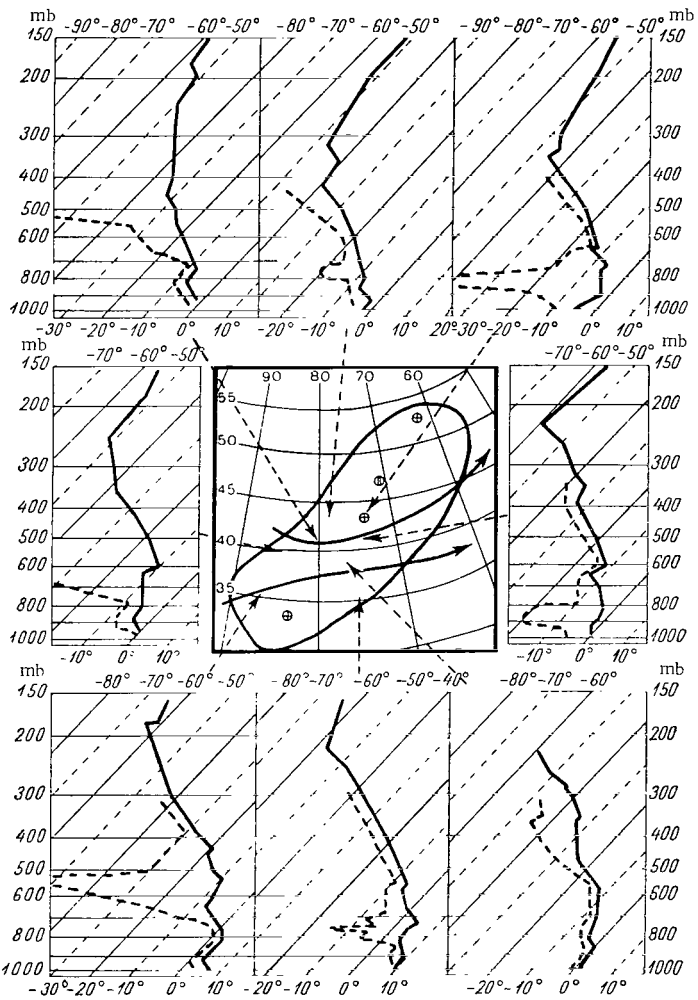

FIGURE 4.54. Data of radio sounding performed at 1200 hr on 20 November 1962, close to the jet-stream region

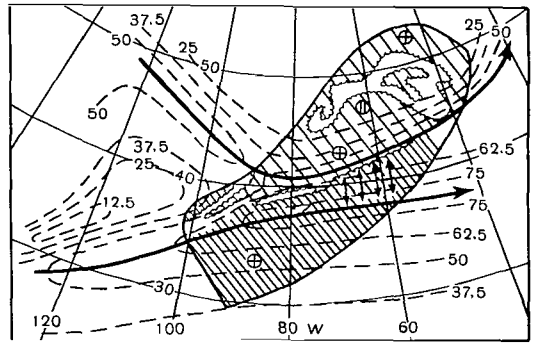

FIGURE 4.55. Nephchart for Photograph 4.68. Isotachs in m/sec

Sequence of operations

1. Analyze the 250-mb chart to detect the jet streams.
2. Compare the cloud picture with nephanalysis data and airborne soundings, laying stress on the dark band of the break in the clouds.
3. Compare the position of jet streams on the 250-mb chart and the position of the dark band of cloud breaks on the satellite picture.
4. Determine on the picture (using the geographical grid) the width d of the dark band of cloud breaks near point M.
5. Calculate for this point the probable width d' of the shadow cast by the upper clouds on the lower ones, using data of the difference in height between the upper cloud boundary to the left and right of the shadow and from the Sun altitude of 18°.
6. Determine the width d'' of the territory viewed from the satellite for a 9° deviation from the local vertical of the camera's optical angle, and for a satellite height $H = 600$ km. Then compare the width with the resolution of the camera and decide on the possibility of identifying this section of territory on the given satellite picture.
7. With data obtained by comparing the values of d, d', and d'', determine on the given area of the picture the existence of shadow cast from top clouds.

II. Initial data

1. Cutout from surface weather chart plotted at 0000 hr on 15 January 1962 (Figure 4.56).
2. Cutout from the 300-mb chart plotted at 0000 hr on 15 January 1962 (Figure 4.57).
3. Cloud photographs taken at 2330 hr on 14 January 1962 by TIROS VII on its orbit No. 3098 (Photograph 4.69).
4. Charts of outgoing radiation measured in the atmospheric window within the 8—12-μ band at 2330 hr on 14 January 1962 by TIROS VII (orbit No. 3098) (Figure 4.58).

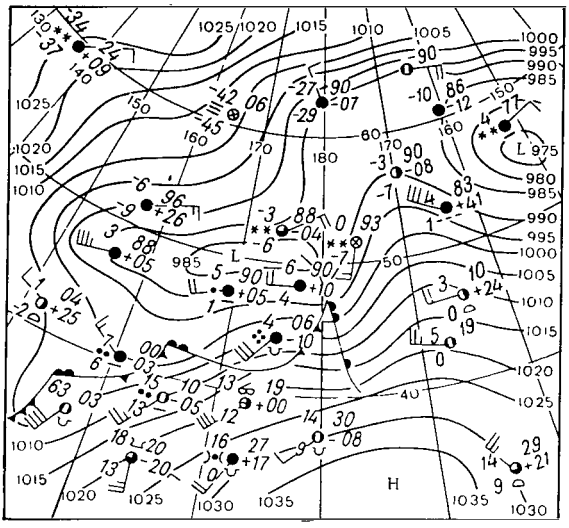

FIGURE 4.56. Cutout from the surface weather chart plotted at 0000 hr on 15 January 1962

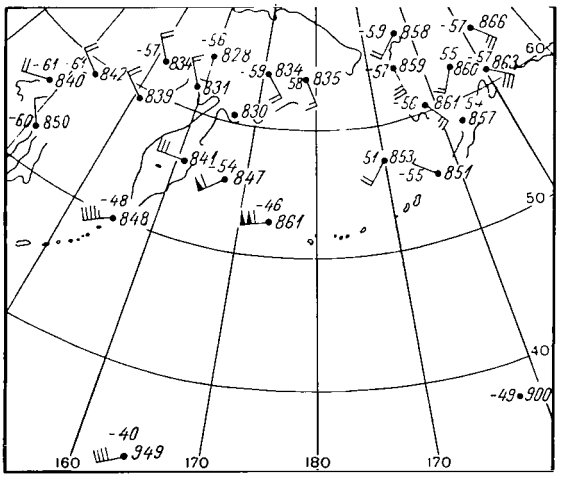

FIGURE 4.57. 300-mb chart plotted at 0000 hr on 15 January 1962

Sequence of operations

1. With the available data on hand, analyze the 300-mb chart and determine the position of the jet-stream axis from the wind and geopotential distribution.

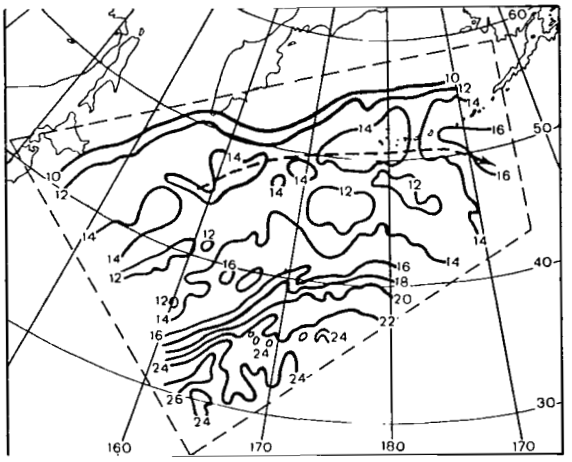

FIGURE 4.58. Chart of outgoing radiation in the 8—12-μ band (Channel 2) plotted at 2330 hr on 14 January 1962

2. Determine the geographical coordinates of several points of the jet-stream axis on the cloud pictures and then plot these points on the 300-mb chart for refining the analysis.

3. Explain the position of the jet-stream axis in the field of outgoing radiation (8—12-μ band) to confirm the analysis of the 300-mb chart and cloud pictures.

4.8. RECONSTRUCTION OF THE GEOPOTENTIAL AND WIND FIELD FROM THE CLOUDINESS FIELD

The practical application of cloud data is made in different ways. One consists in using a physical-statistical approach to establish the relationship between cloudiness and the geopotential field necessary for the transition from the field of cloudiness to that of geopotential.

Musaelyan /5/ advanced a physical-statistical method for using satellite cloud pictures to determine the geopotential and wind field over a given territory and at a given level. Basically the method consists in the following.

Let the extent of cloud cover along each latitude circle or direction x be $S(x)$.

This function may be expanded as the Fourier series

$$S(x) = \frac{S_0}{2} + \sum_{m=1}^{M} S_m \cos mx + \sum_{m=1}^{M} S'_m \sin mx, \tag{4.10}$$

where S_m is the Fourier coefficient and m the wave number.

Similarly, the vertical component of the vorticity $\Omega_h(x)$ at level h may be expressed as

$$\Omega_h(x) = \frac{\delta_0}{2} + \sum_{m=1}^{M} \delta_m \cos mx + \sum_{m=1}^{M} \delta_m \sin mx \tag{4.11}$$

and the horizontal divergence D_h of the speed as

$$D_h(x) = \frac{\gamma_0}{2} + \sum_{m=1}^{M} \gamma_m \cos mx + \sum_{m=1}^{M} \gamma'_m \sin mx, \tag{4.12}$$

where

$$D_h = \frac{\partial u}{\partial x} + \frac{\partial v}{\partial y}; \quad \Omega_h = \frac{\partial v}{\partial x} - \frac{\partial u}{\partial y}, \tag{4.13}$$

u and v being the horizontal components of wind speed.

Such a Fourier series is valid for each line of the chosen rectilinear grid of points, and, if the problem is solved in spherical coordinates, for each latitude circle.

According to some data there is a definite relationship between cloudiness field, vorticity, and speed divergence. With this relationship one can determine the statistical link between the Fourier coefficients by means of the following regression equations:

$$\begin{aligned} \delta_m &= \alpha_m S_m + \beta_m, \\ \gamma_m &= \alpha'_m S_m + \beta'_m. \end{aligned} \tag{4.14}$$

If we have at our disposal cloud fields, charts of baric topography, and wind field plotted for several days at various levels for the middle and upper troposphere, then formulas (4.10) to (4.13) determine the Fourier coefficients for each harmonic. For our purpose 10—15 harmonics are sufficient. Then, using formula (4.5) we determine coefficients β_m and α_m, β_m' and α_m' by the least-square method. These may be taken as constant even for the following day.

Suppose, for the following day, we only have data on the cloudiness field for a certain region, as well as the value H of geopotential and wind-speed components u_b and v_b at the boundary of the given region. Then we introduce a function ω_h defined as

$$\bar{\omega}_h = \Omega_{hi} + D_{hj}. \tag{4.15}$$

From (4.13) and (4.15) we have

$$\nabla^2 u = \mathrm{rot}_h \bar{\omega}_h; \quad \nabla^2 v = \mathrm{div}\, \bar{\omega}_h, \tag{4.16}$$

where $\nabla^2 = \frac{\partial}{\partial x^2} + \frac{\partial}{\partial y^2}$ is the two-dimensional Laplacian operator.

With the statistically determined Fourier coefficients, we can calculate functions Ω_h and D_h, and hence $\bar{\omega}_h$, only using the field of cloud distribution.

Solving equation (4.16) as a Poisson distribution equation for u and v with boundary conditions $u = u_b$ and $v = v_b$ at the limits of the given region, we obtain the wind speed only from the cloudiness field.

Assuming quasisolenoidal conditions for the middle levels of the troposphere, i.e., $\frac{dD_h}{dt} = 0$, we write the following balance (Monge-Ampère) equation for determining the geopotential field:

$$\nabla^2 H = l\Omega_h - \left[\left(\frac{\partial u}{\partial x}\right)^2 + \left(\frac{\partial v}{\partial y}\right)^2 - 2\frac{\partial u}{\partial y}\frac{\partial v}{\partial x}\right] - l_x u - l_y v, \tag{4.17}$$

where $l = 2\omega \sin\varphi$ is the Coriolis parameter, $l_x = \frac{\partial l}{\partial x}$, $l_y = \frac{\partial l}{\partial y}$.

This is the Poisson equation for the geopotential H. Solving it for boundary conditions $H = H_b$ we obtain the geopotential field for the given region using only cloudiness data.

TABLE 4.15. Evaluation of the field of geopotential H and of wind-speed components u and v from satellite cloud-picture data

Date of plotting	H geopotential km $\lvert\delta\rvert$	H geopotential km $\lvert\Delta\rvert$	r	u m/sec $\lvert\delta\rvert$	u m/sec $\lvert\Delta\rvert$	r	v m/sec $\lvert\delta\rvert$	v m/sec $\lvert\Delta\rvert$
Related data								
25 VIII 1963	3	12	0.89	4	14	0.83	4	20
26 VIII	3	13	0.82	5	19	0.86	4	12
27 VIII	3	9	0.82	4	16	0.90	3	12
28 VIII	3	10	0.81	4	16	0.90	4	16
29 VIII	4	13	0.69	5	17	0.91	3	14
30 VIII	5	16	0.33	9	28	0.65	7	27
Independent data								
1 VII 1962	3	14	0.74	5	17	0.94	4	14
2 VII	3	10	0.80	4	20	0.91	4	17
3 VII	2	14	0.86	4	14	0.94	3	17
4 VII	4	14	0.74	5	18	0.93	3	14
5 VII	5	15	0.75	5	20	0.88	4	16
6 VII	5	18	0.37	8	36	0.69	6	28

The data in Table 4.15 refer to the 500-mb level. In this table, r is the correlation coefficient between the calculated and actual fields, $|\delta|$ is the mean absolute error, and $|\Delta|$ is the mean maximum error for the given field.

The above calculations were performed over an area of 4,000 × 4,000 km.

To a first approximation, this method permits the use of cloud data to plot wind and geopotential fields. This is of particular significance for regions with sparse aerological data, e.g., oceans, polar areas, etc.

Despite its obvious usefulness, this method still requires refining for more reliable statistical relations.

Difficulties in calculating the horizontal divergence of speed may be overcome if we use the field of vertical speeds for several levels. In this case, the continuity equation yields

$$D_h = -\frac{\partial \tau}{\partial p} \qquad (4.18)$$

from data on vertical speeds τ. The calculations are rather complex and can be performed only with computers.

Any further development of the method of objective analysis for regions with sparse meteorological observations should be based on a refined geopotential field plotted from cloud data and results of aerological soundings. This is what Musaelyan did when solving some meteorological problems.

The U.S. Weather Bureau /23/ used a similar approach to determine the wind field or jet streams with the aid of satellite cloud-picture data.

The method is as follows. As is known, there is good correlation between the field of vertical speeds in the middle troposphere and the Jacobian that represents the vortex advection. This correlation is

$$w = a\frac{g}{l}(z,\ \nabla^2 z), \tag{4.19}$$

where w is the vertical speed; g is the acceleration of gravity; z is the height of the isobaric surface; and a is the regression coefficient determined statistically.

This correlation means that the field of ascending vertical movements should correspond to a certain cloudiness pattern. According to (4.19), regions of positive w should coincide with regions of maximum cyclonic vortex. The field of descending currents (absence of cloudiness) should correspond to regions of maximum advection of the anticyclonic vortex.

Knowing the predicted values of the geopotential field and having cloudiness data, the analyst corrects by hand the geopotential field (flow lines) to obtain a good agreement between the geopotential field and the Jacobian field calculated by the computer. Such a correction is repeated until the required accuracy is achieved. Such an approach simplifies the analysis of data from regions with sparse meteorological observations. Basically, the problem may be solved entirely by a computer, once the Jacobian has been determined.

4.9. PRACTICAL NEPHANALYSIS

From experience accumulated by numerous meteorological services, particularly in America /23, 24/, the best way of using satellite data is to analyze satellite pictures at central forecasting agencies, and then to transmit data in the form of nephcharts to other interested institutions or consumers. This implies that the correct and efficient use of nephanalysis data is as important practically as other meteorological information. The practical use of nephanalysis data is discussed in /6, 23, 24/.

The time for transmitting nephanalysis data is rather limited /23/, and this and the nature of TIROS orbits is responsible for the irregular reception of satellite data for a given area. Most frequently data are only transmitted from one orbit, but often data from several orbits are linked on a single nephchart.

At present, nephcharts are plotted on maps of polar stereographic projection for temperate and high latitudes, and in Mercator projection for the equator zone (from 20°N to 20°S). Charts in both projections are plotted to a scale of 1:20,000,000. Since only isolated satellites are on a particular orbit, the forecaster has only a limited amount of nephanalysis data, in the form of strips. In view of the small time interval between orbits (1.5 to 2 hours) it is now customary to plot a mosaic chart of nephanalysis from several strips (belts). As shown in /23/, all nephanalysis data taken within ± 6 hours of the required time of observation may be included in a single mosaic pattern, since large-scale cloud systems hardly vary over several hours.* As data are obtained from every new orbit they are incorporated

* Such mosaic patterns may also be plotted from photographs.

in the mosaic pattern of the previous nephanalysis. The final analysis refers to a certain average orbit selected as close as possible to the time of plotting synoptic and aerological charts. If for a given region the satellite orbits are intersected, the most recent data are used.

Study of nephanalysis mosaics showed that nephcharts are more illustrative if the regions fully covered by the angle of view of the satellite camera are hatched, e.g., in blue or green, while regions covered only partly (or to their major part) by satellite observations are hatched in a brighter color. Such hatching, in addition to dotting, reveals the synoptically most important regions and simplifies the identification of synoptical situations permitting rapid orientation both in the use of mosaics and individual, successively plotted nephcharts. With increasing skill, the analyst often may dispense with such hatching, but for the customer's use it is nevertheless helpful.*

For the transmission of nephcharts via facsimile communication lines, meteorological services both in the U.S.A. and the USSR use various legends and symbols. These symbols are not as yet standardized, since this would require relearning to decode, but with time standardization will be inevitable. In the U.S.A. the following standard symbols are already in common use:

Nephchart symbols

cumulus clouds

stratiform clouds

cirrus clouds

thick cumulus and cumulonimbus clouds

boundary between basic cloud systems — fronts, cyclones, or other systems that determine the nature of cloudiness in the viewing field of the satellite

clear boundaries of nonuniform cloudiness

unclearly defined boundary of nonuniform cloudiness

cloud bands

small cloud bands

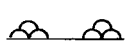
line of clouds

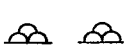
cloud lines, small cloud forms, designated also by

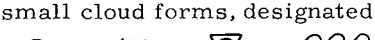

direction of shift of cirrus clouds relative to the anvils of thick cumulus clouds

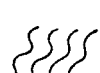
cloud waves (both of the orographic and transverse type)

* When analyzing synoptic charts, the analyst may also dispense with the hatching of precipitation zones, but it may nevertheless be used for receiving a clearer picture.

jet streams

vortex

\+ dense clouds

— thin clouds

The sizes of cloudiness and cloud-free zones are entered according to the following table:

Clouds	Sizes in miles	Cloud-free regions
1	0—30	6
2	30—60	7
3	60—90	8
4	90—120	9

The degree of cloudiness (cloud-cover size) in terms of symbols and designations is recorded as follows:

Most of the sky is cloud-free (< 20% of the sky is covered with clouds)	Open (0)
Large part (20—50%) of the sky is covered with clouds	MOP
A yet larger part (50—80%) of the sky is covered with clouds	MCO
Total cloudiness (80% of the sky is covered with clouds)	C

In addition, nephcharts receive some additional ideograms, e.g., ice, snow, cells, vortex.

In the USSR satellite meteorological data are received at the Main Hydrometeorological Center, where the results of nephanalysis are plotted on charts transmitted via facsimile lines to the consumer.

These charts are a somewhat modified system of ideograms, in line with recent advances in the technique of nephchart plotting (see Table 4.16). Soviet charts also contain additional inscriptions that simplify the reading of charts (Table 4.17).

TABLE 4.16. Symbols on cloud charts

1. Types of clouds

— cumulus clouds

— well developed thick cumulus or cumulonimbus clouds

— cirrus clouds

— stratiform clouds

— stratocumulus clouds

2. Extent of cloud cover

○ — cloud cover over < 20% of the sky

NBL — cloud cover over 20—50% of the sky

ZNCh — cloud cover over 50—80% of the sky 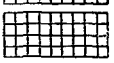

C — cloud cover over > 80% of the sky

3. Sizes of clouds and cloud-free regions

Cloud	Sizes	Cloud-free region
1	0—50 km	6
2	50—100 "	7
3	100—150 "	8
4	150—200 "	9

4. Boundaries

— main cloud systems

 — well developed cloud boundary

 — unclearly developed boundary

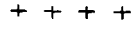 — ice-field boundary

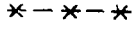 — snowpack (cover) boundary

5. Structure and synoptic interpretation

— point at which cloud bands converge in the form of a spiral

— point usually located in the low-cloud field of cumulus cover; this is the point of spiral-like cloud convergence

— cloud band in the shape of a "comma"

— cloud bands (other symbols may also be used depending on the cloud type)

— short, broken or very thin cloud bands

— banded structure

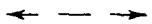 — thin banded structure

SSSS — wavelike clouds (thin or transverse)

— presumed position of jet stream

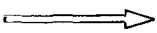 — direction of bands in cirrus clouds that are shifted relative to the cumulonimbus clouds

— dense clouds

 — thin clouds

CELLS — cumulus-cloud structure forming closed or open polygons

ITCZ — intertropical convergence zone

MSC — mesoscale spiral cloud (vortex formation)

TABLE 4.17. Code for drawing up telegrams and schematic cloud charts

Code number	C_a extent of cloud cover		C_t type of clouds		C_d structure of clouds		Code number
	characteristic	symbols	characteristic	symbols	characteristic	symbols	
0	Cloudiness < 20%		No clouds		Structure of clouds undetermined		0
1	Cloudiness 20—50%	NBL	Cumulus clouds		Thin clouds		1
2	Cloudiness 60—80%	ZNCh	Stratiform clouds		Thick dense clouds		2
3	Cloudiness > 80%	C	Cirrus clouds		Possible presence of haze, snow, etc.		3
4	Cloudiness 0—50%		Cirrus and cumulus clouds				
5	Cloudiness 20—80%		Stratiform and cumulus clouds		Convection cells	Cells	4
6	Cloudiness 50—100%		Cumulonimbus clouds		Cloud bands*	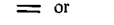	5
7			Cumulonimbus and other cloud forms		Transverse cloud bands*		6
8			Frontal clouds	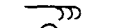	Frontal clouds	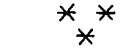	7
					Thick frontal clouds	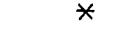	8
9			Unknown type of clouds		Vortex		9

* Recorded according to the direction of cloud bands on the photograph.

Photograph 4.70 shows a picture mosaic of the cloud cover over Greenland and the adjacent areas /23/.

Figure 4.59 shows the results of nephanalysis for this area plotted both on a synoptic chart (Figure 4.59a) and a 500-mb chart (Figure 4.59b).

Such a superposition is very useful, as it permits the analyst to obtain data which he could not obtain from the separate use of satellite or conventional observational data.

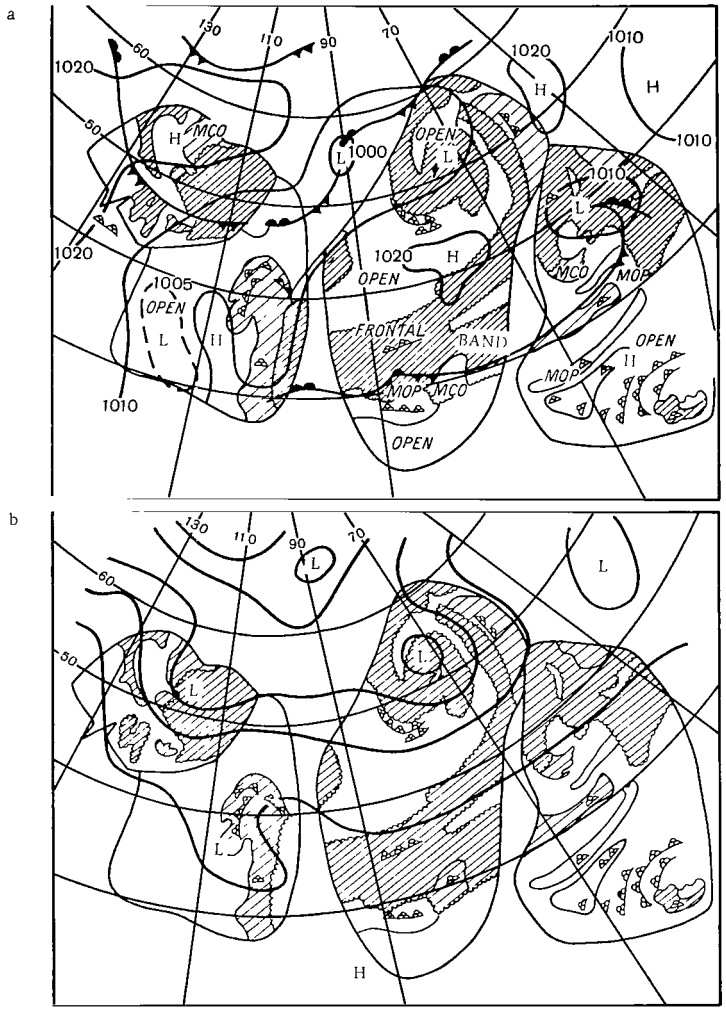

FIGURE 4.59. Schematic nephanalysis (at 1250 hr, 7 September 1962) superimposed on the surface weather chart that was plotted at 1200 hr the same day (a) and on the 500-mb chart plotted at the same day and hour (b)

Experience has shown that for the comparison of cloud-field with circulation data, the use of a 500-mb level chart yields better results. In extreme cases, if there is no suitable agreement between the data in nephcharts and 500-mb charts, an additional comparison should be made with the surface weather chart. This can easily be done using the same map scale and projection for both synoptic and nephanalysis. If at the point for which nephanalysis is being used there exists APT data-acquisition facilities, the received pictures are used for finding such details that cannot be obtained from nephcharts.

As shown in /23/, the international aviation centers in New York and Honolulu used cloud data for predicting flight conditions and safety. When the results of the latest nephanalysis and satellite pictures for the territory along the flight route were available, they were given to the pilot.

Nephanalysis data are of particular value for ocean areas, both for an efficient daily synoptic analysis of these areas and for their climatologic characteristics. These data are also useful for regions with a well-developed meteorological network, for which they furnish numerous additional characteristics and details. Some details determined on the strength of nephanalysis (e.g., cold fronts, internal clouds, etc.) are suitably transferred onto annular weather charts.

The paper in /23/ presents examples of joint interpretation of conventional synoptic and nephanalysis data for temperate latitudes. These examples cover four different synoptic situations for several successive days and different seasons of the year. Thus, e.g., for autumn, American stations analyzed satellite data for regions of the U.S.A. provided with a large conventional meteorological network. Winter cases are interesting in that the territory to be analyzed had only a sparse conventional network. Summer cases chosen for analysis are illustrated by an example of joint utilization of APT and conventional data for regions with a dense network of stations. Both for the spring and winter cases interpretation was conducted jointly with neph- and conventional data for regions with a sparse network.

Consider now in detail the case that refers to the period between 19 and 21 April 1963. On the first day of this period, analysis was performed for the central and eastern regions of the U.S.A. and Canada, i.e., for regions covered with sufficiently dense conventional networks. On 20 and 21 April, the large-scale baric systems shifted toward a region in the Atlantic with a very sparse conventional network. This case is of particular significance, since it illustrates the joint use of conventional and satellite data for regions with sparse networks but of climatologic importance. Figure 4.60 shows nephanalysis data for 19 April 1963 obtained by TIROS V and superimposed upon the surface weather chart (Figure 4.60a) and the 500-mb chart (Figure 4.60b). The chart was plotted for the situation existing at 1200 hr on 19 April 1963. Figure 4.61 presents the same nephanalysis, but superimposed on a synoptic chart for the situation at 0000 hr on 20 April 1963. Photograph 4.71 shows corresponding cloud pictures.

The time for which nephanalysis was carried out does not coincide with the time of observations. In the first case, to obtain full correspondence, the baric systems and fronts must be shifted from their direction of movement by a path that corresponds to a time interval of about 7 hours.

In the second case, this displacement must be carried out in the opposite direction for a path corresponding to a time interval of 5 hours.

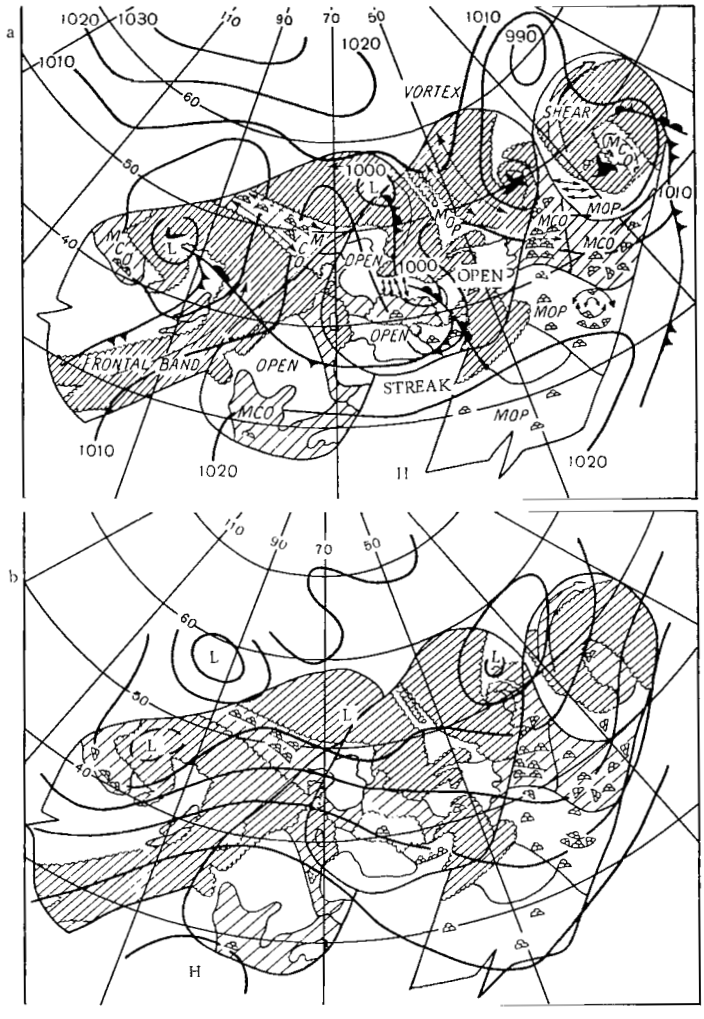

FIGURE 4.60. Schematic nephanalysis according to TIROS V data for 19 April 1963, superimposed on the surface weather chart at 1200 hr 19 April 1963 (a) and on the 500-mb chart for the same data and time (b)

Photograph 4.71 shows the picture that was used for the nephanalysis of the western area of the region shown in the chart.

It should be noted that despite the difference in time, nephdata may be used both for the first and second date of standard observations. However, if necessary, possible displacements in space between cloud systems on nephcharts and the baric centers and fronts on synoptic charts, have to be taken into account.

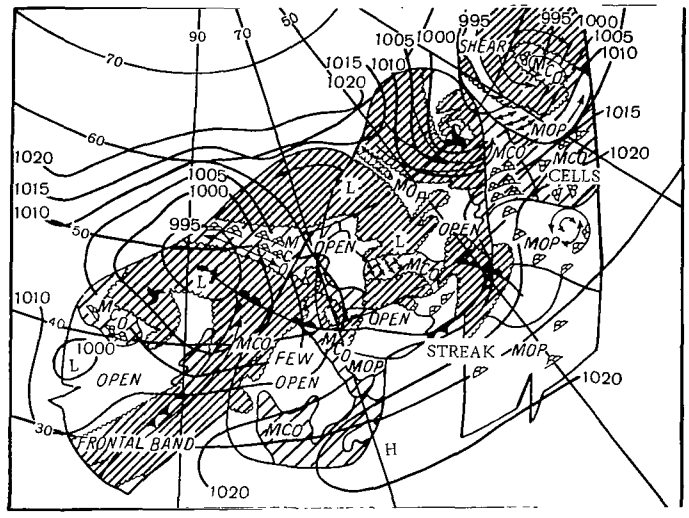

FIGURE 4.61. The same nephanalysis as in Figure 4.60, superimposed on the surface synoptic chart for 0000 hr on 20 April 1963

Consider the western part of the chart. From the nature of cloudiness as discussed in Section 3.4, we may conclude that the cyclone, the center of which was located on the synoptic chart at 42°N, 95°W, is in the state of occlusion. Therefore the meteorologist performed a correct analysis, which is confirmed by satellite data. On the other hand, satellite data permit the refining of the position of frontal cloud bands that correspond to the given cyclone. This is very important for evaluating weather conditions in the given area.

Behind the frontal cloud band on the 500-mb chart there is a high-level trough. As shown above, ascending vertical air and the cloud field associated with such movements are connected with advection of cyclonic vortices. This explains the existence of high-level troughs at the top part of the cloud-band region. This trough could easily be plotted by the analyst since the area has a dense network. In regions with a sparse network, cloud-field observations clearly show the existence of a high-level trough and even permit its position to be refined. Similarly, the cloud-free area in Figure 4.60 with the center at 43°N, 66°W is associated with advection of an anticyclone vortex.* From the direction of upper-air currents at the 500-mb level one may conclude that the observed cloud system is displaced toward a ENE direction.

In Figure 4.62, nephanalysis data for 1428 hr on 20 April 1963 are superimposed on the synoptic chart (Figure 4.62a) and on the 500-mb chart (Figure 4.62b) for 1200 hr on 20 April 1963. Here the observation times almost coincide.

In Figure 4.63, nephanalysis data for 1627 hr on 21 April 1963 are superimposed on the synoptic chart (Figure 4.63a) and on the 500-mb chart (Figure 4.63b) for 1200 hr on 21 April 1963.

Figure 4.62 shows a dense cloud system to the East of the U.S.A., where data of conventional observations are too sparse to permit the evaluation of

* In the jet-stream region, a cyclone vortex should not be taken as a trough and an anticyclone vortex as a ridge, since in such a case we have also to allow for the horizontal shift of wind.

the cloud field over the Atlantic. Thus, in the given example, satellite observations permit the analyst to refine the eastern boundary of frontal cloudiness which is very important for predicting meteorological situations above the oceans.

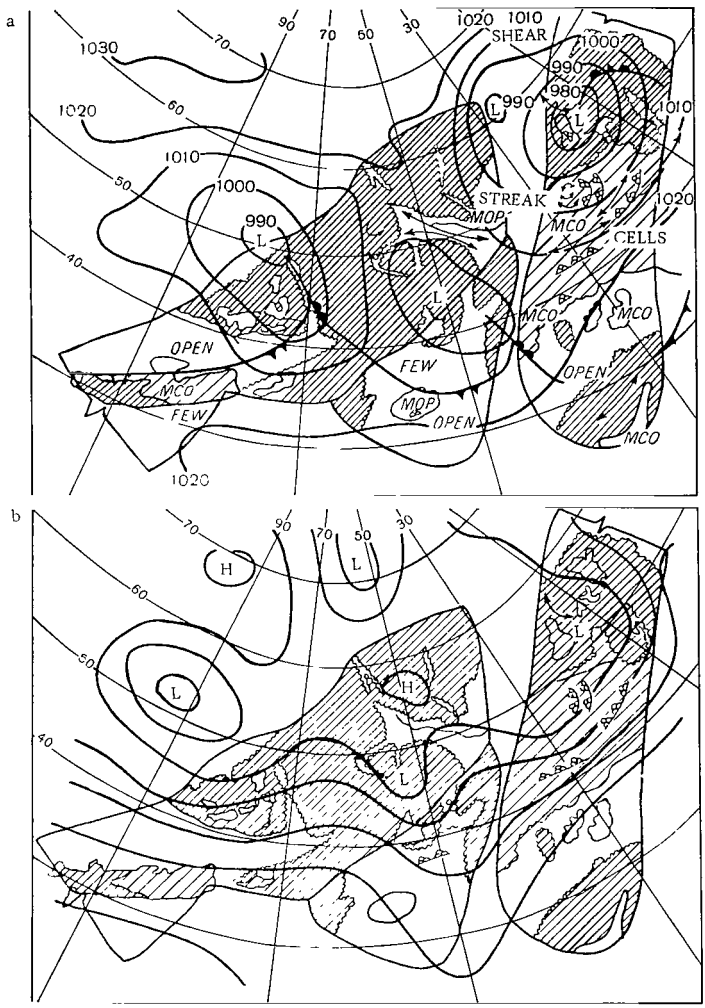

FIGURE 4.62. Schematic nephanalysis superimposed on the synoptic chart at 1200 hr on 20 April 1963 (a) and on the 500-mb chart at the same date and hour (b)

Joint analysis of front systems and cloud fields, according to data in Figure 4.62, permits the assumption that the occlusion point of the cyclone

near the eastern coast of the U.S.A. (western section of the chart) should be displaced by about 5 degrees to the East or even to the North-West. In this case, the agreement between data on cloud systems and fronts will be better.

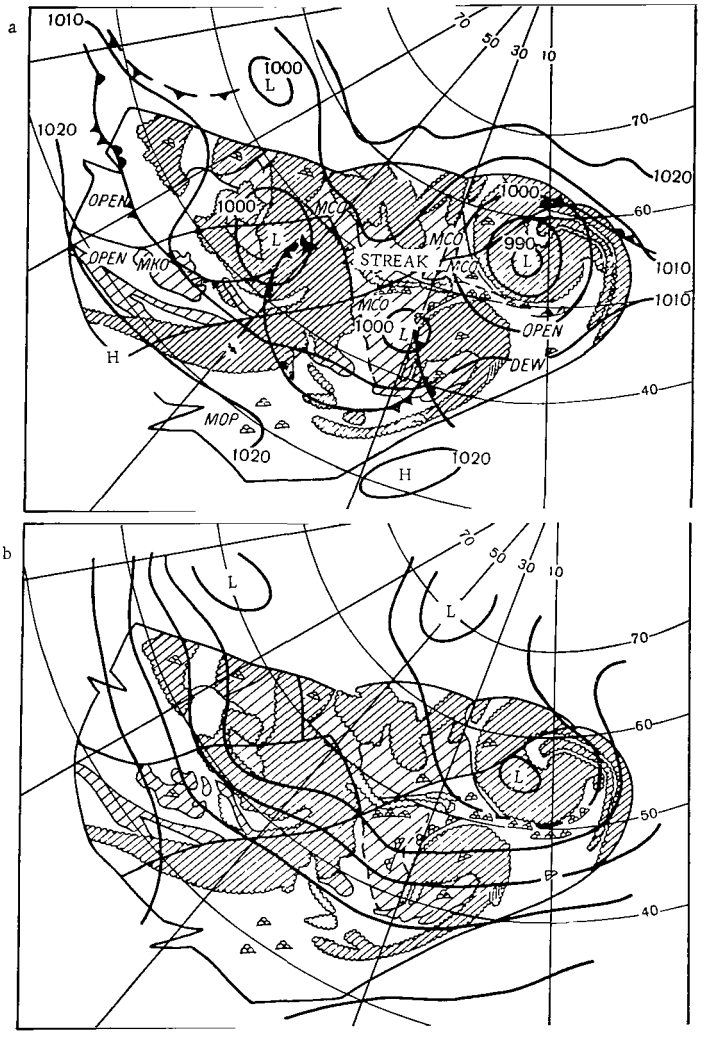

FIGURE 4.63. Schematic nephanalysis superimposed on the synoptic chart at 1200 hr on 21 April 1963 (a) and on the 500-mb chart at the same date and hour (b)

Let us revert to Figure 4.63. A cloud mass in the shape of a "comma" can be noticed in the southeastern part of the chart to the West of Spain. In Figure 4.63a, this cloudiness is linked with the cyclone located at

42°N, 31°W; here, the cyclone has a relatively large occlusion front. Analysis of Figure 4.63b shows that it is this cyclone and its associated cloudiness which determine the weather conditions in Spain and France for the next few days. In other words, the weather in these regions will be determined by the baric systems that form in regions with sparse networks. On the other hand, if the analyst bases his conclusions only on his analysis of fronts, the deterioration of weather conditions will be predicted for 10—12 hours later, as might have been done from an analysis of cloudiness data. Apparently, synoptic analysis for this region requires correction. Frontal systems should shift eastwards by 350—400 km. Therefore, deterioration of weather conditions in Spain and France should be expected up to 12 hours earlier than would be expected from an analysis of fronts only. As is seen, synoptic information permits a considerable refinement of analysis, and hence increases the forecasting accuracy. From the configuration of the cloud system we may conclude that the cyclone associated with this system is in the stage of the onset of occlusion, which in turn does not allow any conclusion as to the large size of the occlusion front.

The 500-mb chart (4.63b) indicates that to the West of the cloud mass we might expect the existence of a high-level trough whose axis passes almost along the 32°N latitude. Such a trough could hardly be detected in the absence of aerological data.

The cloud system in the northeastern region on the chart in Figure 4.62, associated with cyclonic activity, merits closer attention: its center is at 46°N, 15°W. From nephdata alone obtained at 1428 hr on 20 April 1963 it is very difficult to determine the particular development stage of the cyclone. However, joint analysis of aerological and synoptic data clearly points to the connection of the given cloud system with a cyclone which had not yet reached its occlusion stage. The picture taken the next day confirms this conclusion. Actually, Figure 4.63 shows a cloud field of well-developed configuration, characteristic of a cyclone in its occlusion stage. Neph-analysis data confirm this conclusion. This is particularly significant when predicting weather conditions over Great Britain, the North Atlantic, and Norway, since for these regions the cyclone determines the particular weather conditions.

The examples shown do not exhaust the diversity of synoptic situations for which nephdata may have a considerable bearing both on the synoptic analysis and the weather-forecasting accuracy. This is important not only for regions with a sparse nework, but also for the western coasts of the large continents for which, despite the existence of a dense meteorological network, the weather conditions build up in regions with sparse observations. With predominantly western transfer of air masses (westerlies) the frequently occurring failure in weather forecasting is explained by the lack of suitable information, and here the role of nephdata can hardly be overlooked.

When nephdata are used in the U.S, Weather Bureau /23/, it is useful to note the following additional characteristics confirmed by statistical processing.

1. In mid-latitudes with predominant westerlies the cloud system is most frequently located between the high-level trough and the high-level ridge, but slightly ahead of the trough.

Relatively cloud-free regions are located between the trough and the ridge, slightly back from the trough. In other words, cloudiness will correspond to the region of advection of a positive vortex (ascending motion), while absence of cloudiness points to the advection of a negative vortex (descending motion). Analysis of numerous data /23/ showed that in general the cloud cover is associated with advection of a positive vortex ($> 5 \cdot 10^{-10}$ sec^{-2}). The reverse is, however, not necessarily true, i. e., in numerous instances, the absence of cloudiness may also be linked with advection of a positive vortex. These exceptions are understandable, since one can hardly believe that the formation of cloudiness at the 500-mb level will be linked with advection of a vortex only at that particular level. The formation of cloudiness is affected by both dynamic and thermal factors.

2. In regions where the frontal cloud bands extend in a direction normal to the surface front at the cold air side, upper air currents are almost parallel with the front. Where the frontal cloud bands are located at the boundary of the surface front near the warm-air side, or where they are even absent, the air currents in the upper regions are oriented at some angle to the front.

3. If cloud systems are subject to a rapid, daily changing displacement from West to East, the upper-air currents are rather intensive while the amplitude in the isohypse field is low. If the orientation of the cloud system has a clearly expressed meridional character, the amplitude in the isohypse field will probably be much higher.

4. If a vast area of low clouds is located along mountain slopes and the sharp edges of the clouds are alongside the peak of the orographic ridge, the air currents at the lower levels will rise along the slope.

5. Over oceans and lowlands, vast areas of low cloudiness may be associated with cyclonic activity in this area. However, it should be borne in mind that in terms of their climatological characteristics some regions (e.g., oceans, sea areas of California, western Africa, Great Britain, etc.) exhibit the formation of low cloudiness. This fact should be taken into consideration, and for such regions, low cloudiness should not unilaterally be linked with cyclonic activity if there are no other reasons to support this.

To whichever degree satellite-observation techniques are developed, satellite information will not be able to fully replace the standard observation network.

In conclusion, we mention that, in using nephdata, some meteorological services employ telegraph equipment without Roman letters, and so data transmitted in this way will not correspond to the internationally adopted symbol code (Section 3.4). We present a table for converting Russian letters on the T-15 teleprinter into Roman letters corresponding to the code.

А — F	Л — K	Х — I
Б — N	М — C	Ц — P
В — D	Н — R	Ч — O
Г — T	О — J	Ш — Y
Д — L	П — G	Щ — (
Е — E	Р — H	Ю — M
Ж — !	С — X	Я — Z
З — U	Т — B	Ы — S
И — V	У — Q	Й — S
К — W	Ф — A	

EXERCISE 1

Decoding nephanalysis telegrams

Using a telegram with nephanalysis data obtained from the ESSA 1 satellite on 24 February 1966, decode it and transfer the results onto a synoptic chart.

Using the symbols in Table 4.16, plot the chart of schematic nephanalysis, and if possible compare it with the synoptic chart.

Telegram with nephanalysis data obtained from the ESSA I satellite on 24 February 1966

```
ZCZC WSA026-
AUXX KWBC N 240103
BLTN NO 5420
NORTH ATLANTIC WEST AFRICA
NEPAL ESSA 1290 1343Z C 2-
AA690 BB490 CC610 DD620 FF190 GG650 JJ150 KK693 LL240
MM140
06530 AA066 BB090 CC066 BBBBX
30 AAAAA BB099 CC077 DDDDX
30 AAAAA BBCCC CC123 DDDDX
30 AAAGG GGCCC CC134 DXXXX
30 GG101 CC156
30 CC112 FFFFF CC066 FGXXX
29 JJ099 GGGGG FF077 GGGXX
28 JJ112 GG123
27 GG088 JJJJJ GG099
26 GG077 JJ088 GGGGG
05525 GG101 JJ101 GXXXX
24 GG099 JJ112
23 GG099 JJ066 GGJJJ JXXXX
22 GG099 JJJJJ GGJJJ GGGXX
22 GG099 JJJJJ GG077
21 GG088 JJJJJ GG088
21 GG077 JJJJJ GJJGG GGGGX
21 GG077 JJ088 GG066
21 GG088 JJ088 GG066 JXXXX
20 GGFGG JJ099 GG066 JJJXX
04520
20 FFFFG JJ066 GG077 JJJJJ BXXXX
19 FFFFG JJ066 GGGBB KK066 BBXXX
18 FFGGG JJJJG GG066 BB077 LBXXX
17 GGGJJ JJJGG BB112 LLBBX
17 GGGJJ JJJGG BB099 LL077
16 GJJJJ GGGBB BB123 LLLLX
16 GJJJG GGGBB BB123 LLLLX-
16 GJJJG GGGBB BB123 LLLLX-
15 JJJGB BB156 LL077
15 JJJGB BB156 LL077
15 GGGBB BB101 LLLLL BBBBL
03514 GBBBB BB213
13 BB257
13 BB257
12 BB257
12 BB257
11 BB257
11 BB257
11 BB257
```

10 BB257
10 BB257
02509 BB257
09 BB257
08 BB257
08 BB257
08 BB257
07 BB257
06 BMMMM BB190
06 MMBBB BB190
AA690 BB490 CC610 DD620 FF190 GG650 JJ150 KK693 LL240
MM140

EXERCISE 2

Use of nephanalysis data for synoptic studies

1. Copy the meteorological-observational data obtained at 1500 hr on 25 February 1966, on the synoptic chart or on a sheet of tracing paper (Figure 4.64).

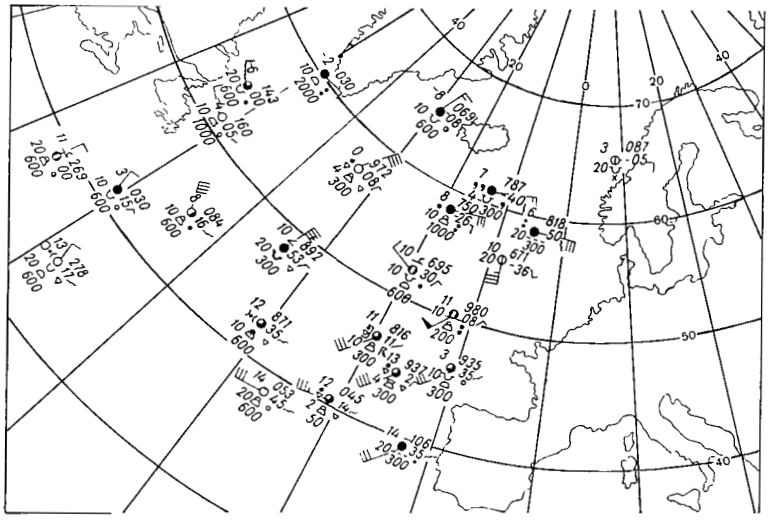

FIGURE 4.64. Cutout from surface weather chart plotted at 1200 hr on 25 February 1966

2. Try to analyze the chart and find the position of the fronts and the cyclone center.

3. Analyze Figure 4.65 with ESSA 1 data obtained at 1232, 1413, and 1553 hr on 25 February 1966.

4. Superimpose the nephchart on the synoptic weather chart.

5. Refine the position of the fronts and the cyclone center.

6. Determine the position of the cold front that passes from the cyclone center to the South close to the western coast of Great Britain and Spain.

Determine the position of the secondary cold front that passes from the cyclone center to the SW. In both cases use satellite data.

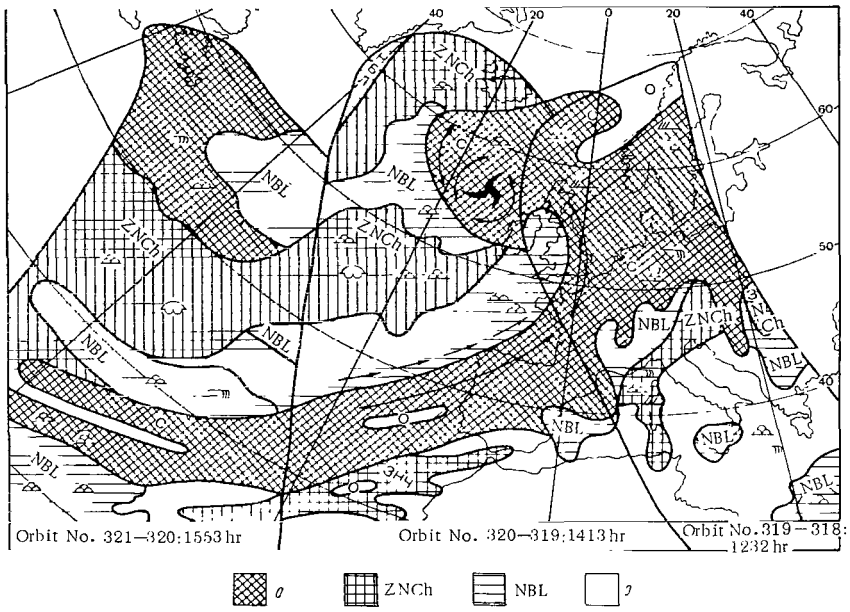

FIGURE 4.65. Schematic nephchart according to data from ESSA 1 obtained on 25 February 1966 [For notation see Table 4.16.]

7. Determine the type of cloudiness in the central and rear areas of the cyclone as well as in its thermal sector.

In the analysis, one must allow for the time difference between the satellite and standard observations.

Bibliography

1. Boldyrev, V.G. Ob ispol'zovanii radiatsionnykh izmerenii so sputnikov v sinopticheskom analize (The Use of Satellite Radiation Data in Synoptic Analysis).— Meteorologiya i Gidrologiya, No. 10. 1962.
2. Bel'tishchev, N.F. Obrabotka televizionnykh izobrazhenii oblachnosti, poluchennykh s meteorologicheskikh sputnikov (The Processing of TV Cloud Pictures Obtained by Meteorological Satellites).— Meteorologiya i Gidrologiya, No. 11. 1962.
3. Malkevich, M.S. Nekotorye voprosy interpretatsii polya ukhodyashchei radiatsii (Some Problems of Interpretation of the Outgoing-Radiation Field).— Trudy GGO, Issue 166. 1964.

4. Minina, L.S. Vikhrevaya struktura oblachnosti po dannym meteorologicheskikh sputnikov (The Vortex Structure of Clouds as Determined from Satellite Data).— Meteorologiya i Gidrologiya, No.1. 1964.
5. Musaelyan, Sh.A. Nekotorye voprosy chislennoi interpretatsii oblachnoi informatsii, postupayushchei s iskusstvennykh sputnikov Zemli (Some Problems of Numerical Interpretation of Cloud Data Obtained by Artificial Satellites).— Trudy GGO, Issue 166. 1964.
6. Kondrat'ev, K.Ya. Meteorologicheskie sputniki (Meteorological Satellites).— Leningrad, Gidrometeoizdat. 1963.
7. Rukovodstvo po kratkosrochnym prognozam pogody. Ch.I (Guidebook on Short-Range Weather Forecasting, Part I).— Leningrad, Gidrometeoizdat. 1964.
8. Klassifikatsiya i terminologiya l'dov, vstrechayushchikhsya v more (Classification and Terminology of Sea Ice).— Leningrad, Gidrometeoizdat. 1954.
9. Sonechkin, D.M. O deshifrirovanii televizionnykh izobrazhenii oblachnosti, poluchennykh s iskusstvennykh sputnikov (Decoding Satellite TV Cloud Pictures).— Meteorologiya i Gidrologiya, No.9. 1962.
10. Boucher, R.J., C.J. Bowley, E.S. Merrit, C.W.C. Rogers, P.E. Sheer, and W.K. Widger. Synoptic Interpretations of Cloud-Vortex Patterns as Observed by Meteorological Satellites.— Final Rep. under Contract No. C.W.b — 10630. Nat. Weather Satellite Center U.S. Weather Bureau. 1963.
11. Conover, J.H. Cloud Interpretation from Satellite Altitudes.— Air Force Cambridge Laboratories Research, Note 81. 1962.
12. Erickson, C.O. and L.F. Hubert. Identification of Cloudforms from TIROS I Pictures.— Meteorological Satellite Laboratory Report, No. 7, Washington. June 1961.
13. Fujita, T., T. Ushijima, W.A. Hass, and G.T. Dellert. Meteorological Interpretation of Convective Nephsystems Appearing in TIROS Cloud Photographs.— Mesometeorology Project, Department of the Geophysical Science University of Chicago, Res. Paper 9. April 1962.
14. Fujita, T.A. Technique for Precise Analysis of Satellite Photographs.— Mesometeorology Project, Department of the Geophysical Sciences, University of Chicago, Res. Paper 17. April 1963.
15. Fujita, T. Use of Pictures for Studies of the Internal Structure of Tropical Storms. (With Ushijima T. Rectified Pictures from TIROS I Orbit 125, R/o 128).— Mesometeorology Project, Department of the Geophysical Sciences, University of Chicago, Res. Paper 25. October 1963.
16. Fujita, T. Outline of a Theory and Examples for Precise Analyses of Satellite Radiation Data.— Mesometeorology Project,

Department of the Geophysical Sciences, Univ. of Chicago, Res. Paper 15. February 1963.
17. Miller, F.R. An Application of TIROS Cloud Observations in Sparse-Data Regions.— Mon. Weath. Rev., Vol. 91, No. 9. 1963.
18. Ninomiya, K. Investigation of a Summer Jet Stream using TIROS and Aerological Data.— Mesometeorology Project, Department of the Geophysical Sciences, University of Chicago, Res. Paper 14. September 1962.
19. Oliver, V.J., R.K. Anderson, and E.W. Ferguson. Some Examples of the Detection of Jet Streams from TIROS Photographs.— Mon. Weath. Rev., Vol. 92, No. 10. 1964.
20. Riehl, H. Waves in the Easterlies and the Polar Front in the Tropics.— Misc. Rpt., No. 17, Univ. of Chicago. 1945.
21. Thiel, E. The Amount of Ice on Planet Earth.— Antarctic Research, Geophys. Monograph., No. 7. 1962.
22. Wark, D.Q. and R.W. Popham. Ice Photography from the Meteorological Satellites TIROS I and TIROS II.— Meteorological Satellite Laboratory Report, No. 8, Washington. March 1962.
23. Widger, W.K., P.E. Sheer, and C.W. Rogers. Practical Interpretation of Meteorological Satellite Data.— Contract No. A.F. 19 (628)—2471, Project No. 6698, Task No. 699802. September 1964.
24. World Meteorological Organization. Inter-Regional Seminar on the Interpretation and Use of Meteorological Satellite Data. Part I, Part II. Tokyo, 27 November—8 December 1964.— Tokyo, Japan Meteorological Agency. 1964.
25. Takahashi, H. Techniques of the Typhoon Forecast.— Geophys. Mag., Vol. 24, No. 1. 1952.
26. Singer, S. and R. Popham. Nonmeteorological Observations from Weather Satellites.— Astron. and Aerospace Eng., Vol. 1, No. 3. 1963.

APPENDIX I

List of pictures in Photographs 4.64 and 4.65

4.64a Tropical low Maria, 0000 hr, 31 August 1961; v_{max} = 15 m/sec, stage C (the time indicated here and below is GMT).

4.64b Tropical storm Elsie, 0406 hr, 16 July 1964; v_{max} = 28 m/sec, stage D.

4.64c Eastern disturbance, 1842 hr, 2 July 1964; v_{max} = 10 m/sec, stage A.

4.64d Tropical low, 1429 hr, 14 June 1964; v_{max} = 12 m/sec, stage B.

4.64e Tropical low, 1703 hr, 5 June 1964; v_{max} = 10 m/sec.

4.64f Eastern disturbance, 1840 hr, 2 July 1964; v_{max} = 10 m/sec, stage A.

4.64g Tropical low, 0028 hr, 27 August 1962; v_{max} = 12—18 m/sec.

4.64h Tropical low Elsie, 0407 hr, 14 July 1964; v_{max} = 15 m/sec, stage C.

4.65a Tropical disturbance Daisy, 1432 hr, 29 September 1962; v_{max} = 15 m/sec, D = 2°, K = 0.

4.65b Tropical low Sarah, 0319 hr, 22 August 1962; v_{max} = 15 m/sec, D = 2.5°, K = 1.

4.65c Tropical storm Ruth, 0403 hr, 14 August 1964; v_{max} = 30 m/sec, D = 4°, K = 2.

4.65d Hurricane Daisy, 1425 hr, 5 September 1962; v_{max} = 42 m/sec, D = 5.5°, K = 3.

4.65e Tropical storm Amy, 2250 hr, 29 August 1962; v_{max} = 22 m/sec, D = 5°, K = 1.

4.65f Tropical storm Sarah, 0604 hr, 14 August 1962; v_{max} = 18—20 m/sec, D = 1.5°, K = 2.

4.65g Typhoon Ruth, 0351 hr, 18 August 1962; v_{max} = 42 m/sec, D = 5°, K = 4 (clear example of concentrated gaps).

4.65h Typhoon Winnie, 0722 hr, 2 July 1964; v_{max} = 50 m/sec, D = 7°, K = 3.

4.65i Typhoon Amy, 2326 hr, 3 September 1962; v_{max} = 65 m/sec, D = 6.5°, K = 4.

4.65j Typhoon Betty, 0600 hr, 3 July 1964; v_{max} = 50 m/sec, D = 3°, K = 4.

4.65k Typhoon Wanda, 0031 hr, 30 August 1962; v_{max} = 40 m/sec, D = 7°, K = 3.

4.65l Typhoon Karen, 0138 hr, 14 November 1962; v_{max} = 70 m/sec, D = 9°, K = 4.

APPENDIX 2

CHARTS FOR ANALYZING TROPICAL CYCLONES

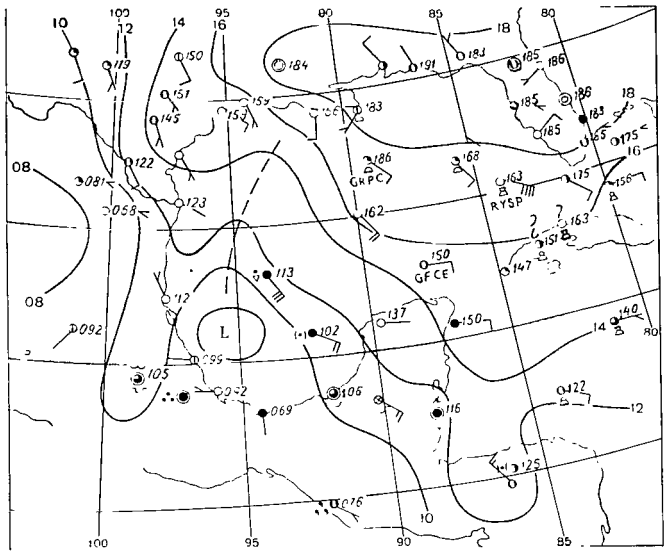

FIGURE 2a. Surface weather chart at 1200 hr on 14 June 1964

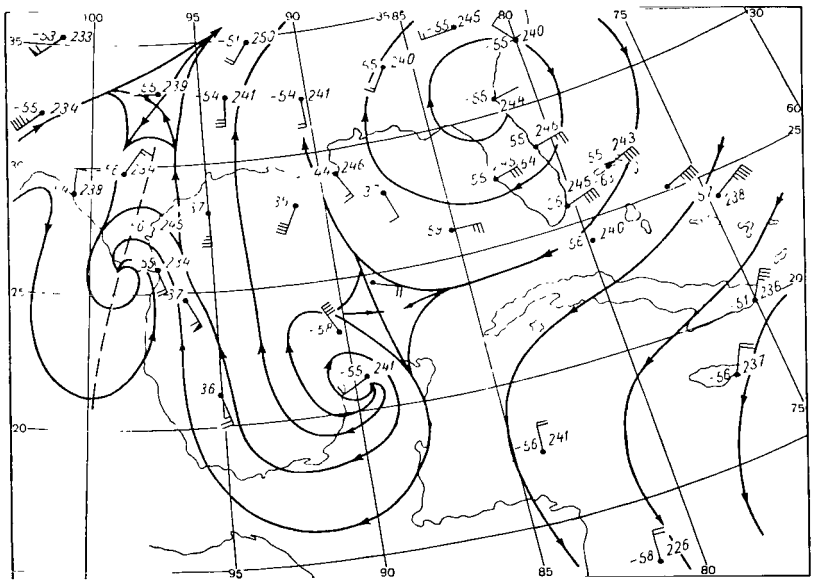

FIGURE 2b. 200-mb chart at 1200 hr on 14 June 1964

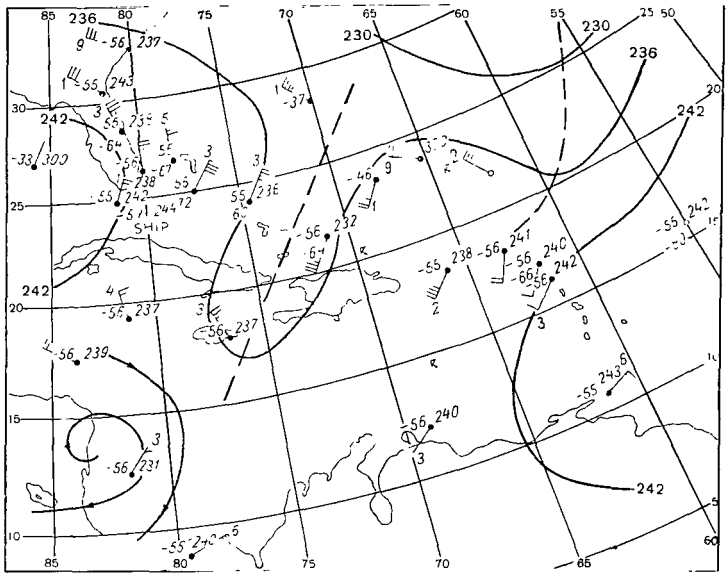

FIGURE 2c. 200-mb chart at 1200 hr on 2 July 1964

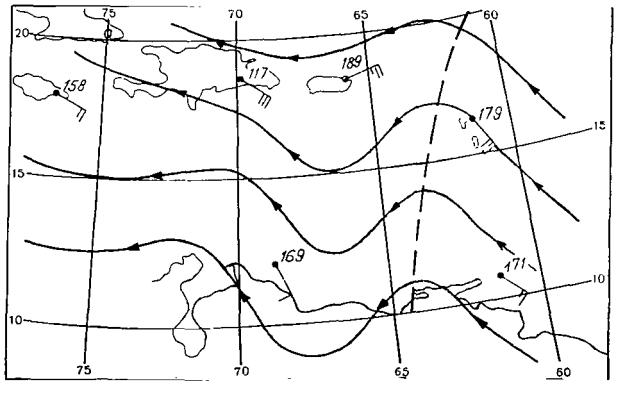

FIGURE 2d. 700-mb chart at 0000 hr on 3 July 1964

PHOTOGRAPHS TAKEN BY METEOROLOGICAL SATELLITES

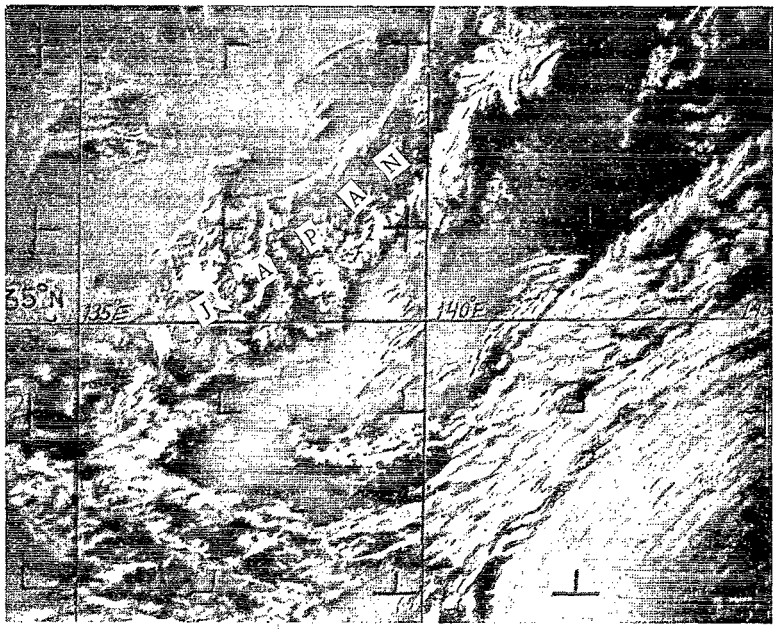

PHOTOGRAPH 1.1. Cloud-distribution pictures from NIMBUS I transmitted by its APT system on 12 September 1964

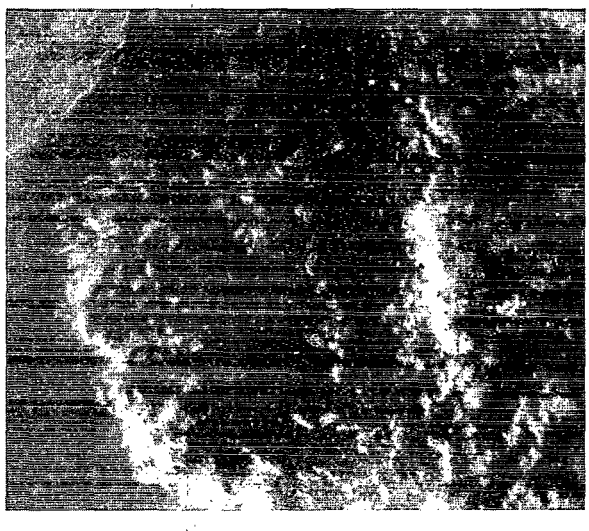

PHOTOGRAPH 2.1. Cloud-distribution picture from TIROS III on 20 July 1961 at 1444 GMT

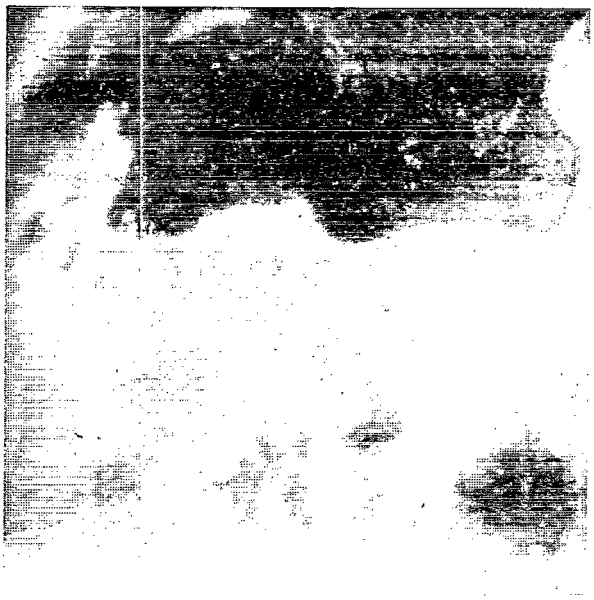

PHOTOGRAPH 2.2. Cloud-distribution picture from TIROS III on 15 July 1961 at 1052 hr

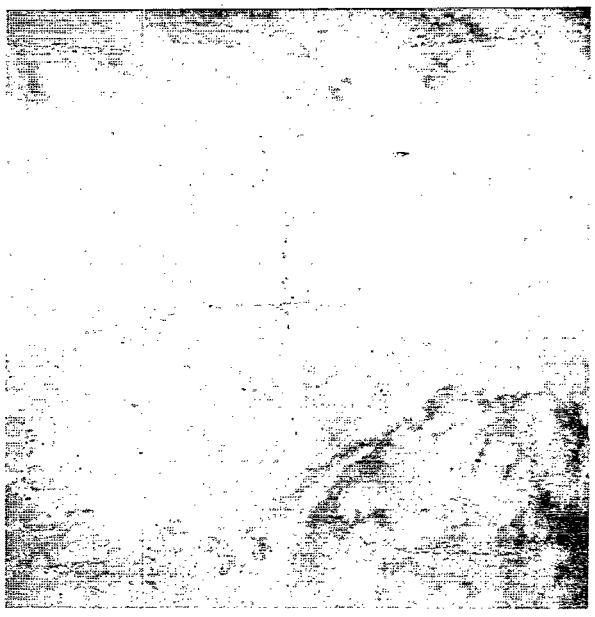

PHOTOGRAPH 2.3. Cloud-distribution picture from TIROS III on 15 July 1961 at 1057 hr

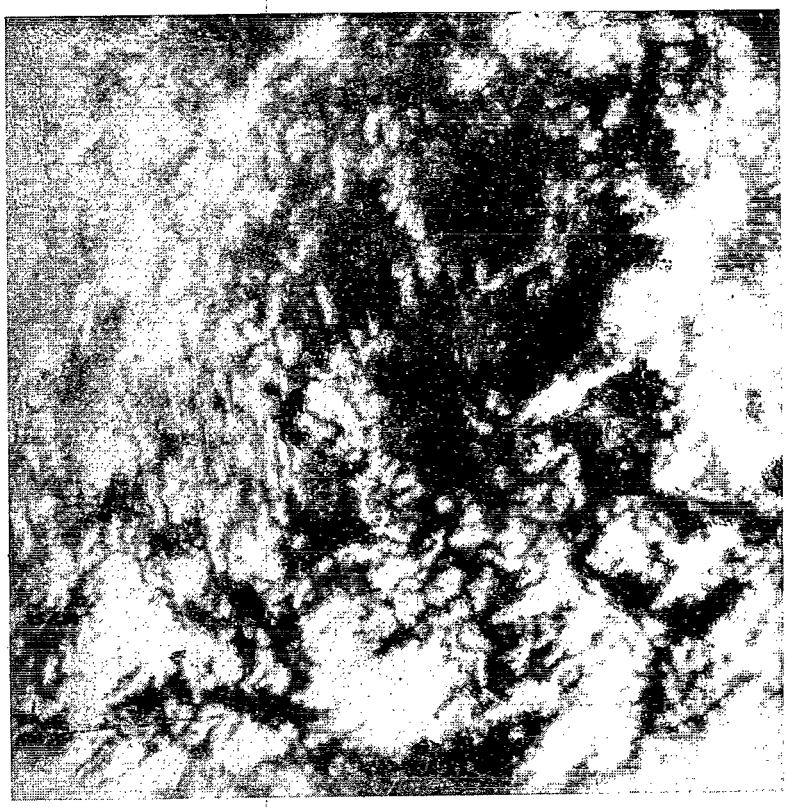

PHOTOGRAPH 2.4. Cloud-distribution picture from TIROS III on 15 July 1961 at 1059hr

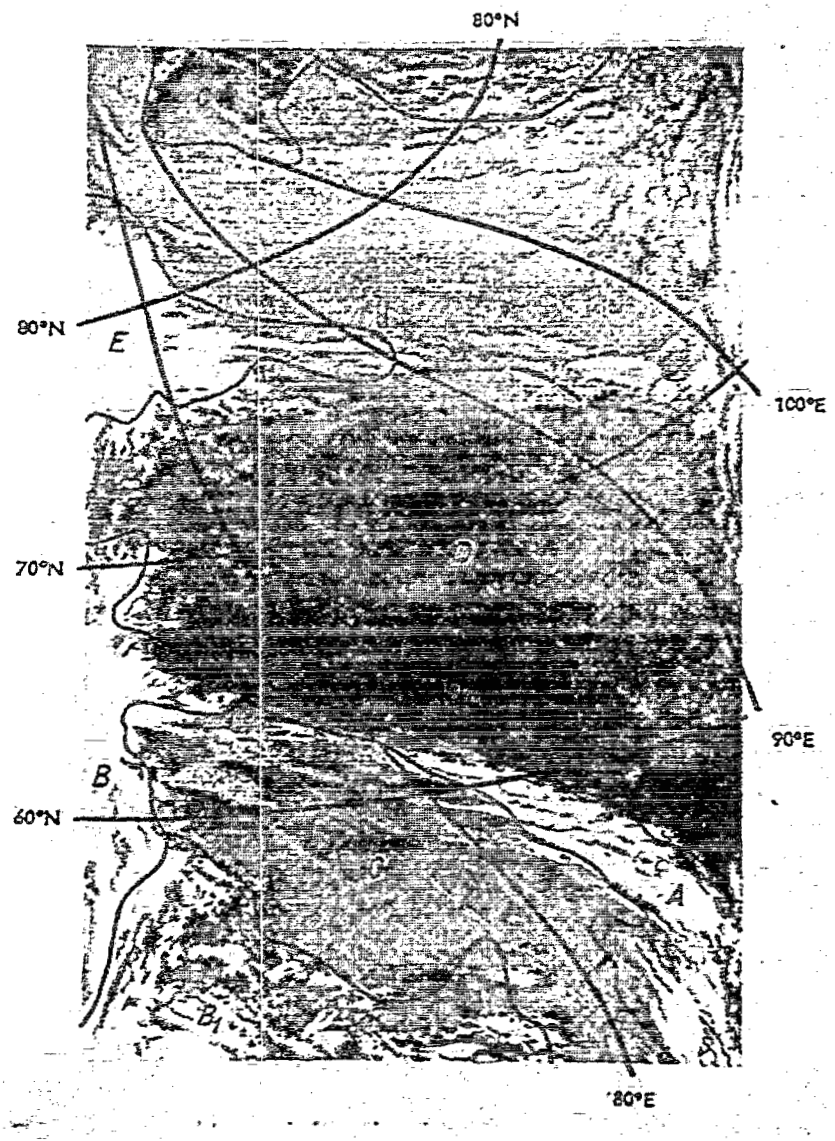

PHOTOGRAPH 2.5. Infrared cloud picture from NIMBUS I on 6 September 1964

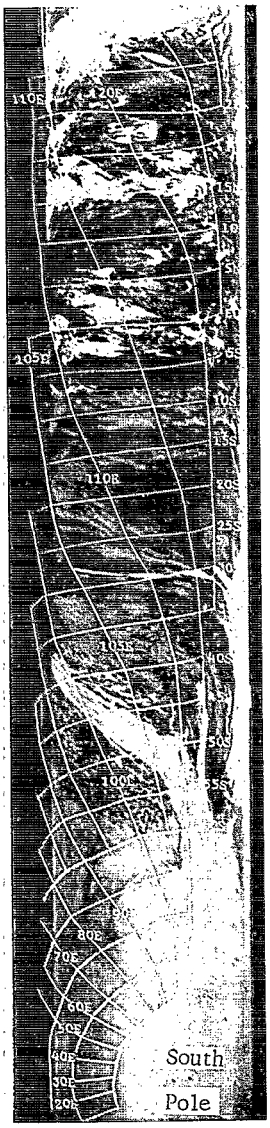

PHOTOGRAPH 2.6. Infrared picture from onboard NIMBUS I (channel 2) with a high-resolution radiometer at a height of 450 to 700 km

PHOTOGRAPH 2.7. Television picture of SE Africa from NIMBUS I (channel 2) at a height of 550 km

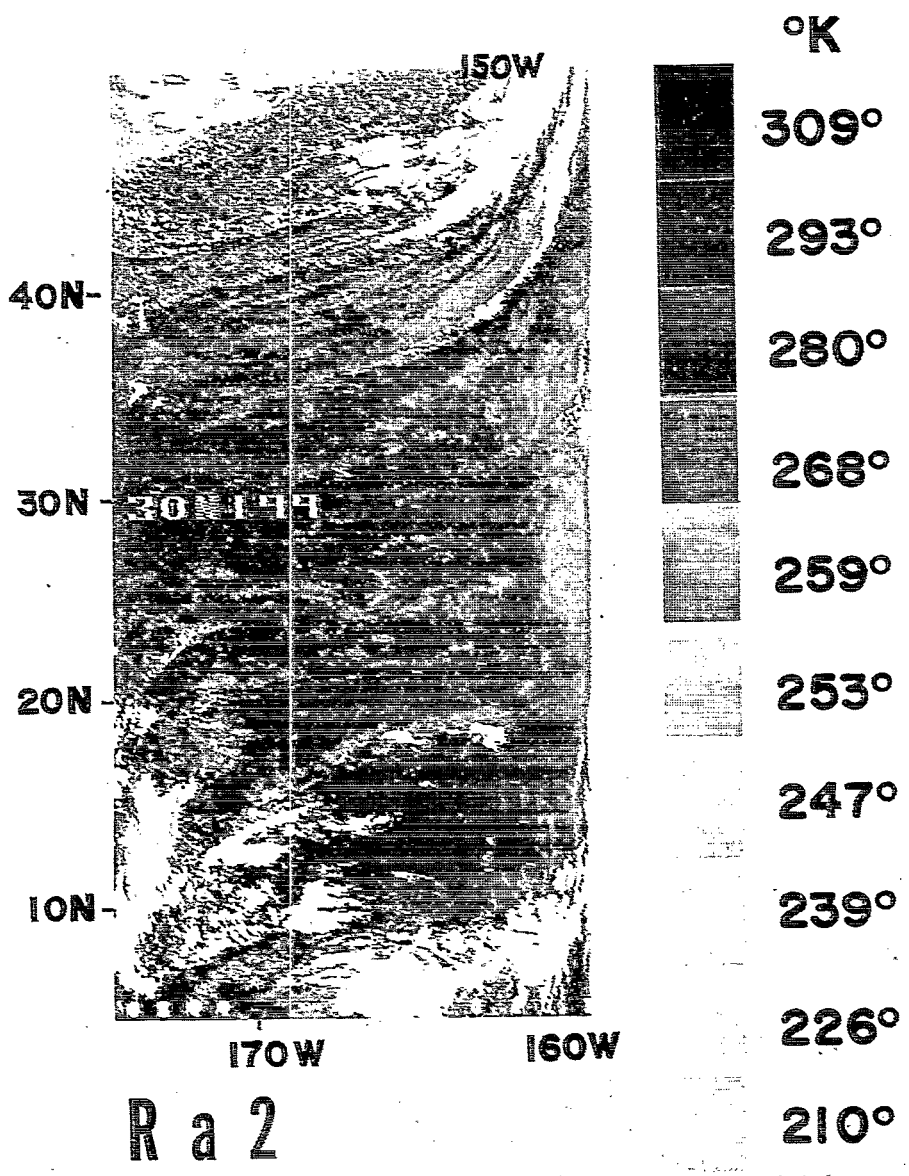

PHOTOGRAPH 2.8. Infrared cloud picture at 1050 hr on 15 September 1964 (the picture contains a scale for conversion from brightness characteristics to temperature of the radiating surface)

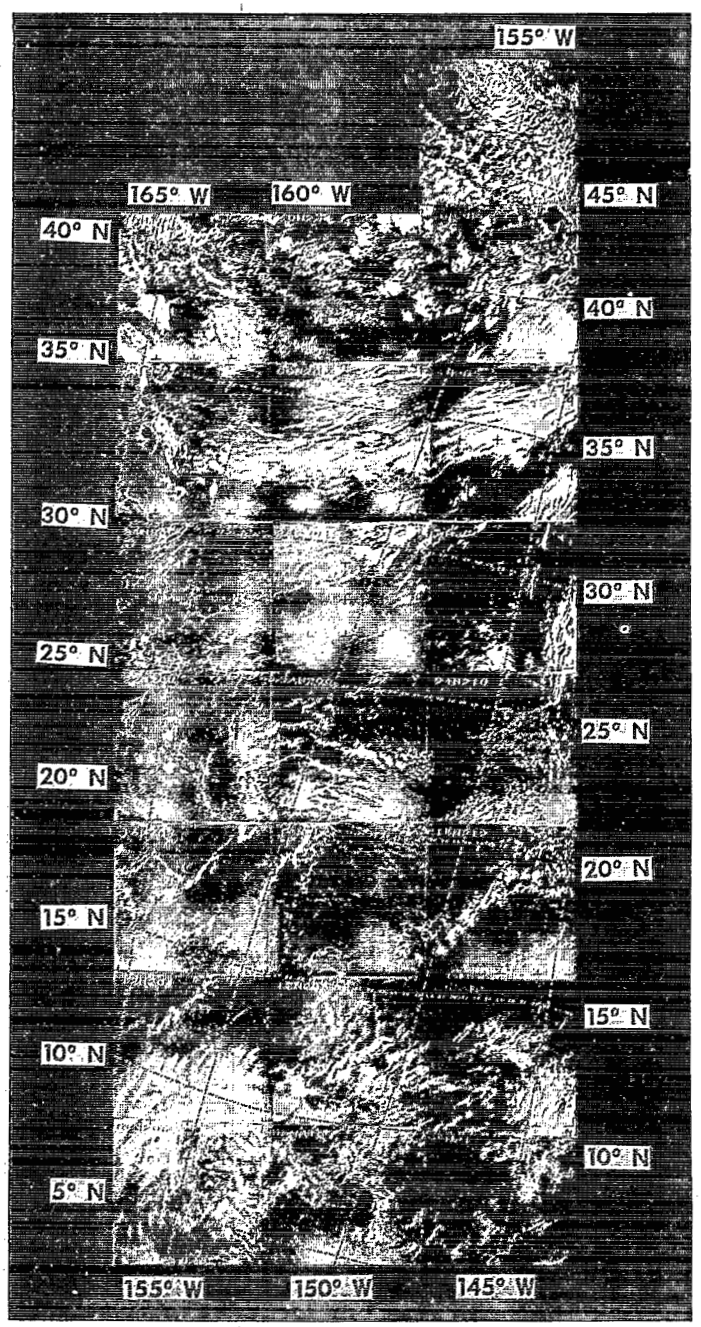

PHOTOGRAPH 2.9. Television cloud pictures at 2143 hr on 15 September 1964

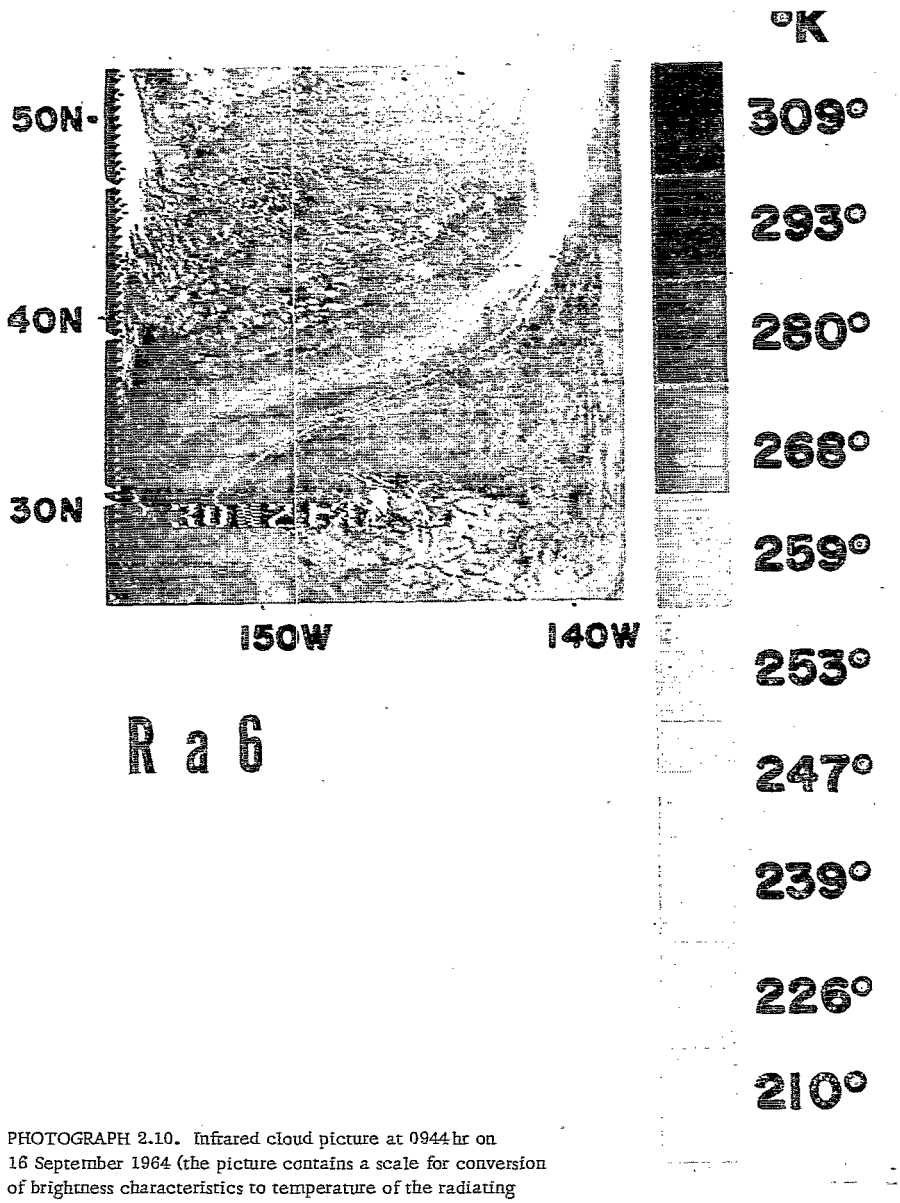

PHOTOGRAPH 2.10. Infrared cloud picture at 0944 hr on 16 September 1964 (the picture contains a scale for conversion of brightness characteristics to temperature of the radiating surface)

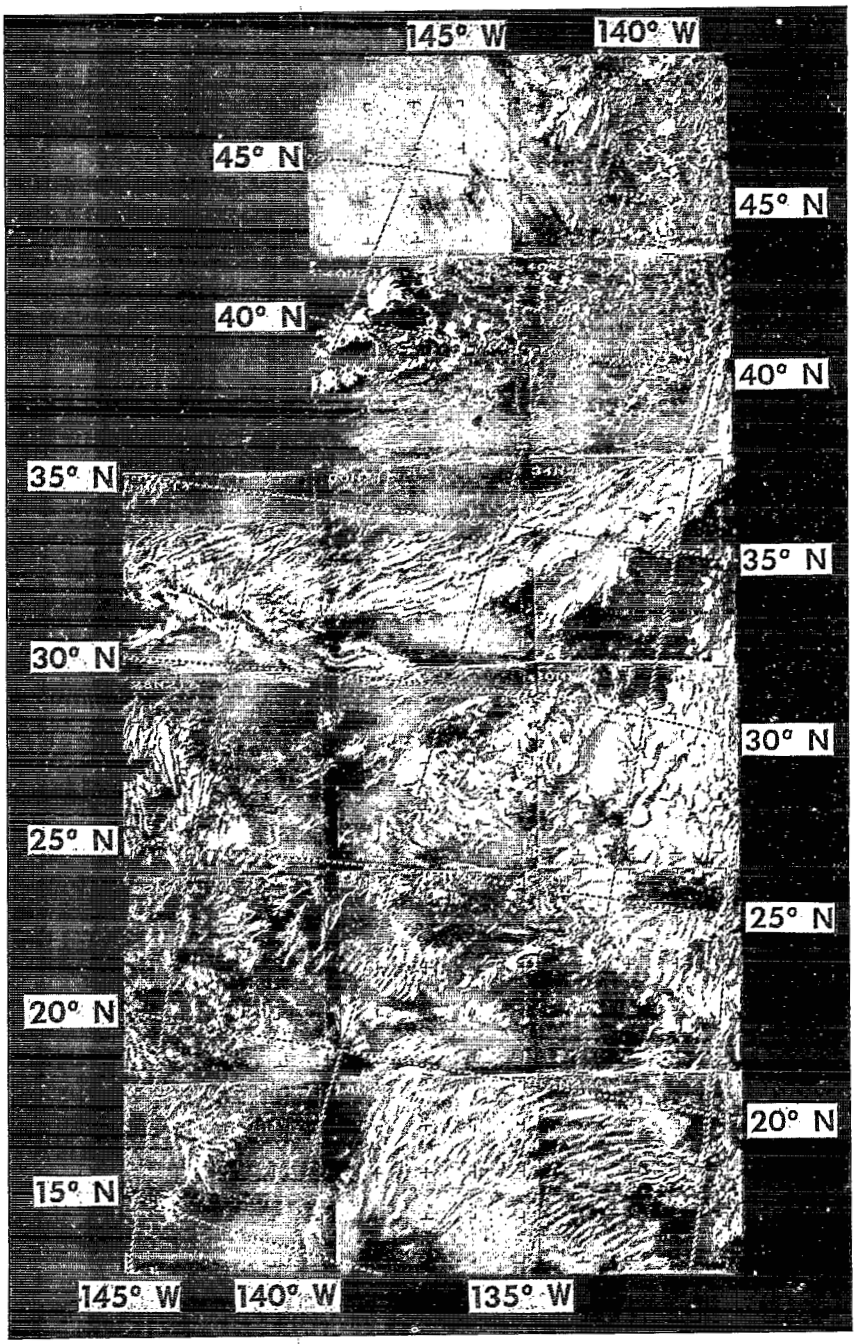

PHOTOGRAPH 2.11. Television cloud pictures at 2042 hr on 16 September 1964

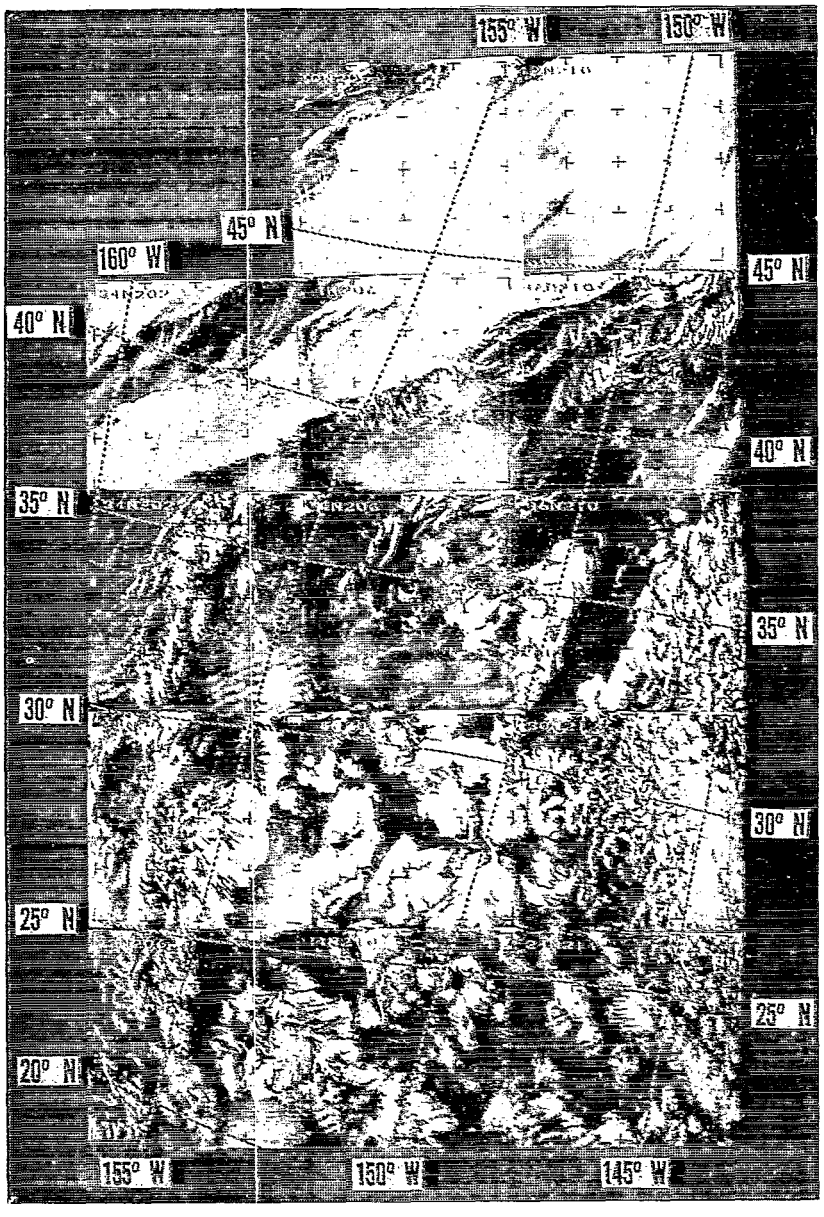

PHOTOGRAPH 2.12. Television cloud pictures at 2129 hr on 20 September 1964

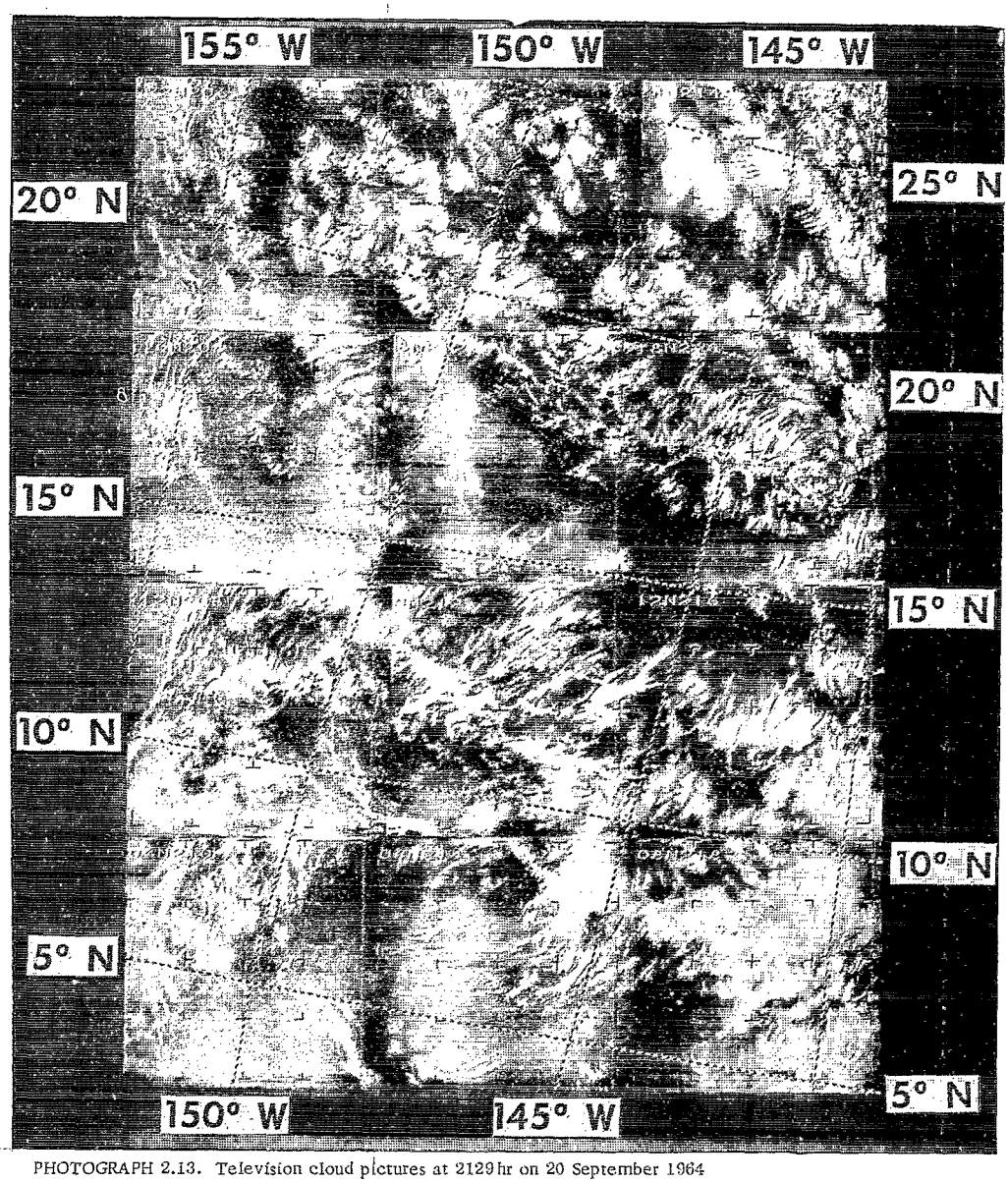

PHOTOGRAPH 2.13. Television cloud pictures at 2129 hr on 20 September 1964

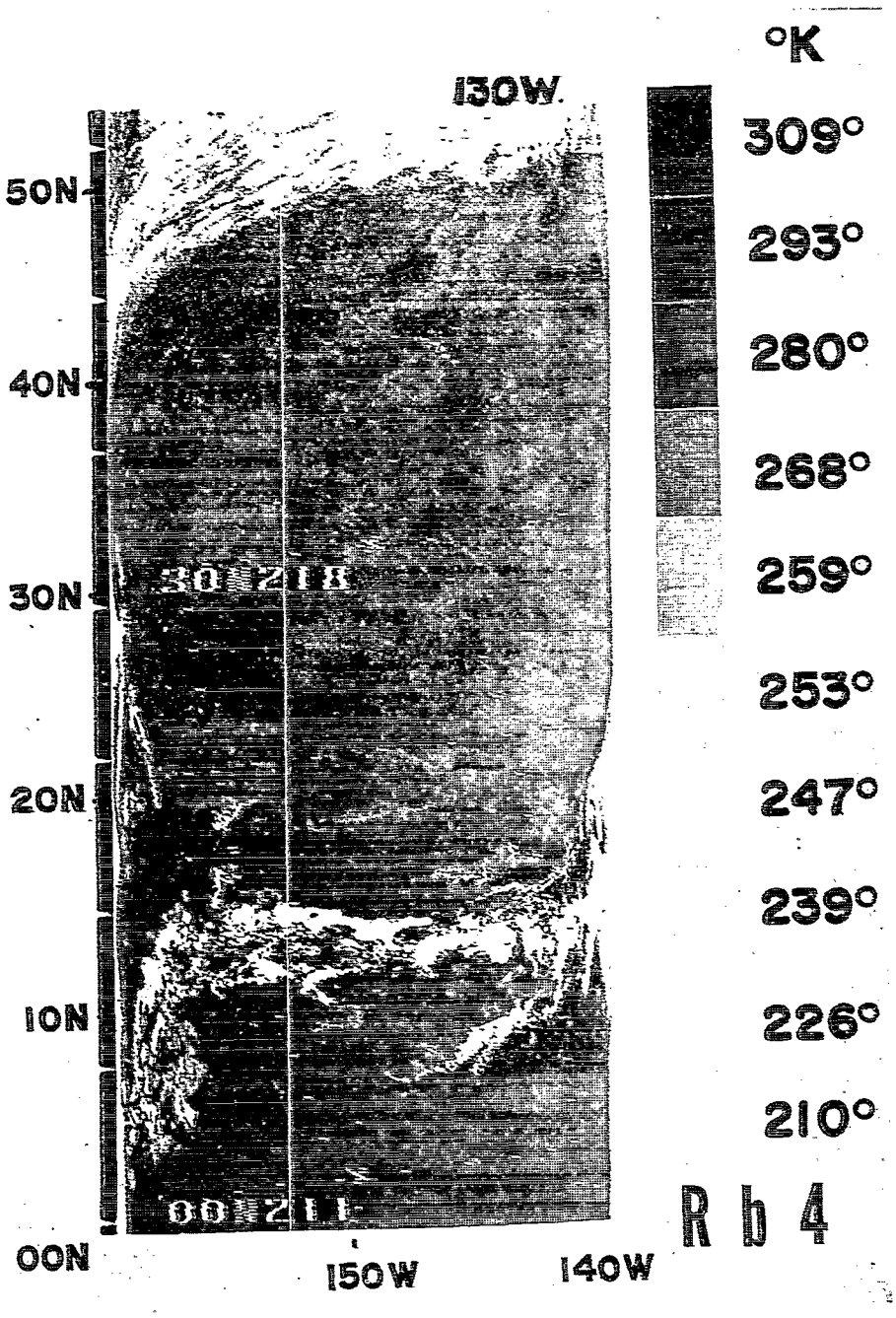

PHOTOGRAPH 2.14. Infrared cloud picture at 0953 hr on 21 September 1964

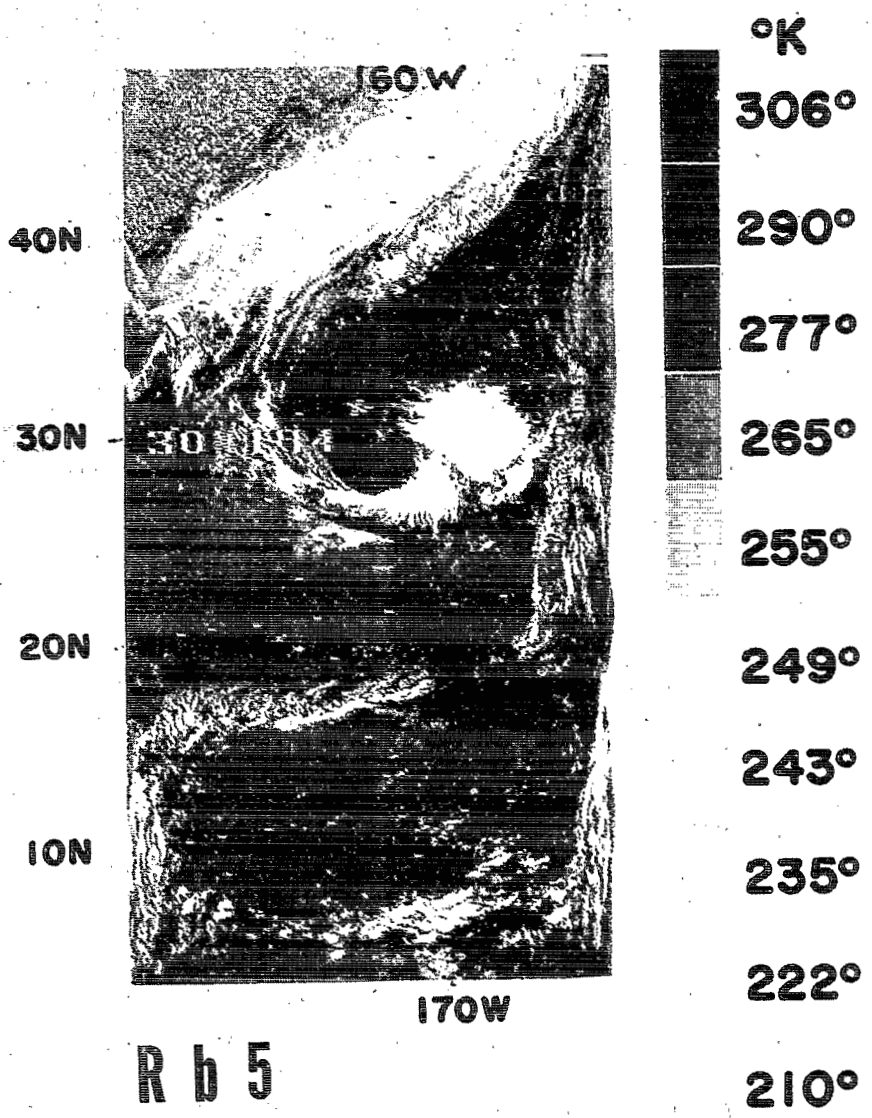

PHOTOGRAPH 2.15. Infrared cloud picture at 1114 hr on 21 September 1964

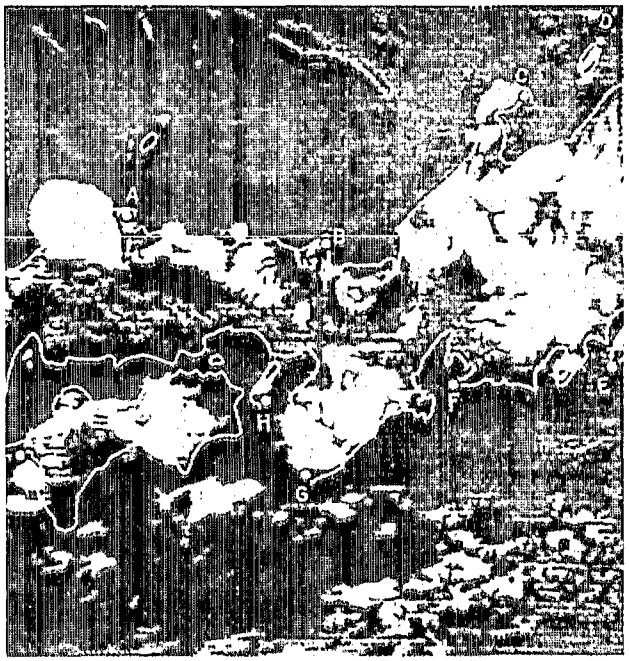

PHOTOGRAPH 3.1. Photograph from TIROS VII at 0525.5 hr on 5 August 1963 showing the raised shoreline and landmarks:

τ — picture inclination angle (23.8°); A — azimuth (117°); H — satellite height (627 km); φ_{SSP} and λ_{SSP} — latitude and longitude of subsatellite point (SSP) (36.0°N, 132.7°W).

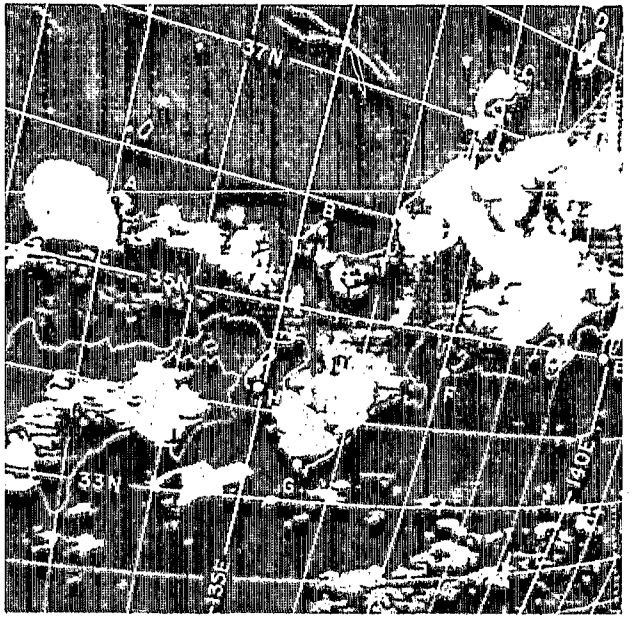

PHOTOGRAPH 3.2. The same as Photograph 3.1, with geographical grid

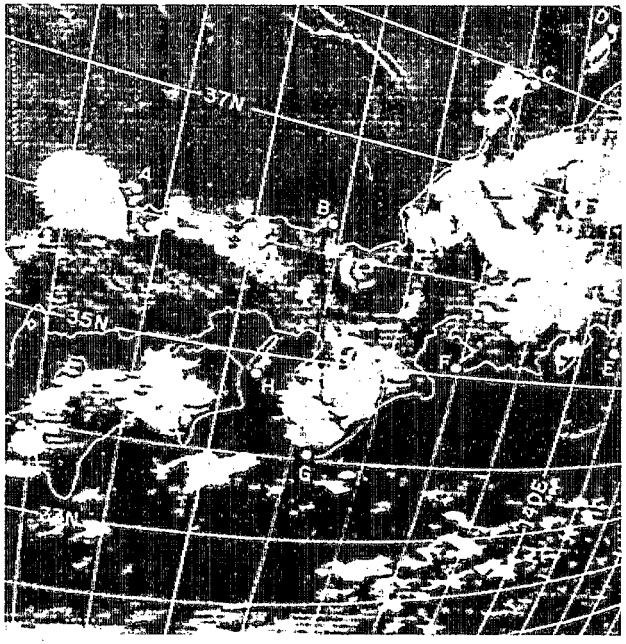

PHOTOGRAPH 3.3. Satellite photograph on 5 August 1963, with a coordinate grid plotted allowing for errors during photography:

actual time of photography 0525.5 hr, H = 627 km, τ = 23.8°, φ_{SSP} = 36°N, A = 117°, λ_{SSP} = 132.7° E; these values were used to correct the following values: time of photography 0525.75 hr, H = 627 km, τ = 23.8°, A = 117°, φ_{SSP} = 36.9°N, λ_{SSP} = 133.4° E.

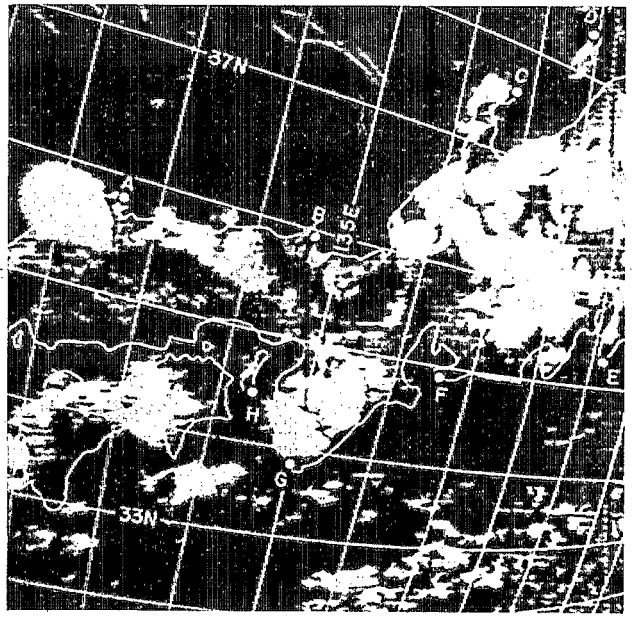

PHOTOGRAPH 3.4. Satellite picture on 5 August 1963, with a coordinate grid plotted allowing for errors in picture angle inclination:

τ_{true} = 23.8°; τ_{used} = 18.8°; other parameters as in Photograph 3.1.

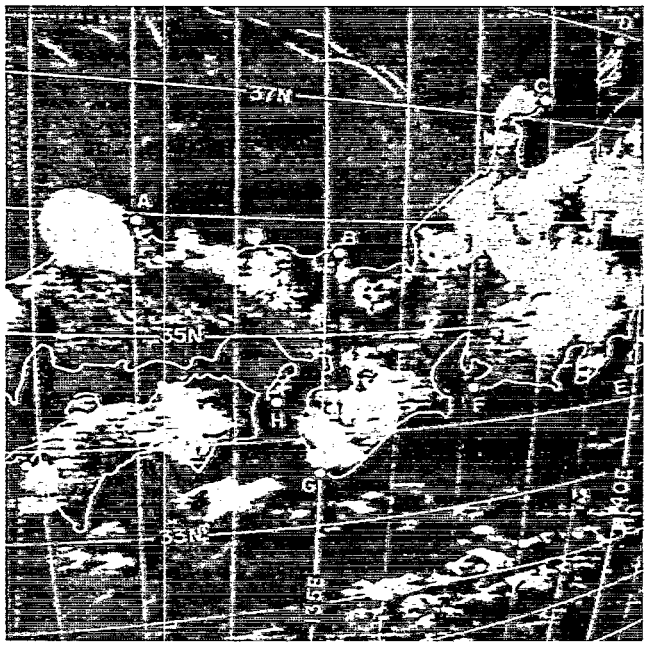

PHOTOGRAPH 3.5. Satellite picture on 5 August 1963, with a geographical grid plotted allowing for errors in the azimuth of the principal line: $A_{true} = 117°$; $A_{used} = 127°$; other parameters as in Photograph 3.1.

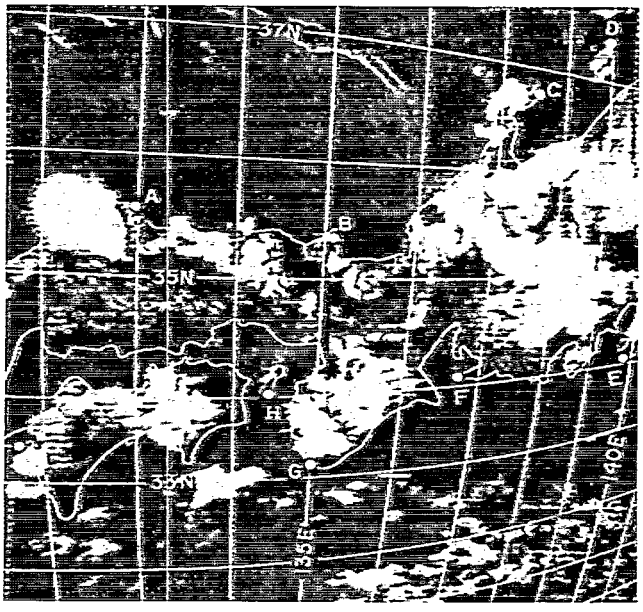

PHOTOGRAPH 3.6. Satellite picture on 5 August 1963, with a geographical grid plotted allowing for errors in determining the SSP

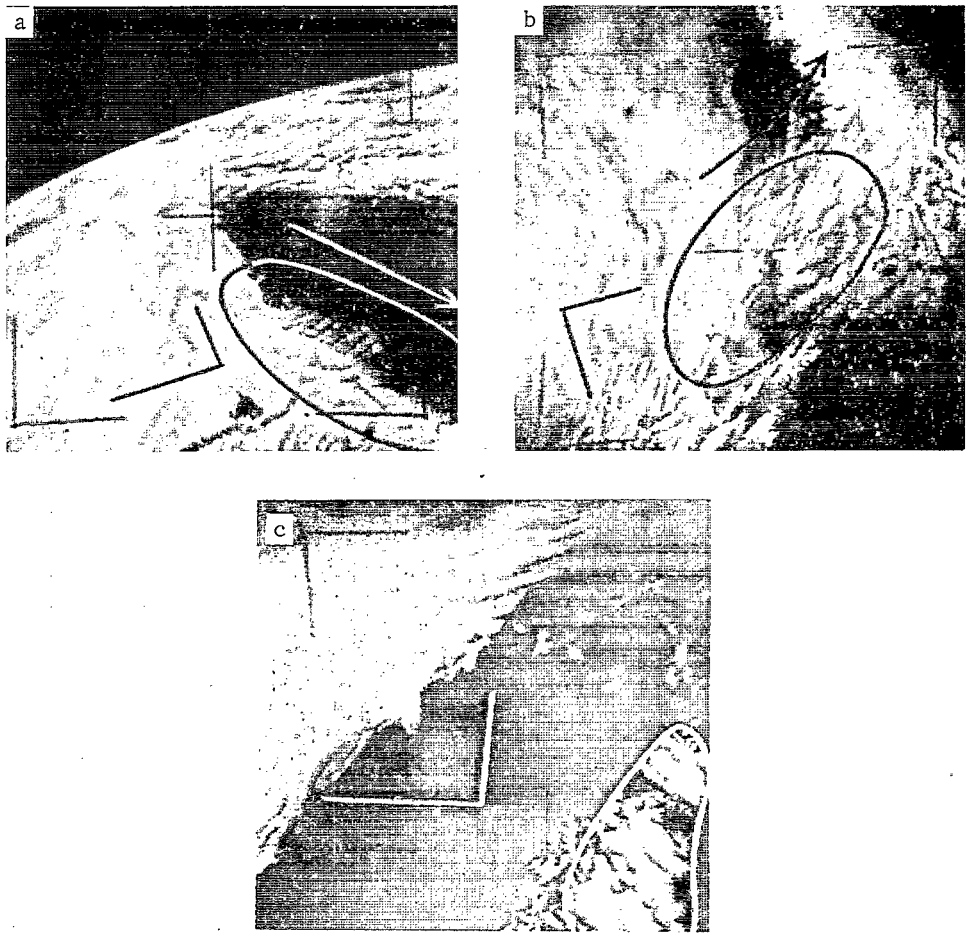

PHOTOGRAPH 4.1. Cirrus clouds (Ci):

a — of wave form; b — cloud bands (stratiform clouds to the left); c — cumulonimbus (Cb) anvils.

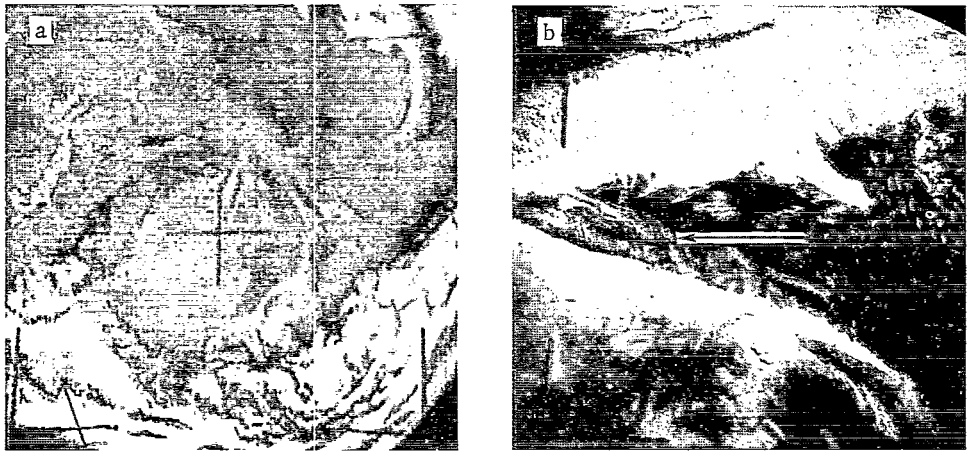

PHOTOGRAPH 4.2. Cirrostratus clouds (Cs):

a — against the background of underlying terrain; b — against the background of lower stratiform clouds.

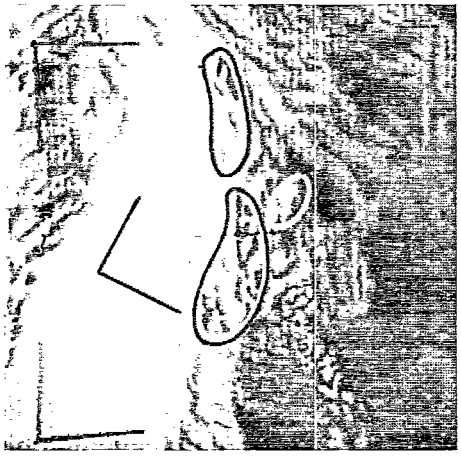

PHOTOGRAPH 4.3. Altocumulus clouds (Ac)

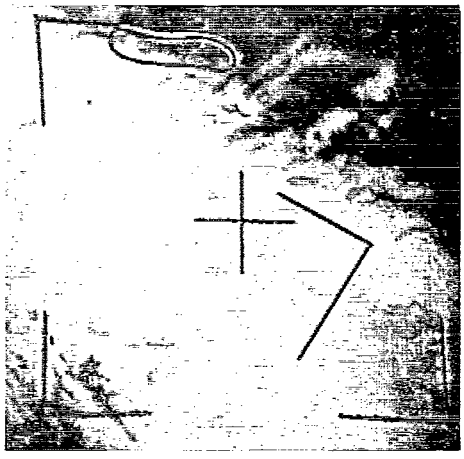

PHOTOGRAPH 4.4. Altostratus clouds (As)

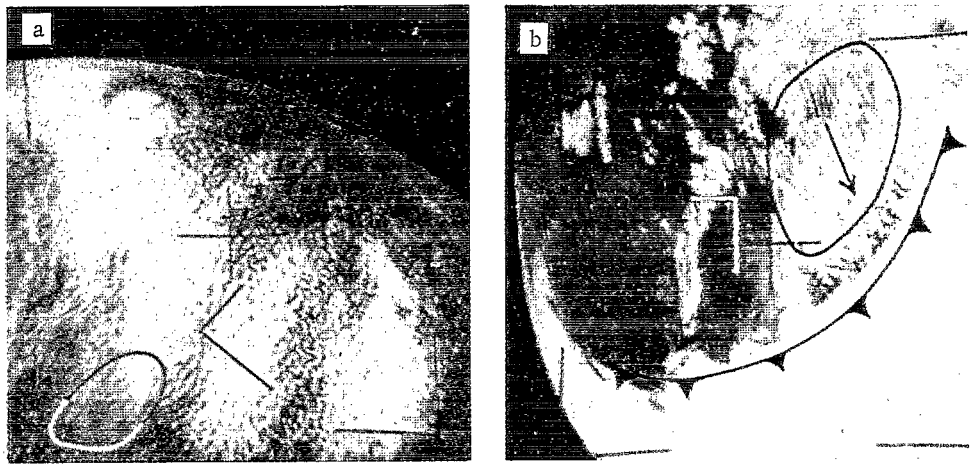

PHOTOGRAPH 4.5. Stratocumulus clouds (Sc):
a — internal clouds; b — behind the cold front.

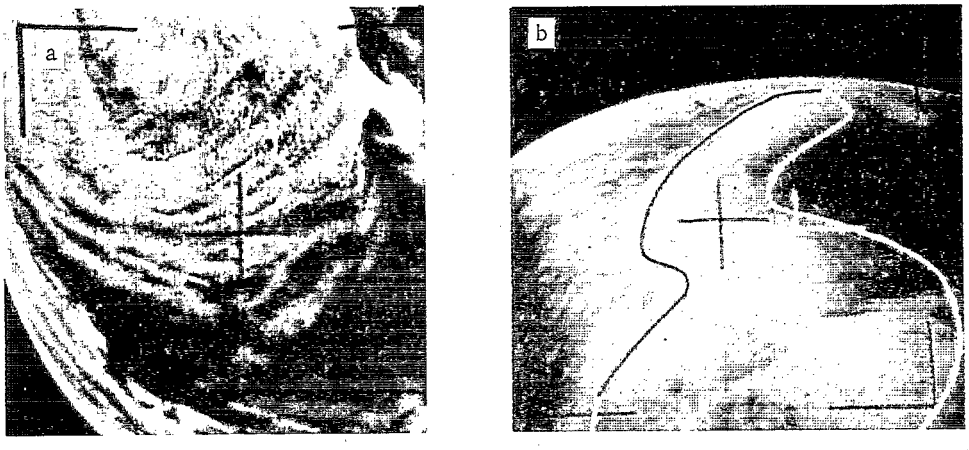

PHOTOGRAPH 4.6. Stratiform clouds (St):
a — seen as fibers; b — St or dust.

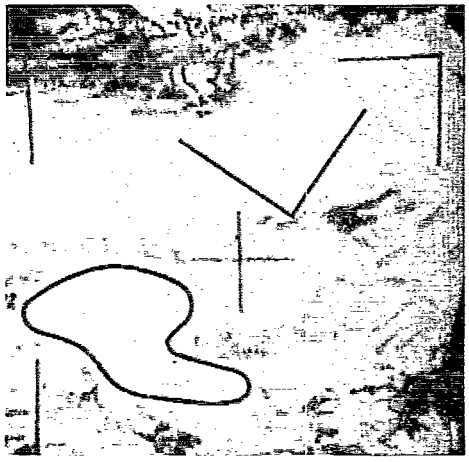

PHOTOGRAPH 4.7. Nimbostratus clouds (Ns)

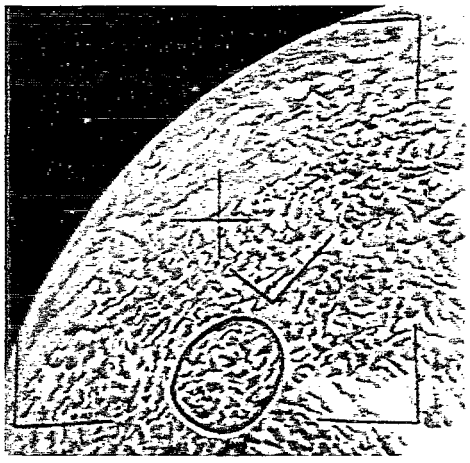

PHOTOGRAPH 4.8. Fair-weather cumulus clouds (Cu hum.) and thick cumulus-congestus clouds (Cu cong.)

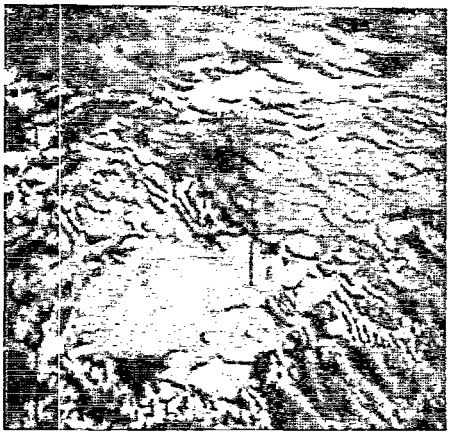

PHOTOGRAPH 4.9. Cumulonimbus (Cb) and accumulations of smaller cloud elements

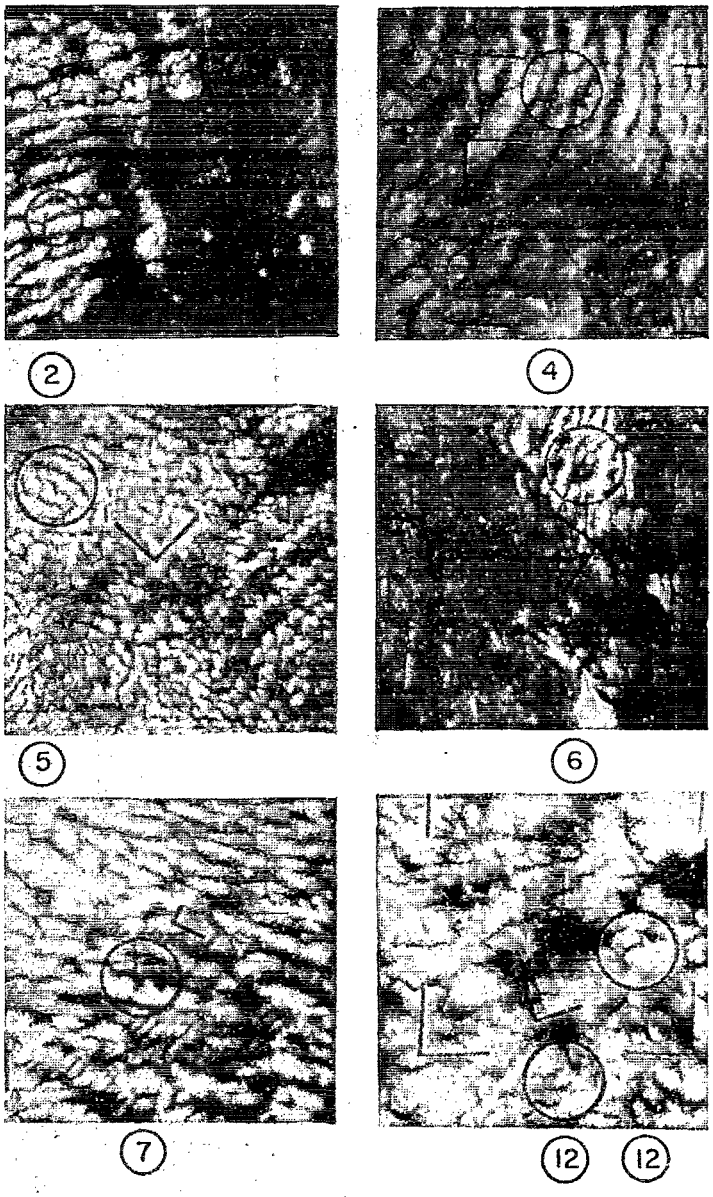

PHOTOGRAPH 4.10. Pictures from satellite camera 1 (numbers in circles

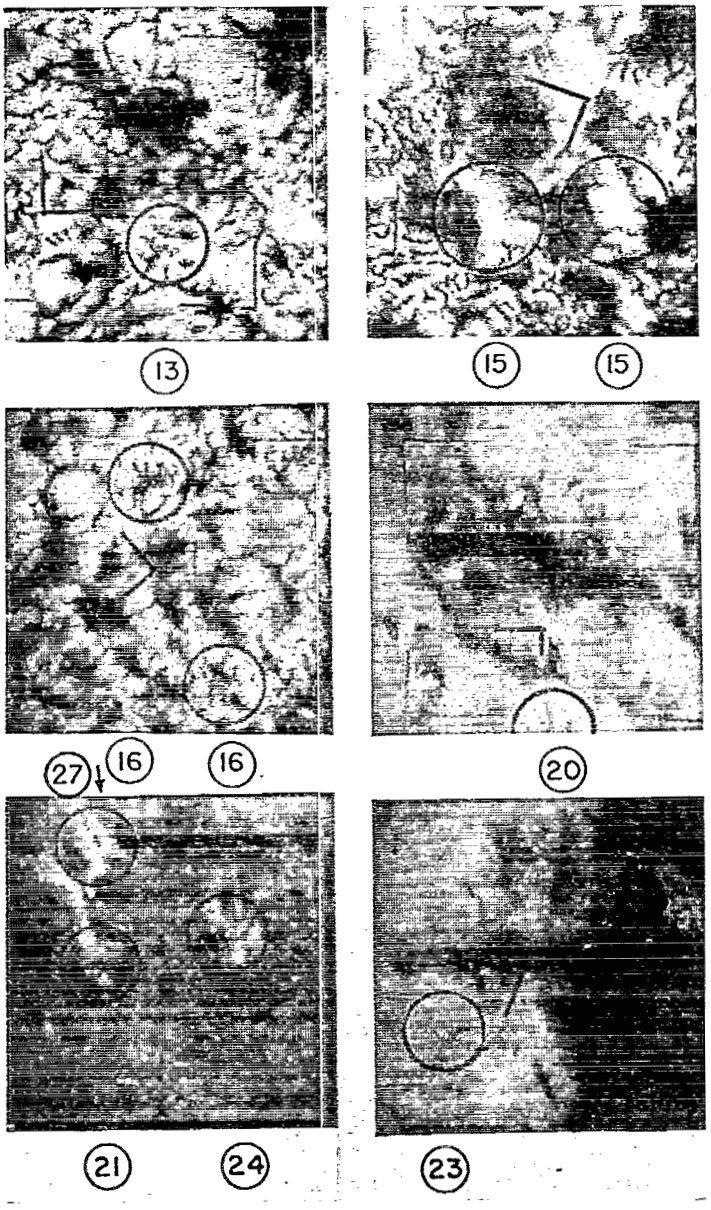

correspond to numbers in Figure 4.6)

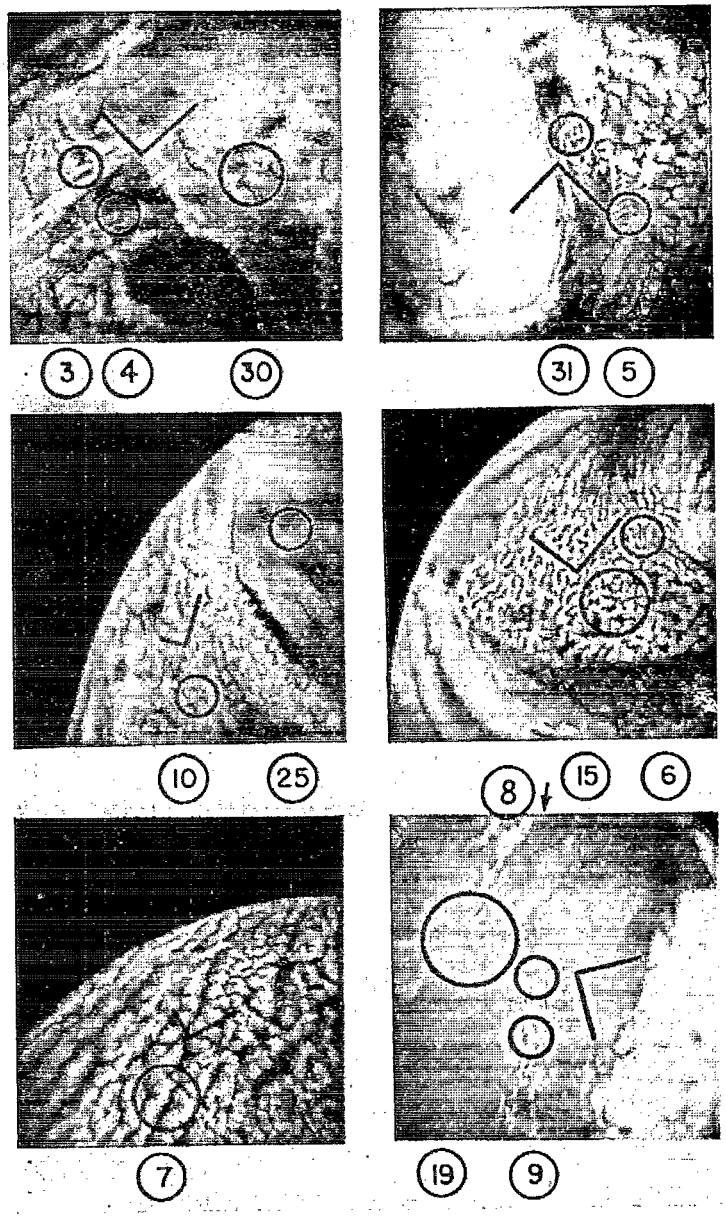

PHOTOGRAPH 4.11. Pictures from satellite camera 2 (numbers in circles

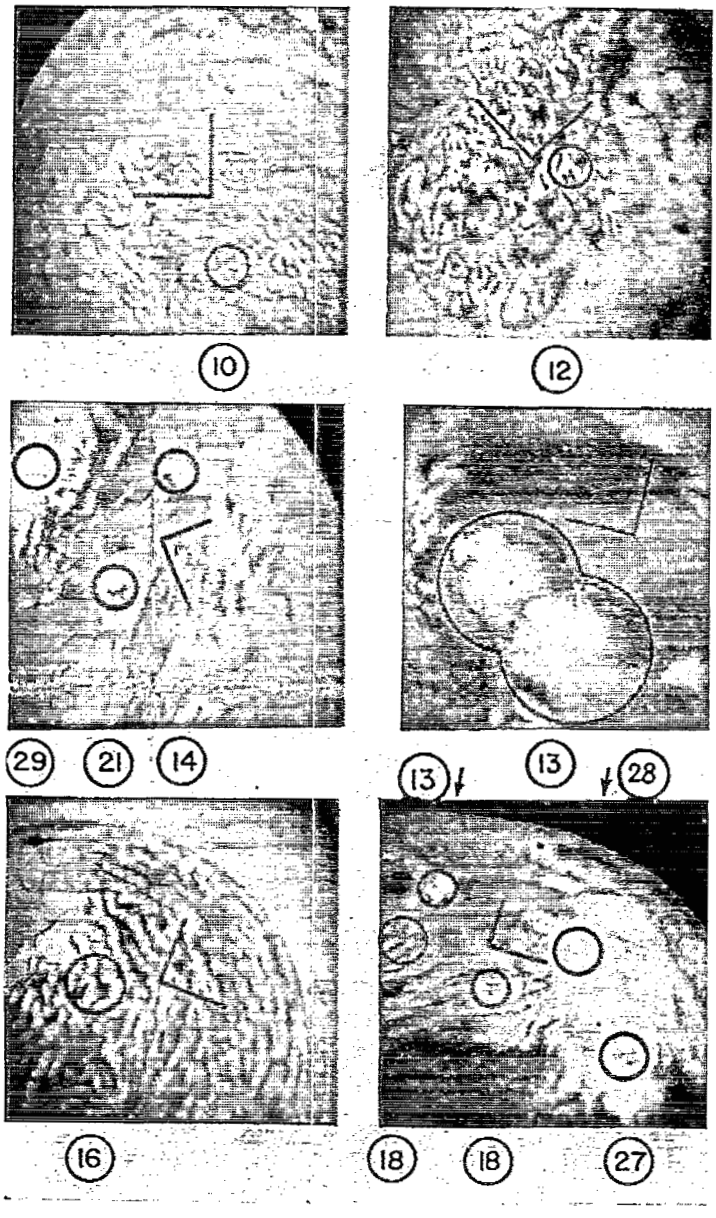

correspond to numbers in Figure 4.7)

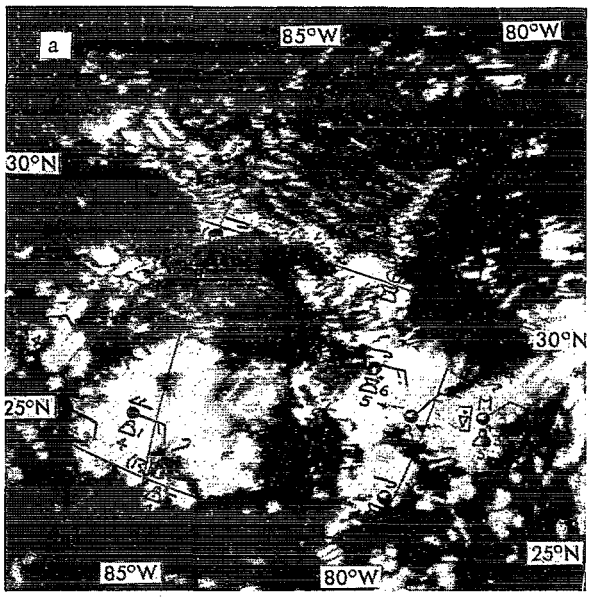

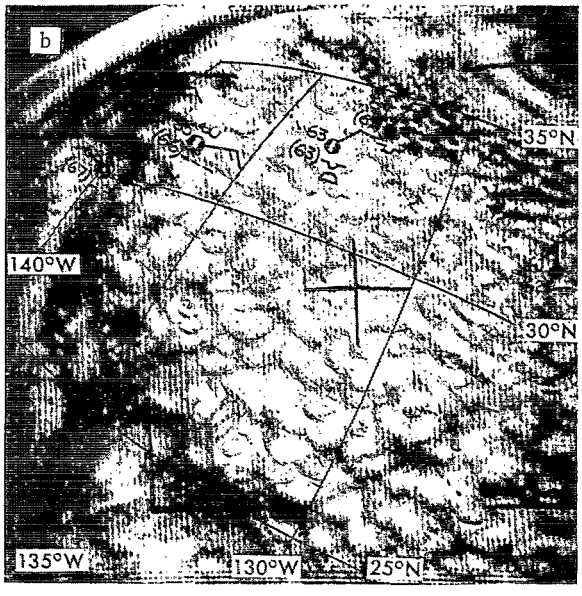

PHOTOGRAPH 4.12. Cumulus clouds in the shape of dense cells:

a — Cu and Sc of uniform areal distribution (from TIROS IV at 2100 hr on 5 June 1962); b — randomly located Cu and Cb (from TIROS V at 1800 hr on 19 August 1962)

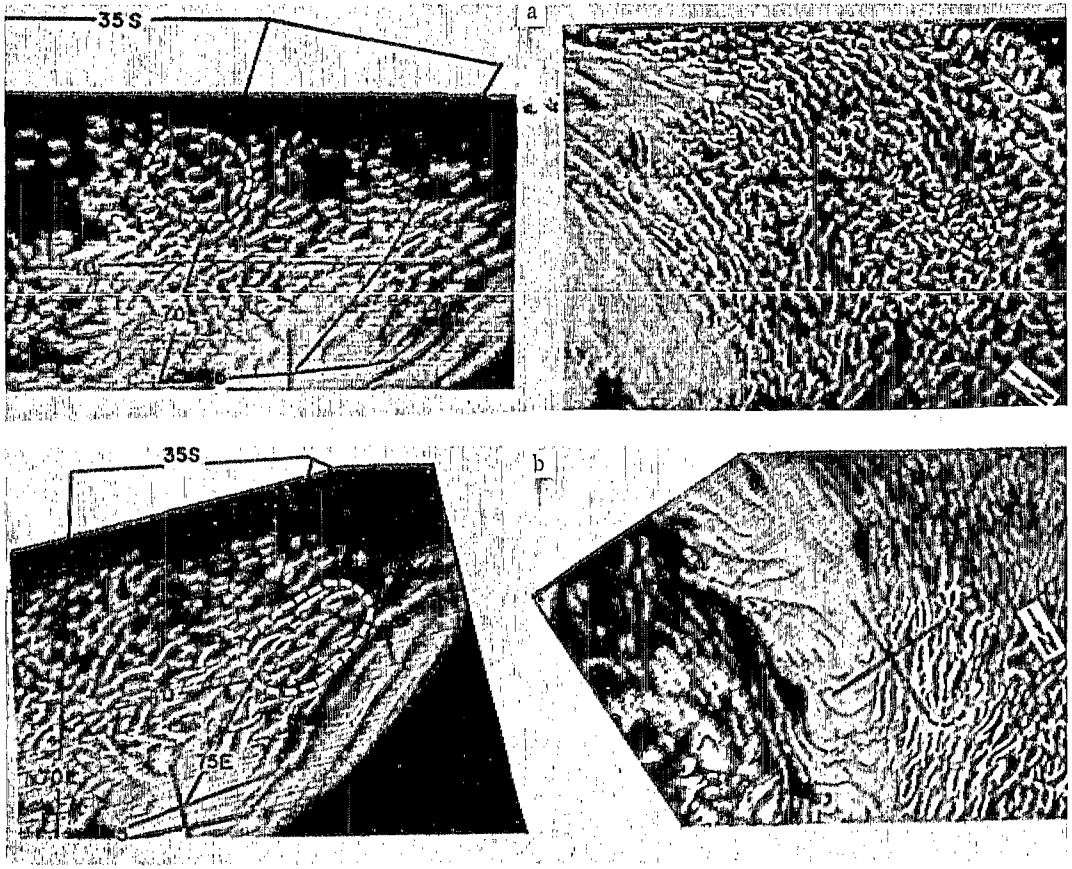

PHOTOGRAPH 4.13. Cumulus clouds in the shape of empty cells:

a — empty cells, in the presence of a weak wind (TIROS V at 1500 hr on 7 October 1962); b — polygonal empty cells in the shape of elliptic chains, in the presence of a strong wind.

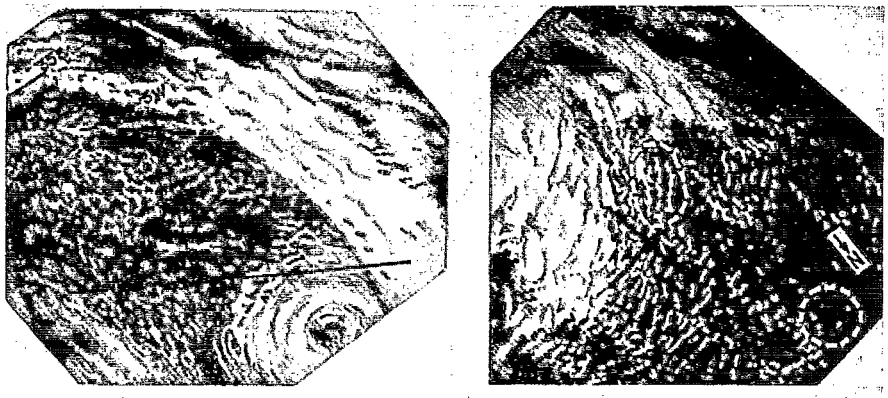

PHOTOGRAPH 4.14. Half-moon cumulus clouds

PHOTOGRAPH 4.15. Vermiform Cu cloud bands (from NIMBUS I during orbit No.3818, frame 2, at 0222 hr on 21 September 1964)

PHOTOGRAPH 4.16. Noncumulus bands of fibratus clouds

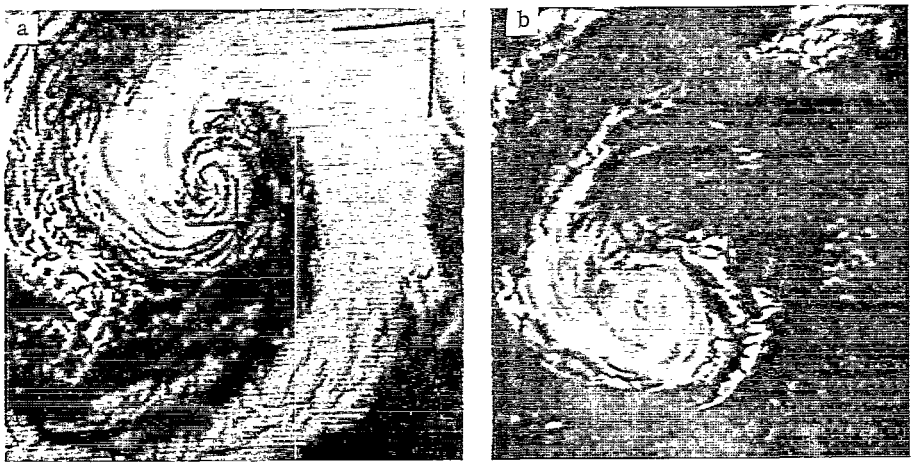

PHOTOGRAPH 4.17. Spiral-like clouds or cloud vortex:

a — in mid-latitude cyclone; b — in developed tropical cyclone.

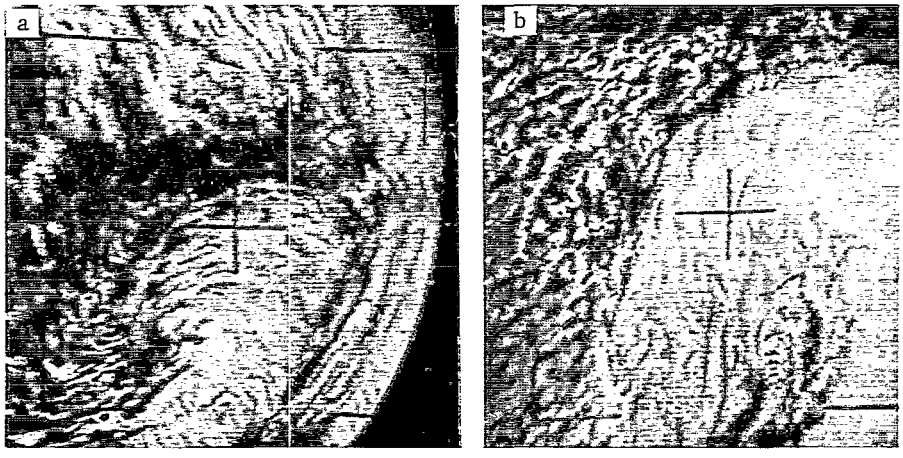

PHOTOGRAPH 4.18. Clouds in the shape of a "comma" (a) and half moon (b)

PHOTOGRAPH 4.19. Principal cloud bands:

a — bands of large-scale cold front; b — bands of varying scale

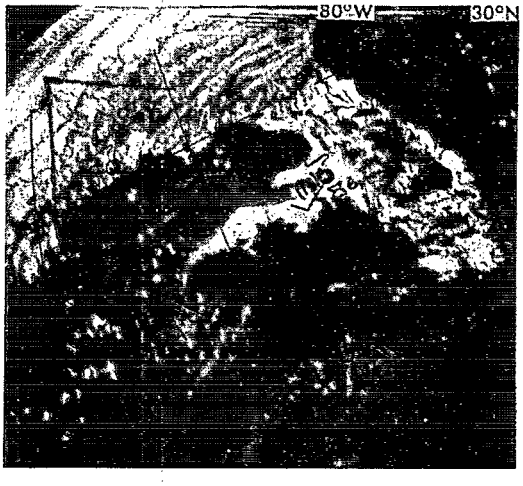

PHOTOGRAPH 4.20. Region of convective clouds of different size and vertical development

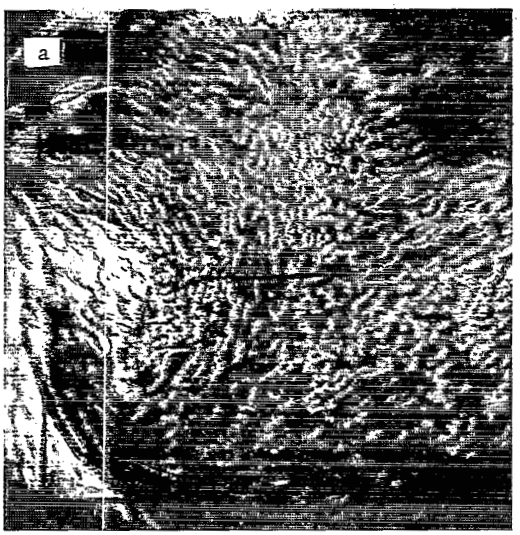

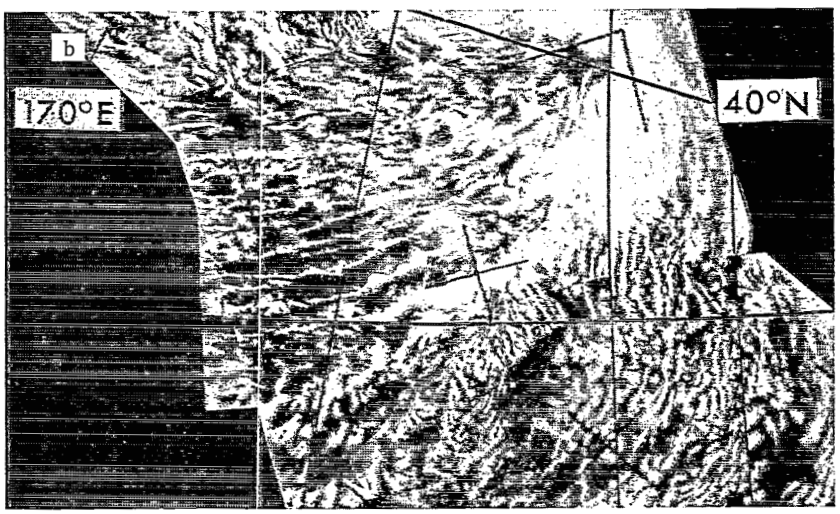

PHOTOGRAPH 4.21. Homogeneous internal clouds of small and medium (meso) scale: a — convective cloud cells; b — rows of convective clouds.

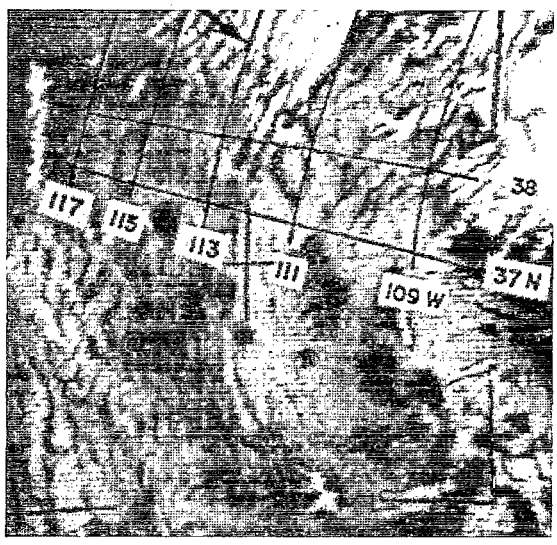

PHOTOGRAPH 4.22. Crest clouds above the Nevada range

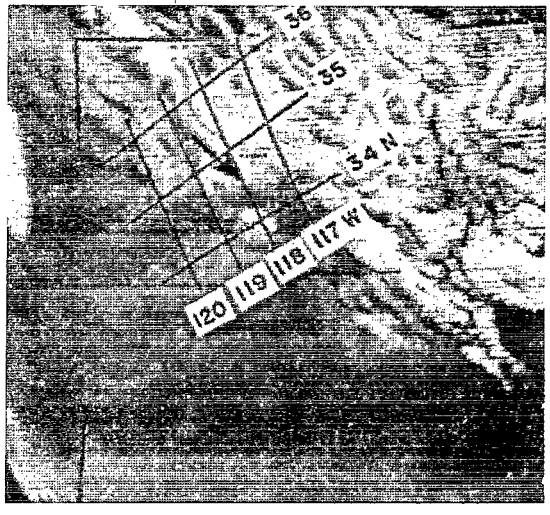

PHOTOGRAPH 4.23. Lenticular clouds over California

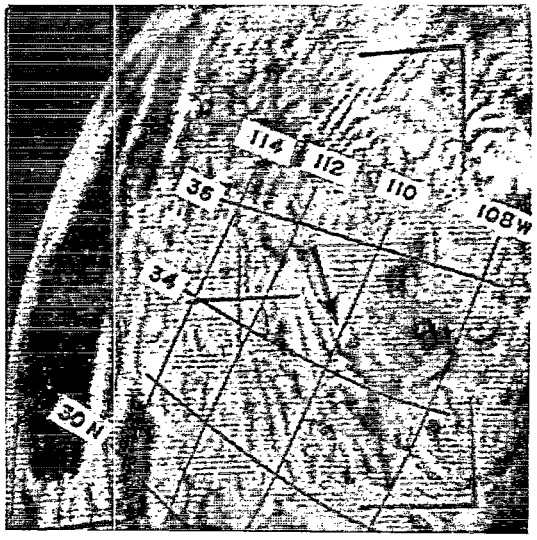

PHOTOGRAPH 4.24. Convergent fibrous clouds

PHOTOGRAPH 4.25. Single cloud lines above Iceland

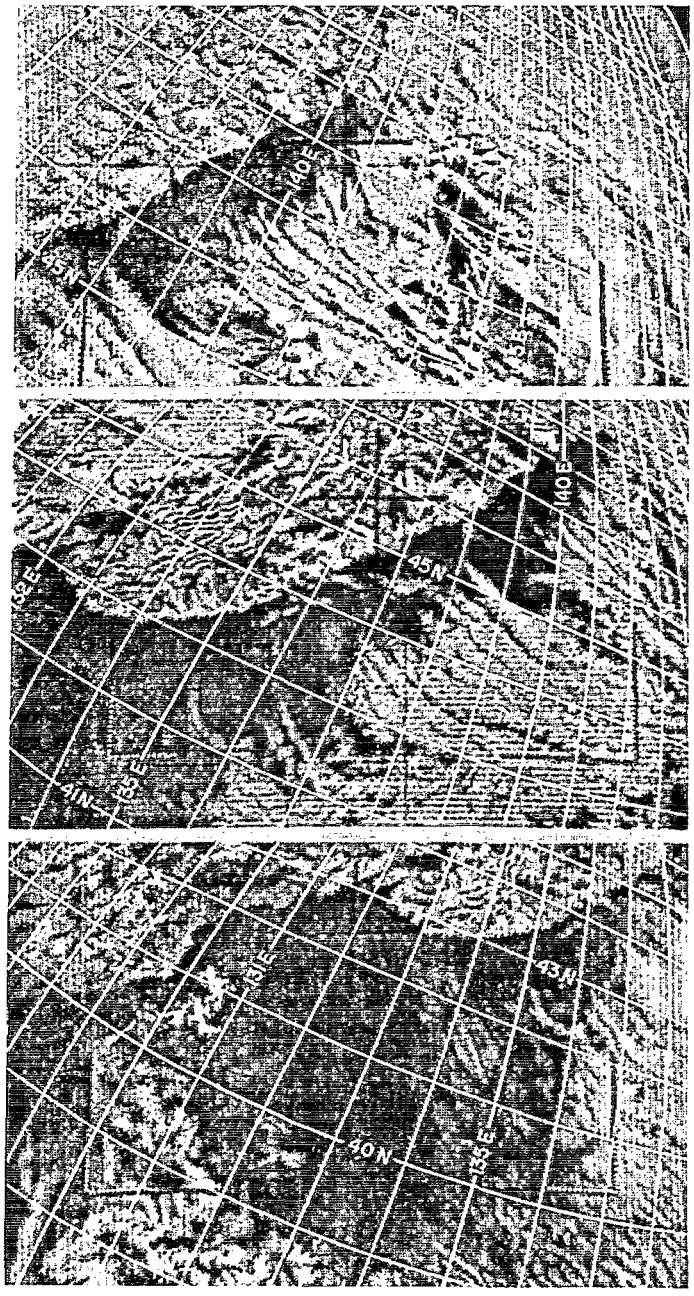

PHOTOGRAPH 4.26. Pictures from TIROS VII (Orbit No.3085, camera 2) on 14 January 1964:

Frame 6 (top): 0226 hr, $\varphi_{SSP} = 44.2°$ N, $\lambda_{SSP} = 139.5°$ E, $H = 642$ km, $\tau = 34.0°$, $A = 2.6°$; frame 8 (middle): 0225 hr, $\varphi_{SSP} = 46.1°$ N, $\lambda_{SSP} = 136.1°$ E, $H = 642$ km, $\tau = 31.5°$, $A = 355.9°$; frame 10 (bottom): 0224 hr, $\varphi_{SSP} = 39.0°$ N, $\lambda_{SSP} = 133.0°$ E, $H = 641$ km, $\tau = 29.2°$, $A = 348.9°$.

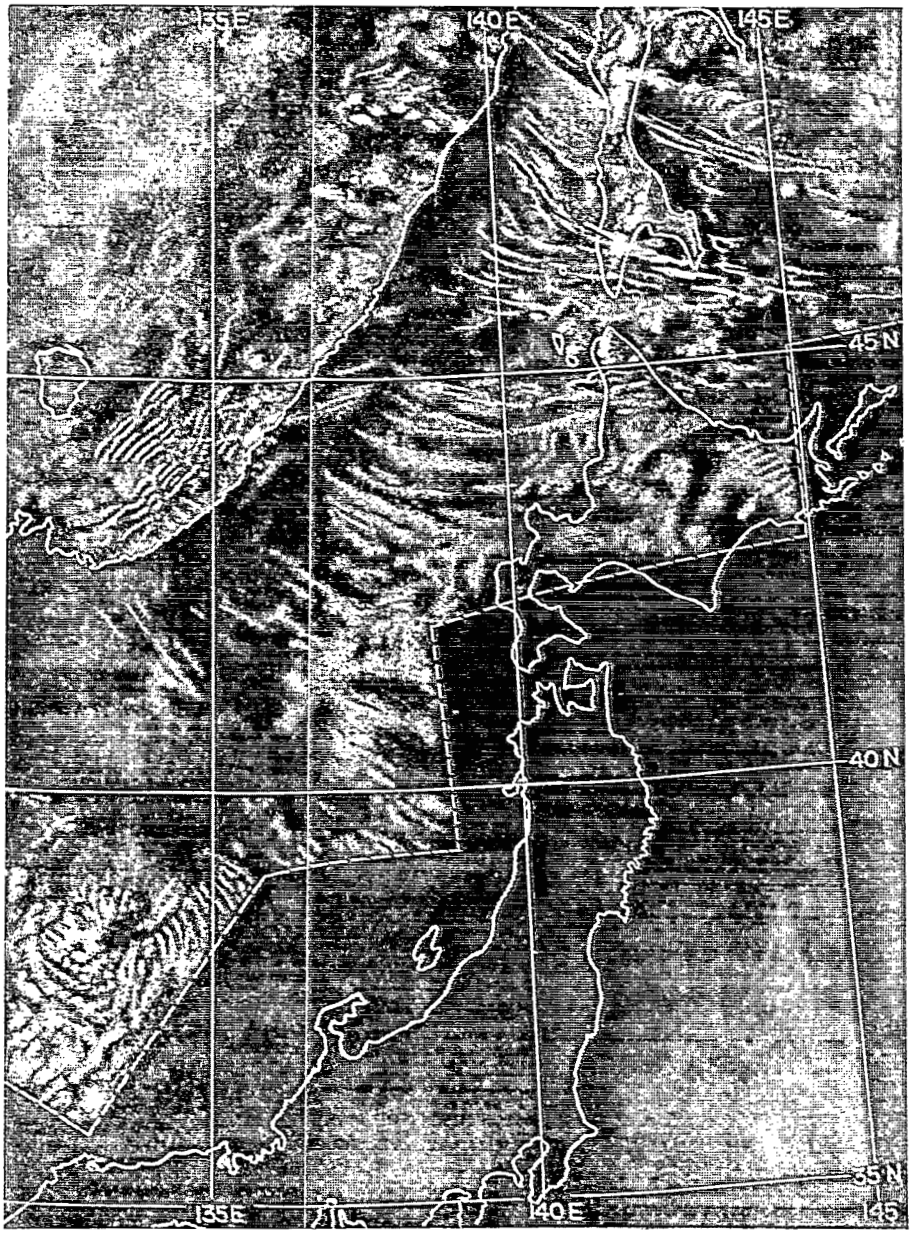

PHOTOGRAPH 4.27. Systematic chart plotted from data on Photograph 4.26

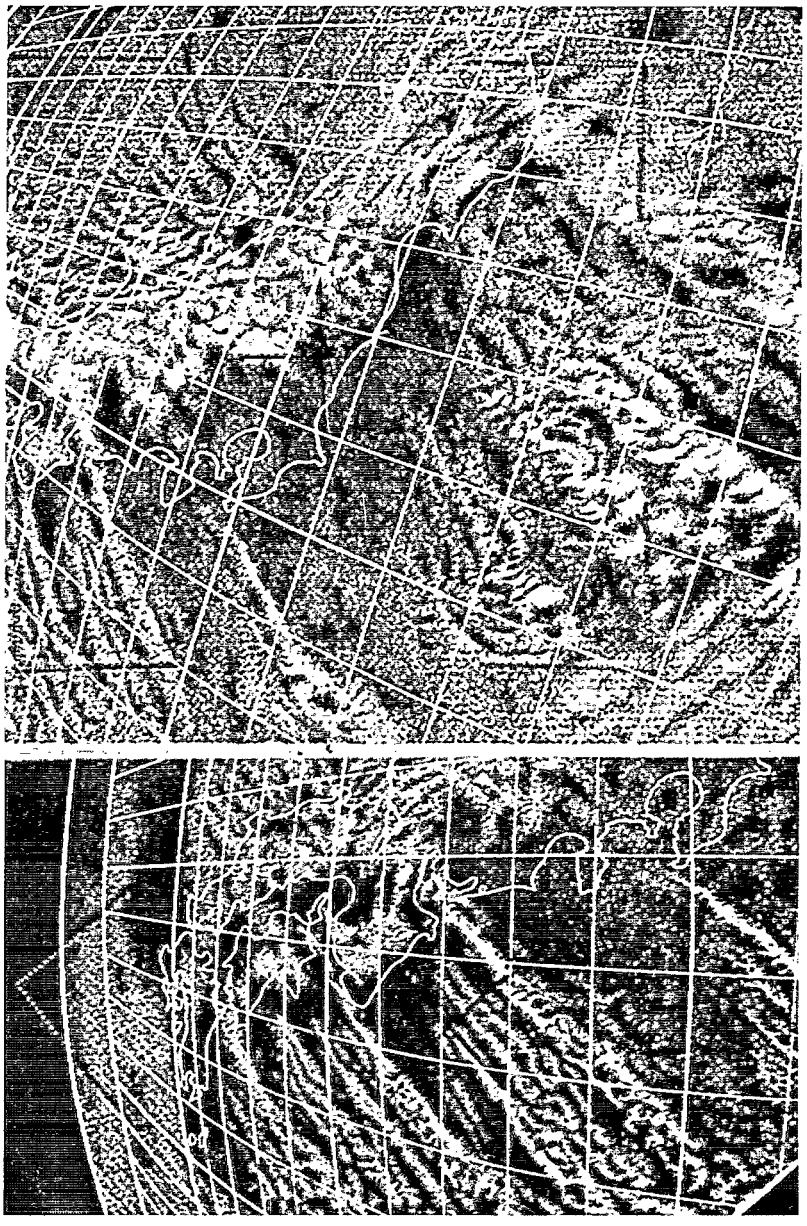

PHOTOGRAPH 4.28. Photograph from TIROS VII (orbit No.3172, camera 2) on 20 January 1964:

Frame 14 (top): 2337.5 hr, $\varphi_{SSP} = 36.7°$N, $\lambda_{SSP} = 144.2°$ E, $H = 639$ km, $\tau = 27.9°$, $A = 270.9°$; frame 16 (bottom): 2336.5 hr, $\varphi_{SSP} = 33.9°$N, $\lambda_{SSP} = 141.6°$ E, $H = 638$ km, $\tau = 30.3°$, $A = 264.4°$.

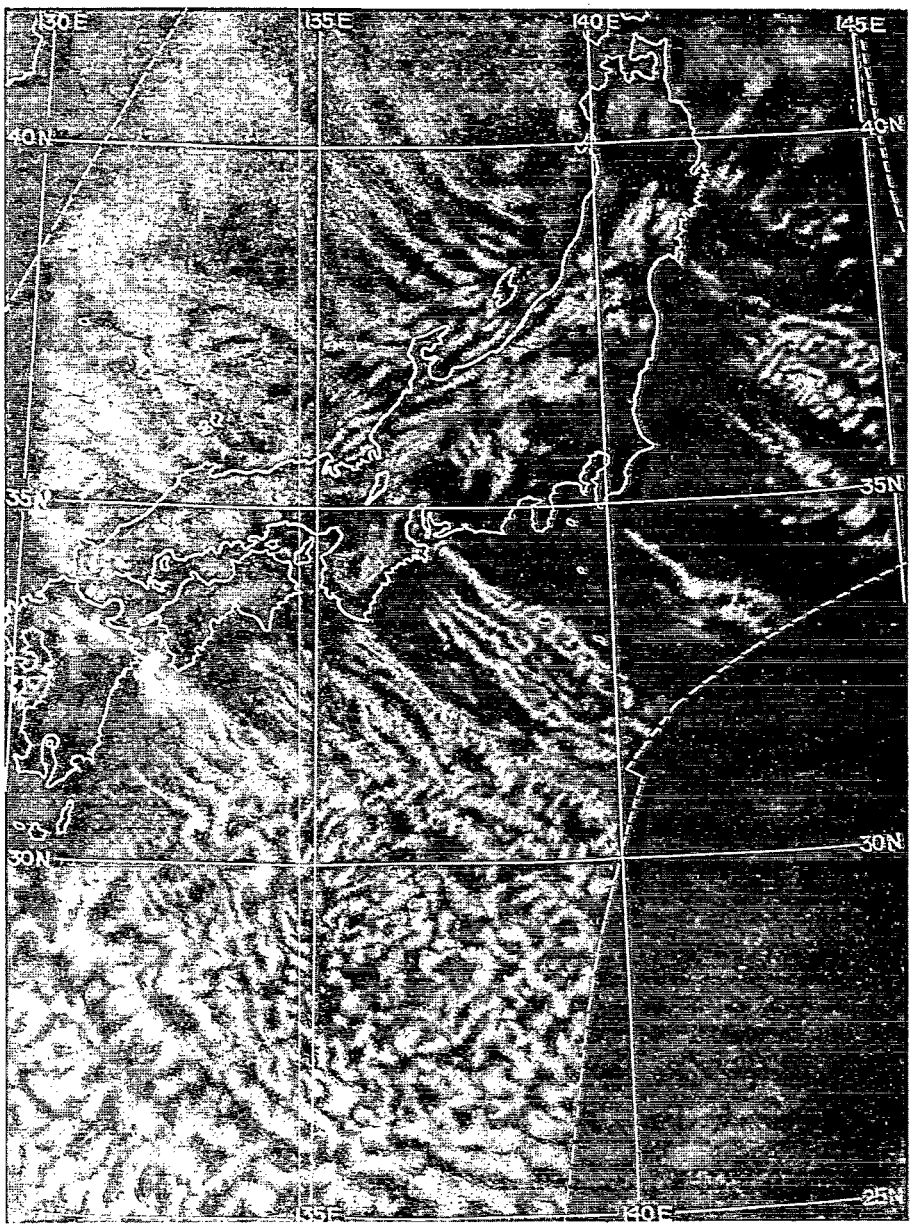

PHOTOGRAPH 4.29. Systematic chart plotted from data in Figure 4.28

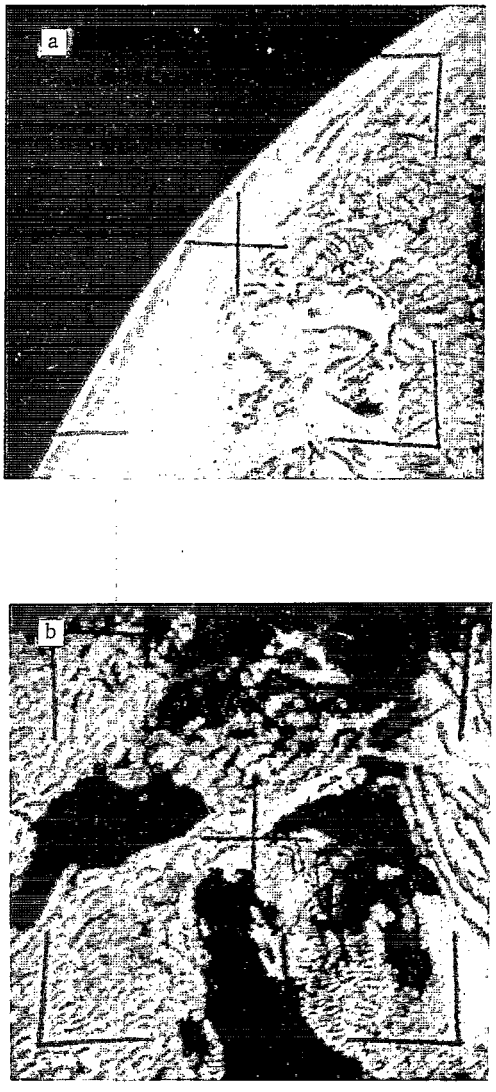

PHOTOGRAPH 4.30. Picture from TIROS IV on 9 February 1962 at a nadir angle of 61° (Lake Michigan and adjacent areas are seen as white spots) (a); same area photographed on 1 April 1962 at a nadir angle of 25° (b)

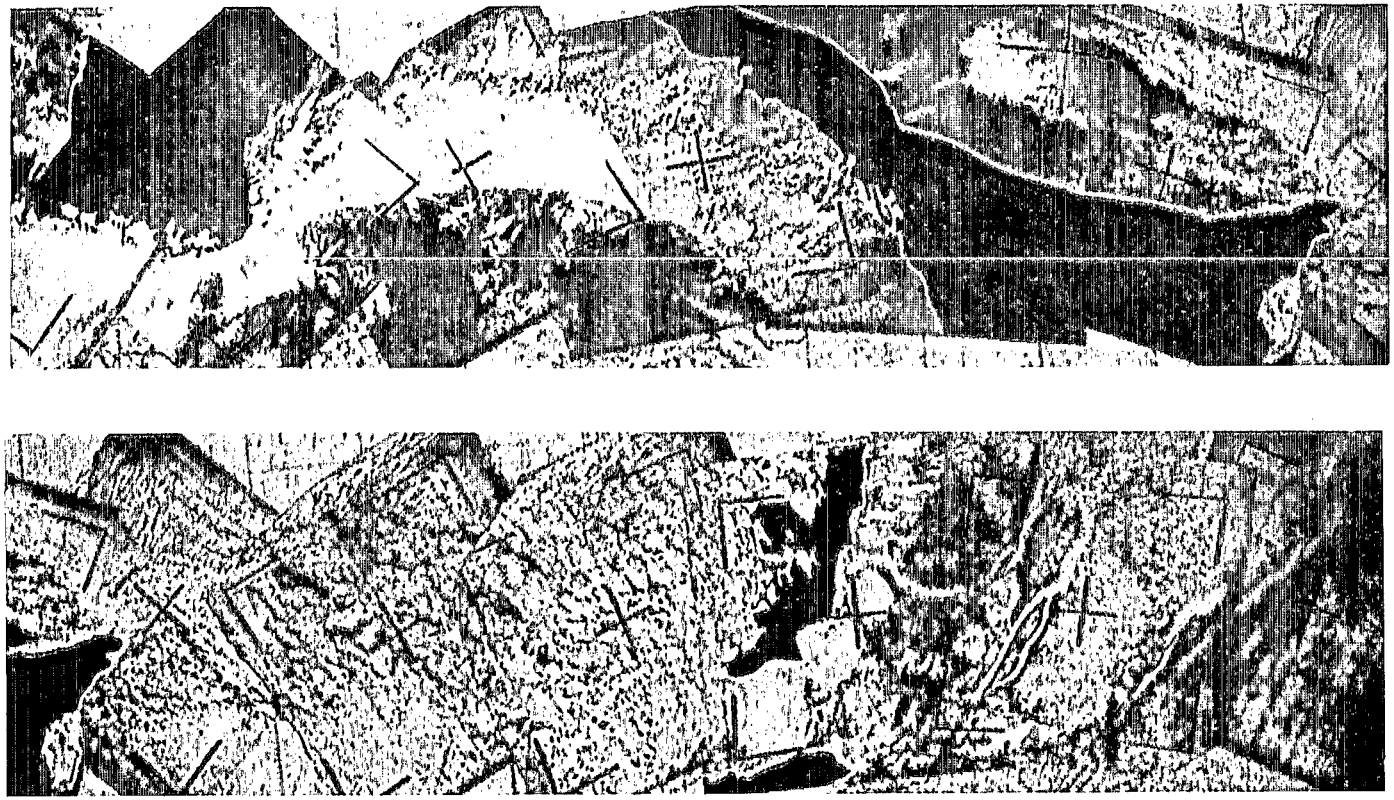

PHOTOGRAPH 4.31. Picture mosaic of ice fields on 22 March 1961 (TIROS satellite); top photograph shows western part of viewed region, bottom part shows eastern part

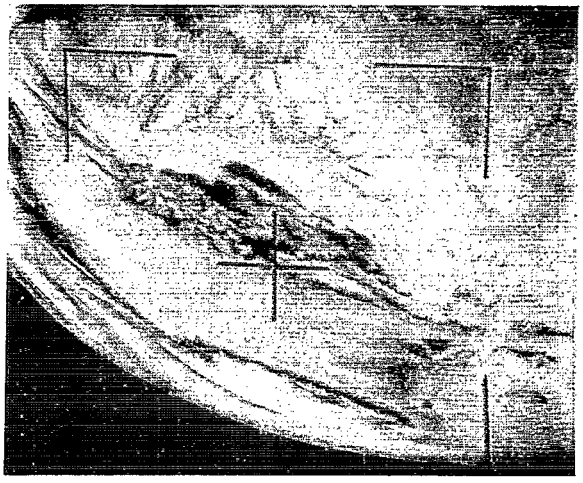

PHOTOGRAPH 4.32. Picture of the St. Lawrence Bay region from TIROS VI on April 1963 (orbit No.3227)

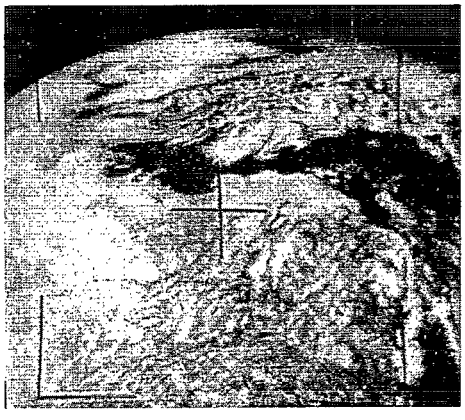

PHOTOGRAPH 4.33. Picture of the St. Lawrence Bay area (TIROS VI, orbit No.3241, April 1963). The photograph was taken two days after that in Photograph 4.32

PHOTOGRAPH 4.34. Same region as in Photograph 4.32. The picture was taken at large nadir angle (orbit No.4334, 1963)

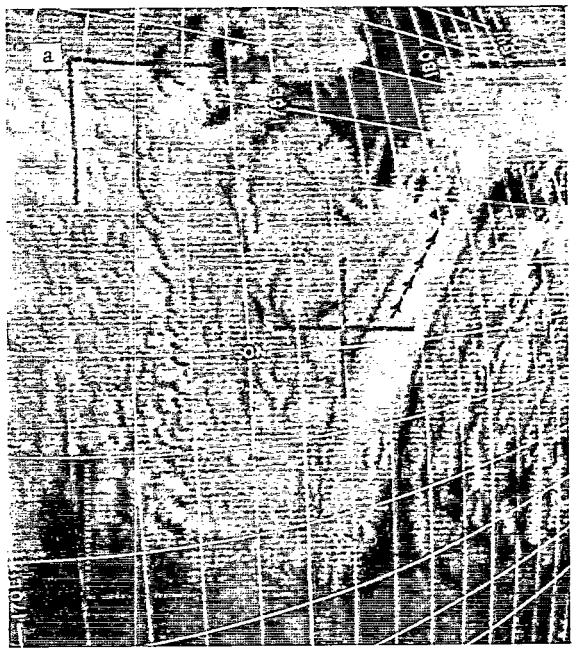

PHOTOGRAPH 4.35. Pictures from TIROS VII on 8 August 1963 (orbit No.735, camera 2, $H = 628$ km):

a — frame 8, 0319.5 hr, $\varphi_{SSP} = 49.8°$N, $\lambda_{SSP} = 170.5°$ E, $\tau = 30.1°$, $A = 87.4°$;
b — frame 6, 0320.5 hr, $\varphi_{SSP} = 51.8°$N, $\lambda_{SSP} = 175.1°$ E, $\tau = 33.3°$, $A = 88.1°$.

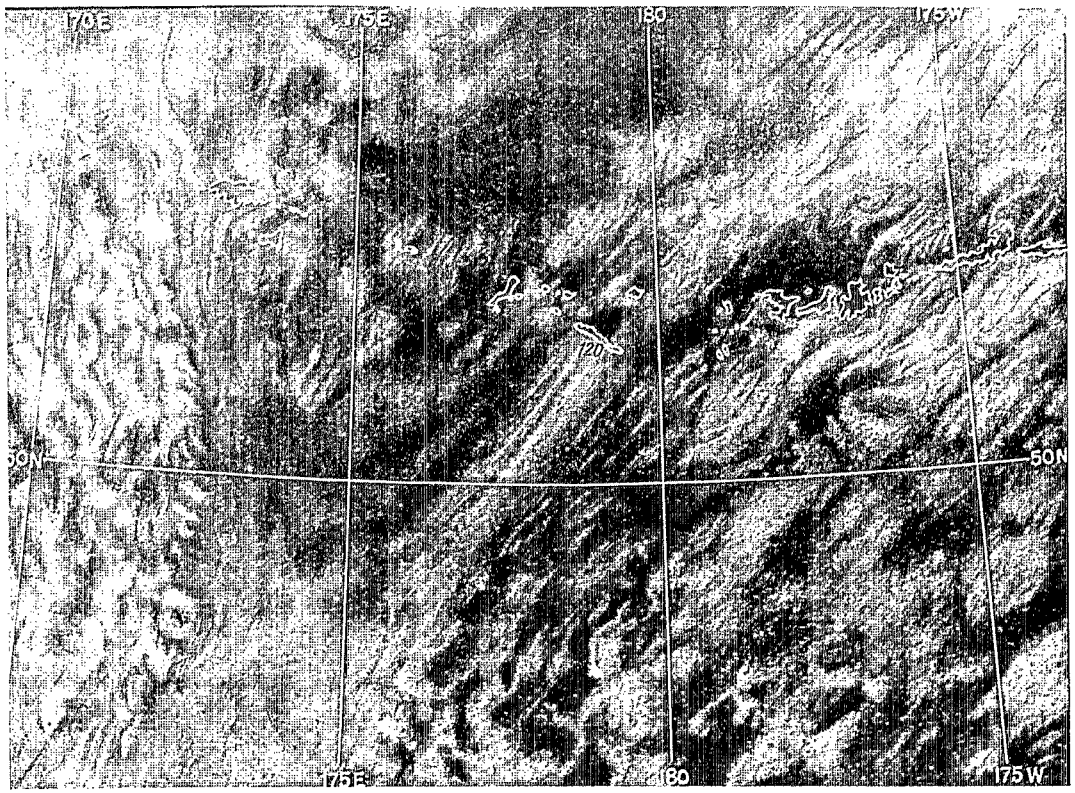

PHOTOGRAPH 4.36. Systematic chart plotted from data in Figure 4.35

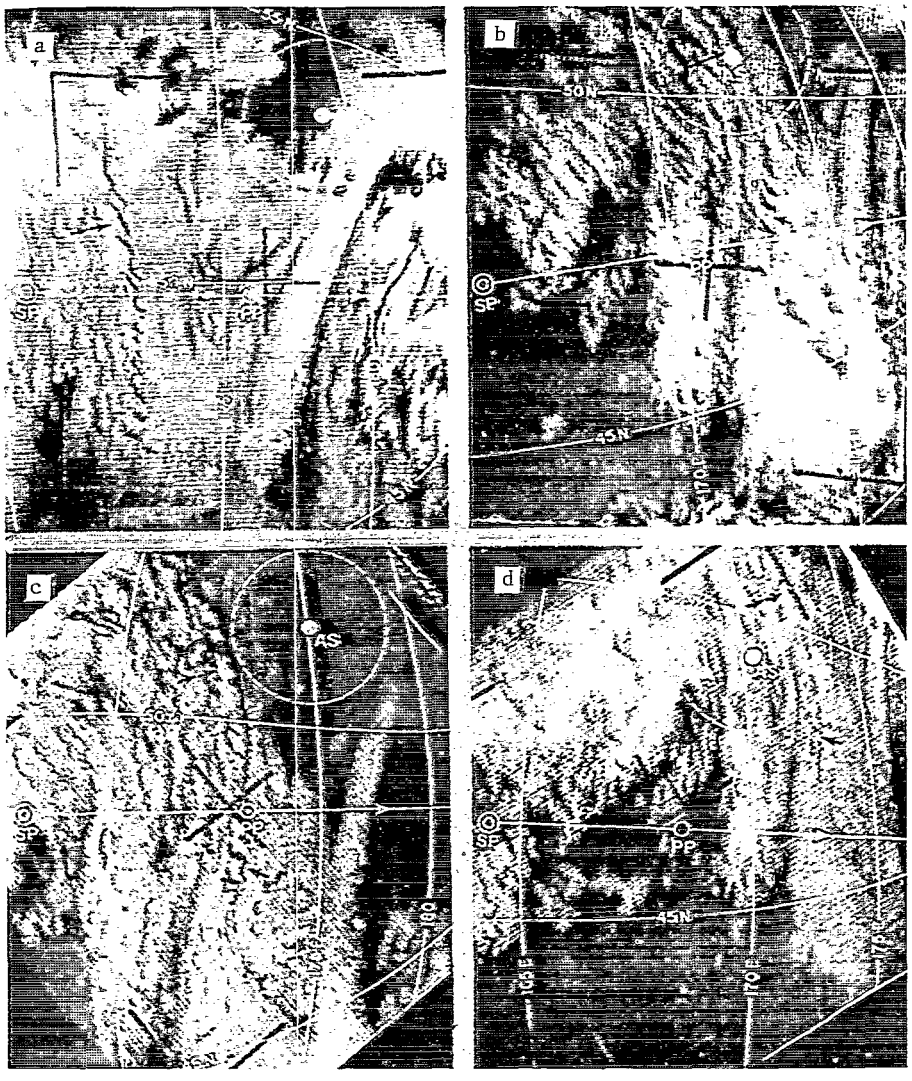

PHOTOGRAPH 4.37. Pictures from TIROS VII on 8 August 1963 (orbit No.735, $H = 628$ km):

a — frame 8, 0319.5 hr, $\varphi_{SSP} = 49.8°$N, $\lambda_{SSP} = 170.5°$E, $\tau = 30.1°$, $A = 87.4°$; b — frame 9, 0320 hr, $\varphi_{SSP} = 48.7°$N, $\lambda_{SSP} = 168.3°$E, $\tau = 28.6°$, $A = 87.4°$; c — frame 10, 0320.5 hr, $\varphi_{SSP} = 47.5°$N, $\lambda_{SSP} = 166.3°$E, $\tau = 27.1°$, $A = 88.0°$; d — frame 11, 0320 hr, $\varphi_{SSP} = 46.3°$N, $\lambda_{SSP} = 164.3°$E, $\tau = 25.6°$, $A = 88.8°$ (for symbols see Chapter 2).

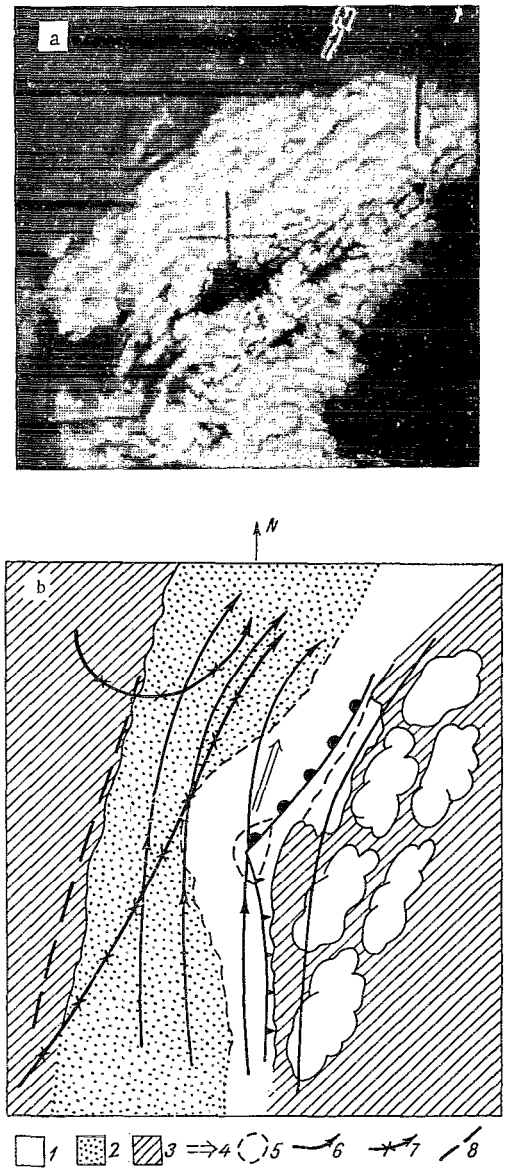

PHOTOGRAPH 4.38. Frontal wave clouds:

a — cloud photograph; b — schematic diagram of clouds, fronts and air currents; 1 — cloud cover; 2 — cloud cover of low reflectivity; 3 — surface of land or ocean; 4 — direction of cyclone displacement; 5 — air currents in the lower troposphere; 6 — air currents in the middle troposphere; 7 — air currents at the tropopause level; 8 — position of high-level trough axis.

PHOTOGRAPH 4.39. Cyclone formation at occlusion point (picture from TIROS V at 1520 hr on 9 September 1962)

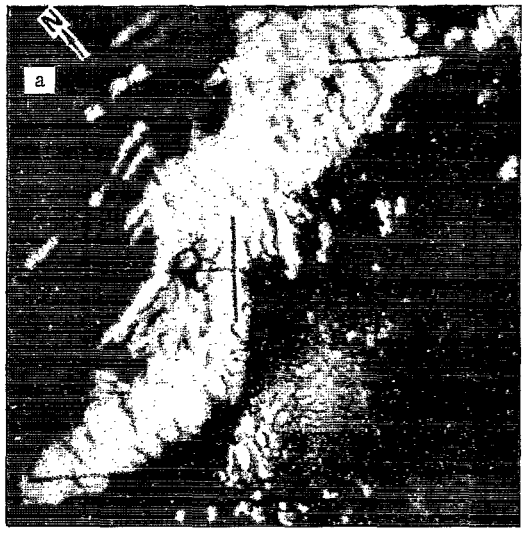

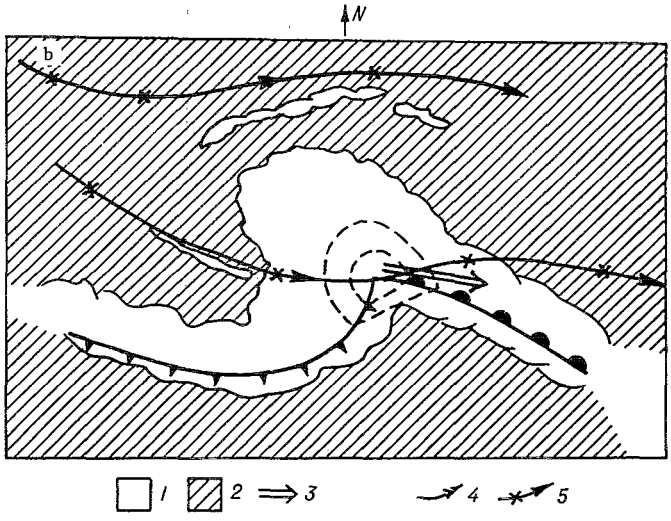

PHOTOGRAPH 4.40. Stage of young cyclone prior to its occlusion:

a — cloud picture; b — schematic diagram of clouds, fronts, and air currents; 1 — cloud cover; 2 — surface of land or ocean; 3 — direction of cyclone movement; 4 — air currents in middle troposphere; 5 — air current at tropopause level.

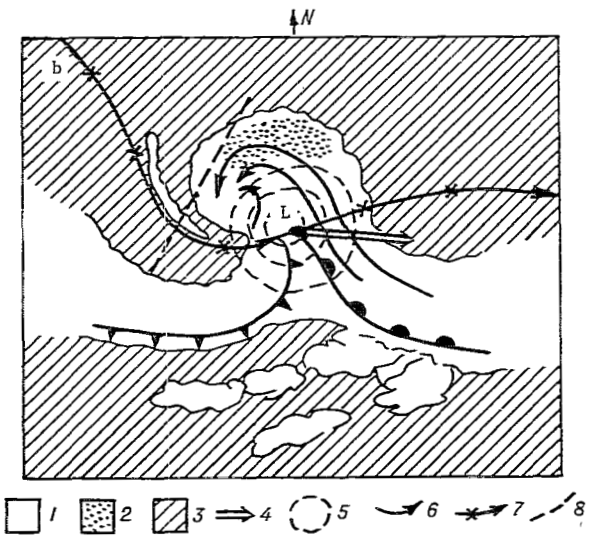

PHOTOGRAPH 4.41. Initial stage of cyclone occlusion.
For symbols see Photograph 4.38.

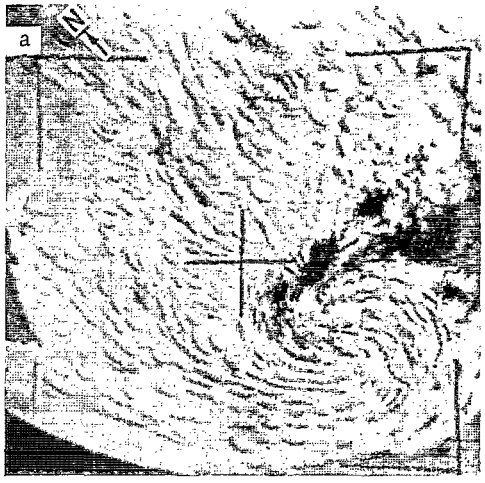

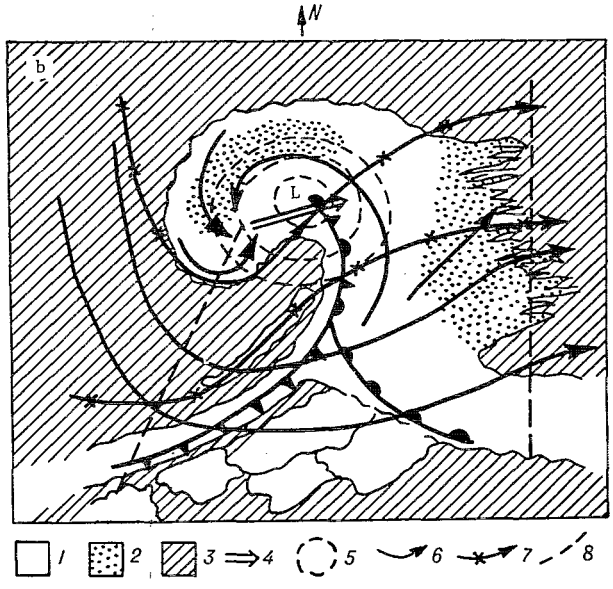

PHOTOGRAPH 4.42. Stage of occluding cyclone (no clouds in the cold air). For symbols see Photograph 4.38.

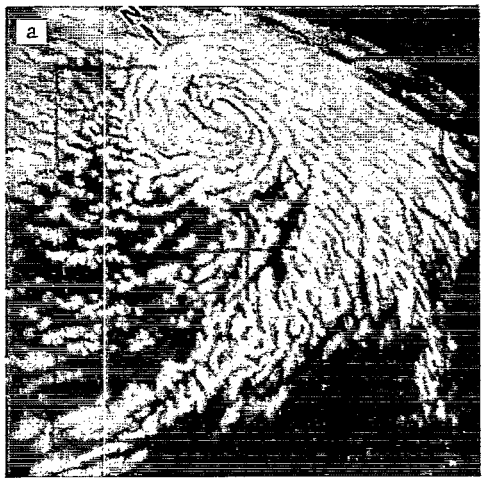

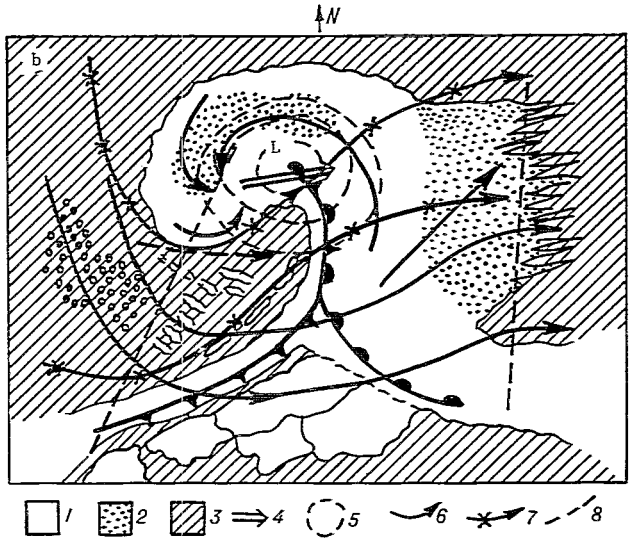

PHOTOGRAPH 4.43. Stage of occluding cyclone (convective clouds in cold air). For symbols see Photograph 4.38.

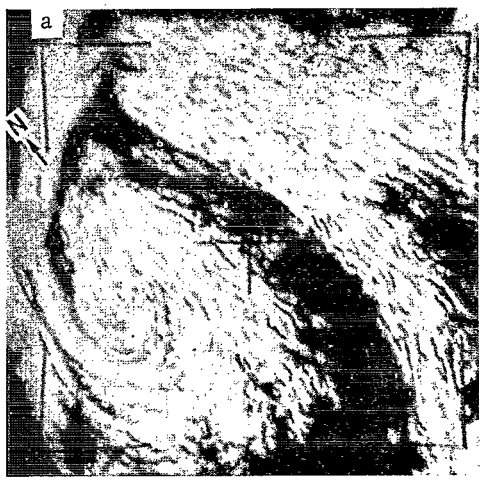

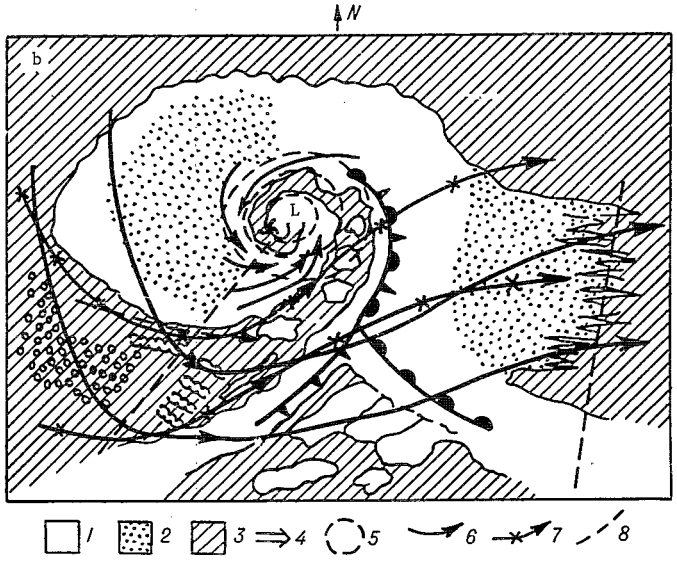

PHOTOGRAPH 4.44. Stage of occluding cyclone (a strip of dry cloud-free atmosphere is seen around the vortex center). For symbols see Photograph 4.38.

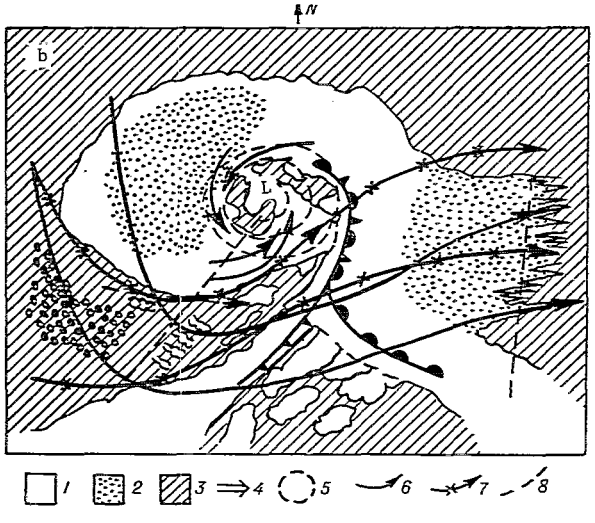

PHOTOGRAPH 4.45. Stage of fully occluded cyclone (start of cloud decay at vortex center). For symbols see Photograph 4.38

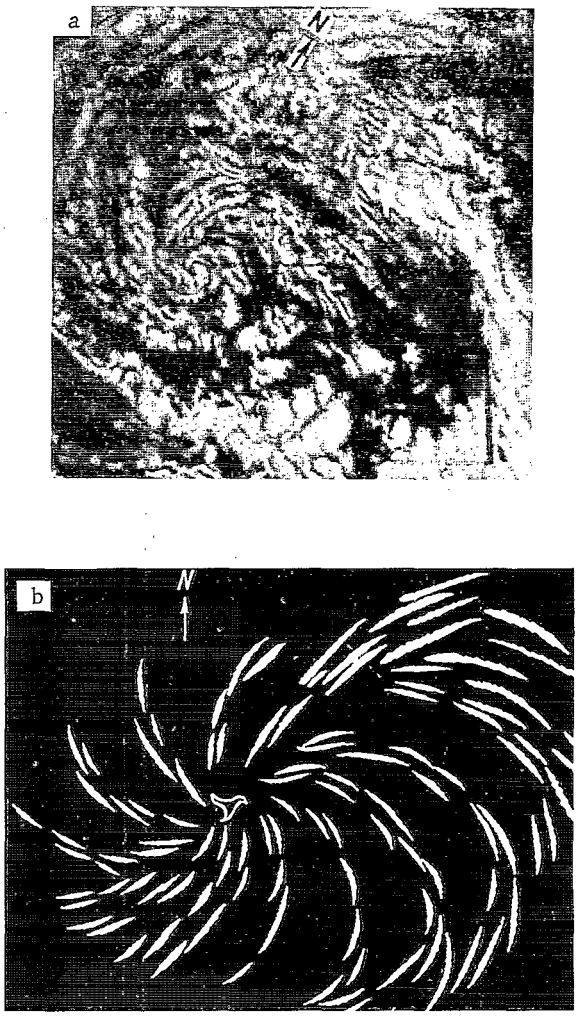

PHOTOGRAPH 4.46. Stage of cyclone decay and filling. For symbols see Photograph 4.38.

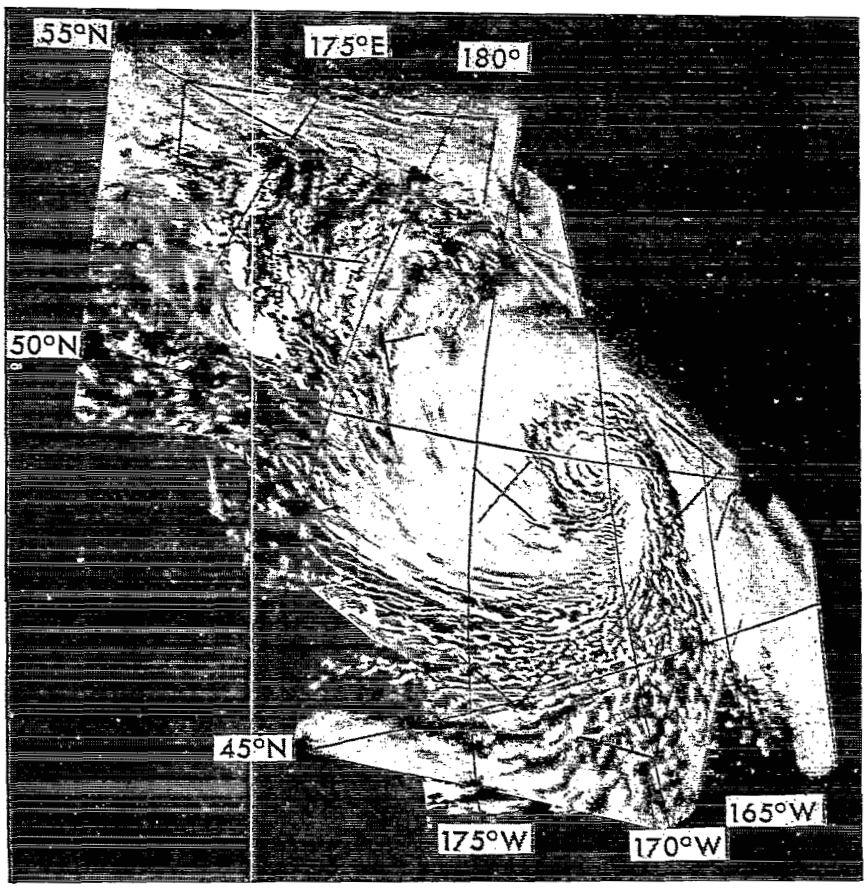

PHOTOGRAPH 4.47. Picture from TIROS VII at 0136 hr on 29 January 1964

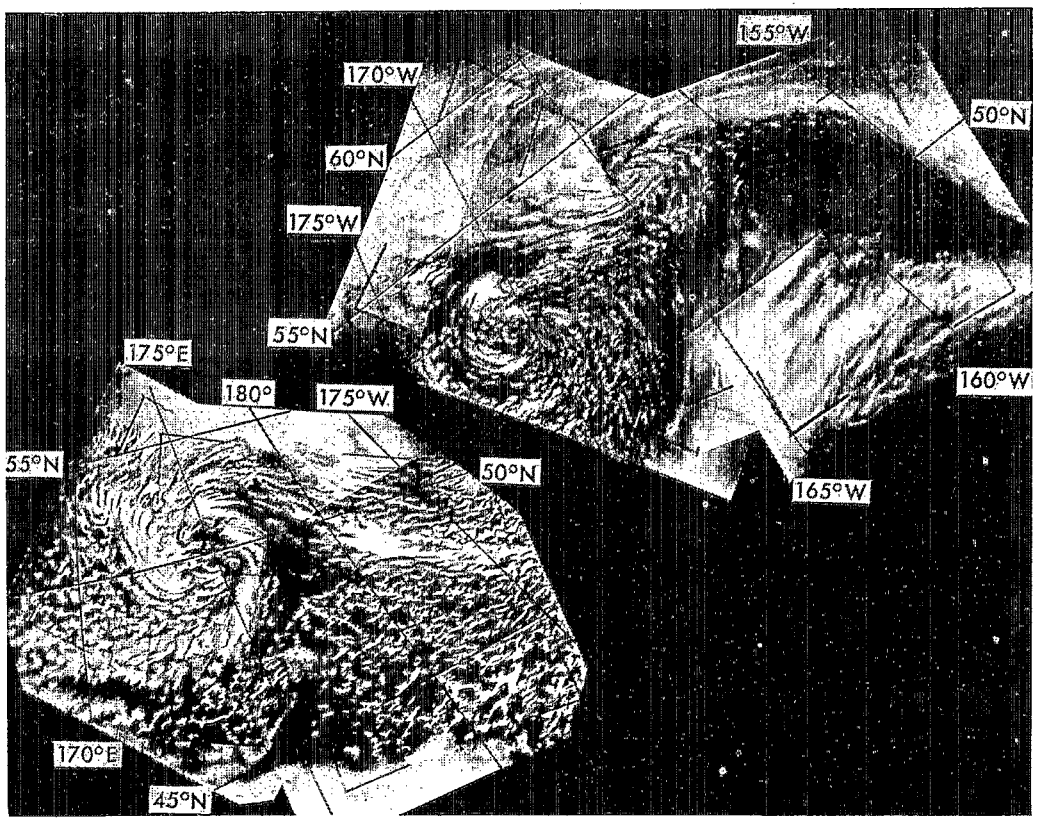

PHOTOGRAPH 4.48. Pictures from TIROS VII at 0157 hr (top) and 0020 hr (bottom) on 30 January 1964

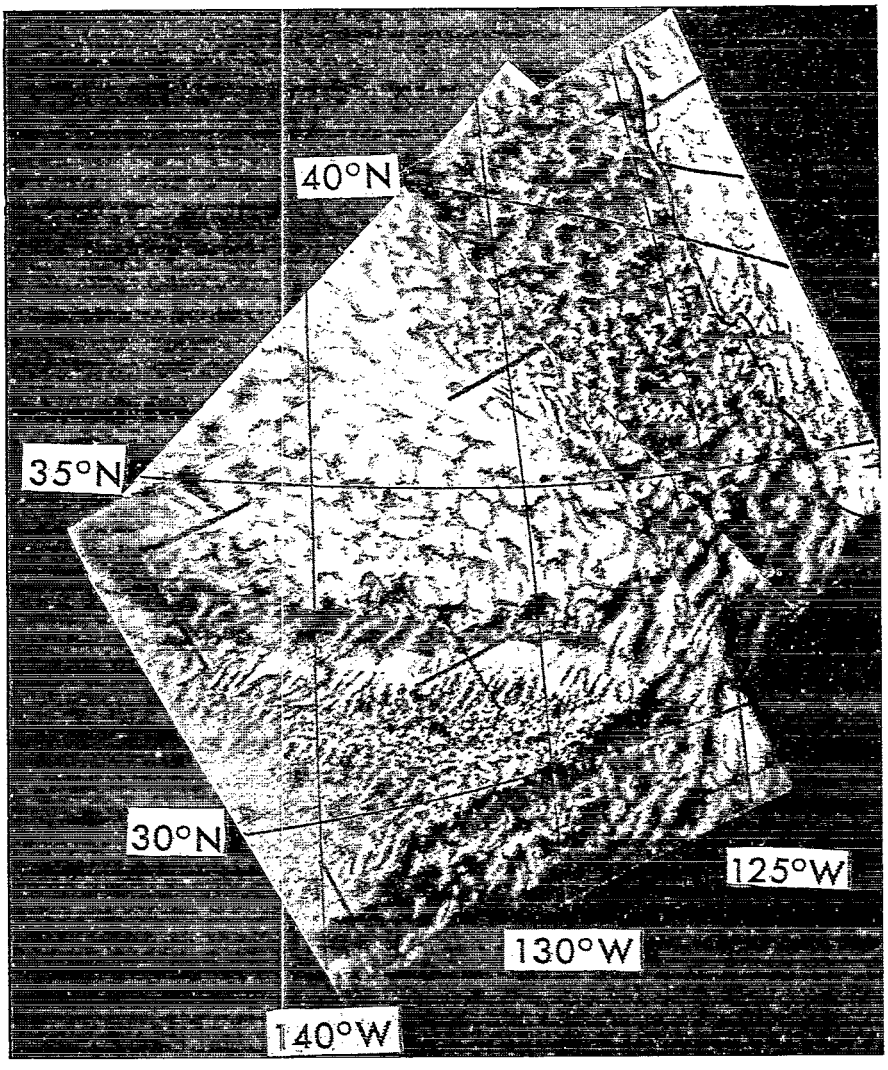

PHOTOGRAPH 4.49. Picture from TIROS V at 2103 hr on 19 April 1963

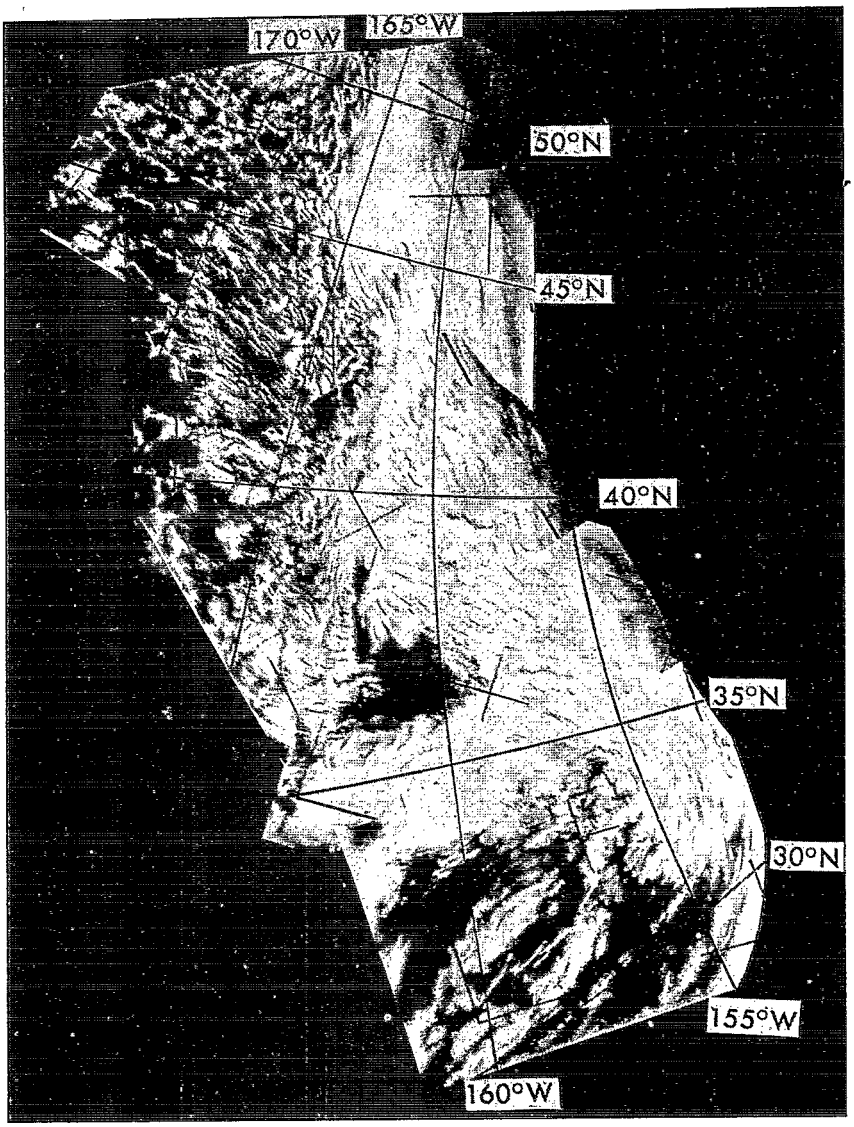

PHOTOGRAPH 4.50. Picture from TIROS VII at 0136 hr on 29 January 1964

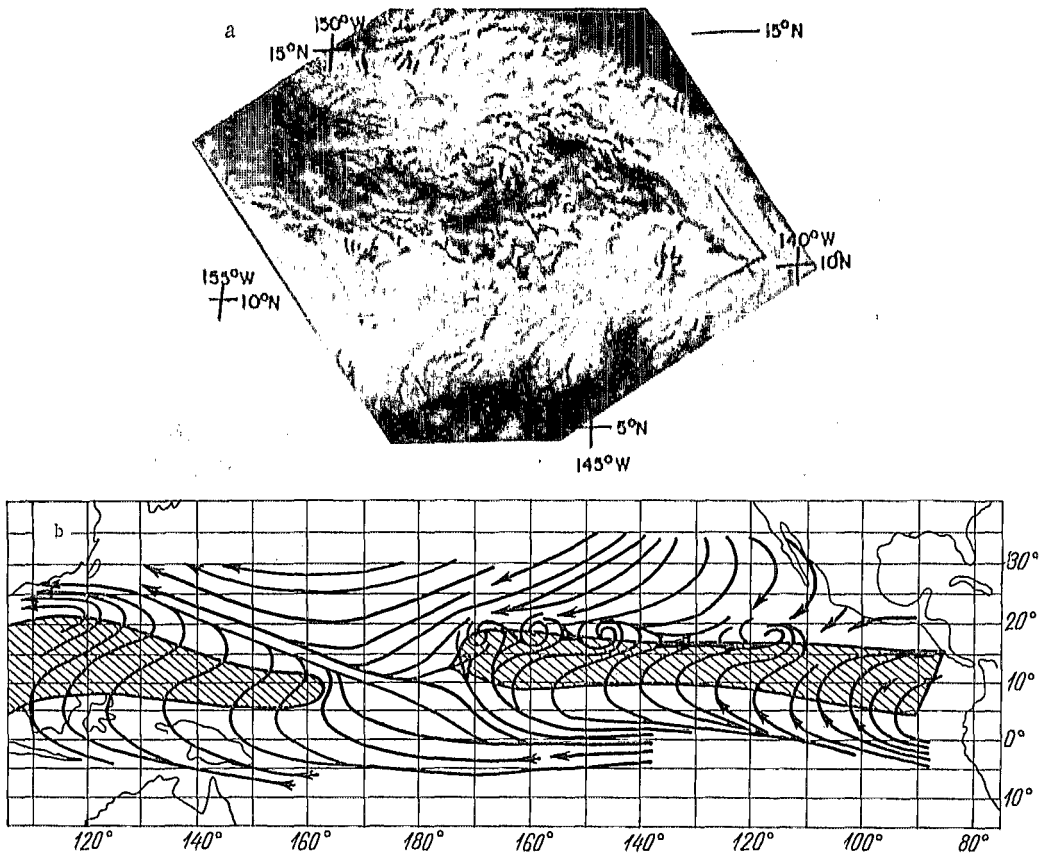

PHOTOGRAPH 4.51. Cloud distribution in the tropical zone and its connection with the monsoon trough:

a — satellite cloud picture showing the principal and secondary cloud bands; b — analysis of flow lines near the Earth surface on 18 August 1961 (dark spots show regions over which cloud bands are located).

PHOTOGRAPH 4.52. Convective cloud towers in the initial stage of development of a tropical cyclone

PHOTOGRAPH 4.53. Early stage of tropical-cyclone development on 15 August 1962

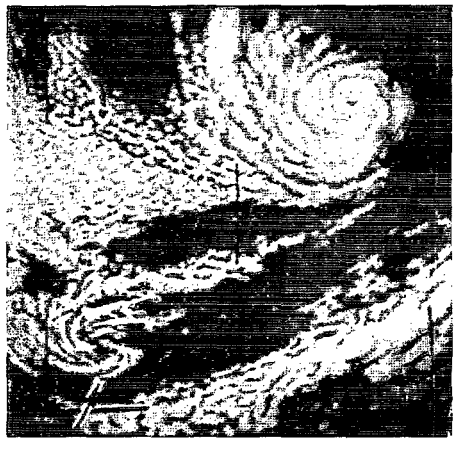

PHOTOGRAPH 4.54. Picture of tropical cyclone with secondary vortex

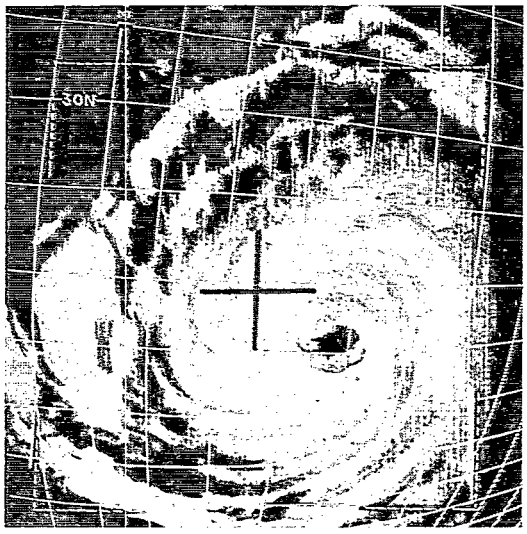

PHOTOGRAPH 4.55. Picture of typhoon on 18 August 1962 (center at 31°N, 141°E). The center of the photograph shows the position of the storm eye

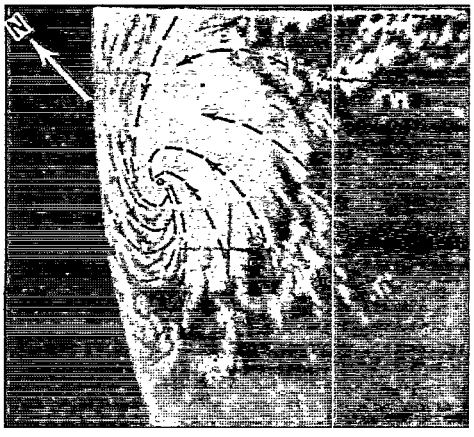

PHOTOGRAPH 4.56. Determination of typhoon center according to the convergence of cirrus spiral cloud bands

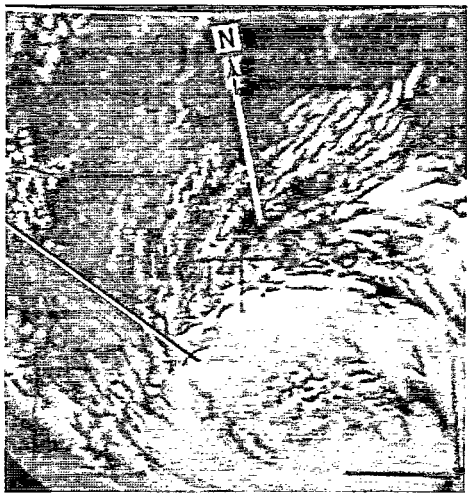

PHOTOGRAPH 4.57. Tropical cyclone Wanda on 29 August 1962 (17°N, 127°E). The arrow indicates the shift.

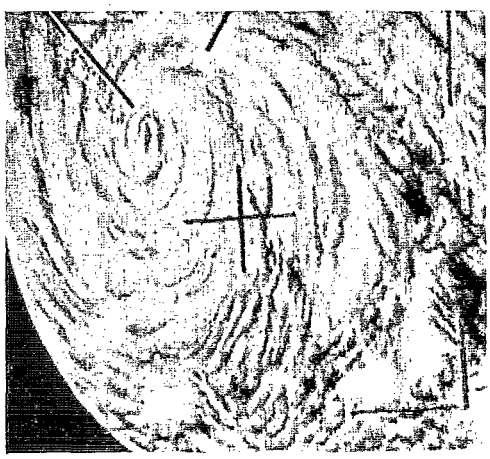

PHOTOGRAPH 4.58. Cyclone Wanda on 30 August 1962 (20°N, 123.6°E). The arrow indicates the shift

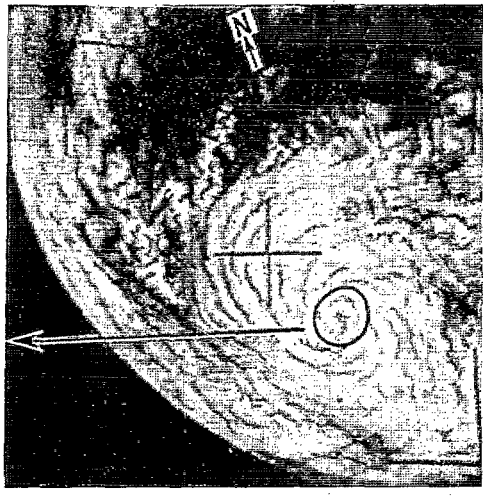

PHOTOGRAPH 4.59. Typhoon Amy on 3 September 1962 (20.5°N, 125.5°E). The bright circle shows the zone of strong winds; the arrow shows the direction of wind displacement

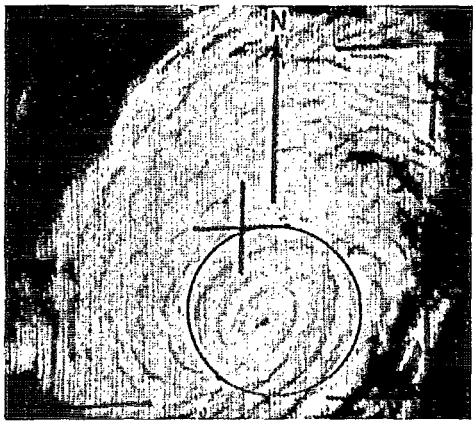

PHOTOGRAPH 4.60. Typhoon Jean on 8 November 1962 (14.5°N, 114.5°E). Bright circle in the region of the eye delineated by a dark rim indicates a zone of strong winds

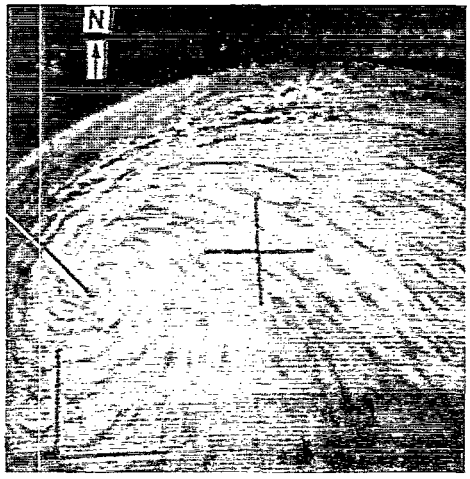

PHOTOGRAPH 4.61. Asymmetric location of cloud cover in typhoon Opal on 4 August 1962. Arrow shows direction of wind displacement

PHOTOGRAPH 4.62. Cloud picture of cyclone Daisy on 5 October 1962. Cirrus cloud bands show the direction of flow lines

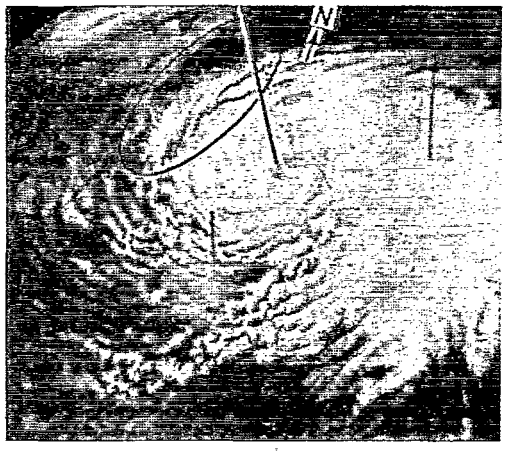

PHOTOGRAPH 4.63. Squall lines of typhoon Daisy on 4 October 1962. Arrow shows the flow direction

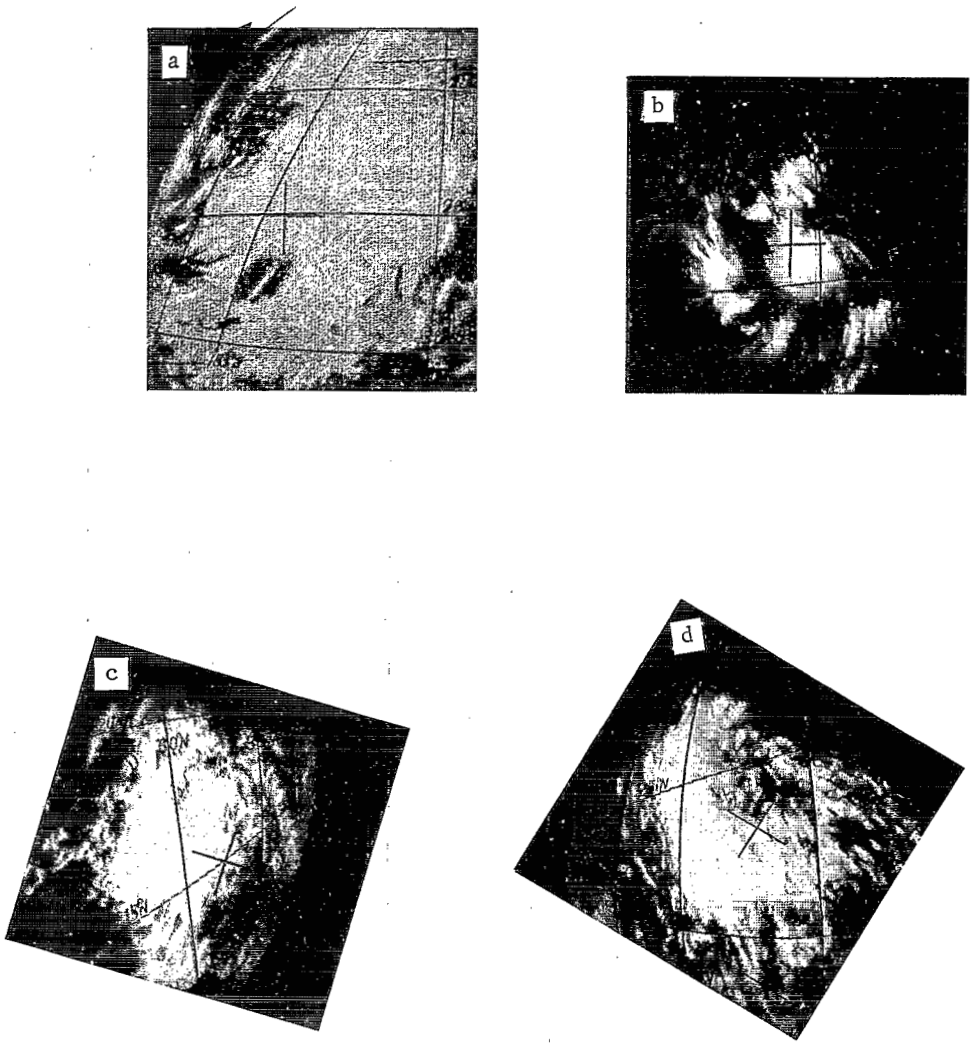

PHOTOGRAPH 4.64. Pictures of tropical cyclones at various development stages. For details see Appendix 1

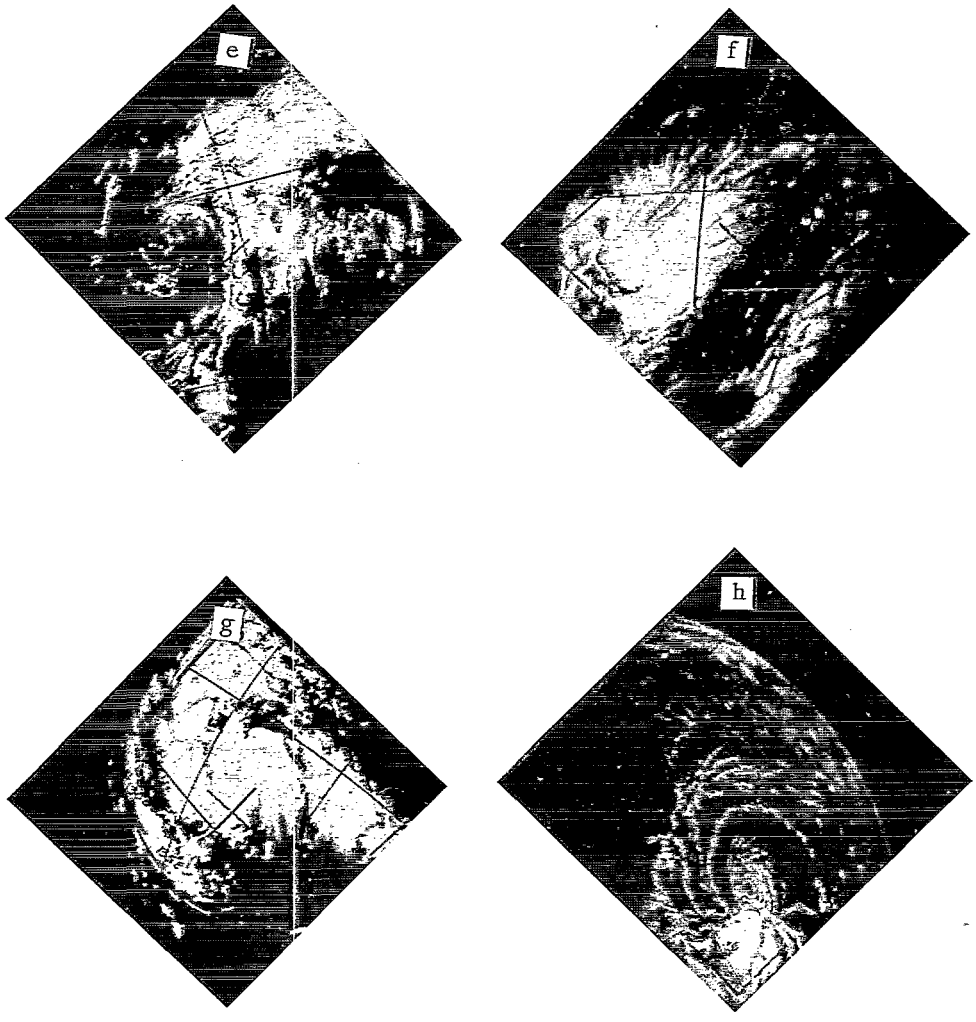
e
f
g
h

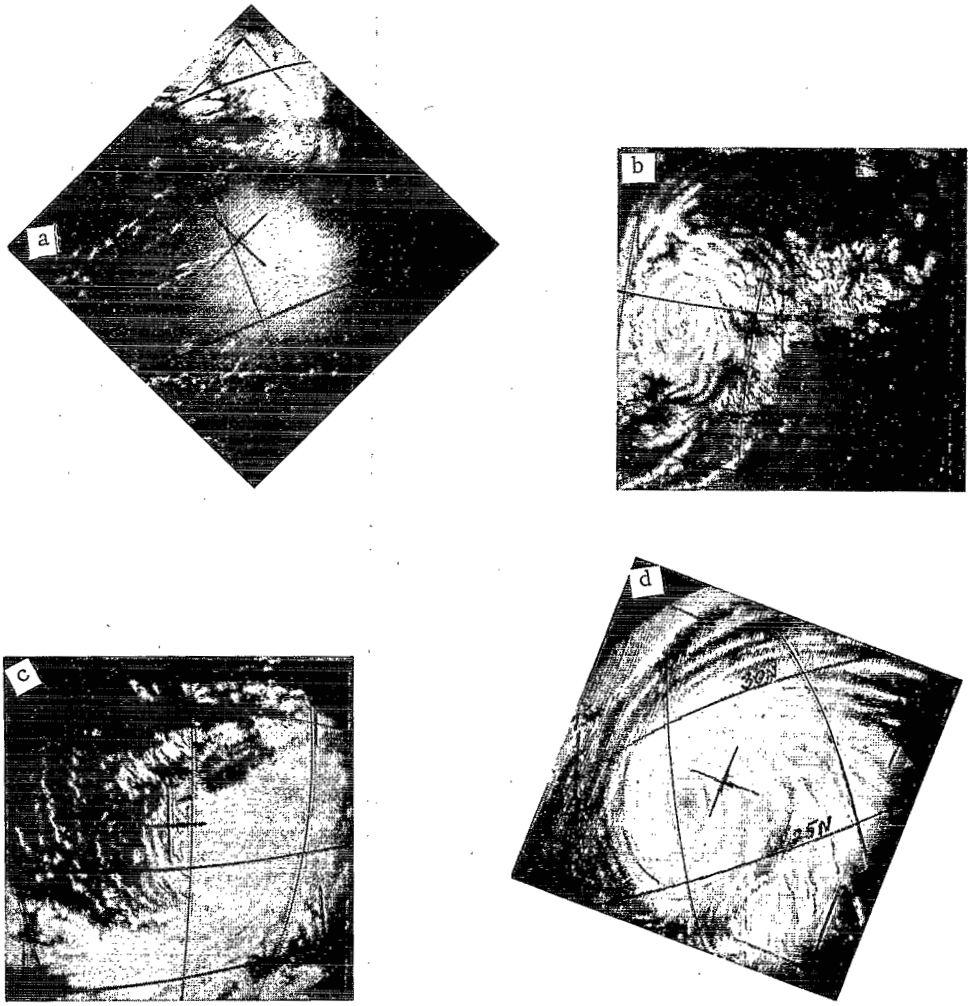

PHOTOGRAPH 4.65. (a–h). Pictures of tropical cyclones with varying diameter of cloud cover. For details see

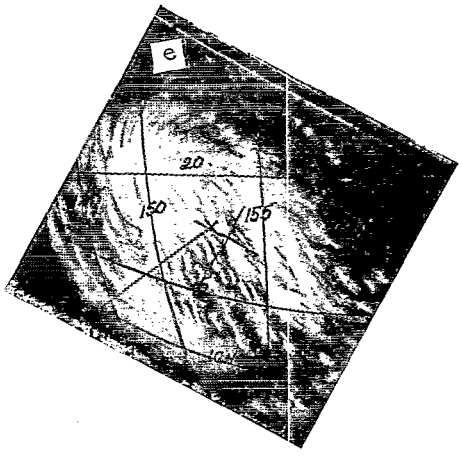

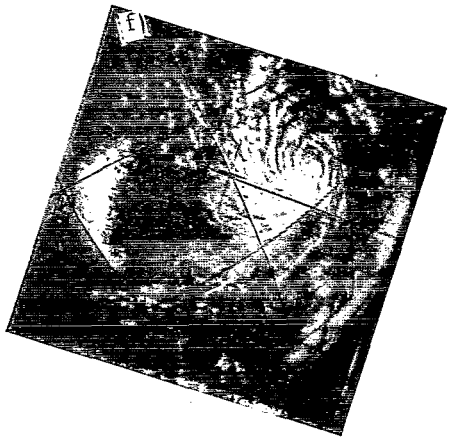

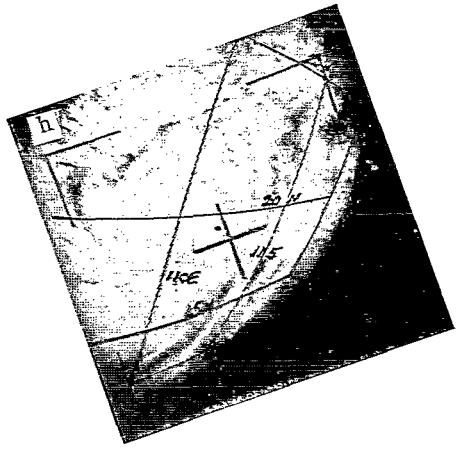

Appendix 1

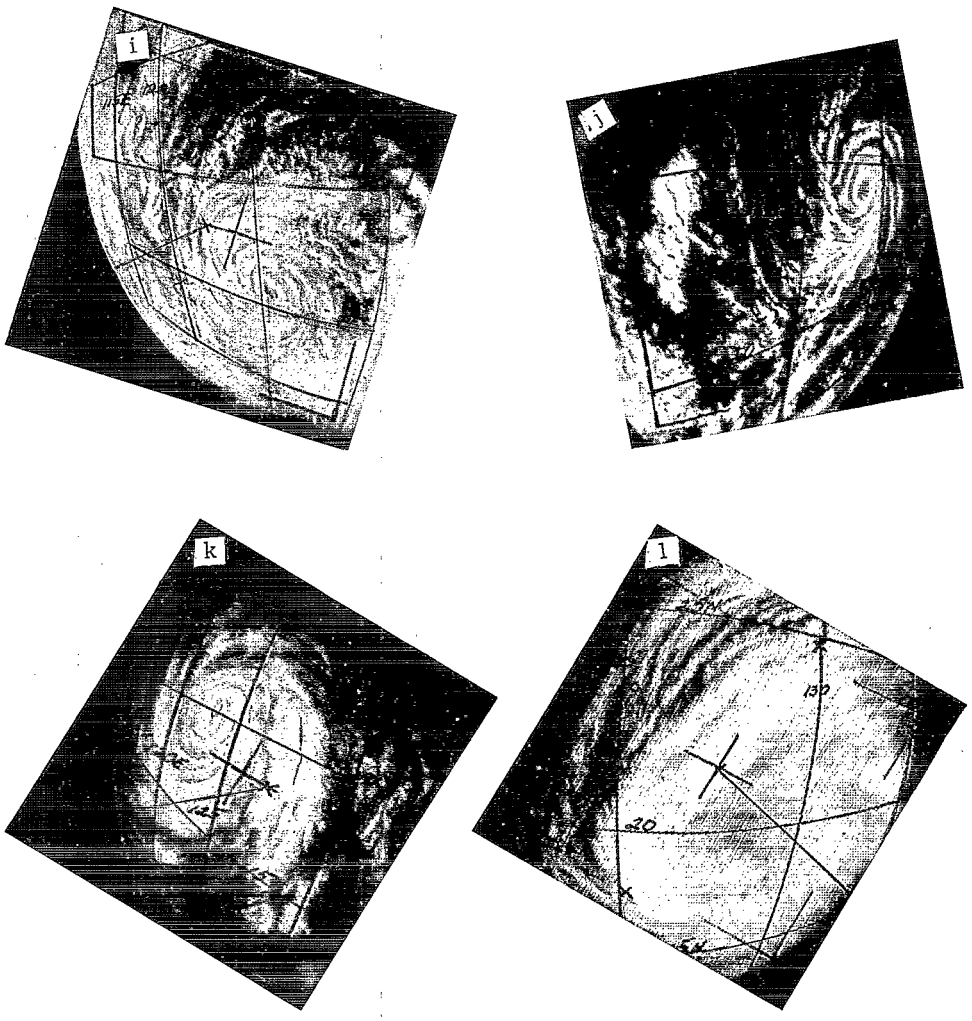

PHOTOGRAPH 4.65 (i–l). Pictures of tropical cyclones with varying diameter of cloud cover. For details see Appendix 1

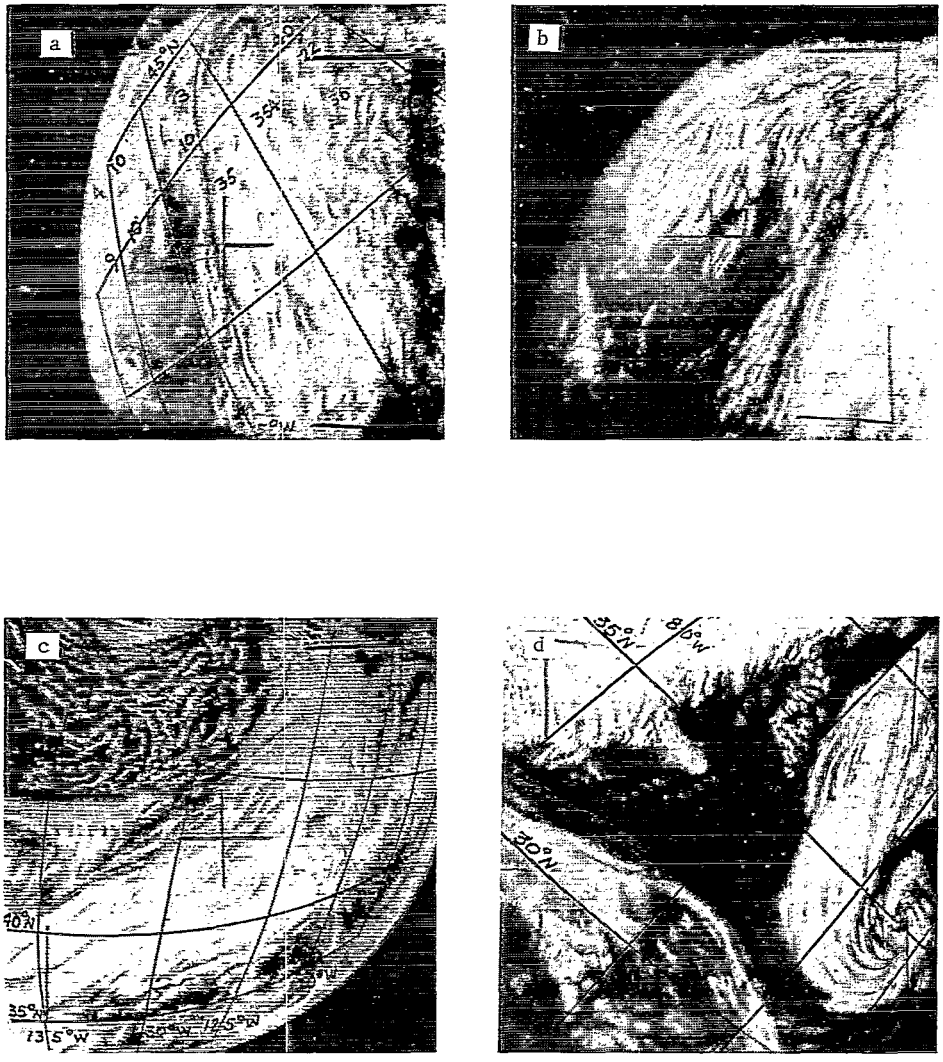

PHOTOGRAPH 4.66. Pictures from TIROS V:

a — 1312 hr, 4 October 1962; b — 1311 hr, 4 October 1962; c — 2220 hr, 1 December 1962; d — 1830 hr, 5 December 1962.

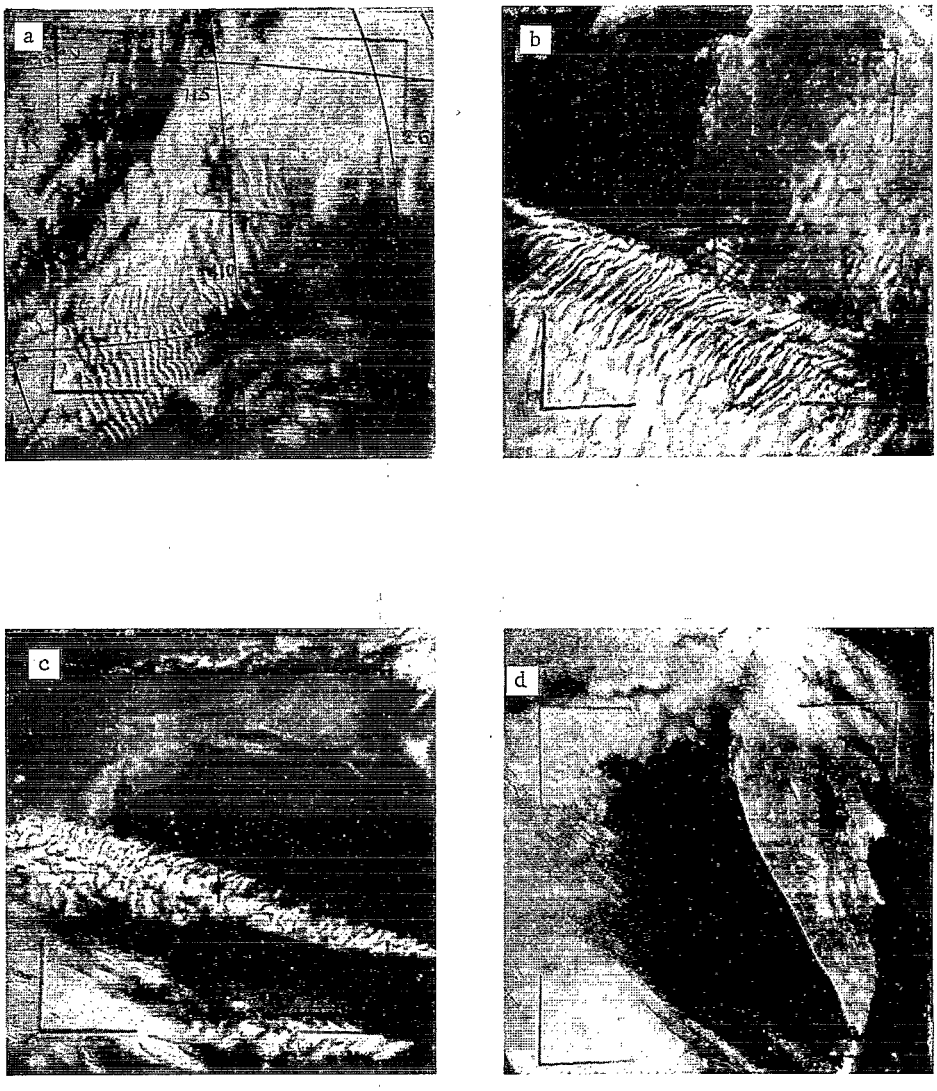

PHOTOGRAPH 4.67. Pictures from TIROS VI (a) and TIROS VII (b, c, d):

a — 1705 hr, 15 November 1962; b — 1920 hr, 7 January 1964; c — 1740 hr, 23 June 1963; d — 0404 hr, 10 April 1964.

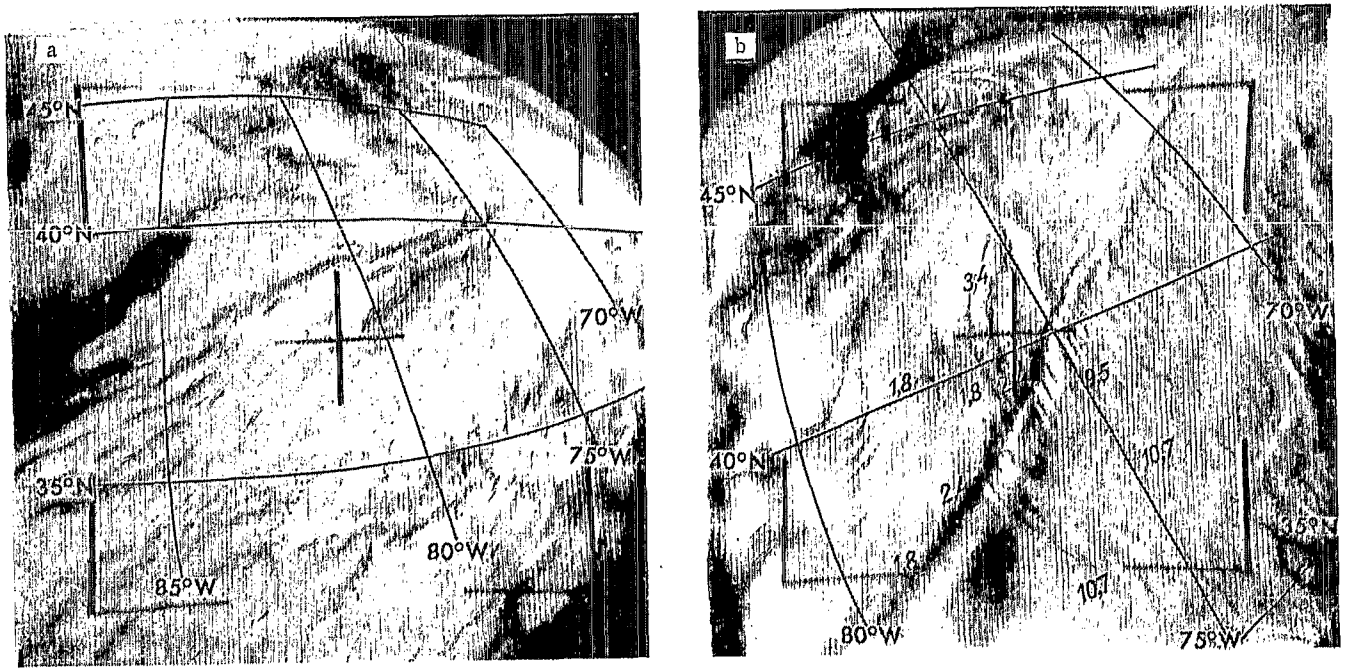

PHOTOGRAPH 4.68. Pictures from TIROS VI (a) and TIROS V (b) showing the heights (in km) of the top cloud boundary according to airborne data: a — 1358 hr, 20 November 1962; b — 1447 hr, 20 November 1962.

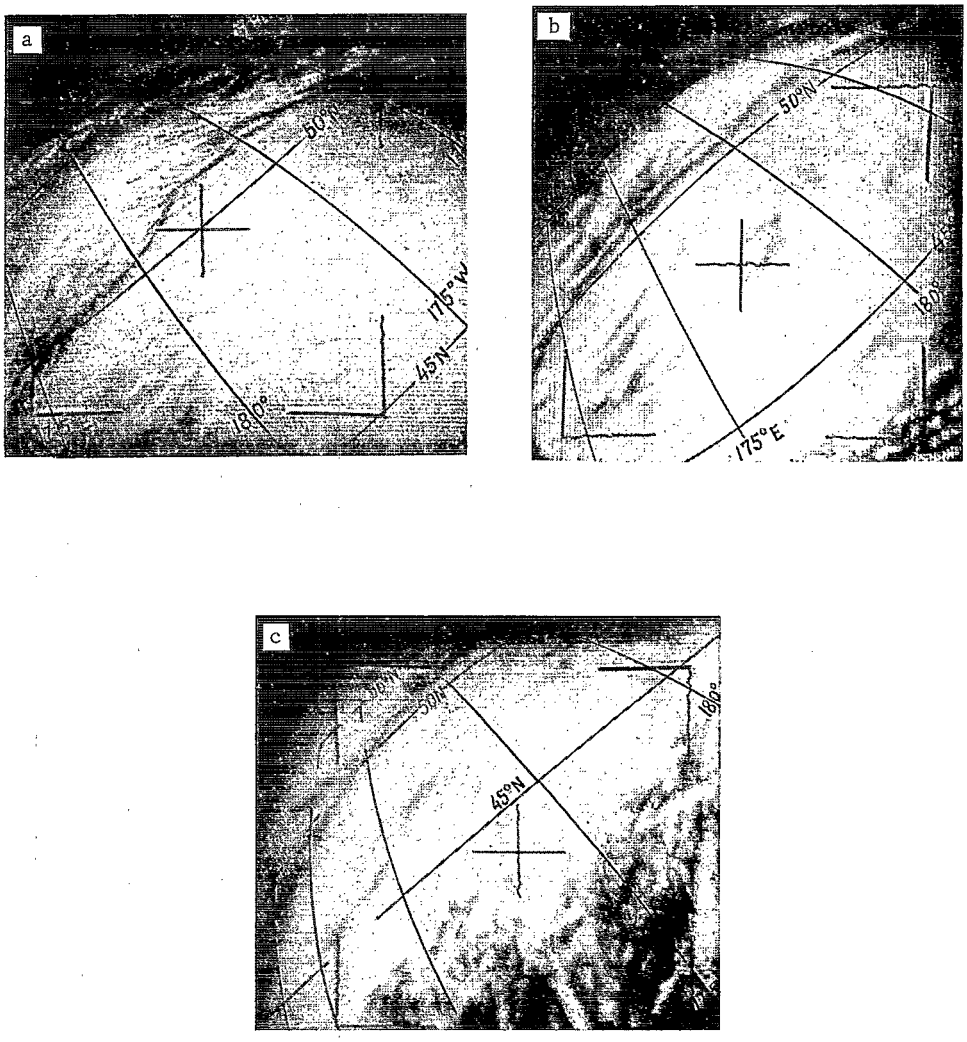

PHOTOGRAPH 4.69. Pictures from TIROS VII (frames 1, 3, and 5) at 2330 hr, 14 January 1962

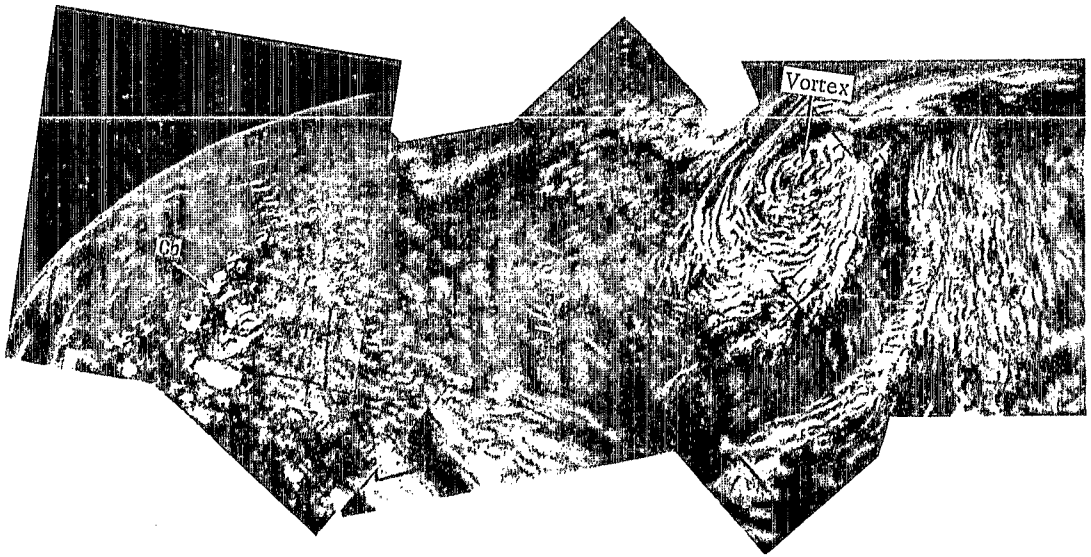

PHOTOGRAPH 4.70. Picture mosaic of cloud cover according to TIROS V data at 1250 hr, 7 September 1962. The picture show a well-developed cyclone, cloud-free regions, lines of cumulonimbus clouds and zones of fog.

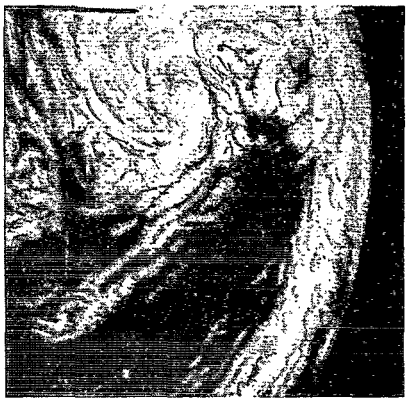

PHOTOGRAPH 4.71. Cloud pictures from TIROS V at 1925 hr, 19 April 1963

National Aeronautics and Space Administration
WASHINGTON, D. C. 20546

POSTAGE AND FEES PAID
NATIONAL AERONAUTICS AND
SPACE ADMINISTRATION

OFFICIAL BUSINESS

050 001 45 51 3DS 70272 00903
AIR FORCE WEAPONS LABORATORY /WLOL/
KIRTLAND AFB, NEW MEXICO 87117

ATT E. LOU BOWMAN, CHIEF,TECH. LIBRARY

NASA TT F-511
TT 68-50310

Printed in Jerusalem, Israel

[5143]